

LEVEL

12

ADA10444

NSWC TR 80-238

COMPUTATIONAL AND EXPERIMENTAL
DETERMINATION OF FRAGMENTATION
FOR NATURALLY FRAGMENTING WARHEADS

by
WILLIS MOCK, JR.
WILLIAM H. HOLT
Weapons Systems Department

DTIC
ELE
FEB 3 1982
H

MAY 1981

Approved for public release, distribution unlimited

BEST
AVAILABLE COPY

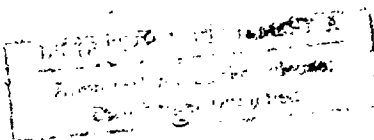


NAVAL SURFACE WEAPONS CENTER

Danlrgen, Virginia 22448

Silver Spring, Maryland 20910

DTIC FILE COPY



82 02 02 128

UNCLASSIFIED

SECURITY CLASSIFICATION OF THIS PAGE (When Data Entered)

REPORT DOCUMENTATION PAGE		READ INSTRUCTIONS BEFORE COMPLETING FORM
1 REPORT NUMBER NSWC TR 80-238	2 GOVT ACCESSION NO. AP-110 4441	3 RECIPIENT'S CATALOG NUMBER
4 TITLE (and Subtitle) COMPUTATIONAL AND EXPERIMENTAL DETERMINATION OF FRAGMENTATION FOR NATURALLY FRAGMENTING WARHEADS		5 TYPE OF REPORT & PERIOD COVERED Final
7 AUTHOR(s) Willis Mock, Jr. William H. Holt		6 PERFORMING ORG. REPORT NUMBER
9 PERFORMING ORGANIZATION NAME AND ADDRESS Naval Surface Weapons Center (G35) Dahlgren, VA 22448		8. CONTRACT OR GRANT NUMBER(s) 11
11 CONTROLLING OFFICE NAME AND ADDRESS Naval Sea Systems Command Washington, DC 20362		10 PROGRAM ELEMENT, PROJECT, TASK AREA & WORK UNIT NUMBERS 62332N/F32392 SF-32-392-391
14 MONITORING AGENCY NAME & ADDRESS (if different from Controlling Office)		12 REPORT DATE May 1981
		13 NUMBER OF PAGES 453
		15. SECURITY CLASS. (of this report) UNCLASSIFIED
		15a. DECLASSIFICATION/DOWNGRADING SCHEDULE
16 DISTRIBUTION STATEMENT (of this Report) Approved for public release; distribution unlimited.		
17 DISTRIBUTION STATEMENT (of the abstract entered in Block 20, if different from Report)		
18 SUPPLEMENTARY NOTES		
19 KEY WORDS (Continue on reverse side if necessary and identify by block number) shock waves spall brittle fracture gas gun HF-1 steel Hugoniot equation fracture Armco iron computational modeling fragmentation shear fracture		
20 ABSTRACT (Continue on reverse side if necessary and identify by block number) A computational and experimental investigation of the fragmentation response of Armco iron and HF-1 steel explosively filled cylinders and an HF-1 steel projectile is presented. SRI International Lagrangian finite-difference stress wave propagation codes that contain brittle fracture and shear banding models were used for the computational simulations. Gas gun Hugoniot and soft-recovery experiments were performed for HF-1 steel to determine input parameters for the brittle fracture model. Cylinder and projectile fragment mass distributions were experimentally (see back)		

DD FORM 1473
1 JAN 73EDITION OF 1 NOV 65 IS OBSOLETE
S/N 0102-LF-014-6601

UNCLASSIFIED

SECURITY CLASSIFICATION OF THIS PAGE (When Data Entered)

UNCLASSIFIED

SECURITY CLASSIFICATION OF THIS PAGE (When Data Entered)

ABSTRACT (Continued)
(20)

determined for comparison with the simulations. Cylinder computations and experiments were performed for two heat treatments of HF-1 steel to investigate microstructural changes on the fragmentation behavior. Computed stress, particle velocity, and crack concentration histories are presented for an HF-1 steel cylinder. A scheme was devised for characterizing the recovered fragments from the cylinder and projectile experiments with respect to their fracture surfaces.

UNCLASSIFIED

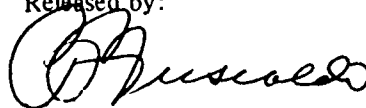
SECURITY CLASSIFICATION OF THIS PAGE (When Data Entered)

FOREWORD

A computational and experimental investigation of the fragmentation response of naturally fragmenting munitions is presented. This work is in support of an effort to develop a computational design tool for ordnance applications. Funding for this work was provided by NAVSEA Task No. SF-32-392-391.

This report was reviewed and approved by C. A. Cooper, Head, Gun Systems and Munitions Division.

Released by:



CAPT R. P. FUSCALDO

Assistant for Weapons Systems

Weapons Systems Department

Accession For	
NTIS GRA&I	<input checked="checked" type="checkbox"/>
DTIC TAB	<input type="checkbox"/>
Unannounced	<input type="checkbox"/>
Justification	
By _____	
Distribution/	
Availability Codes	
Dist _____	
A	



ACKNOWLEDGEMENTS

The authors would like to acknowledge C. R. Crowe for helping plan and perform some of the experiments reported herein. They would like to acknowledge L. Seaman of SRI International for providing the latest versions of the FUFF and TROTT computer programs and for many helpful discussions concerning their use. They would also like to thank O. H. Griffin* for assistance with the implementation and use of these programs.

*Presently with Bendix Advanced Technology Center, Columbus, MD 21045

TABLE OF CONTENTS

	Page
FOREWORD.....	iii
ACKNOWLEDGEMENTS.....	v
LIST OF ILLUSTRATIONS.....	ix
LIST OF TABLES.....	ix
I. INTRODUCTION.....	1
II. MATERIALS	2
III. MECHANICAL AND ACOUSTICAL EXPERIMENTS.....	4
IV. HUGONIOT EQUATION OF STATE EXPERIMENTS	11
V. DYNAMIC FRACTURE EXPERIMENTS.....	17
VI. COMPUTATION OF DYNAMIC FRACTURE PARAMETERS	32
VII. ARMCO IRON FRAMING CAMERA EXPERIMENT	42
VIII. EXPERIMENTAL DETERMINATION OF FRAGMENT MASS DISTRIBUTIONS.....	46
IX. COMPUTATION OF FRAGMENT MASS DISTRIBUTIONS.....	69
X. SUMMARY AND RECOMMENDATIONS	79
REFERENCES	80
APPENDIXES	
A- TRANSVERSE TENSILE MEASUREMENTS FOR HF-1 STEEL	A-1
B- OSCILLOSCOPE RECORDS FOR HF-1 STEEL HUGONIOT EXPERIMENTS.....	B-1
C- EXPRESSIONS FOR TRANSFORMING THE HUGONIOT EQUATION OF STATE FROM A LINEAR SHOCK VELOCITY-PARTICLE VELOCITY RELATIONSHIP INTO A STRESS-COMPRESSION RELATIONSHIP	C-1

TABLE OF CONTENTS (Continued)

	Page
D PHOTOGRAPHS OF THE SPALL FRACTURE SPECIMENS OF HF-1 STEEL	D-1
E CRACK DISTRIBUTIONS FOR SPALL FRACTURE SPECIMENS OF HF-1 STEEL . . .	E-1
F DIGITIZED CRACK COORDINATES FOR THE SPALL FRACTURE SPECIMENS OF HF-1 STEEL	F-1
G - COMPUTER LISTINGS OF THE INPUT PARAMETERS USED IN THE PUFF COMPUTATIONS FOR THE HF-1 STEEL SPALL FRACTURE EXPERIMENTS.	G-1
H COMPUTED STRESS, PARTICLE VELOCITY, AND CRACK CONCENTRATION VERSUS TIME PLOTS FOR THE CELL OF MAXIMUM DAMAGE FOR THE HF-1 STEEL SPALL FRACTURE SPECIMENS.	H-1
I COMPUTED STRESS, PARTICLE VELOCITY, AND CRACK CONCENTRATION VERSUS TIME PLOTS FOR EACH COMPUTATIONAL CELL FOR THE HF-1 STEEL, HEAT TREATMENT B, SPALL FRACTURE SHOT 144	I-1
J COMPUTATION OF DYNAMIC FRACTURE PARAMETERS FOR HEAT TREATMENT A OF HF-1 STEEL WITH STRINGER CRACKS EXCLUDED	J-1
K - FRAMING CAMERA PHOTOGRAPHS FOR EXPLOSIVE-FILLED ARMCO IRON CYLINDER EXPERIMENT	K-1
L PHOTOGRAPHS OF FRAGMENT TYPES FROM ARMCO IRON AND HF-1 STEEL CYLINDER FRAGMENT RECOVERY EXPERIMENTS.	L-1
M RESULTS OF THE ARMCO IRON CYLINDER, THE HF-1 STEEL CYLINDER, AND THE HF-1 STEEL PROJECTILE FRAGMENT RECOVERY EXPERIMENTS . . .	M-1
N - COMPUTER LISTINGS FOR THE ARMCO IRON AND HF-1 STEEL CYLINDRICAL PUFF AND TROTT COMPUTATIONS	N-1
O SUMMARY OF THE COMPUTATIONAL CRACK DISTRIBUTION RESULTS AND THE CALCULATED FRAGMENT MASS DISTRIBUTION RESULTS FOR THE ARMCO IRON AND HF-1 STEEL CYLINDER EXPERIMENTS AND THE HF-1 STEEL PROJECTILE EXPERIMENT	O-1
P COMPUTED STRESS, PARTICLE VELOCITY, AND CRACK CONCENTRATION VERSUS TIME PLOTS FOR EACH COMPUTATIONAL CELL FOR THE HF-1 STEEL, HEAT TREATMENT B, CYLINDER EXPERIMENTTS	P-1
DISTRIBUTION	

LIST OF ILLUSTRATIONS

Figure		Page
1	Microstructure of Armco iron	3
2	Microstructure of HF-1 steel with heat treatment A	5
3	Microstructure of HF-1 steel with heat treatment B	5
4	True stress-true strain and engineering stress-strain curves for longitudinal tensile specimens of Armco iron.	6
5	True stress-true strain and engineering stress-strain curves for longitudinal tensile specimens of HF-1 steel with heat treatment A.	6
6	Engineering stress-strain curves for transverse tensile specimens of HF-1 steel with heat treatments A and B.	8
7	Macrophotographs of the fracture surfaces for the transverse tensile specimens of HF-1 steel	8
8	Longitudinal and shear echo pulses for HF-1 steel specimens with heat treatment A	10
9	Schematic of muzzle region of gas gun for a shock transit-time experiment	12
10	Shock velocity-particle velocity relationship for HF-1 steel.	14
11	Stress-particle velocity relationship for HF-1 steel.	15
12	Stress-compression and pressure-compression relationships for HF-1 steel	16
13	Schematic of muzzle region of gas gun for a spall fracture experiment	18
14	Simplified schematic of the spall fracture process	18
15	Schematic of soft recovery technique	19
16	Schematic of sectioned specimen to reveal fracture damage	20
17	Effect of increasing impactor velocity on fracture damage for 6.35-mm-thick HF-1 steel specimens with heat treatment A.	22
18	Effect of increasing impactor velocity on fracture damage for 6.35-mm-thick HF-1 steel specimens with heat treatment B.	23
19	SEM micrographs of the fracture surface for the full-spalled HF-1 steel, heat treatment A, specimen in Shot 88	27
20	Micrographs of cracks for the HF-1 steel, heat treatment A, specimen in Shot 110	28
21	Micrographs of cracks for the HF-1 steel, heat treatment A, specimen in Shot 90	29
22	Micrographs of cracks for the HF-1 steel, heat treatment B, specimen in Shot 144	30
23	Micrographs of cracks for the HF-1 steel, heat treatment B, specimen in Shot 142	31
24	Experimental and computed nucleation rate and growth curves for HF-1 steel with heat treatment A	37
25	Experimental and computed nucleation rate and growth curves for HF-1 steel with heat treatment B	38

LIST OF ILLUSTRATIONS (Continued)

Figure		Page
26	Computed stress-time profiles for selected computational cells for the HF-1 steel, heat treatment B, specimen in Shot 144.	41
27	Computed crack concentration-time profiles for those computational cells in which tensile fracture occurred for the HF-1 steel, heat treatment B, specimen in Shot 144.	41
28	Framing camera photograph of Armco iron cylinder prior to detonation of the composition B explosive.	43
29	Armco iron cylinder outer radius versus time plot.	43
30	Armco iron cylinder outer surface at various times after explosive detonation. .	45
31	Evolution of Armco iron cylinder surface cracks as a function of time.	47
32	Schematic of explosive-filled cylinder experiment.	49
33	Explosive-filled HF-1 steel cylinder with heat treatment B for experiment 5. .	50
34	Photographs of HF-1 steel projectile with heat treatment A.	51
35	Schematic examples of fragment types from the Armco iron and HF-1 steel cylinder experiments.	53
36	Schematic through cylinder or projectile wall showing the possible formation of fragment types from the intersections of brittle and shear fracture surfaces.	54
37	Fragment mass distributions (versus the square root of the fragment mass) for the cylinder and projectile experiments.	55
38	Fragment mass distributions (versus the fragment mass) for the cylinder and projectile experiments.	56
39	Fragment mass distributions for the Armco iron cylinder experiments.	60
40	Fragment mass distributions for the HF-1 steel, heat treatment A, cylinder experiments.	61
41	Fragment mass distributions for the HF-1 steel, heat treatment B, cylinder experiments.	62
42	Fragment mass distributions for the HF-1 steel, heat treatment A, projectile experiment.	63
43	Photographs of the reconstructed nose for the projectile experiment.	66
44	Comparison of fragment mass distributions for the HF-1 steel, heat treatment A, cylinder experiments and the projectile experiment excluding 41 large nose fragments.	66
45	Brittle fracture crack distributions for the Armco iron and HF-1 steel cylinder PUFF computations and for the HF-1 steel projectile TROTT computation using the BFRAC2 subroutine.	71
46	Brittle and shear fracture crack distributions for the HF-1 steel cylinder PUFF computations using the BFRAC2 and SHEAR2 subroutines.	72

LIST OF ILLUSTRATIONS (Continued)

Figure		Page
47	Comparison of measured and calculated fragment mass distributions for the Armco iron cylinder.	74
48	Comparison of measured and calculated fragment mass distributions for the HF-1 steel cylinders with heat treatments A and B.	75
49	Comparison of measured and calculated fragment mass distributions for the HF-1 steel cylinders with heat treatment A.	76
50	TROTT simulation of the exploding HF-1 steel projectile at selected times	78
51	Framing camera photograph of AISI 3140 steel projectile approximately 78 μ s after explosive detonation.	79
B-1	Oscilloscope records for Shot 117.	B-3
B-2	Oscilloscope records for Shot 118.	B-4
B-3	Oscilloscope record for Shot 120	B-5
B-4	Oscilloscope records for Shot 152.	B-6
B-5	Oscilloscope records for Shot 153.	B-7
D-1	Sectioned HF-1 steel specimens with heat treatment A for Shots 95, 110, and 98	D-3
D-2	Sectioned HF-1 steel specimens with heat treatment A for Shots 92, 91, and 90	D-4
D-3	Sectioned HF-1 steel specimens with heat treatment A for Shots 94, 89, and 113	D-5
D-4	Sectioned HF-1 steel specimens with heat treatment A for Shots 88, 111, and 112.	D-6
D-5	Sectioned HF-1 steel specimens with heat treatment B for Shots 154, 145, and 144	D-7
D-6	Sectioned HF-1 steel specimens with heat treatment B for Shots 143, 142, and 150	D-8
D-7	Sectioned HF-1 steel specimens with heat treatment B for Shots 148, 149, and 142	D-9
D-8	Sectioned HF-1 steel specimens with heat treatment B for Shots 146 and 151 . .	D-10
E-1	Crack distributions for Shot 95.	E-3
E-2	Crack distributions for Shot 110.	E-6
E-3	Crack distributions for Shot 98.	E-9
E-4	Crack distributions for Shot 92.	E-12
E-5	Crack distributions for Shot 91.	E-15
E-6	Crack distributions for Shot 90.	E-18
E-7	Crack distributions for Shot 94.	E-21
E-8	Crack distributions for Shot 113.	E-24
E-9	Crack distributions for Shot 88.	E-27
E-10	Crack distributions for Shot 111.	E-30
E-11	Crack distributions for Shot 112.	E-33

LIST OF ILLUSTRATIONS (Continued)

Figure		Page
E-12	Crack distributions for Shot 154.....	E-36
E-13	Crack distributions for Shot 145.....	E-39
E-14	Crack distributions for Shot 144.....	E-42
E-15	Crack distributions for Shot 143.....	E-45
E-16	Crack distributions for Shot 142.....	E-48
E-17	Crack distributions for Shot 150.....	E-51
E-18	Crack distributions for Shot 148.....	E-54
E-19	Crack distributions for Shot 149.....	E-57
E-20	Crack distributions for Shot 146.....	E-60
E-21	Crack distributions for Shot 151.....	E-63
F-1	Listing of digitized crack coordinates for the spall fracture specimens of HF-1 steel.....	F-3
G-1	PUFF input parameters for Shots 110 and 98.....	G-3
G-2	PUFF input parameters for Shots 92 and 91.....	G-4
G-3	PUFF input parameters for Shots 90 and 94.....	G-5
G-4	PUFF input parameters for Shots 113 and 111.....	G-6
G-5	PUFF input parameters for Shots 112 and 154.....	G-7
G-6	PUFF input parameters for Shots 145 and 144.....	G-8
G-7	PUFF input parameters for Shots 143 and 142.....	G-9
G-8	PUFF input parameters for Shots 150 and 148.....	G-10
G-9	PUFF input parameters for Shots 149 and 146.....	G-11
G-10	PUFF input parameters for Shot 151.....	G-12
H-1	Computed shock histories in cell 23 for Shot 110.....	H-3
H-2	Computed shock histories in cell 23 for Shot 98.....	H-4
H-3	Computed shock histories in cell 23 for Shot 92.....	H-5
H-4	Computed shock histories in cell 23 for Shot 91.....	H-6
H-5	Computed shock histories in cell 23 for Shot 90.....	H-7
H-6	Computed shock histories in cell 23 for Shot 94.....	H-8
H-7	Computed shock histories in cell 20 for Shot 113.....	H-9
H-8	Computed shock histories in cell 24 for Shot 111.....	H-10
H-9	Computed shock histories in cell 23 for Shot 112.....	H-11
H-10	Computed shock histories in cell 22 for Shot 154.....	H-12
H-11	Computed shock histories in cell 22 for Shot 145.....	H-13
H-12	Computed shock histories in cell 23 for Shot 144.....	H-14
H-13	Computed shock histories in cell 23 for Shot 143.....	H-15
H-14	Computed shock histories in cell 23 for Shot 142.....	H-16
H-15	Computed shock histories in cell 25 for Shot 150.....	H-17
H-16	Computed shock histories in cell 21 for Shot 148.....	H-18
H-17	Computed shock histories in cell 20 for Shot 149.....	H-19

LIST OF ILLUSTRATIONS (Continued)

Figure		Page
H-18	Computed shock histories in cell 23 for Shot 146.....	H-20
H-19	Computed shock histories in cell 26 for Shot 151.....	H-21
I-1	Computed stress histories in cell 1 for Shot 144.....	I-3
I-2	Computed stress histories in cell 2 for Shot 144.....	I-3
I-3	Computed stress histories in cell 3 for Shot 144.....	I-4
I-4	Computed stress histories in cell 4 for Shot 144.....	I-4
I-5	Computed stress histories in cell 5 for Shot 144.....	I-5
I-6	Computed stress histories in cell 6 for Shot 144.....	I-5
I-7	Computed stress histories in cell 7 for Shot 144.....	I-6
I-8	Computed stress histories in cell 8 for Shot 144.....	I-6
I-9	Computed stress histories in cell 10 for Shot 144.....	I-7
I-10	Computed stress histories in cell 11 for Shot 144.....	I-7
I-11	Computed stress histories in cell 12 for Shot 144.....	I-8
I-12	Computed stress histories in cell 13 for Shot 144.....	I-8
I-13	Computed stress histories in cell 14 for Shot 144.....	I-9
I-14	Computed stress histories in cell 15 for Shot 144.....	I-9
I-15	Computed stress histories in cell 16 for Shot 144.....	I-10
I-16	Computed stress histories in cell 17 for Shot 144.....	I-10
I-17	Computed stress histories in cell 18 for Shot 144.....	I-11
I-18	Computed stress histories in cell 19 for Shot 144.....	I-11
I-19	Computed stress histories in cell 20 for Shot 144.....	I-12
I-20	Computed stress histories in cell 21 for Shot 144.....	I-12
I-21	Computed stress histories in cell 22 for Shot 144.....	I-13
I-22	Computed stress histories in cell 23 for Shot 144.....	I-13
I-23	Computed stress histories in cell 24 for Shot 144.....	I-14
I-24	Computed stress histories in cell 25 for Shot 144.....	I-14
I-25	Computed stress histories in cell 26 for Shot 144.....	I-15
I-26	Computed stress histories in cell 27 for Shot 144.....	I-15
I-27	Computed stress histories in cell 28 for Shot 144.....	I-16
I-28	Computed stress histories in cell 29 for Shot 144.....	I-16
I-29	Computed particle velocity histories in cells 1 and 2 for Shot 144.....	I-17
I-30	Computed particle velocity histories in cells 3 and 4 for Shot 144.....	I-17
I-31	Computed particle velocity histories in cells 5 and 6 for Shot 144.....	I-18
I-32	Computed particle velocity histories in cells 7 and 8 for Shot 144.....	I-18
I-33	Computed particle velocity histories in cells 10 and 11 for Shot 144.....	I-19
I-34	Computed particle velocity histories in cells 12 and 13 for Shot 144.....	I-19
I-35	Computed particle velocity histories in cells 14 and 15 for Shot 144.....	I-20
I-36	Computed particle velocity histories in cells 16 and 17 for Shot 144.....	I-20
I-37	Computed particle velocity histories in cells 18 and 19 for Shot 144.....	I-21

LIST OF ILLUSTRATIONS (Continued)

Figure		Page
I-38	Computed particle velocity histories in cells 20 and 21 for Shot 144	I-21
I-39	Computed particle velocity histories in cells 22 and 23 for Shot 144	I-22
I-40	Computed particle velocity histories in cells 24 and 25 for Shot 144	I-22
I-41	Computed particle velocity histories in cells 26 and 27 for Shot 144	I-23
I-42	Computed particle velocity histories in cells 28 and 29 for Shot 144	I-23
I-43	Computed crack concentration histories in cells 14 and 15 for Shot 144	I-24
I-44	Computed crack concentration histories in cells 16 and 17 for Shot 144	I-24
I-45	Computed crack concentrations histories in cells 18 and 19 for Shot 144	I-25
I-46	Computed crack concentration histories in cells 20 and 21 for Shot 144	I-25
I-47	Computed crack concentration histories in cells 22 and 23 for Shot 144	I-26
I-48	Computed crack concentration histories in cells 24 and 25 for Shot 144	I-26
I-49	Computed crack concentration histories in cells 26 and 27 for Shot 144	I-27
J-1	Crack distributions for Shot 98 with stringer cracks excluded.	J-3
J-2	Crack distributions for Shot 92 with stringer cracks excluded.	J-6
J-3	Crack distributions for Shot 91 with stringer cracks excluded.	J-9
J-4	Crack distributions for Shot 90 with stringer cracks excluded.	J-12
J-5	Crack distributions for Shot 94 with stringer cracks excluded.	J-15
J-6	Crack distributions for Shot 113 with stringer cracks excluded.	J-18
J-7	Crack distributions for Shot 111 with stringer cracks excluded	J-21
J-8	Experimental and computed nucleation rate and growth curves for HF-1 steel with heat treatment A with stringer cracks excluded	J-24
J-9	PUFF input parameters for Shots 110 and 98 with stringer cracks excluded. ...	J-25
J-10	PUFF input parameters for Shots 92 and 91 with stringer cracks excluded.	J-26
J-11	PUFF input parameters for Shots 90 and 94 with stringer cracks excluded.	J-27
J-12	PUFF input parameters for Shots 113 and 111 with stringer cracks excluded. ..	J-28
J-13	PUFF input parameters for Shot 112 with stringer cracks excluded	J-29
J-14	Computed shock histories in cell 23 for Shot 110 with stringer cracks excluded	J-30
J-15	Computed shock histories in cell 23 for Shot 98 with stringer cracks excluded.	J-31
J-16	Computed shock histories in cell 23 for Shot 92 with stringer cracks excluded.	J-32
J-17	Computed shock histories in cell 23 for Shot 91 with stringer cracks excluded.	J-33
J-18	Computed shock histories in cell 23 for Shot 90 with stringer cracks excluded.	J-34
J-19	Computed shock histories in cell 23 for Shot 94 with stringer cracks excluded.	J-35
J-20	Computed shock histories in cell 20 for Shot 113 with stringer cracks excluded.	J-36

LIST OF ILLUSTRATIONS (Continued)

Figure		Page
J-21	Computed shock histories in cell 24 for Shot 111 with stringer cracks excluded.	J-37
J-22	Computed shock histories in cell 24 for Shot 112 with stringer cracks excluded.	J-38
K-1	Frames 1 and 2 for Armco iron framing camera experiment.	K-3
K-2	Frames 3 and 4 for Armco iron framing camera experiment.	K-4
K-3	Frames 5 and 6 for Armco iron framing camera experiment.	K-5
K-4	Frames 7 and 8 for Armco iron framing camera experiment.	K-6
K-5	Frames 9 and 10 for Armco iron framing camera experiment.	K-7
K-6	Frames 11 and 12 for Armco iron framing camera experiment.	K-8
K-7	Frames 14 and 15 for Armco iron framing camera experiment.	K-9
K-8	Frames 16 and 17 for Armco iron framing camera experiment.	K-10
K-9	Frames 18 and 19 for Armco iron framing camera experiment.	K-11
K-10	Frames 20 and 21 for Armco iron framing camera experiment.	K-12
K-11	Frames 22 and 23 for Armco iron framing camera experiment.	K-13
K-12	Frames 24 and 25 for Armco iron framing camera experiment.	K-14
L-1	Type 1 Armco iron cylinder fragment (Fragment mass: 1551.0 gr).	L-3
L-2	Type 1 Armco iron cylinder fragment (Fragment mass: 437.4 gr).	L-4
L-3	Type 2A Armco iron cylinder fragment.	L-5
L-4	Type 2B Armco iron cylinder fragment.	L-6
L-5	Type 3A Armco iron cylinder fragment.	L-7
L-6	Type 3B Armco iron cylinder fragment.	L-8
L-7	Type 4A Armco iron cylinder fragment.	L-9
L-8	Type 4B Armco iron cylinder fragment.	L-10
L-9	Type 1 HF-1 steel cylinder fragment with heat treatment A.	L-11
L-10	Type 2A HF-1 steel cylinder fragment with heat treatment A.	L-12
L-11	Type 2B HF-1 steel cylinder fragment with heat treatment A.	L-13
L-12	Type 3A HF-1 steel cylinder fragment with heat treatment A.	L-14
L-13	Type 3B HF-1 steel cylinder fragment with heat treatment A.	L-15
L-14	Type 4A HF-1 steel cylinder fragment with heat treatment A.	L-16
L-15	Type 4B HF-1 steel cylinder fragment with heat treatment A.	L-17
L-16	Type 4C HF-1 steel cylinder fragment with heat treatment A.	L-18
L-17	Type 1 HF-1 steel cylinder fragment with heat treatment B.	L-19
L-18	Type 2A HF-1 steel cylinder fragment with heat treatment B.	L-20
L-19	Type 2B HF-1 steel cylinder fragment with heat treatment B.	L-21
L-20	Type 3A HF-1 steel cylinder fragment with heat treatment B.	L-22
L-21	Type 3B HF-1 steel cylinder fragment with heat treatment B.	L-23
L-22	Type 4A HF-1 steel cylinder fragment with heat treatment B.	L-24
L-23	Type 4B HF-1 steel cylinder fragment with heat treatment B.	L-25
L-24	Type 4C HF-1 steel cylinder fragment with heat treatment B.	L-26

LIST OF ILLUSTRATIONS (Continued)

Figure		Page
N-1	Computer listing of input parameters and output results at 600 time cycles for the Armco iron cylindrical PUFF computation using the BFRACT2 subroutine	N-3
N-2	Computer listing of input parameters and output results at 500 time cycles for the HF-1 steel, heat treatment A, cylindrical PUFF computation using the BFRACT2 subroutine	N-6
N-3	Computer listing of input parameters and output results at 500 time cycles for the HF-1 steel, heat treatment B, cylindrical PUFF computation using the BFRACT2 subroutine	N-9
N-4	Computer listing of input parameters and output results at 500 time cycles for the HF-1 steel, heat treatment A, cylindrical PUFF computation using the BFRACT2 and SHEAR2 subroutines	N-12
N-5	Computer listing of input parameters and output results at 500 time cycles for the HF-1 steel, heat treatment B, cylindrical PUFF computation using the BFRACT 2 and SHEAR2 subroutines	N-16
N-6	Computer listing of input parameters, grid layout, and output results at 500 time cycles for the HF-1 steel, heat treatment A, TROTT computation using the BFRACT2 subroutine	N-20
P-1	Computed stress histories in cell 1 for the HF-1 steel, heat treatment B, cylinder experiments	P-3
P-2	Computed stress histories in cell 2 for the HF-1 steel, heat treatment B, cylinder experiments	P-3
P-3	Computed stress histories in cell 3 for the HF-1 steel, heat treatment B, cylinder experiments	P-4
P-4	Computed stress histories in cell 4 for the HF-1 steel, heat treatment B, cylinder experiments	P-4
P-5	Computed stress histories in cell 5 for the HF-1 steel, heat treatment B, cylinder experiments	P-5
P-6	Computed stress histories in cell 6 for the HF-1 steel, heat treatment B, cylinder experiments	P-5
P-7	Computed stress histories in cell 7 for the HF-1 steel, heat treatment B, cylinder experiments	P-6
P-8	Computed stress histories in cell 8 for the HF-1 steel, heat treatment B, cylinder experiments	P-6
P-9	Computed stress histories in cell 9 for the HF-1 steel, heat treatment B, cylinder experiments	P-7
P-10	Computed stress histories in cell 10 for the HF-1 steel, heat treatment B, cylinder experiments	P-7
P-11	Computed stress histories in cell 12 for the HF-1 steel, heat treatment B, cylinder experiments	P-8
P-12	Computed stress histories in cell 13 for the HF-1 steel, heat treatment B, cylinder experiments	P-8

LIST OF ILLUSTRATIONS (Continued)

Figure		Page
P-13	Computed stress histories in cell 14 for the HF-1 steel, heat treatment B, cylinder experiments	P-9
P-14	Computed stress histories in cell 15 for the HF-1 steel, heat treatment B, cylinder experiments	P-9
P-15	Computed stress histories in cell 16 for the HF-1 steel, heat treatment B, cylinder experiments	P-10
P-16	Computed stress histories in cell 17 for the HF-1 steel, heat treatment B, cylinder experiments	P-10
P-17	Computed stress histories in cell 18 for the HF-1 steel, heat treatment B, cylinder experiments	P-11
P-18	Computed stress histories in cell 19 for the HF-1 steel, heat treatment B, cylinder experiments	P-11
P-19	Computed stress histories in cell 20 for the HF-1 steel, heat treatment B, cylinder experiments	P-12
P-20	Computed stress histories in cell 21 for the HF-1 steel, heat treatment B, cylinder experiments	P-12
P-21	Computed particle velocity histories in cells 1 and 2 for the HF-1 steel, heat treatment B, cylinder experiments	P-13
P-22	Computed particle velocity histories in cells 3 and 4 for the HF-1 steel, heat treatment B, cylinder experiments	P-13
P-23	Computed particle velocity histories in cells 5 and 6 for the HF-1 steel, heat treatment B, cylinder experiments	P-14
P-24	Computed particle velocity histories in cells 7 and 8 for the HF-1 steel, heat treatment B, cylinder experiments	P-14
P-25	Computed particle velocity histories in cells 9 and 10 for the HF-1 steel, heat treatment B, cylinder experiments	P-15
P-26	Computed particle velocity histories in cells 12 and 13 for the HF-1 steel, heat treatment B, cylinder experiments	P-15
P-27	Computed particle velocity histories in cells 14 and 15 for the HF-1 steel, heat treatment B, cylinder experiments	P-16
P-28	Computed particle velocity histories in cells 16 and 17 for the HF-1 steel, heat treatment B, cylinder experiments	P-16
P-29	Computed particle velocity histories in cells 18 and 19 for the HF-1 steel, heat treatment B, cylinder experiments	P-17
P-30	Computed particle velocity histories in cells 20 and 21 for the HF-1 steel, heat treatment B, cylinder experiments	P-17
P-31	Computed crack concentration histories in cell 12 for the HF-1 steel, heat treatment B, cylinder experiments	P-18

LIST OF ILLUSTRATIONS (Continued)

Figure		Page
P-32	Computed crack concentration histories in cell 13 for the HF-1 steel, heat treatment B, cylinder experiments	P-18
P-33	Computed crack concentration histories in cell 14 for the HF-1 steel, heat treatment B, cylinder experiments	P-19
P-34	Computed crack concentration histories in cell 15 for the HF-1 steel, heat treatment B, cylinder experiments	P-19
P-35	Computed crack concentration histories in cell 16 for the HF-1 steel, heat treatment B, cylinder experiments	P-20
P-36	Computed crack concentration histories in cell 17 for the HF-1 steel, heat treatment B, cylinder experiments	P-20
P-37	Computed crack concentration histories in cell 18 for the HF-1 steel, heat treatment B, cylinder experiments	P-21
P-38	Computed crack concentration histories in cell 19 for the HF-1 steel, heat treatment B, cylinder experiments	P-21
P-39	Computed crack concentration histories in cell 20 for the HF-1 steel, heat treatment B, cylinder experiments	P-22
P-40	Computed crack concentration histories in cell 21 for the HF-1 steel, heat treatment B, cylinder experiments	P-22

LIST OF TABLES

Table		Page
1	Chemical analysis of Armco iron and HF-1 steel	3
2	Summary of tensile-pull measurements for transverse-direction specimens of HF-1 steel	7
3	Summary of mechanical properties for Armco iron and HF-1 steel	9
4	Ultrasonic velocity measurements and elastic constants for HF-1 steel	10
5	Summary of Hugoniot experiments for HF-1 steel	13
6	Summary of spall fracture experiments for HF-1 steel	21
7	Summary of crack measurements for spall fracture specimens of HF-1 steel ..	25
8	Summary of experimental volume crack-size distribution parameters for spall fracture specimens of HF-1 steel	26
9	Summary of experimental and computed nucleation and growth values for spall fracture specimens of HF-1 steel with heat treatment A	35
10	Summary of experimental and computed nucleation and growth values for spall fracture specimens of HF-1 steel with heat treatment B	36
11	Dynamic fracture parameters for heat treatments A and B of HF-1 steel and Armco iron	39
12	Armco iron cylinder outer radius versus time values near the mid-length position of the cylinder	44
13	Configuration details for explosive-filled cylinder and projectile experiments.	48
14	Definitions of fragment types used for characterization of recovered fragments from the explosive-filled cylinder and projectile experiments	52
15	Average fragment mass results for cylinder and projectile experiments	58
16	Summary of results for typed fragments from cylinder and projectile experiments	64
17	Average fragment mass results for typed fragments from cylinder and projectile experiments	65
18	Summary of measurements on type-1 fragments from cylinder and projectile experiments	68
A-1	Tensile-pull measurements for transverse-direction specimens of HF-1 steel ..	A-3
J-1	Summary of experimental volume crack-size distribution parameters for spall fracture specimens of HF-1 steel with heat treatment A with stringer cracks excluded ...	J-39
J-2	Summary of experimental and computed nucleation and growth values for spall fracture specimens of HF-1 steel with heat treatment A with stringer cracks excluded	J-40
J-3	Dynamic fracture parameters for heat treatment A of HF-1 steel with stringer cracks excluded	J-41
M-1	Mass distribution and characterization of Armco iron cylinder fragments from experiment 1	M-3
M-2	Mass distribution and characterization of Armco iron cylinder fragments from experiment 2	M-4

LIST OF TABLES (Continued)

Table		Page
M-3	Mass distribution and characterization of HF-1 steel cylinder fragments with heat treatment A from experiment 3	M-8
M-4	Mass distribution and characterization of HF-1 steel cylinder fragments with heat treatment A from experiment 4	M-9
M-5	Mass distribution and characterization of HF-1 steel cylinder fragments with heat treatment B from experiment 5	M-11
M-6	Mass distribution and characterization of HF-1 steel cylinder fragments with heat treatment B from experiment 6	M-13
M-7	Mass distribution and characterization of HF-1 steel projectile fragments with heat treatment A from experiment 7	M-15
M-8	Measurements on twenty-five selected type 1 Armco iron cylinder fragments from experiment 1	M-18
M-9	Measurements on twenty-five selected type 1 Armco iron cylinder fragments from experiment 2	M-19
M-10	Measurements on the type 1 HF-1 steel cylinder fragments with heat treatment A from experiment 3	M-20
M-11	Measurements on the type 1 HF-1 steel cylinder fragments with heat treatment A from experiment 4	M-21
M-12	Measurements on the type 1 HF-1 steel cylinder fragments with heat treatment B from experiment 5	M-22
M-13	Measurements on the type 1 HF-1 steel cylinder fragments from experiment 6	M-24
M-14	Measurements on twenty selected type 1 HF-1 steel projectile fragments with heat treatment A from experiment 7	M-26
O-1	Summary of brittle fracture crack distribution results for the Armco iron cylindrical PUFF computation	O-3
O-2	Calculated fragment mass distribution results for the Armco iron cylinder using the brittle fracture crack distribution results from Table O-1	O-4
O-3	Summary of brittle fracture crack distribution results for the HF-1 steel, heat treatment A, cylindrical PUFF computation	O-5
O-4	Calculated fragment mass distribution results for the HF-1 steel cylinder with heat treatment A using the brittle fracture crack distribution results from Table O-3	O-6
O-5	Summary of brittle fracture crack distribution results for the HF-1 steel, heat treatment B, cylindrical PUFF computation	O-7
O-6	Calculated fragment mass distribution results for the HF-1 steel cylinder with heat treatment B using the brittle fracture crack distribution results from Table O-5	O-8
O-7	Summary of brittle and shear fracture crack distribution results for the HF-1 steel, heat treatment A, cylindrical PUFF computation	O-9

LIST OF TABLES (Continued)

Table		Page
O-8	Calculated fragment mass distribution results for the HF-1 steel cylinder with heat treatment A using the brittle and shear fracture crack distribution results from Table O-7	O-10
O-9	Summary of brittle and shear fracture crack distribution results for the HF-1 steel, heat treatment B, cylindrical PUFF computation.	O-11
O-10	Calculated fragment mass distribution results for the HF-1 steel cylinder with heat treatment B using the brittle and shear fracture crack distribution results from Table O-9	O-12
O-11	Calculated fragment mass distribution results for the HF-1 steel projectile with heat treatment A using the brittle fracture crack distribution results from the TROTT computation	O-13

I. INTRODUCTION

In this report a computational and experimental investigation of the fragmentation of Armco iron and HF-1 steel explosively loaded cylinders and an HF-1 steel projectile is presented. The computational simulations were performed with SRI International Lagrangian finite-difference computer programs.^{1,2} Cylinder and projectile fragment mass distributions were experimentally determined for comparison with the computations. The PUFF 8¹ one-dimensional and TROTT² two-dimensional stress wave propagation codes were used for the cylinder and projectile computations, respectively. The SHEAR2^{1,3,4} shear band model and the BFRACT2¹ brittle fracture model simulated the fracture processes. These nucleation and growth models are subroutines in the stress wave propagation codes.

The original version of the computational shear band model SHEAR1⁵ was developed by SRI as part of a joint NSWC-SRI experimental and analytical effort to simulate the fragmentation behavior of naturally fragmenting munitions.⁶ In that work the PUFF 8 computer program containing the SHEAR1 and BFRACT2 fracture models was used by SRI to compute fragment mass distributions for cylinders of Armco iron and a selected heat treatment of HF-1 steel.⁵ The HF-1 steel brittle fracture parameters that were used as input to the BFRACT2 fracture model were determined at NSWC via gas gun impact and soft recovery experiments. Fragment mass distributions for the cylinders were experimentally determined at NSWC for comparison with the SRI computations.⁶ SRI refined the original shear band model under joint sponsorship of the Army Ballistic Research Laboratory, the Advanced Research Projects Agency, and NSWC.³ The new shear band model SHEAR2 was then used with the PUFF 8 and TROTT computer programs to calculate fragment mass distributions for Armco iron and HF-1 steel cylinders and an HF-1 steel projectile, respectively.³

In the present work, computations were made for a different heat treatment of HF-1 steel⁷ and also for the previous heat treatment that was used in the earlier work. The two heat treatments produced different microstructures and resulted in different fracture parameters. This allowed the predictive capability of the BFRACT2 model to be tested for small changes in the fracture parameters for HF-1 steel. The fracture parameters for the previous heat treatment of HF-1 steel⁶ were redetermined for these calculations. Computations were also made for an Armco iron cylinder. The SHEAR2 and BFRACT2 fracture models were used together in some of the com-

putations, since the recovered fragments had both shear and brittle fracture surfaces. For those cases where the models could not be used together, the BFRACT2 model was used to simulate the fracture processes because the recovered fragments had more brittle than shear fracture surface area. Some of the results presented in the earlier report (Reference 6) are presented in this report in more detail for completeness.

The materials are described in Section II. Static tensile-pull measurements and ultrasonic velocity measurements for HF-1 steel are presented in Section III. HF-1 steel Hugoniot measurements are presented in Section IV. Section V describes the HF-1 steel gas gun impact and soft recovery experiments. The calculated dynamic fracture parameters for HF-1 steel that were used as input for the cylinder and projectile simulations are given in Section VI. The results of a framing camera experiment for an explosively loaded Armco iron cylinder are presented in Section VII. Section VIII contains the fragment mass distribution results of the Armco iron and HF-1 steel explosively loaded cylinder experiments and the HF-1 steel projectile experiment. A new characterization scheme for grouping the recovered fragments with respect to their fracture surfaces is presented in this section. The fragment mass distribution computations are presented in Section IX. Section X contains the summary. Appendixes A through P contain tables, photographs, computer listings, computer plots, and other information concerning this work.

II. MATERIALS

The Armco iron material used for the exploding cylinder experiments was purchased from Corey Steel Company, Chicago, Illinois, as a 127-mm-diameter hot-rolled bar. It was used in the as-received condition. The chemical analysis is given in Table 1. The microstructure of the material shown in Figure 1 consists primarily of a single-phase polycrystalline aggregate with ASTM grain size number of approximately 2.5 to 3. A few inclusions are also present; these are probably oxides.

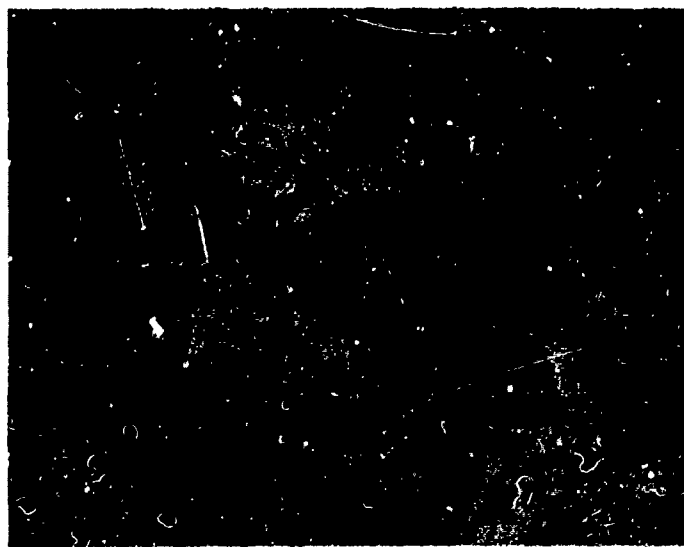
The HF-1 steel material that was used in this investigation was purchased from Norris Industries, Pomona, California, in cylinder form and as a 127-mm-diameter hot-rolled bar. The chemical analysis of this silico-manganese steel is given in Table 1. Two heat treatments were

Table 1. Chemical analysis of Armco iron and HF-1 steel.

Element	Armco Iron ^a (wt %)	HF-1 Steel ^b (wt %)
C	0.004	1.08
Mn	Trace	1.83
Si	Trace	0.86
P	Trace	0.011
S	0.025	0.0001
Al	0.0002	0.006
Mo	Trace	0.07
Ni	0.0001	Trace
Cr	Trace	0.15
O	0.010	—
N	0.001	—
Cd	0.003	—
Mg	0.001	—

^aDetermined by Corey Steel Company, Chicago, Illinois.

^bDetermined by NSWC, Dahlgren, Virginia.



200 μ m

Figure 1. Microstructure of Armco iron.

considered to investigate microstructural changes on fragmentation behavior. Heat treatment A material was austenized at $843\pm 4^\circ\text{C}$ for 4 hr and then quenched in warm oil at 60°C to form martensite. The martensite was tempered at $566\pm 4^\circ\text{C}$ for 2 hr and then air-cooled. Figure 2 shows the microstructure for this heat treatment at two different magnifications. It consists mainly of tempered martensite with some dispersed carbide precipitates and retained austenite. Heat treatment B material was used in the work of Reference 6. Heat treatment B material was austenized at $927\pm 4^\circ\text{C}$ for 1 hr, transferred to $782\pm 4^\circ\text{C}$ for 1 hr to form grain boundary cementite, and then air-cooled to form pearlite.⁷ The microstructure for this heat treatment is shown in Figure 3. It consists mainly of a cementite network and a fine pearlite structure.

III. MECHANICAL AND ACOUSTICAL EXPERIMENTS

In this section tensile-pull and ultrasonic velocity measurements are presented for the materials. This information will be useful for comparison with the shock-wave measurements to be presented in later sections. Tensile-pull results are presented for Armco iron and the two heat treatments of HF-1 steel. Results are presented for longitudinal (parallel to the material rolling direction) and transverse (perpendicular to the material rolling direction) tensile specimens. Figures 4 and 5 give stress-strain curves for longitudinal tensile specimens of Armco iron and heat treatment A of HF-1 steel, respectively. Both true and engineering stress-strain curves are shown in these figures. The crosses indicate specimen fracture. Stress-strain curves for transverse tensile specimens of heat treatments A and B of HF-1 steel are shown in Figure 6. Two experiments were performed for each HF-1 steel heat treatment. This figure was constructed from the measurements listed in Table A-1. The specimen dimensions and experimental details for the transverse tensile-pull measurements are given in this table. Table 2 summarizes the transverse tensile-pull measurements for the two HF-1 steel heat treatments. The heat treatment B transverse tensile specimens fractured at a lower stress (about 20% less) and a lower strain (about 70% less) than the heat treatment A transverse tensile specimens. Photographs of the fracture surfaces for two specimens are shown in Figure 7. Table 3 summarizes the mechanical property measurements for the materials. The extent of the directional character of the mechanical properties for heat treatment A of HF-1 steel is shown in this table.

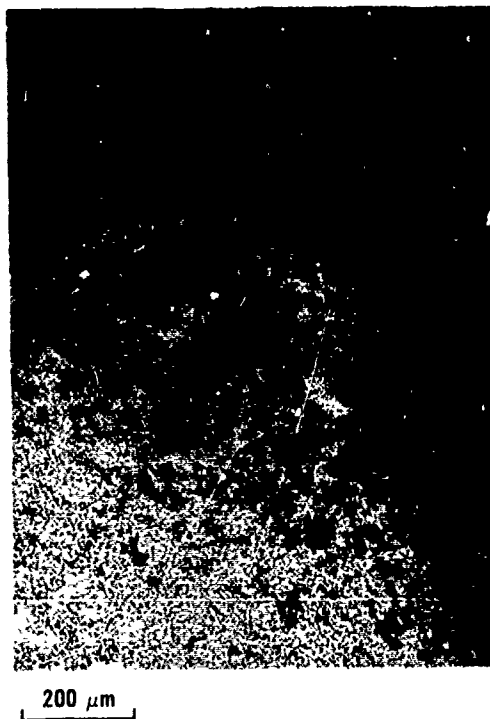


Figure 2. Microstructure of HF-1 steel with heat treatment A.

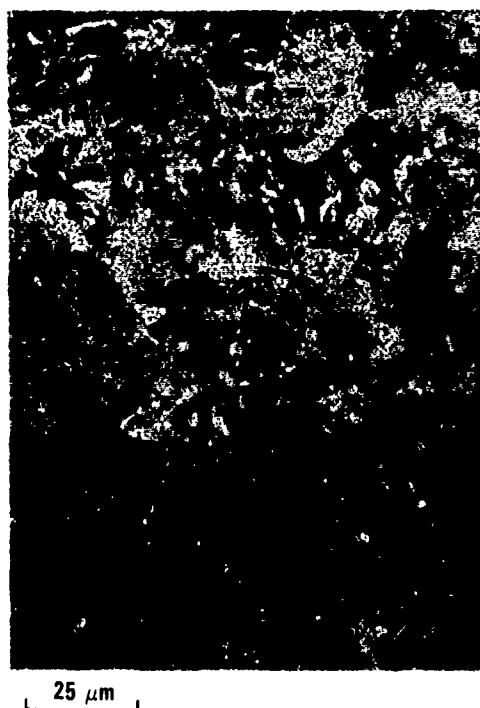
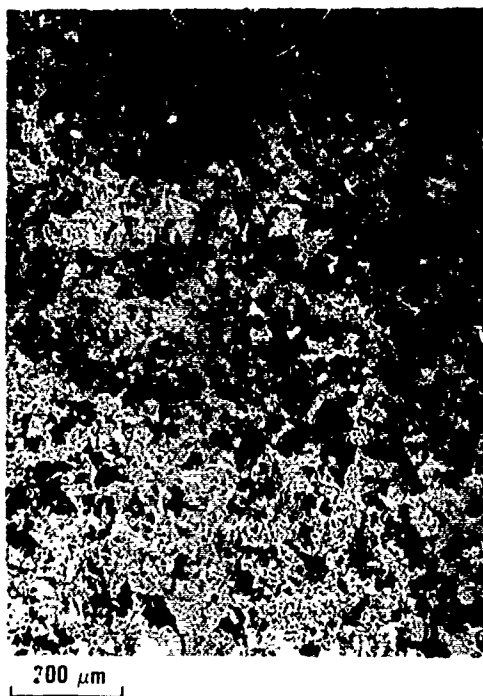


Figure 3. Microstructure of HF-1 steel with heat treatment B.

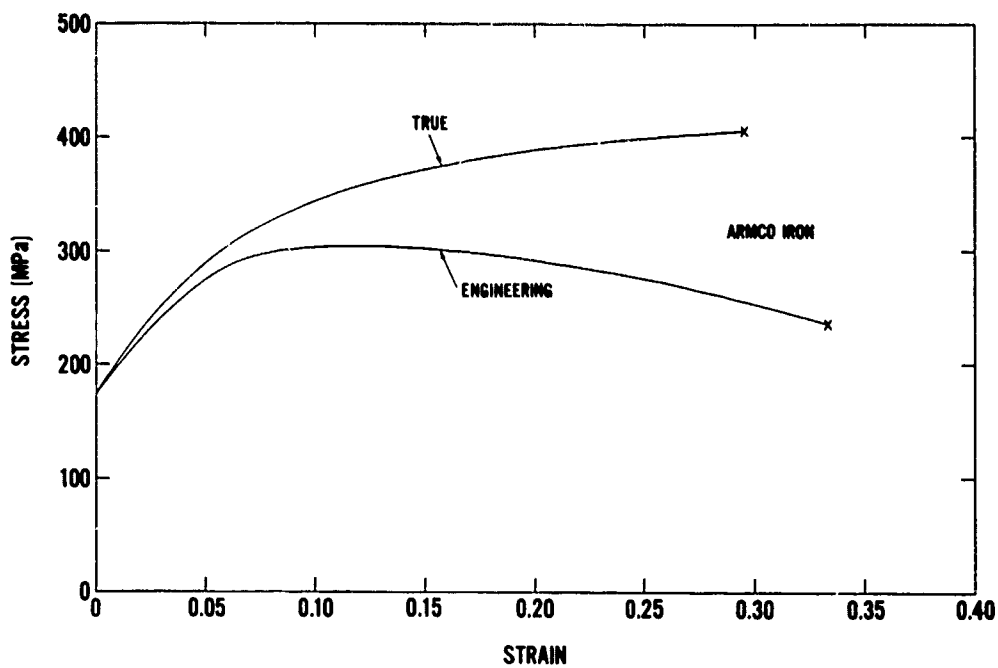


Figure 4. True stress-true strain and engineering stress-strain curves for longitudinal tensile specimens of Armco iron.

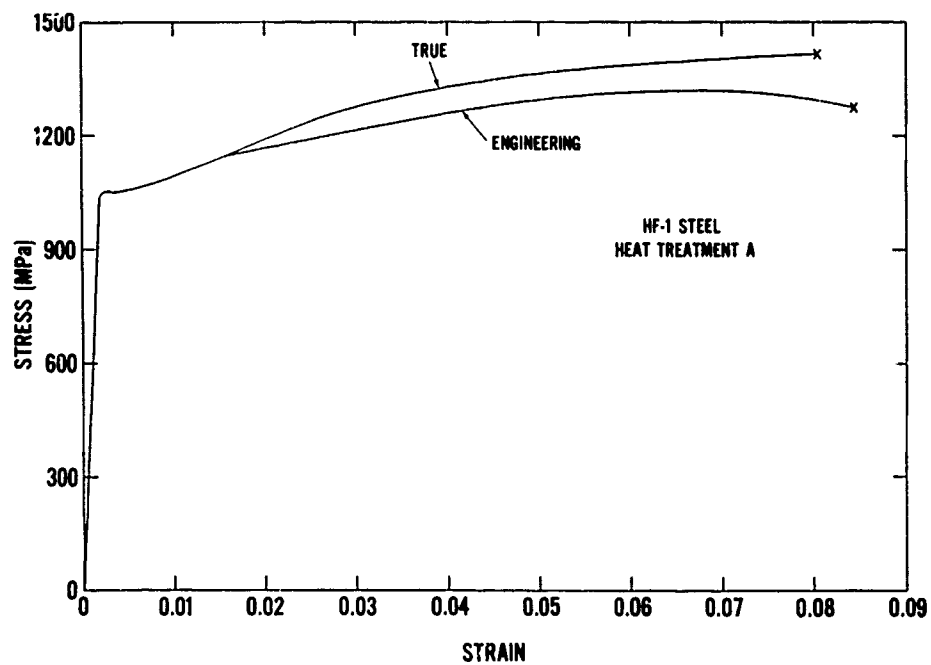


Figure 5. True stress-true strain and engineering stress-strain curves for longitudinal tensile specimens of HF-1 steel with heat treatment A.

Table 2. Summary of tensile-pull measurements for transverse-direction specimens of HF-1 steel.

Experiment No.	Heat Treatment ^a	Initial Specimen Diameter (mm)	Young's Modulus ^b (MPa) ^c	0.2% Offset Yield Strength (MPa)	Ultimate Tensile Strength ^d (MPa)	Percent Elongation ^e	Percent Reduction in Area ^f
1	A	4.70	194	947	1090	2.7	3.3
2	A	4.71	191	1013	1120	4.0	2.7
3	B	4.70	192	855	885	—	—
4	B	4.70	176	858	879	1.0	0.8

^a Specimens 1 and 2 had a hardness of R_C 39. Specimens 3 and 4 had a hardness of R_C 43. Two hardness values were measured for each disk prior to fabricating a tensile-pull specimen.

^b Obtained from the slope of the elastic-region part of the stress-strain curves in Figure 6. The value for experiment 4 is about 8% less than the values for the other experiments and is therefore probably more uncertain.

^c 1 megapascal (MPa) = 145.0 psi. 1 gigapascal (GPa) = 10^3 MPa.

^d The ultimate tensile strength is the stress at fracture. The average strain at fracture for heat treatments A and B is 0.0247 and 0.0074, respectively.

^e The final central-region length for specimens 1, 2, and 4 was 19.6, 13.2, and 12.8 mm, respectively. The final length for specimen 3 was not measured.

^f The final central-region diameter of the necked-down fracture region for specimens 1, 2, and 4 was 4.62, 4.64, and 4.69 mm, respectively. The final diameter for specimen 3 was not measured. The fracture regions for specimens 3 and 4 occurred at the edge of the central region and in the middle of the central region, respectively.

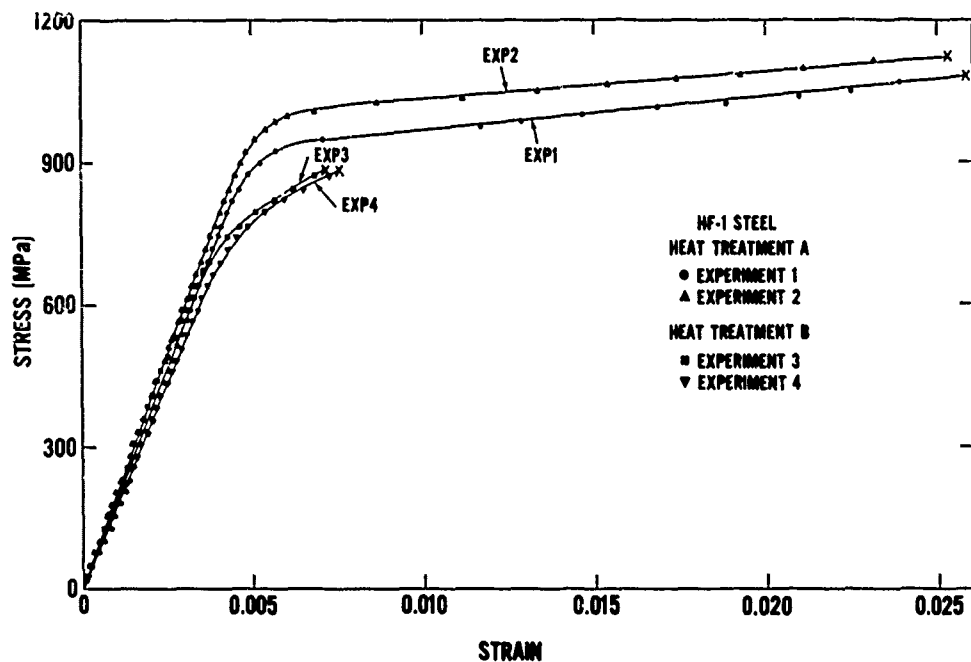


Figure 6. Engineering stress-strain curves for transverse tensile specimens of HF-1 steel with heat treatments A and B.

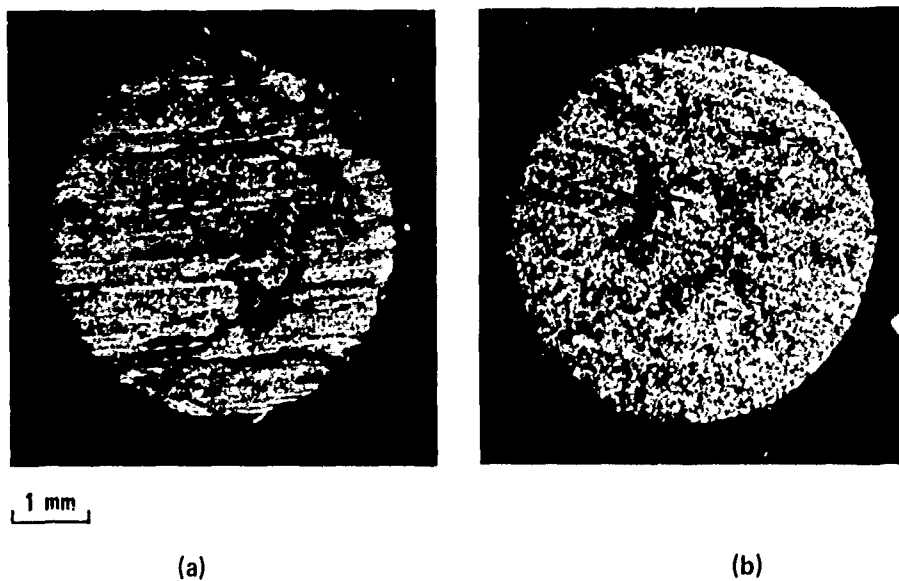


Figure 7. Macrophotographs of the fracture surfaces for the transverse tensile specimens of HF-1 steel with (a) heat treatment A in experiment 1 and (b) heat treatment B in experiment 3.

Table 3. Summary of mechanical properties for Armco iron and HF-1 Steel.

Material	Heat Treatment	Hardness	Tensile-Pull Direction ^a	0.2% Offset Yield Strength (MPa)	Ultimate Tensile Strength (MPa)	Percent Elongation	Percent Reduction in Area
Armco iron	None	R _B 40	Longitudinal	180	300	34	57
HF-1- Steel	A	R _C 40	Longitudinal	1040	1320	8.4	14
	A	R _C 39	Transverse	980	1105	3.4	3.0
HF-1 Steel	B	R _C 43	Transverse	857	882	1.0	0.8

^a The longitudinal tensile properties for Armco iron and for heat treatment A of HF-1 steel are averages for three and five measurements, respectively. The longitudinal tensile measurements were performed on standard 6.35-mm ASTM E-68 tensile specimens; the percent elongation results are for 25.4-mm gage. The transverse tensile properties for heat treatments A and B of HF-1 steel are both averages for two measurements. The details of the transverse tensile measurements are given in Tables 2 and A-1.

Zero-stress longitudinal and shear wave velocity measurements have been performed for the two heat treatments of HF-1 steel using the ultrasonic pulse-echo technique. The longitudinal wave velocity measurements were performed with a 6.5-MHz Dapco transducer. A 1.6-MHz Panametrics transducer was used for the shear wave velocity measurements. The transducers were used with an ultrasonic pulser/receiver (Panametrics 5050 PR). A high-viscosity fluid (Dapco couplant paste) was used to couple the transducers to the specimens. The time between the echos was measured with an oscilloscope (Tektronix R7704) and a digital delay plug-in unit (Tektronix 7D11). The unit was checked for accuracy with a digital delay pulse generator (Berkeley Nucleonics 7040). Table 4 summarizes the ultrasonic velocity measurements and the calculated elastic constants for the two heat treatments of HF-1 steel.

Figure 8 shows ultrasonic pulses for HF-1 steel specimens with heat treatment A. To measure the time difference between echos, the first positive peak in the pulse is aligned with a selected graticule line. The digital delay unit is then used to move the pulse train across the display in 1-ns increments until the same part of the next pulse is aligned with the fiducial graticule. The wave velocity data for each measurement was obtained by averaging the time differences for five or more successive echos.

Table 4. Ultrasonic velocity measurements and elastic constants for HF-1 steel.

Heat Treat- ment	Density ρ_0 (Mg/m ³)	Longitudinal Wave Velocity ^a C_L (km/s)	Shear Wave Velocity ^b C_S (km/s)	Bulk Wave Velocity ^c C_B (km/s)	Poisson's Ratio ^d ν	Young's Modulus ^e E (GPa)	Bulk Modulus ^f K (GPa)	Shear Modulus ^g G (GPa)
A	7.77 ^h	5.93 ^{i,j}	3.25 ^{l,k}	4.59	0.285	211	164	82.1
B	7.77 ^h	5.92 ^j	3.24 ^{j,k}	4.58	0.286	210	164	81.6

^a Measured for a nominal center frequency of 6.5 MHz of a broadband pulse.

^b Measured for a nominal center frequency of 1.6 MHz of a broadband pulse.

$$^c C_B^2 = C_L^2 \cdot (4/3) - C_S^2$$

$$^d \nu = [(C_L/C_S)^2 - 2] / [2(C_L/C_S)^2 - 2]$$

$$^e E = 2(1 + \nu)C_S^2 \rho_0$$

$$^f K = E / [3(1 - 2\nu)]$$

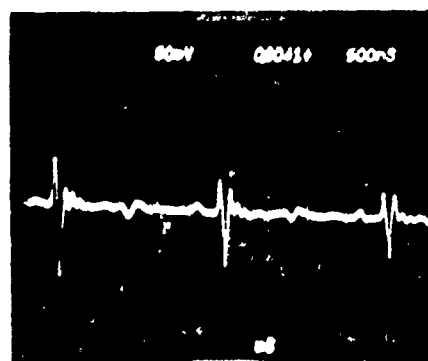
$$^g G = E / [2(1 + \nu)]$$

^h Average for two specimens. Each specimen was 6.36-mm thick.

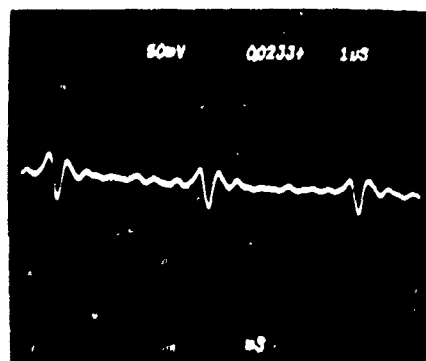
ⁱ Average of four measurements on two specimens.

^j The scatter in the measurements was 0.5% or less.

^k Average of six measurements on two specimens.



(a)



(b)

Figure 8. Longitudinal and shear echo pulses for HF-1 steel specimens with heat treatment A. steel. (a) Longitudinal echo pulses. The vertical scale is 50 mV/div and the horizontal scale is 0.5 μ s/div. (b) Shear echo pulses. The vertical scale is 50 mV/div and the horizontal scale is 1 μ s/div.

IV. HUGONIOT EQUATION OF STATE EXPERIMENTS

A series of Hugoniot experiments has been performed for heat treatments A and B of HF-1 steel. The resulting Hugoniot equation of state was used as input to the computer programs for calculating the shock stress in HF-1 steel. The measurements were performed with a 40-mm-bore diameter gas gun.⁸ Both direct-impact and transit-time experiments were performed. In the direct-impact experiment, an HF-1 steel disk was impacted directly onto a quartz gauge to measure the HF-1 steel shock stress and particle velocity. In the transit-time experiments, an HF-1 steel disk was impacted onto an HF-1 steel specimen that was backed with a quartz gauge. Figure 9 is a schematic of the muzzle region of the gas gun for this type of experiment. The impact time and impact planarity are measured with the four charged tilt pins that are centered around the specimen. The tilt pin ends are positioned in the plane of the impact face of the specimen to within 1 μm . The average projectile velocity at impact is measured with the three charged pins in the side of the barrel and the specimen tilt pins. The quartz gauge measures the stress-time profile at the specimen-quartz interface. Elastic and plastic wave velocities in the specimen are determined by measuring the time between the impact of the front surface of the specimen and the arrival of the stress waves at the specimen back surface. A digital delay generator (Berkeley Nucleonics 7040) is used for producing two reference pulses that are time delayed with respect to each other by a predetermined amount. The initial pulse is recorded on the tilt data trace, and the delayed pulse is recorded on the quartz gauge data trace.

The oscilloscope records for the five Hugoniot experiments are given in Appendix B. Shots 117, 118, and 120 were performed for heat treatment A material; Shots 152 and 153 were performed for heat treatment B material. All the experiments were shock transit-time experiments except Shot 120, which was a direct impact experiment. The tilt data record for the transit-time experiments is a series of voltage pulses corresponding to the contact of the tilt pins by the impactor disk. The tilt angle or impact planarity is measured from this record. The quartz gauge current record for each shot shows an HF-1 steel elastic wave followed by a slower-moving plastic wave. A rising transition region occurs between the elastic wave front and the peak of the plastic wave for both HF-1 steel heat treatments. A similar phenomenon has been observed by Jones et al.⁹ for SAE 4340 steel and attributed to work hardening and wave dispersion. This is in contrast to Armco iron, which exhibits an elastic wave followed by stress relaxation and then a gradual rise to the plastic wave.¹⁰

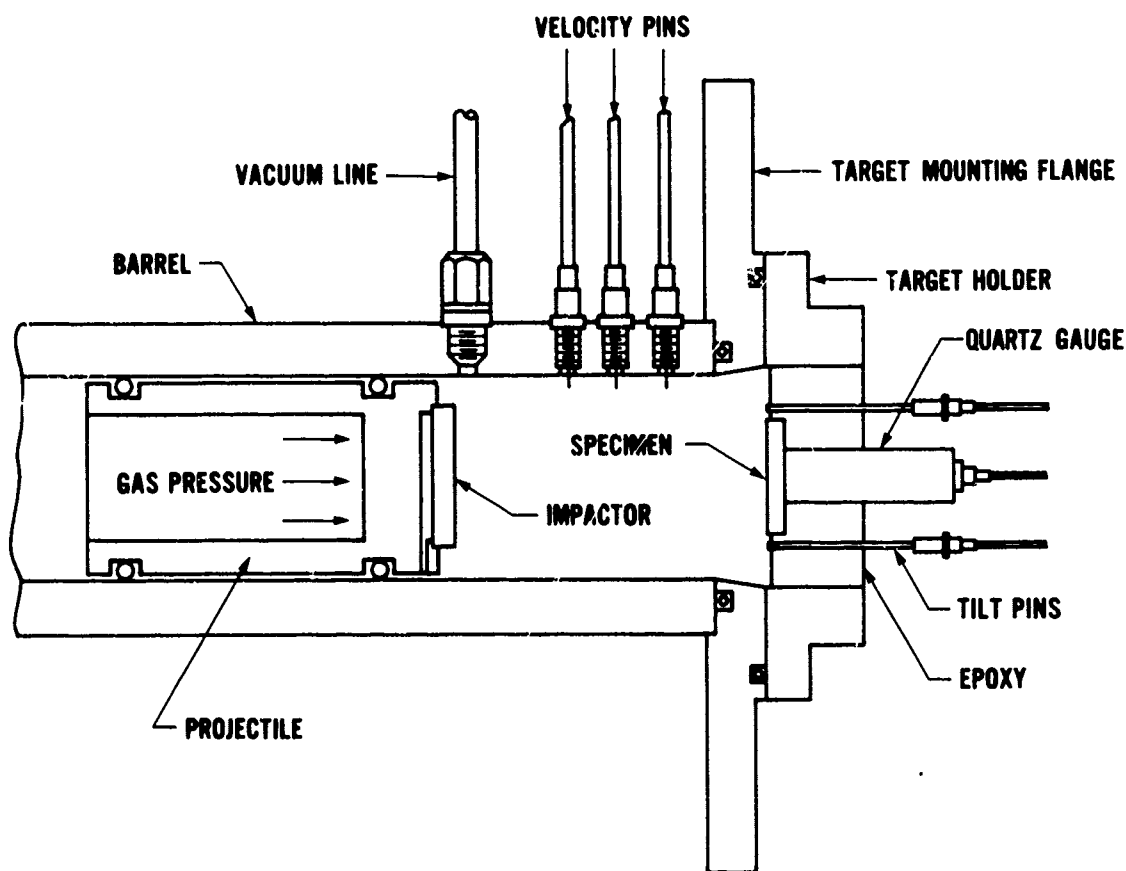


Figure 9. Schematic of muzzle region of gas gun for a shock transit-time experiment.

Table 5 summarizes the shock wave measurements and calculations for HF-1 steel. A brief description of each shot is given in the third column of the table. The average measured density for the HF-1 steel disks is $\rho_0 = 7.774 \text{ Mg/m}^3$. Impact tilt was measured from the rise time of the quartz gauge pulse for Shot 120. The average tilt value for the shots is 0.84 mrad. Values for wave velocity, stress particle velocity, and strain are given for the elastic and plastic waves. An average value of 2.2 GPa was obtained for the Hugoniot elastic limit (HEL) for heat treatment A material. The hardness for this material is $R_C 40$. An average HEL value of 2.4 GPa was obtained for heat treatment B material with a hardness of $R_C 43$. Jones et al.⁹ obtained a value of 2.0 GPa for the HEL of SAE 4340 steel with a thickness of 19.9 mm and a hardness of $R_C 40$. Minshall¹¹ measured an elastic wave velocity of 5.95 km/s and an HEL of 2.5 GPa for 25.4-mm-thick 4340 steel with a hardness of $R_C 35$.

Table 5. Summary of Hugoniot experiments for HF-1 steel.

Shot No.	Heat Treatment	Description of Shot	Elastic Wave ^a					Plastic Wave ^b									
			Impactor Diameter (mm)	Impactor Thickness (mm)	Initial Specimen Density (Mg/m ³)	Specimen Diameter (mm)	Specimen Thickness (mm)	Density ρ_0 (Mg/m ³)	Impactor Velocity ^c U_0 (km/s)	Tilt ^d (mrad)	Wave Velocity ^e C_L (km/s)	Stress ^f σ_e (GPa)	Particle Velocity ^g u_e (km/s)	Wave Velocity ^h U_s (km/s)	Stress ⁱ σ_H (GPa)	Particle Velocity ^j u_p (km/s)	Compression ^k $\Delta V/V_0$
117 ^m	A	HF-1 \rightarrow HF-1/tilt pins, quartz gauge	35.58	3.183	7.771	27.93	6.359	7.777	0.339	0.77	5.94	2.09	0.045	0.0076	-	0.169	-
118	A	HF-1 \rightarrow HF-1/tilt pins, quartz gauge	35.57	3.183	7.776	27.91	3.186	7.772	0.354	0.74	5.95	2.33	0.050	0.0085	4.87	0.177	0.0345
120	A	HF-1 \rightarrow quartz gauge	35.59	3.183	7.766	-	-	-	0.315	1.29	-	-	-	-	-	0.088	-
152	B	HF-1 \rightarrow HF-1/tilt pins, quartz gauge	35.58	3.188	7.771	27.96	6.358	7.773	0.370	0.74	5.81	2.43	0.054	0.0092	4.83	0.150	0.0292
153	B	HF-1 \rightarrow HF-1/tilt pins, quartz gauge	35.58	3.186	7.770	27.95	6.357	7.775	0.236	0.67	5.88	2.45	0.054	0.0091	4.83	0.118	0.0255

^a Average values for the elastic wave velocity C_L, particle velocity u_e, and elastic compression η_e = ΔV/V₀ for both heat treatments are 5.89 km/s, 0.051 km/s, and 0.0086, respectively. Average values for the Hugoniot elastic limit σ_e are 2.2 and 2.4 GPa, respectively, for heat treatments A and B.

^b A straight-line least-squares fit of the three U_s, u_p data points and the ultrasonic bulk wave velocity of 4.59 km/s (from Table 4) gives U_s = 4.60 + 1.61 u_p for the shock velocity-particle velocity Hugoniot relation.

^c Average of three measurements except Shot 120, which is the average of two measurements. The estimated uncertainty is 1% or less.

^d Average of measurements from two oscilloscope records. The estimated uncertainty is about 5%.

^e Calculated using the measured elastic and plastic wave transit times through the specimen disks. The estimated wave velocity uncertainty is about 2%.

^f σ_e = [(2C_L + Z)/(2C_L)] σ_H is the calculated stress in quartz from the measured quartz gauge current. Z = ρ₀ U_q where ρ₀ = 2.65 Mg/m³ is the initial quartz density and U_q is the calculated quartz wave velocity.

^g u_e = u_e/C_L.

^h The compression η_e = ΔV/V₀ = 1 - V/V₀ = u_e/C_L where V₀ = 1/ρ₀.

ⁱ For the transmitted wave experiments q_H = σ_e + ρ₀ (U_s - u_e)/C_L where ρ₀ = ρ₀/(1 - u_e/C_L) and u_p = U_s/2. For the direct impact experiment (Shot 120) q_H = σ_H.

^j For the transmitted wave experiments u_p = U_s/2. For the direct impact experiment (Shot 120) u_p = U_s - u_e where u_e is the calculated quartz particle velocity.

^k The compression η = ΔV/V₀ = 1 - V/V₀ where V/V₀ = (1 - u_e/C_L)/(U_s - u_e) and V = 1/ρ.

^l Only the beginning of the plastic wave was recorded in this shot, since the separation of the elastic and plastic waves was greater than the quartz gauge read time.

^m Shunted guard-ring quartz gauges were used for these experiments. In Shots 117, 118, and 120 the diameter and thickness of the quartz disks were 9.53 and 1.27 mm, respectively. The inner electrode diameter and insulating gap width were 3.81 and 0.13 mm, respectively. The read time was approximately 0.22 μs. In Shots 152 and 153 the diameter and thickness of the quartz disks were 25.40 and 6.35 mm, respectively. The inner electrode diameter and insulating gap width were 6.35 and 0.13 mm, respectively. The read time was approximately 1.11 μs. The gauges were purchased from Valpey-Fisher Corp., Holliston, Massachusetts 01748.

A value for the one-dimensional static yield strength σ_Y can be calculated for heat treatment A material using the equation $\sigma_Y = [(1-\nu)/(1-2\nu)]Y$ where ν is Poisson's ratio and Y is the longitudinal yield strength. For this material $Y = 1.04$ GPa from Table 3 and $\nu = 0.285$ from Table 4. The calculated value of $\sigma_Y = 1.7$ GPa is not as large as the measured HEL value of 2.2 GPa for heat treatment A material, indicating some strain-rate dependence for HF-1 steel. The ultrasonic longitudinal wave velocity of 5.93 km/s from Table 4 is in good agreement with the average elastic wave velocity value of 5.89 km/s.

Figure 10 gives the shock velocity-particle velocity data points for HF-1 steel. The Hugoniot relationship $U_s = 4.60 + 1.61 u_p$ was obtained from a straight-line least-squares fit to the three U_s - u_p plastic wave data points from Table 5 and the average value for the ultrasonic bulk wave velocity from Table 4. The Hugoniot curves for Armco iron¹⁰ and 304 stainless steel¹² are shown for comparison.

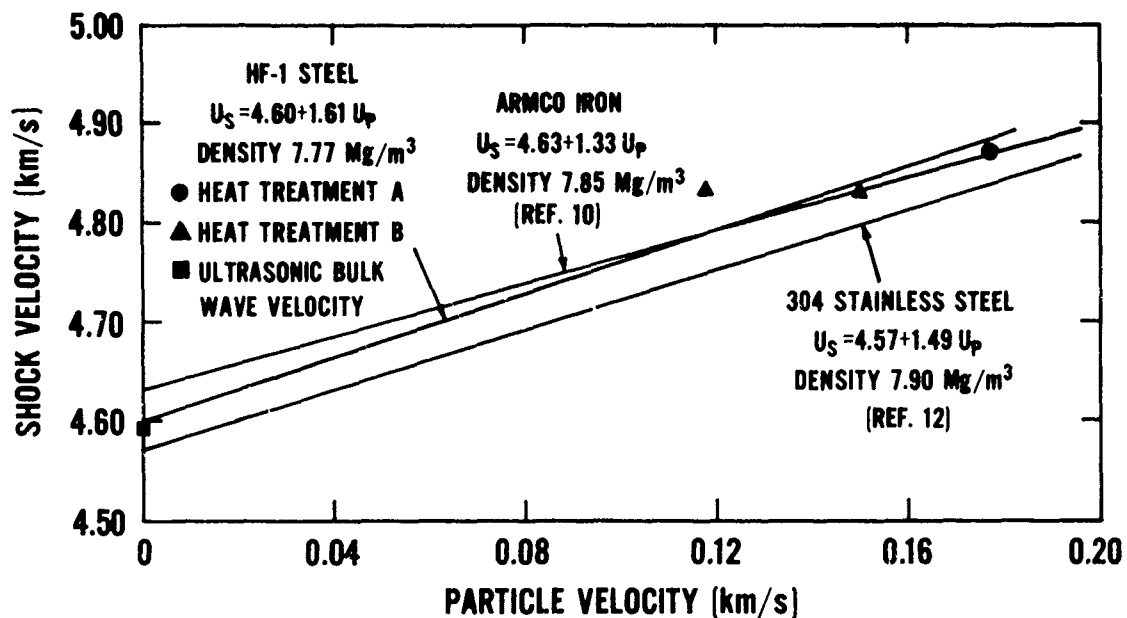


Figure 10. Shock velocity-particle velocity relationship for HF-1 steel.

The stress-particle velocity Hugoniot relation and data points for HF-1 steel are shown in Figure 11. A maximum stress of 7.11 GPa was obtained for these shots. The stress-particle velocity relationship was taken to be a straight line up to a particle velocity of $u_e \approx 0.051$ km/s, the average particle velocity at the elastic limit. The stress at this particle velocity is $\sigma_e \approx 2.3$ GPa, the average HEL value for the two heat treatments of HF-1 steel. Above a particle velocity of 0.051 km/s the stress-particle velocity relationship was obtained from the equation $\sigma_H = \sigma_e + \rho_e (U_s - u_e) (u_p - u_e)$ where $\rho_e = \rho_0 / (1 - u_e / C_L)$. Here ρ_e and $C_L = 5.89$ km/s are the density and wave velocity at the elastic limit, respectively. Using the HF-1 steel shock velocity-particle velocity relationship $U_s = 4.60 + 1.61 u_p$ and the measured values for the other parameters gives $\sigma_H = 0.51 + 35.0 u_p + 12.6 u_p^2$ for $u_p \geq 0.051$ km/s. Here σ_H is in gigapascals.

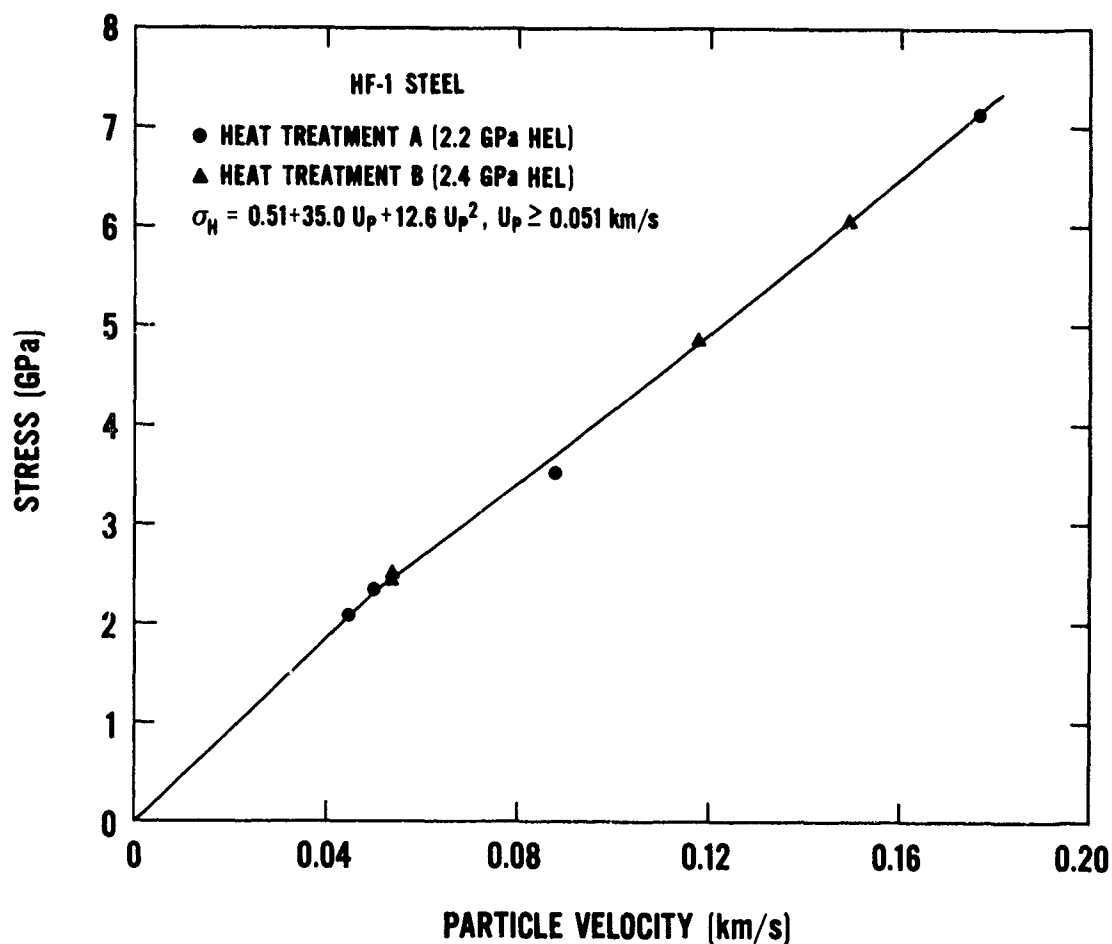


Figure 11. Stress-particle velocity relationship for HF-1 steel.

Figure 12 gives the Hugoniot stress and pressure relationships for HF-1 steel. Equation (C-22) of Appendix C was used to transform the linear shock velocity-particle velocity relationship into the stress-compression relationship. The compression $\mu = V_0/V - 1$ where V_0 and V are initial and final specific volumes, respectively. The stress relationship is valid above the elastic limit compression $\mu_e = 0.0087$. In the elastic region the stress is given by $\sigma_H = 270 \mu / (1 + \mu)$. At the elastic limit compression μ_e , the stress is $\sigma_e = 2.3$ GPa. The HF-1 steel hydrostat was obtained by subtracting the deviator stress $\sigma_D = 0.91$ GPa from the stress relationship. The hydrostat is part of the input data for the SRI computer programs. The Armco iron hydrostat¹³ that was used in the computer programs is shown in Figure 12 for comparison with the HF-1 steel hydrostat.

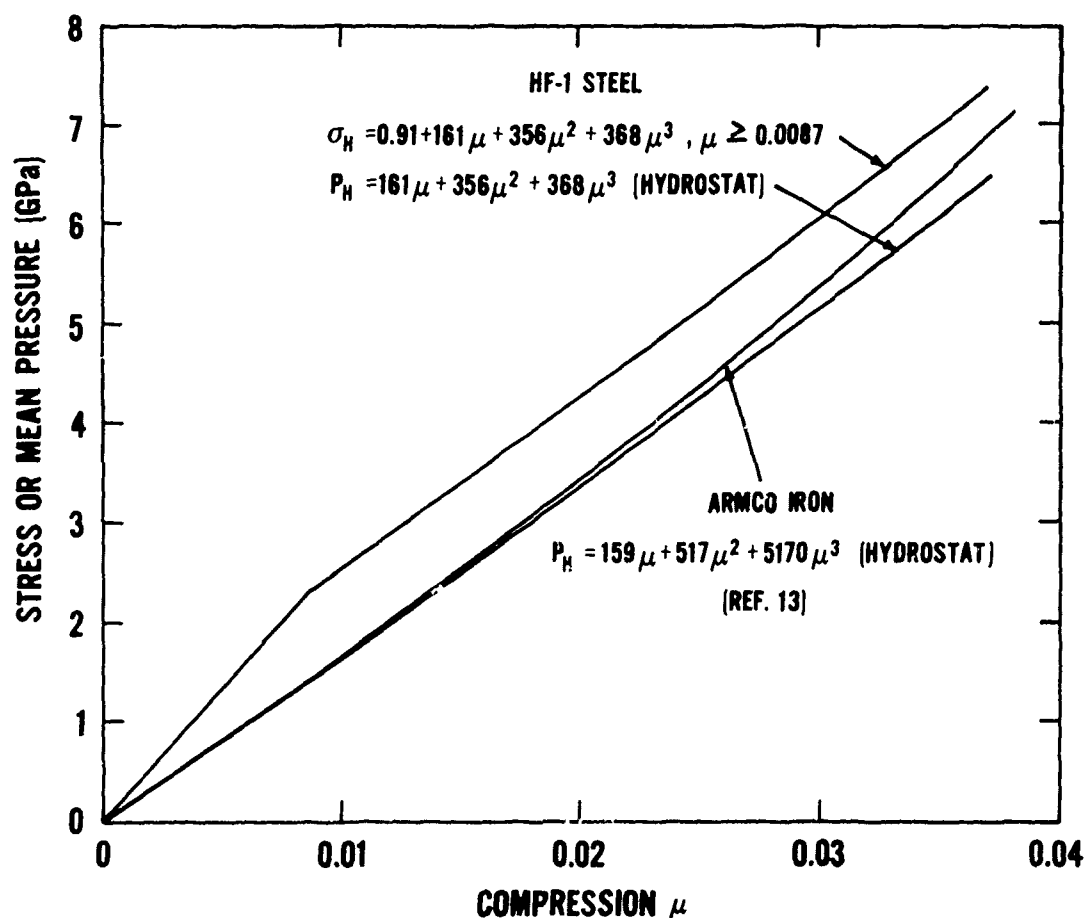


Figure 12. Stress-compression and pressure-compression relationships for HF-1 steel.

V. DYNAMIC FRACTURE EXPERIMENTS

A series of spall fracture experiments has been performed for heat treatments A and B of HF-1 steel. The purpose of the experiments was to obtain a quantitative measure of fracture damage in this material for use in calculating dynamic fracture parameters. The procedure is as follows. Differing amounts of spall fracture are produced in the specimens under known impact conditions. The specimens are soft recovered, sectioned on a diameter, and polished to reveal the microscopic spall fracture. The numbers of cracks, their lengths, and orientations with respect to the impact plane are digitized. The surface distributions are converted to volume distributions using the SRI statistical transformation computer program BABS3.^{14,15}

Figure 13 shows the muzzle region of the gas gun for a spall fracture experiment. The specimen is held in a stainless steel mounting ring with a low-melting-point alloy (Cerroband alloy). For spall fracture to occur, the experimental conditions must cause tensile stresses in the specimen. Figure 14 is a simplified schematic of the spall process. The impactor thickness is less than the specimen thickness. In the first step after impact, a plane shock wave propagates into both the impactor and specimen. In the next step, one wave reaches the back surface of the impactor, while the other wave continues into the specimen. The wave in the impactor is reflected as a rarefaction wave and propagates back through the impactor toward the specimen. Subsequently, a rarefaction wave moves into the specimen from its free surface. When the two plane rarefaction waves interact, the result is a tensile stress in the specimen. The tensile stress occurs because in rarefaction waves, material is accelerated in a direction opposite to the rarefaction propagation direction. If the tensile stress amplitude and duration are sufficient, spall fracture occurs. The compressive stress amplitude is determined from the impact velocity and the Hugoniot equation of state of the materials used. The stress duration is controlled by the thickness of the impactor.

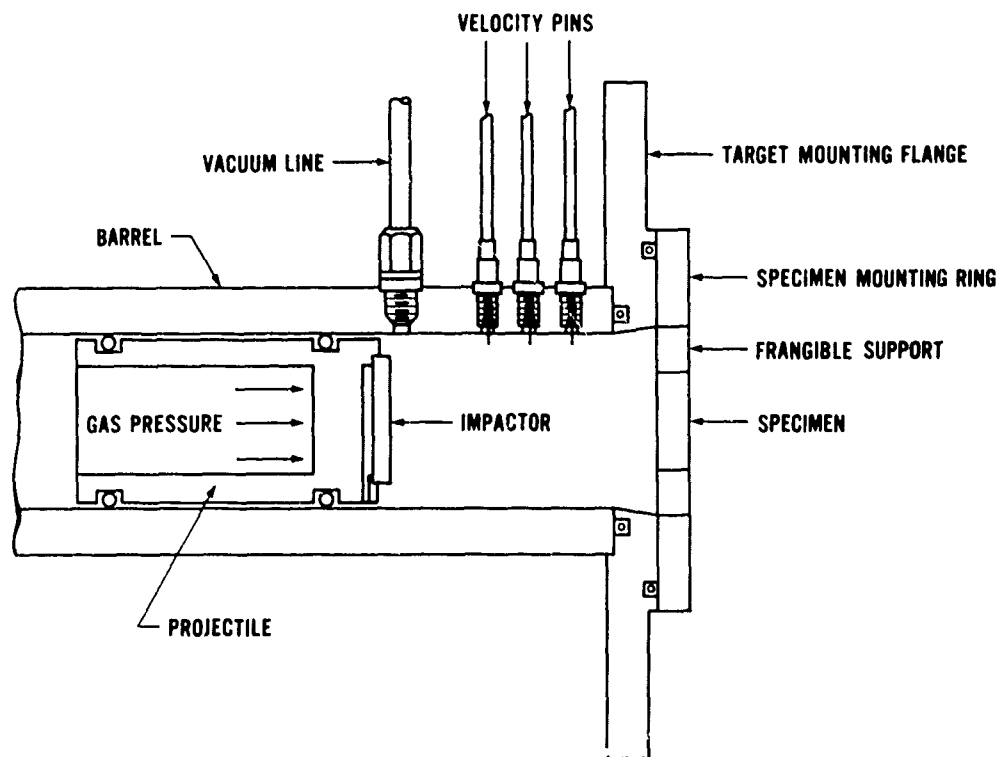


Figure 13. Schematic of muzzle region of gas gun for a spall fracture experiment.

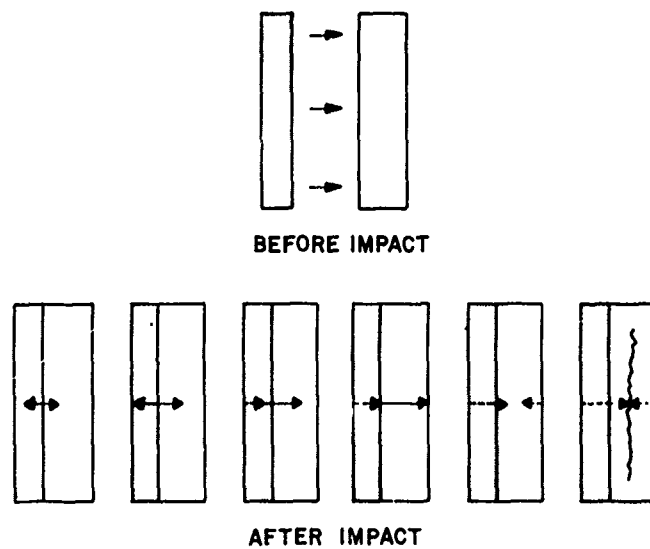


Figure 14. Simplified schematic of the spall fracture process. After impact the time sequence of wave interactions is shown from left to right. The solid and dashed lines indicate the propagation of compression and rarefaction waves, respectively.

When performing the spall fracture experiments, the impacted specimen is soft recovered to minimize any unintentional damage.¹⁶ Figure 15 shows the operation of the soft recovery system. The system consists of a steel box mounted on a track and a rag cage. The box is filled with laminated sheets of plywood. A hole through the plywood core is larger than the specimen diameter but smaller than the diameter of the impactor and projectile. Figure 15(a) shows conditions prior to impact. Figure 15(b) shows conditions shortly after impact. The projectile and impactor are caught in the separator box, and the box moves along the track as momentum is transferred to it. The specimen passes unhindered through the separator box and moves toward the rag cage. In Figure 15(c) the box is stopped by shock absorbers at the end of the track, and the specimen is soft recovered in the rags. The recovered specimen is sectioned along a diameter, mounted, and metallographically polished to reveal the crack distribution as schematically shown in Figure 16.

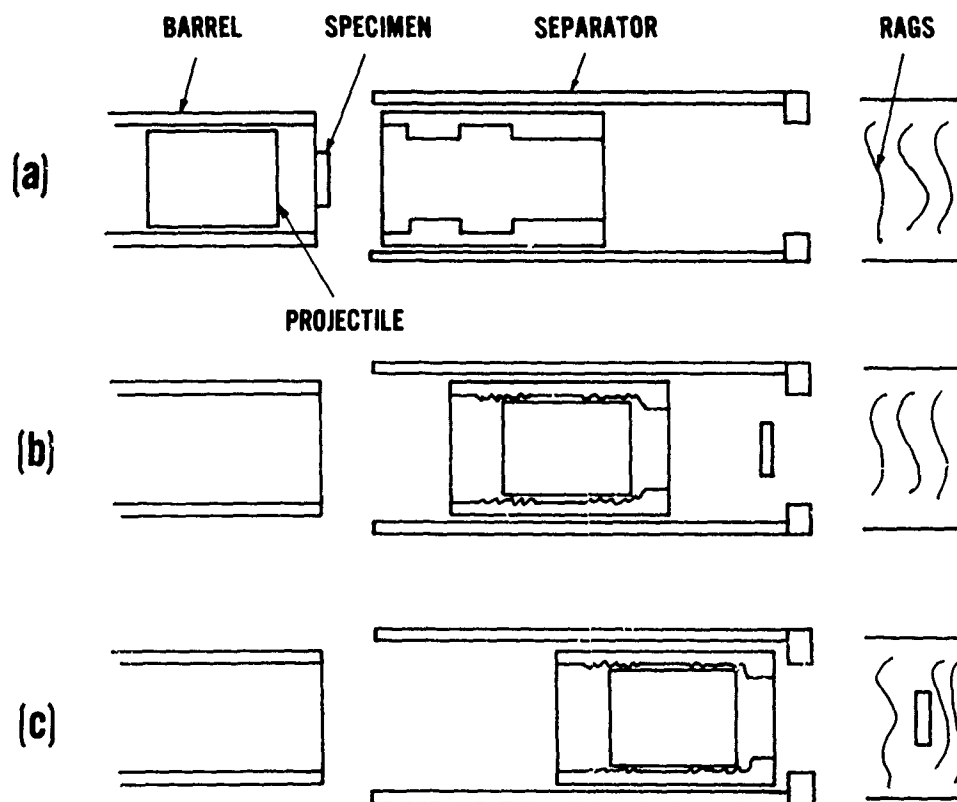


Figure 15. Schematic of soft recovery technique. (a) Before impact. (b) In-flight capture of projectile and impactor. (c) Soft recovery of specimen.

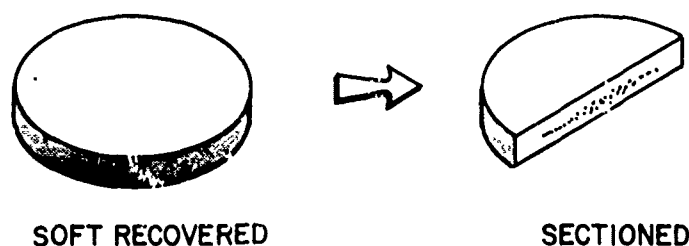


Figure 16. Schematic of sectioned specimen to reveal fracture damage.

A summary of the spall fracture experiments performed for HF-1 steel is presented in Table 6. Twelve experiments were performed for heat treatment A material, and eleven experiments were performed for heat treatment B material. The impactor disks were nominally 1.15-, 1.59-, and 2.37-mm thick. The specimen disks were nominally 3.18- and 6.35-mm thick. The impactor velocities ranged from 0.120 to 0.276 km/s. The last column of the table gives a qualitative degree of fracture damage for the specimens as determined by microscopic observation. Typical compressive stress amplitudes ranged from about 2 to 5 GPa, and typical stress durations were fractions of a microsecond.

To obtain the crack distributions the sectioned specimens are first macrophotographed at about 5X magnification using a Bausch and Lomb L camera. During this procedure it is very important to illuminate the specimen with diffuse light so that all the cracks are visible in the photograph. Appendix D contains these photographs for all the sectioned specimens of HF-1 steel. Figures 17 and 18 show the effect of increasing impactor velocity on the specimen fracture damage for heat treatments A and B of HF-1 steel, respectively. For these shots the impactor and specimen thicknesses were 2.37 and 6.35 mm, respectively. The specimens in Figures 17(a) and 18(b) were impacted at the same velocity. The increased fracture damage shown in Figure 18(b), compared with Figure 17(a), suggests that the fracture threshold stress is less for heat treatment B material than heat treatment A material.

Table 6. Summary of spall fracture experiments for HF-1 steel.

Shot No. ^{a,b}	Heat Treatment	Initial Impactor Diameter (mm)	Initial Impactor Thickness ^c (mm)	Initial Impactor Density ^d (Mg/m ³)	Initial Specimen Diameter (mm)	Initial Specimen Thickness ^e (mm)	Initial Specimen Density ^d (Mg/m ³)	Specimen Thickness After Soft Recovery ^e (mm)	Impactor Velocity (km/s)	Qualitative Degree of Specimen Damage
95	A	35.59	2.369	7.776	27.96	6.312	7.779	6.312	0.130	Incipient
110	A	35.59	2.371	7.774	27.96	6.348	7.773	6.359	0.149	Light
98	A	35.58	2.371	7.764	27.94	6.349	7.777	6.374	0.160	Medium
92	A	35.57	2.372	7.765	18.89	6.336	7.771	6.358	0.180	Medium
91	A	35.58	2.373	7.763	27.97	6.342	7.772	6.359	0.183	Medium
90	A	35.59	2.370	7.774	27.93	6.351	7.768	6.391	0.191	Heavy
94	A	35.57	2.369	7.777	27.92	6.358	7.777	6.485	0.200	Heavy
89 ⁸	A	35.59	1.609	7.697	27.91	3.179	7.773	No measurement	0.120	No Damage
113	A	35.59	1.596	7.761	27.95	3.189	7.768	3.200	0.202	Medium
88	A	35.59	1.596	7.755	28.17	3.190	No measurement	—	0.276	Complete Separation
111	A	35.56	1.156	7.772	27.96	3.185	7.773	3.192	0.193	Light
112	A	35.59	1.159	7.753	27.95	3.192	7.765	3.202	0.204	Medium
134	A	35.59	2.373	7.768	27.97	6.350	7.770	6.403	0.0937	Medium
145	B	35.58	2.375	7.768	27.96	6.353	7.773	6.360	0.116	Medium
144	B	35.56	2.372	7.765	27.96	6.353	7.771	6.444	0.148	Heavy
143	B	35.59	2.374	7.769	27.96	6.350	7.772	6.462	0.169	Heavy
142	B	35.58	2.374	7.772	27.95	6.358	7.773	6.568	0.191	Heavy
150	B	35.57	1.577	7.771	27.99	6.355	7.773	6.393	0.152	Medium
148	B	35.57	1.579	7.762	27.99	3.183	7.752	3.193	0.172	Light
149	B	35.59	1.580	7.760	27.95	3.183	7.765	3.239	0.194	Medium
147 ⁸	B	35.59	1.146	7.750	27.99	3.184	7.766	3.185	0.147	No Damage
146	B	35.59	1.158	7.741	27.97	3.180	7.767	2.93	0.167	Medium
151	B	35.59	1.150	7.754	27.97	6.360	7.772	6.392	0.190	Medium

^a The septa ator-box plywood core used for separating the projectile and impactor disk from the specimen disk consisted of 22 pieces of 12.7-mm-thick plywood. For the majority of the shots the plywood arrangement from the entrance hole to the exit hole was as follows: 16 pieces alternating between 76- and 35-mm-diameter holes, and 4 pieces with 35-mm-diameter holes.

^b Except for Shots 88 and 89, the perpendicularity of the mounted impactor disk face with respect to the side of the projectile was measured. The average value of the deviation from perpendicularity was 0.005 mm over the 35.6-mm-diameter face of the disk, this gives an angular deviation of 140 μ rad.

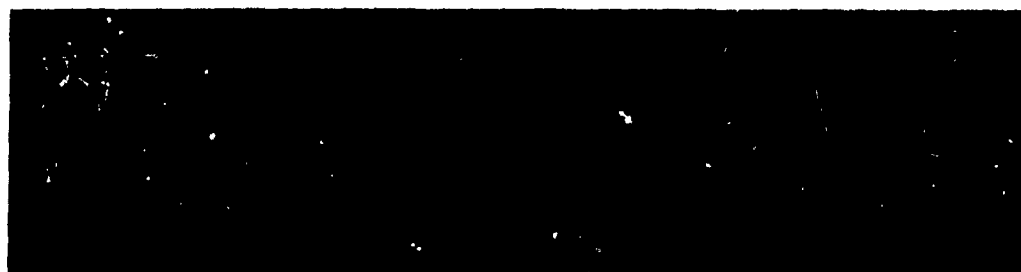
^c The surfaces were flat and parallel to within 0.003 mm.

^d The average value for the impactor and specimen densities is 7.768 Mg/m³.

^e The average specimen thickness for a 10-mm-diameter region in the center of the disk.

^f Average of two measurements, the estimated uncertainty is 1% or less.

^g Although no damage was produced in planes parallel to the specimen faces in Shots 89 and 147, a crack perpendicular to the faces occurred in the specimens. The crack length was about 65% of the specimen thickness for each shot.



(a) Shot 110, 0.149 km/s.



(b) Shot 98, 0.160 km/s.



(c) Shot 90, 0.191 km/s.



4 mm

(d) Shot 94, 0.200 km/s.

Figure 17. Effect of increasing impactor velocity on fracture damage for 6.35-mm-thick HF-1 steel specimens with heat treatment A. The impactor thickness was 2.37 mm. The bottom edge of each specimen is the impact surface.



(a) Shot 154, 0.094 km/s.



(b) Shot 144, 0.143 km/s.



(c) Shot 143, 0.169 km/s.



(d) Shot 142, 0.191 km/s.

Figure 18. Effect of increasing impactor velocity on fracture damage for 6.35-mm-thick HF-1 steel specimens with heat treatment B. The impactor thickness was 2.37 mm. The bottom edge of each specimen is the impact surface.

For crack counting, each 5X photograph was enlarged again and arranged together to form a 24X composite photograph of the specimen surface. Cracks were marked as straight-line segments on a clear plastic sheet that was placed over the photograph. Using this procedure the original crack-counting photograph was not marked. Only cracks in the approximate central one-third region of the specimen were counted. This was done to ensure that the measured cracks were not influenced by stress relief wave effects from the edge of the specimen. The general crack counting criterion used was to count the longest segment as a crack and each intersecting segment as a crack. If the intersecting crack extended through the primary crack, its length was taken as extending from tip to tip. If the intersecting crack stopped at the primary crack or appeared to extend through the primary crack with a relative displacement, each segment was treated as an individual crack. Table 7 summarizes the crack measurements for the spall fracture specimens of HF-1 steel. The specimen magnification factors, region of damage, and number of measured cracks are listed for each shot.

The cracks for each specimen were digitized by mounting the plastic sheet with the indicated cracks on a digitizer table (Computer Equipment Corporation Model TF-10C Digitizer) to determine the coordinates of the cracks. The digitized crack data was then used as input to a computer program that divided the damage region into a series of zones parallel to the specimen faces. The average zone width was 0.40 mm. The length, orientation, and location of the midpoint of each crack relative to the impact face was calculated. Each crack was assigned to a zone based on its midpoint. This computer program was written to interface with the SRI BABS3 program that calculated surface and volume crack-size distributions for each damage zone.

The parameters N_0 and R_1 are obtained for each damage zone containing cracks by fitting the equation $N_g = N_0 \exp(-R/R_1)$ to the volume crack-size distribution. Here N_g is the number of cracks per unit volume with radius greater than R , N_0 is the total number of cracks per unit volume, and R_1 is the average crack radius. The zone of maximum damage is taken as that zone in which $N_0 R_1^2$ is a maximum. The N_0 and R_1 values for the zone of maximum damage are used for each specimen to calculate the dynamic fracture parameters. Appendix E contains computer-generated plots for each sectioned specimen of HF-1 steel (excluding the no-damage Shots 89 and 147). Each figure shows plots of the digitized cracks, and the computed surface and volume crack-size distributions for each damage zone. Appendix F lists the digitized crack coordinates for all the counted cracks. Table 8 summarizes the N_0 and R_1 values for each spall fracture specimen of HF-1 steel. The N_0 and R_1 values determined for Shots 95 and 88 were not used for calculating dynamic fracture parameters.

Table 7. Summary of crack measurements for spall fracture specimens of HF-1 steel.

Shot No.	Heat Treatment	Ratio of Specimen Thickness After Soft Recovery to Initial Specimen Thickness R	Specimen Thickness		Specimen Length L	Region of Damage (mm)		Number of Digitized Cracks ^e
			Magnification from Crack Counting Photograph ^a W	Magnification from Crack Counting Photograph ^b L		Length ^c	Width ^d	
95 ^f	A	1.000	23.5	23.8	10.16	2.61	8	
110	A	1.002	23.6	23.8	10.16	2.14	38	
98	A	1.004	23.7	23.9	10.16	0.04	89	
92	A	1.003	23.6	23.8	6.86	1.82	40	
91	A	1.003	23.5	23.8	10.16	3.12	84	
90	A	1.006	23.5	23.8	10.16	3.10	153	
94	A	1.020	23.6	23.9	10.16	2.44	143	
89 ^g	A	—	—	—	—	—	0	
113	A	1.003	23.7	23.9	10.16	1.55 ^h	107	
88	A	1.00 ⁱ	23.5 ^j	23.8 ^j	10.16	0.49 ^j	23 ^j	
111	A	1.003	23.5	23.8	10.16	0.86	65	
112	A	1.003	23.6	23.8	10.16	1.33	95	
154	B	1.008	24.1	24.2	10.16	0.95	50	
145	B	1.001	23.6	23.6	10.16	2.00	58	
144	B	1.014	23.7	23.6	10.16	3.37	209	
143	B	1.018	23.5	23.4	10.16	4.18	281	
142	B	1.033	23.5	23.1	10.16	3.08	261	
150	B	1.004	23.7	23.8	10.16	1.63	74	
148	B	1.003	23.8	24.0	5.94	0.86	25	
149	B	1.017	23.3	23.2	10.16	1.07	104	
147 ^k	B	1.060	—	—	—	—	0	
146	B	1.004	23.6	23.9	10.16	1.89	268	
151	B	1.005	23.5	23.7	10.16	2.61	170	

^a The photographic magnification is given by $P = \frac{L}{W}$ (Fig. 1). P_p is the specimen thickness in the center of the crack counting photograph, P_p is the measured specimen thickness after soft recovery (Table 6), and $P = 0.987$ is a factor that accounts for the slight tilting of the specimen damage plane about the specimen diameter during the initial photographing of the damage region. The width magnification is given by $W = PFR$. The factor R , which is given in this table, changes the specimen thickness after impact to that before impact because the crack widths were neglected in the damage distribution analysis.

^b The length magnification L is given by the photographic magnification P .

^c The damage region was taken to be approximately the central one-third of the sectioned specimen surface. This was done to ensure that the measured cracks were not influenced by stress relief waves from the edge of the specimen. A crack was considered to be in the central region if its center was in this region. In Shot 92 the length of the damage region was less than that for the majority of shots since the specimen diameter was only 18.9 mm. In Shot 148 the length of the damage region was only 5.94 mm because cracks were produced only on the approximate central one-fifth of the sectioned specimen surface.

^d Determined from the end points of the two cracks that define the width of the region.

^e For some of the shots for both heat treatments some cracks occurred along the stinger impurities in the material. (Stinger impurities are elongated impurity regions produced during the material fabrication process. For these specimens the impurities were parallel to the shock wave propagation direction). To determine the importance of the stinger cracks, dynamic fracture parameters were also obtained for heat treatment A material with them excluded. Forty-four stinger cracks were measured for heat treatment A material, three for Shot 92, four for Shot 91, three for Shot 90, fourteen for Shot 94, nine for Shot 113, and nine for Shot 112.

^f Due to the small number of measured cracks for this shot, the computer-generated damage distributions were not used for determining dynamic fracture parameters.

^g Cracks were not measured for the no-damage Shots 89 and 147.

^h The width of the damage region is 1.22 mm if the nine stinger cracks for this shot are not included.

ⁱ For this full spall shot the factor R was taken to be 1.00 and the photographic magnification P was taken as the average value for the heat treatment A shots.

^j Only cracks in one half of the specimen (the impact surface piece) for this full-spall shot were digitized. Since cracks for the entire damage region were not measured, the computer-generated damage distribution for this shot was not used in the data analysis for determining the dynamic fracture parameters.

Table 8. Summary of experimental volume crack-size distribution parameters for spall fracture specimens of HF-1 steel.^a

Shot No.	Heat Treatment	Number of Cracks per Unit Volume N_0 ($10^4/\text{cm}^3$)	Average Crack Radius R_1 (μm)	Distance from Specimen Impact Surface to Midpoint of Zone of Maximum Damage (mm)
95 ^b	A	0.03	-1822.2	2.73
110	A	0.74	150.3	4.04
98	A	2.55	121.1	3.96
92	A	2.89	103.9	4.40
91	A	8.49	54.2	4.00
90	A	4.96	99.7	4.19
94	A	7.37	94.2	4.17
89 ^c	A	—	—	—
113	A	7.92	66.6	1.84
88 ^d	A	3.92	107.6	1.51
111	A	5.36	75.5	2.19
112	A	7.48	84.7	2.09
154	B	1.45	200.3	3.15
145	B	1.24	190.5	3.73
144	B	4.26	127.0	3.36
143	B	7.10	88.7	4.58
142	B	3.68	132.5	4.32
150	B	4.25	114.9	4.22
148	B	4.58	99.1	2.01
149	B	6.64	97.7	1.58
147 ^c	B	—	—	—
146	B	9.64	99.3	2.03
151	B	6.32	115.8	4.51

^a The parameters N_0 and R_1 were obtained for each damage zone of each specimen by fitting the equation $N_g = N_0 \exp(-R/R_1)$ to the volume crack-size distribution. Here N_g is the number of cracks per unit volume with radius greater than R . Plots of the volume crack-size distributions for each damage zone of each specimen are given in Appendix E. The parameters N_0 and R_1 listed in this table are the values for the zone of maximum damage.

^b This shot was not used for determining dynamic fracture parameters due to the small number of measured cracks, hence, the unrealistic negative value for the average crack radius.

^c Cracks were not measured for the no-damage Shots 89 and 147.

^d This full-spall shot was not used for determining dynamic fracture parameters. Only cracks in one half of the specimen were digitized.

Scanning electron microscope (SEM) photographs of the fracture surface for the full-spalled heat treatment A specimen in Shot 88 are shown in Figure 19. These micrographs can be compared with the fracture surface for the low-strain-rate heat treatment A transverse tensile specimen in Figure 7(a). Micrographs of cracks were made for some of the sectioned specimen surfaces in order to obtain a detailed comparison of the spall fracture for the two heat treatments of HF-1 steel. The specimens were etched with either 2% Nital or 4% Picral solutions. Figures 20 and 21 are crack micrographs for the heat treatment A specimens in Shots 110 and 90, respectively. Figures 22 and 23 are crack micrographs for the heat treatment B specimens in Shots 144 and 142, respectively. The impactor velocity for Shots 110 and 144 was 0.149 km/s. The impactor velocity for Shots 90 and 142 was 0.191 km/s. Cracks occurred primarily through the grain boundary cementite for heat treatment B material, although some cracks occurred in the pearlite microstructure.

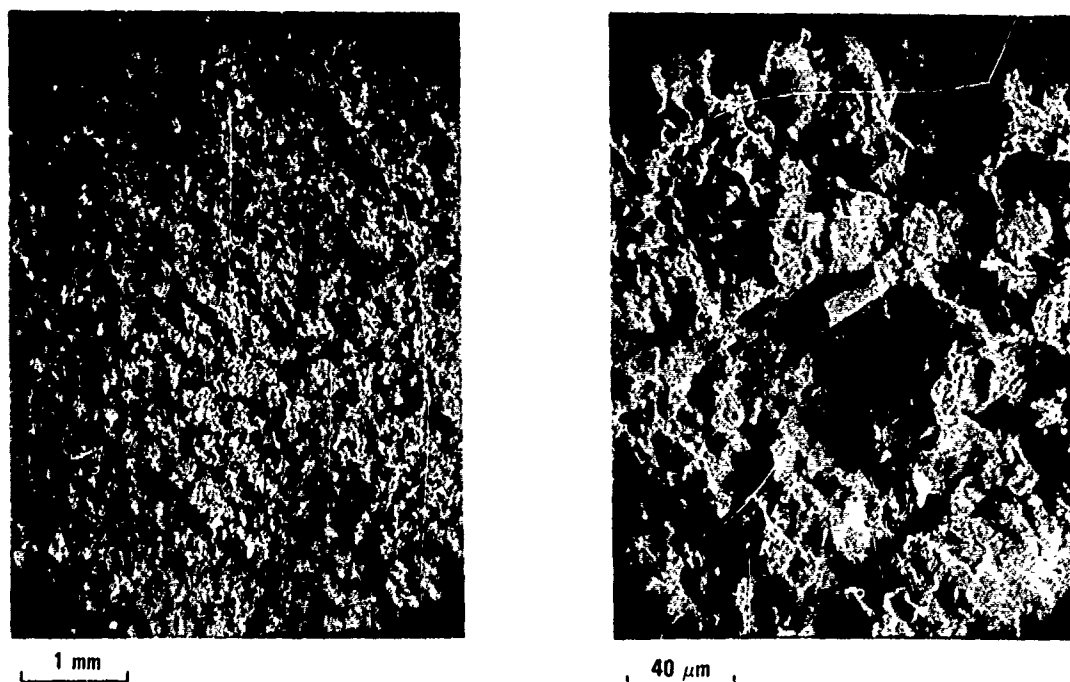
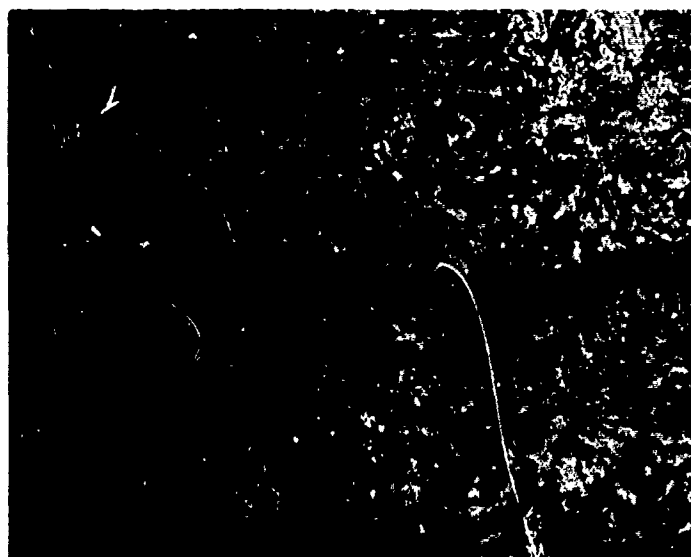


Figure 19. SEM micrographs of the fracture surface for the full-spalled HF-1 steel, heat treatment A, specimen in Shot 88.



200 μm

(a)



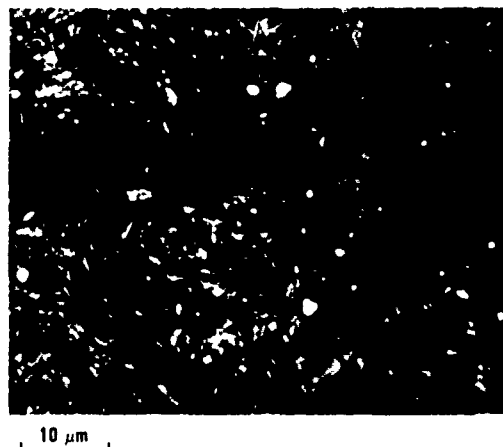
25 μm

(b)

Figure 20. Micrographs of cracks for the HF-1 steel, heat treatment A, specimen in Shot 110.
(a) View of multiple cracks. (b) High-magnification view of a crack.



(a)

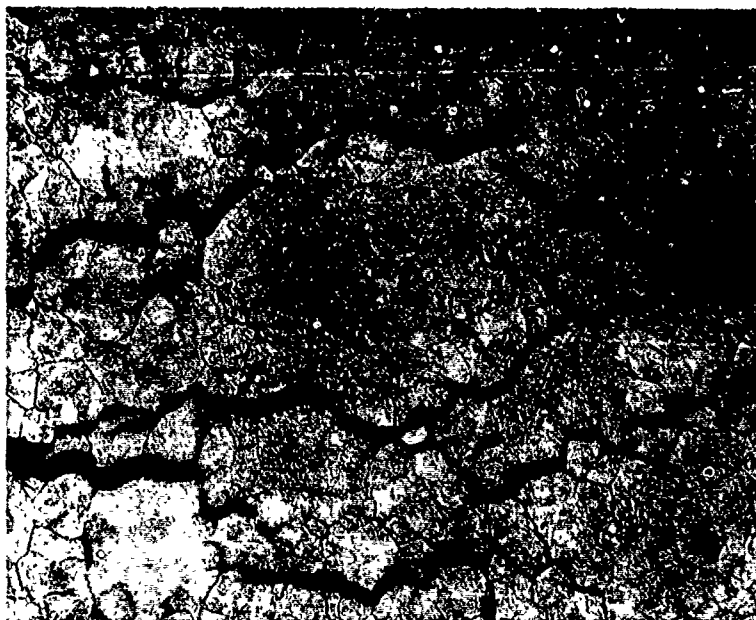


(b)



(c)

Figure 21. Micrographs of cracks for the HF-1 steel, heat treatment A, specimen in Shot 90. (a) View of multiple cracks. (b) High-magnification view of a crack. (c) High-magnification view of cracks around material impurity.

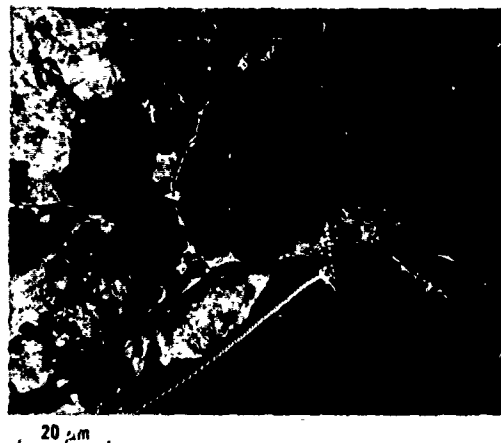


200 μm

Figure 22. Micrograph of cracks for the HF-1 steel, heat treatment B, specimen in Shot 144. Cracks occurred primarily through the grain boundary cementite.



(a)



(b)



(c)

Figure 23. Micrographs of cracks for the HF-1 steel, heat treatment B, specimen in Shot 142. (a) View of multiple cracks. (b) High-magnification view of grain boundary cementite cracks extending into an adjacent grain. (c) High-magnification view of grain boundary crack.

VI. COMPUTATION OF DYNAMIC FRACTURE PARAMETERS

In this section the dynamic fracture parameters are calculated for heat treatments A and B of HF-1 steel. Initially, PUFF 8 computations assuming no fracture damage were made for the twelve heat treatment A and the eleven heat treatment B spall fracture experiments of the last section. The material properties determined in the previous sections were used as input in the computations. For a computation, the impactor thickness was divided into 8 computational cells, numbered 1 through 8, beginning at the impactor free surface. The specimen thickness was divided into 20 computational cells, numbered 10 through 29, beginning at the specimen impact surface. The initial maximum tensile stress σ_m for each specimen was determined from these computations. (Compressive stresses have positive values; tensile stresses have negative values.) A maximum tensile stress of -2.5 GPa was obtained for the heat treatment A specimen in Shot 95. This value was taken as the nucleation threshold stress σ_{no} for heat treatment A material, since the experimental crack density for this shot was only 300 cracks/cm³ (see Table 8), a value considered negligible.¹⁷ For the no-damage Shot 89, a maximum tensile stress of -2.4 GPa was calculated, a value less than the nucleation threshold stress. For heat treatment B material, a shot near the threshold stress was not obtained for the 2.37-mm-thick impactor disks. All the experimental crack density values in Table 8 for this heat treatment are larger than 1000 cracks/cm³, except Shot 147, which was a no-damage shot for a 1.15-mm-thick impactor. In Shot 154 (the lowest velocity shot) a 6.35-mm-thick specimen was impacted at 0.094 km/s with a 2.37-mm-thick impactor. The maximum tensile stress for this shot was -2.1 GPa. The nucleation threshold stress for heat treatment B material was estimated by plotting the experimental crack density values from Table 8 versus the maximum tensile stress values for the no-damage PUFF 8 computations. The stress-axis intercept of this plot was -1.8 GPa. This value was therefore taken as the nucleation threshold stress for heat treatment B material. The growth threshold stress σ_{go} for both heat treatments of HF-1 steel was taken as -0.1 GPa.⁶ The nucleation and growth threshold stress values, σ_{no} and σ_{go} , respectively, are two of the six dynamic fracture parameters. To obtain initial estimates for the remaining parameters, it is necessary to obtain estimates for the spall fracture nucleation and growth times, Δt_n and Δt_g , respectively, for each of the shots for the zone of maximum stress. The nucleation time is the time interval for which the initial tensile stress pulse exceeds the nucleation threshold stress. The growth time is the time interval for which the initial tensile stress pulse exceeds the nucleation threshold stress until it decreases to the growth threshold stress.

The nucleation rate for cracks \dot{N} and the growth rate for cracks \dot{R} are given, respectively, by

$$\dot{N} = \dot{N}_0 \exp \left[\frac{\sigma - \sigma_{no}}{\sigma_1} \right] , \quad (1)$$

and

$$\dot{R} = T_1 (\sigma - \sigma_{go}) R , \quad (2)$$

where σ is the applied tensile stress, \dot{N}_0 is the nucleation threshold rate, σ_1 is the nucleation sensitivity parameter, R is the crack radius, and T_1 is the growth coefficient. Integrating Equation (2) gives

$$\ln R = \ln R_0 + T_1 \sigma t , \quad (3)$$

where R_0 is the nucleation size parameter. Here the growth threshold stress σ_{go} is assumed to be negligible. \dot{N}_0 , σ_1 , R_0 , and T_1 are the remaining four dynamic fracture parameters.

A first estimate for the nucleation parameters is obtained by plotting the values $\ln(N_0/\Delta t_n)$ versus the stress above threshold $\sigma_m - \sigma_{no}$ for each of the shots for each heat treatment. The N_0 values were obtained from Table 8, and the σ_m and Δt_n values were obtained from the initial no-damage PUFF computations. A straight-line least-squares fit to the nucleation data gives initial estimates for the intercept \dot{N}_0 and slope σ_1^{-1} . A first estimate for the growth parameters is obtained by plotting the values $\ln R_1$ versus $\sigma_m \Delta t_g$ for each of the shots for each heat treatment. The R_1 values were obtained from Table 8, and the Δt_g values were obtained from the initial no-damage PUFF computations. A straight-line least-squares fit to the growth data gives initial estimates for the intercept R_0 and the slope T_1 . Data for Shots 95, 89, 88, and 147 was not used in these estimates or any later computations.

The parameters σ_{no} and σ_{go} and the initial estimates for the parameters \dot{N}_0 , σ_1 , R_0 , and T_1 are then used in a first iteration of PUFF 8 computations using the BFRAC22 subroutine, which allows fracture to occur. In these computations, crack densities N_0 and radii R_1 are computed for each specimen cell in which fracture occurs. The cell of maximum damage for a specimen is taken as the cell in which the computed value $N_0 R_1^2$ is a maximum at a time when the tensile pulse has decreased to the ~ 0.1 GPa threshold growth stress. The cell of maximum damage is not necessarily the same as the cell of maximum stress for the initial no-damage PUFF computations. Using the results of these computations, nucleation and growth plots are again constructed. Straight-line least-squares fits to the experimental and computational data are obtained for each plot. The N_0 and R_1 values from Table 8 were again used to construct the $\ln(N_0/\Delta t_n)$ and $\ln R_1$ values, respectively for the experimental curves. For the computational curves, the computed N_0 and R_1 values were used. A table is then constructed consisting of the initial set of dynamic fracture parameters \dot{N}_0 , σ_1 , R_0 , and T_1 and the experimental and computed intercept and slope values from the nucleation and growth plots. Ratios of the corresponding experimental and computed intercept and slope values are determined. A new set of fracture parameters is obtained by multiplying the appropriate parameter by the appropriate ratio. The new set of dynamic fracture parameters is then used in a second series of PUFF 8 computations using the BFRAC22 subroutine. Nucleation and growth plots are again obtained and then a new set of dynamic fracture parameters. This iterative process is continued until the experimental and computed nucleation and growth curves agree. The dynamic fracture parameters used for this final iteration are then taken as the dynamic fracture parameters for the material.

Six iterations with the PUFF 8 computer program using the BFRAC22 subroutine were performed to obtain the dynamic fracture parameters for heat treatments A and B of HF-1 steel. Tables 9 and 10 give the experimental and computed nucleation and growth values that were obtained using the final set of dynamic fracture parameters for heat treatments A and B, respectively. These values are plotted in Figures 24 and 25. Straight-line least-squares fits to the experimental and computed values are shown in the figures. The experimental and computed intercept and slope values for the heat treatment A nucleation rate curves in Figure 24(a) are 15.1 and 16.9 cracks/cm³-ns and -12.9 and -12.0 GPa⁻¹, respectively. The experimental and computed intercept and slope values for the heat treatment A growth curves in Figure 24(b) are 68.3 and 68.4 μm and -0.137 and -0.141 GPa⁻¹ μs^{-1} , respectively. The experimental and computed intercept and slope values for the heat treatment B nucleation rate curves in Figure 25(a) are 12.3 and 12.5 cracks/cm³-ns and -5.56 and -5.54 GPa⁻¹, respectively. The experimental and

Table 9. Summary of experimental and computed nucleation and growth values for spall fracture specimens of HF-1 steel with heat treatment A.^a

Shot No.	Distance from Specimen				Time at which Tensile Stress Exceeds				Tensile Stress above Threshold				Computed Nucleation Rate			
	Experimental Crack Density ^c N_0 ($10^3/\text{cm}^3$)	Experimental Average Crack Radius ^c R_1 (μm)	Cell of Maximum Damage ^d	Impact Surface to Midpoint of Cell of Maximum Damage ^d (mm)	Computed Crack Density N_0 ($10^3/\text{cm}^3$)	Computed Average Crack Radius R_1 (μm)	Time of Maximum Compressive Stress (μs)	Maximum Compressive Stress (GPa)	Time of Maximum Tensile Stress (μs)	Maximum Tensile Stress (GPa)	Nucleation Time ^e Δt_n (μs)	Growth Time ^f Δt_g (μs)	Product $\sigma_m \Delta t_g$ (GPa μs)	Experimental Nucleation Rate $N_0/\Delta t_n$ ($\text{no./cm}^3\text{-ns}$)	Computed Nucleation Rate $N_0/\Delta t_n$ ($\text{no./cm}^3\text{-ns}$)	
95 ^b	—	—	—	—	—	—	—	—	—	—	—	—	—	—	—	—
110	0.74	150.3	23	4.28	1.23	91.3	—	3.09	1.16	-2.58	1.89	0.27	-0.08	-2.31	26.9	44.7
98	2.55	121.1	23	4.29	1.78	94.3	1.16	3.28	1.16	-2.61	1.86	0.29	-0.11	-2.46	86.8	60.6
92	2.89	103.9	23	4.23	3.88	102.2	1.16	3.64	1.16	-2.66	1.83	0.34	-0.16	-2.83	84.7	114
91	8.49	54.2	23	4.28	4.19	103.5	1.16	3.69	1.16	-2.67	1.83	0.35	-0.17	-2.89	24.5	121
90	4.96	99.7	23	4.29	4.98	106.8	1.16	3.84	1.16	-2.66	1.83	0.36	-0.18	-3.04	139	140
94	7.37	94.2	23	4.29	5.96	110.2	1.15	4.00	1.15	-2.70	1.83	0.36	-0.20	-3.22	203	164
89 ^b	—	—	—	—	—	—	—	—	—	—	—	—	—	—	—	—
113	7.92	66.5	20	1.67	7.84	89.7	0.48	4.07	0.48	-2.71	1.02	0.33	-0.21	-1.29	237	235
88 ^b	—	—	—	—	—	—	—	—	—	—	—	—	—	—	—	—
111	5.36	75.5	24	2.31	5.95	80.5	0.58	3.76	0.58	-2.76	0.90	0.17	-0.26	-1.52	315	349
112	7.48	84.7	23	2.15	7.18	83.6	0.55	4.02	0.55	-2.73	0.90	0.21	-0.23	-1.57	349	335

^a These computed nucleation and growth values for heat treatment A material were calculated using dynamic fracture parameters (Table 11) obtained after six iterations with the PUFF 8 stress-wave computer program for planar geometry.

^b These shots were not used for determining dynamic fracture parameters. Only a few spall fracture cracks were produced in Shot 95. No cracks were measured for the no-damage PUFF 8 computations. The nucleation threshold stress for heat treatment A material was taken as -2.5 GPa, the maximum tensile stress of -2.5, -2.4, and -4.1 GPa were obtained for Shots 95, 89, and 88, respectively, from the initial no-damage PUFF 8 computations.

^c These experimental parameters were obtained from Table 8 for the zone of maximum damage for each specimen (see Appendix E).

^d The location of the cell of maximum damage does not necessarily correspond to the experimentally determined zone of maximum damage.

^e The nucleation time is the time interval that the initial tensile stress pulse exceeds the -2.5 GPa nucleation threshold stress.

^f The growth time is the time interval that the initial tensile stress pulse exceeds the -2.5 GPa nucleation threshold stress until it decreases to the -0.1 GPa growth threshold stress.

Table 10. Summary of experimental and computed nucleation and growth values for spall fracture specimens of HF-1 steel with heat treatment B.^a

Shot No.	Experimental Crack Density ^c N_0 ($10^4/\text{cm}^3$)	Experimental Average Crack Radius ^c R_1 (μm)	Cell of Maximum Damage	Distance from Impact Surface to Midpoint of Cell of Maximum Damage (mm)	Computed Crack Density N_0 ($10^4/\text{cm}^3$)	Computed Average Crack Radius R_1 (μm)	Time of Computed Crack Density and Radius (μs)	Maximum Compressive Stress (GPa)	Time of Maximum Compressive Stress (μs)	Time of Maximum Tensile Stress (μs)	Time at which Tensile Stress Exceeds Threshold ^f (μs)	Tensile Stress above Threshold ^f (GPa)	Tensile Stress Growth Product $\sigma_m \Delta t_g$ (GPa μs)	Experimental Nucleation Rate $N_0/\Delta t_g$ ($10^4/\text{cm}^3\text{-ms}$)	Computed Nucleation Rate $N_0/\Delta t_g$ ($10^4/\text{cm}^3\text{-ms}$)
154	1.45	200.3	22	3.97	1.27	120.0	2.62	2.08	0.97	-2.03	1.45	-0.23	-2.06	43.6	38.4
145	1.24	190.5	22	3.97	2.89	121.6	2.84	2.52	1.06	-2.09	1.65	-0.29	-2.57	24.9	58.1
144	4.26	127.6	23	4.29	4.26	124.3	3.01	3.07	1.16	-2.13	1.79	-0.33	-2.78	82.6	82.5
143	7.10	88.7	23	4.29	5.24	129.4	3.08	3.44	1.16	-2.18	1.79	-0.38	-2.96	137	101
142	3.68	132.5	23	4.29	6.69	137.2	3.09	3.84	1.16	-2.23	1.80	-0.43	-3.31	69.2	126
150	4.25	114.9	25	4.93	3.44	107.6	2.75	2.80	1.17	-2.14	1.56	-0.34	-2.22	113	91.3
148	4.58	99.1	21	1.83	6.36	105.4	1.53	3.52	0.51	-2.28	0.98	-0.48	-1.39	120	166
149	6.63	97.7	20	1.67	8.18	108.7	1.55	3.92	0.47	-2.31	1.00	-0.51	-1.52	148	183
147 ^b	—	—	—	—	—	—	—	—	—	—	—	—	—	—	—
146	9.64	99.3	23	2.15	5.13	99.4	1.34	3.38	0.55	-2.26	0.91	-0.46	-1.42	342	182
151	6.32	115.8	26	5.25	3.21	95.9	2.63	2.69	1.15	-2.17	1.48	-0.37	-1.53	218	111

^a These computed nucleation and growth values for heat treatment B material were calculated using dynamic fracture parameters obtained after six iterations with the PUFF 8 stress-wave computer program for planar geometry. The nucleation threshold stress for heat treatment B material was taken as 1.8 GPa. This value was estimated by taking the stress axis intercept of the plot of the experimental crack density values from this table versus the maximum tensile stress values for these shots determined from the no-damage PUFF 8 computation.

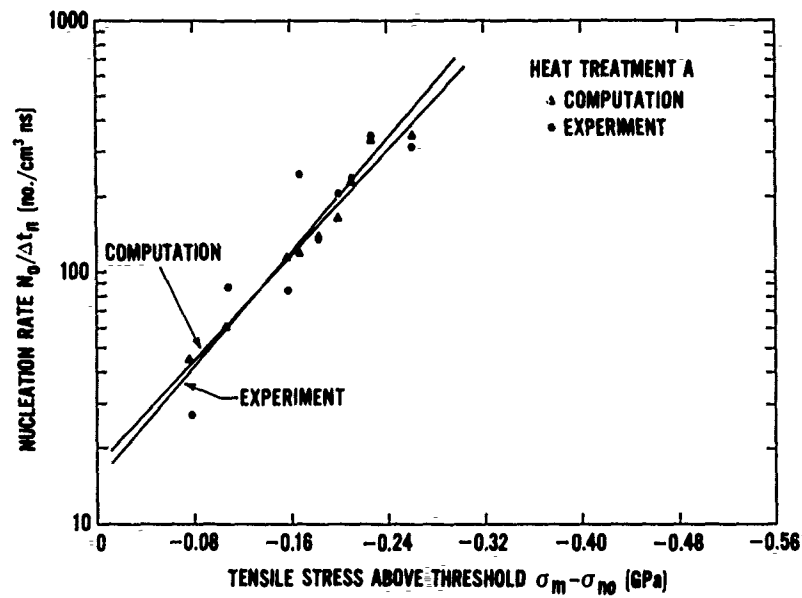
^b The no-damage Shot 147 was not used for determining dynamic fracture parameters. A maximum tensile stress of 2.7 GPa was obtained for this shot from the no-damage PUFF 8 computation.

^c These experimental parameters were obtained from Table 8 for the zone of maximum damage for each specimen (See Appendix E).

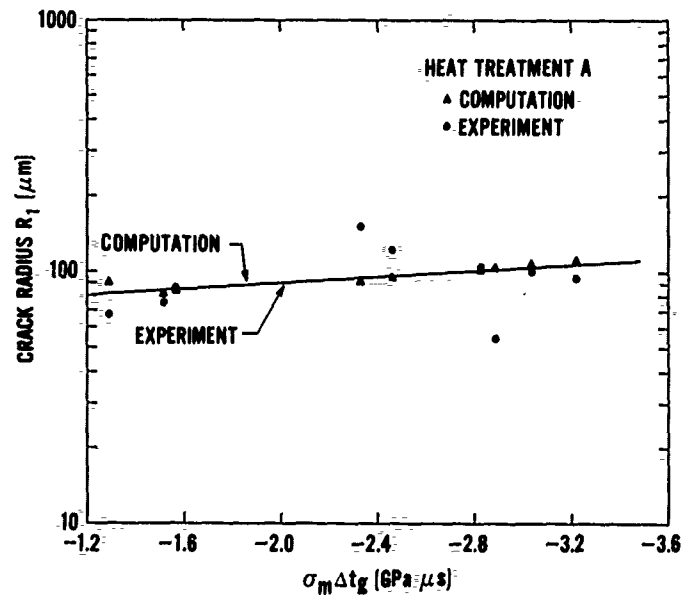
^d The location of the cell of maximum damage does not necessarily correspond to the experimentally determined zone of maximum damage.

^e The nucleation time is the time interval that the initial tensile stress pulse exceeds the 1.8 GPa nucleation threshold stress.

^f The growth time is the time interval that the initial tensile stress pulse exceeds the 1.8 GPa nucleation threshold stress until it decreases to the -0.1 GPa growth threshold stress.

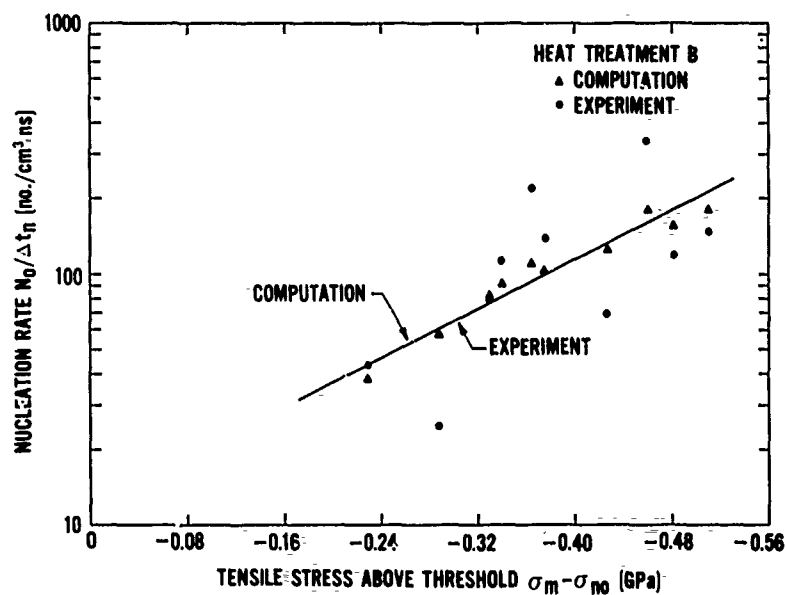


(a)

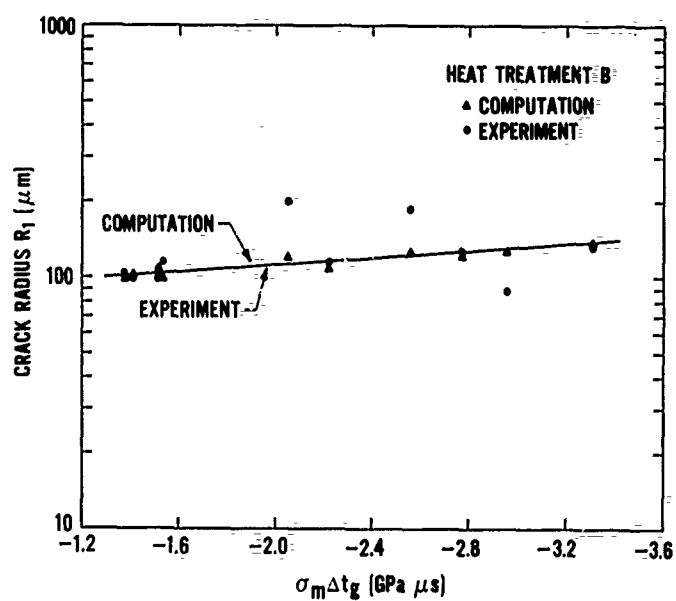


(b)

Figure 24. Experimental and computed nucleation-rate and growth curves for HF-1 steel with heat treatment A. (a) Nucleation rate curves. (b) Growth curves. The points in these plots are from Table 9 and were obtained using the final set of dynamic fracture parameters for this heat treatment of HF-1 steel in a PUFF 8 computation.



(a)



(b)

Figure 25. Experimental and computed nucleation rate and growth curves for HF-1 steel with heat treatment B. (a) Nucleation rate curves. (b) Growth curves. The points in these plots are from Table 10 and were obtained using the final set of dynamic fracture parameters for this heat treatment of HF-1 steel in a PUFF 8 computation.

computed intercept and slope values for the heat treatment B growth curves in Figure 25(b) are 82.7 and 82.8 μm and -0.148 and $-0.152 \text{ GPa}^{-1} \mu\text{s}^{-1}$, respectively. For the nucleation rate curves, all the experimental points were used in the curve fits, since considerable scatter was evident in the data. For the growth curves, the experimental points for Shots 110, 91, and 113 for heat treatment A material and the points for Shots 154, 145, and 143 for heat treatment B material were not used in the curve fits, since they were out of range of the majority of the experimental points.

Table 11 summarizes the dynamic fracture parameters for heat treatments A and B of HF-1 steel. Also shown for comparison are the previously determined dynamic fracture parameters for Armco iron.¹ For the two heat treatments of HF-1 steel, larger differences occurred in the nucleation parameters than in the growth parameters. The nucleation threshold stress is about 40% higher and the nucleation threshold rate is about 30% lower for heat treatment A material than for heat treatment B material. This suggests that heat treatment A material is a somewhat tougher material with respect to crack nucleation than heat treatment B material.

Table 11. Dynamic fracture parameters for heat treatments A and B of HF-1 steel and Armco iron.

Parameter ^a	Description	Units	Heat Treatment A of HF-1 Steel	Heat Treatment B of HF-1 Steel	Armco Iron ^b
T_1	Growth coefficient:	$\text{GPa}^{-1} \mu\text{s}^{-1}$	-0.377	-0.387	-5.5
σ_{go}	Growth threshold stress	GPa	-0.1	-0.1	-0.02
R_0	Nucleation size parameter	μm	65.6	81.8	0.5
\dot{N}_0	Nucleation threshold rate	$\text{no. cm}^{-3} \text{ns}^{-1}$	90.0	125	4600
σ_{no}	Nucleation threshold stress	GPa	-2.5	-1.8	-0.3
σ_1	Nucleation sensitivity parameter	GPa	-0.0588	-0.174	-0.53

^a In the BFRAC2 brittle fracture subroutine, these parameters are listed as T1, T2, T3, T4, T5, and T6, respectively, with different units. For example, for heat treatment A material, the values are $T1 = -3.77 \times 10^{-5} \text{ cm}^2/\text{dyne-s}$, $T2 = -1.0 \times 10^9 \text{ dyne/cm}^2$, $T3 = 6.56 \times 10^{-3} \text{ cm}$, $T4 = 9.00 \times 10^{10} \text{ cm}^{-3} \text{ s}^{-1}$, $T5 = -2.50 \times 10^{10} \text{ dyne/cm}^2$, and $T6 = -5.88 \times 10^8 \text{ dyne/cm}^2$.

^b These dynamic fracture parameters for Armco iron were taken from Reference 1 and are shown here for comparison with the HF-1 steel values.

Input listings for the PUFF 8 computations using the final set of dynamic fracture parameters are given in Appendix G for the HF-1 steel spall fracture shots. A detailed explanation of the meaning of each of the input parameters can be found in Reference 1. A brief description is as follows: The impactor velocity is given by UZERO. $RHOS = 7.774 \text{ g/cm}^3$ is the average impactor and specimen density. The EQST parameters (EQSTC, EQSTD, EQSTE, EQSTG, EQSTH, and EQSTS from left to right in the EQST line) give the equation of state parameters. The parameters EQSTC, EQSTD, and EQSTS represent C, D, and S, respectively, in the Hugoniot pressure-compression relation $P_H = C\mu + D\mu^2 + S\mu^3$ where $\mu = V_0/V - 1$. V_0 and V are the initial and final specific volumes, respectively. For HF-1 steel (see Figure 12), $EQSTC = 1.605 \times 10^{12} \text{ dyne/cm}^2$, $EQSTD = 3.561 \times 10^{12} \text{ dyne/cm}^2$, and $EQSTS = 3.683 \times 10^{12} \text{ dyne/cm}^2$. The parameters EQSTE, EQSTG, and EQSTH are the sublimation energy, Grüneisen parameter, and the vapor expansion coefficient, respectively. The sublimation energy was taken as $7.36 \times 10^{10} \text{ erg/g}$.^{1,18} The Grüneisen parameter γ_0 is calculated from the equation $\gamma_0 = \beta C_0^2 / C_p$ where β is the volume thermal expansion coefficient, C_p is the specific heat at constant pressure, and C_0 is the bulk sound speed. For iron at 25°C , the linear thermal expansion coefficient is $11.7 \times 10^{-6} \text{ }^\circ\text{K}^{-1}$ and the specific heat at constant pressure is $0.448 \times 10^7 \text{ erg/g-}^\circ\text{K}$.¹⁹ From Figure 10, $C_0 = 4.60 \text{ km/s}$ for HF-1 steel. Using these values the Grüneisen parameter γ_0 is 1.66. The parameter $EQSTH = 0.25$ for metals.¹ The TSR1 and TSR2 lines give the dynamic fracture parameters (see Table 11) and other input parameters for the BFRAC2 subroutine.¹ The two YO values represent the HF-1 steel yield strength and shear modulus. The yield strength Y was calculated from the deviator stress $\sigma_D = 0.907 \text{ GPa}$ (see Figure 12) using the equation $Y = (3/2)\sigma_D$. This gives $Y = 1.361 \times 10^{10} \text{ dyn/cm}^2$. The shear modulus G is obtained from the equation $\sigma_D = (4/3)G\mu_e / (1 + \mu_e)$ where $\mu_e = 0.00867$ is the HF-1 steel elastic limit compression. Using this and the value for μ_D gives $G = 7.912 \times 10^{11} \text{ dyne/cm}^2$. The number of computational cells and thickness for an impactor and specimen are given in the last two lines of a PUFF listing, respectively.

Appendix H gives computed stress, particle velocity, and crack concentration versus time plots for the cell of maximum damage for the HF-1 steel spall fracture shots. Appendix I gives computed stress, particle velocity, and crack concentration versus time plots for each impactor and specimen computational cell for the HF-1 steel, heat treatment B, Shot 144. This appendix is included so that selected shock histories can be observed for all computational cells for a typical shot. Figures 26 and 27 give propagation-direction stress histories and crack concentration histories, respectively, for selected computational cells for this shot. These figures were constructed from some of the plots in Appendix I. They indicate in a graphic manner the time evolution of these selected properties.

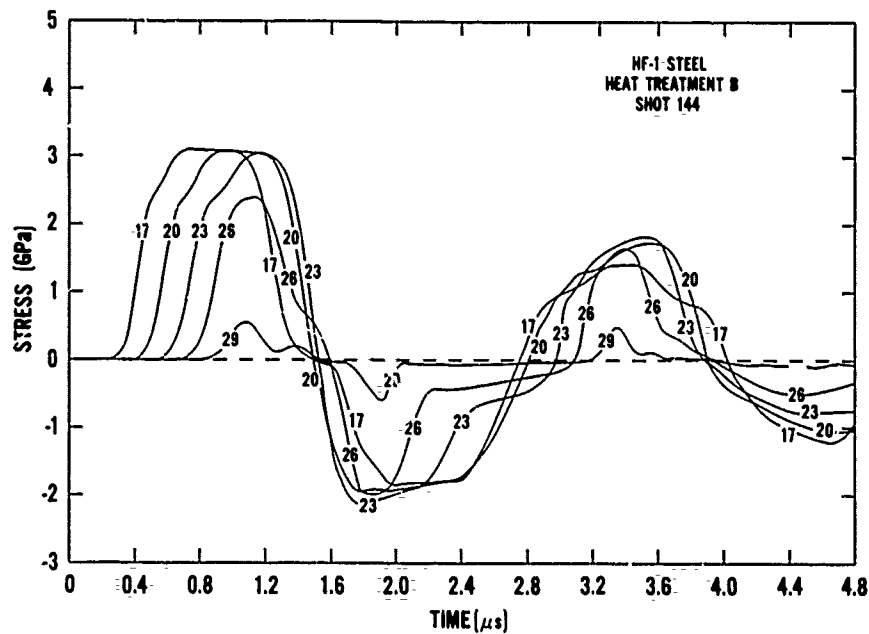


Figure 26. Computed stress-time profiles for selected computational cells for the HF-1 steel, heat treatment B, specimen in Shot 144. The stress is parallel to the shock propagation direction. The cell numbers are indicated on the profiles. This figure was constructed from plots in Appendix I.

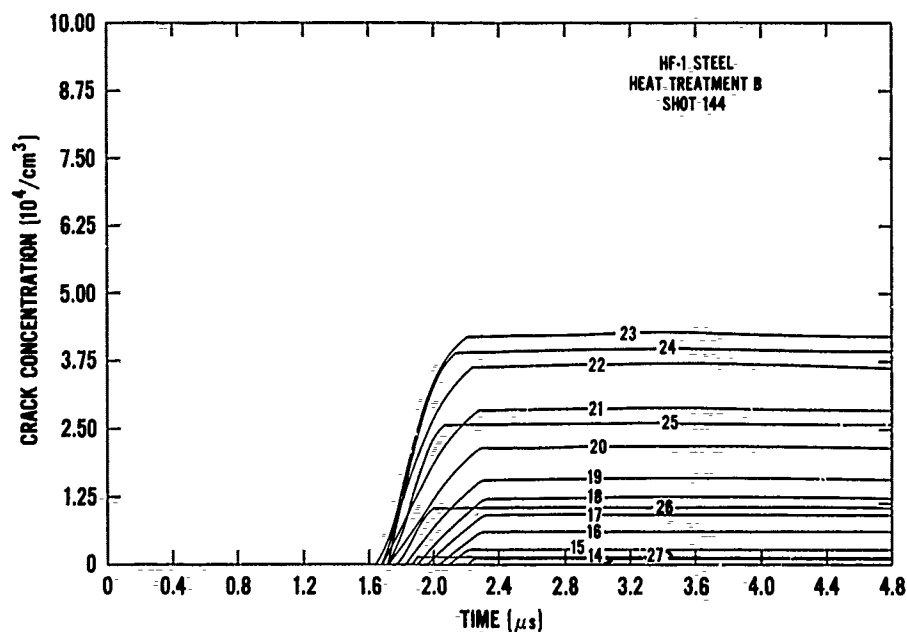


Figure 27. Computed crack concentration-time profiles for those computational cells in which tensile fracture occurred for the HF-1 steel, heat treatment B, specimen in Shot 144. The cell numbers are indicated on the profiles. This figure was constructed from plots in Appendix I.

In Table 7 of Section V, it was pointed out that for some of the shots for both heat treatments of HF-1 steel some cracks occurred along the stringer impurities in the material. A total of 44 stringer cracks were counted for heat treatment A material. This corresponds to about 5% of the total number of digitized cracks for this heat treatment. The stringer cracks were in most cases parallel to the shock wave propagation direction. We were interested in determining the significance of the stringer cracks on the computed dynamic fracture parameters. The fracture parameters for heat treatment A material with stringer cracks excluded were therefore determined for comparison with the parameters in Table 11. Appendix J contains the tables and figures for this computation. With the exception of an appreciable decrease in the nucleation threshold rate \dot{N}_0 , the exclusion of the stringer cracks did not significantly affect the dynamic fracture parameters for heat treatment A material.

VII. ARMCO IRON FRAMING CAMERA EXPERIMENT

In this section, the results of a framing-camera experiment for an explosive-filled Armco iron cylinder are presented. The cylinder had inside and outside diameters of 76.2 and 114.3 mm, respectively, and was 381 mm long. It was filled with 4.10 kg of cast-in-place composition B explosive that extended beyond the cylinder to minimize end effects. Figure 28 shows the explosive-filled cylinder prior to detonating the explosive on the right end. The explosive extended 64 and 90 mm beyond the cylinder on the right and left ends, respectively. Large and small grid patterns were placed on the cylinder surface in an attempt to measure the strain history of the expanding cylinder using the Moire interference technique. This procedure (described in detail in References 5 and 6) was not successful because there was insufficient detail in the film to resolve the interference patterns. The Moire grid patterns, which extended 191 mm along the cylinder axis, can be seen in the middle of the cylinder in Figure 28. The gross strain history of the cylinder was obtained by measuring its diameter in the framing camera photographs. A square grid pattern with a 25.4-mm spacing was placed behind the cylinder for reference.

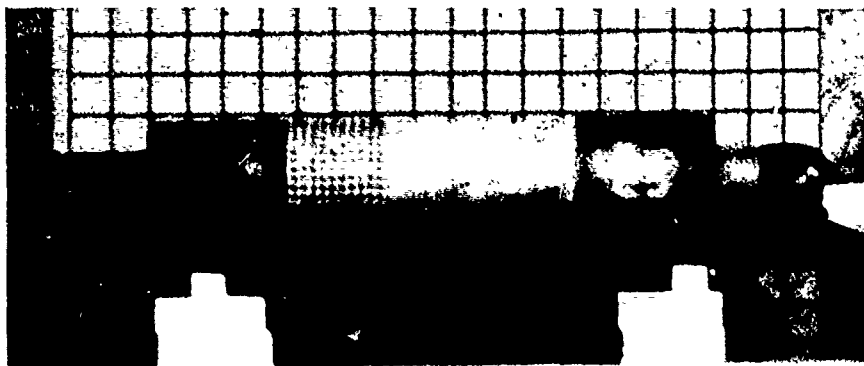


Figure 28. Framing camera photograph of Armco iron cylinder prior to detonation of the composition B explosive.

The Armco iron framing camera photographs are given in Appendix K. The cylinder outer radius was measured at a point near its mid-length on 21 photographs. Table 12 summarizes the measurements. Figure 29 is a plot of these values as a function of time. The slope of the radius-time plot increased during the initial stages of cylinder expansion (from about 25 to 65 μ s). During the final stages of cylinder expansion (from about 65 to 95 μ s), the slope was essentially constant at a value of about 1 km/s. The decreased cylinder acceleration that occurred during the final stages of expansion may be due to explosive relief wave effects from the ends of the cylinder and possibly around the partially formed fragments.

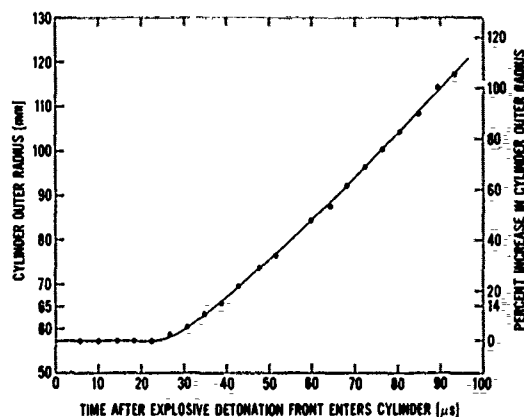


Figure 29. Armco iron cylinder outer radius versus time plot. The data points were obtained from Table 12. Visible cracks first appeared on the cylinder surface at a radius of about 65 mm (14% increase in radius). This corresponds to about 37 μ s after the detonation front entered the cylinder and about 14 μ s after the detonation front passed the position where the outer radius was measured.

Table 12. Armco iron cylinder outer radius versus time values near the mid-length position of the cylinder.

Frame No. ^a	Time After Explosive Detonation Front Enters Cylinder ^a (μ s)	Axial Position of Explosive Detonation Front in Cylinder ^a (mm)	Cylinder Outer Radius ^b (mm)
1	6	47	57.2
2	10	80	57.2
3	14	114	57.2
4	18	147	57.2
5	23	180	57.2
6	27	214	58.9
7	31	247	60.3
8	35	281	63.5
9	39	314	65.7
10	43	348	69.4
11	48	381	73.3
12	52	—	76.3
13	56	—	—
14	60	—	84.4
15	64	—	87.9
16	68	—	92.2
17	73	—	96.5
18	77	—	100.6
19	81	—	104.3
20	85	—	108.9
21	89	—	114.3
22	93	—	117.2
23	98	—	—
24	102	—	—
25	106	—	—

- ^a Twenty-five framing camera photographs were obtained for the explosive-filled Armco-iron cylinder experiment. The time between frames is 4.17 μ s. The zero for the time scale was taken at the time when the explosive detonation front was located at the entrance end of the cylinder. The detonation front was assumed to be located at the exit end of the 381-mm-long cylinder in frame 11 (see Appendix K). Using this information and the 8.02-km/s detonation velocity for composition B explosive²⁰ the time corresponding to each frame and to the axial position of the detonation front for frames 1 through 10 was obtained. The composition B explosive detonation front entered the end of the cylinder about 8 μ s after initiation of the detonation. The explosive extended about 64 mm beyond the end of the cylinder on the detonation side. The photograph for frame 13 is missing.
- ^b The cylinder outer radius was measured at a position of 178 mm (or 47%) from the detonation-front entrance end of the cylinder (the right end in Figure 28). This position corresponds to the seventh vertical gradicule line that intersects the top of the cylinder in Figure 28. Gradicule lines 0 and 15 correspond to the right and left ends of the cylinder, respectively, in this figure. Two methods were used to measure the expanding cylinder radius: The diameter was measured directly until the lower surface of the cylinder became obscured in frame 20. The position of the upper surface was measured from a fixed horizontal gradicule line until the upper surface became obscured by smoke in frame 23. The radius values listed for frames 6 through 19 (excluding frame 13) are average values for these two methods. The values listed for frames 20, 21, and 22 were obtained with the second method. The gradicule lines are 25.4 mm apart.

Figure 30 gives the Armco iron cylinder outer radius for various times after explosive detonation. The maximum observed increase in radius was about 150%. The angle θ between the expanding outer surface and the initial position of the cylinder wall was observed to increase with time. This angle increased from 0.07 to 0.14 rad in a continuous manner as the outer surface moved from its position at 14 μ s to its position at 106 μ s. The Taylor formula,²¹ $V = 2D \sin(\theta/2)$, where D is the explosive detonation velocity, can be used to estimate the cylinder velocity V during the final stages of cylinder expansion. Using $\theta = 0.14$ rad and $D = 8.02$ km/s for composition B explosive²⁰ gives $V = 1.1$ km/s. This value is in good agreement with the velocity value of 1 km/s estimated from Figure 29.

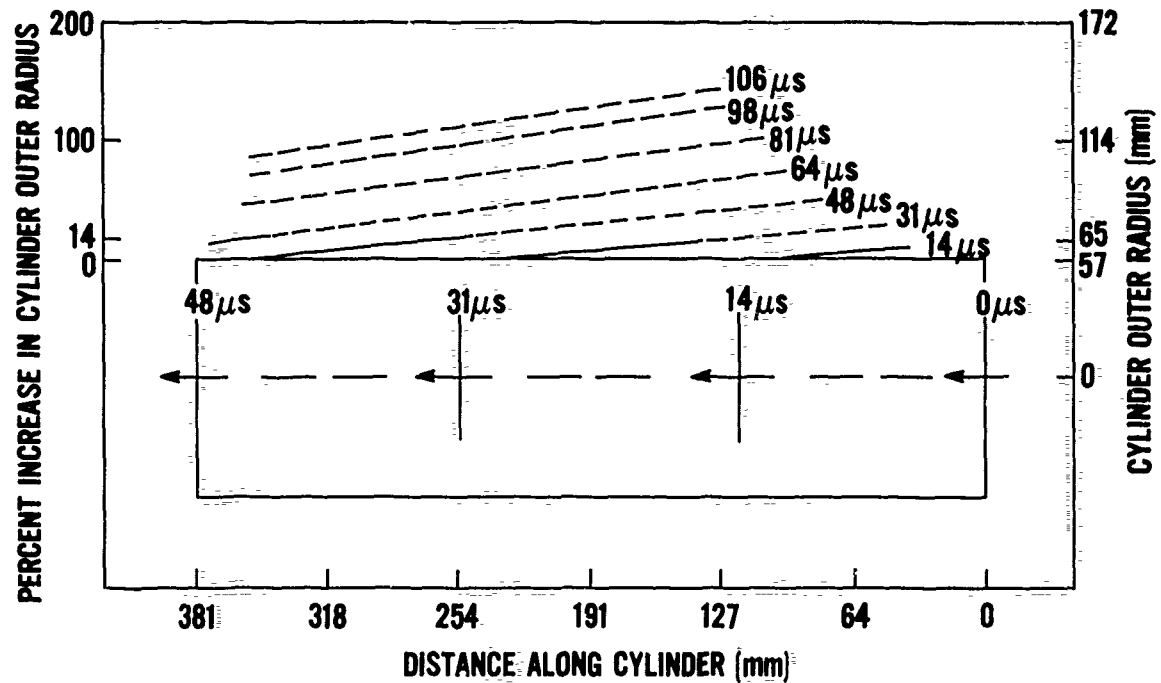


Figure 30. Armco iron cylinder outer surface at various times after explosive detonation. All times are measured with respect to when the detonation front entered the cylinder. The position of the detonation front in the cylinder is also given. The cylinder surface is represented by a dashed line when cracks were observed at that position. The surface positions at the times 14, 31, 48, 64, 81, 98, and 106 μ s correspond to framing camera photographs 3, 7, 11, 15, 19, 23, and 25, respectively, which are presented in Appendix K.

Figure 31 shows the initiation and growth of a series of Armco iron cylinder surface cracks as a function of time. The cracks were first observed about 40 to 50 μ s after the detonation front entered the cylinder. They may have been initiated sooner but were not visible. About 20 surface cracks were initiated in the region of observation. The cracks were about 10 to 20 mm in length. After about 60 μ s of growth and coalescence, the number of surface cracks decreased to about half the original number, but the average crack length increased to about 30 to 50 mm. This type of crack data may be more appropriate for obtaining dynamic fracture parameters for use in exploding cylinder simulations than the one-dimensional spall fracture experiments described in the previous sections. The dynamic fracture parameters may be very different for the two types of experiments. Fewer cracks would probably be produced for framing camera experiments (tens of cracks over a large area in Figure 31) as compared to spall fracture experiments (in some cases, hundreds of cracks in a small area, see Appendix E) due to the different strain rates. It may also be possible to use framing camera cylinder experiments to observe the growth and coalescence of surface shear cracks for those materials in which shear fractures occur through the entire wall of the cylinder.

VIII. EXPERIMENTAL DETERMINATION OF FRAGMENT MASS DISTRIBUTIONS

A series of Armco iron and HF-1 steel exploding cylinder experiments and an HF-1 steel projectile experiment²² were performed to provide fragment mass distributions for comparison with the computations and for future model development of the fracture processes. These experiments were conducted at the NSWC Sawdust Pit Facility.²³ Table 13 gives the configuration details for the experiments. A schematic of an explosive-filled cylinder experiment is shown in Figure 32. The cast-in-place composition B explosive extended beyond the cylinder to minimize end effects. Figure 33 shows the explosive-filled HF-1 steel cylinder for experiment 5. A projectile similar to the one used in experiment 7 is shown in Figure 34. The projectile was sectioned to show its inner surface and wall thickness.

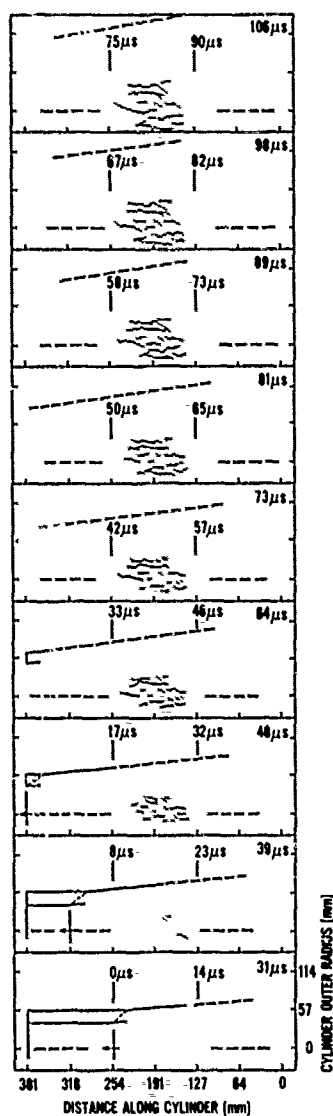


Figure 31. Evolution of Armco iron cylinder surface cracks as a function of time. The times after the detonation wave has entered the cylinder are given in the upper right corner of each frame. The times at 127 and 247 mm on each frame correspond to the times after the detonation front has reached these positions, respectively. The calculated position of the detonation front is shown in the first three frames. The position of the cylinder outer surface is shown in each frame. A dashed line represents the surface after cracks were observed at that position. The inner surface of the cylinder is also shown prior to shock compression. The sloped dashed line in the cylinder wall in the first three frames separates shocked and unshocked material. The evolution of a group of cracks in the center of the cylinder is shown as they become visible and grow. These frames (beginning at the bottom) correspond to framing camera photographs 7, 9, 11, 15, 17, 19, 21, 23, and 25, respectively. The scale for the outer radius of the cylinder is labeled only in the first frame.

Table 13. Configuration details for explosive-filled cylinder and projectile experiments.

Experiment No. ^a	Configuration and Material	Length (mm)	Inside Diameter (mm)	Outside Diameter (mm)	Wall Thickness (mm)	Mass (kg)	Hardness	Explosive Mass ^b (kg)	Fraction of Explosive Mass Inside Cylinder ^c	Explosive Mass to Metal Mass Ratio ^d (C/M)
1	Armco Iron Cylinder	203.0	76.2	114.3	19.1	9.13	R _B 40	2.75	0.57	0.17
2	Armco Iron Cylinder	203.0	76.2	114.3	19.1	9.16	R _B 40	2.77	0.57	0.17
3	HF-1 Steel Cylinder, Heat Treatment A	203.0	76.2	120.7	22.3	10.94	R _C 39	2.75	0.57	0.14
4	HF-1 Steel Cylinder, Heat Treatment A	203.0	76.2	120.7	22.3	10.96	R _C 39	2.75	0.57	0.14
5	HF-1 Steel Cylinder, Heat Treatment B	202.3	75.9	120.0	22.1	10.57	R _C 36 ^e	2.76	0.57	0.15
6	HF-1 Steel Cylinder, Heat Treatment B	202.4	75.9	120.4	22.3	10.77	R _C 36 ^e	2.68	0.57	0.14
7 ^f	HF-1 Steel Projectile	565.4 ^g	90.1 ^h	126.1 ^h	18.0 ^h	25.21 ⁱ	R _C 38-39	3.11	Not Applicable	0.12 ^j

^a Explosive experiments 1 through 7 correspond, respectively, to NSWC/DL Fragmentation Tests 2872, 2873, 2874, 2875, 2924, 2925, and 2824.

^b Cast-in-place composition B explosive was used in experiments 1 through 6. PBXN-106 explosive cast in a 0.20-kg mass, 1.52-mm-thick polyethylene encapsulating beaker was used in experiment 7.

^c To minimize end effects the explosive extended approximately 90 mm beyond the end of the cylinder on the detonator end and approximately 64 mm beyond the end of the cylinder on the opposite end. The diameter of the explosive was the same both inside and outside the cylinder. The inside surface of each cylinder was painted with MIL-C-450 cavity paint prior to inserting the composition B explosive. The explosive was detonated with an Engineer's Special blasting cap that was placed in a 7.14-mm-diameter by 6.35-mm-deep hole in the end of the explosive.

^d For the cylinder experiments, calculated using the estimated explosive mass inside the cylinder.

^e Average of nine measurements on each end of the cylinder. The hardness measurements varied from about R_C 35 to 37 from the inside to the outside cylinder wall.

^f The projectile was nose-initiated with an M564 fuse that had been modified for still detonation. The fuse mass was 0.84 kg. In addition to the hardness values listed in this table, other mechanical properties of the projectile material include the following: 1.06-GPa 0.2% yield strength, 1.2-GPa ultimate tensile strength, 8-9% elongation, and 14-18% reduction in area. The projectile dimensions listed in this table were not measured for the projectile used in experiment 7 but for a projectile from the same lot. The diameter and thickness tolerances between projectiles are a few percent.

^g Length of the assembled two-piece projectile, but not including the length of the fuse.

^h These values correspond to the 102-mm-long uniform region of the aft projectile section beginning at the joint.

ⁱ Sum of masses of the forward (11.59 kg) and aft (13.62 kg) projectile sections.

^j The C/M ratio for the 102-mm-long uniform region of the aft projectile section is 0.21; this value was obtained by using 7.77 and 1.64 Mg/m³, respectively, for the densities of HF-1 steel and PBXN-106 explosive.

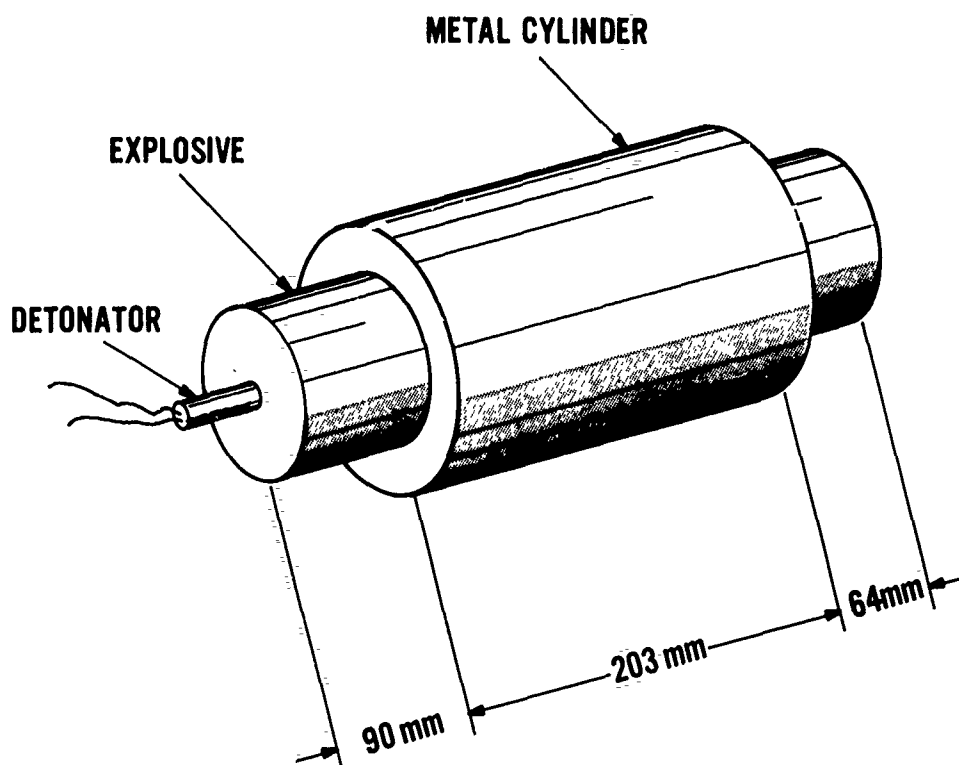
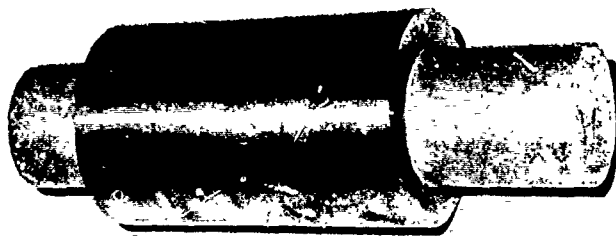


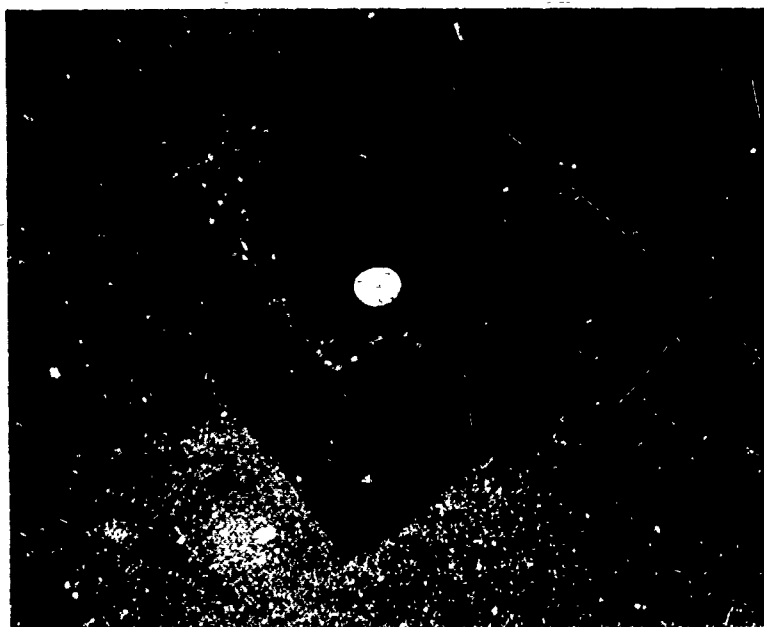
Figure 32. Schematic of explosive-filled cylinder experiment.

After detonation the fragments for each experiment were captured in a large volume of sawdust and then recovered by mechanical screen and magnetic separation techniques. Mass distributions were determined by weighing and counting the fragments. Fragments smaller than 1 gr (0.0648 g) were not counted due to their large numbers. At least 98.9% of the metal mass was recovered in all the experiments. For these thick-walled cylinder and projectile experiments both brittle and shear fracture surfaces were observed.

The observation of brittle and shear fractures in cylinder fragmentation was reported in the early work of Mott.²⁴ For the purpose of the present work a fragment classification scheme was devised to further characterize the recovered fragments according to their cylindrical and fracture surfaces. The brittle fracture surfaces usually occurred near the cylinder (or projectile) outer surface; the shear fracture surfaces usually occurred near the cylinder (or projectile) inner surface. Table 14 defines the eight fragment types. Schematic examples of these fragment types are given in Figure 35. Photographs of the fragment types from the Armco iron and HF-1 steel cylinder



(a)

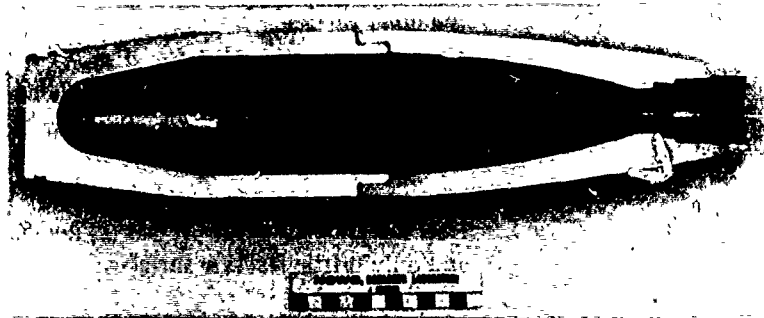


(b)

Figure 33. Explosive-filled HF-1 steel cylinder with heat treatment B for experiment 5. (a) After fabrication and (b) in styrofoam box with lid removed prior to filling of sawdust recovery pit.



(a)



(b)

Figure 34. Photographs of (a) outer surface and (b) inner surface of sectioned HF-1 steel projectile with heat treatment A.

experiments are given in Appendix L. Figure 36 is a schematic of a cross section through the cylinder or projectile wall showing the possible formation of the fragment types during fragmentation. It is not known whether all the fragment types were formed at about the same time after explosive detonation or whether they were formed at different times. It may be possible that many type 1 and type 2A fragments formed initially and then later broke up into fragment types 2B, 3A, 4A, and 4B. A fragment characterization scheme that is similar to the present one, but limited to four fragment types, has been independently devised.²⁵

Appendix M contains the detailed results for the experiments. Tables M-1 through M-7 give the mass distribution results for the typed fragments for each experiment. Tables M-8 through M-14 give dimension measurements and strain calculations for selected type 1 fragments from each experiment.

Table 14. Definitions of fragment types used for characterization of recovered fragments from the explosive-filled cylinder and projectile experiments.

Fragment Type	Definition ^a
1	Has both the inner and outer surfaces of the cylinder (or projectile). Usually has brittle fracture surfaces near the outer surface and shear fracture surfaces near the inner surface.
2A	Has the outer surface of the cylinder (or projectile), and both brittle fracture (usually near the outer surface) and shear fracture surfaces.
2B	Has the outer surface of the cylinder (or projectile), and only brittle fracture surfaces.
3A	Has the inner surface of the cylinder (or projectile), and both brittle fracture and shear fracture (usually near the inner surface) surfaces.
3B	Has the inner surface of the cylinder (or projectile) and only shear fracture surfaces.
4A	Has only brittle and shear fracture surfaces.
4B	Has only brittle fracture surfaces.
4C	Has only shear fracture surfaces.

^a These definitions do not include the fragment end surfaces (the end surfaces were usually perpendicular to the cylinder axis). The fragment end surfaces usually were brittle fracture surfaces. Sometimes a fragment end surface contained the end surface of the cylinder or a shear fracture surface.

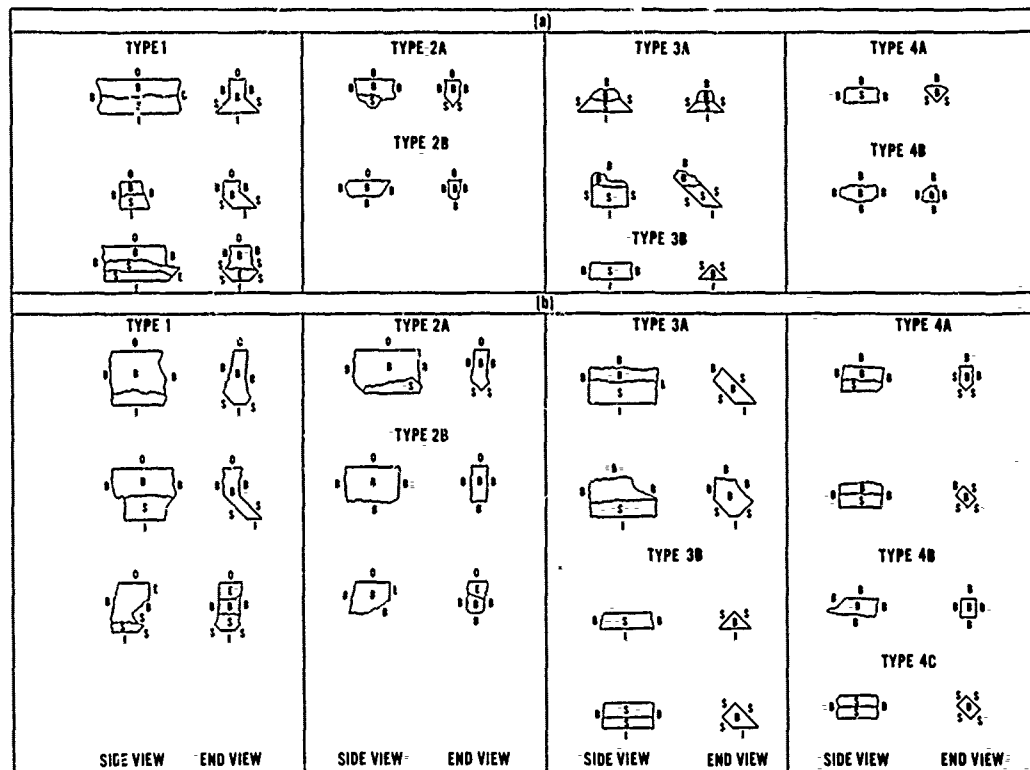


Figure 35 Schematic examples of fragment types from the (a) Armco iron and (b) HF-1 steel cylinder experiments. These examples may not correspond to the most common fragments of a given type. The inner, outer, and end surfaces of the cylinder are indicated by the letters I, O, and E, respectively. Brittle and shear fracture surfaces are indicated by the letters B and S, respectively. Two views are shown for each fragment; a side view (looking perpendicular to the cylinder axis) and an end view (looking parallel to the cylinder axis). The shear fracture surfaces made angles of approximately 45° with the inner cylinder surface (fragment end view). No type 4C fragments were observed for the Armco iron experiments.

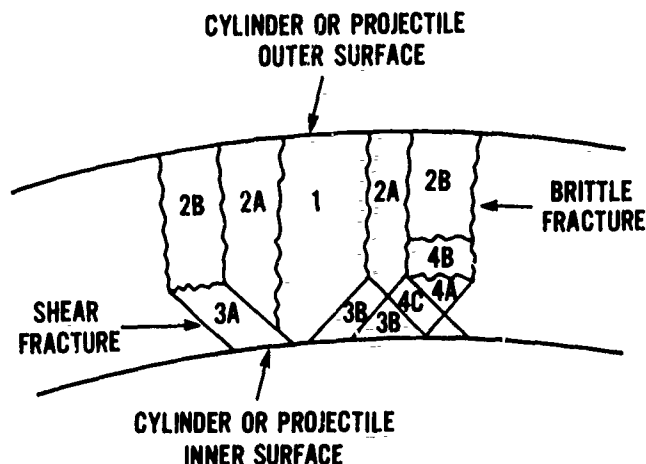


Figure 36. Schematic through cylinder or projectile wall showing the possible formation of fragment types from the intersections of brittle and shear fracture surfaces. The fragment types are defined in Table 14.

Figure 37 is a semilogarithmic plot of the number of fragments with mass greater than m versus the square root of the fragment mass for each experiment. Mott and Linfoot²⁶ found experimentally that the fragment mass distributions for many projectiles and cylindrical warheads could be approximated by an empirical equation of the form

$$N(>m) = N_0 \exp [-(m/\mu)^{1/2}] \quad (4)$$

where $N(>m)$ is the number of fragments with mass greater than m , N_0 is the total number of fragments, m is the fragment mass, and μ is a fragmentation size parameter. Exponents other than $1/2$ have been used in Equation (4) for representing fragment mass distribution data.⁶ Figure 37 suggests that Equation (4) may not adequately represent the fragment mass distribution data for the present experiments, except possibly for the Armco iron experiments, if the small fragment masses are excluded. Fragment mass distribution results are plotted versus the fragment mass in Figure 38. Figure 38(a) is a plot of the number of fragments with mass greater than m and Figure 38(b) is a plot of the average number of fragments per 1-gr interval. To construct Figure 38(b) some of the mass groups for an experiment (given in Tables M-1 through M-7) were combined into larger mass groups before calculating the average number of fragments, especially if the smaller mass groups had only a few fragments. The values in Figure 38(b) were plotted at a fragment mass corresponding to the midpoint of the appropriate mass group. Figure 38(a) suggests that for the HF-1 steel cylinder experiments an exponent of 1 rather than $1/2$ in Equation (4) is a

more adequate representation of the fragment mass distribution data. Table 15 summarizes the average fragment mass results for the cylinder and projectile experiments. The average fragment masses are 97 gr for the Armco iron cylinder experiments, 15 gr for the HF-1 steel, heat treatment A, cylinder experiments, 12 gr for the HF-1 steel, heat treatment B, cylinder experiments, and 21 gr for the HF-1 steel, heat treatment A, projectile experiment. The HF-1 steel cylinder results indicate that heat treatment B material is more brittle than heat treatment A material.

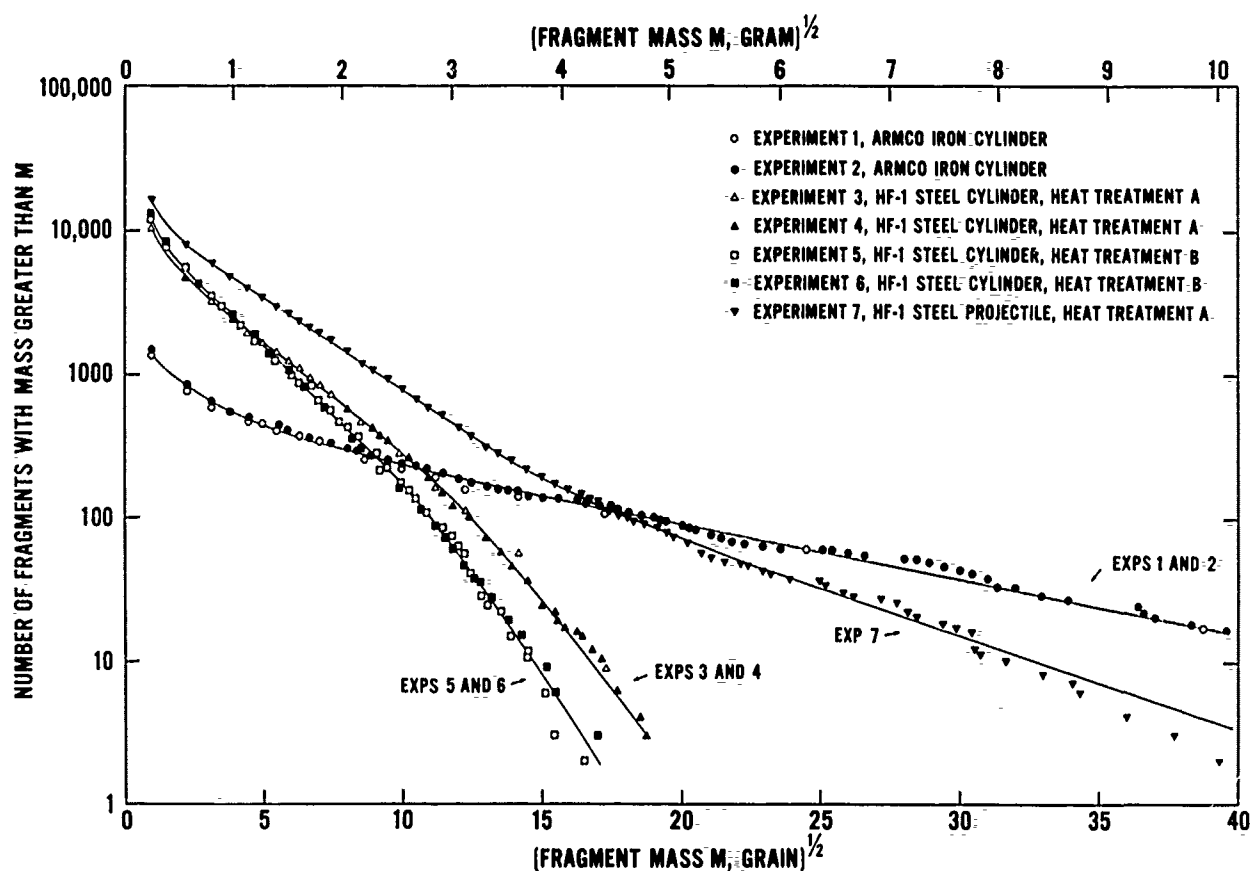
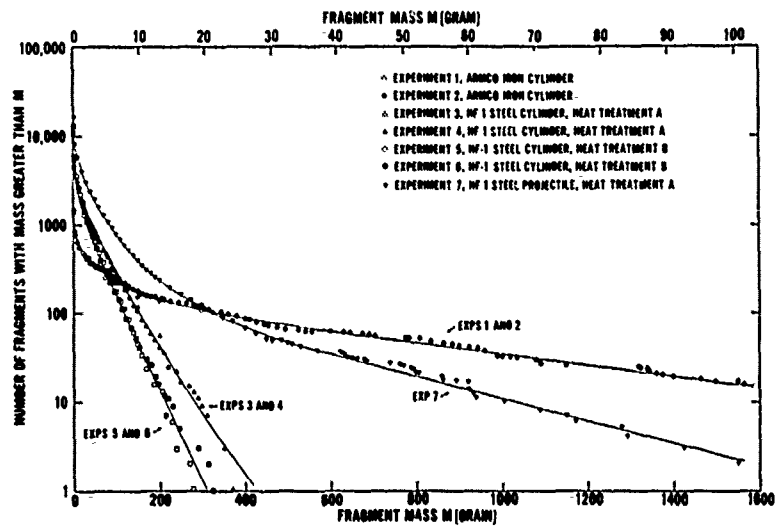
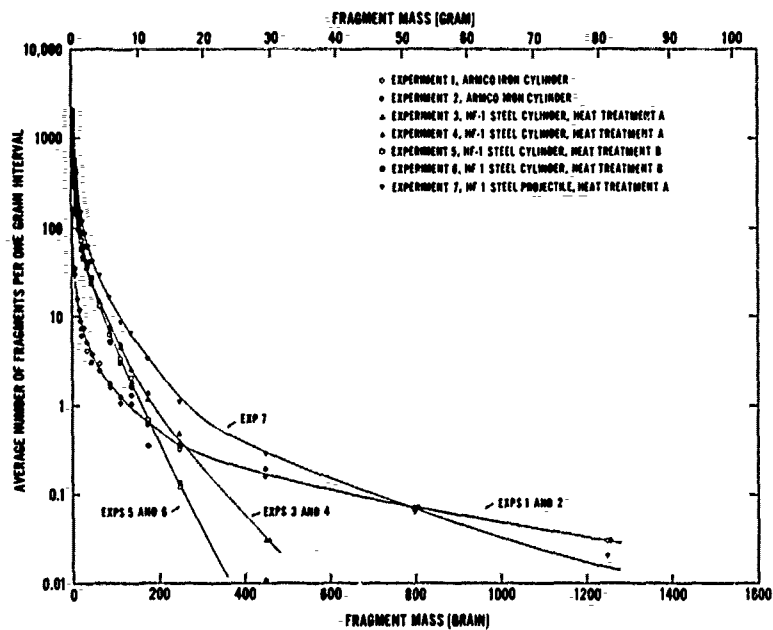


Figure 37. Fragment mass distributions (versus the square root of the fragment mass) for the cylinder and projectile experiments.



(a)



(b)

Figure 38. Fragment mass distributions (versus the fragment mass) for the cylinder and projectile experiments. (a) Cumulative number of fragments. (b) Average number of fragments.

It can be shown that the fragmentation size parameter μ in Equation (4) is related to the average fragment mass \bar{m} , where

$$\bar{m} = \frac{\int_0^{\infty} m dN}{\int_0^{\infty} dN} \quad (5)$$

Here dN is the number of fragments between m and $m + dm$. From Equation (4) $dN = N_0 e^{-x} dx$ where x has been substituted for $(m/\mu)^{1/2}$. Equation (5) then becomes

$$\bar{m} = \frac{\mu \int_0^{\infty} e^{-x} x^2 dx}{\int_0^{\infty} e^{-x} dx} \quad (6)$$

Evaluating the integrals gives $\mu = \bar{m}/2$. It is possible to derive a general relationship between μ and \bar{m} to account for the different exponents that can be used in Equation (4). Rewriting Equation (4) for a general exponent gives

$$N(>\bar{m}) = N_0 \exp [-(m/\mu)^{1/n}], \quad (7)$$

where $n = 1, 2, 3, \dots$. Using $x = (m/\mu)^{1/n}$, Equation (5) becomes

$$\bar{m} = \frac{\mu \int_0^{\infty} e^{-x} x^n dx}{\int_0^{\infty} e^{-x} dx} \quad (8)$$

Evaluating Equation (8) gives $\mu = \bar{m}/n!$. Therefore, for exponents of 1 and 1/3 in Equation (7) $\mu = \bar{m}$ and $\bar{m}/6$, respectively.

Table 15. Average fragment mass results for cylinder and projectile experiments.

Experiment No.	Total Number of Fragments Greater than 1 gr ^a	Fragment Mass Greater than 1 gr ^a (kg)	Average Fragment Mass for Fragments Greater than 1 gr		Total Recovered Fragment Mass ^b (kg)	Fraction of Metal Mass Recovered
			(gr)	(g)		
1	1395	8.99	99.5	6.45	9.08	0.995
2	1457	9.01	95.4	6.18	9.12	0.996
3	10181	10.33	15.7	1.01	10.89	0.996
4	10740	10.32	14.8	0.96	10.93	0.997
5	12132	9.70	12.3	0.80	10.46	0.989
6	12927	9.88	11.8	0.76	10.65	0.989
7 ^c	16403	22.23	20.9	1.36	25.07	0.994

^a Fragments with a mass less than 1 gr (0.0648 g) were not counted.

^b Approximately 1, 5, and 7% of the total recovered mass was in the 0 to 1-gr mass group for cylinder experiments 1 and 2, 3 and 4, and 5 and 6, respectively. Approximately 3% of the total recovered fragment mass was in the 0 to 1-gr mass group for the projectile experiment 7.

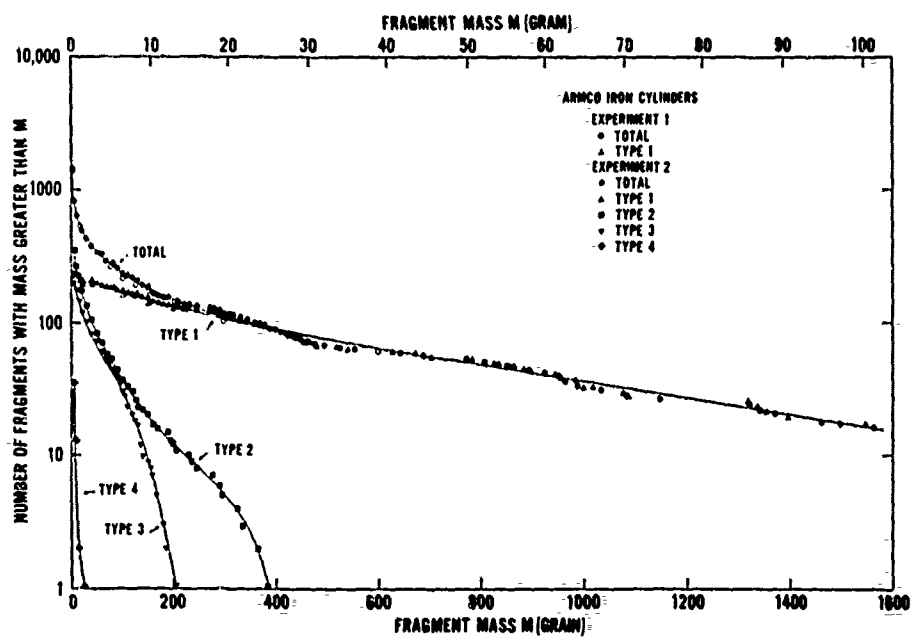
^c Includes only fragments from the forward and aft projectile sections and not the fuse fragments.

Figures 39 through 42 give the fragment mass distribution results for the typed fragments for the cylinder and projectile experiments. Fragment types 2, 3, and 4 are the sums of types 2A and 2B, types 3A and 3B, and types 4A, 4B, and 4C, respectively. Table 16 summarizes the results for the typed fragments for the experiments. The average fragment mass results for the typed fragments are given in Table 17.

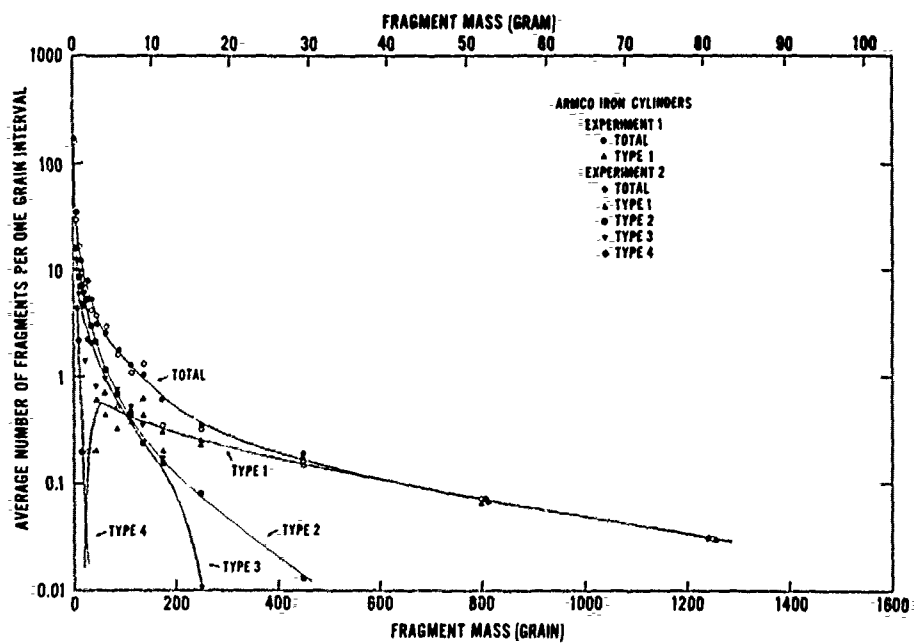
For the Armco-iron cylinder experiments only type 1 fragments were observed for the larger fragment masses. For experiment 2, fragment types 2, 3, and 4 were observed for fragment masses less than about 400, 200, and 25 gr, respectively. No type 4C fragments were observed for this experiment. The number of type 1 fragments increased with decreasing fragment mass except for the smallest masses. About 25% of the recovered fragments were type 1. For the HF-1 steel, heat treatment A, cylinder experiment 4, fragment types 1, 2, and 3 were observed for the largest fragment masses. Type 4 fragments were observed for masses less than about 125-gr. Fragment types 1 and 2 were observed for the largest fragment masses for the heat treatment B, experiment

5. Fragment types 3 and 4 were observed for fragment masses less than about 175 and 105 gr, respectively. Only about 1% of the fragments from the HF-1 steel cylinder experiments were type 1. About 35% of the fragments were type 4 as compared with about 4% type 4 fragments from the Armco iron experiment 2.

For the projectile experiment 7 only type 1 fragments were observed for the larger fragment masses. Fragment types 2, 3, and 4 were observed for fragment masses less than about 550, 450, and 150 gr, respectively. Almost all of the large type 1 fragments originated from the nose region of the projectile. The reconstructed nose is shown in Figure 43. The reconstructed nose mass was about 2.5 kg, which corresponds to about 10% of the initial projectile mass. Since the nose region of the projectile was not in direct contact with the explosive charge, this region was probably subjected to a lower strain rate than the remainder of the projectile. Figure 44 shows that the projectile fragment mass distribution is changed appreciably if the large nose fragments are excluded. The mass of the largest fragments decreases from about 1600 to 800 gr. The mass of the largest fragments for the cylinder experiments was about 400 gr.

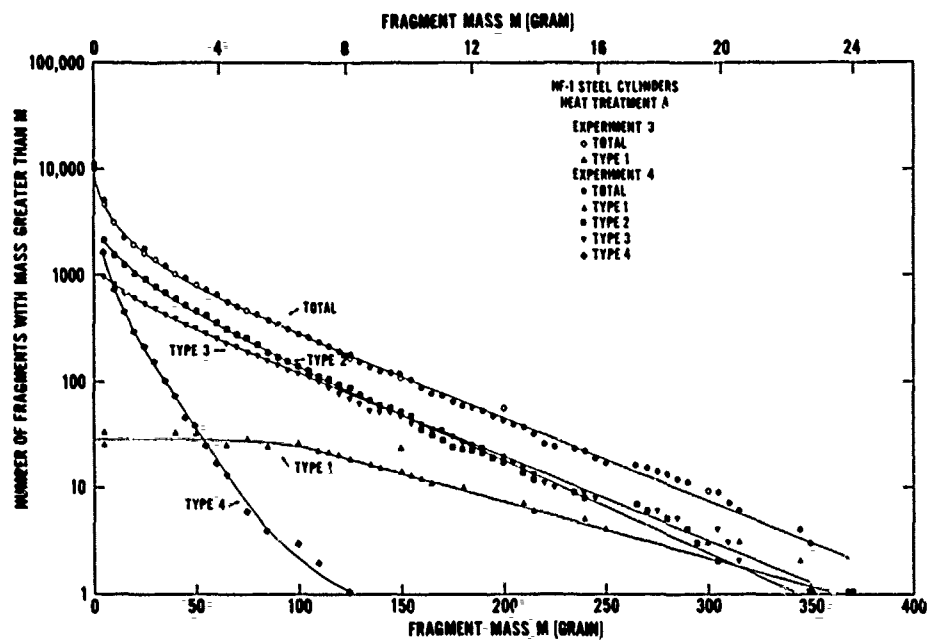


(a)

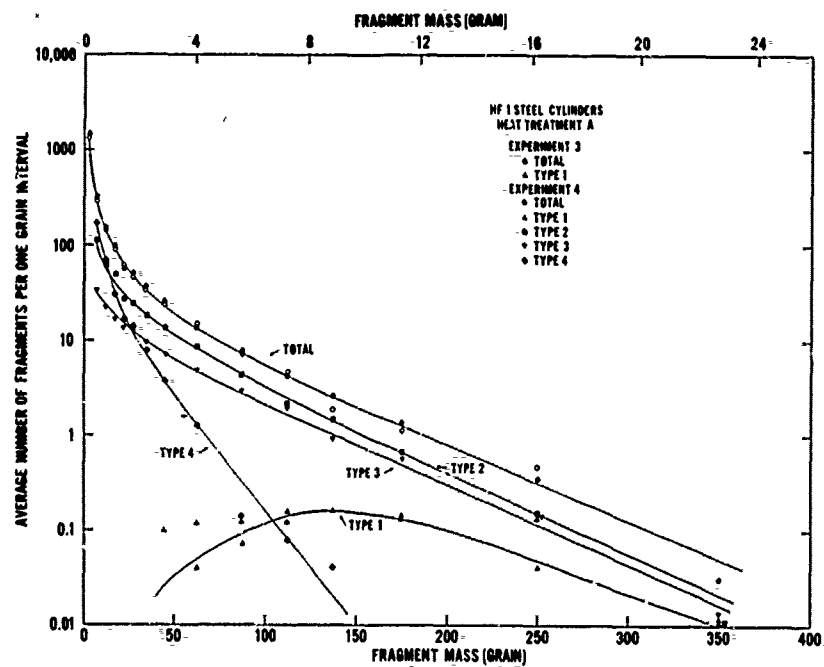


(b)

Figure 39. Fragment mass distributions for the Armco iron cylinder experiments. (a) Cumulative number of fragments. (b) Average number of fragments.

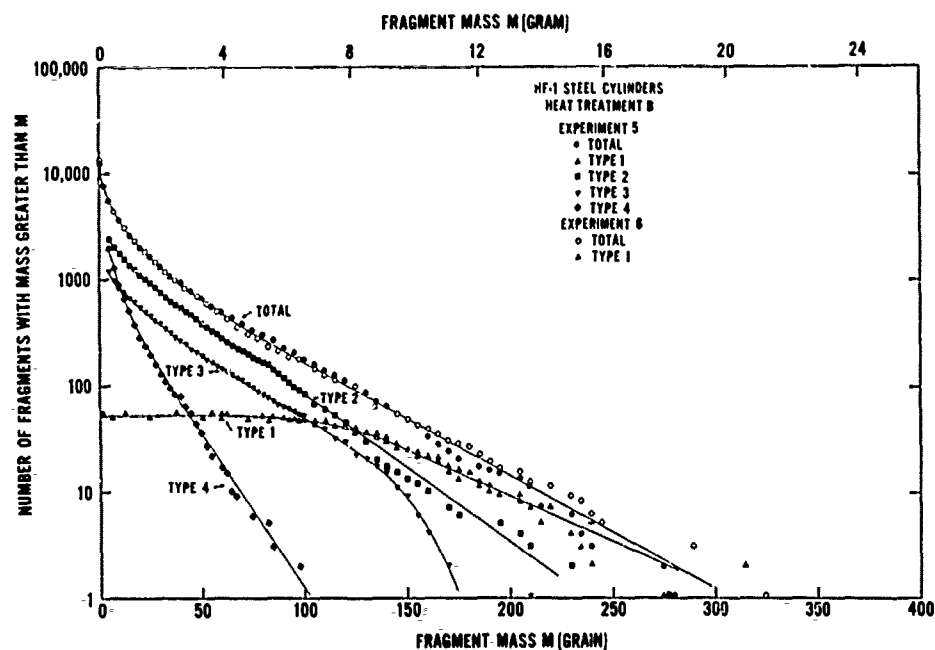


(a)

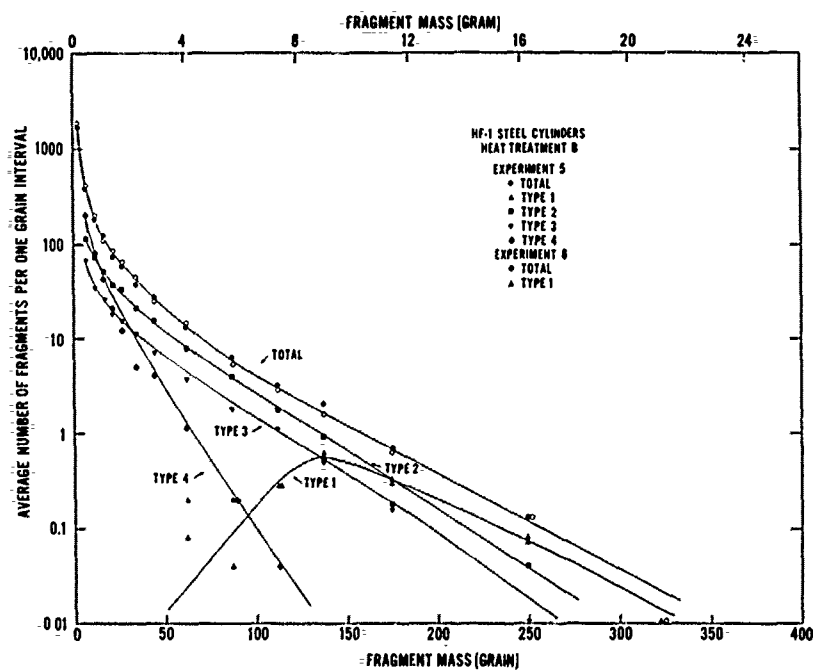


(b)

Figure 40. Fragment mass distributions for the HF-1 steel, heat treatment A, cylinder experiments. (a) Cumulative number of fragments. (b) Average number of fragments.

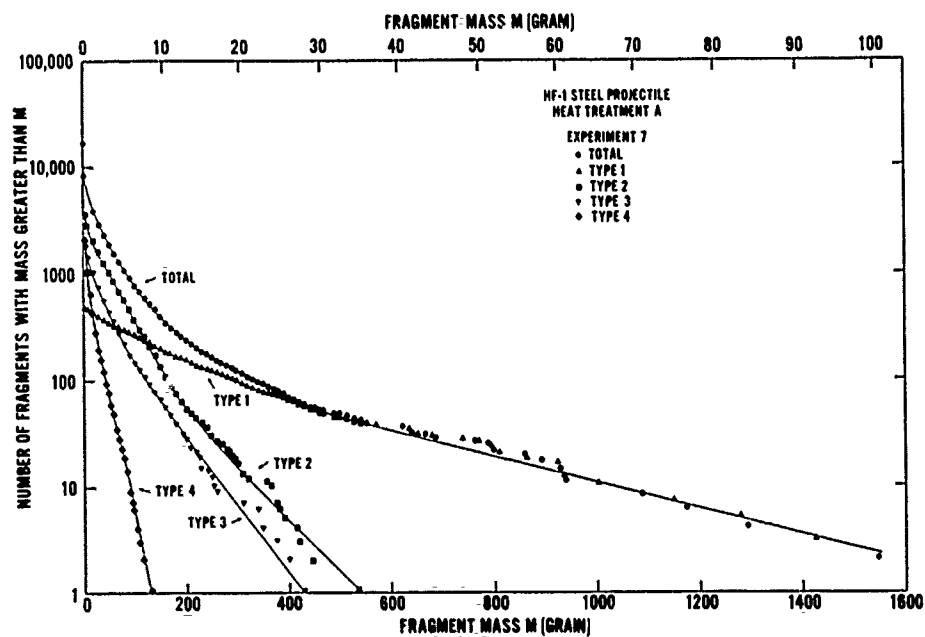


(a)

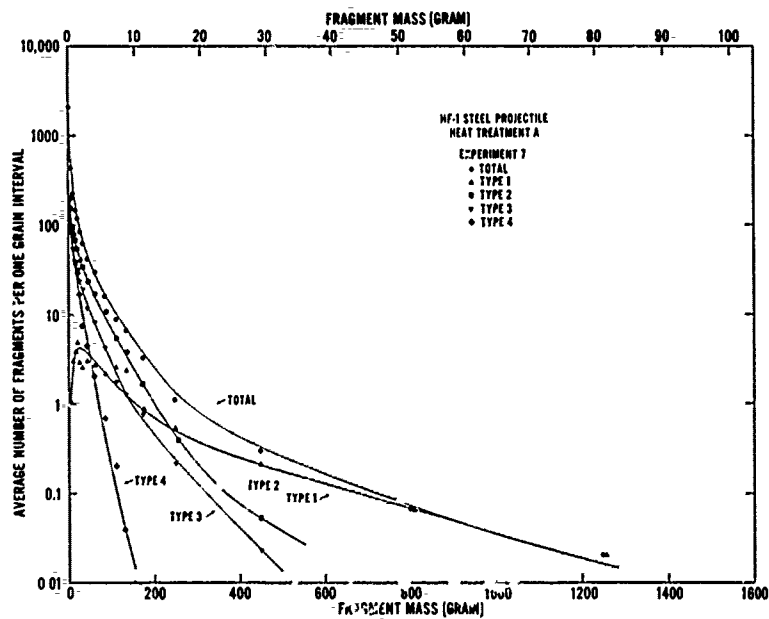


(b)

Figure 41. Fragment mass distributions for the HF-1 steel, heat treatment B, cylinder experiments. (a) Cumulative number of fragments. (b) Average number of fragments.



(a)



(b)

Figure 11. Fragment mass distributions for the HF-1 steel, heat treatment A, projectile experiment. (a) Cumulative number of fragments. (b) Average number of fragments.

Table 16. Summary of results for typed fragments from cylinder and projectile experiments.^a

Experiment No.	Number of Fragments ^b										Total Number of Fragments Greater	Mass of Fragments ^c										Total Fragment Mass Greater	Total Recovered Fragment Mass		
	Type 2					Type 3						Type 4													
	Type 1	Type 2A	Type 2B	Total	Type 3A	Type 3B	Total	Type 4A	Type 4B	Type 4C		Total	Type 1	Type 2A	Type 2B	Total	Type 3A	Type 3B	Total	Type 4A	Type 4B			Type 4C	Total
1 ^d	206 (27.2)	-	-	-	-	-	-	-	-	-	758 (100.0)	734 (80.9)	-	-	-	-	-	-	-	-	-	-	-	890 (98.0)	908 (100.0)
2	195 (24.0)	181 (22.4)	164 (20.2)	117 (14.4)	117 (14.4)	236 (29.1)	28 (3.5)	7 (0.9)	0 (0)	35 (4.3)	811 (100.0)	728 (79.7)	0.81 (8.9)	0.16 (1.8)	0.97 (10.7)	0.43 (4.7)	0.21 (2.4)	0.64 (7.1)	0.02 (0.2)	0.004 (0.04)	0 (0)	0.02 (0.2)	891 (97.7)	912 (100.0)	
3 ^d	33 (0.7)	-	-	-	-	-	-	-	-	-	4660 (100.0)	0.42 (3.9)	-	-	-	-	-	-	-	-	-	-	951 (87.3)	1089 (100.0)	
4	25 (0.5)	455 (9.5)	1683 (35.2)	2138 (44.7)	836 (17.5)	962 (20.1)	938 (19.6)	716 (15.0)	3 ¹ (0.1)	1657 (34.7)	4782 (100.0)	0.29 (2.6)	2.34 (21.4)	2.40 (22.0)	4.74 (43.4)	2.73 (25.0)	0.19 (1.8)	2.92 (26.8)	1.05 (9.6)	0.44 (4.0)	0.003 (0.02)	1.49 (13.6)	944 (86.4)	1093 (100.0)	
5	55 (1.0)	350 (6.4)	1954 (36.0)	2303 (42.4)	900 (16.6)	266 (4.9)	1166 (21.5)	1004 (18.5)	890 (16.4)	1903 (35.1)	5428 (100.0)	0.52 (5.0)	1.66 (15.8)	2.71 (25.9)	4.37 (41.7)	1.91 (18.2)	0.28 (2.7)	2.19 (20.9)	1.02 (9.7)	0.61 (5.9)	0.01 (-1)	1.64 (15.7)	872 (83.3)	1046 (100.0)	
6 ^d	49 (0.9)	-	-	-	-	-	-	-	-	-	5631 (100.0)	0.51 (4.8)	-	-	-	-	-	-	-	-	-	-	879 (82.5)	1065 (100.0)	
7 ^e	472 ^f (5.9)	1558 (19.4)	2099 (26.1)	3657 (45.5)	1458 (18.2)	421 (5.2)	1879 (23.4)	1528 (19.0)	458 (5.7)	2026 (25.2)	8034 (100.0)	6.23 (24.9)	6.78 (27.0)	13.4 (13.3)	10.12 (40.3)	4.16 (16.6)	0.52 (2.1)	4.68 (18.7)	1.62 (6.5)	0.34 (1.4)	0.04 (0.1)	2.00 (8.0)	23.03 (91.9)	2507 (100.0)	

^a Only fragments greater than 5 gr (0.32 g) were characterized. This includes all type 1 fragments. Fragment types 2, 3, and 4 were all observed in the 0 to 1 and 1 to 5-gr mass groups but were not characterized. These results were obtained from Tables M-1 through M-7.
^b The numbers in parentheses give the percentages of fragments of a given type with mass greater than 5 gr.
^c The numbers in parentheses give the percentages of the total fragment mass for a given fragment type.
^d Only type 1 fragments were characterized for these experiments.
^e Includes only fragments from the forward and aft projectile sections.
^f Approximately 59% of the type 1 fragments (277 fragments) came from the thin-walled joint regions of the forward and aft section (210 fragments), the thin-walled nose region on the forward section (15 fragments), and the thick-walled region of the forward section (52 fragments).

Table 17. Average fragment mass results for typed fragments from cylinder and projectiles experiments.^a

Experiment No.	Type 1		Type 2		Type 3		Type 4		Type 4C		Average Fragment Mass for Fragments Greater than 5 gr													
	Type 1A		Type 2B		Type 3A		Type 3B		Type 4A			Type 4B												
	(g)	(gr)	(g)	(gr)	(g)	(gr)	(g)	(gr)	(g)	(gr)		(g)	(gr)											
1 ^b	550.1	35.65	-	-	-	-	-	-	-	-	-	-	181.2	11.74										
2	575.7	37.31	69.1	4.48	15.2	0.99	43.5	2.82	55.5	3.60	28.5	1.85	42.1	2.73	9.4	0.61	8.8	0.57	0	9.3	0.60	169.6	10.99	
3 ^b	196.4	12.73	-	-	-	-	-	-	-	-	-	-	-	-	-	-	-	-	-	-	-	-	31.5	2.04
4	175.9	11.40	79.3	5.14	22.0	1.43	34.2	2.22	50.4	3.26	23.8	1.54	46.9	3.04	17.3	1.12	9.4	0.61	13.5	0.87	13.9	0.90	30.5	1.97
5	146.1	9.46	73.0	4.73	21.4	1.39	23.9	1.90	32.7	2.12	16.1	1.04	28.9	1.88	15.7	1.02	10.6	0.69	10.5	0.68	13.3	0.86	24.8	1.61
6 ^b	161.8	10.48	-	-	-	-	-	-	-	-	-	-	-	-	-	-	-	-	-	-	-	-	24.1	1.56
7	203.7	13.20	67.2	4.36	24.6	1.59	42.7	2.77	44.1	2.86	18.9	1.22	38.4	2.49	16.3	1.06	13.5	0.74	14.1	0.91	15.2	0.99	44.2	2.87

^a Only fragments greater than 5 gr (0.32 g) were characterized. The average values in this table were calculated from the results in Table 16.

^b Only type 1 fragments were characterized for these experiments.

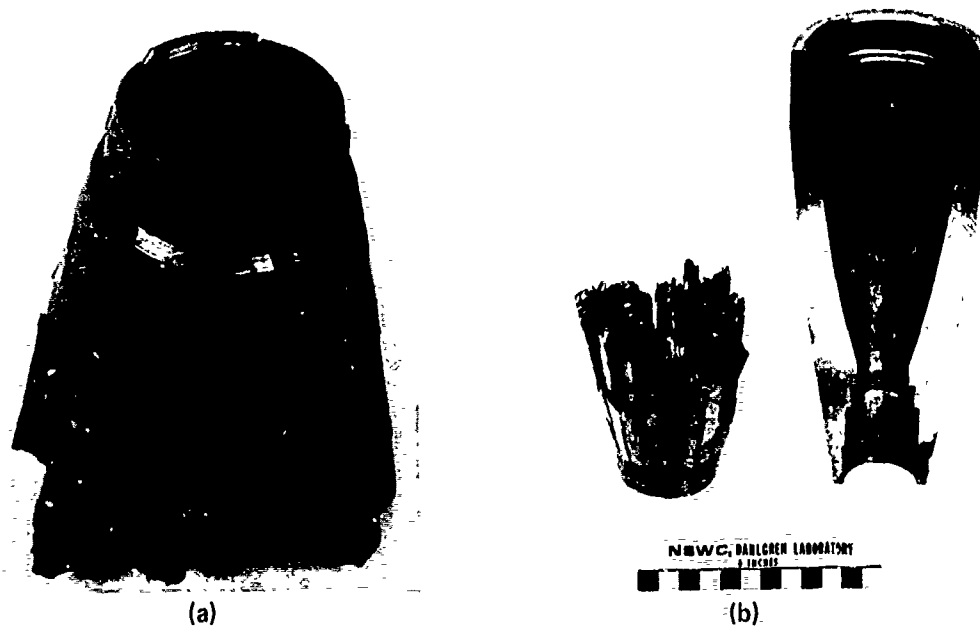


Figure 43. Photographs of the reconstructed nose for the projectile experiment. A sectioned forward projectile piece is compared with the reconstructed nose in (b).

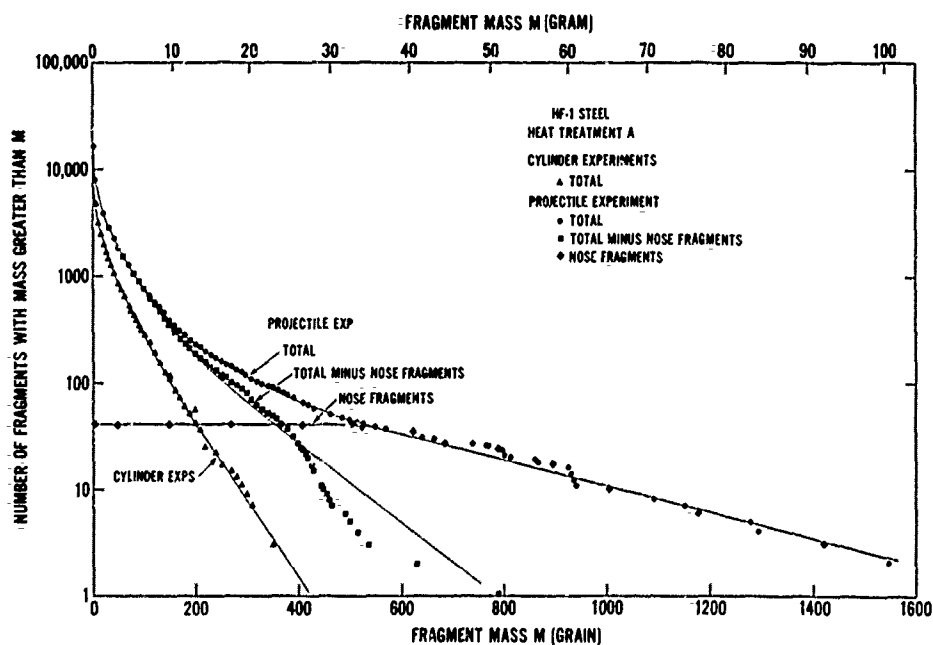


Figure 44. Comparison of fragment mass distributions for the HF-1 steel, heat treatment A, cylinder experiments and the projectile experiment excluding 41 large nose fragments.

The dimension measurements given in Tables M-8 through M-14 for selected type 1 fragments from the cylinder and projectile experiments include the fragment mass, wall thickness, maximum fragment width and length, and average fraction of wall thickness with brittle fracture. Radial and plastic strain values were calculated using the initial and final wall thickness values. The measurements and calculations are summarized in Table 18. The values for the average fraction of the wall thickness with brittle fracture are 0.56, 0.76, and 0.80 for the Armco iron, HF-1 steel with heat treatment A, and HF-1 steel with heat treatment B cylinder experiments, respectively. This value is 0.69 for fragments from the central uniform region of the HF-1 steel projectile. These results agree with the decreased ductility of these materials as given by the percent elongation values in Table 3. Average engineering radial strain values for the type 1 fragments from the Armco iron, HF-1 steel with heat treatment A, and HF-1 steel with heat treatment B cylinder experiments are 0.35, 0.12, and 0.13, respectively. This value is 0.11 for fragments from the central uniform region of the HF-1 steel projectile. It is possible to estimate the final outside diameters corresponding to these residual strain values using the formula $(d_o - a_o) a_o = (d_f - a_f) a_f$. Here d_o and d_f are the initial and final outside diameters, respectively, and a_o and a_f are the initial and final wall thicknesses, respectively. This formula was obtained by assuming that the cross-sectional area of the cylinder or projectile remained constant during explosive expansion. Using diameter and thickness values from Tables 13 and 18, the average percent increase in the outside diameters corresponding to the residual strain values is 39, 8, and 10% for the Armco iron, HF-1 steel with heat treatment A, and HF-1 steel with heat treatment B cylinders, respectively. The percent increase for the HF-1 steel projectile is 9%. These results indicate that during explosive expansion the Armco iron cylinders were at a much larger diameter than the HF-1 steel cylinders and projectile when the increase in the plastic radial strain effectively ceased.

Table 18. Summary of measurements on type 1 fragments from cylinder and projectile experiments.^a

Experiment No.	Total Number of Type 1 Fragments	Number of Type 1 Fragments Measured	Fragment Mass (gr) (g)		Wall Thickness (mm)	Average Fraction of Wall Thickness with Brittle Fracture ^b	Fragment Width ^c (mm)	Maximum Fragment Length ^d (mm)	Engineering Radial Strain ^e	True Radial Strain ^f	Homogeneous Plastic Strain ^g
1	206 ^h	25	550.1 ⁱ	35.64 ⁱ	12.6	0.53	9 17	66	0.34	0.42	0.72
2	195	25	575.7 ⁱ	37.31 ⁱ	12.3	0.57	10 17	72	0.36	0.45	0.78
3	33 ^h	33	191.9	12.43	19.7	0.77	8.3 9.9	21.8	0.12	0.12	0.22
4	25	25	175.9	11.40	19.9	0.75	6.9 8.7	21.0	0.11	0.11	0.19
5	55	55	146.1	9.46	19.0	0.80	7.3 9.2	19.4	0.14	0.15	0.26
6	49	49	161.3	10.48	19.5	0.80	7.9 10.0	21.4	0.12	0.13	0.22
7	472	10 ^j	203.7 ⁱ	13.20 ⁱ	16.0	0.69	11.0 8.4	40.9	0.11	0.12	0.20
		5 ^k			8.7	0.90	6.6 6.5	19.3	0.10	0.10	0.17
		5 ^l			7.3	0.78	5.5 5.6	19.1	0.16	0.18	0.30

^a The values listed in this table are average values for the fragment measurements given in Tables M-8 through M-14.

^b These values are the average of measurements from the cylinder (or projectile) outer surface to the beginning of the shear fracture surface on each side of the fragment. The estimated uncertainty in these values is 10-20%.

^c The two values listed are the average maximum width of the brittle fracture region near the cylinder (or projectile) outer surface and the average maximum width of the shear fracture region near the cylinder (or projectile) inner surface.

^d The fragment length is parallel to the cylinder (or projectile) axis.

^e The engineering radial strain is $(a_0 - a_f)/a_0$ where a_0 and a_f are the initial and final wall thicknesses, respectively.

^f The true radial strain³ is $-\ln(a_f/a_0)$.

^g The homogeneous plastic strain³ is $-\sqrt{3} \ln(a_f/a_0)$.

^h Six fragments were removed from the distribution prior to the characterization of the fragments; therefore the total number of type 1 fragments may be greater.

ⁱ Average value for total number of type 1 fragments.

^j Fragments from the 102-mm-long uniform region of the aft projectile section.

^k Fragments from the joint region of the forward projectile section.

^l Fragments from the joint region of the aft projectile section.

IX. COMPUTATION OF FRAGMENT MASS DISTRIBUTIONS

In this section, computed fragment mass distribution results are presented for Armco iron and HF-1 steel explosive-filled cylinders and an HF-1 steel projectile. The computations are compared with the experiments of the last section. Cylindrical PUFF and TROTT computations were performed to simulate the exploding cylinders and the projectile, respectively. The fracture processes were simulated with the BFRACT2 brittle fracture model and the SHEAR2 shear band model. Brittle and shear fracture crack distribution results were obtained from the computations. Fragment mass distributions were then calculated from the crack distributions.

Computer listings of the input parameters and the output results for the PUFF and TROTT computations are given in Appendix N. Four computations (Figures N-1, N-2, N-3, and N-6) were performed using the BFRACT2 model to simulate the fracture processes (the recovered fragments had more brittle than shear fracture surface area, see Table 18). These computations were for explosive-filled cylinders of Armco iron and HF-1 steel with heat treatments A and B, and for an HF-1 steel projectile with heat treatment A. Two computations (Figures N-4 and N-5) were performed using the BFRACT2 and SHEAR2 fracture models together (the recovered fragments had both brittle and shear fracture surfaces). These computations were for explosive-filled cylinders of HF-1 steel with heat treatments A and B.

Input parameters for the composition B explosive, for Armco iron (excluding the yield strength, nucleation threshold stress, and strain hardening parameter), and for the HF-1 steel SHEAR2 subroutine were obtained from Reference 1. The PBXN-106 and CH6 explosive input parameters and the cell and coordinate layout for the projectile computation were obtained from Reference 3. The HF-1 steel input parameters for the Hugoniot equation of state and for the BFRACT2 subroutine (excluding the nucleation threshold stress) were obtained from Sections IV and VI, respectively. The longitudinal-direction yield strength values of 0.18 and 1.04 GPa for Armco iron and HF-1 steel with heat treatment A, respectively, obtained from Table 3, were used in the computations. The transverse-direction yield strength values in Table 3 were not used, since only isotropic material properties can be treated in the computations. The longitudinal tensile-pull direction is parallel to the cylinder axis for the exploding cylinder experiments. Since a longitudinal-direction yield strength value was not determined for HF-1 steel with heat treatment B, the heat treatment A value was used for all the HF-1 steel computations. The larger 1.36-GPa

yield strength value for HF-1 steel determined from the Hugoniot measurements (Section IV) was used only in the PUFF computations for the high-strain-rate spall fracture experiments (Appendix G). Armco iron and HF-1 steel nucleation threshold stress values of -0.18 and -1.04 GPa, respectively, were used in the computations. For these simulations, it was assumed that cracks nucleated when the tensile stress exceeded the yield strength.

Strain hardening parameters for Armco iron and HF-1 steel with heat treatment A were obtained from the true stress-true strain curves in Figures 4 and 5, respectively. The strain hardening parameter is defined as the increase in the yield strength from $\mu = \mu_{EL}$ to $\mu = 0.2$, where the true strain $\mu = V_0/V - 1$ and the elastic limit strain $\mu_{EL} = Y/(2G)$.²⁷ Here V_0 and V are the initial and final specific volumes, respectively, Y is the initial yield strength, and G is the shear modulus. An Armco iron strain hardening parameter of 0.21 GPa was obtained from Figure 4 from the difference in the true stress value of 0.39 GPa at $\mu = 0.2$ and the elastic stress value of 0.18 GPa at $\mu_{EL} = 0.001$. An HF-1 steel strain hardening parameter of 0.94 GPa was obtained from Figure 5 from the difference in the extrapolated true stress value of 1.98 GPa at $\mu = 0.2$ and the elastic stress value of 1.04 GPa at $\mu_{EL} = 0.007$. (The extrapolated stress value was obtained by fitting a straight line through the elastic stress and strain values and the 1.41-GPa stress and 0.0804 strain values at fracture.)

The crack distribution output results for the computations are given in Figures N-1(b), N-2(b), N-3(b), N-4(b), N-5(b), N-6(b), and N-6(c). Results are given for each computational cell containing Armco iron or HF-1 steel. These results are summarized and average crack distribution values for the metal cylinder or projectile are given in Tables O-1, O-3, O-5, O-7, O-9, and O-11. For each simulation the average crack density (\bar{N}_0) and the average crack radius (\bar{R}_1) are obtained for the activated cracks with each orientation by averaging the crack distribution values for the computational cells. These average values are obtained from the equations

$$\bar{N}_0 = \frac{\sum_i N_{0i} V_i}{\sum_i V_i} \quad , \quad (9)$$

and

$$\bar{R}_1 = \frac{\sum_i N_{0i} V_i R_{1i}}{\sum_i N_{0i} V_i} \quad , \quad (10)$$

where \bar{N}_{0i} and \bar{R}_{1i} are the crack density and average crack radius, respectively, for each computational cell and V_i is the cell volume. The summation is over the appropriate computational cells. The \bar{N}_0 and \bar{R}_1 values obtained for each computation are given as footnotes in the tables in Appendix O. Figure 45 gives plots of the brittle axial and brittle circumferential crack distributions for the Armco iron and HF-1 steel cylinder computations, and the brittle circumferential crack distribution for the HF-1 steel projectile computation using the BFRACT2 subroutine. Figure 46 gives plots of the brittle axial, brittle circumferential, and shear crack distributions for the HF-1 steel cylinder computations using the BFRACT2 and SHEAR2 subroutines. For each computation, more axial cracks were activated than circumferential or shear cracks. Figure 46 indicates that for the HF-1 steel cylinder computations the number of shear cracks is a few orders of magnitude less than the number of axial or circumferential cracks, but the average crack radius is larger.

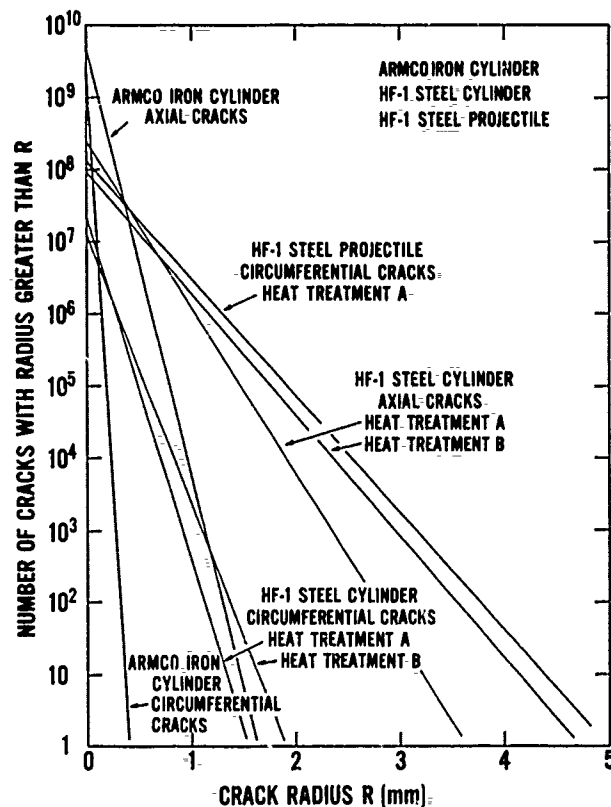


Figure 45. Brittle fracture crack distributions for the Armco-iron and HF-1-steel cylinder PUFF computations and for the HF-1 steel projectile TROTT computation using the BFRACT2 subroutine. These average crack distributions were determined from the results in Tables O-1, O-3, O-5, and O-11.

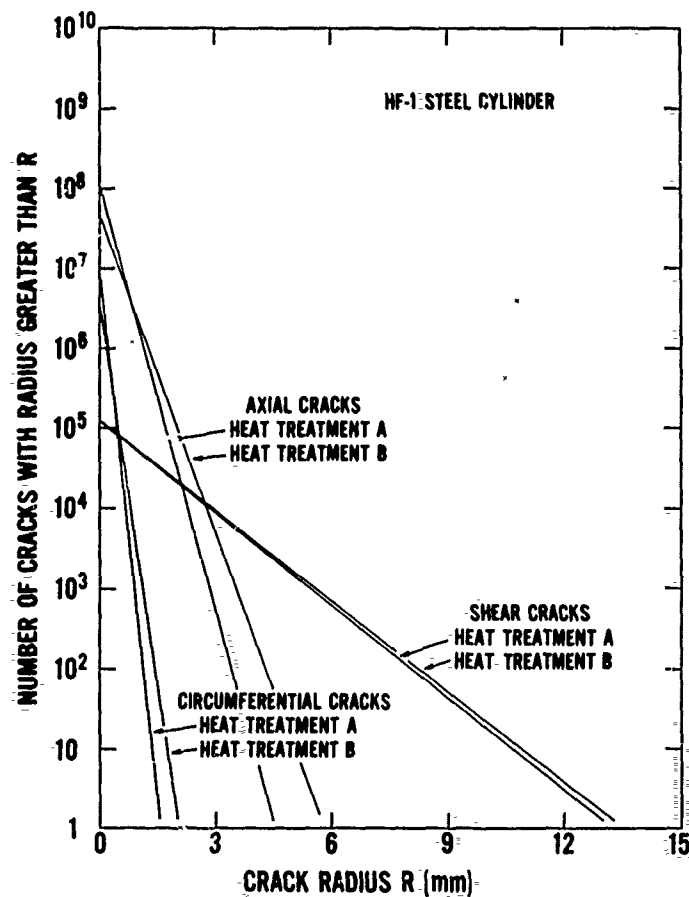


Figure 46. Brittle and shear fracture crack distributions for the HF-1 steel cylinder PUFF computations using the BFRACT2 and SHEAR2 subroutines. These average crack distributions were determined from the results in Tables O-7, and O-9.

In the SHEAR2 subroutine, shear bands nucleate when the plastic shear strain exceeds a threshold value. For these HF-1 steel computations, a threshold value of 0.17 was used since "contained" exploding HF-1 steel cylinder experiments performed at SRI indicate that shear bands begin to nucleate at an equivalent plastic strain of 0.29 (and therefore a shear strain of $0.29/\sqrt{3} = 0.17$).³ For the HF-1 steel cylinder computations using the BFRACT2 and SHEAR2 subroutines, brittle fracture began at the outer cylinder surface and propagated inward and shear bands began at the inner cylinder surface and propagated outward. Brittle fracture was nucleated in 40% of the HF-1 steel computational cells; shear bands were nucleated in the remaining cells. For the recovered HF-1 steel type 1 fragments, brittle fracture extended from the outer surface inward for about 75 to 80% of the wall thickness; the remaining 20 to 25% of the wall thickness

was shear fracture (Table 18, Figures L-9 and L-17). To nucleate brittle fracture in 80% of the computational cells, it was necessary to increase the plastic shear strain threshold to 0.45 for the computations; this corresponds to an equivalent plastic strain of 0.78. Average homogeneous plastic strain values of 0.21 and 0.24 were obtained for the HF-1 steel cylinder fragments with heat treatments A and B, respectively (Table 18). These values are somewhat smaller than the equivalent plastic strain threshold value of 0.29 used in the computations. The Armco iron fragments had about 75% homogeneous plastic strain.

The computed crack distributions in Figures 45 and 46 were used to calculate fragment mass distributions for the cylinders and projectile. All computed fragments were assumed to be type 1. For the computations using the BFRACT2 subroutine, each type 1 fragment contained the inner and outer cylinder (or projectile) surfaces, two fracture surfaces with brittle axial cracks perpendicular to the cylinder (or projectile) axis, and two fracture surfaces with brittle circumferential cracks perpendicular to cylinder (or projectile) circumference. For the HF-1 steel cylinder computations using the BFRACT2 and SHEAR2 subroutines together, each fragment had two additional fracture surfaces with shear cracks on planes 45° between the radial and circumferential axes. All fragments were assumed to have no internal cracks and to be formed from the same number of surface cracks. In order to use all the cracks to form fragments, each fragment was also assumed to have the same ratio of the number of cracks of each orientation as determined by the crack distribution results. Tables O-2, O-4, O-6, O-8, O-10, and O-11 give the calculated fragment mass distribution results. The detailed procedure for obtaining the distributions is given in footnotes in the tables. For these simulations, an iterative procedure was used to select the number of cracks per fragment. This parameter was varied until the calculated fragment mass distribution gave the best agreement with experiment. Figures 47, 48, and 49 are comparisons of the calculations and experiments.

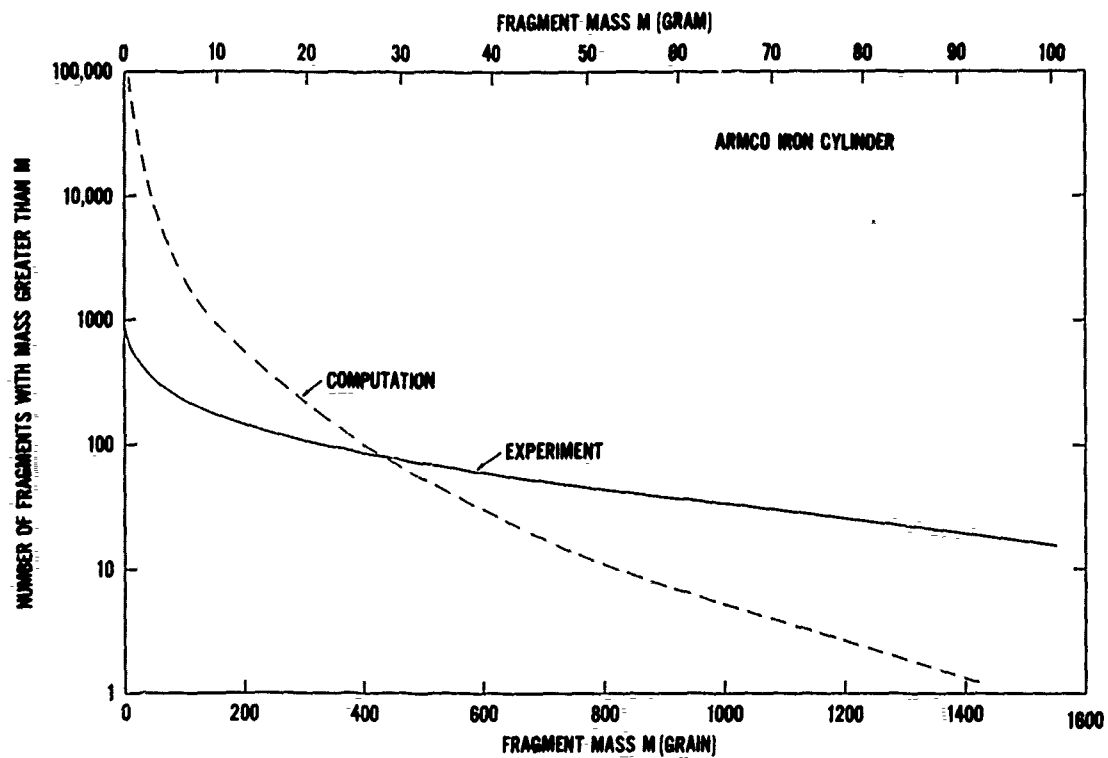


Figure 47. Comparison of measured and calculated fragment mass distributions for the Armco iron cylinder. The brittle fracture crack distributions in Figure 45 were used to obtain the calculated fragment mass distribution. The calculations are given in Table O-2.

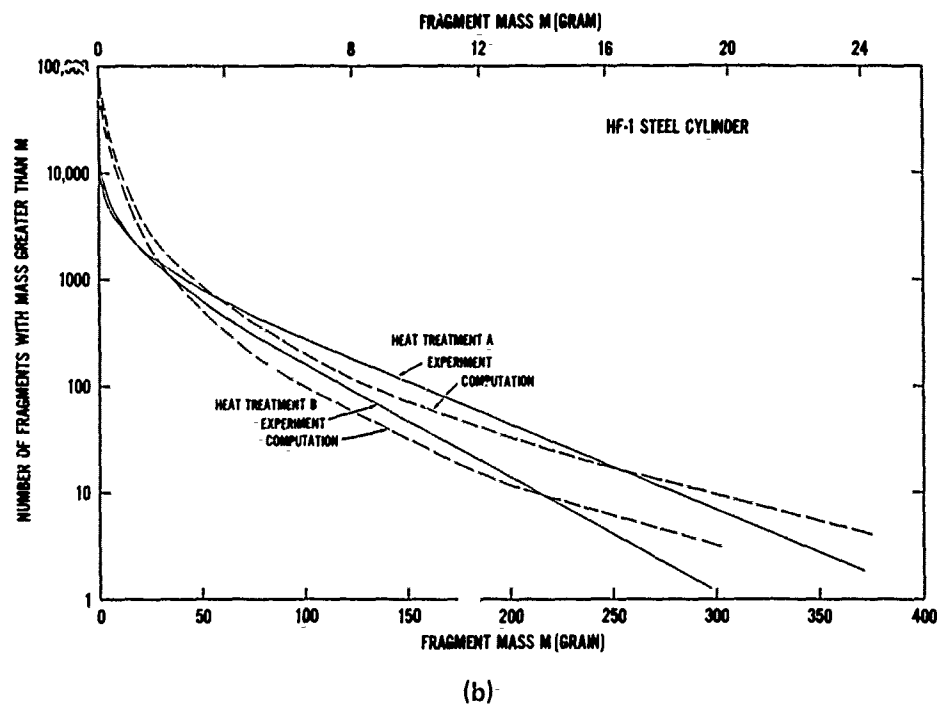
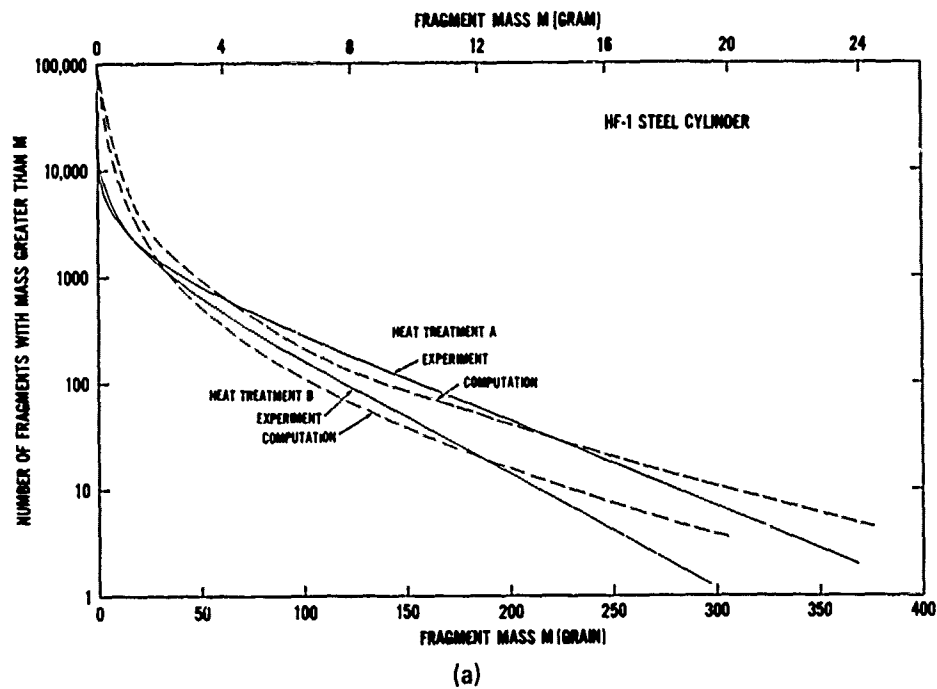


Figure 48. Comparison of measured and calculated fragment mass distributions for the HF-1 steel cylinders with heat treatments A and B. (a) The brittle fracture crack distributions in Figure 45 were used to obtain the calculated fragment mass distributions. The calculations are given in Tables O-4 and O-6. (b) The brittle and shear fracture crack distributions in Figure 46 were used to obtain the calculated fragment mass distributions. The calculations are given in Tables O-8 and O-10.

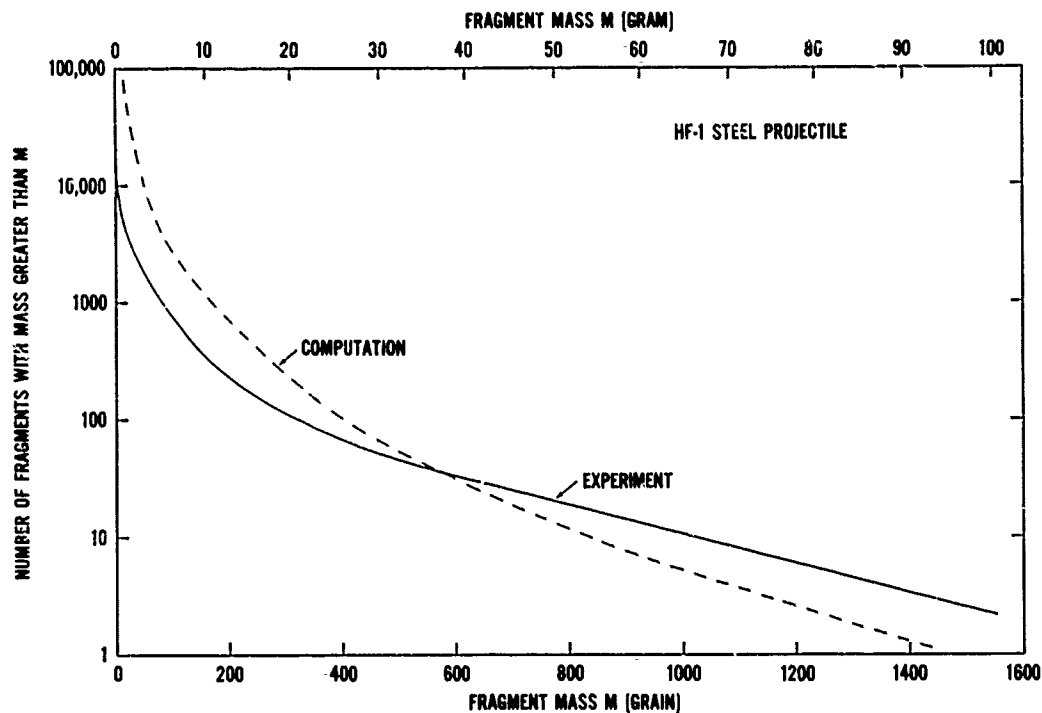


Figure 49. Comparison of measured and calculated fragment mass distributions for the HF-1 steel cylinders with heat treatment A. The brittle fracture crack distribution in Figure 45 was used to obtain the calculated fragment mass distribution. The calculations are given in Table O-11.

The Armco iron computation in Figure 47 is not in good agreement with experiment. Many more cracks were activated than were actually needed to form fragments. Better agreement between computation and experiment may be achieved if dynamic fracture parameters could be determined from framing camera photographs that show the growth and coalescence of exploding cylinder surface cracks (see Figure 31). A computation using the BFRAC2 and SHEAR2 subroutines together was also performed for an explosive-filled Armco iron cylinder. It was not possible to calculate a fragment mass distribution for this case since type 1 fragments could not be formed because the total computed shear band crack area was insufficient to form fragments. This shear band crack area was only about 0.8 and 0.2% of the total axial and circumferential crack areas, respectively.

The HF-1 steel cylinder computations in Figure 48 are in reasonable agreement with experiment. About twice as many cracks were used to form heat treatment A fragments than heat treatment B fragments. This is due to a larger average brittle crack radius for heat treatment B

material compared to heat treatment A material resulting from the different dynamic fracture parameters for the two heat treatments. A comparison of Figures 48(a) and 48(b) indicates that the use of the SHEAR2 subroutine in the PUFF computations had a negligible affect on the computed fragment mass distributions. Appendix P gives the computed stress, particle velocity, and crack concentration versus time plots for each computational cell for the HF-1 steel, heat treatment B, cylindrical PUFF computation using the BFRACT2 subroutine. Input parameters and output results for this computation are given in Figure N-3. This appendix is included so that selected shock histories can be observed in all computational cells for a cylindrical PUFF computation.

The calculated and measured HF-1 steel projectile fragment mass distributions in Figure 49 are in reasonable agreement with each other. Since only circumferential cracks were activated for this computation, an axial crack distribution equivalent to the circumferential crack distribution was assumed in order to form fragments. A TROTT computation using the BFRACT2 and SHEAR2 subroutines together was attempted but was not successful due to some unresolved computer code and subroutine incompatibilities.

Figure 50 is a series of computer plots for the TROTT simulation of the HF-1 steel projectile after explosive detonation. Brittle fracture is initiated in the cells nearest the outer wall and propagates inward in agreement with proposed fragmentation models.⁷ Fracture occurs in all cells except those in the fuse region. Figure 43 shows that the fuse region fragmented into a few tens of mainly large type 1 fragments. The joint region of the projectile was not simulated in the computation. Figure 51 is a framing camera photograph of an AISI 3140 steel projectile approximately 72 μ s after explosive detonation that is shown for comparison with the TROTT simulation. (A framing camera experiment for an HF-1 steel projectile has not been performed.) The AISI 3140 material has an R_c 40 hardness and a 1100-MPa yield strength.²⁸ These mechanical properties are similar to those for HF-1 steel (Table 3). The maximum expansion of the AISI 3140 steel projectile diameter is about 51%. This value is in reasonable agreement with a maximum computational expansion of 58% at 73 μ s after explosive detonation for the HF-1 steel projectile simulation in Figure 50.

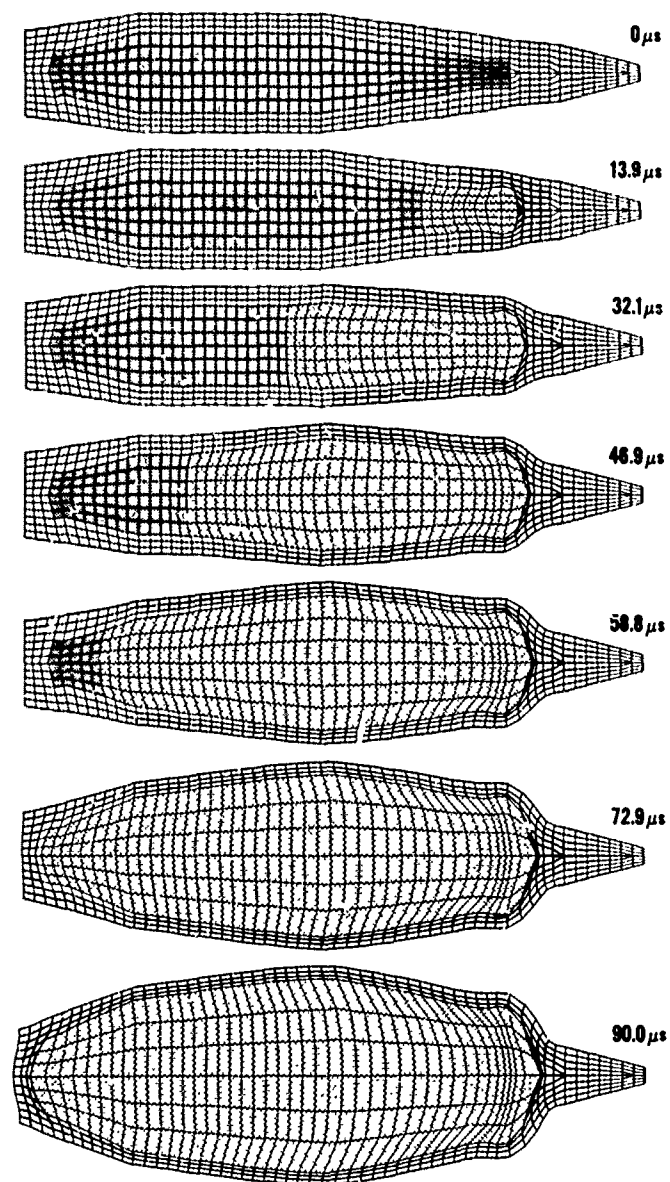


Figure 50. TROTT simulation of the exploding HF-1 steel projectile at selected times. The CH6 primary explosive in the fuse is detonated at $0 \mu s$ and subsequently detonates the PBXN-106 secondary explosive. Prior to detonation the light and dark cells are HF-1 steel and explosive, respectively. The dotted cells represent reacted explosive. As the detonation front propagates from right to left in the projectile, brittle fracture is initiated in HF-1 steel cells in the outer wall region and moves inward. The dark HF-1 steel cells indicate that brittle fracture has occurred in these cells. The HF-1 steel cells in the fuse region did not fracture and were not used in the calculation of the fragment mass distribution.



Figure 51. Framing camera photograph of AISI 3140 steel projectile approximately 78 μ s after explosive detonation. The mechanical properties for this material are similar to those for HF-1 steel with heat treatment A. Cracks cover the entire surface of the projectile in agreement with the computer plot at 73 μ s after explosive detonation for the HF-1 steel projectile simulation in Figure 50.

X. SUMMARY AND RECOMMENDATIONS

The fragmentation of Armco iron and HF-1 steel explosive-filled cylinders and an HF-1 steel projectile has been simulated with the SRI PUFF 8 and TROTT computer programs. The BFRACT2 brittle fracture model and the SHEAR2 shear band model simulated the fracture processes. Cylinder computations were performed for two heat treatments of HF-1 steel. Gas gun impact Hugoniot and soft recovery experiments were performed for both HF-1 steel heat treatments to determine input parameters for the computations. A series of exploding cylinder experiments and a projectile experiment were performed to provide fragment mass distributions for comparison with the computations. A scheme was devised for characterizing the recovered fragments from the experiments. A framing camera experiment for an explosive-filled Armco iron cylinder was performed in which the initiation and growth of cylinder surface cracks was observed as a function of time. This type of brittle crack data may be useful for the direct determination of dynamic fracture parameters for use in exploding cylinder simulations.

While considerable progress has been made in the computational simulation of naturally fragmenting munitions, further refinements are needed before a detailed computational design tool is available. For example, future computational efforts should consider the fragment characterization results of Section VIII and the assumptions in Section IX that lead to the formation of fragments. Specifically, attempts should be made to calculate fragment mass distributions that include more than one fragment type (Figures 39 through 42) and to have fragments that contain internal cracks and shear bands (Appendix L). The mechanisms of axial crack formation should be further investigated since these cracks are probably formed after circumferential crack formation (Figure 31). Analytical techniques should also be extended to permit the use of the BFRACT2 and SHEAR2 subroutines together in two-dimensional TROTT computations.

REFERENCES

1. L. Seaman, *SRI PUFF 8 Computer Program for One-Dimensional Stress Wave Propagation*, Volume 2, Contract DAAK11-77-C-0083, Army Ballistic Research Laboratory, Aberdeen Proving Ground, MD (August 1978).
2. L. Seaman and D. R. Curran, *TROTT Computer Program for Two-Dimensional Stress Wave Propagation*, Volume 3, Contract DAAK11-77-C-0083, Army Ballistic Research Laboratory, Aberdeen Proving Ground, MD (August 1978).
3. D. C. Erlich, L. Seaman, D. A. Shockey, and D. R. Curran, *Development and Application of a Computational Shear Band Model*, Contract DAAE05-76-C-0762, Army Ballistic Research Laboratory, Aberdeen Proving Ground, MD (May 1977).
4. D. C. Erlich, L. Seaman, D. R. Curran, and L. A. Shockey, *A Preliminary Study of Armor Penetration by Shear Banding*, Volume 1, Contract DAAK11-77-C-0083, Army Ballistic Research Laboratory, Aberdeen Proving Ground, MD (August 1978).

5. L. Seaman, D. A. Shockey, D. R. Curran, and R. E. Tokheim, *Development of a Shear Band Model for Fragmentation in Exploding Cylinders*, Contract N00178-74-C-0450, Naval Surface Weapons Center, Dahlgren, VA (August 1975).
6. C. R. Crowe, W. H. Holt, W. Mock, Jr., and O. H. Griffin, *Dynamic Fracture and Fragmentation of Cylinders*, NSWC/DL TK-3449, Naval Surface Weapons Center, Dahlgren, VA (November 1976).
7. B. P. Bardes, *Mechanism of Fragmentation of Silico-Manganese Steels*, R-1918, Frankford Arsenal, Philadelphia, PA (March 1969).
8. W. Mock, Jr. and W. H. Holt, *The NSWC Gas Gun Facility for Shock Effects in Materials*, NSWC/DL TR-3473, Naval Surface Weapons Center, Dahlgren, VA (July 1976).
9. O. E. Jones, F. W. Neilson, and W. B. Benedick, "Dynamic Yield Behavior of Explosively Loaded Metals Determined by a Quartz Transducer Technique," *Journal of Applied Physics*, Vol. 33, p.3224 (1962).
10. L. M. Barker, " α -Phase Hugoniot for Iron," *Journal of Applied Physics*, Vol 46, p. 2544 (1975).
11. F. S. Minshall, "The Response of Iron and Iron Alloys to Shock Waves," *Response of Metals to High Velocity Deformation*, edited by P. G. Shewman, Interscience Publishers, New York, p. 149 (1961).
12. *Selected Hugoniots*, LA-4167-MS, prepared by Group GMX-6, Los Alamos Scientific Laboratory, Los Alamos, NM (May 1969).
13. B. J. Kohn, *Compilation of Hugoniot Equations of State*, AFWL-TR-69-38, Air Force Weapons Laboratory, Kirtland Air Force Base, NM (April 1969).
14. The computer program BABS3 was provided by L. Seaman of SRI International, Menlo Park, CA.

15. L. Seaman, D. R. Curran, and R. C. Crewdson, *Transformation of Observed Crack Traces on a Section to True Crack Density for Fracture Calculations*, Poulter Laboratory Technical Report 002-78, SRI International, Menlo Park, CA (February 1978).
16. W. H. Holt and W. Mock, Jr., "Soft Recovery of Shocked Specimens for Dynamic Fracture Studies," *Review of Scientific Instruments*, Vol. 47, p. 210 (1976).
17. L. Seaman of SRI International has assumed that a specimen has negligible fracture damage if the crack density is less than about 1000 cracks/cm^3 . (private communication).
18. D. R. Strull et al., *JANAF Thermochemical Tables*, Dow Chemical Company, Contract AF 04(611)-7554, sponsored by Project Principia of the Advanced Research Projects Agency, August 1965, with Addenda published in August 1966 and August 1967.
19. *Handbook of Physics and Chemistry*, 57th edition, 1976-1977, edited by R. C. Weast, CRC Press, Cleveland, OH (1976).
20. O. E. Jones, "Metal Response Under Explosive Loading," *Behavior and Utilization of Explosives in Engineering Design*, proceedings of the 12th Annual Symposium held 2-3 March 1972, published by New Mexico Section of American Society of Mechanical Engineers, p. 125 (1972).
21. Ibid., J. E. Kennedy, "Explosive Output for Driving Metal," p. 109.
22. Experimental details and the recovered fragments for the HF-1 steel projectile experiment were provided by D. L. Brunson, W. S. Burnley, J. R. Thompson, and L. S. Sullivan of NSWC, Dahlgren, VA.
23. D. J. Ammerman, *Fragmentation Test Facilities, Methods, and Data Processing Used at NWL*, NWL TN-T-2/73, Naval Weapons Laboratory, Dahlgren, VA (1973).
24. N. F. Mott, *A Theory of the Fragmentation of Shells and Bombs*, AC 4035, Ministry of Supply, London, Great Britain (May 1943).

25. *Fracture Mechanism in Naturally Fragmenting Materials*, Report MOU/FM/1/75, A Cooperative Research and Development Project, The Australian Department of Defence and the U. S. Department of the Army, Frankford Arsenal, Philadelphia, PA (October 1975).
26. N. F. Mott and E. H. Linfoot, *A Theory of Fragmentation*, AC 3348, Ministry of Supply, London, Great Britain (January 1943).
27. L. Seaman, *SRI PUFF 3 Computer Code for Stress Wave Propagation*, Technical Report No. AFWL-TR-70-51, Air Force Weapons Laboratory, Kirtland Air Force Base, NM (September 1970).
28. The framing camera photograph for the AISI 3140 steel projectile and the mechanical properties for this material were provided by D. R. Monn of NSWC, Dahlgren, VA.

APPENDIX A

TRANSVERSE TENSILE MEASUREMENTS FOR HF-1 STEEL

Table A-1. Tensile-pull measurements for transverse-direction specimens of HF-1 steel.^{a,b}

Heat Treatment A				Heat Treatment B			
Experiment 1		Experiment 2		Experiment 3		Experiment 4	
Stress (MPa)	Strain ($\mu\text{m/m}$)	Stress (MPa)	Strain ($\mu\text{m/m}$)	Stress (MPa)	Strain ($\mu\text{m/m}$)	Stress (MPa)	Strain ($\mu\text{m/m}$)
0	0	0	0	0	0	0	0
25.7	152	25.6	80	25.7	205	25.6	100
51.3	313	51.1	210	51.3	312	51.2	235
77.0	492	76.7	318	77.0	408	76.8	356
102.6	660	102.3	452	102.6	500	102.4	496
128.3	813	127.9	580	128.3	632	128.0	642
153.9	962	153.4	708	153.9	766	153.6	795
180.0	1094	179.0	840	180.0	905	179.2	945
205.3	1236	204.6	984	205.3	1044	204.8	1118
230.9	1368	230.2	1125	230.9	1168	230.4	1292
256.7	1494	255.7	1265	256.6	1286	256.0	1458
282.2	1633	281.3	1395	282.2	1414	281.6	1595
307.9	1776	306.9	1515	307.9	1530	307.2	1730
333.5	1902	332.5	1652	333.5	1670	332.8	1875
359.2	2036	358.0	1796	359.2	1800	358.4	2045
384.8	2180	383.6	1930	384.8	1925	384.0	2202
410.5	2304	409.2	2068	410.5	2054	409.6	2350
436.2	2440	434.8	2192	436.2	2195	435.2	2490
461.8	2562	460.3	2325	461.8	2340	460.8	2630
487.5	2684	485.9	2454	487.5	2500	486.4	2788
513.1	2814	511.5	2588	513.1	2638	512.0	2940
538.8	2944	537.0	2715	538.8	2790	537.6	3092
564.4	3076	562.6	2834	564.4	2950	563.2	3235
590.2	3200	588.2	2962	590.1	3090	588.8	3390
615.8	3334	613.8	3110	615.8	3240	614.4	3536
641.4	3460	639.3	3250	641.4	3404	640.0	3695
667.1	3590	664.9	3388	667.1	3590	665.6	3874
692.7	3733	690.5	3525	692.7	3770	691.2	4064
718.4	3874	716.1	3662	744.0	4280	716.8	4284
744.0	4028	741.6	3792	769.7	4655	742.4	4555
769.7	4160	767.2	3928	795.4	5150	768.0	4900
795.4	4310	792.8	4070	821.0	5675	793.6	5395

Table A-1. Tensile-pull measurements for transverse-direction specimens of HF-1 steel.^{a,b} (Cont'd)

Heat Treatment A				Heat Treatment B			
Experiment 1		Experiment 2		Experiment 3		Experiment 4	
Stress (MPa)	Strain ($\mu\text{m/m}$)	Stress (MPa)	Strain ($\mu\text{m/m}$)	Stress (MPa)	Strain ($\mu\text{m/m}$)	Stress (MPa)	Strain ($\mu\text{m/m}$)
821.0	4452	818.4	4210	846.7	6225	819.2	5940
846.7	4642	843.9	4348	872.3	6850	844.8	6555
872.3	4886	869.5	4465	885.2 ^c	7170 ^c	870.4	7295
898.0	5268	895.1	4650			879.4 ^c	7525 ^c
923.6	5786	920.6	4844				
949.3	7110	946.0	5084				
975.0	11700	971.8	5416				
987.8	12960	984.6	5710				
1000.6	14790	997.4	6090				
1013.4	16960	1010.2	6858				
1026.3	18830	1022.9	8670				
1039.1	21020	1035.7	11200				
1051.9	22500	1048.5	13370				
1064.7	23980	1061.3	15420				
1090.4 ^c	—	1074.1	17382				
		1086.9	19360				
		1099.7	21300				
		1112.5	23180				
		1120.1 ^c	25325 ^c				

^a The transverse tensile specimens were fabricated from 6.35-mm-thick disks of HF-1 steel (the same group of disks that was used for the gas gun experiments). The disks were cut from a bar of HF-1 steel. The cylindrical axis of the specimens was transverse to the axis of the bar. The specimens were dumbbell shaped with a central-region diameter of 4.70 mm. For experiments 1 and 3, the total length and central-region length of the specimens was 35.6 and 19.1 mm, respectively. For experiments 2 and 4, the total length and central-region length of the specimens was 27.9 and 12.7 mm, respectively.

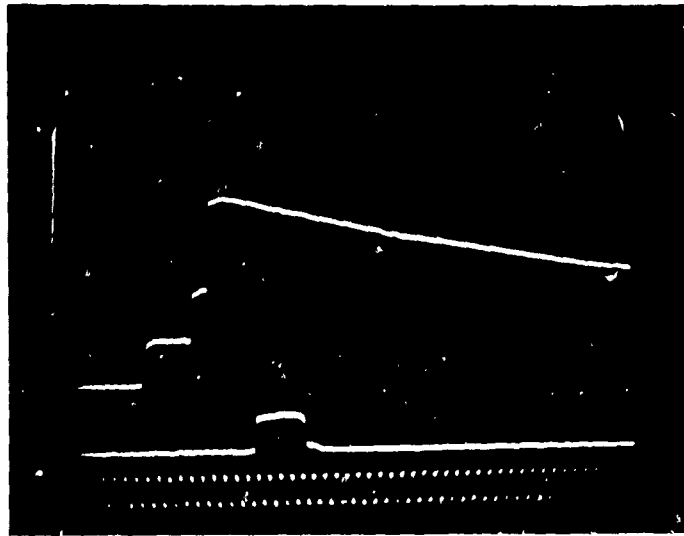
^b The specimens were pulled in a tensile-testing machine at a constant crosshead speed. The strain measurements were made with a portable strain indicator (Vishay Instruments, Inc. Model P-350). Strain gauges (Micro-Measurements Gage Type EA-06-125BT-120, $120.0 \pm 0.3\%$ Ω resistance, $2.11 \pm 0.5\%$ gage factor, 3.18-mm long, 1.57-mm grid width, were used for experiments 1 and 3; Micro-Measurements Gage Type EA-06-062AP-120, $120.0 \pm 0.3\%$ Ω resistance, $2.085 \pm 0.5\%$ gage factor, 1.57-mm long, 1.57-mm grid width, were used for experiments 2 and 4) were attached to the central region of the specimens with epoxy.

^c Stress and strain at fracture. For experiment 1 the strain of fracture was not recorded.

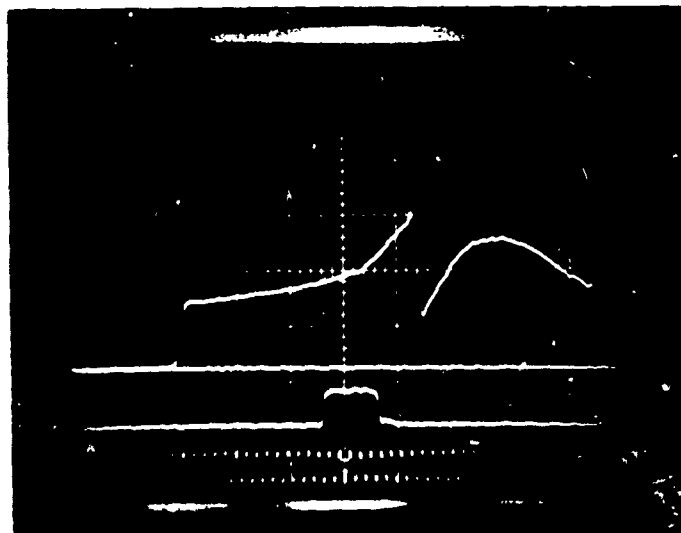
APPENDIX B

OSCILLOSCOPE RECORDS FOR HF-1 STEEL HUGONIOT EXPERIMENTS

(Figures B-1, B-2, and B-3 are the oscilloscope records for heat treatment A material. Figures B-4 and B-5 are oscilloscope records for heat treatment B material. All the experiments were shock transit time experiments except Shot 120 (Figure A-3), which was a direct impact experiment.)

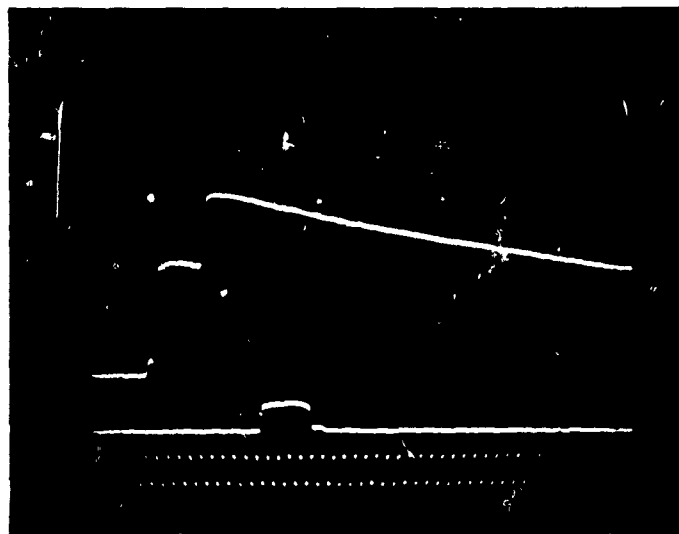


(a)

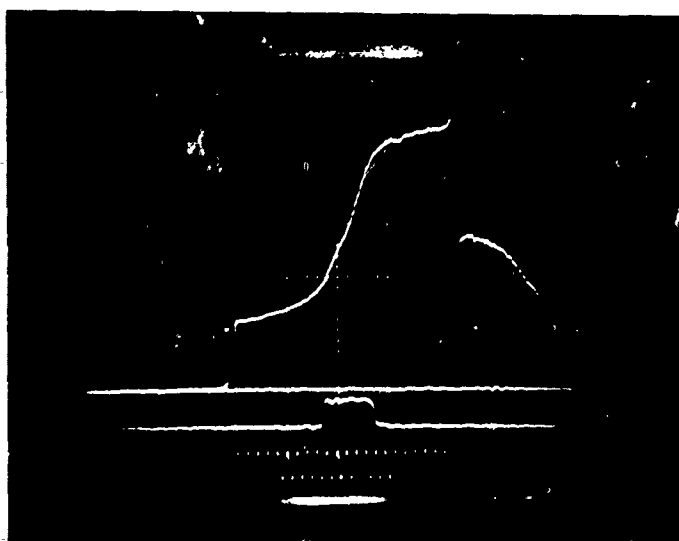


(b)

Figure B-1. Oscilloscope records for Shot 117. Time increases from left to right. (a) Tilt data record. The vertical scale is 4 V/div and the horizontal scale is 50 ns/div. The middle trace is an initial time reference square pulse. The lower trace is a 10-ns-period time calibration signal. (b) Current record from back-surface quartz gauge. The vertical scale is 100 mA/div and the horizontal scale is 50 ns/div. The middle trace is a time reference square pulse delayed by 1120 ns with respect to the initial time reference square pulse in (a) for wave velocity measurements. The lower trace is a 10-ns-period time calibration signal. Only the beginning of the plastic wave was recorded for this shot.



(a)

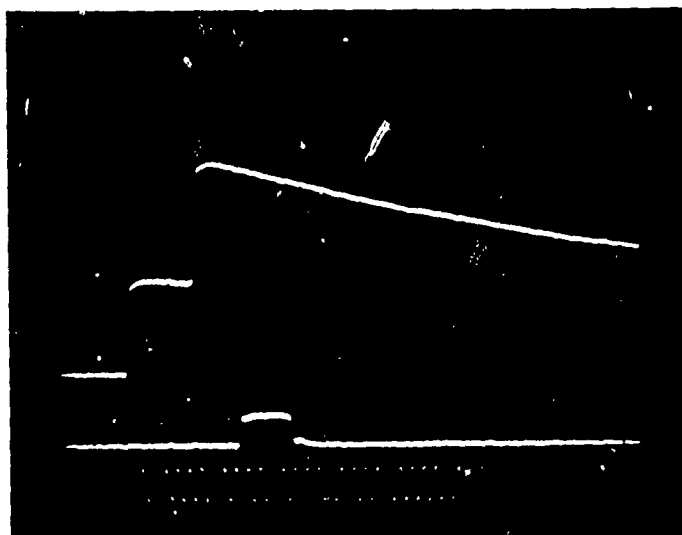


(b)

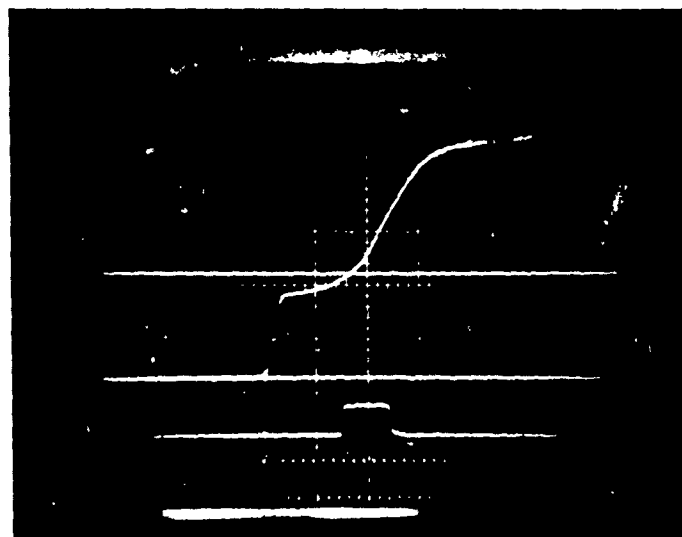
Figure B-2. Oscilloscope records for Shot 118. Time increases from left to right. (a) Tilt data record. The vertical scale is 4 V/div and the horizontal scale is 50 ns/div. The middle trace is an initial time reference square pulse. The lower trace is a 10-ns-period time calibration signal. (b) Current record from back-surface quartz gauge. The vertical scale is 100 mA/div and the horizontal scale is 50 ns/div. The middle trace is a time reference square pulse delayed by 535 ns with respect to the initial time reference square pulse in (a) for wave velocity measurements. The lower trace is a 10-ns-period time calibration signal.



Figure B-3. Oscilloscope record for Shot 120. Current record from direct impact onto a quartz gauge. Time increases from left to right. The vertical scale is 100 mA/div and the horizontal scale is 50 ns/div. The lower trace is a 10-ns-period time calibration signal.

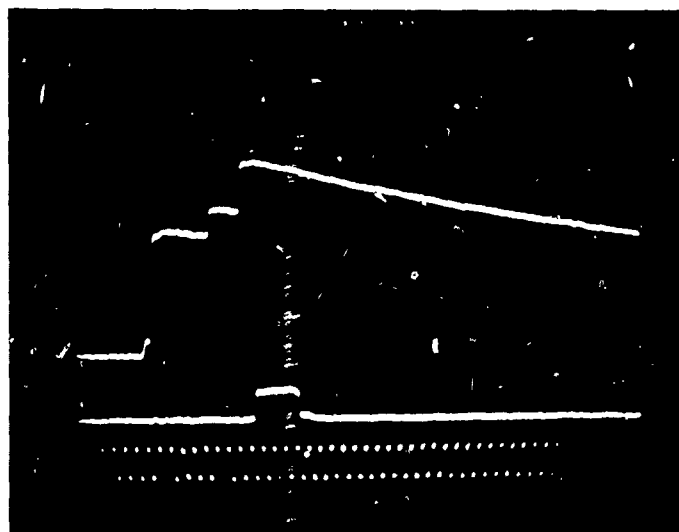


(a)

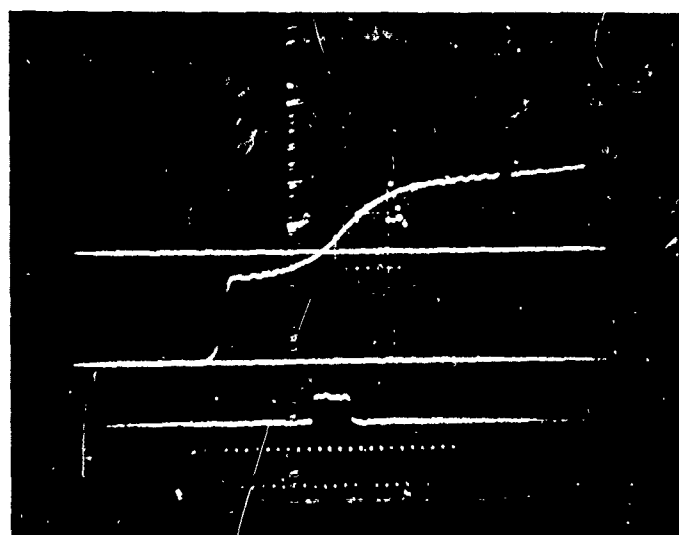


(b)

Figure B-4. Oscilloscope records for Shot 152. Time increases from left to right. (a) Tilt data record. The vertical scale is 4 V/div and the horizontal scale is 50 ns/div. The middle trace is an initial time reference square pulse. The lower trace is a 10-ns-period time calibration signal. (b) Current record from back-surface quartz gauge. The current calibration trace (upper horizontal line) has an amplitude of 100 mA. The horizontal scale is 100 ns/div. The middle trace is a time reference square pulse delayed by 1140 ns with respect to the initial time reference square pulse in (a) for wave velocity measurements. The lower trace is a 20-ns-period time calibration signal.



(a)



(b)

Figure B-5. Oscilloscope records for Shot 153. Time increases from left to right. (a) Tilt data record. The vertical scale is 4 V/div and the horizontal scale is 50 ns/div. The middle trace is an initial time reference square pulse. The lower trace is a 10-ns-period time calibration signal. (b) Current record from back-surface quartz gauge. The current calibration trace (upper horizontal line) has an amplitude of 100 mA. The horizontal scale is 100 ns/div. The middle trace is a time reference square pulse delayed by 1180 ns with respect to the initial time reference square pulse in (a) for wave velocity measurements. The lower trace is a 20-ns-period time calibration signal.

APPENDIX C

EXPRESSIONS FOR TRANSFORMING THE HUGONOT EQUATION OF STATE FROM A LINEAR SHOCK VELOCITY-PARTICLE VELOCITY RELATIONSHIP INTO A STRESS-COMPRESSION RELATIONSHIP

In this appendix, expressions are derived for converting the Hugoniot equation of state from a stress-particle velocity ($\sigma_H - u_p$) relationship into a stress-compression ($\sigma_H - \mu$) relationship. Here the compression

$$\mu = \frac{V_0}{V} - 1, \quad (C-1)$$

where V_0 and V are initial and final specific volumes, respectively.

In the elastic region the momentum ($\sigma_H - u_p$) and mass conservation equations^{C-1} are, respectively,

$$\sigma_H = \rho_0 C_L u_p, \quad u_p \leq u_e, \quad (C-2)$$

and

$$\frac{V}{V_0} = 1 - \frac{u_p}{C_L}, \quad u_p \leq u_e, \quad (C-3)$$

where $\rho_0 = 1/V_0$ is the initial density, C_L is the longitudinal wave velocity, and u_e is the particle velocity at the elastic limit. Eliminating V/V_0 from Equations (C-1) and (C-3) gives

$$\frac{u_p}{C_L} = \frac{\mu}{1 + \mu}, \quad \mu \leq \mu_e, \quad (C-4)$$

where μ_e is the compression at the elastic limit. Substituting this equation into Equation (C-2) gives

$$\sigma_H = \rho_0 C_L^2 \frac{\mu}{1 + \mu}, \quad \mu \leq \mu_e, \quad (C-5)$$

for the stress-compression relationship.

This equation can be transformed further by using expressions for the adiabatic bulk modulus K and shear modulus G for an isotropic material,

$$K = \rho_0 C_B^2 = \rho_0 \left(C_L^2 - \frac{4}{3} C_B^2 \right), \quad (C-6)$$

and

$$G = \rho_0 C_S^2, \quad (C-7)$$

where C_B and C_S are the bulk and shear wave velocities, respectively. Substituting these equations into Equation (C-5) gives

$$\sigma_H = \frac{4}{3} G \frac{\mu}{1 + \mu} + K \frac{\mu}{1 + \mu}, \quad \mu \leq \mu_e. \quad (C-8)$$

In this form of the stress-compression relationship the stress is the sum of shear and hydrostatic components. If the deviator stress σ_D is defined as

$$\sigma_D = \frac{4}{3} G \frac{\mu_e}{1 + \mu_e}, \quad (C-9)$$

then at the elastic limit ($\mu = \mu_e$) σ_H becomes

$$\sigma_e = \sigma_D + K \frac{\mu_e}{1 + \mu_e}. \quad (C-10)$$

The deviator stress is a measure of the ability of a material to support shear.

For the plastic region, an ideal elastic-plastic wave structure is assumed with equilibrium initial and final states. The momentum and mass conservation relations C^{-1} become, respectively,

$$\sigma_H = \sigma_e + \rho_e (U_s - u_e)(u_p - u_e), \quad u_p \geq u_e, \quad (C-11)$$

and

$$\frac{V}{V_0} = \left(1 - \frac{\mu_e}{C_L} \right) \left(\frac{U_s - u_p}{U_s - u_e} \right), \quad u_p \geq u_e. \quad (C-12)$$

where $\rho_e = \rho_0 (1 + \mu_e)$ is the density at the elastic limit and U_s is the shock velocity. Substituting $V_e/V_0 = 1 - u_e/C_L$ from Equation (C-3) into Equation (C-12) and simplifying gives

$$\frac{V}{V_e} = 1 - \frac{u_p - u_e}{U_s - u_e}, \quad u_p \geq u_e. \quad (C-13)$$

Using $V/V_e = (1 + \mu_e)/(1 + \mu)$ from Equation (C-1) in Equation (C-13) gives

$$\frac{u_p - u_e}{U_s - u_e} = \frac{\mu - \mu_e}{1 + \mu}, \quad \mu \geq \mu_e. \quad (C-14)$$

Inserting $u_p - u_e$ from this equation into Equation (C-11) gives

$$\sigma_H = \sigma_e + \rho_e (U_s - u_e)^2 \chi, \quad \mu \geq \mu_e, \quad (C-15)$$

where

$$\chi = \frac{\mu - \mu_e}{1 + \mu} = (1 + \mu_e) \left(\frac{\mu}{1 + \mu} - \frac{\mu_e}{1 + \mu_e} \right). \quad (C-16)$$

Equations (C-15) can be reduced further by assuming an analytical form for the $U_s - u_p$ relationship. A linear relationship

$$U_s = C_0 + su_p \quad (C-17)$$

is taken because it has been found that this form represents the Hugoniot for many materials.^{C-2} The parameter C_0 for many materials is usually very nearly equal to C_B , the bulk sound velocity at zero stress.^{C-3} Substituting Equation (C-17) into Equation (C-15) and using Equation (C-10) and the equation $C_0 - u_e + su_p = (C_0 - u_e + su_e)/(1 - s\chi)$ gives

$$\sigma_H = \sigma_D + K \frac{\mu_e}{1 + \mu_e} + \rho_e (C_0 - u_e + su_e)^2 \frac{\chi}{(1 - s\chi)^2}, \quad \mu \geq \mu_e, \quad (C-18)$$

for the stress-compression relationship in the plastic region. At the elastic limit, Equation (C-18) becomes $\sigma_H = \sigma_e$ since $\chi = 0$ at $\mu = \mu_e$.

For $\mu \geq \mu_e$ the deviatoric stress σ_D can be defined as the difference between the stress-compression relationship and the hydrostat. If the material strain hardens, the deviatoric stress will be a function of μ .^{C-1}

Equation (C-18) can be expressed as a series expansion in terms of the compression μ . The term $\chi/(1-s\chi)^2$ in Equation (C-18) can be written as

$$\frac{\chi}{(1-s\chi)^2} = \frac{(1+\mu)(\mu-\mu_e)}{[1+s\mu_e-(s-1)\mu]^2} \quad (C-19)$$

Expanding the denominator gives

$$\begin{aligned} \frac{\chi}{(1-s\chi)^2} = \frac{-\mu_e + (1-\mu_e)\mu + \mu^2}{(1+s\mu_e)^2} & \left[1 + 2\left(\frac{s-1}{1+s\mu_e}\right)\mu + 3\left(\frac{s-1}{1+s\mu_e}\right)^2\mu^2 \right. \\ & \left. + 4\left(\frac{s-1}{1+s\mu_e}\right)^3\mu^3 + 5\left(\frac{s-1}{1+s\mu_e}\right)^4\mu^4 + \dots \right] \end{aligned} \quad (C-20)$$

Regrouping terms gives

$$\begin{aligned} \frac{\chi}{(1-s\chi)^2} = \frac{1}{(1+s\mu_e)^2} & \left[-\mu_e + [-2p\mu_e + (1-\mu_e)]\mu + [-3p^2\mu_e + 2p(1-\mu_e) + 1]\mu^2 \right. \\ & \left. + [-4p^2\mu_e + 3p(1-\mu_e) + 2]p\mu^3 + [-5p^2\mu_e + 4p(1-\mu_e) + 3]p^2\mu^4 + \dots \right] \end{aligned} \quad (C-21)$$

where $p = (s-1)/(1+s\mu_e)$. Substituting Equation (C-21) into Equation (C-18) and taking $K = \rho_0 C_0^2$ gives after reducing

$$\begin{aligned} \sigma_{II} = \sigma_D + K & \left(1 - \frac{\left[1 - \mu_e \left(\frac{C_L}{C_0} - 1 \right) + s\mu_e \frac{C_L}{C_0} \right]^2}{(1+s\mu_e)^2} \right) \frac{\mu_e}{1+\mu_e} \\ & + K \frac{\left[1 - \mu_e \left(\frac{C_L}{C_0} - 1 \right) + s\mu_e \frac{C_L}{C_0} \right]^2}{(1+s\mu_e)^2} \left(\frac{(1-s\mu_e)}{(1+s\mu_e)} \mu \right. \\ & + \frac{[(2s-1)(1-s\mu_e) + s\mu_e(s+1)]}{(1+s\mu_e)^2} \mu^2 + \frac{(s-1)[(3s-1)(1-s\mu_e) + 2s\mu_e(s+1)]}{(1+s\mu_e)^3} \mu^3 \\ & \left. + \frac{(s-1)^2[(4s-1)(1-s\mu_e) + 3s\mu_e(s+1)]}{(1+s\mu_e)^4} \mu^4 + \dots \right), \quad \mu \geq \mu_e \end{aligned} \quad (C-22)$$

Equation (C-22) can be simplified because for most materials $\mu_e \ll 1$, $s \cong 1.5$, and $C_L/C_0 \cong 1$.^{C-2} Therefore, neglecting the μ_e terms gives

$$\sigma_H = \sigma_D + K\mu + K(2s-1)\mu^2 + K(s-1)(3s-1)\mu^3 + K(s-1)^2(4s-1)\mu^4 + \dots, \quad \mu \geq \mu_e. \quad (C-23)$$

This equation gives a simpler form for the stress-compression relationship than Equation (C-22). Only the initial density ρ_0 and the two parameters in the linear shock velocity-particle relationship $U_s = C_0 + s u_p$ are necessary to determine the coefficients. For HF-1 steel the calculated coefficients for this equation only differed by a few percent from the more complicated coefficients in Equation (C-22). For most materials the coefficients in Equation (C-23) are evaluated through the μ^3 term. Christman et al.^{C-1} calculated a zero-pressure Grüneisen parameter $\gamma_0 = 2s-1$ using the Dugdale and MacDonald Grüneisen formula.^{C-4} The coefficient of the μ^2 term in Equation (C-23) can therefore be represented by $K\gamma_0$ where γ_0 is a zero-pressure Grüneisen parameter estimate and K is the low-pressure bulk modulus. This observation was initially made by Rice et al.^{C-5}

The results of this section could have been expressed in terms of the compression η where

$$\eta = 1 - \frac{V}{V_0}. \quad (C-24)$$

Using Equation (C-1) for the compression μ , it can be shown that $(1 + \mu)(1 - \eta) = 1$, which gives the relations $\eta = \mu/(1 + \mu)$ and $\mu = \eta/(1 - \eta)$.

REFERENCES

- C-1. D. R. Christman, W. M. Isbell, S. G. Babcock, A. R. McMillian, and S. J. Green, *Measurements of Dynamic Properties of Materials, Vol. III, 6061-T6 Aluminum*, DASA 2501-3, General Motors Technical Center, Warren, MI (November 1971).

- C-2 R. G. McQueen, S. P. Marsh, J. W. Taylor, J. N. Fritz, and W. J. Carter, "The Equation of State of Solids from Shock Wave Studies," *High Velocity Impact Phenomena*, edited by R. Kinslow, Academic Press, New York, p. 293 (1970).
- C-3. G. E. Duvall and R. A. Graham, "Phase Transitions Under Shock Wave Loading," *Reviews of Modern Physics*, Vol. 49, p. 523 (1977).
- C-4. J. S. Dugdale and D. K. C. MacDonald, "The Thermal Expansion of Solids," *Physical Review*, Vol. 89, p. 832 (1953).
- C-5. M. H. Rice, R. G. McQueen, and J. M. Walsh, "Compression of Solids by Strong Shock Waves," *Solid State Physics, Vol. 6*, edited by F. Seitz and D. Turnbull, Academic Press, New York, p. 1 (1958).

APPENDIX D

PHOTOGRAPHS OF THE SPALL FRACTURE SPECIMENS OF HF-1 STEEL

(The impactor velocity, initial impactor thickness, and initial specimen thickness are given for each shot. Cracks were digitized for all the shots except the no-damage Shots 89 and 147. Cracks were measured in the approximate central one-third region of the sectioned specimen face. The bottom edge of each specimen is the impact surface. The specimen magnification is approximately 5X).



(a) Shot 95, 0.130-km/s impactor velocity, 2.37-mm-thick impactor, 6.31-mm-thick specimen.



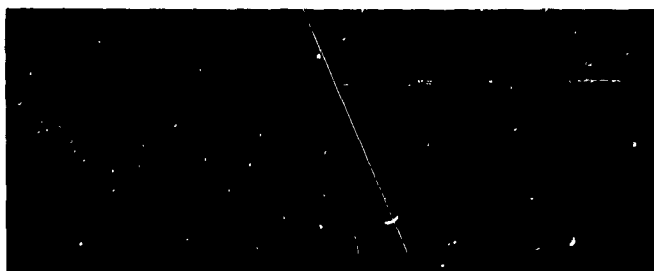
(b) Shot 110, 0.149-km/s impactor velocity, 2.37-mm-thick impactor, 6.35-mm-thick specimen.



4 mm

(c) Shot 98, 0.160-km/s impactor velocity, 2.37-mm-thick impactor, 6.35-mm-thick specimen.

Figure D-1. Sectioned HF-1 steel specimens with heat treatment A for (a) Shot 95, (b) Shot 110, and (c) Shot 98.



(a) Shot 92, 0.180-km/s impactor velocity, 2.37-mm-thick impactor, 6.34-mm-thick specimen.



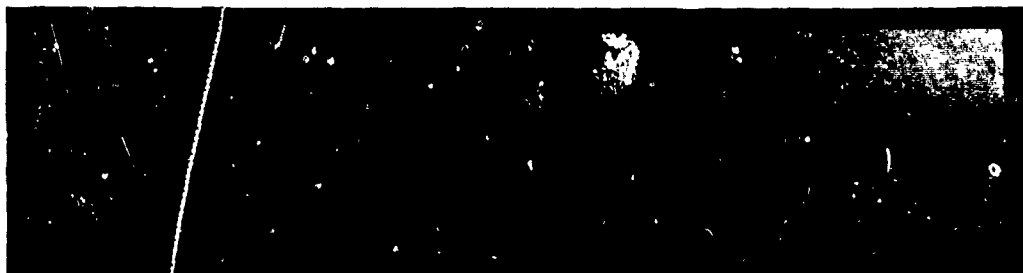
(b) Shot 91, 0.183-km/s impactor velocity, 2.37-mm-thick impactor, 6.34-mm-thick specimen.



4 mm

(c) Shot 90, 0.191-km/s impactor velocity, 2.37-mm-thick impactor, 6.35-mm-thick specimen.

Figure D-2. Sectioned HF-1 steel specimens with heat treatment A for (a) Shot 92, (b) Shot 91, and (c) Shot 90.



(a) Shot 94, 0.200-km/s impactor velocity, 2.37-mm-thick impactor, 6.36-mm-thick specimen.



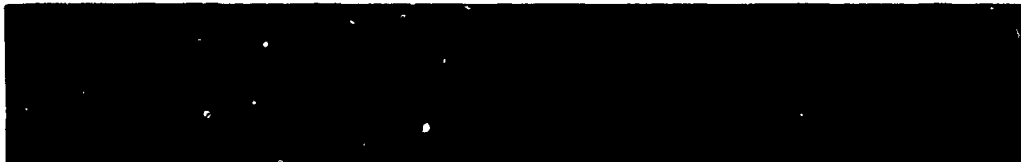
(b) Shot 89, 0.120-km/s impactor velocity, 1.61-mm-thick impactor, 3.18-mm-thick specimen.



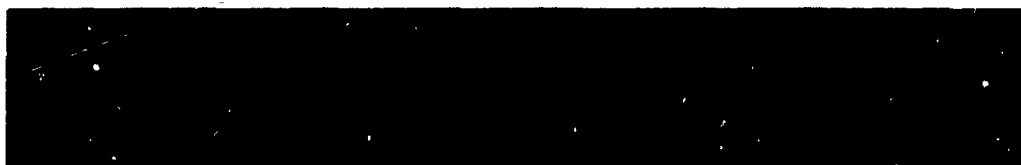
4 mm

(c) Shot 113, 0.202-km/s impactor velocity, 1.60-mm-thick impactor, 3.19-mm-thick specimen.

Figure D-3. Sectioned HF-1 steel specimens with heat treatment A for (a) Shot 94, (b) Shot 89, and (c) Shot 113.



(a) Shot 88, 0.276-km/s impactor velocity, 1.60-mm-thick impactor, 3.19-mm-thick specimen.
Only half of the full-spalled specimen is shown.



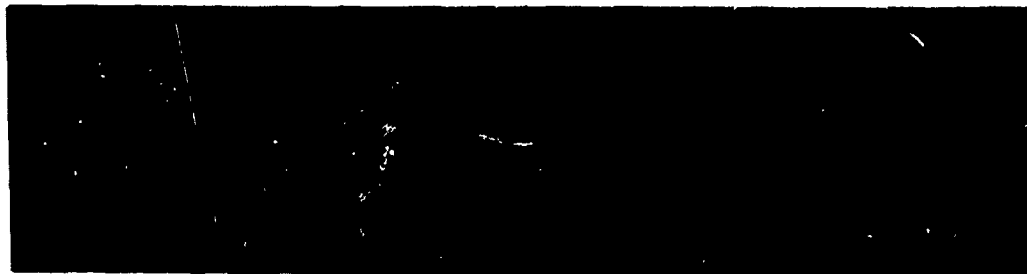
(b) Shot 111, 0.193-km/s impactor velocity, 1.16-mm-thick impactor, 3.19-mm-thick specimen.



4 mm

(c) Shot 112, 0.204-km/s impactor velocity, 1.16-mm-thick impactor, 3.19-mm-thick specimen.

Figure D-4. Sectioned HF-1 steel specimens with heat treatment A for (a) Shot 88, (b) Shot 111, and (c) Shot 112.



(a) Shot 154, 0.094-km/s impactor velocity, 2.37-mm-thick impactor, 6.35-mm-thick specimen.



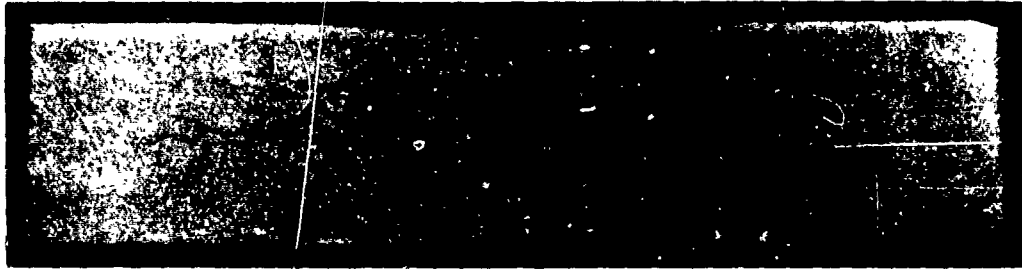
(b) Shot 145, 0.116-km/s impactor velocity, 2.38-mm-thick impactor, 6.35-mm-thick specimen.



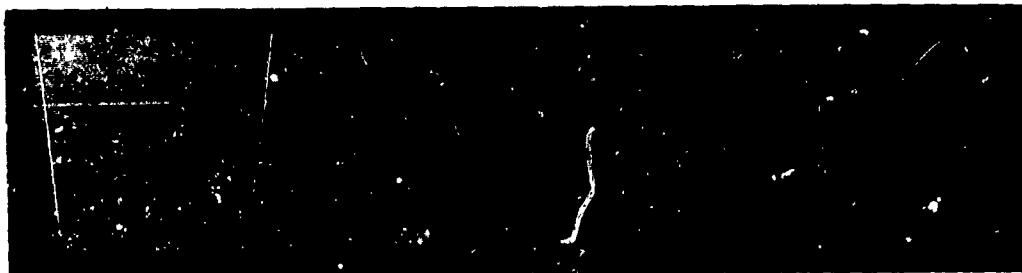
4 mm

(c) Shot 144, 0.148-km/s impactor velocity, 2.37-mm-thick impactor, 6.35-mm-thick specimen.

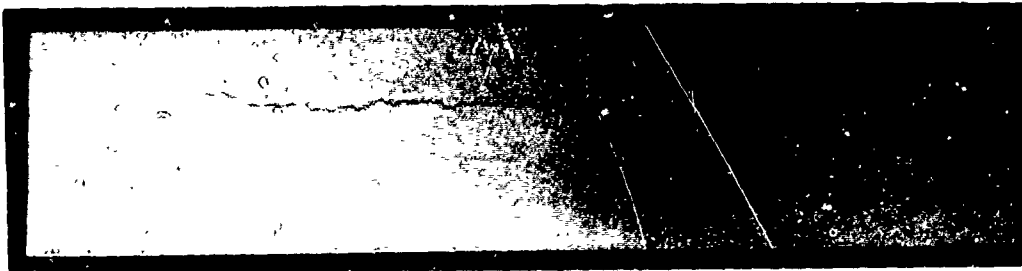
Figure D-5. Sectioned HF-1 steel specimens with heat treatment B for (a) Shot 154, (b) Shot 145, and (c) Shot 144.



(a) Shot 143, 0.169-km/s impactor velocity, 2.37-mm-thick impactor, 6.35-mm-thick specimen.



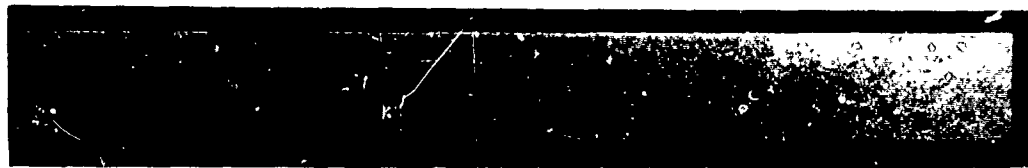
(b) Shot 142, 0.191-km/s impactor velocity, 2.37-mm-thick impactor, 6.36-mm-thick specimen.



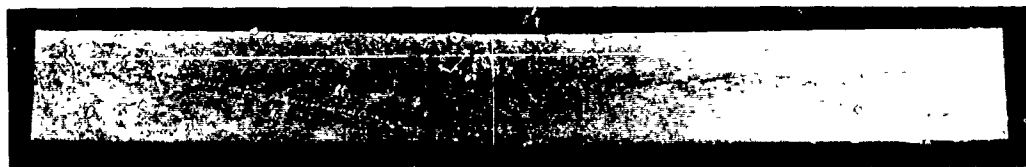
4 mm

(c) Shot 150, 0.152-km/s impactor velocity, 1.58-mm-thick impactor, 6.36-mm-thick specimen.

Figure D-6. Sectioned HF-1 steel specimens with heat treatment B for (a) Shot 143, (b) Shot 142, and (c) Shot 150.



(a) Shot 148, 0.172-km/s impactor velocity, 1.58-mm-thick impactor, 3.18-mm-thick specimen.



(b) Shot 149, 0.194-km/s impactor velocity, 1.58-mm-thick impactor, 3.18-mm-thick specimen.

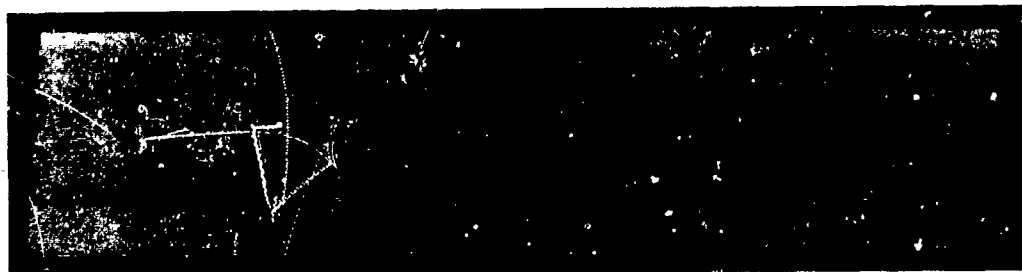


(c) Shot 147, 0.147-km/s impactor velocity, 1.15-mm-thick impactor, 3.18-mm-thick specimen.

Figure D-7. Sectioned HF-1 steel specimens with heat treatment B for (a) Shot 148, (b) Shot 149, and (c) Shot 147.



(a) Shot 146, 0.167-km/s impactor velocity, 1.16-mm-thick impactor, 3.18-mm-thick specimen.



4 mm

(b) Shot 151, 0.190-km/s impactor velocity, 1.15-mm-thick-impactor, 6.36-mm-thick specimen.

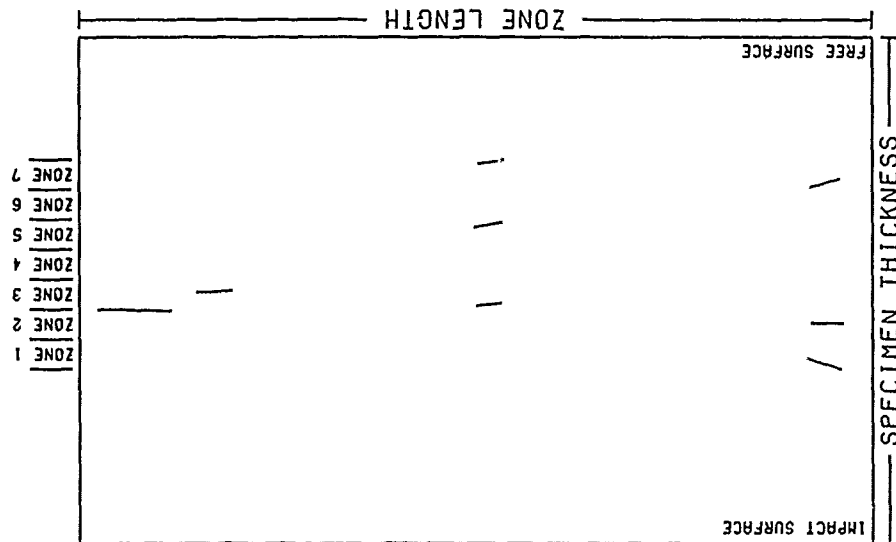
Figure D-8. Sectioned HF-1 steel specimens with heat treatment B for (a) Shot 146 and (b) Shot 151.

APPENDIX E

CRACK DISTRIBUTIONS FOR SPALL FRACTURE SPECIMENS OF HF-1 STEEL

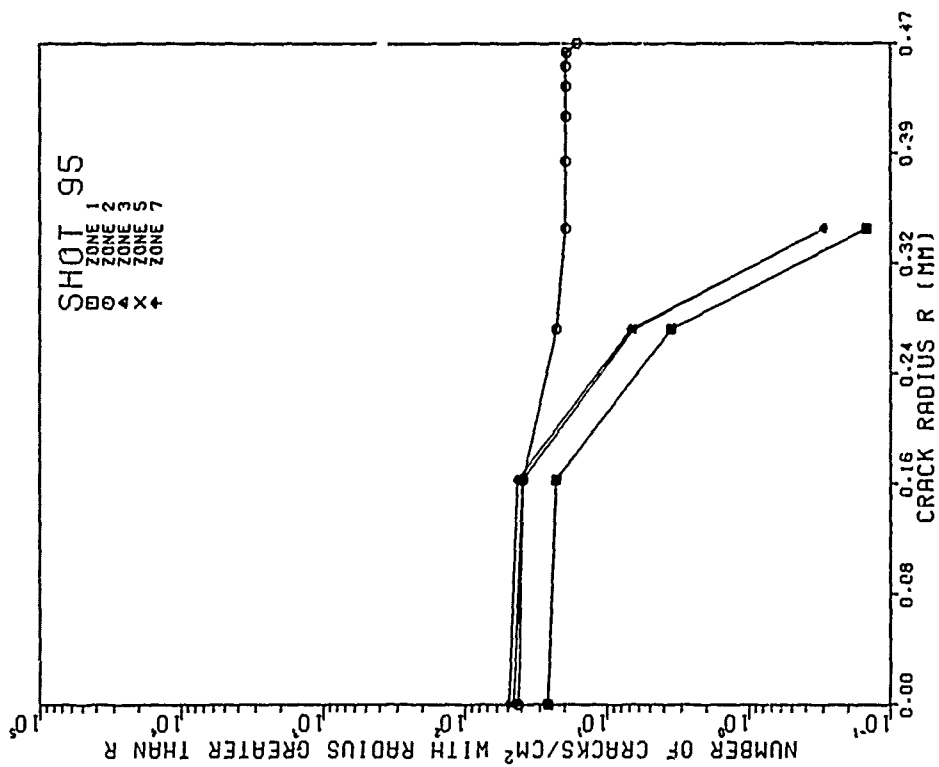
(Figures are presented for eleven heat treatment A specimens (Shots 95 through 112) and ten heat treatment B specimens (Shots 154 through 151). Figures are not presented for the no-damage Shots 89 and 147. Each figure contains five plots. Plots (a) and (b) are distributions for the digitized cracks. Cracks were measured in the approximate central one-third region of the sectioned specimen face. A crack was considered to be in the central region if its midpoint was in the region. Plots (c), (d), and (e) are crack-size distributions that were calculated from the digitized cracks using the SRI statistical transformation computer program BABS3. The dashed line in plot (d) of each figure is a fit of the equation $N_g = N_0 \exp(-R/R_1)$ to the volume crack-size distribution for the zone of maximum damage. Here N_g is the number of cracks per unit volume with radius greater than R_1 . The calculated values for N_0 and R_1 for the zone of maximum damage are given in the plot. The spall plane in plots (b) and (e) is taken as the difference in the specimen and impactor thicknesses.)

SHOT 95
 IMPACTOR VELOCITY 0.130 MM/S
 IMPACTOR THICKNESS 2.37 MM
 SPECIMEN THICKNESS 6.31 MM
 NUMBER OF CRACKS 8
 NUMBER OF ZONES 7
 ZONE LENGTH 10.16 MM
 ZONE WIDTH 0.37 MM
 IMPACT SURFACE TO ZONE1 2.17 MM

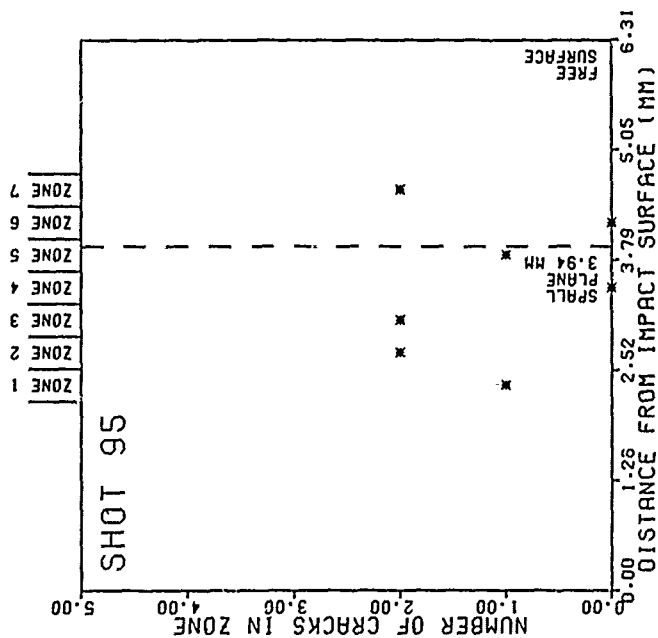


(a)

Figure E-1. Crack distributions for Shot 95. (a) Digitized cracks on sectioned specimen surface. (b) Number of digitized cracks as a function of position. (c) Surface crack-size distributions. (d) Volume crack-size distributions. (e) Volume density of cracks as a function of position.



(c)



(b)

Figure E-1. (Continued)

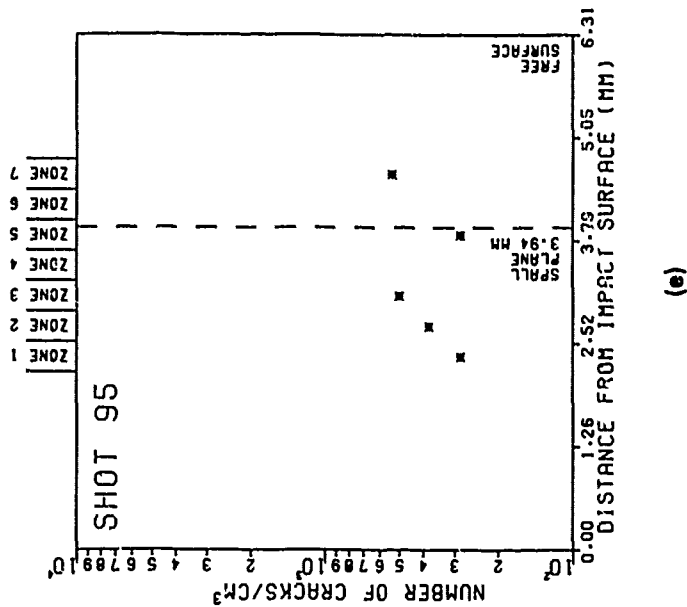
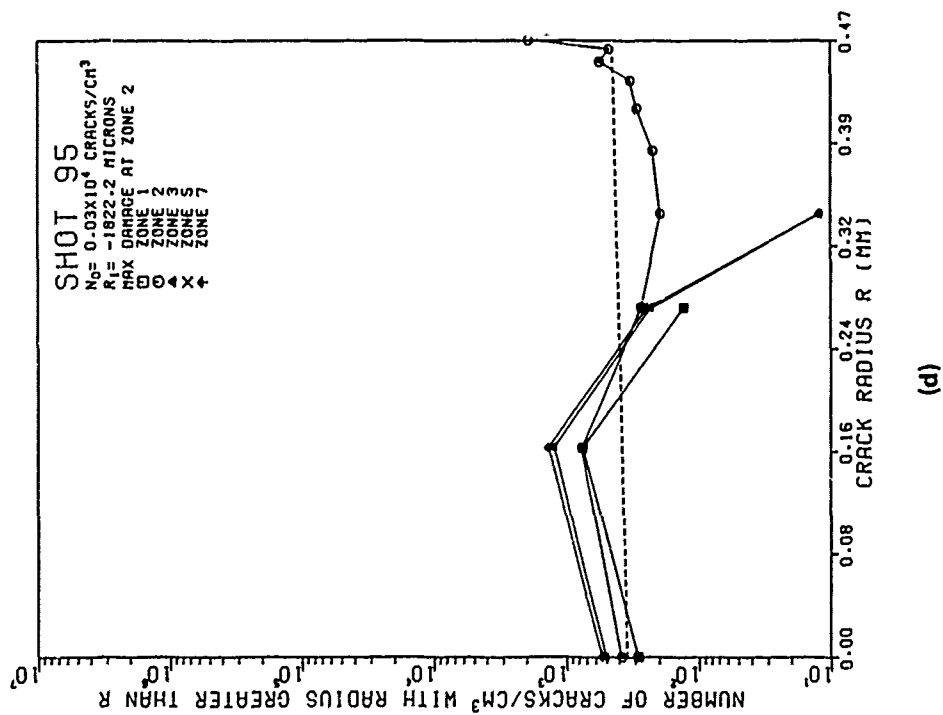
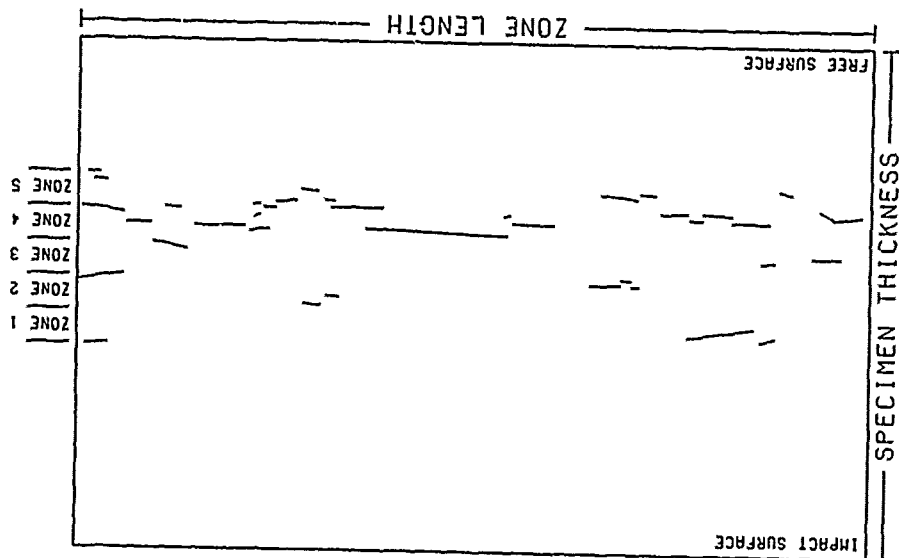


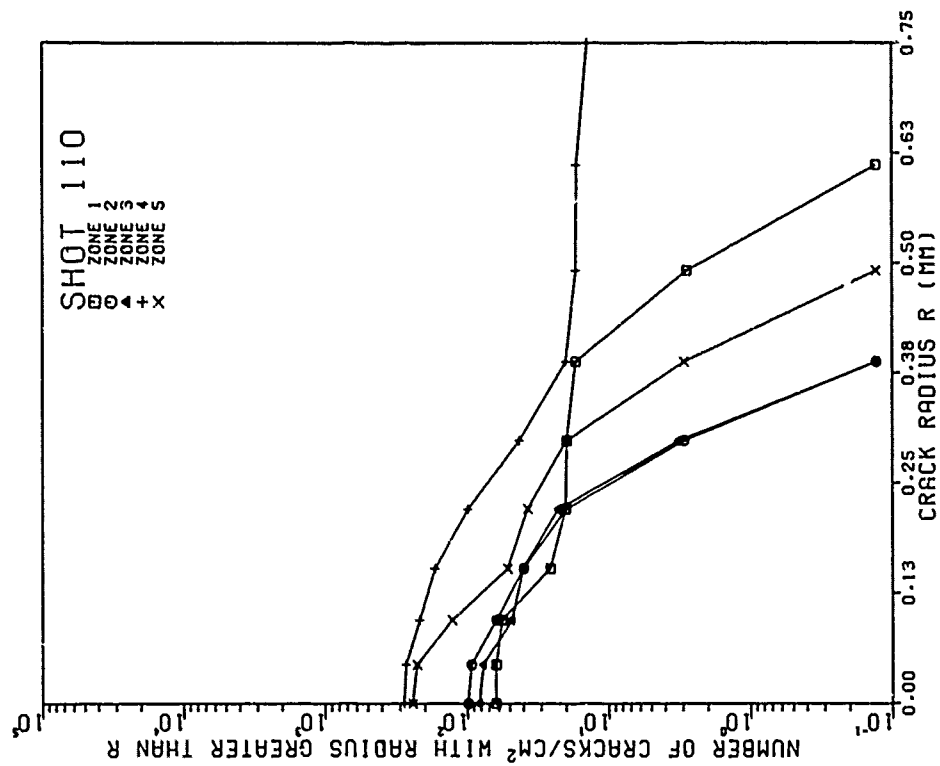
Figure E-1. (Continued)

SHOT 110
 IMPACTOR VELOCITY 0.149 KM/S
 IMPACTOR THICKNESS 2.37 MM
 SPECIMEN THICKNESS 6.35 MM
 NUMBER OF ZONES 5
 ZONE LENGTH 10.16 MM
 ZONE WIDTH 0.43 MM
 IMPACT SURFACE TO ZONE1 2.54 MM

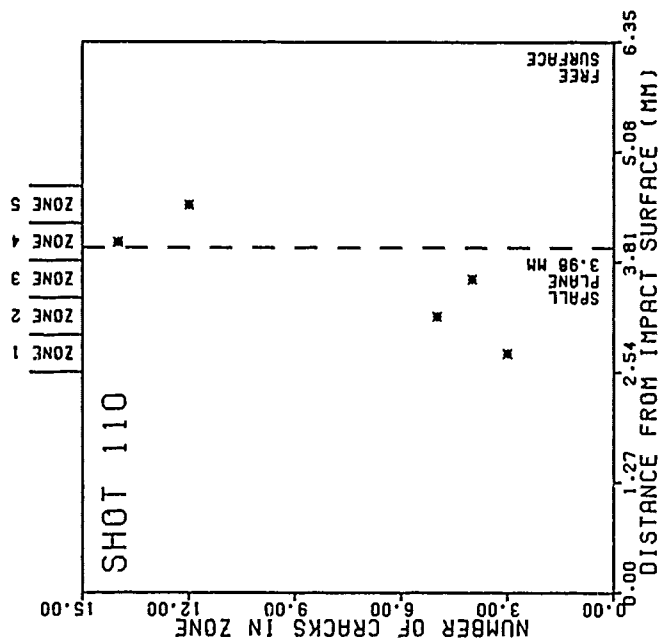


(a)

Figure E-2. Crack distributions for Shot 110. (a) Digitized cracks on sectioned specimen surface. (b) Number of digitized cracks as a function of position. (c) Surface crack-size distributions. (d) Volume crack-size distributions. (e) Volume density of cracks as a function of position.



(c)



(b)

Figure E-2. (Continued)

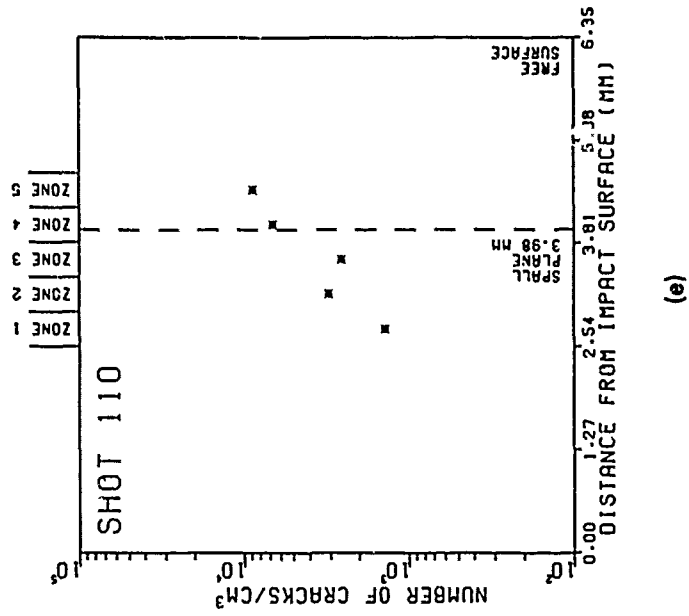
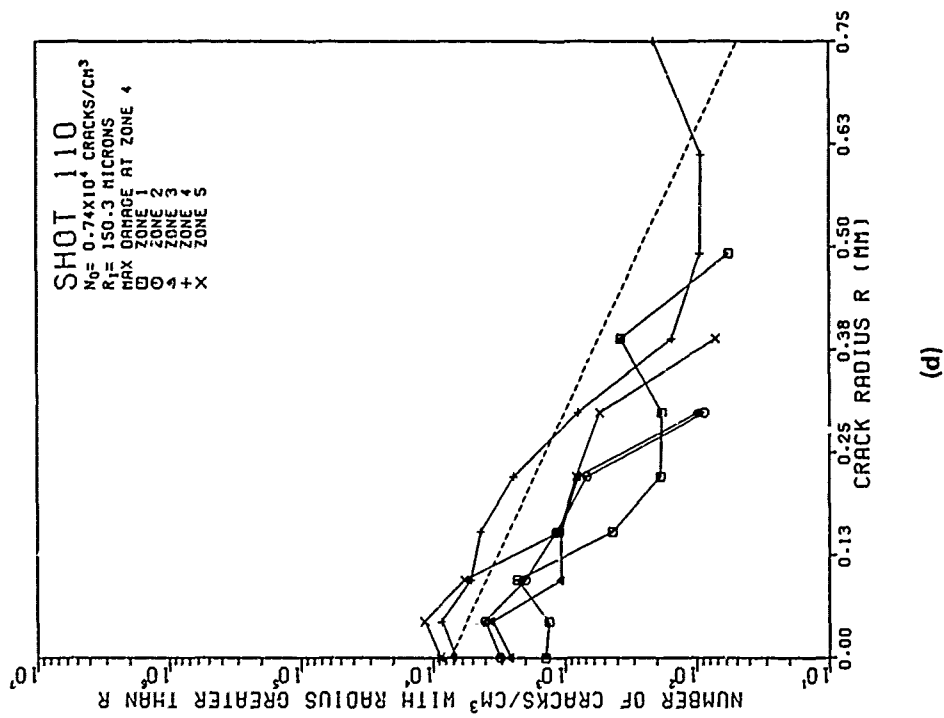
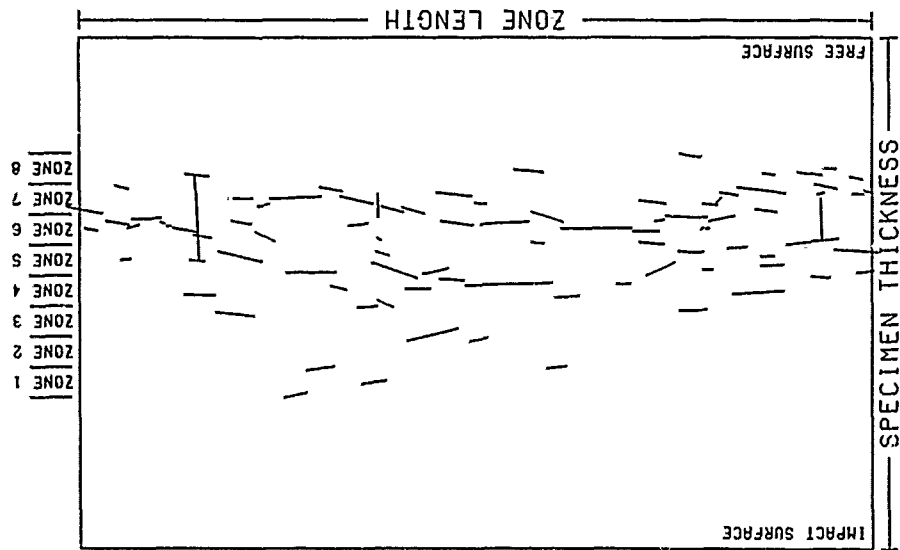


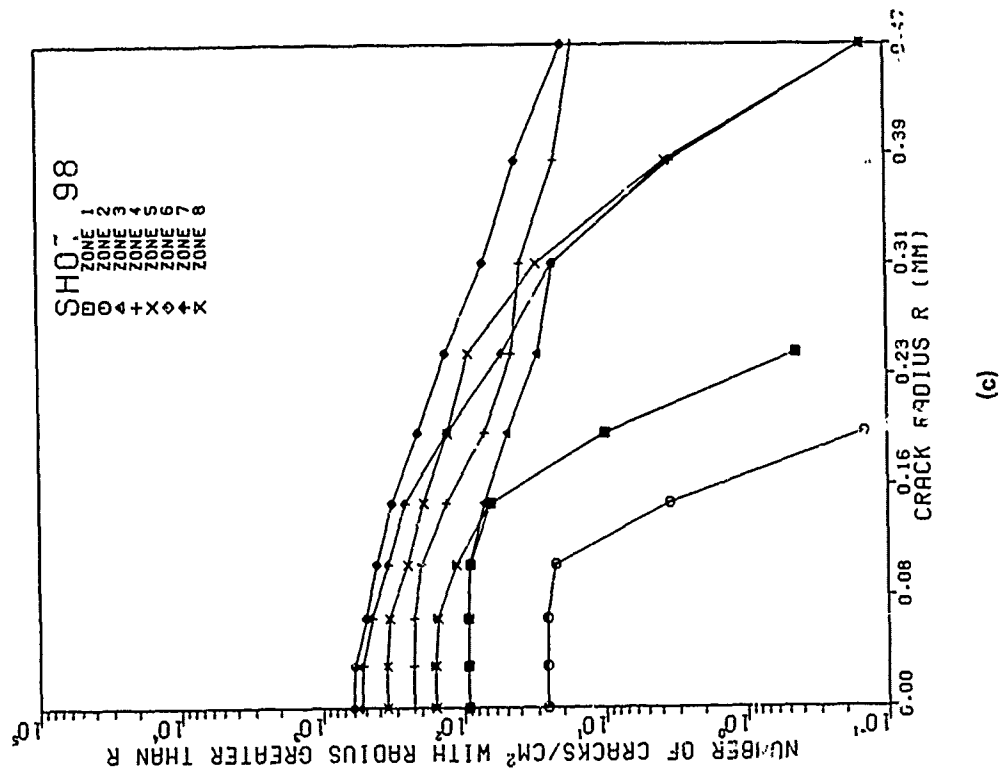
Figure E-2. (Continued)

SHOT 98
 IMPACTOR VELOCITY 0.160 MM/S
 IMPACTOR THICKNESS 2.37 MM
 SPECIMEN THICKNESS 6.35 MM
 NUMBER OF ZONES 8
 ZONE LENGTH 10.16 MM
 ZONE WIDTH 0.38 MM
 IMPACT SURFACE TO ZONE1 1.87 MM

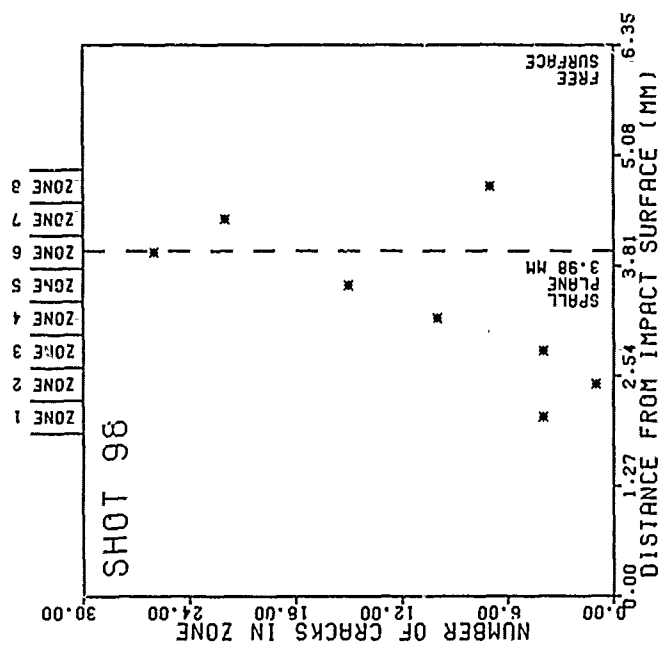


(a)

Figure E-3. Crack distributions for Shot 98. (a) Digitized cracks on sectioned specimen surface. (b) Number of digitized cracks as a function position. (c) Surface crack-size distributions. (d) Volume crack-size distributions. (e) Volume density of cracks as a function of position.



(c)



(b)

Figure E-3. (Continued)

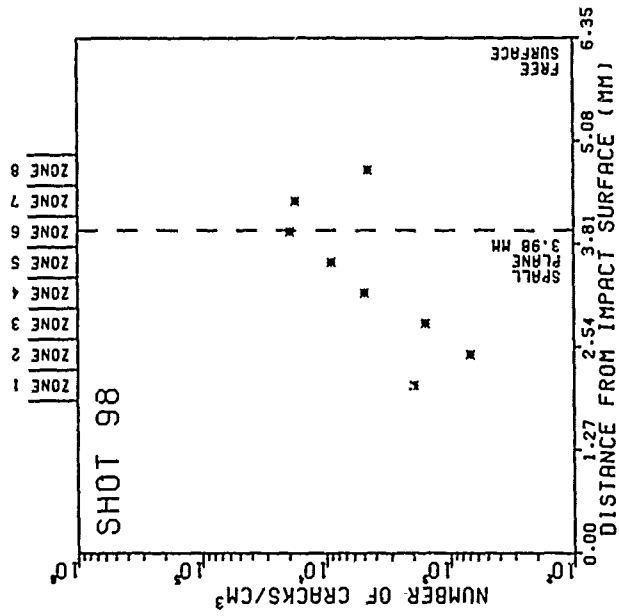
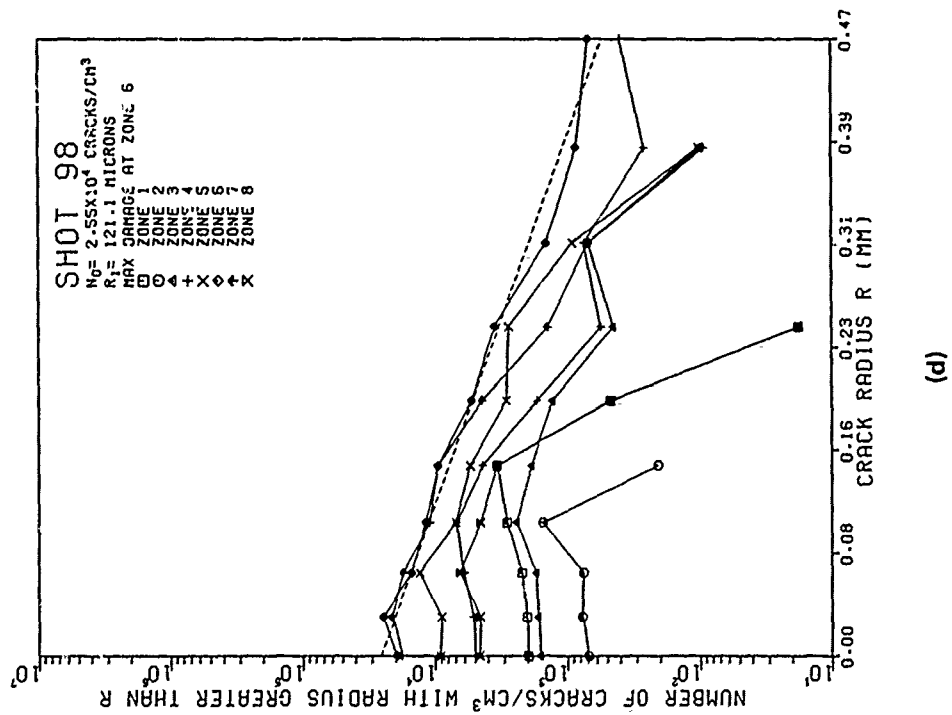
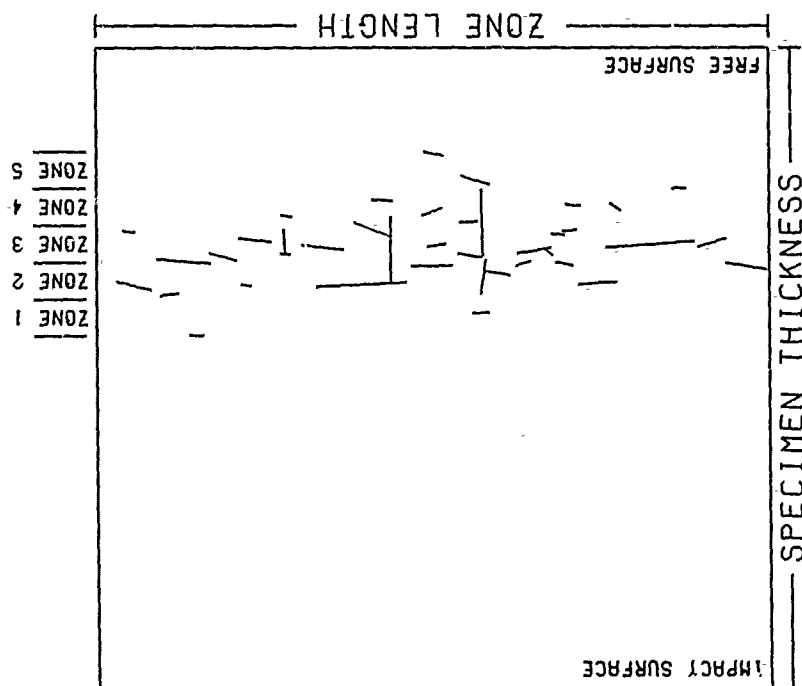


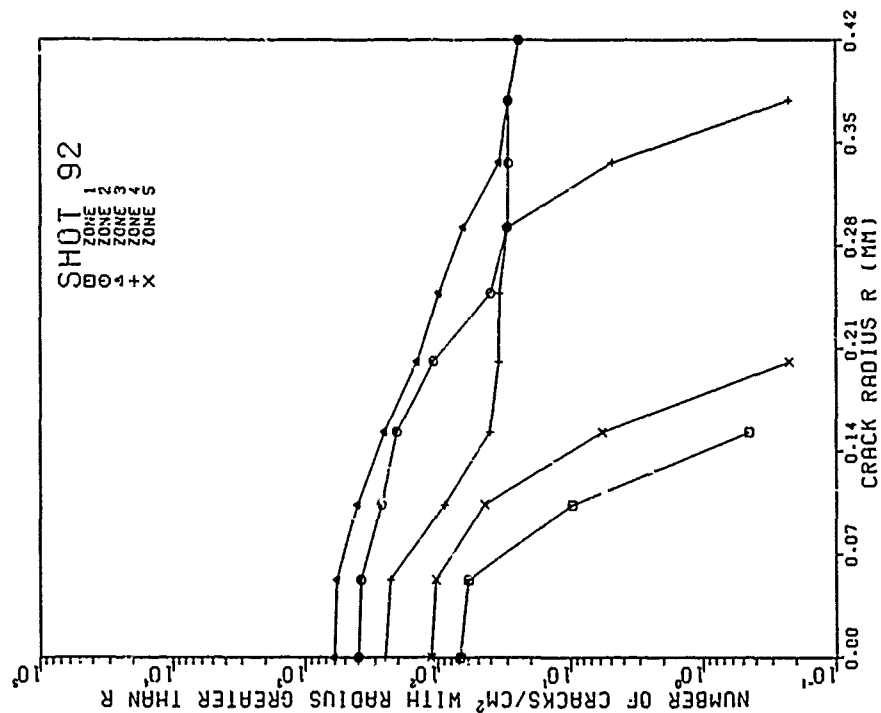
Figure E-3. (Continued)

SHOT 92
 IMPACTOR VELOCITY 0.180 KM/S
 IMPACTOR THICKNESS 2.38 MM
 SPECIMEN THICKNESS 6.34 MM
 NUMBER OF CRACKS 40
 NUMBER OF ZONES 5
 ZONE LENGTH 6.86 MM
 ZONE WIDTH 0.36 MM
 IMPACT SURFACE TO ZONE1 3.49 MM

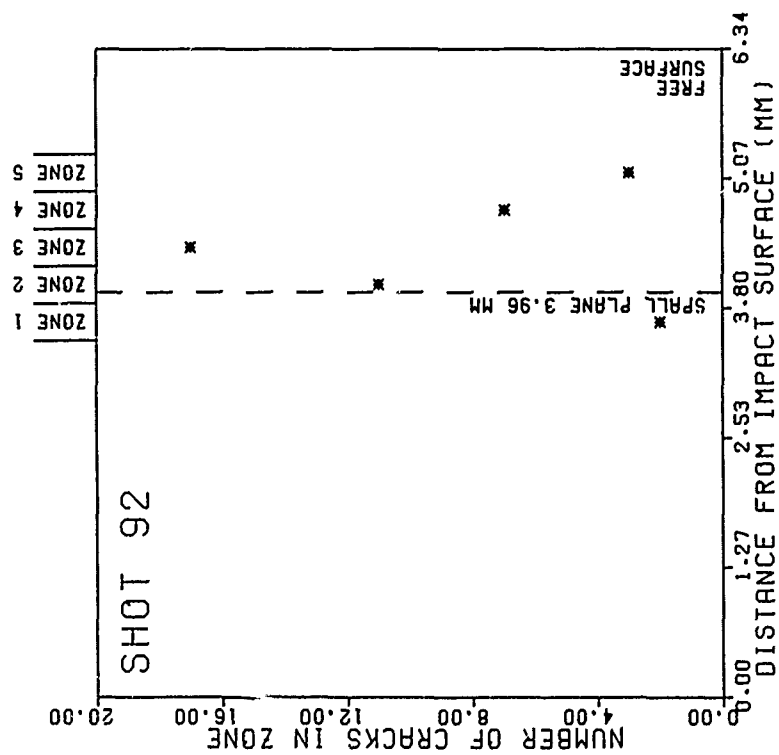


(a)

Figure E-4. Crack distributions for Shot 92. (a) Digitized cracks on sectioned specimen surface. (b) Number of digitized cracks as a function of position. (c) Surface crack-size distributions. (d) Volume crack-size distributions. (e) Volume density of cracks as a function of position.

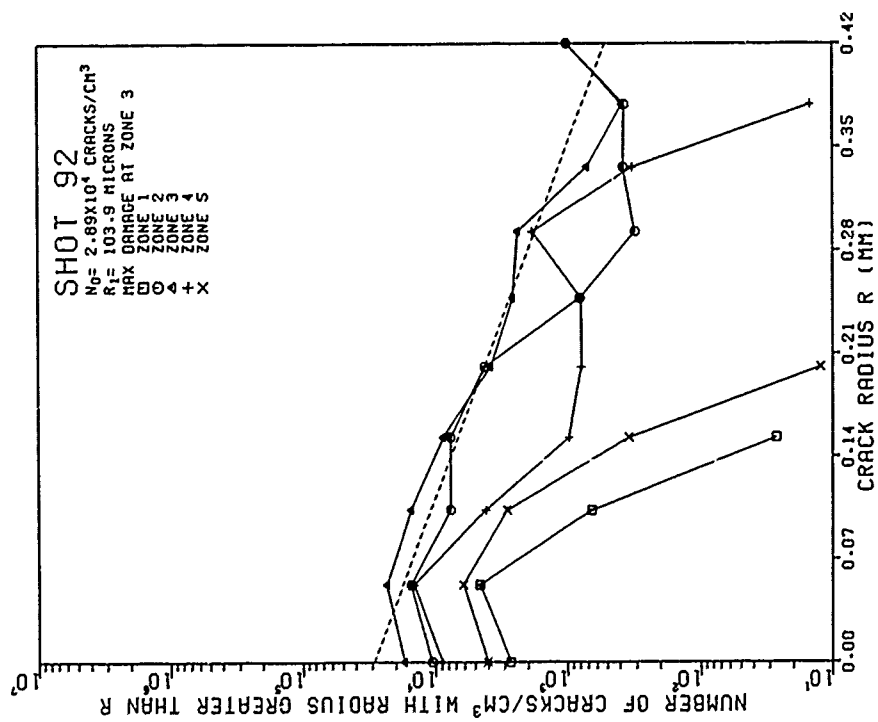


(c)

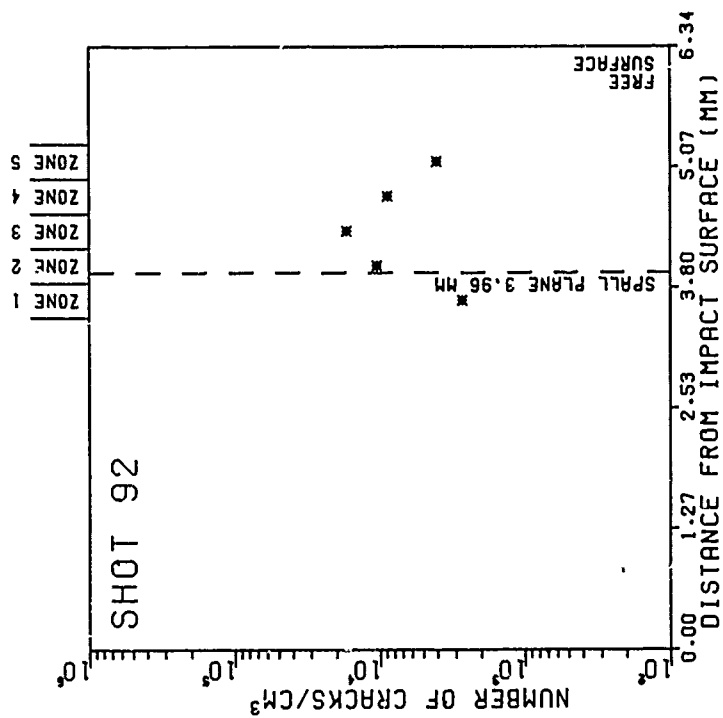


(b)

Figure E-4. (Continued)



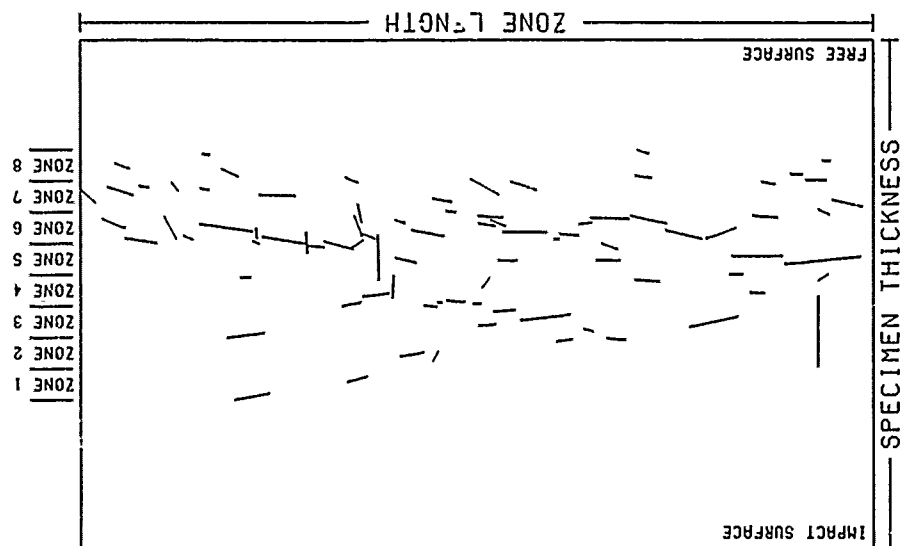
(d)



(e)

Figure E-4. (Continued)

SHOT 91
 IMPACTOR VELOCITY 0.183 KM/S
 IMPACTOR THICKNESS 2.37 MM
 SPECIMEN THICKNESS 6.34 MM
 NUMBER OF CRACKS 84
 NUMBER OF ZONES 8
 ZONE LENGTH 10.16 MM
 ZONE WIDTH 0.39 MM
 IMPACT SURFACE TO ZONE1 1.85 MM



(a)

Figure E-5. Crack distributions for Shot 91. (a) Digitized cracks on sectioned specimen surface. (b) Number of digitized cracks as a function of position. (c) Surface crack-size distributions. (d) Volume crack-size distributions. (e) Volume density of cracks as a function of position.

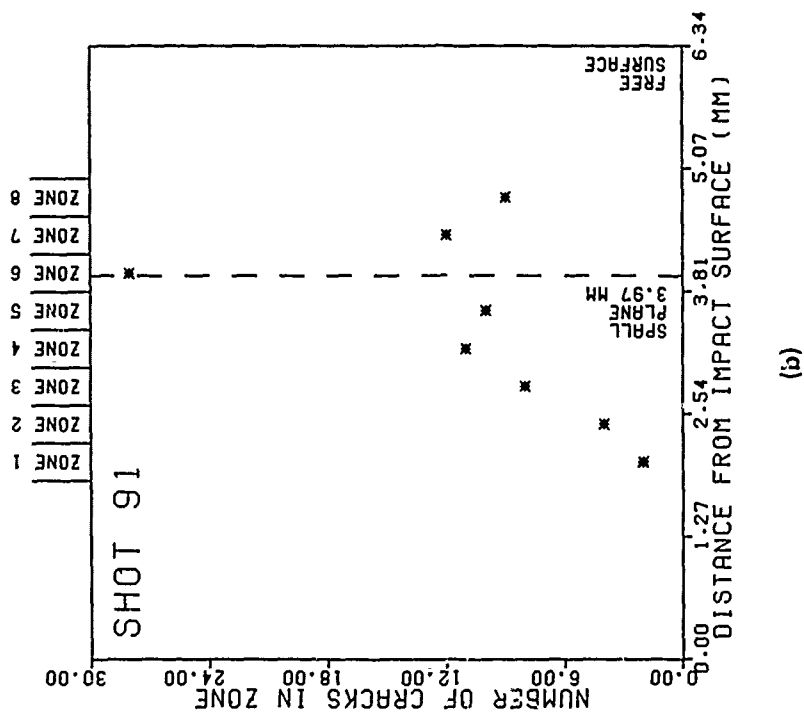
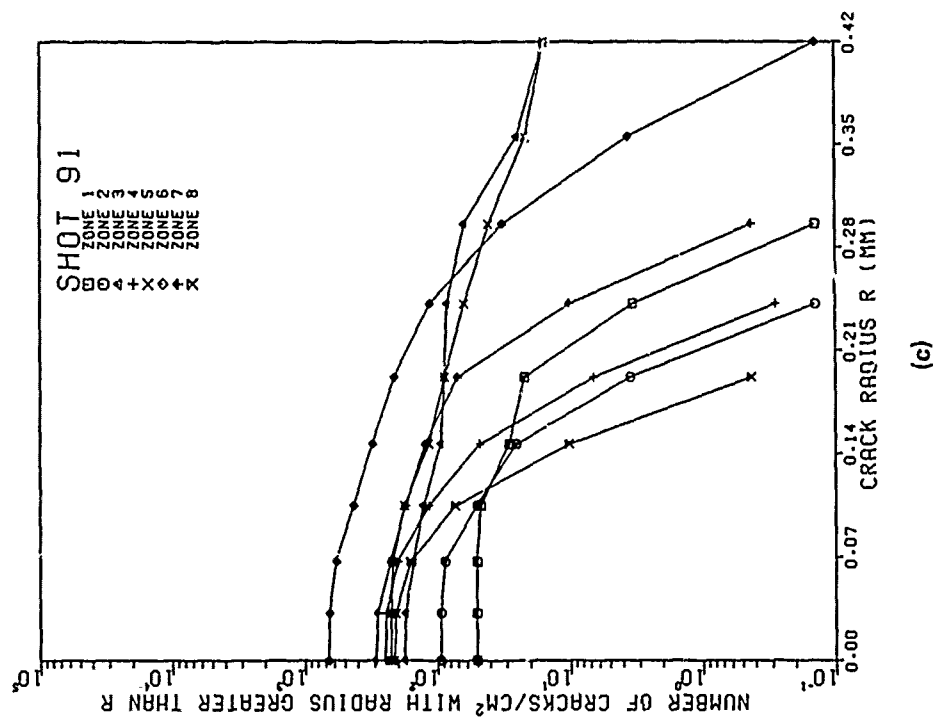
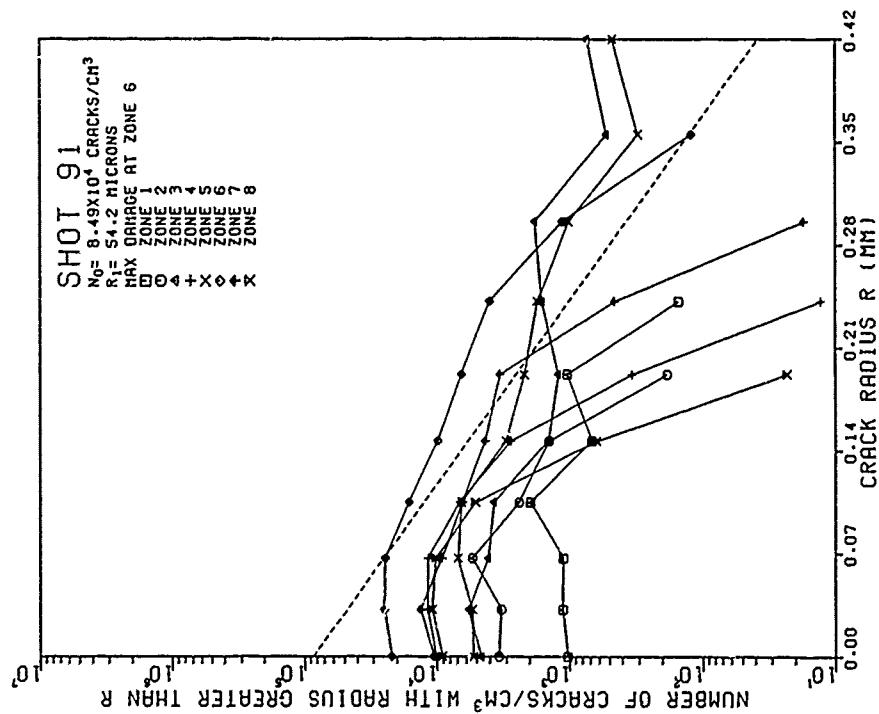
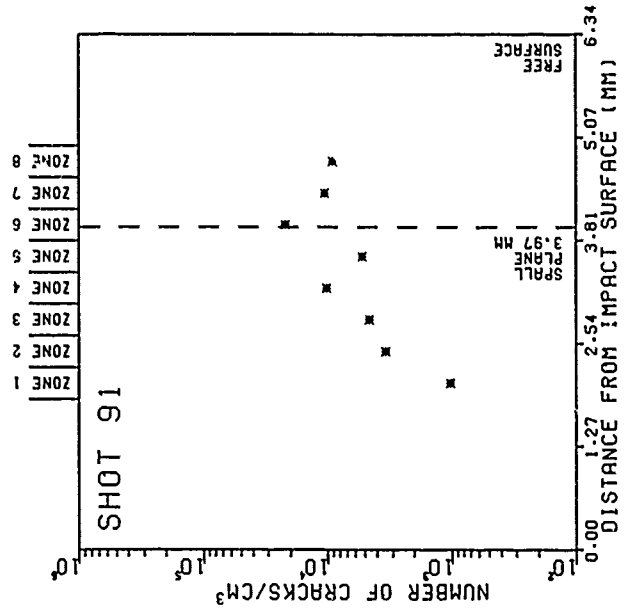


Figure E-5. (Continued)



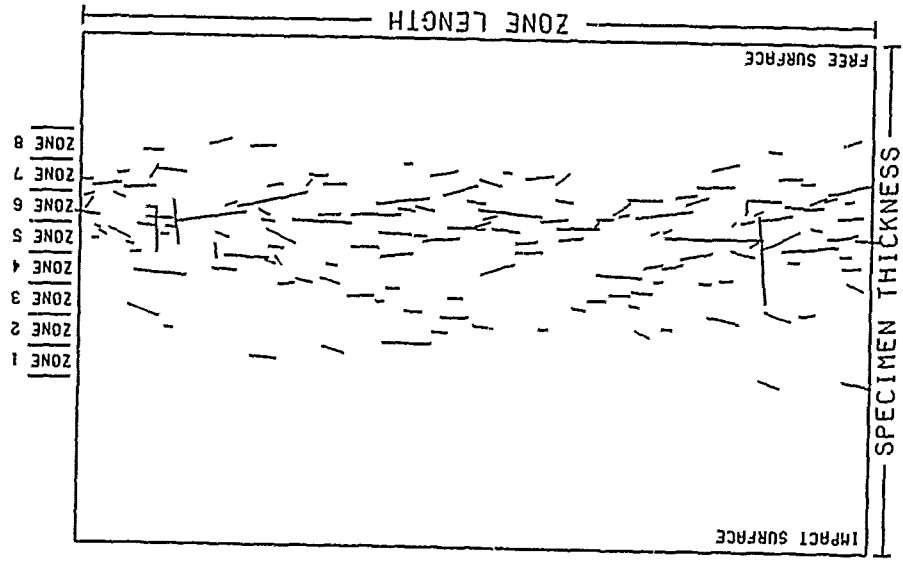
(d)



(e)

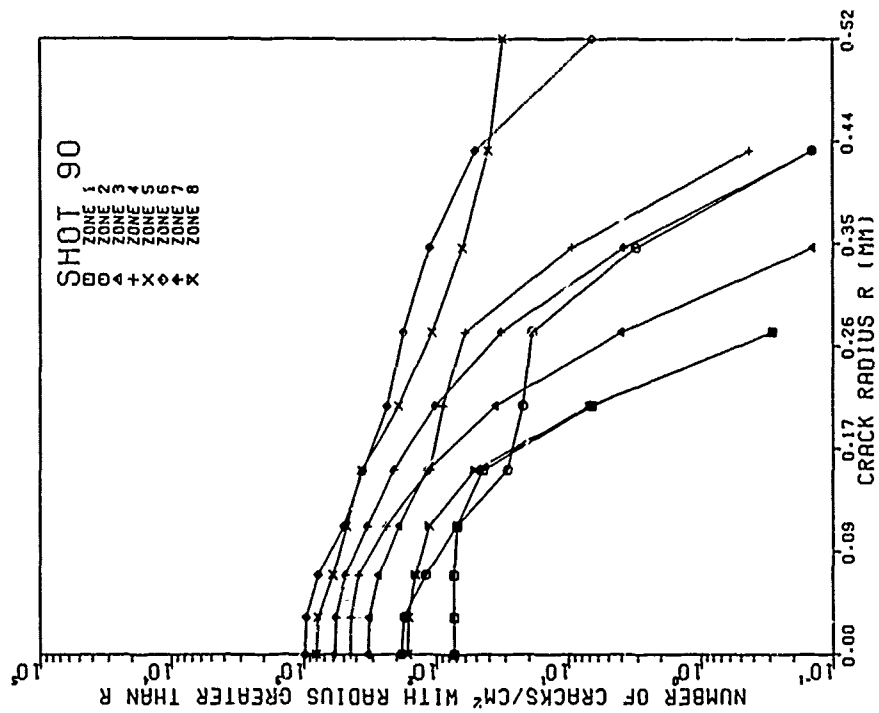
Figure E-5. (Continued)

SHOT 90
 IMPACTOR VELOCITY 0.191 KM/S
 IMPACTOR THICKNESS 2.37 MM
 SPECIMEN THICKNESS 6.35 MM
 NUMBER OF CRACKS 153
 NUMBER OF ZONES 8
 ZONE LENGTH 10.16 MM
 ZONE WIDTH 0.39 MM
 IMPACT SURFACE TO ZONE1 2.05 MM

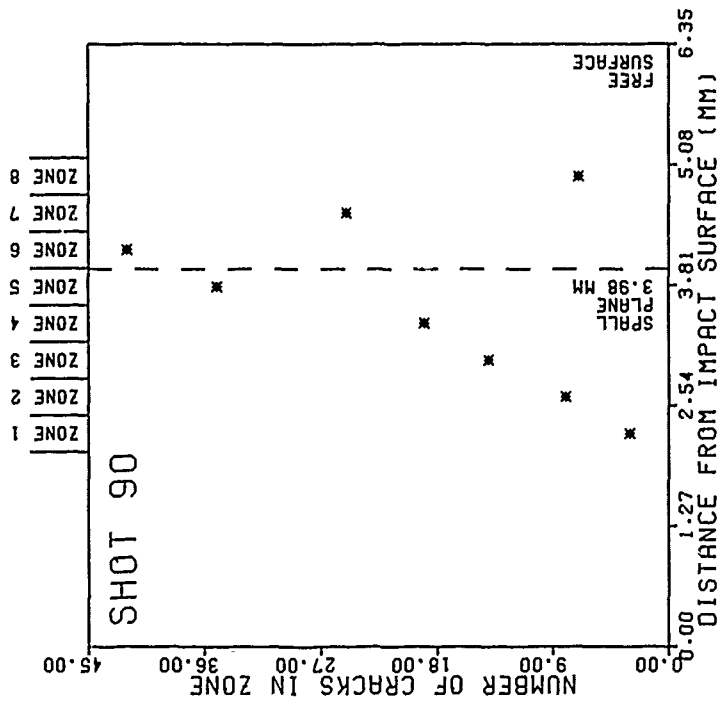


(a)

Figure E-6. Crack distributions for Shot 90. (a) Digitized cracks on sectioned specimen surface. (b) Number of digitized cracks as a function of position. (c) Surface crack-size distributions. (d) Volume crack-size distributions. (e) Volume density of cracks as a function of position.

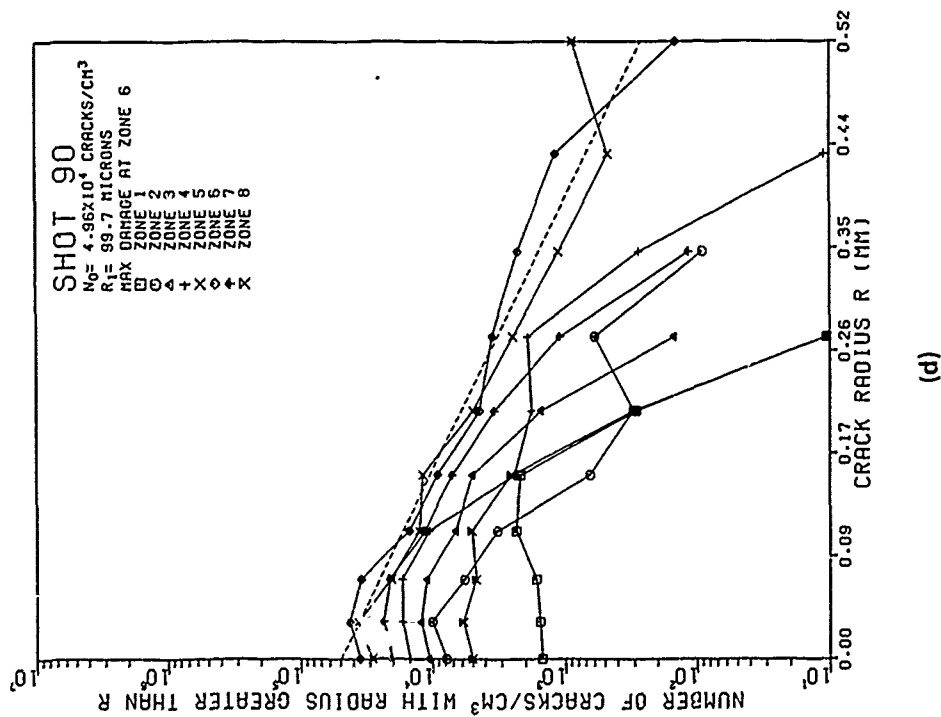


(c)

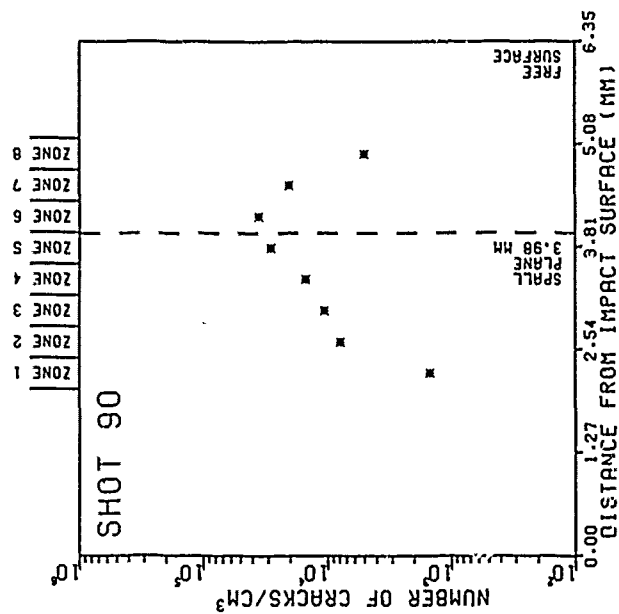


(b)

Figure E-6. (Continued)



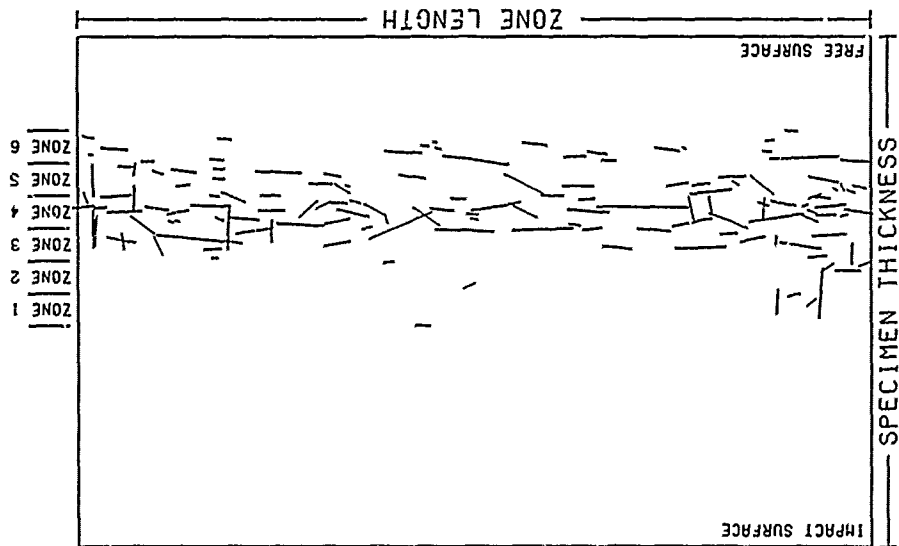
(d)



(e)

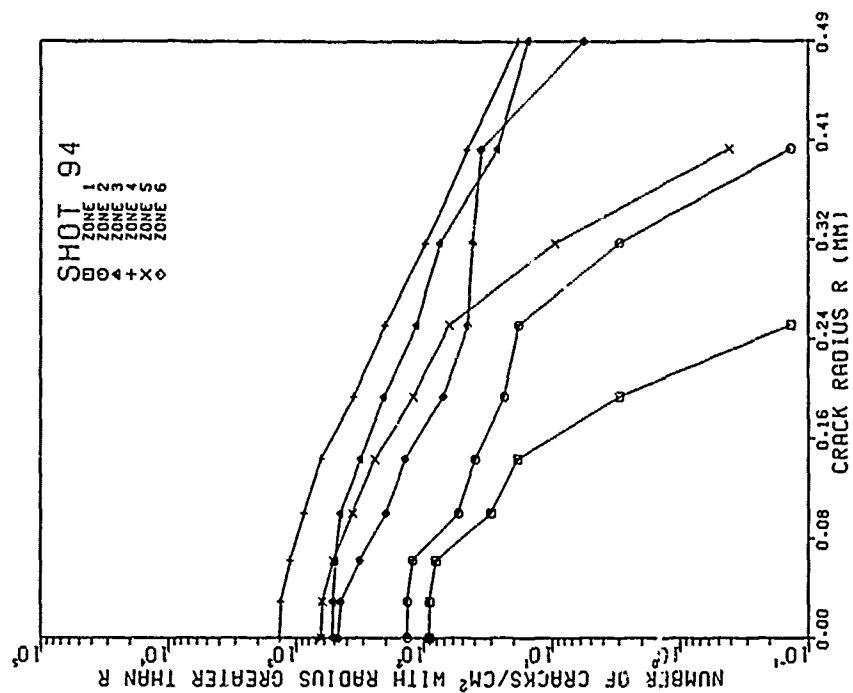
Figure E-6. (Continued)

SHOT 94
 IMPACTOR VELOCITY 0.200 MM/S
 SPECIMEN THICKNESS 2.36 MM
 SPECIMEN THICKNESS 2.36 MM
 NUMBER OF CRACKS 143
 NUMBER OF ZONES 6
 ZONE LENGTH 19.16 MM
 ZONE WIDTH 0.41 MM
 IMPACT SURFACE TO ZONE1 2.75 MM

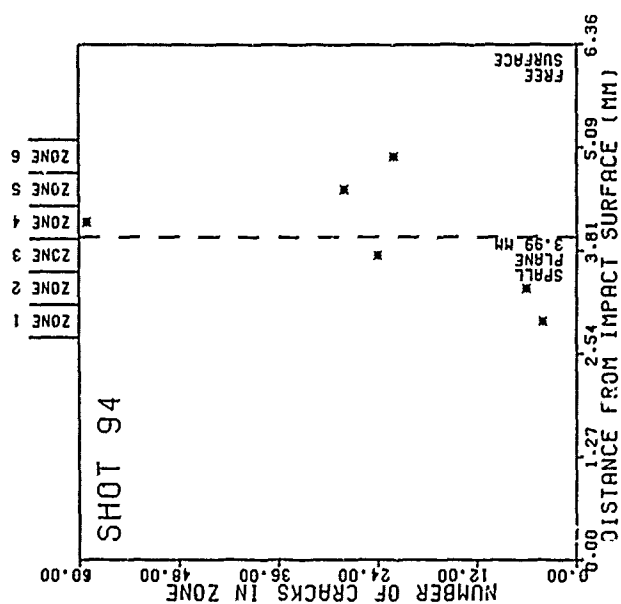


(a)

Figure E-7. Crack distributions for Shot 94. (a) Digitized cracks on sectioned specimen surface. (b) Number of digitized cracks as a function of position. (c) Surface crack-size distributions. (d) Volume crack-size distributions. (e) Volume density of cracks as a function of position.

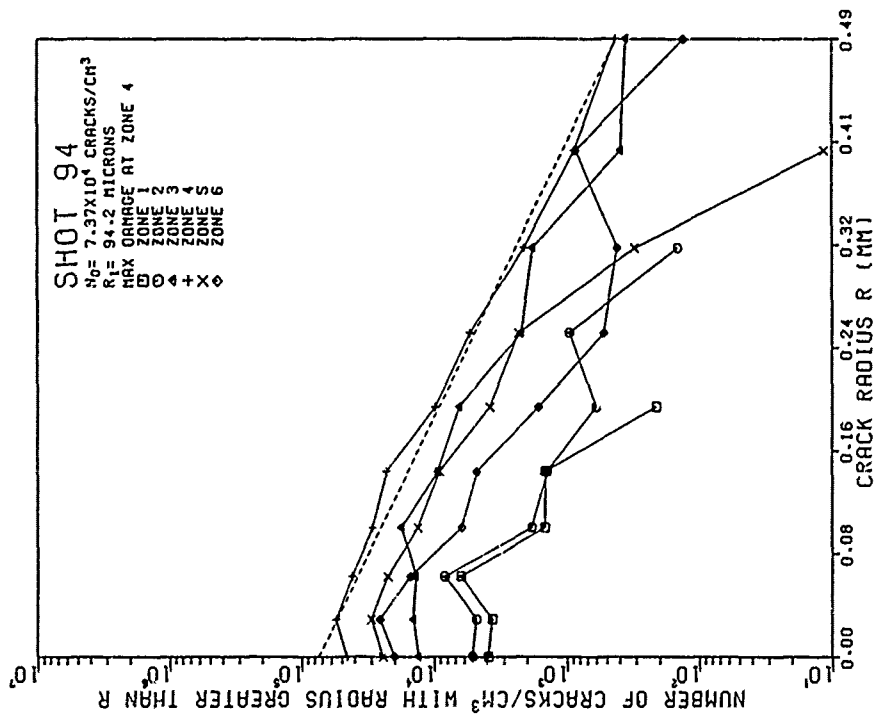


(c)

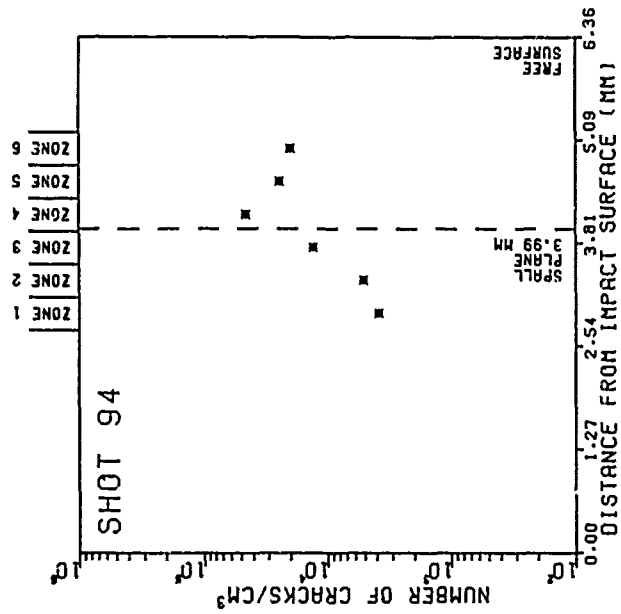


(b)

Figure E-7. (Continued)



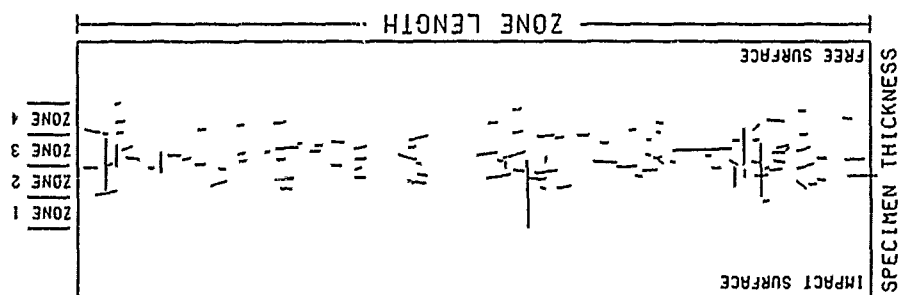
(d)



(e)

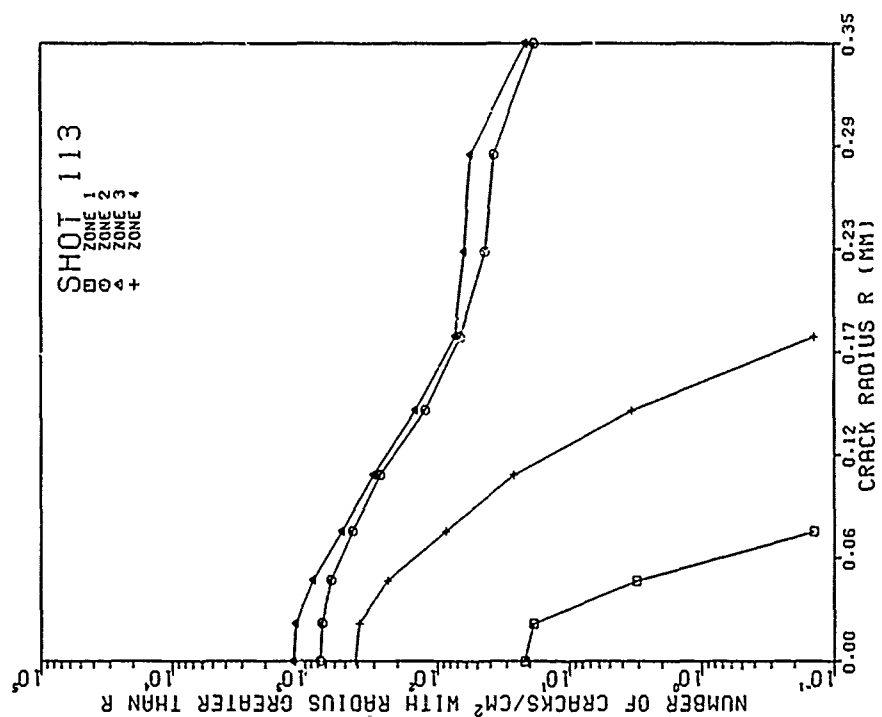
Figure E-7. (Continued)

SHOT 113
 IMPACTOR VELOCITY 0.202 KM/S
 IMPACTOR THICKNESS 1.60 MM
 SPECIMEN THICKNESS 3.19 MM
 NUMBER OF CRACKS 107
 NUMBER OF ZONES 4
 ZONE LENGTH 10.16 MM
 ZONE WIDTH 0.35 MM
 IMPACT SURFACE TO ZONE1 0.87 MM

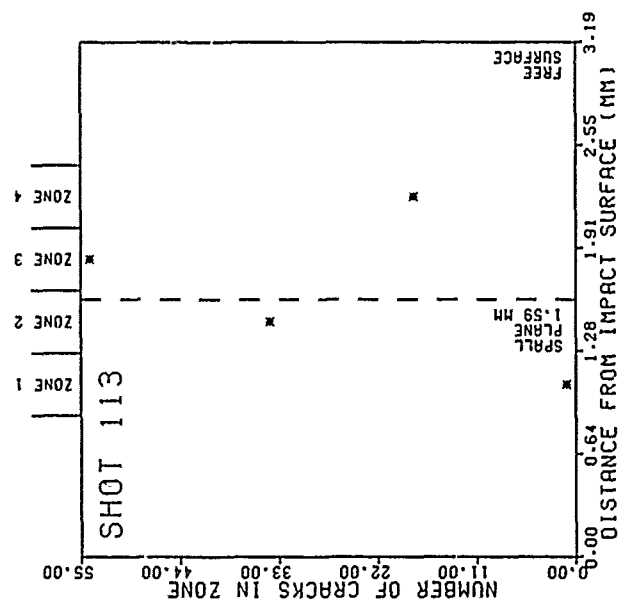


(a)

Figure E-8. Crack distributions for Shot 113. (a) Digitized cracks on sectioned specimen surface. (b) Number of digitized cracks as a function of position. (c) Surface crack-size distributions. (d) Volume crack-size distributions. (e) Volume density of cracks as a function of position.

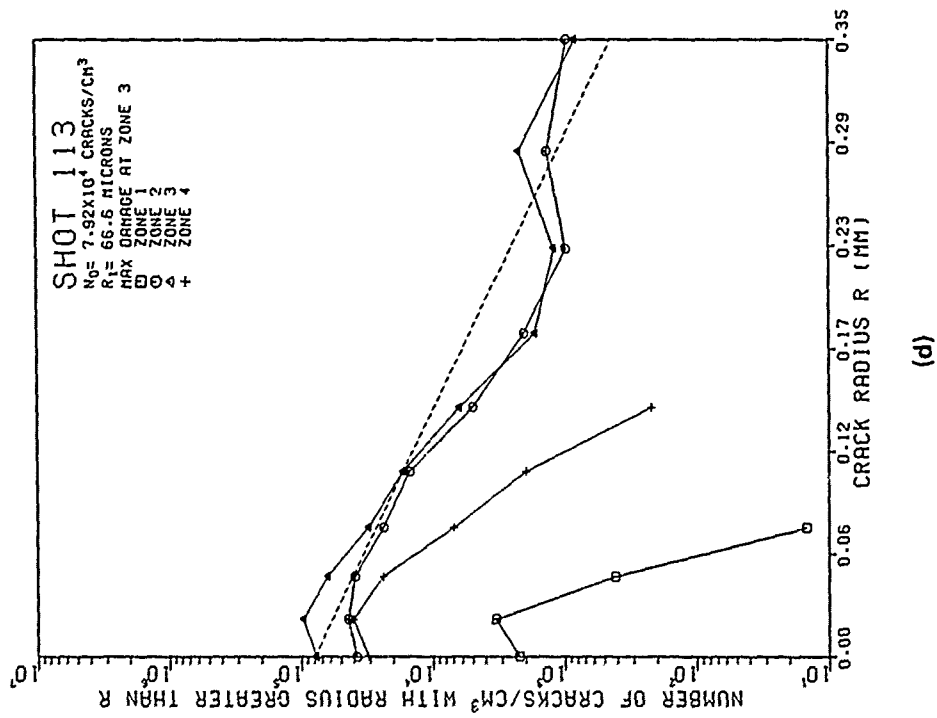


(c)

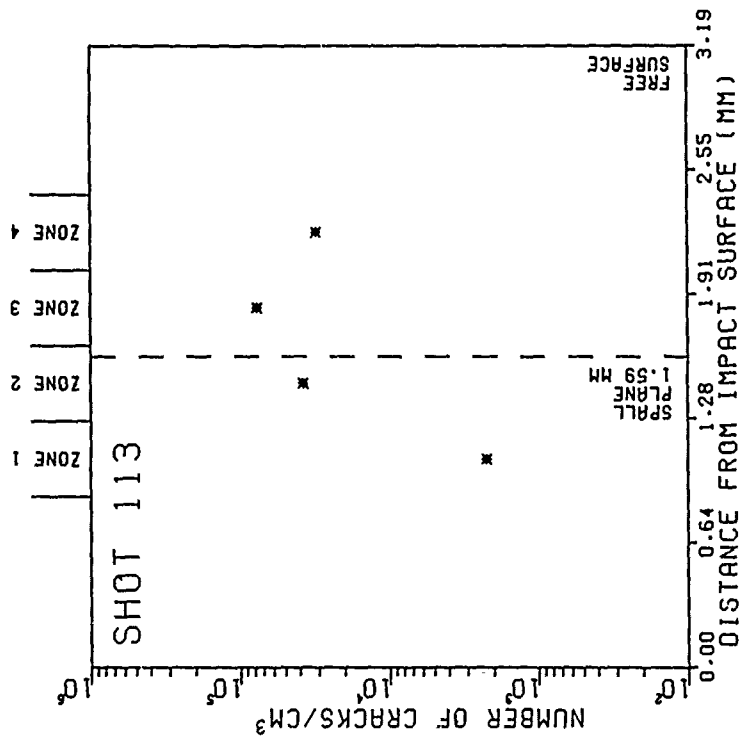


(b)

Figure E-8. (Continued)



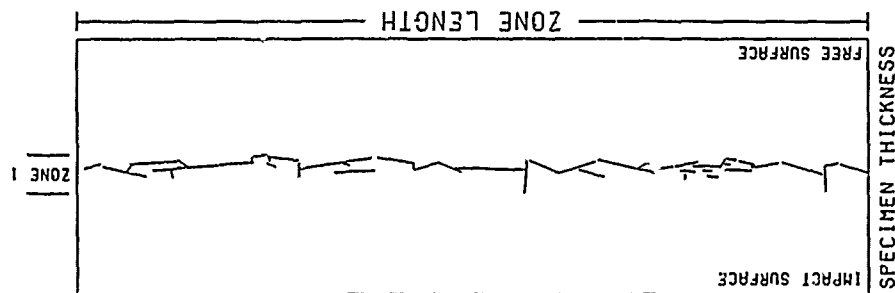
(d)



(e)

Figure E-8. (Continued)

SHOT 88
 IMPACTOR VELOCITY 0.276 KM/S
 IMPACTOR THICKNESS 1.60 MM
 SPECIMEN THICKNESS 3.19 MM
 NUMBER OF CRACKS 43
 NUMBER OF ZONES 1
 ZONE LENGTH 1.16 MM
 ZONE WIDTH 0.48 MM
 IMPACT SURFACE TO ZONE 1 1.26 MM



(a)

Figure E-9. Crack distributions for Shot 88. The cracks from only one half of this full-spalled specimen were digitized. This shot was not used for calculating dynamic fracture parameters for heat treatment A material. (a) Digitized cracks on sectioned specimen surface. (b) Number of digitized cracks as a function of position. (c) Surface crack-size distribution. (d) Volume crack-size distribution. (e) Volume density of cracks as a function of position.

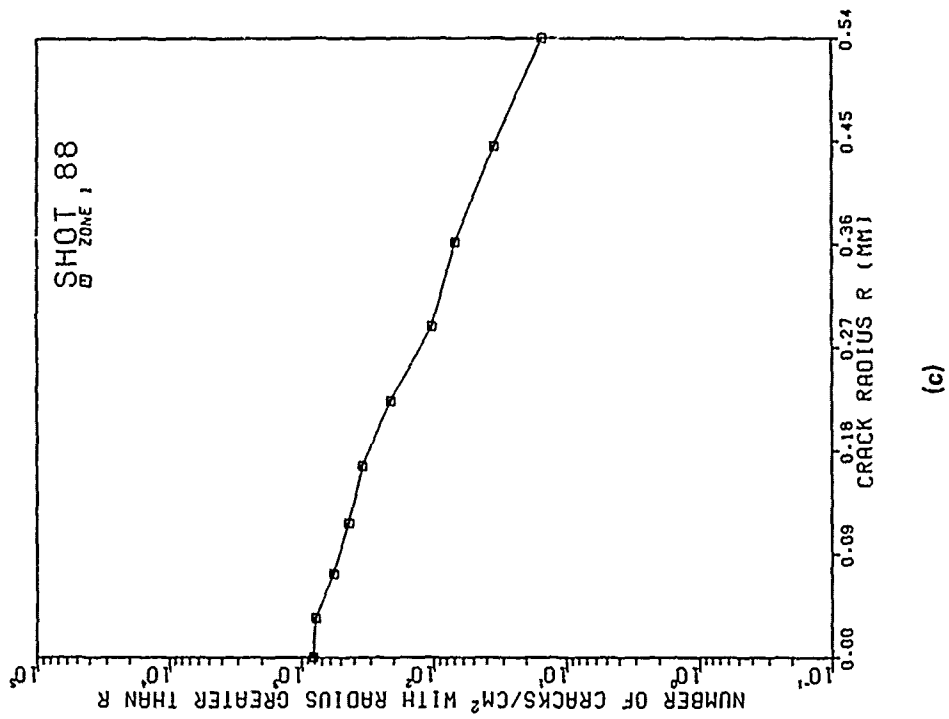
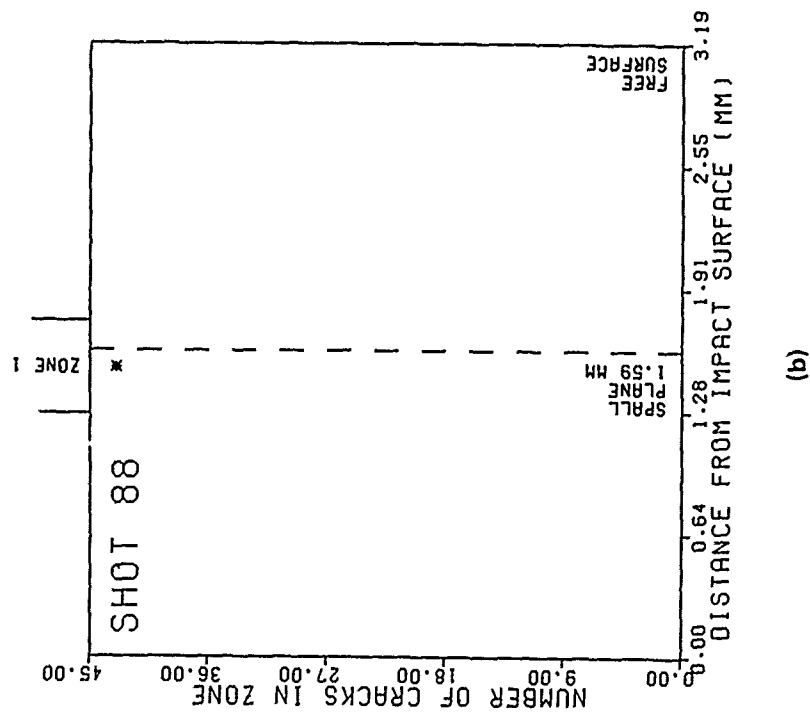
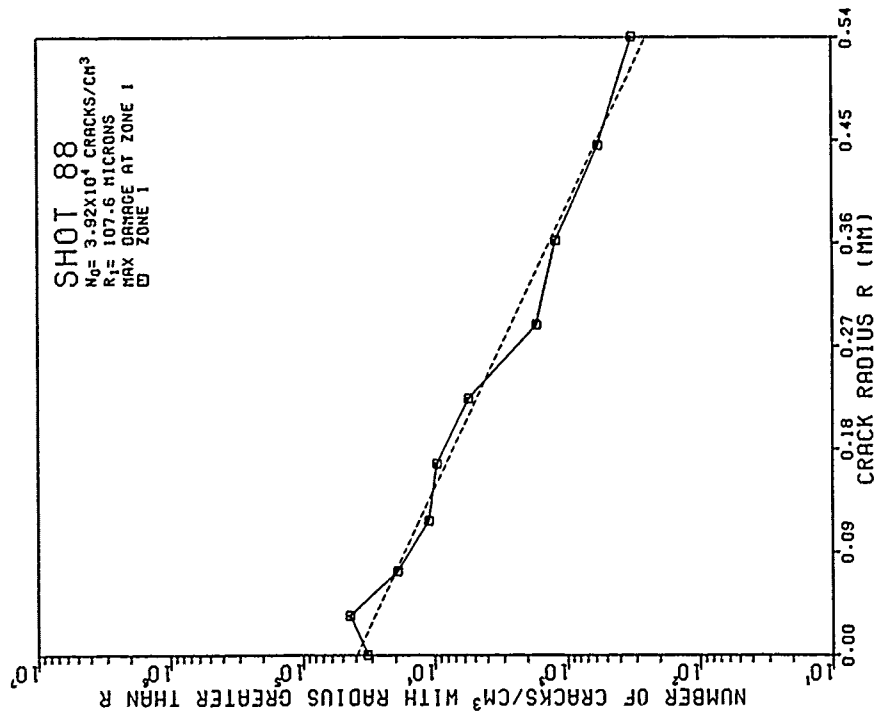
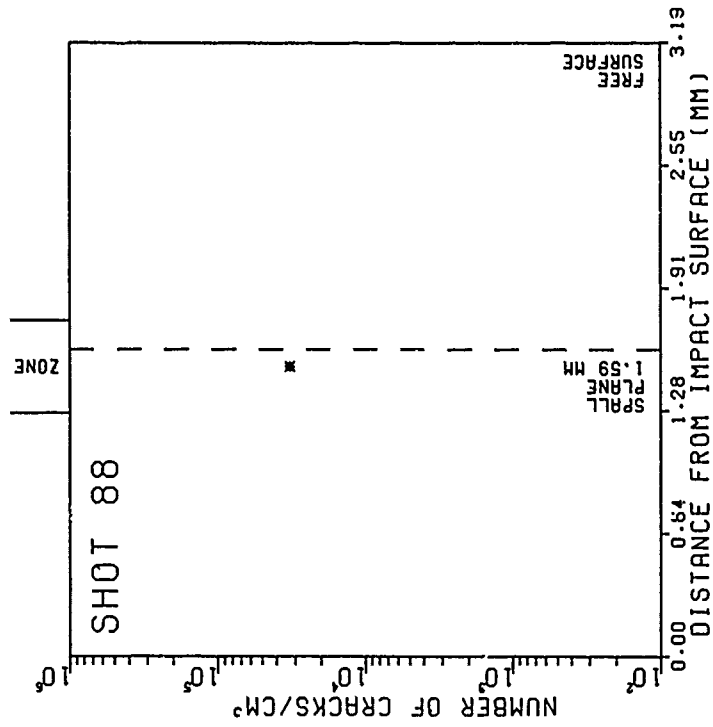


Figure E-9. (Continued)



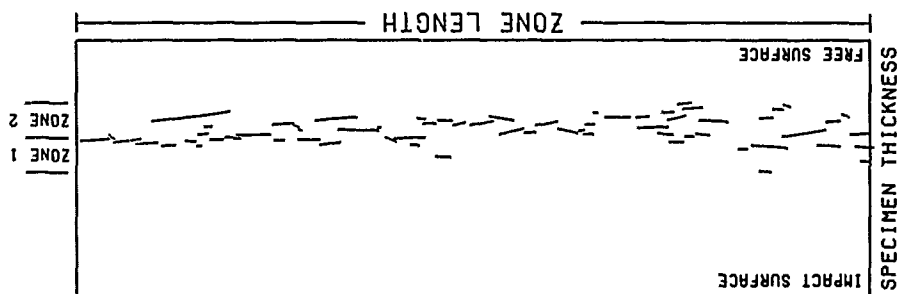
(d)



(e)

Figure E-9. (Continued)

SHOT 111
 IMPACTOR VELOCITY 0.193 KM/S
 IMPACTOR THICKNESS 1.16 MM
 SPECIMEN THICKNESS 3.19 MM
 NUMBER OF CRACKS 65
 NUMBER OF ZONES 2
 ZONE LENGTH 10.16 MM
 ZONE WIDTH 0.43 MM
 IMPACT SURFACE TO ZONE1 1.54 MM



(a)

Figure E-10. Crack distributions for Shot 111. (a) Digitized cracks on sectioned specimen surface. (b) Number of digitized cracks as a function of position. (c) Surface crack-size distributions. (d) Volume crack-size distributions. (e) Volume density of cracks as a function of position.

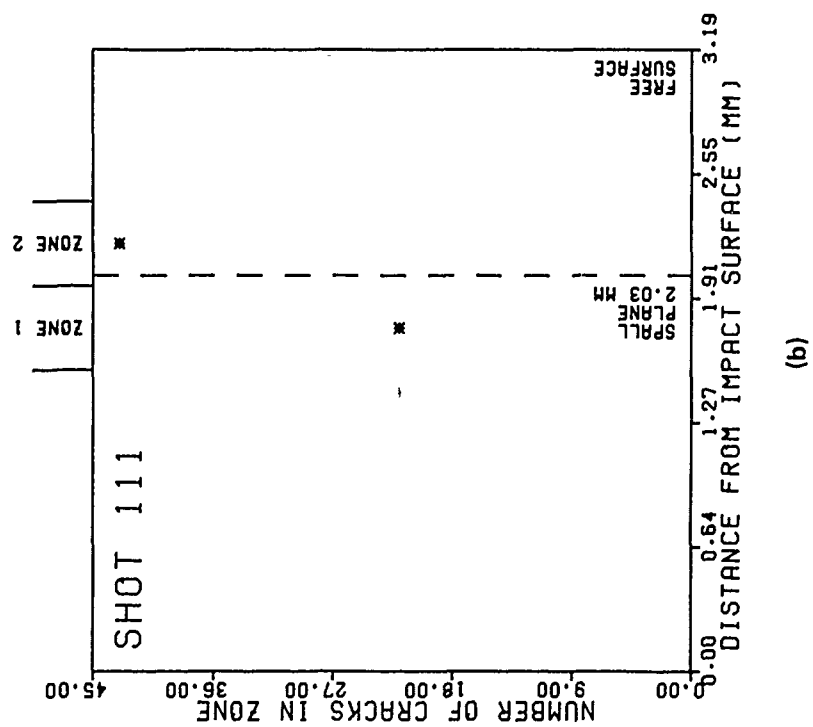
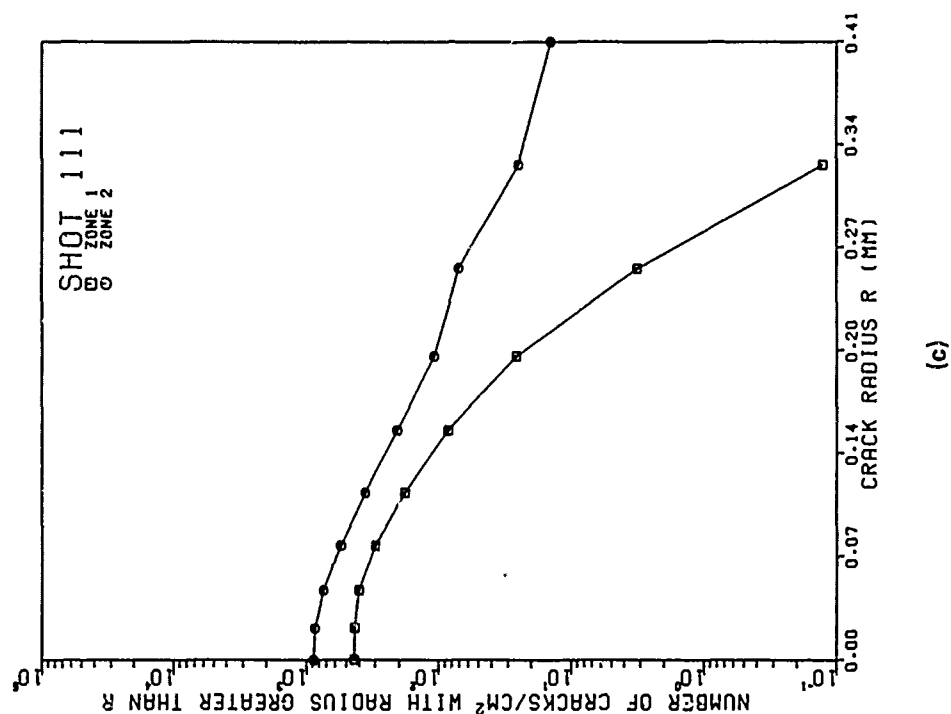
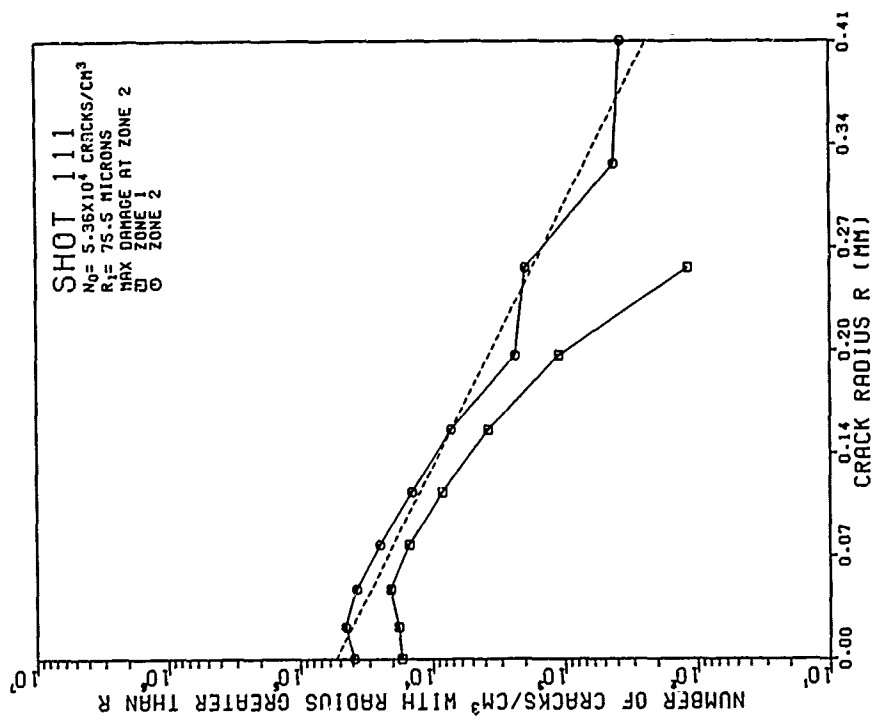
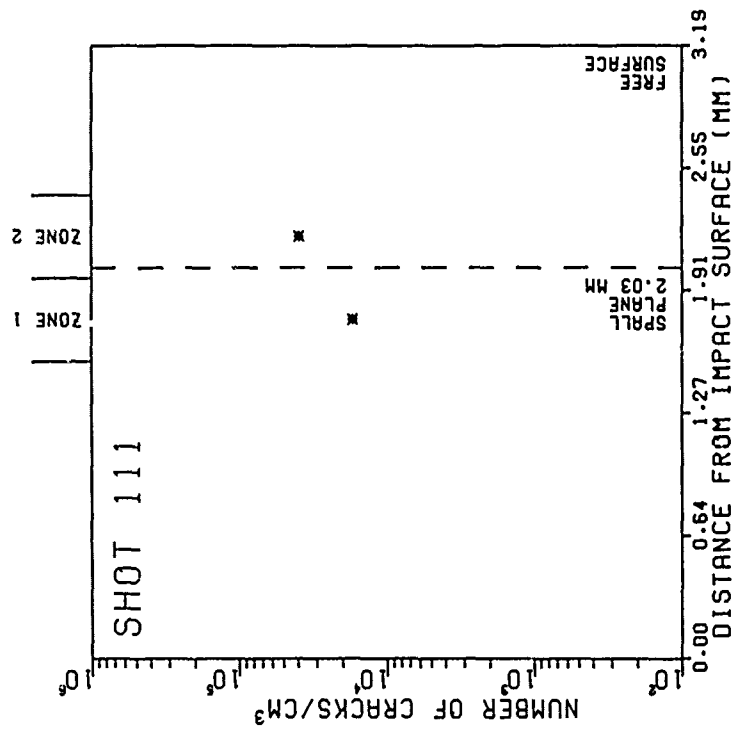


Figure E-10. (Continued)



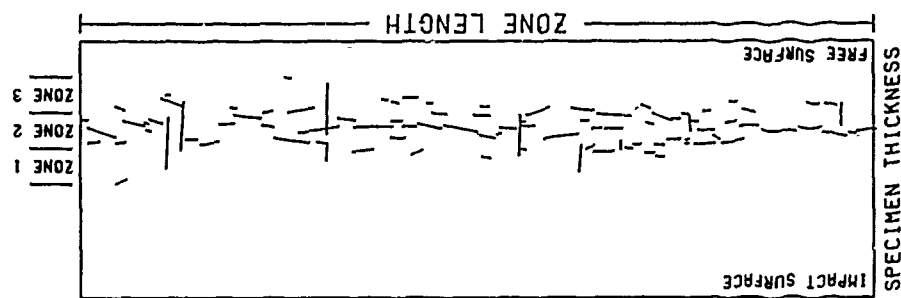
(d)



(e)

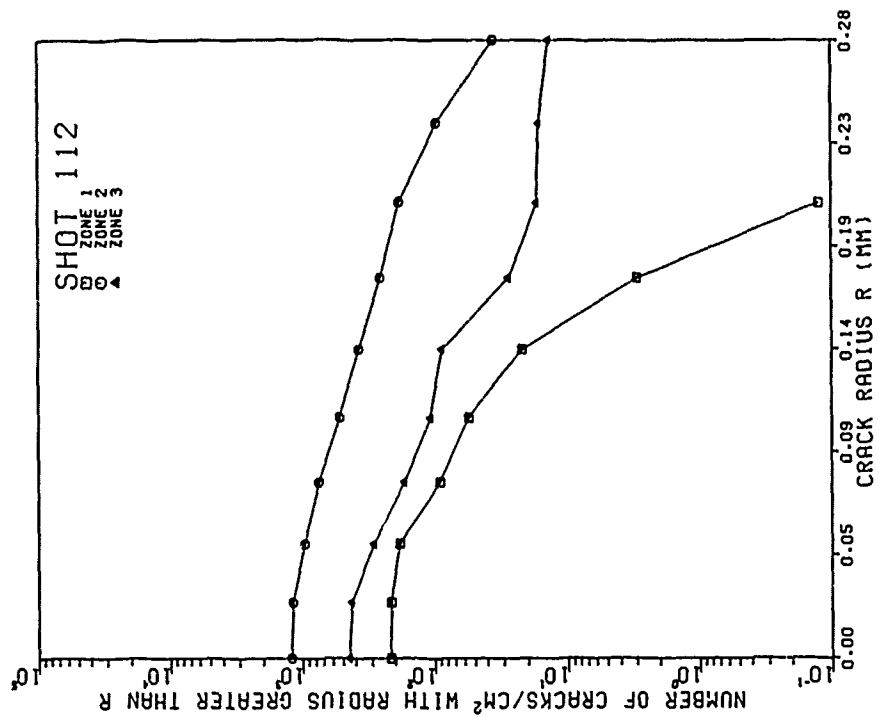
Figure E-10. (Continued)

SHOT 112
 IMPACTOR VELOCITY 0.204 KM/S
 IMPACTOR THICKNESS 1.16 MM
 SPECIMEN THICKNESS 3.19 MM
 NUMBER OF CRACKS 95
 NUMBER OF ZONES 3
 ZONE LENGTH 10.16 MM
 ZONE WIDTH 0.44 MM
 IMPACT SURFACE TO ZONE1 1.42 MM

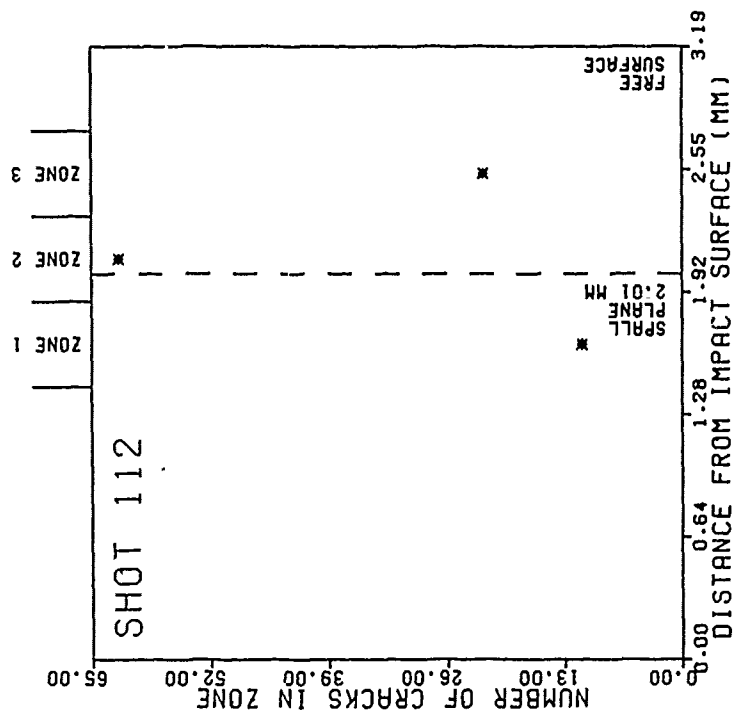


(a)

Figure E-11. Crack distributions for Shot 112. (a) Digitized cracks on sectioned specimen surface. (b) Number of digitized cracks as a function of position. (c) Surface crack-size distributions. (d) Volume crack-size distributions. (e) Volume density of cracks as a function of position.

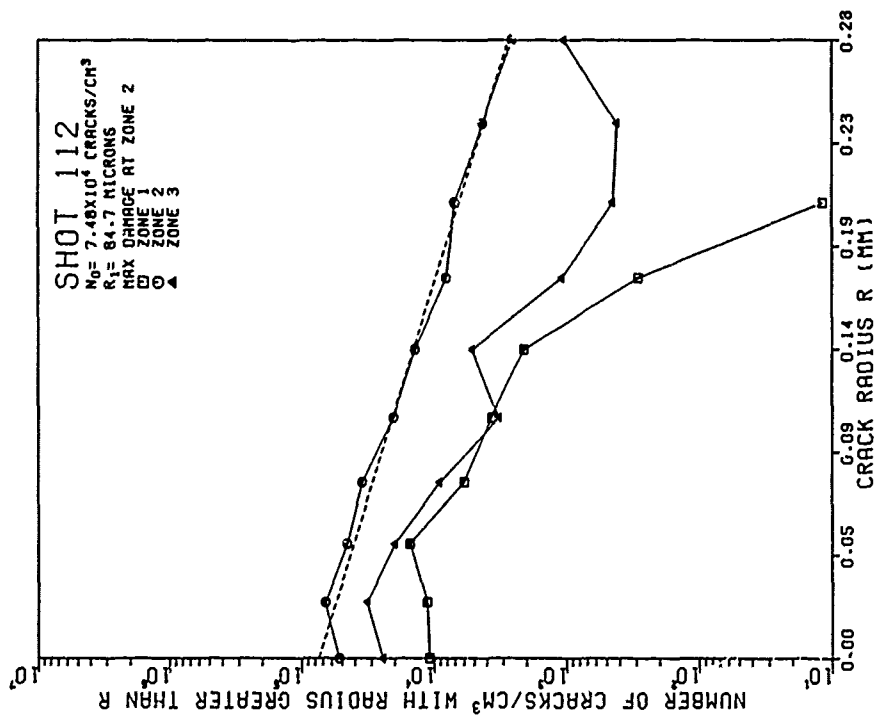


(c)

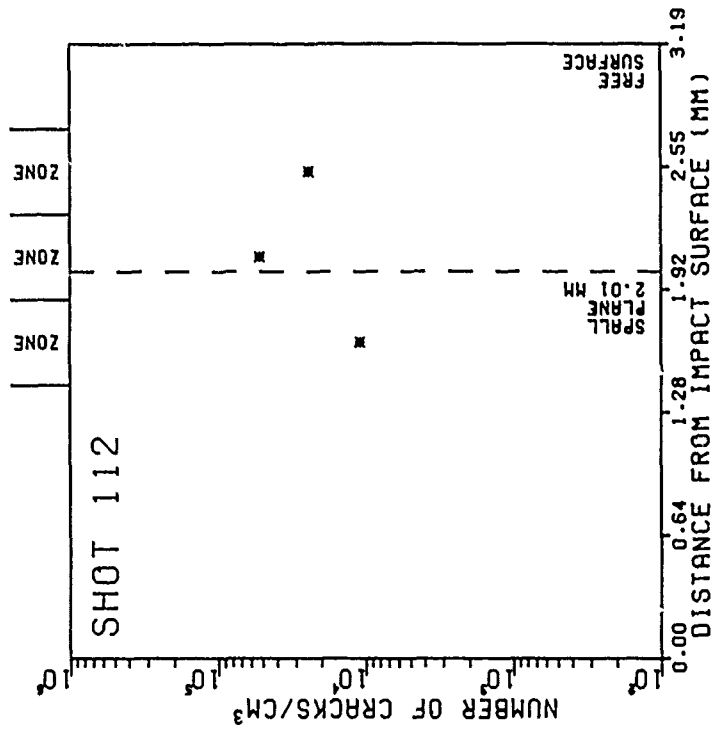


(b)

Figure E-11. (Continued)



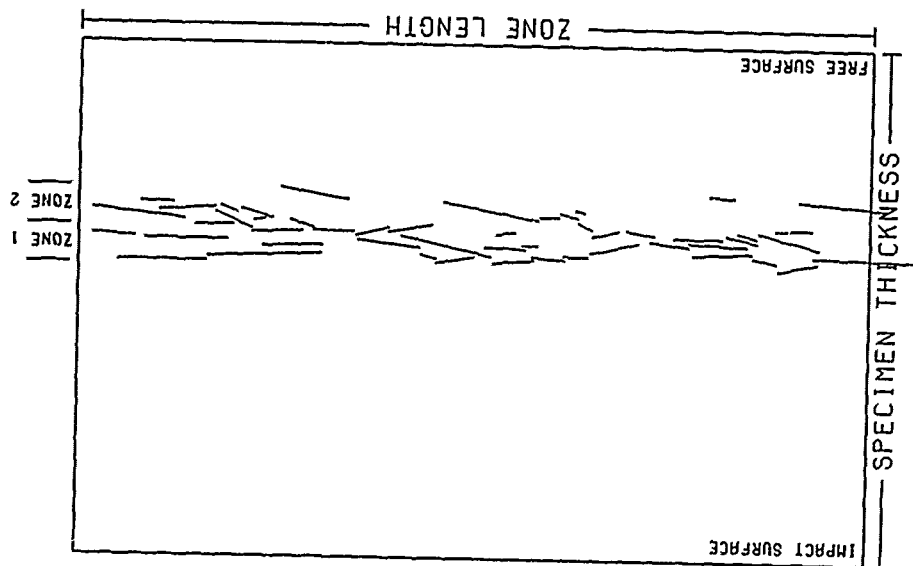
(d)



(e)

Figure E-11. (Continued)

SHOT 154
 IMPACTOR VELOCITY 0.094 KM/S
 IMPACTOR THICKNESS 2.37 MM
 SPECIMEN THICKNESS 6.35 MM
 NUMBER OF CRACKS 30
 NUMBER OF ZONES 2
 ZONE LENGTH 10.16 MM
 ZONE WIDTH 0.48 MM
 IMPACT SURFACE TO ZONE1 3.61 MM



(a)

Figure E-12. Crack distributions for Shot 154. (a) Digitized cracks on sectioned specimen surface. (b) Number of digitized cracks as a function of position. (c) Surface crack-size distributions. (d) Volume crack-size distributions. (e) Volume density of cracks as a function of position.

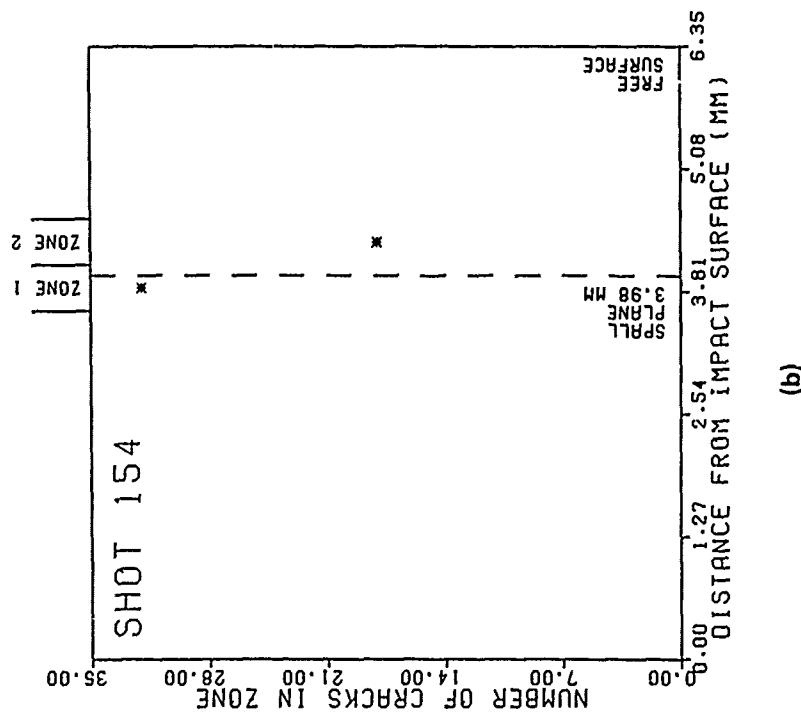
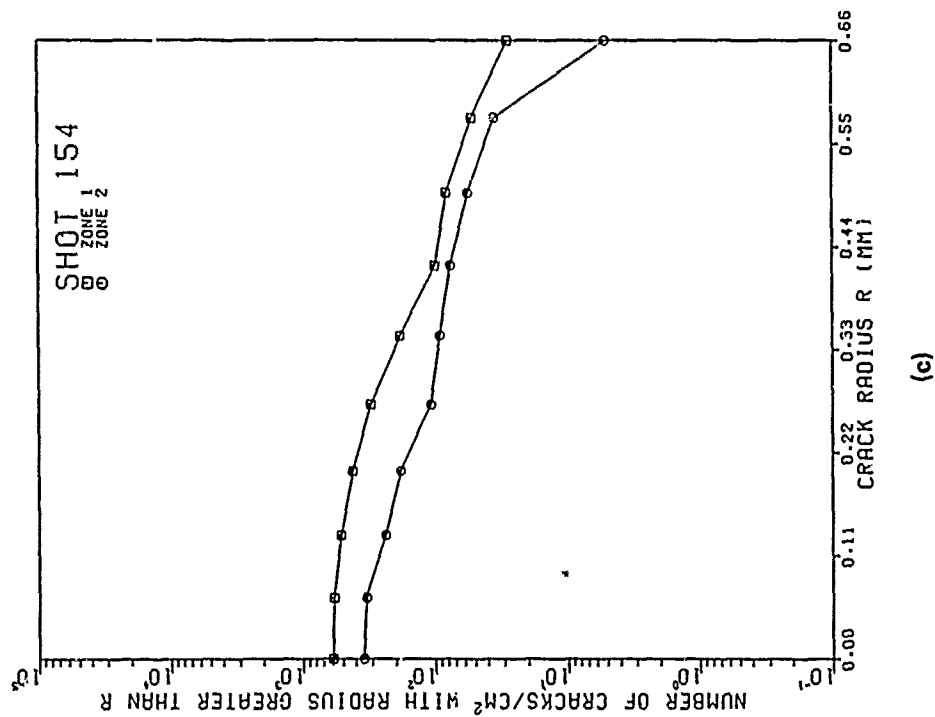
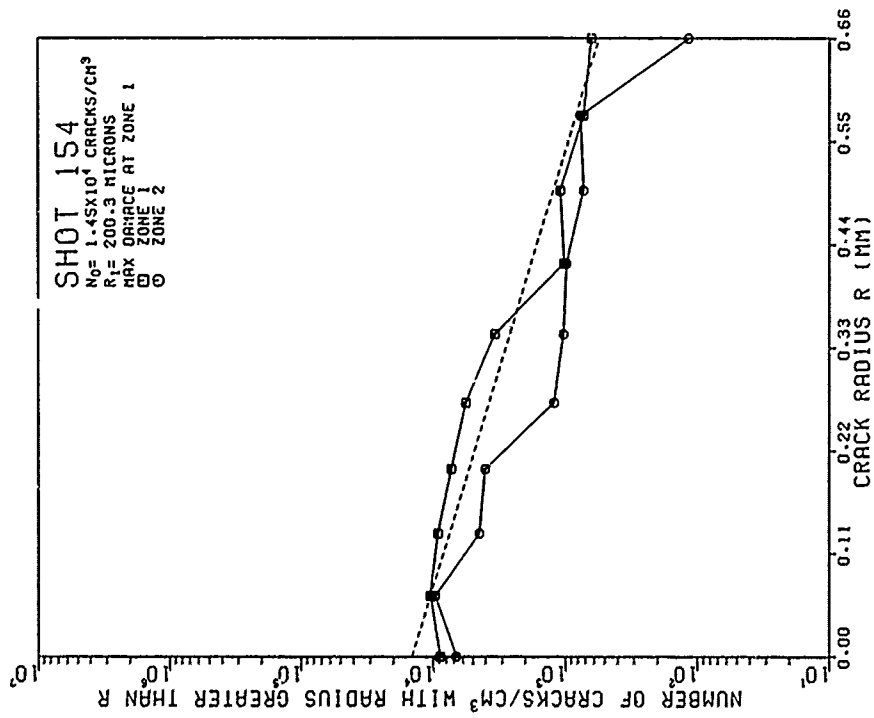
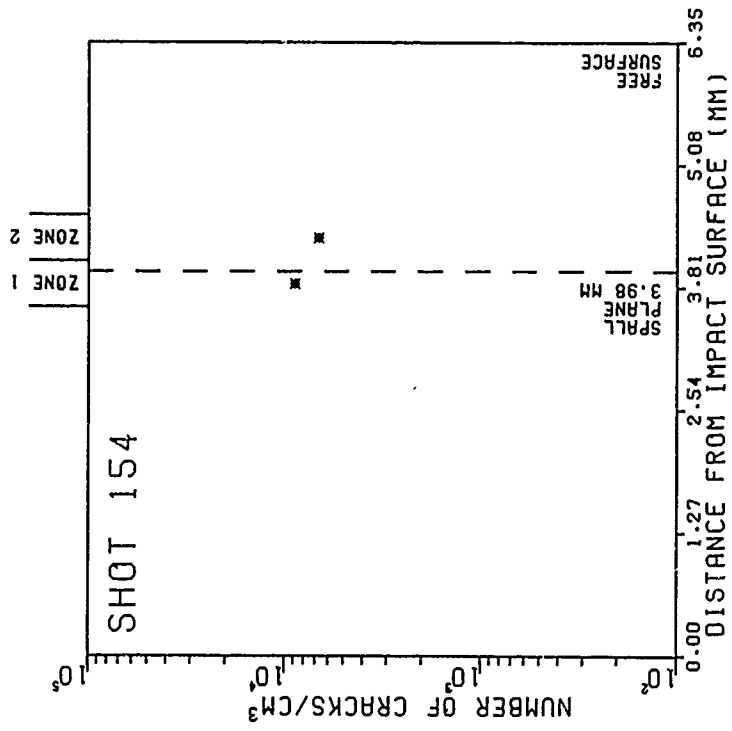


Figure E-12. (Continued)



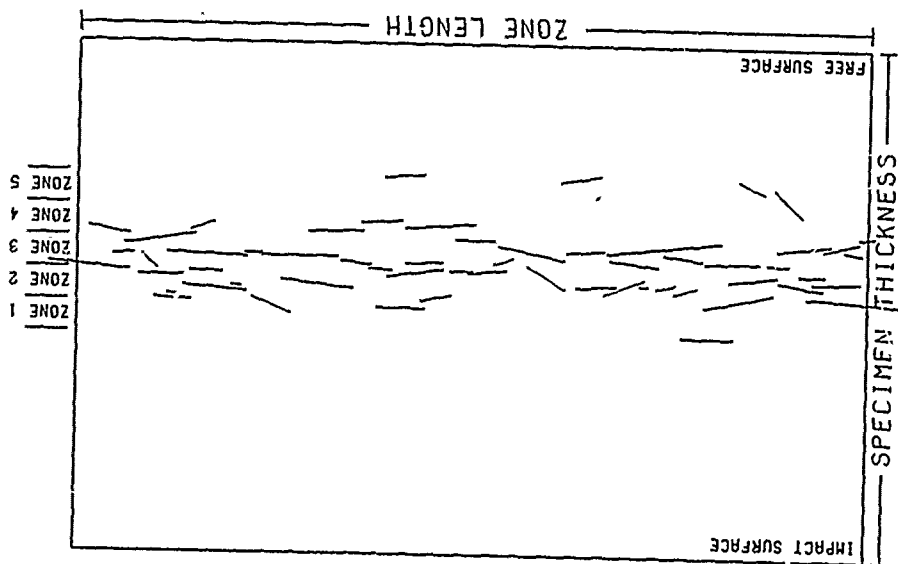
(d)



(e)

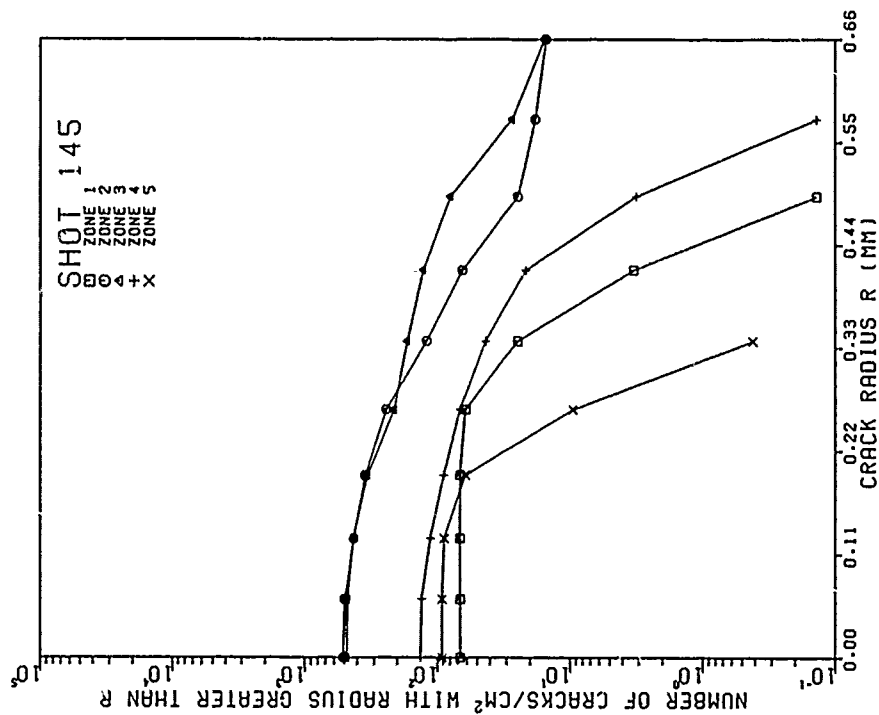
Figure E-12. (Continued)

SHOT 145
 IMPACTOR VELOCITY 0.116 KM/S
 IMPACTOR THICKNESS 2.37 MM
 SPECIMEN THICKNESS 6.35 MM
 NUMBER OF CRACKS 58
 NUMBER OF ZONES 5
 ZONE LENGTH 10.16 MM
 ZONE WIDTH 0.40 MM
 IMPACT SURFACE TO ZONE1 2.73 MM

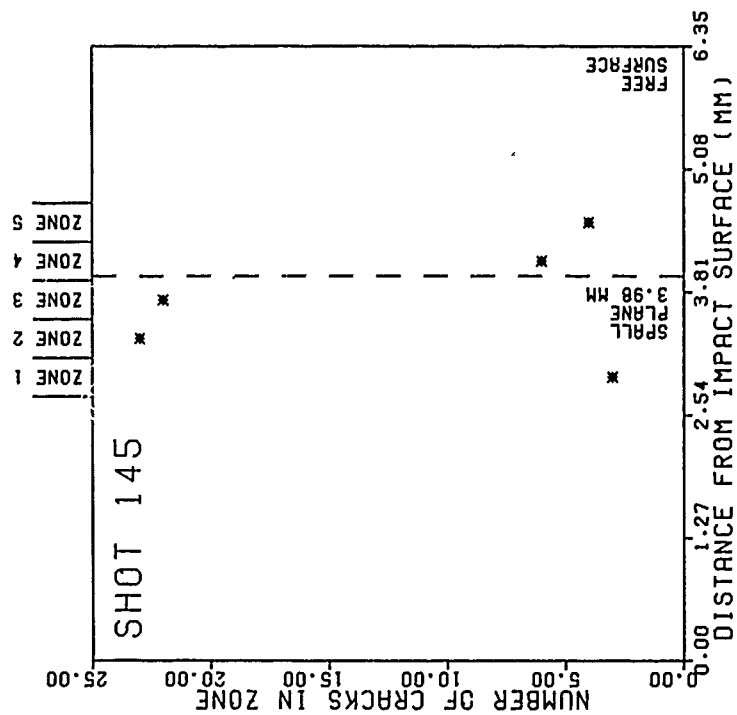


(a)

Figure E-13. Crack distributions for Shot 145. (a) Digitized cracks on sectioned specimen surface. (b) Number of digitized cracks as a function of position. (c) Surface crack-size distributions. (d) Volume crack-size distributions. (e) Volume density of cracks as a function of position.



(c)



(b)

Figure E-13. (Continued)

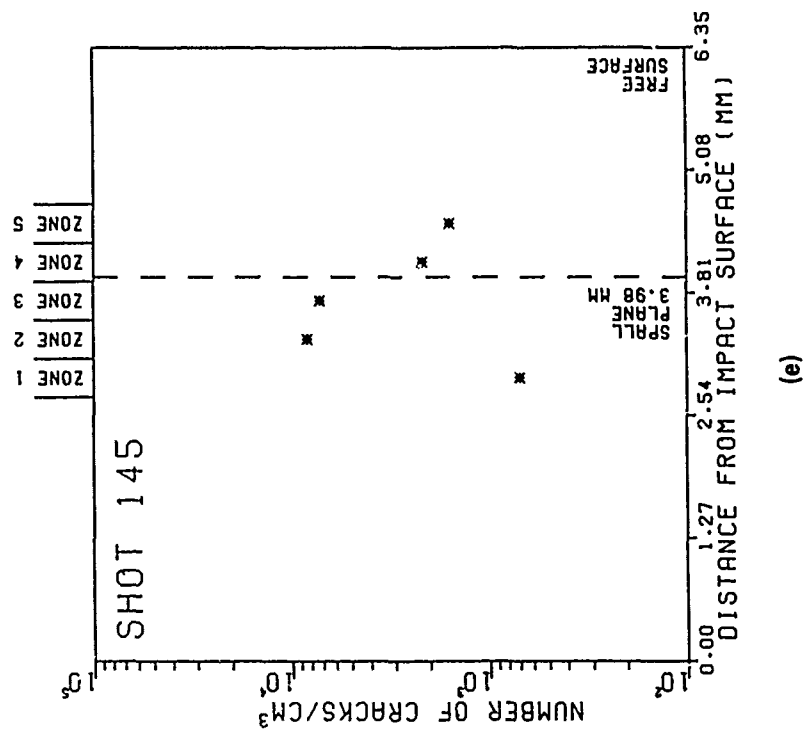
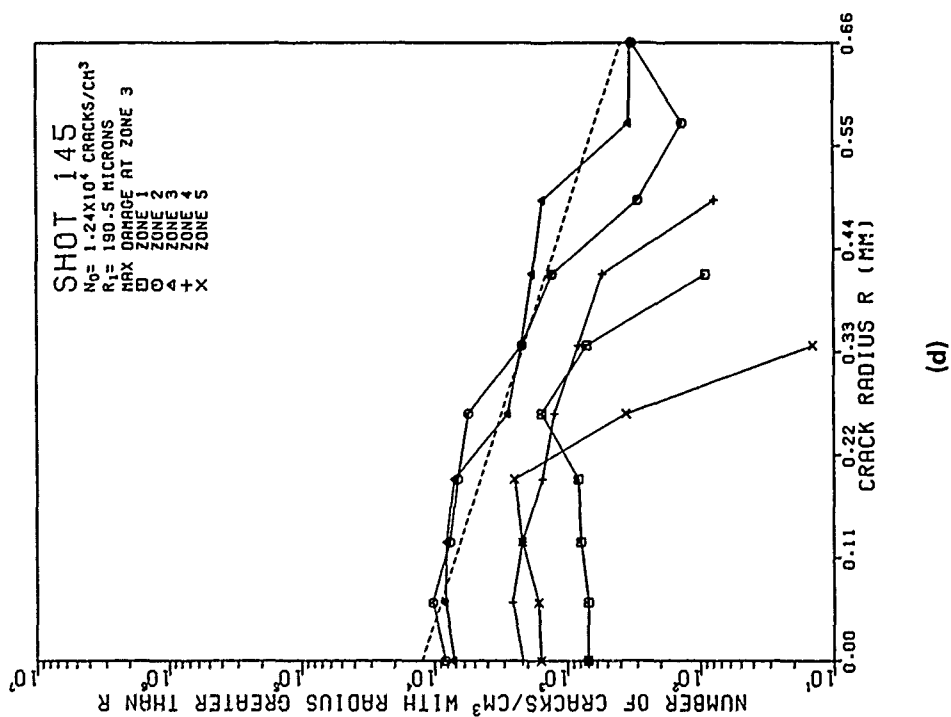
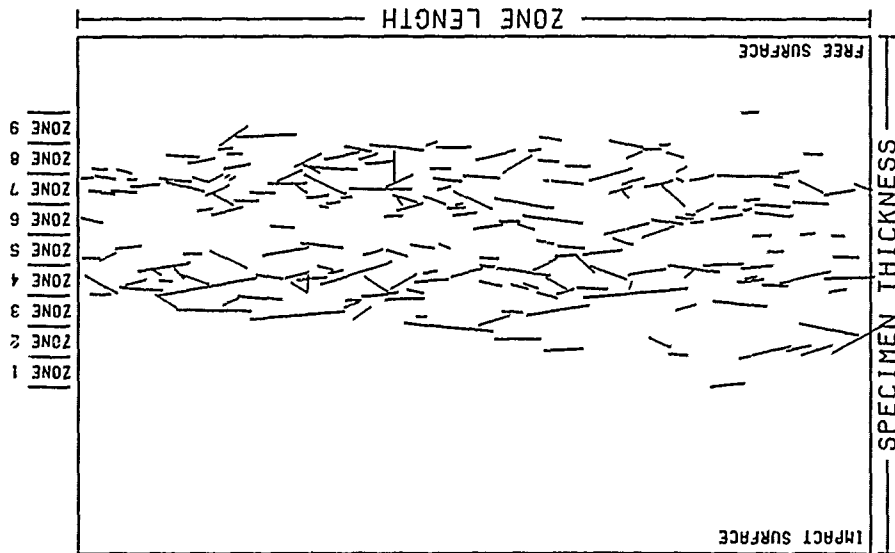


Figure E-13. (Continued)

SHOT 144
 IMPACTOR VELOCITY 0.148 KM/S
 IMPACTOR THICKNESS 2.37 MM
 SPECIMEN THICKNESS 6.35 MM
 NUMBER OF CRACKS 209
 NUMBER OF ZONES 9
 ZONE LENGTH 10.16 MM
 ZONE WIDTH 0.37 MM
 IMPACT SURFACE TO ZONE1 2.05 MM



(a)

Figure E-14. Crack distributions for Shot 144. (a) Digitized cracks on sectioned specimen surface. (b) Number of digitized cracks as a function of position. (c) Surface crack-size distributions. (d) Volume crack-size distributions. (e) Volume density of cracks as a function of position.

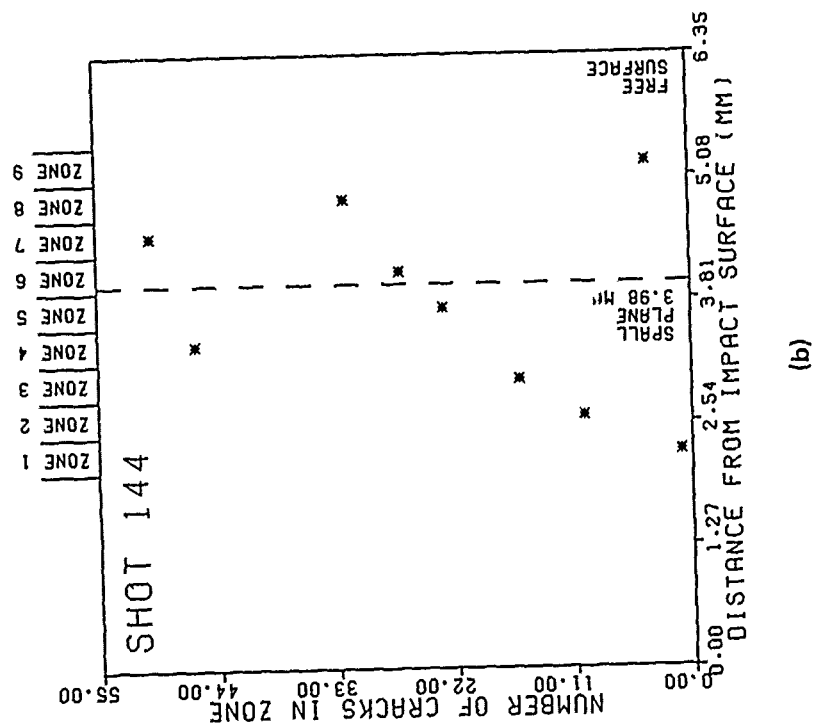
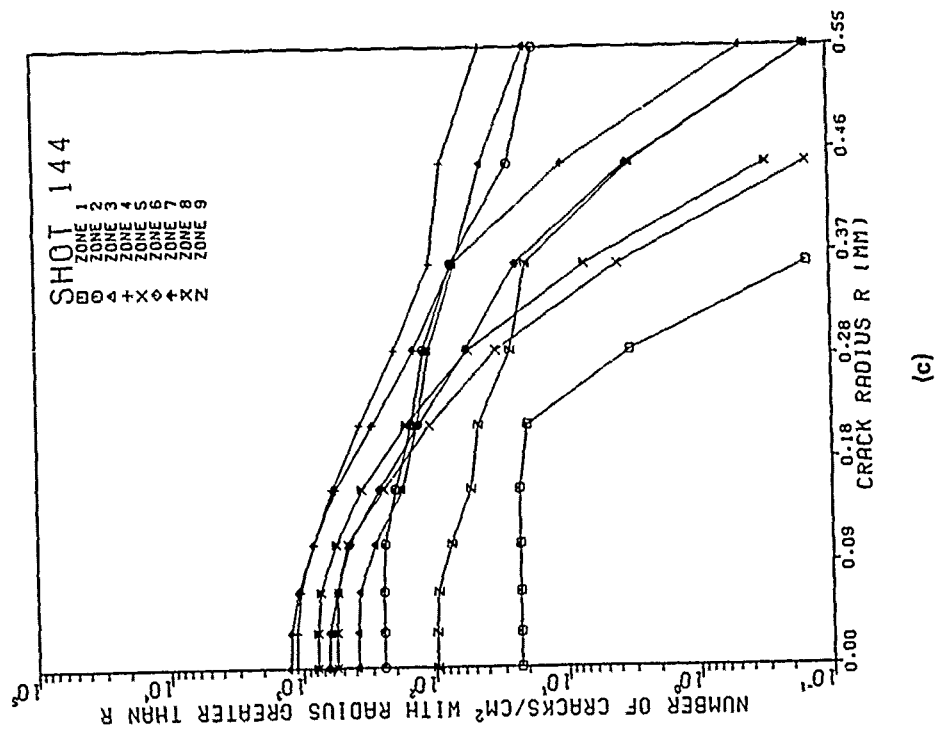


Figure E-14. (Continued)

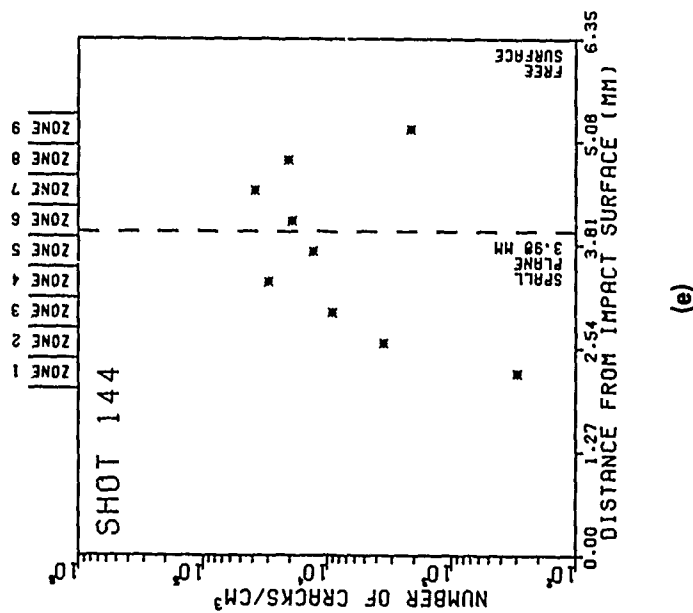
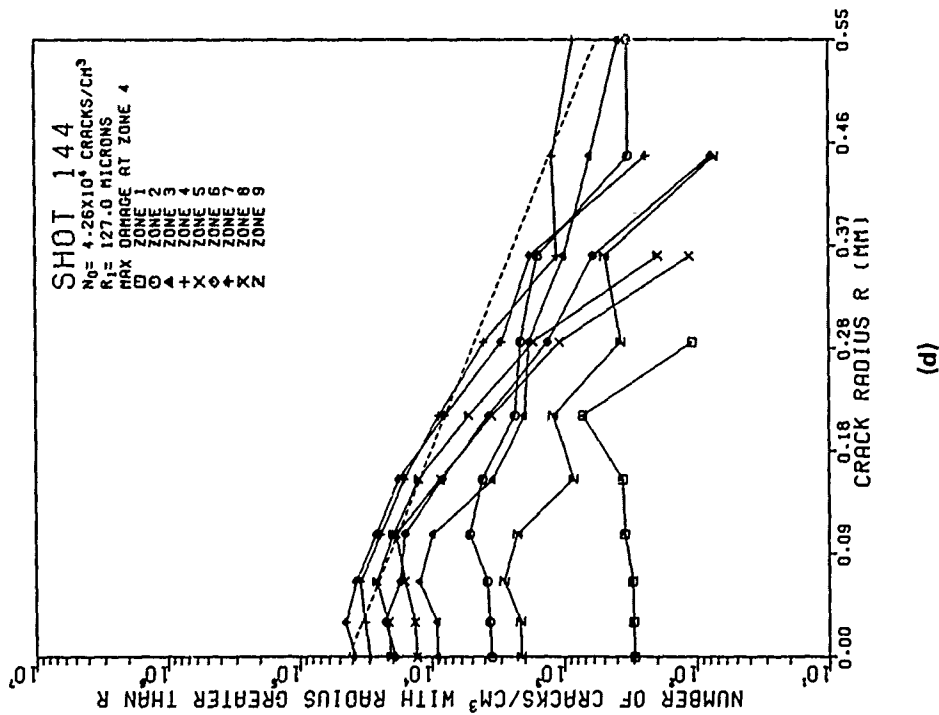
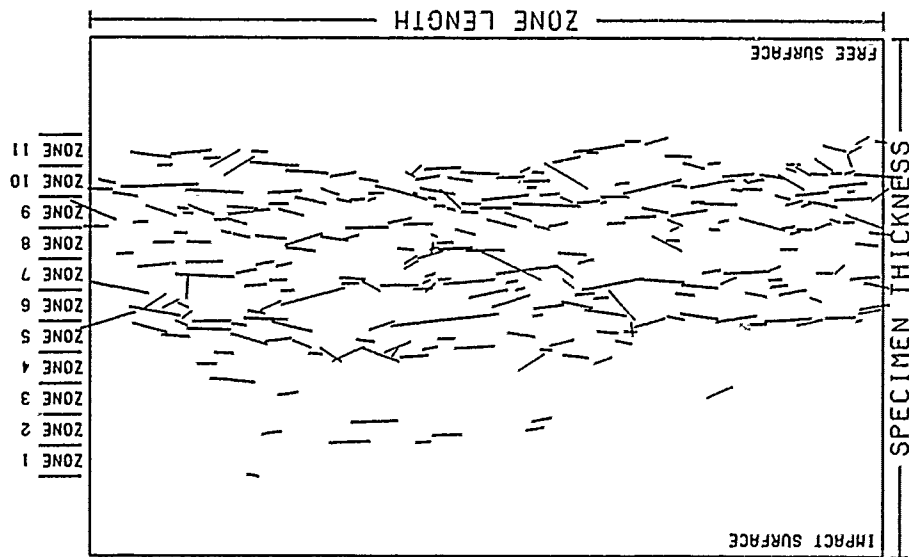


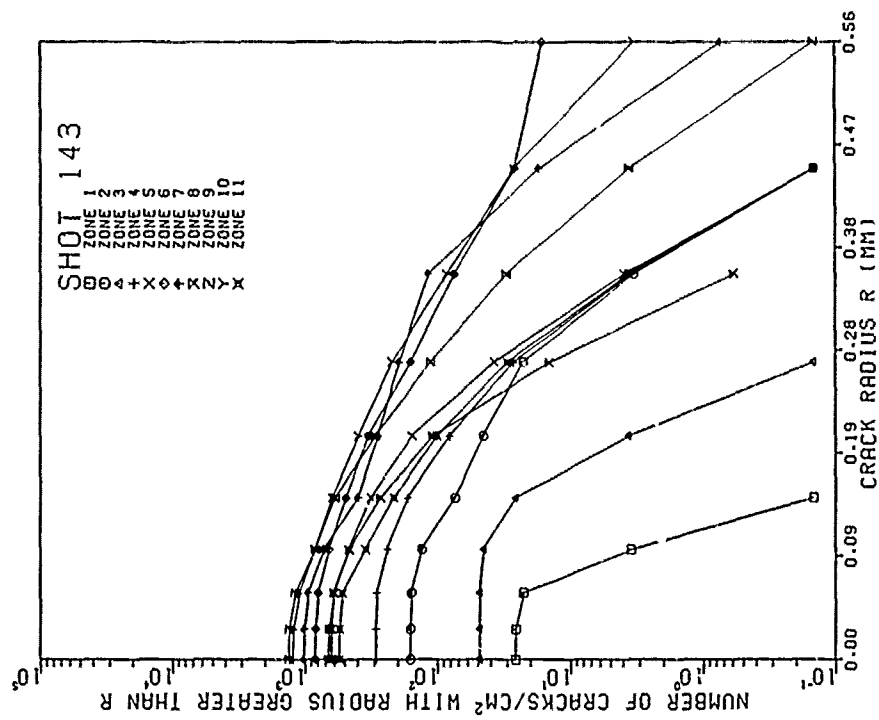
Figure E-14. (Continued)

SHOT 143
 IMPACTOR VELOCITY 0.169 KM/S
 IMPACTOR THICKNESS 2.97 MM
 SPECIMEN THICKNESS 6.35 MM
 NUMBER OF CRACKS 281
 NUMBER OF ZONES 11
 ZONE LENGTH 10.16 MM
 ZONE WIDTH 0.38 MM
 IMPACT SURFACE TO ZONE1 0.97 MM

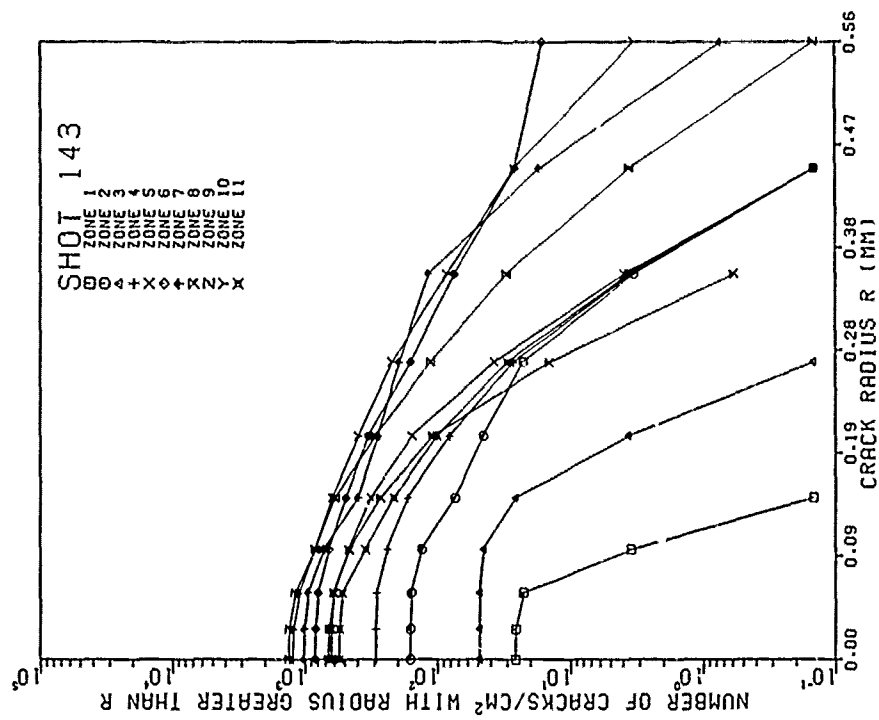


(a)

Figure E-15. Crack distributions for Shot 143. (a) Digitized cracks on sectioned specimen surface. (b) Number of digitized cracks as a function of position. (c) Surface crack-size distributions. (d) Volume crack-size distributions. (e) Volume density of cracks as a function of position.

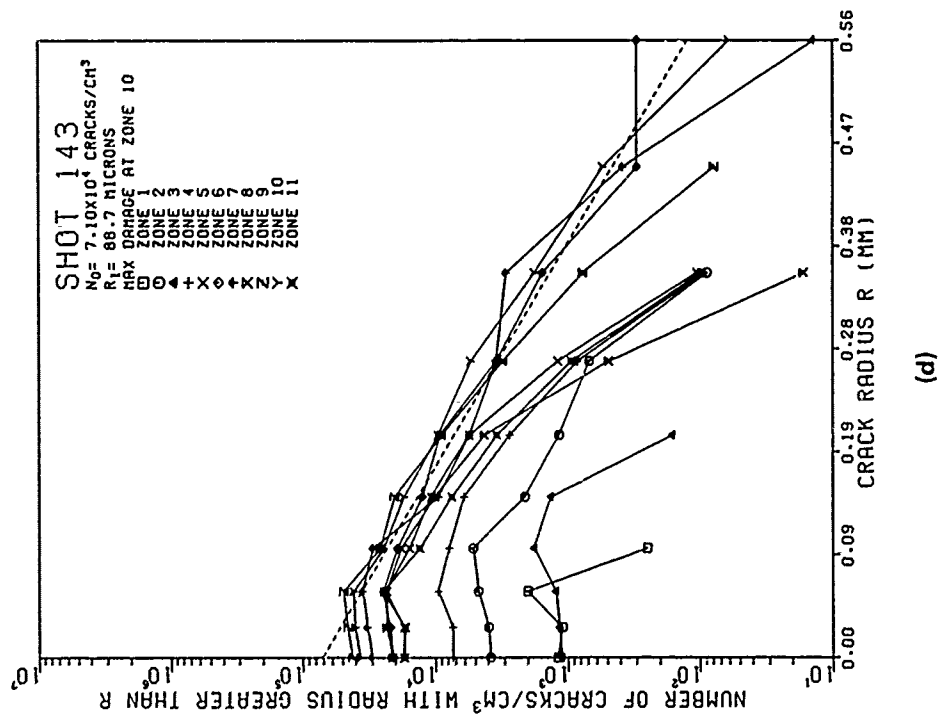


(b)

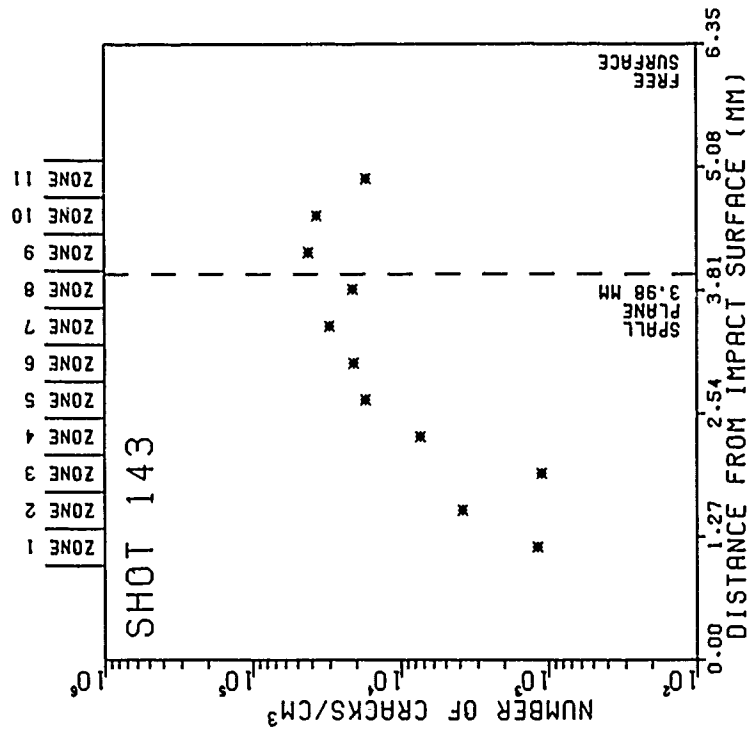


(c)

Figure E-15. (Continued)



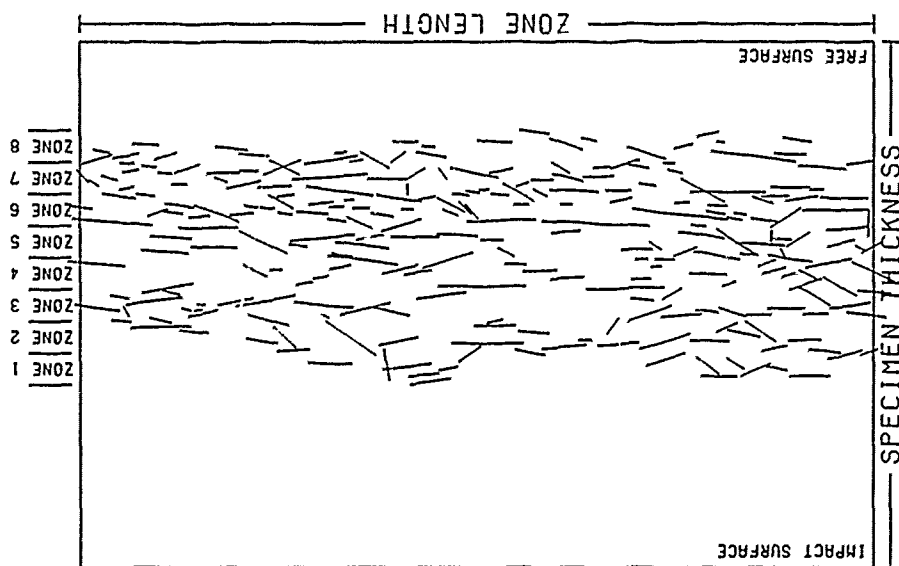
(d)



(e)

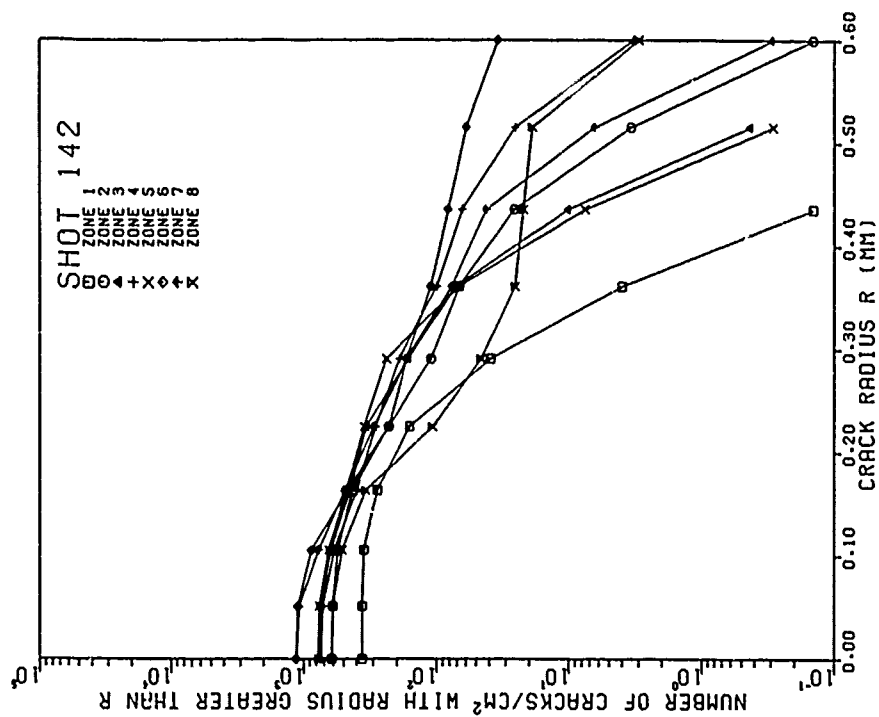
Figure E-15. (Continued)

SHOT 142
 IMPACTOR VELOCITY 0.191 KM/S
 IMPACTOR THICKNESS 2.37 MM
 SPECIMEN THICKNESS 6.36 MM
 NUMBER OF ZONES 8
 ZONE LENGTH 0.79 MM
 ZONE WIDTH 0.38 MM
 IMPACT SURFACE TO ZONE1 2.21 MM

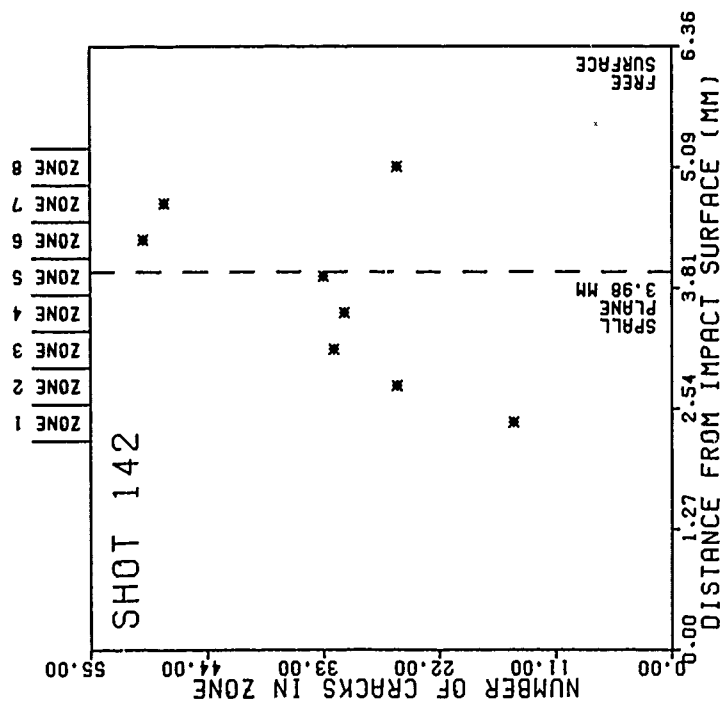


(a)

Figure E-16. Crack distributions for Shot 142. (a) Digitized cracks on sectioned specimen surface. (b) Number of digitized cracks as a function of position. (c) Surface crack-size distributions. (d) Volume crack-size distributions. (e) Volume density of cracks as a function of position.

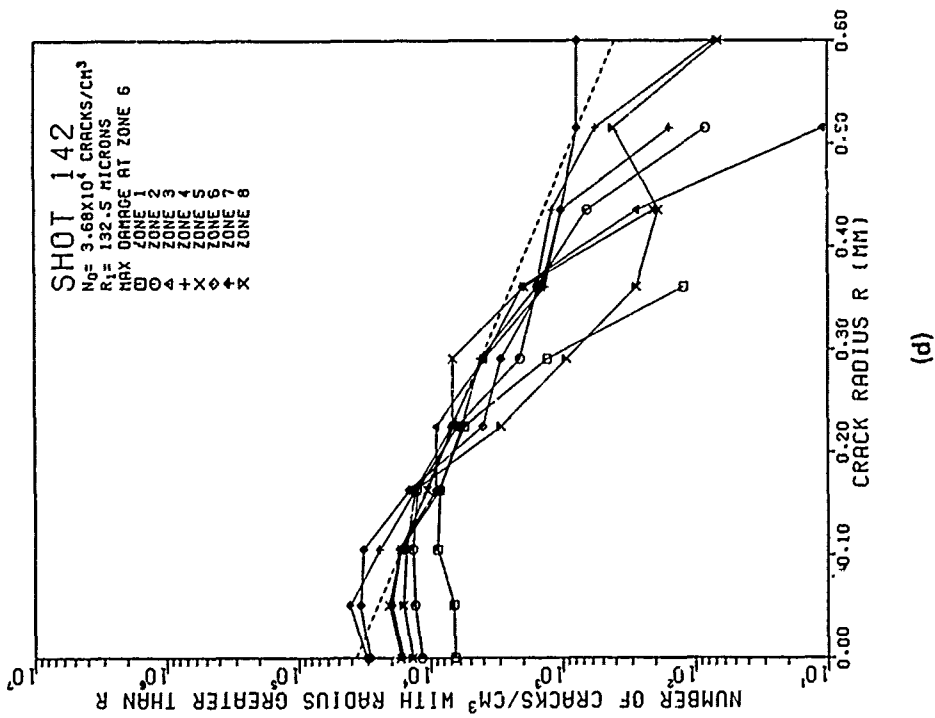


(c)

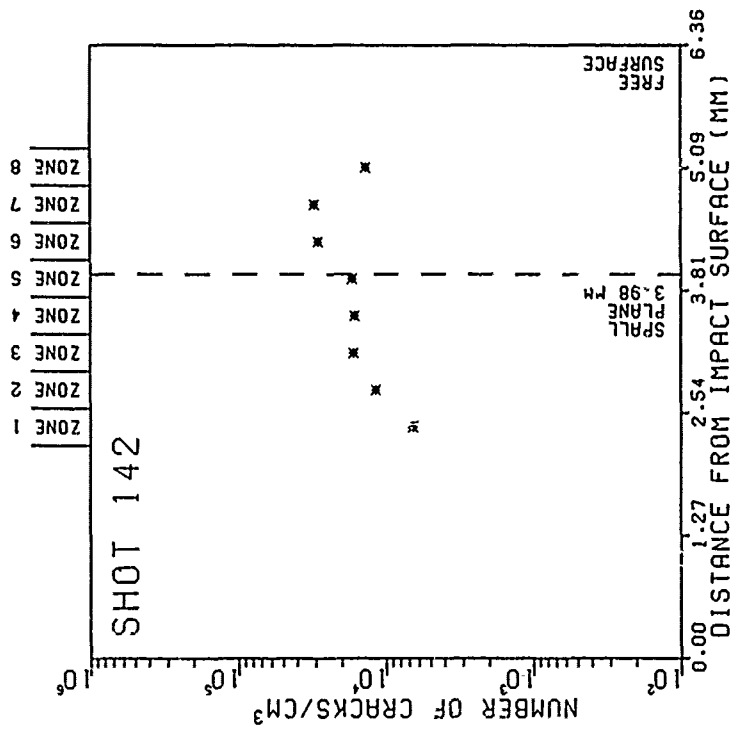


(b)

Figure E-16. (Continued)



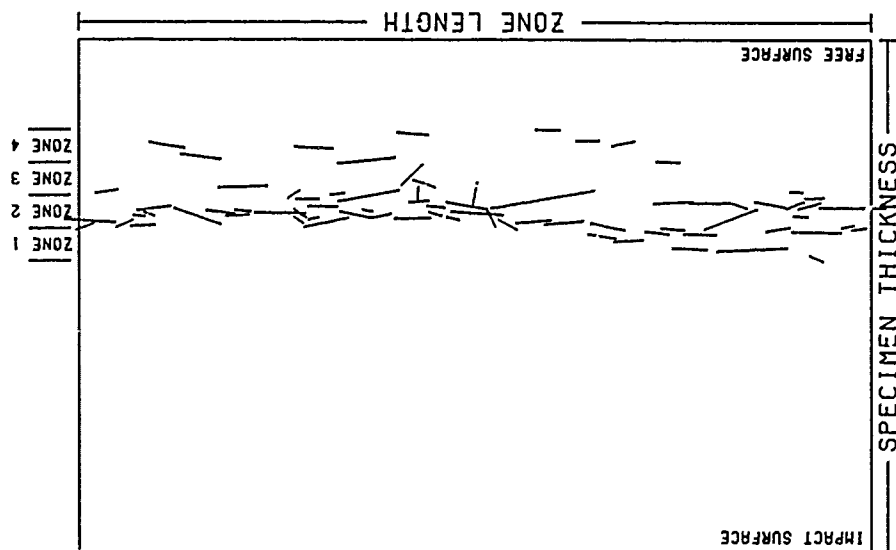
(d)



(e)

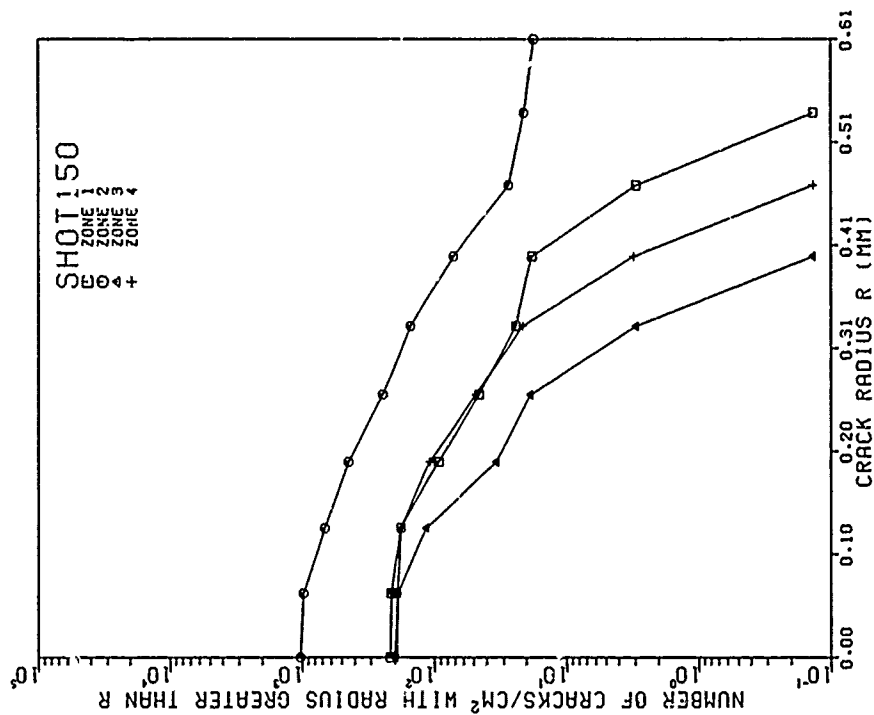
Figure E-16. (Continued)

SHOT 150
 IMPACTOR VELOCITY 0.152 KM/S
 IMPACTOR THICKNESS 1.58 MM
 SPECIMEN THICKNESS 6.36 MM
 NUMBER OF CRACKS 74
 NUMBER OF ZONES 4
 ZONE LENGTH 10.16 MM
 ZONE WIDTH 0.41 MM
 IMPACT SURFACE TO ZONE1 3.61 MM

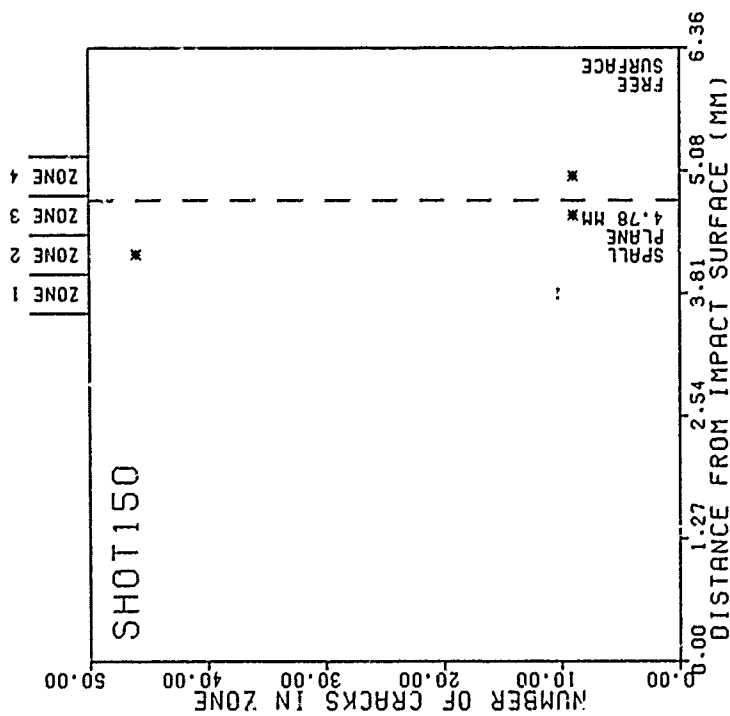


(a)

Figure E-17. Crack distributions for Shot 150. (a) Digitized cracks on sectioned specimen surface. (b) Number of digitized cracks as a function of position. (c) Surface crack-size distributions. (d) Volume crack-size distributions. (e) Volume density of cracks as a function of position.



(c)



(b)

Figure E-17. (Continued)

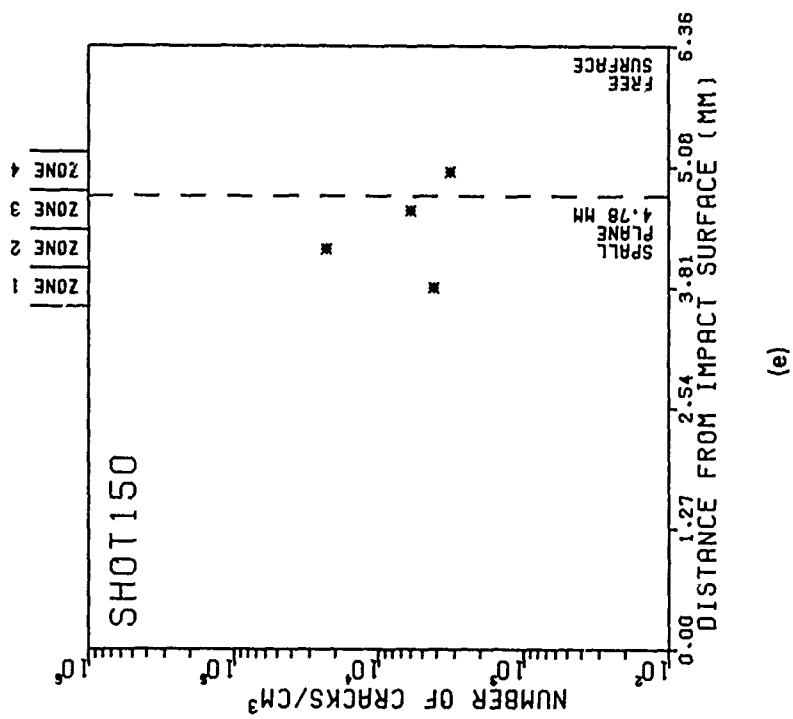
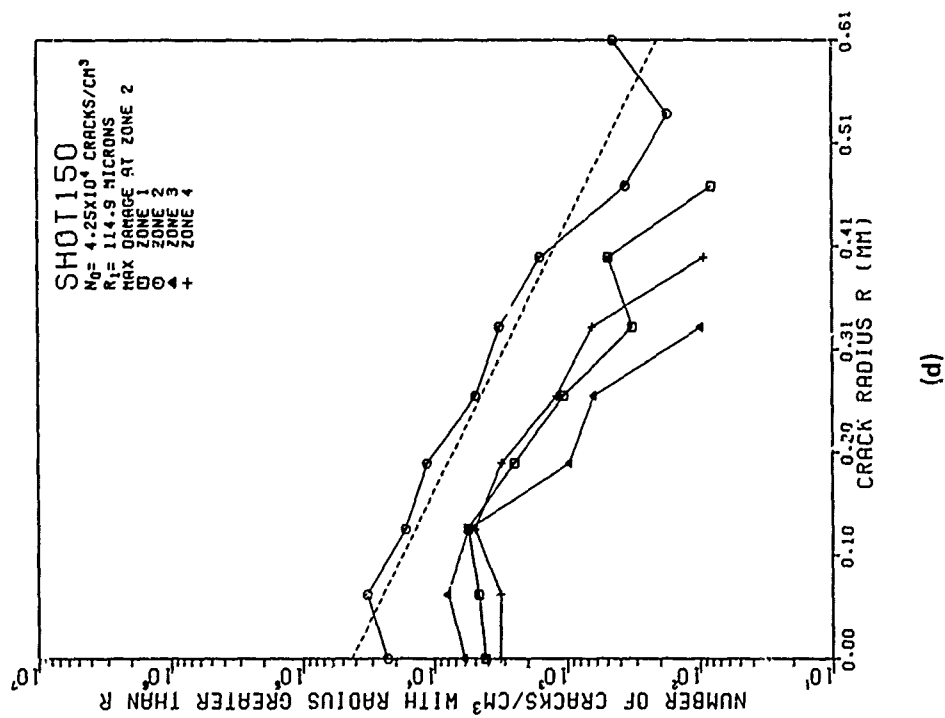
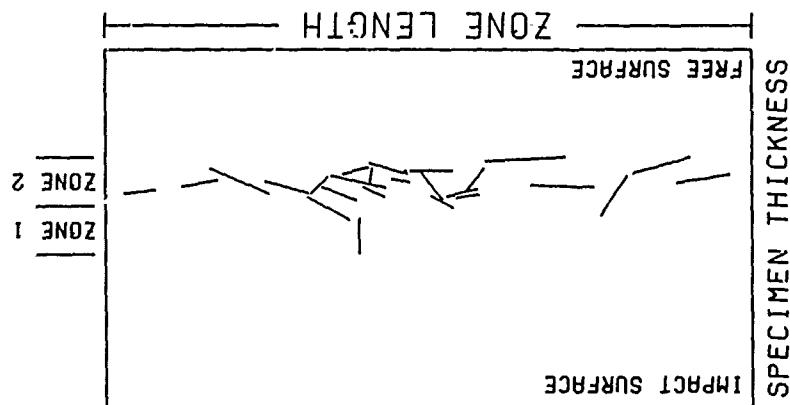


Figure E-17. (Continued)

SHOT 148
 IMPACTOR VELOCITY 0.172 KM/S
 IMPACTOR THICKNESS 1.58 MM
 SPECIMEN THICKNESS 3.18 MM
 NUMBER OF CRACKS 25
 NUMBER OF ZONES 2
 ZONE LENGTH 5.94 MM
 ZONE WIDTH 0.43 MM
 IMPACT SURFACE TO ZONE1 1.36 MM



(a)

Figure E-18. Crack distributions for Shot 148. (a) Digitized cracks on sectioned specimen surface. (b) Number of digitized cracks as a function of position. (c) Surface crack-size distributions. (d) Volume crack-size distributions. (e) Volume density of cracks as a function of position.

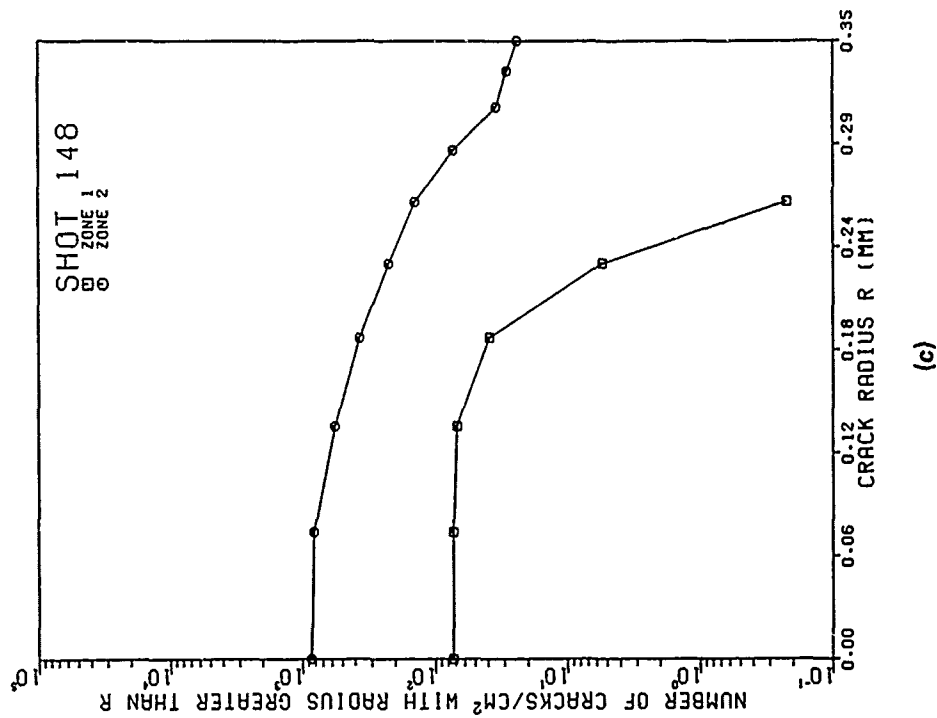
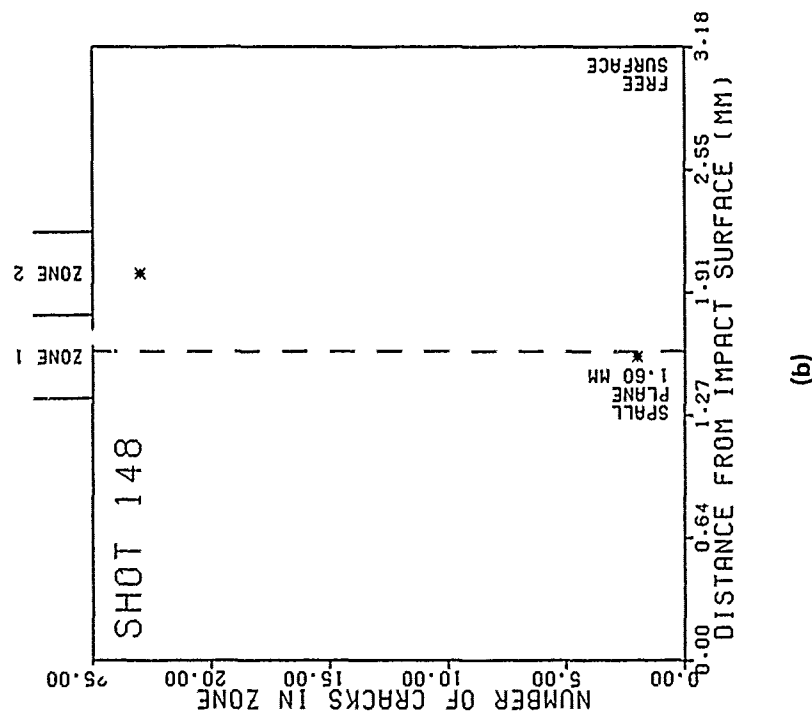
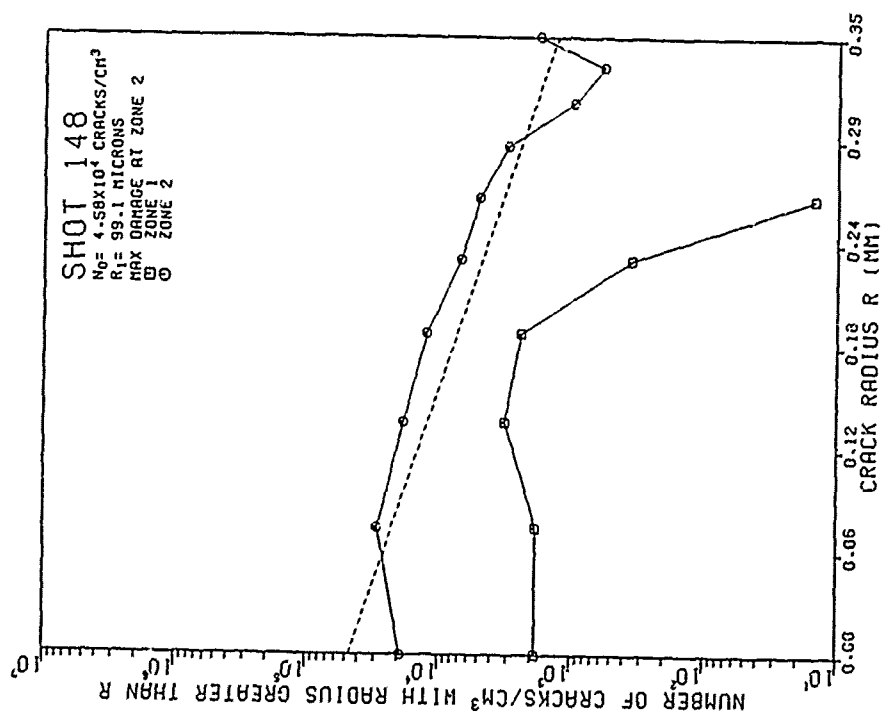
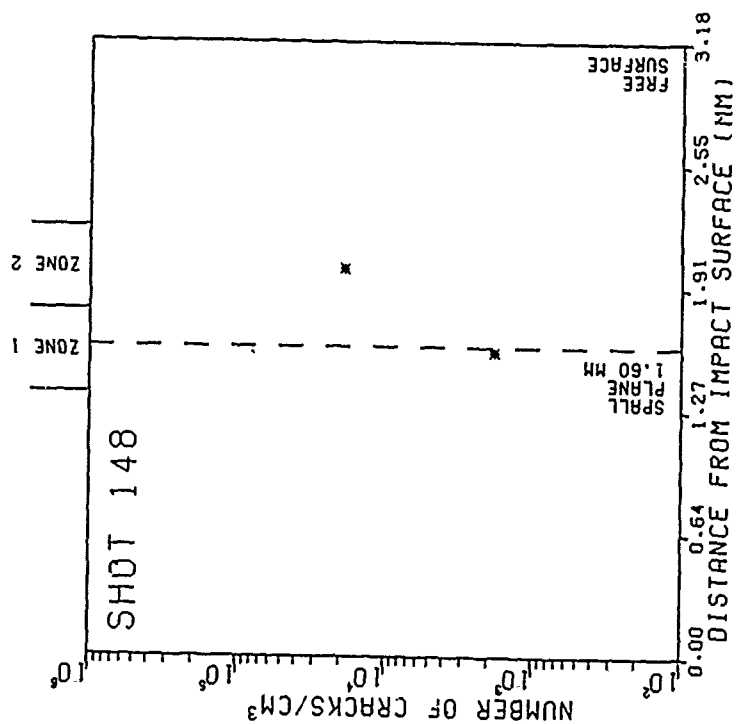


Figure E-18. (Continued)



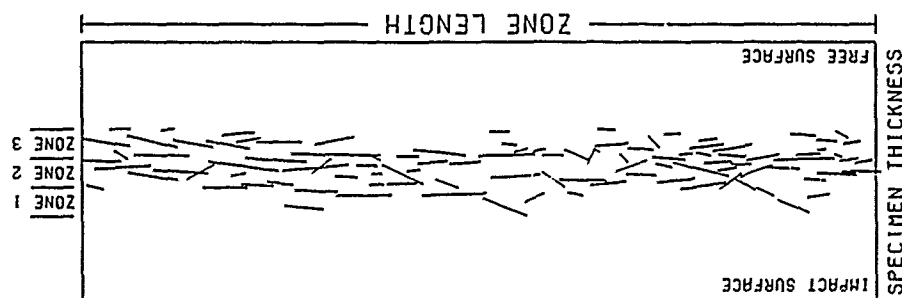
(d)



(e)

Figure E-18. (Continued)

SHOT 149
 IMPACTOR VELOCITY 0.194 KM/S
 IMPACTOR THICKNESS 1.58 MM
 SPECIMEN THICKNESS 3.18 MM
 NUMBER OF CRACKS 104
 NUMBER OF ZONES 3
 ZONE LENGTH 10.16 MM
 ZONE WIDTH 0.36 MM
 IMPACT SURFACE TO ZONE1 1.05 MM



(a)

Figure E-19. Crack distributions for Shot 149. (a) Digitized cracks on sectioned specimen surface. (b) Number of digitized cracks as a function of position. (c) Surface crack-size distributions. (d) Volume crack-size distributions. (e) Volume density of cracks as a function of position.

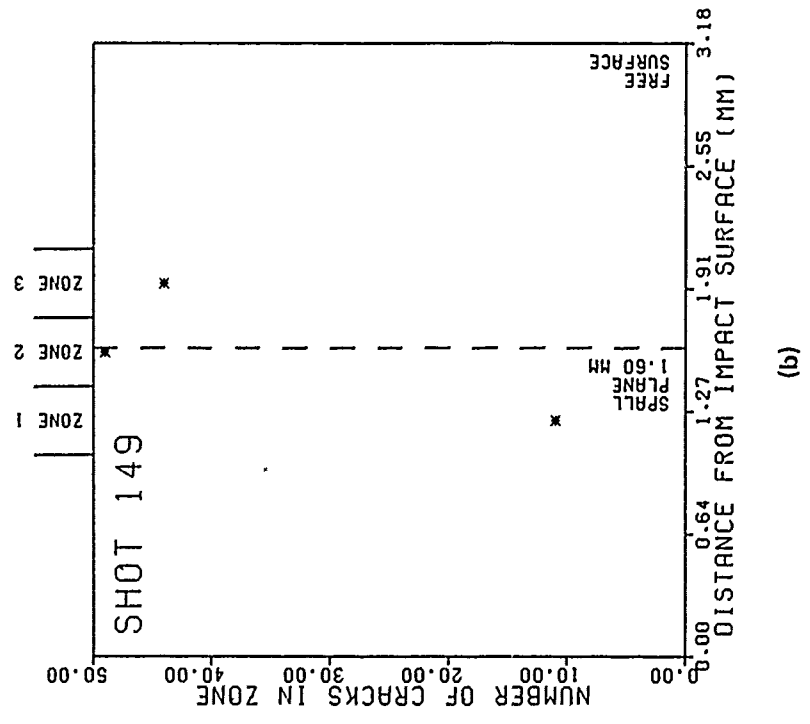
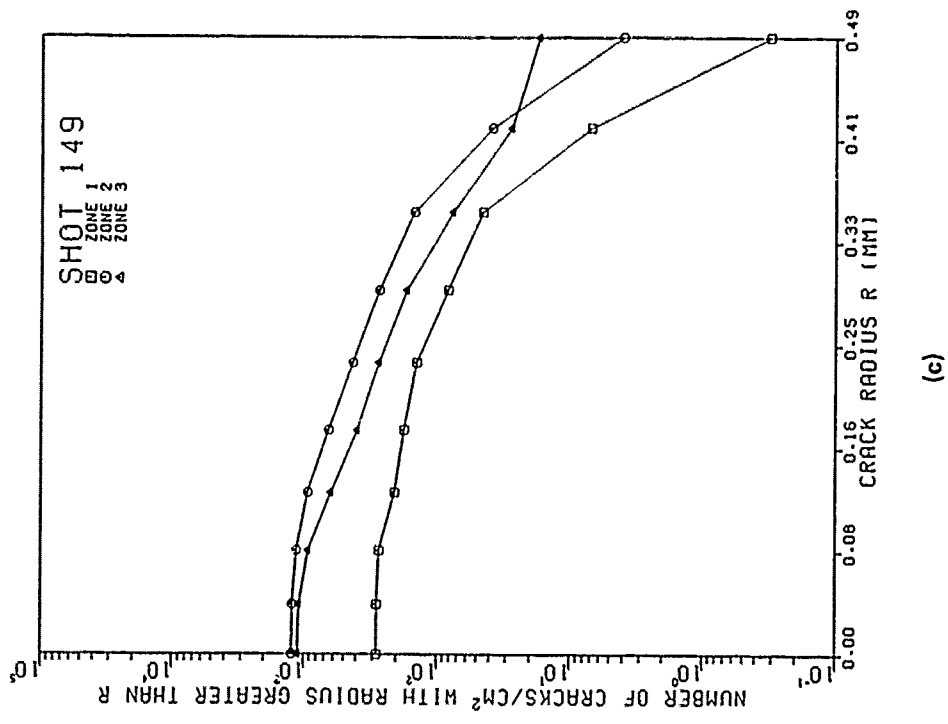


Figure E-19. (Continued)

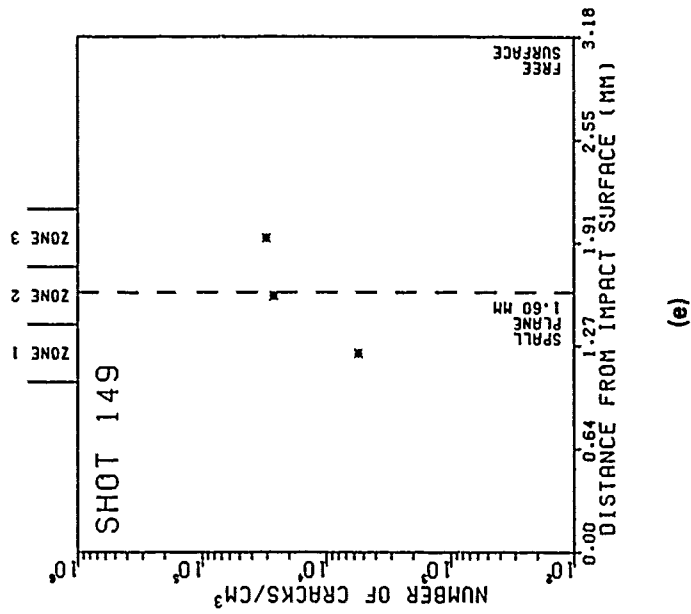
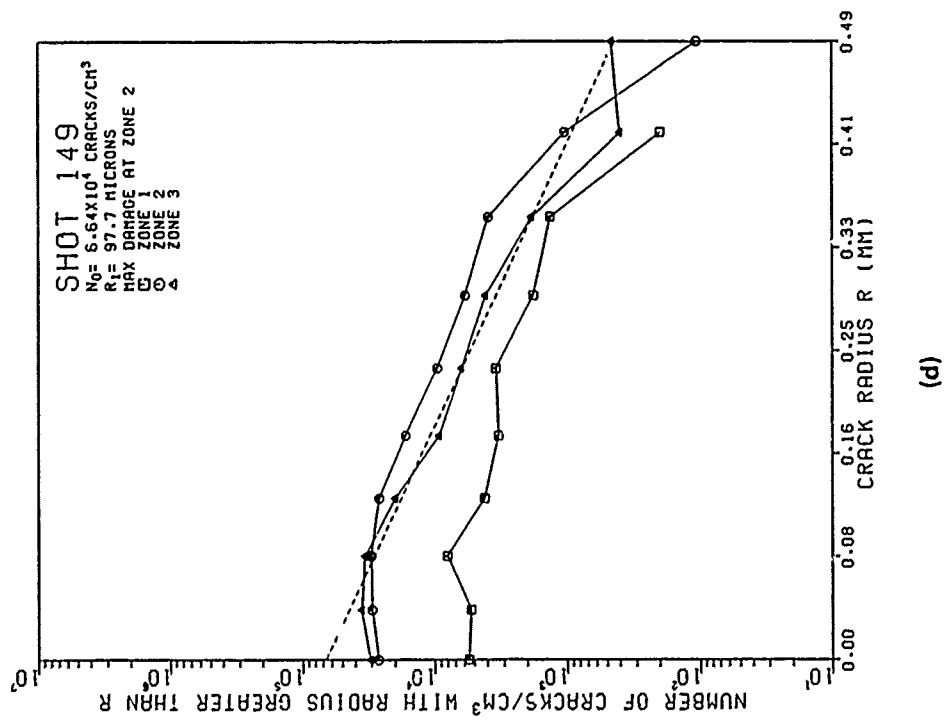
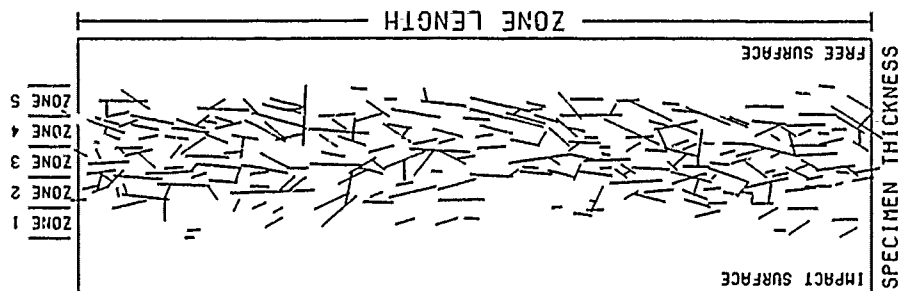


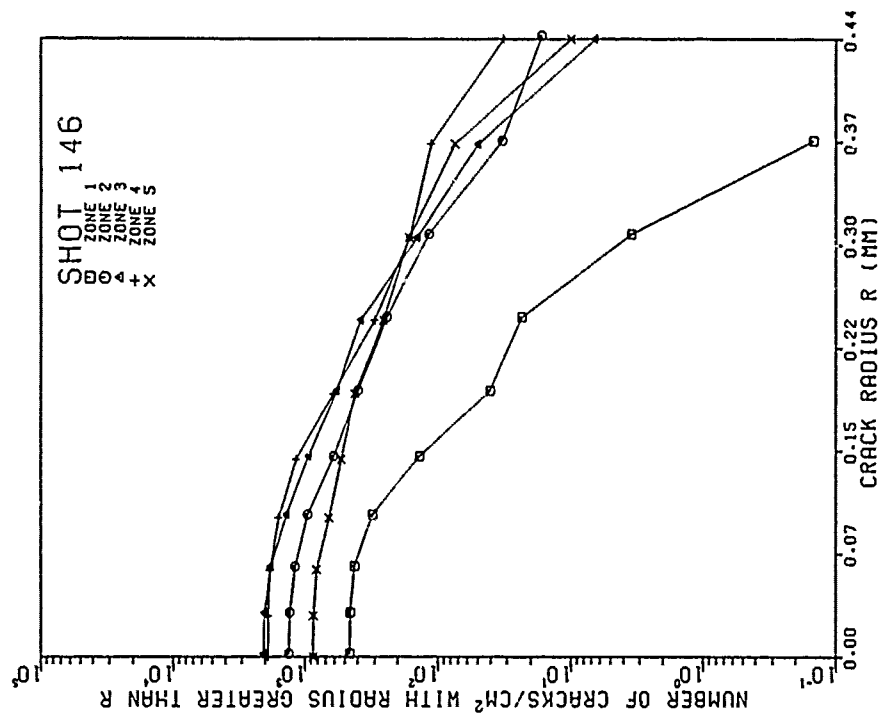
Figure E-19. (Continued)

SHOT 146
 IMPACTOR VELOCITY 0.167 KM/S
 IMPACTOR THICKNESS 1.16 MM
 SPECIMEN THICKNESS 3.18 MM
 NUMBER OF ZONES 5
 ZONE LENGTH 10.16 MM
 ZONE WIDTH 0.38 MM
 IMPACT SURFACE TO ZONE1 0.71 MM

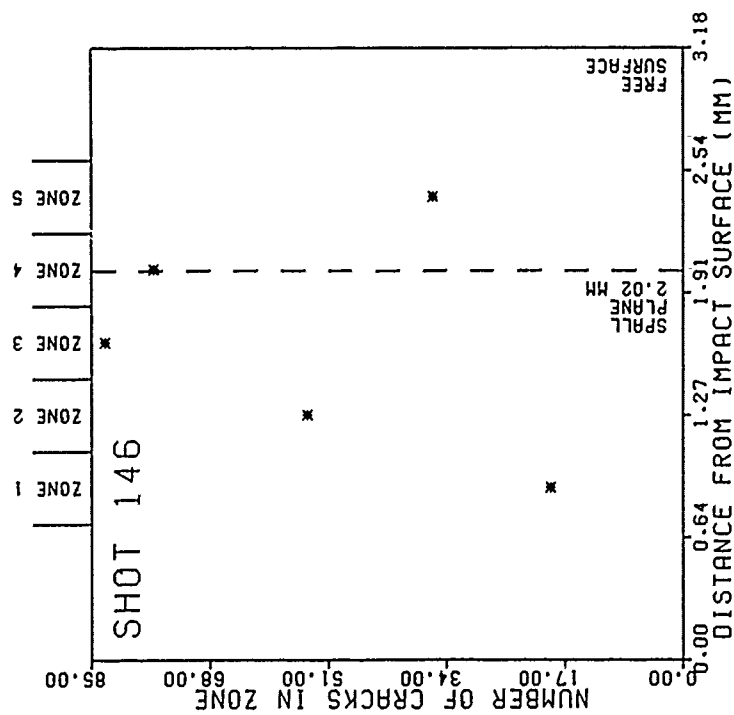


(a)

Figure E-20. Crack distributions for Shot 146. (a) Digitized cracks on sectioned specimen surface. (b) Number of digitized cracks as a function of position. (c) Surface crack-size distributions. (d) Volume crack-size distributions. (e) Volume density of cracks as a function of position.

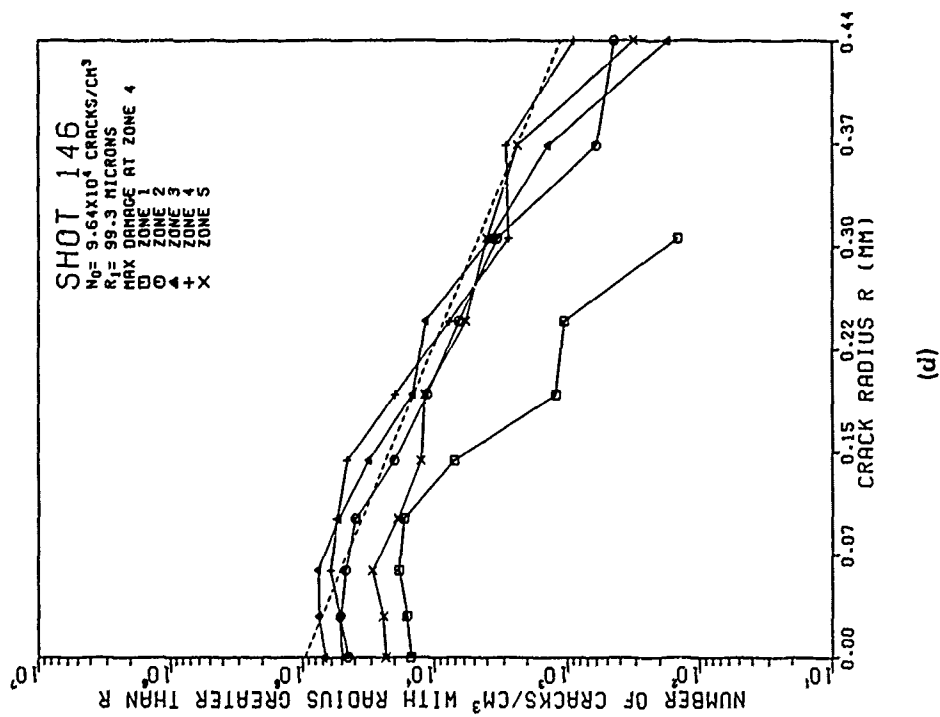


(c)

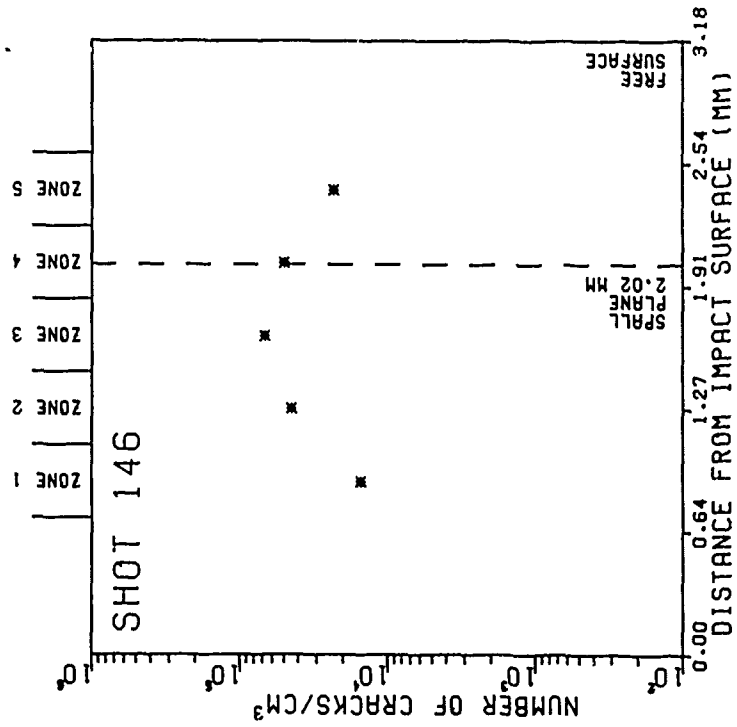


(b)

Figure E-20. (Continued)



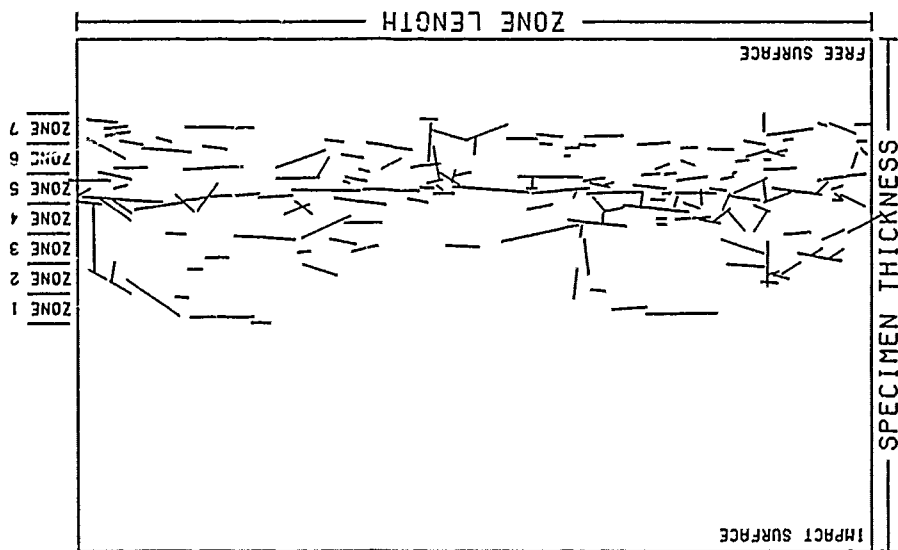
(d)



(e)

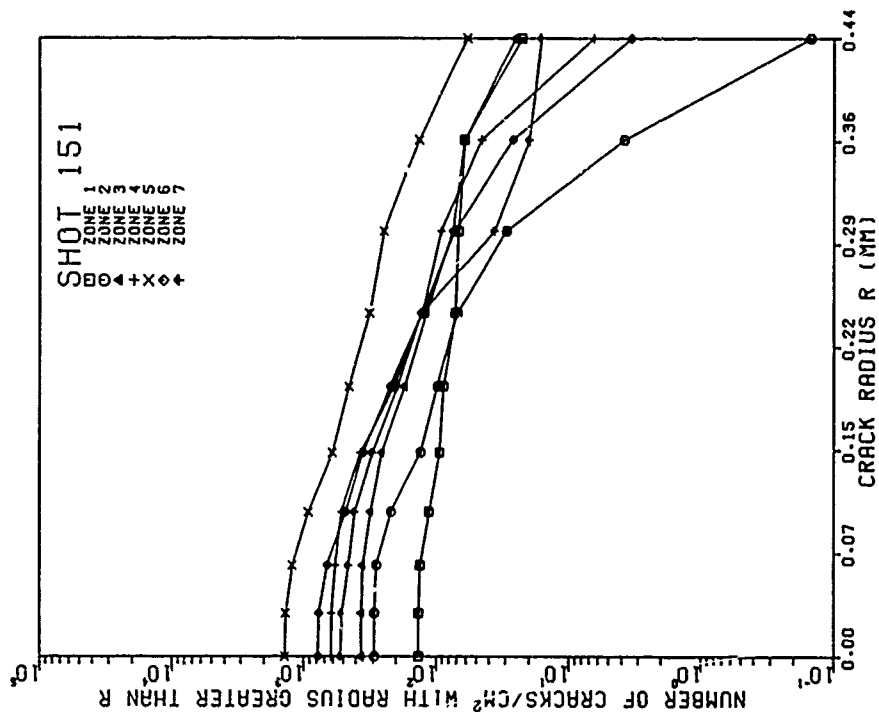
Figure E-20. (Continued)

SHOT 151
 IMPACTOR VELOCITY 0.190 KM/S
 IMPACTOR THICKNESS 1.15 MM
 SPECIMEN THICKNESS 5.36 MM
 NUMBER OF CRACKS 170
 ZONE LENGTH 10.16 MM
 ZONE WIDTH 0.37 MM
 IMPACT SURFACE 10 ZONE1 2.83 MM

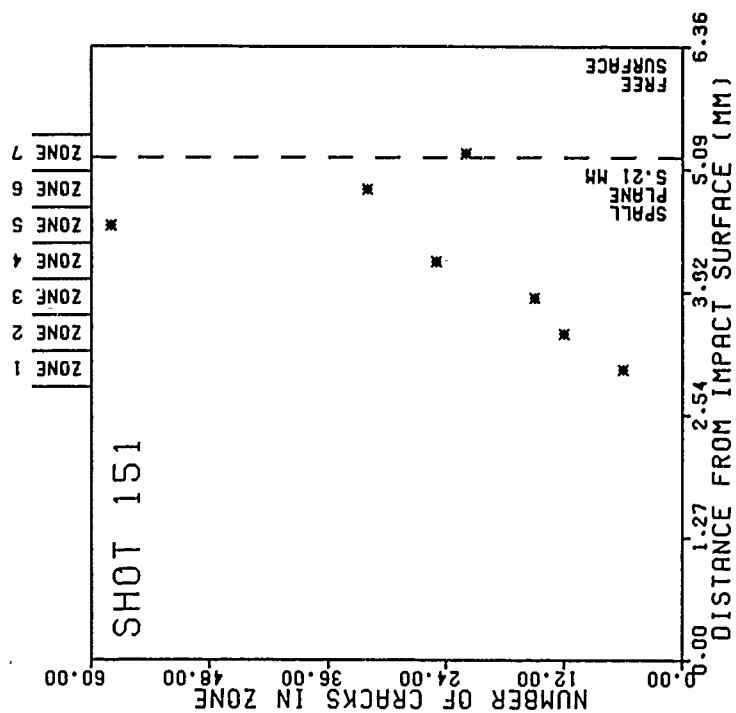


(a)

Figure E-21. Crack distributions for Shot 151. (a) Digitized cracks on sectioned specimen surface. (b) Number of digitized cracks as a function of position. (c) Surface crack-size distributions. (d) Volume crack-size distributions. (e) Volume density of cracks as a function of position.

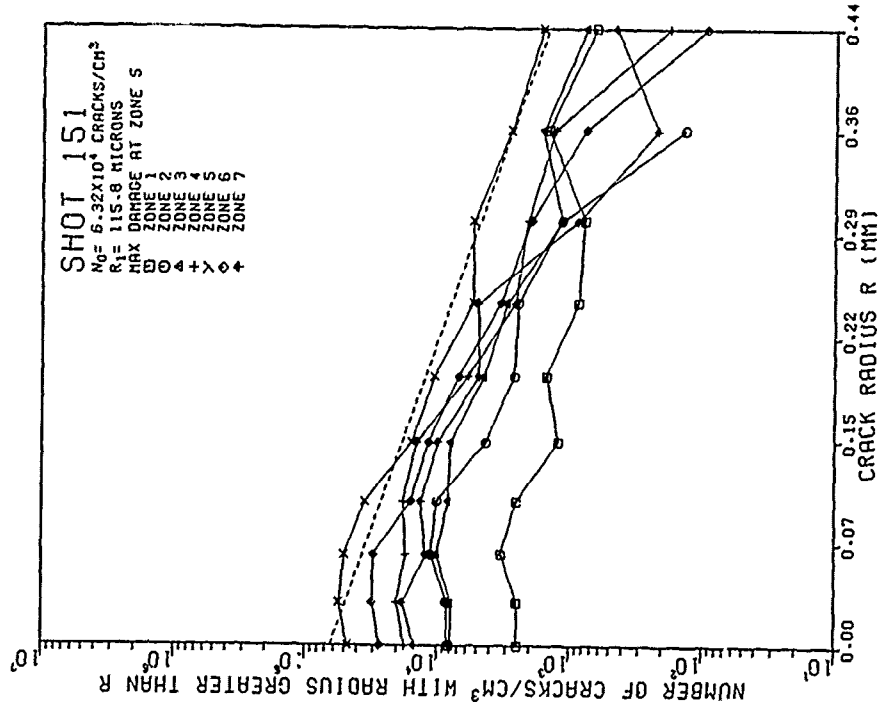


(c)

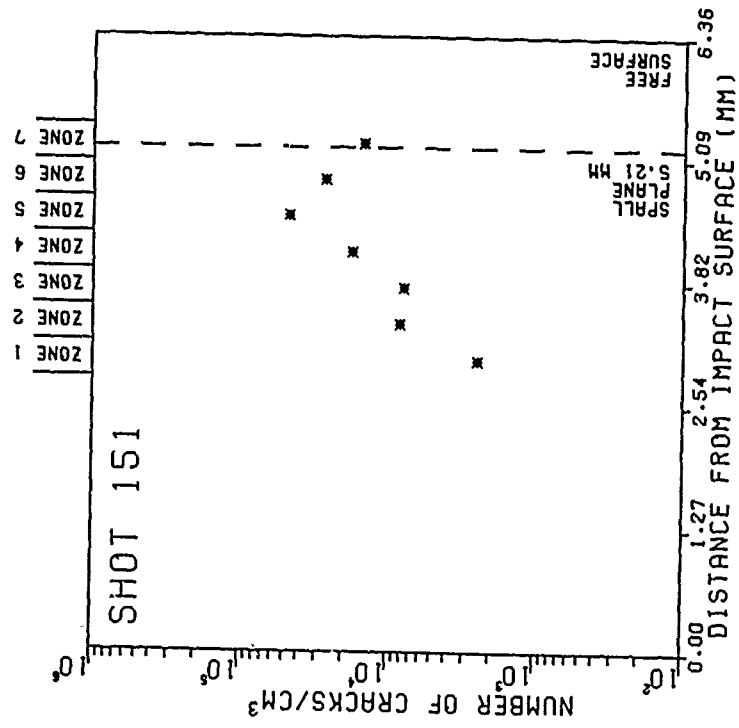


(b)

Figure E-21. (Continued)



(d)



(e)

Figure E-21. (Continued)

APPENDIX F

DIGITIZED CRACK COORDINATES FOR THE SPALL FRACTURE SPECIMENS OF HF-1 STEEL

(Digitized crack coordinates are presented for all the counted cracks for heat treatments A and B of HF-1 steel. Plot (a) of each figure in Appendix E shows the digitized crack distribution for each shot. The upper left corner of each plot is the coordinate system origin for the digitized crack values. Four values are listed for each crack in row form. The initial two values are the coordinates of one endpoint position of a crack measured in the specimen length and thickness directions, respectively. The final two values are the coordinates of the other endpoint position of the crack measured in the specimen length and thickness directions, respectively. These values are given in inches. The cracks given in the eight columns on the left side of a page are continued at the top of the eight columns on the right side. The specimen length and thickness magnification factors are given in Table 7. The cracks were measured on enlarged photographs of the sectioned specimen surfaces. The heat treatment A stringer cracks (three for Shot 98, four for Shot 92, two for Shot 91, three for Shot 90, fourteen for Shot 94, nine for Shot 113, and nine for Shot 112) are listed last for the shots that contain them.)

1.64880	1.71000	2.25800	1.78328	2.17730	3.59338	2.78518	5.51710	2.26700	2.44938	2.44338	3.43668	2.36068	3.32738	2.44268	3.23240
2.73570	3.49580	2.32588	3.47058	2.18328	3.18330	2.24228	4.22160	2.23120	3.29388	2.55888	3.23688	2.35088	3.22658	2.96758	4.27690
2.25250	3.53380	3.29810	3.45190	3.26830	3.49558	3.39798	3.55888	2.73000	4.15700	2.77780	4.21950	2.93520	4.17580	3.28720	4.18870
3.26250	3.57250	3.27420	3.59820	3.32960	3.97698	3.36978	3.55888	3.90590	4.12250	3.99760	4.42960	3.55628	3.95798	4.19540	4.03130
3.39220	2.91370	3.21550	2.91420	3.38558	2.92540	3.36978	2.83260	2.87320	3.82250	3.33440	3.82748	2.97308	3.75778	3.27888	3.73630
3.64710	2.21460	2.21460	2.21460	3.23320	2.11568	3.38360	2.27520	2.66440	3.82250	3.33440	3.82748	2.97308	3.75778	3.27888	3.73630
3.77900	3.79280	3.90120	3.74998	4.23490	4.03518	4.38360	3.99440	2.96440	3.82250	3.33440	3.82748	2.97308	3.75778	3.27888	3.73630
4.40880	3.48960	4.51580	3.68218	3.97230	3.67128	4.37418	3.68158	2.93720	3.82250	3.33440	3.82748	2.97308	3.75778	3.27888	3.73630
3.78840	3.37000	4.02870	3.25990	4.66368	4.25768	5.03408	4.88110	3.57120	2.81448	3.77220	2.81448	3.78220	2.81448	3.55368	2.98140
5.17330	3.22760	5.48270	4.12990	4.76710	3.83568	5.03408	4.88110	3.57120	2.81448	3.77220	2.81448	3.78220	2.81448	3.55368	2.98140
5.32560	3.76850	5.10880	3.71448	4.77520	3.74888	5.99448	3.62188	4.35388	2.68328	4.47988	2.68328	4.47988	2.68328	4.62368	2.54120
5.64538	3.51750	5.18200	3.56498	5.75990	3.62188	5.99448	3.62188	3.62220	3.35258	4.00488	3.35258	4.00488	3.35258	4.62368	2.54120
4.82100	3.03318	4.11700	3.11700	4.80820	2.83568	5.25728	3.31620	3.62220	3.35258	4.00488	3.35258	4.00488	3.35258	4.62368	2.54120
4.26510	2.83958	4.34510	2.83100	4.11590	2.73958	4.28620	2.74830	3.62220	3.35258	4.00488	3.35258	4.00488	3.35258	4.62368	2.54120
4.77130	2.81720	4.83170	2.82550	5.28480	2.73128	5.21550	2.75188	5.08878	4.03920	5.18148	4.03920	5.18148	4.03920	5.62128	4.18130
6.84308	2.56498	6.98770	2.58130	5.28480	2.62970	5.08100	2.69870	5.08878	4.03920	5.18148	4.03920	5.18148	4.03920	5.62128	4.18130
6.32598	2.52998	6.15720	2.50238	5.71670	2.38648	5.88160	2.48670	4.85180	3.79828	5.82178	3.79828	5.82178	3.79828	5.92968	4.88160
6.85520	2.29568	6.56020	2.27650	5.98390	3.73698	6.44440	3.75720	4.85180	3.79828	5.82178	3.79828	5.82178	3.79828	5.92968	4.88160
7.82250	3.66558	7.26480	3.75918	6.79190	3.32318	6.44440	3.75720	4.85180	3.79828	5.82178	3.79828	5.82178	3.79828	5.92968	4.88160
6.25638	3.51688	6.44168	3.45638	6.79190	3.32318	6.44440	3.75720	4.85180	3.79828	5.82178	3.79828	5.82178	3.79828	5.92968	4.88160
5.65930	3.09590	6.95860	3.08188	7.81380	3.37130	8.13198	2.94318	5.76850	3.57088	6.31678	3.57088	6.31678	3.57088	6.62328	4.81960
7.31068	3.16270	7.95840	3.15938	8.46168	2.95848	8.28780	2.94318	5.76850	3.57088	6.31678	3.57088	6.31678	3.57088	6.62328	4.81960
8.07820	2.55350	7.80580	2.66978	8.16748	2.29448	8.33688	2.94318	5.76850	3.57088	6.31678	3.57088	6.31678	3.57088	6.62328	4.81960
8.46830	3.83458	8.36950	3.81578	8.66188	3.27938	9.16788	3.39210	5.53538	2.53588	5.66578	2.53588	5.66578	2.53588	6.09678	2.76300
8.46830	3.83458	8.36950	3.81578	8.66188	3.27938	9.16788	3.39210	5.53538	2.53588	5.66578	2.53588	5.66578	2.53588	6.09678	2.76300
8.46830	3.83458	8.36950	3.81578	8.66188	3.27938	9.16788	3.39210	5.53538	2.53588	5.66578	2.53588	5.66578	2.53588	6.09678	2.76300
3.55700	3.14650	3.57650	3.86340	9.82840	4.01520	9.98880	3.94140	6.22550	3.18228	6.77628	3.18228	6.77628	3.18228	6.98678	2.97250
8.65270	2.91750	8.65550	2.90678	3.76840	3.62250	3.75950	2.88518	6.22550	3.18228	6.77628	3.18228	6.77628	3.18228	6.98678	2.97250

Figure F-1. (Continued)

Figure F-1. (Continued)

[illegible]

Figure F-1. (Continued)

Figure F-1. (Continued)

SHOT 143 201 CRACKS

Figure F-1. (Continued)

F-9

Figure F-1. (Continued)

Figure F-1. (Continued)

5.95750	3.60330	6.01800	3.74613	6.04913	3.58130	6.18130	3.17170
5.95620	3.23640	5.91463	2.86374	6.12950	3.00260	6.29928	2.96170
5.94950	3.60440	6.51920	5.73090	6.26550	3.70170	6.27278	3.88840
6.15140	4.07150	6.28000	3.91950	6.28830	3.90020	6.51990	3.94750
6.07990	4.10530	6.75550	4.52478	6.74360	4.12080	6.72440	3.97060
6.50770	3.97480	7.30100	3.89320	6.63390	4.20570	7.01608	4.16950
6.73660	4.32170	6.95090	4.93740	7.95950	4.25750	7.05980	4.16950
7.00230	4.35518	7.18110	4.84140	7.95950	4.25750	7.05980	4.16950
7.45190	4.47580	6.81220	4.59440	7.52550	4.25750	7.05980	4.16950
7.20070	4.47800	7.35910	4.43440	7.97620	4.53130	8.24290	4.61170
7.66310	4.27390	7.31413	4.30420	7.81393	4.33540	7.74220	4.44180
6.97440	4.10878	7.61650	4.11530	7.43860	4.15570	7.44950	4.35990
6.94540	4.03960	6.93920	4.03420	7.11870	3.95330	7.15010	3.97060
6.90810	3.81980	7.03020	3.81780	6.91140	3.75650	7.13190	3.97060
7.13280	3.81560	7.58410	3.83240	7.52540	3.75650	7.13190	3.97060
7.42090	3.91840	7.96680	4.11020	7.75708	3.98460	7.74220	3.97060
7.43310	4.11370	8.24560	4.28598	7.75448	4.08270	8.12620	3.67930
8.15100	4.24680	8.20900	4.30330	8.15570	4.01820	8.58703	4.01290
8.06600	3.97630	8.24650	3.98461	8.06900	3.67110	8.21980	4.12190
7.67640	3.58390	8.14350	3.42260	7.74830	3.29110	8.20180	3.98460
7.95350	4.71620	8.13060	4.67280	8.18400	5.02760	8.19420	3.26520
8.22040	4.77190	8.78300	4.85170	8.42240	4.71600	8.24290	4.82520
8.20760	4.59810	8.42560	4.54250	8.34810	4.71600	8.24290	4.82520
8.15260	4.91250	8.52720	4.84091	8.97000	4.28090	8.51130	4.84090
9.27050	4.49340	9.46750	4.80273	9.29340	4.78660	9.28020	4.80270
3.13410	4.62440	9.41010	4.55090	3.29168	4.78660	9.28020	4.78030
4.42330	4.25730	9.39403	4.33360	4.99500	4.57540	9.23540	4.59810
8.20550	4.17350	9.86600	4.09630	8.79890	4.15750	9.13220	4.19920
9.00890	4.03160	9.13500	4.02970	9.03528	4.10310	8.95420	4.24360
9.40280	4.09210	9.33230	3.95980	9.18840	4.10310	9.12708	4.03170
8.42820	3.63960	8.72730	3.66120	8.97940	3.56000	9.02700	3.66120
8.59440	3.76240	9.10820	3.75683	8.40020	3.59730	8.81390	3.69880
8.23250	3.55750	8.22510	3.04461	8.14948	3.17780	8.61870	3.31540
8.24250	3.18310	8.37210	3.21230	8.30180	3.09460	8.35850	3.07850
6.37360	2.77020	6.78690	2.83340	6.78420	3.17220	8.49170	3.12880
					2.72150	7.63510	2.73540

Figure F-1. (Continued)

APPENDIX G

COMPUTER LISTINGS OF THE INPUT PARAMETERS USED IN THE PUFF COMPUTATIONS FOR THE HF-1 STEEL SPALL FRACTURE EXPERIMENTS

(The nucleation and growth values in Tables 9 and 10 were obtained from PUFF computations using the input parameters in this appendix. Figures G-1 through G-5(a) give the input parameters for the computations for the heat treatment A experiments. Figures G-5(b) through G-10 give the input parameters for the computations for the heat treatment B experiments. The input parameters for the BFRACT2 fracture model are given in the TSR1 and TSR2 lines of each listing. The HF-1 steel equation of state data is given in the EQST and Y0 lines. An explanation of the these parameters is given in Section VI and Reference 1.)

***** SRI PUFF 8 *****
 DATE = 11/16/78
 IDENT HF-1 STEEL. SHOT 92. 590 FPS. DAMAGE.
 NTEGT= 0 NJEUIT= 3 NREZON= 0 NALPHA
 JEDITS= S1,10,11,12,13,14,15,16,17,18,19,20,21,22,23,24,25,26,27,28,29
 JEDITS= NEM,13,20,21,22,23,24,25,26,27,28
 JEDITS= NET,19,20,21,22,23,24,25,26,27,28
 NEDIT= 5 JCYCS= 3,000E+00 TS= 1,000E-05 IN= 5
 NTRLS= 1 MATFL= 150 CKS= 1,800E+04 IN= 5 , CM, SEC
 IN= 5 , CM/SEC
 HF1 STEEL RHOS= 7,774E+03 CFP = 050 DPY = 001 NVAR= 10 IN= 5 G/CM3
 EQST = 1,605E+12 3,561E+12 7,360E+10 1,660E+00 2,500E-01 3,603E+12 0 IN= 5 DYN/CM2,=, ERG/G, , DYN/CM2, ERG/G
 TSRI = -3,770E-05-1,000E+09 6,560E-03 9,000E+10-2,500E-01-5,600E+08 0 IN= 5
 TSRI = -2,500E+10 0 2,500E-01 5,000E-01 4,000E-01 3,000E+00 0 IN= 5
 Y0= 1,361E+10 7,912E+11 0 0 0 0 0 IN= 5 DYN/CM2, DYN/CM2, DYN/CM2,
 NLAYER= 2 JNAT= 1 0 0 0 0 0 0 IN= 5
 NZONES= 1 8 CELLS IN 2,372E-01 CM IN= 5 CM, CH,
 NZONES= 1 20 CELLS IN 6,336E-01 CM IN= 5 CM, CH,

(a)

***** SRI PUFF 8 *****
 DATE = 11/16/78
 IDENT HF-1 STEEL. SHOT 91. 601 FPS. DAMAGE.
 NTEGT= 0 NJEUIT= 3 NREZON= 0 NALPHA
 JEDITS= S1,10,11,12,13,14,15,16,17,18,19,20,21,22,23,24,25,26,27,28,29
 JEDITS= NEM,19,20,21,22,23,24,25,26,27,28
 JEDITS= NET,19,20,21,22,23,24,25,26,27,28
 NEDIT= 5 JCYCS= 3,000E+00 TS= 1,000E-05 IN= 5
 NTRLS= 1 MATFL= 150 CKS= 1,800E+04 IN= 5 , CM, SEC
 IN= 5 , CM/SEC
 HF1 STEEL RHOS= 7,774E+03 CFP = 050 DPY = 001 NVAR= 10 IN= 5 G/CM3
 EQST = 1,605E+12 3,561E+12 7,360E+10 1,660E+00 2,500E-01 3,603E+12 0 IN= 5 DYN/CM2,=, ERG/G, , DYN/CM2, ERG/G
 TSRI = -3,770E-05-1,000E+09 6,560E-03 9,000E+10-2,500E-01-5,600E+08 0 IN= 5
 TSRI = -2,500E+10 0 2,500E-01 5,000E-01 4,000E-01 3,000E+00 0 IN= 5
 Y0= 1,361E+10 7,912E+11 0 0 0 0 0 IN= 5 DYN/CM2, DYN/CM2, DYN/CM2,
 NLAYER= 2 JNAT= 1 1 0 0 0 0 0 IN= 5
 NZONES= 1 8 CELLS IN 2,373E-01 CM IN= 5 CM, CH,
 NZONES= 1 20 CELLS IN 6,342E-01 CM IN= 5 CM, CH,

(b)

Figure G-2. PUFF input parameters for (a) Shot 92 and (b) Shot 91.

A-4

```

DATE = 11/16/78
IDENT HF-1 STEEL. SHOT 90. 626 FPS. DAMAGE.
NTEDIT= 0 NJEDIT= 3 NREZON= 0 NALPHA
JEDITS= S1,10,11,12,13,14,15,16,17,18,19,20,21,22,23,24,25,26,27,28,29
JEDITS= NEM,19,20,21,22,23,24,25,26,27,28
JEDITS= NET,19,20,21,22,23,24,25,26,27,28
NEDIT= 5 JCYCS= 3.000E+00 TS= 1.000E-05 IN= 5 , , CH, SEC
NMTRLS= 1 MATFL= 150 CKS= 1.910E+04 IN= 5 , , CH/SEC
          1 UZERO= 0.000000000 IN= 5 , , CH/SEC

HF1 STEEL
EQST = 1.605E+12 3.561E+12 7.774E+00 CFP = 050 DPY = 001 NVAR= 10 IN= 5 G/CM3
TSR1 = -3.770E-05 -1.000E+09 6.560E-03 9.000E+10 2.500E-01 3.603E+12 IN= 5 DYN/CM2,=, ERG/G, , DYN/CM2, ERG/G
TSR2 = -2.500E+10 0. 2.500E-01 5.000E-01 4.000E-01 3.000E+00 0. IN= 5
Y0= 1.361E+10 7.912E+11 0. 0. 0. 0. IN= 5 DYN/CM2, DYN/CM2, DYN/CM2,

NLAYER= 2 JMAT= 1 1 0 0 0 0 0 0 IN= 5
NZONES= 1 8 CELLS IN 2.370E-01 CM IN= 5 CM, CM,
NZONES= 1 20 CELLS IN 6.351E-01 CM IN= 5 CM, CM,

```

(a)

```

DATE = 11/16/78
IDENT HF-1 STEEL. SHOT 94. 655 FPS. DAMAGE.
NTEDIT= 0 NJEDIT= 3 NREZON= 0 NALPHA
JEDITS= S1,10,11,12,13,14,15,16,17,18,19,20,21,22,23,24,25,26,27,28,29
JEDITS= NEM,19,20,21,22,23,24,25,26,27,28
JEDITS= NET,19,20,21,22,23,24,25,26,27,28
NEDIT= 5 JCYCS= 3.000E+00 TS= 1.000E-05 IN= 5 , , CH, SEC
NMTRLS= 1 MATFL= 150 CKS= 2.000E+04 IN= 5 , , CH/SEC
          1 UZERO= 0.000000000 IN= 5 , , CH/SEC

HF1 STEEL
EQST = 1.605E+12 3.561E+12 7.774E+00 CFP = 050 DPY = 001 NVAR= 10 IN= 5 G/CM3
TSR1 = -3.770E-05 -1.000E+09 6.560E-03 9.000E+10 2.500E-01 3.603E+12 IN= 5 DYN/CM2,=, ERG/G, , DYN/CM2, ERG/G
TSR2 = -2.500E+10 0. 2.500E-01 5.000E-01 4.000E-01 3.000E+00 0. IN= 5
Y0= 1.361E+10 7.912E+11 0. 0. 0. 0. IN= 5 DYN/CM2, DYN/CM2, DYN/CM2,

NLAYER= 2 JMAT= 1 1 0 0 0 0 0 0 IN= 5
NZONES= 1 8 CELLS IN 2.369E-01 CM IN= 5 CM, CM,
NZONES= 1 20 CELLS IN 6.350E-01 CM IN= 5 CM, CM,

```

(b)

Figure G-3. PUFF input parameters for (a) Shot 90 and (b) Shot 94.

DATE = 11/16/78
 IDENT HF-1 STEEL. SHOT 113. 662 FPS DAMAGE.
 NTEDT= 0 NJEDIT= 3 NREZON= 0 NALPHA
 JEDITS= S1,10,11,12,13,14,15,16,17,18,19,20,21,22,23,24,25,26,27,28,29
 NEM,16,17,18,19,20,21,22,23,24,25
 NET,16,17,18,19,20,21,22,23,24,25
 JEDITS= 5 JCYCS= 150 CKS= 3.000E+00 TS= 1.000E-05 IN= 5 CM, SEC
 NMTRLS= 1 MATFL= 1 UZERO= 2.020E+04 IN= 5 CM/SEC
 HF1 STEEL
 EQST = 1.605E+12 3.561E+12 7.774E+00 CFP = 050 DRY = 001 NVAR= 10
 TSRI = -3.770E-05-1.000E+09 6.560E-03 1.660E+00 2.500E-01 3.683E+12 0.
 TSRI = -2.500E+10 0. 2.500E-01 5.000E-01 4.000E-01 3.000E+00 0.
 Y8= 1.351E+10 7.912E+11 0. 0. 0. 0.
 NLAYER= 2 JNAT= 1 1 0 0 0 0 0 0 0 0
 NZONES= 1 8 CELLS IN 1.596E-01 CM 0.
 NZONES= 1 20 CELLS IN 3.169E-01 CM 0.

(a)

DATE = 11/16/78
 IDENT HF-1 STEEL. SHOT 111. 633 FPS. DAMAGE.
 NTEDT= 0 NJEDIT= 3 NREZON= 0 NALPHA
 JEDITS= S1,10,11,12,13,14,15,16,17,18,19,20,21,22,23,24,25,26,27,28,29
 NEM,19,20,21,22,23,24,25,26,27,28
 NET,19,20,21,22,23,24,25,26,27,28
 JEDITS= 5 JCYCS= 150 CKS= 3.000E+00 TS= 1.000E-05 IN= 5 CM, SEC
 NMTRLS= 1 MATFL= 1 UZERO= 1.930E+04 IN= 5 CM/SEC
 HF1 STEEL
 EQST = 1.605E+12 3.561E+12 7.774E+00 CFP = 050 DRY = 001 NVAR= 10
 TSRI = -3.770E-05-1.000E+09 6.560E-03 1.660E+00 2.500E-01 3.683E+12 0.
 TSRI = -2.500E+10 0. 2.500E-01 5.000E-01 4.000E-01 3.000E+00 0.
 Y8= 1.351E+10 7.912E+11 0. 0. 0. 0.
 NLAYER= 2 JNAT= 1 1 0 0 0 0 0 0 0 0
 NZONES= 1 8 CELLS IN 1.156E-01 CM 0.
 NZONES= 1 20 CELLS IN 3.105E-01 CM 0.

(b)

Figure G-4. PUFF input parameters for (a) Shot 113 and (b) Shot 111.

DATE = 11/16/76
IDENT HF-1 STEEL, HT 8, SHOT 145, 379 FPS, DAMAGE.
NTEOT= 0 NJEDIT= 3 NREZON= 0 NALPHA
JEDITS= S1,10,11,12,13,14,15,16,17,18,19,20,21,22,23,24,25,26,27,28,29
JEDITS= NEM,19,20,21,22,23,24,25,26,27,28
JEDITS= NET,19,20,21,22,23,24,25,26,27,28
NEDIT= 5 JCYCS= 150 CKS= 3.000E+00 TS= 1.000E-05 IN= 5
NMTRLS= 1 MATFL= 1 UZERO= 1.160E+04 IN= 5
HF1 STEEL RHOS= 7.774E+00 CFP = 050 DPY = 001 NVAR= 10 IN= 5 G/CM3
EQST = 1.605E+12 3.561E+12 7.360E+10 1.660E+00 2.500E-01 3.683E+12 0. IN= 5 DYN/CM2,=, ERG/G, , DYN/CM2, ERG/G
TSR1 = -3.870E-05-1.000E+09 8.180E-03 1.248E+11-1.800E+10-1.740E+09 0. IN= 5
TSR2 = -1.800E+10 0. 2.500E-01 5.000E-01 4.000E-01 3.000E+00 0. IN= 5
Y0= 1.361E+10 7.912E+11 0. 0. 0. 0. IN= 5 DYN/CM2, DYN/CM2, DYN/CM2,
NLAYER= 2 JMATE 1 1 0 0 0 0 0 0 IN= 5
NZONES= 1 8 CELLS IN 2.375E-01 CM IN= 5 CH, CH,
NZONES= 1 20 CELLS IN 6.353E-01 CM IN= 5 CH, CH,

(a)

DATE = 11/16/76
IDENT HF-1 STEEL, HT 8, SHOT 144, 405 FPS, DAMAGE.
NTEOT= 0 NJEDIT= 3 NREZON= 0 NALPHA
JEDITS= S1,10,11,12,13,14,15,16,17,18,19,20,21,22,23,24,25,26,27,28,29
JEDITS= NEM,19,20,21,22,23,24,25,26,27,28
JEDITS= NET,19,20,21,22,23,24,25,26,27,28
NEDIT= 5 JCYCS= 150 CKS= 3.000E+00 TS= 1.000E-05 IN= 5
NMTRLS= 1 MATFL= 1 UZERO= 1.480E+04 IN= 5
HF1 STEEL RHOS= 7.774E+00 CFP = 050 DPY = 001 NVAR= 10 IN= 5 G/CM3
EQST = 1.605E+12 3.561E+12 7.360E+10 1.660E+00 2.500E-01 3.683E+12 0. IN= 5 DYN/CM2,=, ERG/G, , DYN/CM2, ERG/G
TSR1 = -3.870E-05-1.000E+09 8.180E-03 1.248E+11-1.800E+10-1.740E+09 0. IN= 5
TSR2 = -1.800E+10 0. 2.500E-01 5.000E-01 4.000E-01 3.000E+00 0. IN= 5
Y0= 1.361E+10 7.912E+11 0. 0. 0. 0. IN= 5 DYN/CM2, DYN/CM2, DYN/CM2,
NLAYER= 2 JMATE 1 1 0 0 0 0 0 0 IN= 5
NZONES= 1 8 CELLS IN 2.372E-01 CM IN= 5 CH, CH,
NZONES= 1 20 CELLS IN 6.353E-01 CM IN= 5 CH, CH,

(b)

Figure G-6. PUFF input parameters for (a) Shot 145 and (b) Shot 144.

DATE = 11/16/78
 IDENT HF-1 STEEL, HT 8, SHOT 143, 554 FPS. DAMAGE.
 NTEOT= 0 NJECIT= 3 NREZON= 0 NALPHA
 JEDITS= S1,10,11,12,13,14,15,16,17,18,19,20,21,22,23,24,25,26,27,28,29
 JEDITS= NEM,19,20,21,22,23,24,25,26,27,28
 JEDITS= NET,19,20,21,22,23,24,25,26,27,28
 NEDIT= 5 JCYCS= 3,000E+00 TS= 1,000E-05 IN= 5 , IN= 5
 NMTRLS= 1 MATFL= 150 CKS= 1,590E+04 IN= 5 , IN= 5 , CM, SEC
 1 UZERO= 0000000000 IN= 5 , IN= 5 , CM/SEC

HF1 STEEL
 EQST = RHOS= 7.774E+00 CFP = 050 DPY = 001 NVAR= 10
 1,605E+12 3,561E+12 7,360E+10 1,660E+00 2,500E-01 3,683E+12 0.
 TSRI = -3,870E-05-1,000E+09 8,180E-03 1,248E+11-1,800E+10-1,740E+09 0.
 YSR2 = -1,800E+10 0. 2,500E-01 5,000E-01 4,000E-01 3,000E+00 0.
 Y0= 1,361E+10 7,912E+11 0. 0. 0. 0. 0.

MLAYER= 2 JMAT= 1 1 0 0 0 0 0 0 0 0
 NZONES= 1 8 CELLS IN 2,374E-01 CM IN= 5
 NZONES= 1 20 CELLS IN 6,350E-01 CM IN= 5 CM, CM,
 IN= 5 CM, CM,

(a)

DATE = 11/16/78
 IDENT HF-1 STEEL, HT 8, SHOT 142, 628 FPS. DAMAGE.
 NTEOT= 0 NJECIT= 3 NREZON= 0 NALPHA
 JEDITS= S1,10,11,12,13,14,15,16,17,18,19,20,21,22,23,24,25,26,27,28,29
 JEDITS= NEM,19,20,21,22,23,24,25,26,27,28
 JEDITS= NET,19,20,21,22,23,24,25,26,27,28
 NEDIT= 5 JCYCS= 3,000E+00 TS= 1,000E-05 IN= 5 , IN= 5
 NMTRLS= 1 MATFL= 150 CKS= 1,910E+04 IN= 5 , IN= 5 , CM, SEC
 1 UZERO= 0000000000 IN= 5 , IN= 5 , CM/SEC

HF1 STEEL
 EQST = RHOS= 7.774E+00 CFP = 050 DPY = 001 NVAR= 10
 1,605E+12 3,561E+12 7,360E+10 1,660E+00 2,500E-01 3,683E+12 0.
 TSRI = -3,870E-05-1,000E+09 8,180E-03 1,248E+11-1,800E+10-1,740E+09 0.
 YSR2 = -1,800E+10 0. 2,500E-01 5,000E-01 4,000E-01 3,000E+00 0.
 Y0= 1,361E+10 7,912E+11 0. 0. 0. 0. 0.

MLAYER= 2 JMAT= 1 1 9 0 0 0 0 0 0 0
 NZONES= 1 8 CELLS IN 2,374E-01 CM IN= 5
 NZONES= 1 20 CELLS IN 6,350E-01 CM IN= 5 CM, CM,
 IN= 5 CM, CM,

(b)

Figure G-7. PUFF input parameters for (a) Shot 143 and (b) Shot 142.

DATE = 11/16/78
 IDENT HF-1 STEEL, HT 8. SHOT 150. 499 FPS. DAMAGE.
 NEDIT= 0 NJEDIT= 3 NREZON= 0 NALPHA
 JEDITS= S1,10,11,12,13,14,15,16,17,18,19,20,21,22,23,24,25,26,27,28,29
 NET,20,21,22,23,24,25,26,27,28,29
 JEDITS= NET,20,21,22,23,24,25,26,27,28,29
 NEDIT= 5 JCYCS= 150 CKS= 3.000E+00 TS= 1.000E-05 IN= 5
 NMTRLS= 1 MATFL= 1 UZERO= 1.520E+04 IN= 5 , , CM, SEC
 IN= 5 , , CM/SEC

HF1 STEEL
 EQST = RHUS= 7.774E+00 CFP = 050 DPY = 001 NVAR= 10
 TSRI = 1.605E+12 3.561E+12 7.360E+10 1.660E+00 2.500E-01 3.683E+12 0.
 TSRI = -3.470E-05-1.000E+09 8.180E-03 1.248E+11-1.800E+10-1.740E+09 0.
 TSRI = -1.800E+10 0. 2.500E-01 5.000E-01 4.000E-01 3.000E+00 0.
 Y0= 1.361E+10 7.912E+11 0. 0. 0. 0. 0.

NLAYER= 2 JMAT= 1 1 0 0 0 0 0 0 0 0
 NZONES= 1 8 CELLS IN 1.577E-01 CM 0.
 NZONES= 1 20 CELLS IN 6.355E-01 CM 0.

(a)

DATE = 11/16/78
 IDENT HF-1 STEEL, HT 8. SHOT 148. 566 FPS. DAMAGE.
 NEDIT= 0 NJEDIT= 3 NREZON= 0 NALPHA
 JEDITS= S1,10,11,12,13,14,15,16,17,18,19,20,21,22,23,24,25,26,27,28,29
 NET,20,21,22,23,24,25,26,27,28,29
 JEDITS= NET,20,21,22,23,24,25,26,27,28,29
 NEDIT= 5 JCYCS= 150 CKS= 3.000E+00 TS= 1.000E-05 IN= 5
 NMTRLS= 1 MATFL= 1 UZERO= 1.720E+04 IN= 5 , , CM, SEC
 IN= 5 , , CM/SEC

HF1 STEEL
 EQST = RHUS= 7.774E+00 CFP = 050 DPY = 001 NVAR= 10
 TSRI = 1.605E+12 3.561E+12 7.360E+10 1.660E+00 2.500E-01 3.683E+12 0.
 TSRI = -3.470E-05-1.000E+09 8.180E-03 1.248E+11-1.800E+10-1.740E+09 0.
 TSRI = -1.800E+10 0. 2.500E-01 5.000E-01 4.000E-01 3.000E+00 0.
 Y0= 1.361E+10 7.912E+11 0. 0. 0. 0. 0.

NLAYER= 2 JMAT= 1 1 0 0 0 0 0 0 0 0
 NZONES= 1 8 CELLS IN 1.579E-01 CM 0.
 NZONES= 1 20 CELLS IN 3.183E-01 CM 0.

(b)

Figure G-8. PUFF input parameters for (a) Shot 150 and (b) Shot 148.

DATE = 11/16/76
 IDENT HF-1 STEEL, HT 8. SHOT 149. 637 FPS. DAMAGE.
 NTEOT= 0 NJEOT= 3 NREZON= 0 NALPHA
 JEDITS= S1,10,11,12,13,14,15,16,17,18,19,20,21,22,23,24,25,26,27,28,29
 JEDITS= NEM,16,17,18,19,20,21,22,23,24,25
 JEDITS= NET,16,17,18,19,20,21,22,23,24,25
 NEDIT= 5 JCYCS= 150 CKS= 3.000E+00 TS= 1.000E-05 IN= 5 , IN= 5
 NMTRL= 1 MATFL= 1 UZERO= 1.940E+04 IN= 5 , IN= 5 , CM, SEC
 HF1 STEEL RHOSE= 7.774E+00 CFP = 050 DPT = 001 NVAR= 10
 EQST = 1.605E+12 3.561E+12 7.360E+10 1.660E+00 2.500E-01 3.683E+12 0
 TSRI = -3.870E-05 -1.000E+09 8.180E-03 1.248E+11 -1.800E+10 -1.740E+09 0
 TSRI = -1.800E+10 0 2.500E-01 5.000E-01 4.000E-01 3.000E+00 0
 Y0= 1.361E+10 7.912E+11 0 0 0 0 0
 NLAYER= 2 JNATE= 1 1 0 0 0 0 0 0 0 0 0 0
 NZONES= 1 8 CELLS IN 1.580E-01 CM IN= 5 , IN= 5 CM, CM
 NZONES= 1 20 CELLS IN 3.160E-01 CM IN= 5 , IN= 5 CM, CM

(a)

DATE = 11/16/76
 IDENT HF-1 STEEL, HT 8. SHOT 146. 547 FPS. DAMAGE.
 NTEOT= 0 NJEOT= 3 NREZON= 0 NALPHA
 JEDITS= S1,10,11,12,13,14,15,16,17,18,19,20,21,22,23,24,25,26,27,28,29
 JEDITS= NEM,19,20,21,22,23,24,25,26,27,28
 JEDITS= NET,19,20,21,22,23,24,25,26,27,28
 NEDIT= 5 JCYCS= 150 CKS= 3.000E+00 TS= 1.000E-05 IN= 5 , IN= 5
 NMTRL= 1 MATFL= 1 UZERO= 1.670E+04 IN= 5 , IN= 5 , CM, SEC
 HF1 STEEL RHOSE= 7.774E+00 CFP = 050 DPT = 001 NVAR= 10
 EQST = 1.605E+12 3.561E+12 7.360E+10 1.660E+00 2.500E-01 3.683E+12 0
 TSRI = -3.870E-05 -1.000E+09 8.180E-03 1.248E+11 -1.800E+10 -1.740E+09 0
 TSRI = -1.800E+10 0 2.500E-01 5.000E-01 4.000E-01 3.000E+00 0
 Y0= 1.361E+10 7.912E+11 0 0 0 0 0 0 0 0 0 0
 NLAYER= 2 JNATE= 1 1 0 0 0 0 0 0 0 0 0 0
 NZONES= 1 8 CELLS IN 1.580E-01 CM IN= 5 , IN= 5 CM, CM
 NZONES= 1 20 CELLS IN 3.160E-01 CM IN= 5 , IN= 5 CM, CM

(b)

Figure G-9. PUFF input parameters for (a) Shot 149 and (b) Shot 146.

```

***** SRI PUFF 8 *****
DATE = 11/16/78
IDENT HF-1 STEEL, HT 0, SHOT 151, 625 FPS, DAMAGE.
NTEDT= 0 NJEDIT= 3 NREZON= 0 NALPHA
JEDITS= S1,10,11,12,13,14,15,16,17,18,19,20,21,22,23,24,25,26,27,28,29
JEDITS= NEM,20,21,22,23,24,25,26,27,28,29
JEDITS= NET,20,21,22,23,24,25,26,27,28,29
NEDIT= 5 JOYCS= 150 GKS= 3.000E+00 TS= 1.000E-05 IN= 5 , IN= 5 , CM, SEC
NMTRLS= 1 MATFL= 1 UZERO= 1.300E+04 0000000000 IN= 5 , IN= 5 , CM/SEC

HF1 STEEL RHOSE= 7.774E+00 CFP = 050 UFY = 001 NVAR= 10
EQST = 1.605E+12 3.561E+12 7.360E+10 1.660E+00 2.500E-01 3.683E+12 0.
TSR1 = -3.870E-05-1.000E+09 8.180E-03 1.248E+11-1.800E+10-1.748E+09 0.
TSR2 = -1.800E+10 0. 2.500E-01 5.000E-01 4.000E-01 3.000E+00 0.
Y0= 1.361E+10 7.912E+11 0. 0. 0. 0. 0.

NLAYER= 2 JHAT= 1 1 0 0 0 0 0 0 0 0 0 0 0 0 0 0 0 0 0 0
NZONES= 1 8 CELLS IN 1.150E-01 CM 0. 0. 0. 0. 0. 0. 0. 0. 0. 0. 0. 0. 0. 0. 0. 0. 0. 0. 0.
NZONES= 1 20 CELLS IN 6.360E-01 CM 0. 0. 0. 0. 0. 0. 0. 0. 0. 0. 0. 0. 0. 0. 0. 0. 0. 0. 0. 0.

```

Figure G-10. PUFF input parameters for Shot 151.

APPENDIX H

COMPUTED STRESS, PARTICLE VELOCITY, AND CRACK CONCENTRATION VERSUS TIME PLOTS FOR THE CELL OF MAXIMUM DAMAGE FOR THE HF-1 STEEL SPALL FRACTURE SPECIMENS

(The input parameters in Appendix G (with the appropriate JEDIT parameters) were used in PUFF 8 computations to produce these plots. No plots are presented for the threshold-damage Shot 95, the no-damage Shots 89 and 147, and the full-spall Shot 88. Tables 9 and 10 summarize some of the stress and crack density values. The stress and crack concentration values are computed at the cell midpoints. The particle velocity values are computed at the cell edge nearest the impact surface. Each specimen was divided into 20 computational cells of equal width, numbered 10 through 29 beginning at the specimen impact surface. Plots (a) and (b) refer to principal stresses in the direction of shock wave propagation and orthogonal to that direction, respectively. Compressive and tensile stress values are positive and negative, respectively. Plots (c) and (d) give the particle velocity in the shock propagation direction and the generated crack concentration for cracks oriented in planes perpendicular to that direction, respectively.)

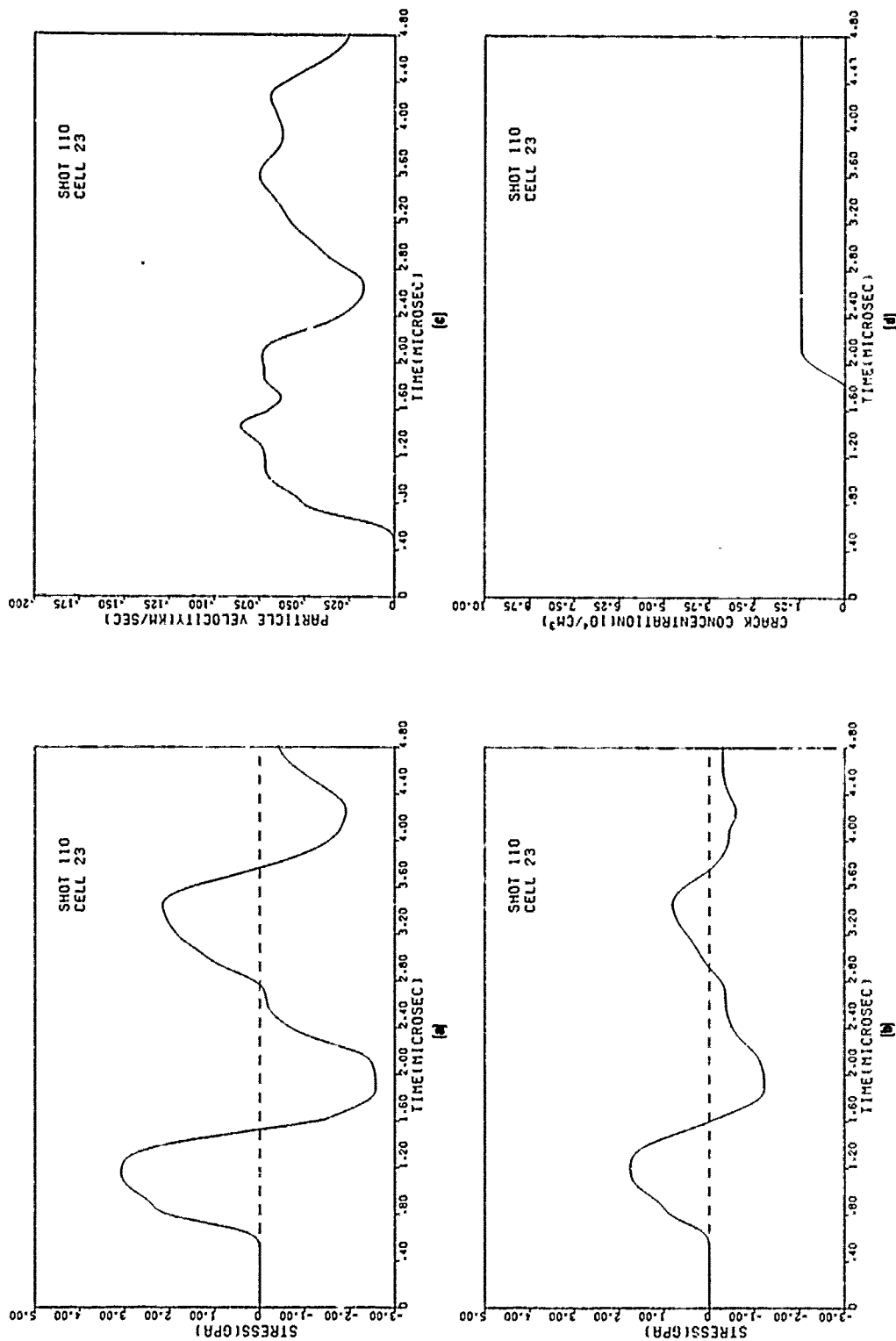


Figure H-1. Computed shock histories in cell 23 for Shot 110. (a) Parallel stress. (b) Perpendicular stress. (c) Particle velocity. (d) Crack concentration.

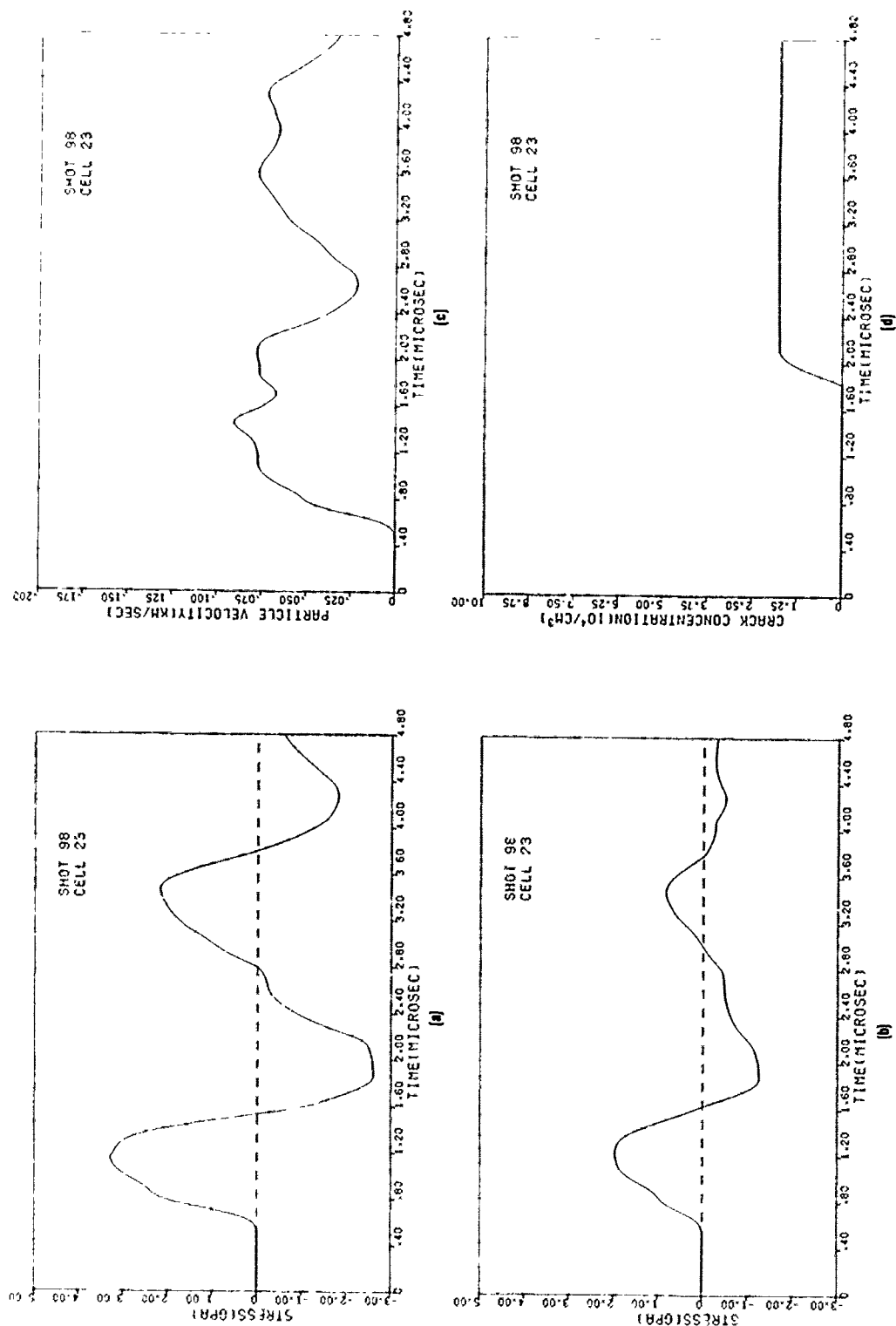


Figure H-2. Computed shock histories in cell 23 for Shot 98. (a) Parallel Stress. (b) Perpendicular stress. (c) Particle velocity. (d) Crack concentration.

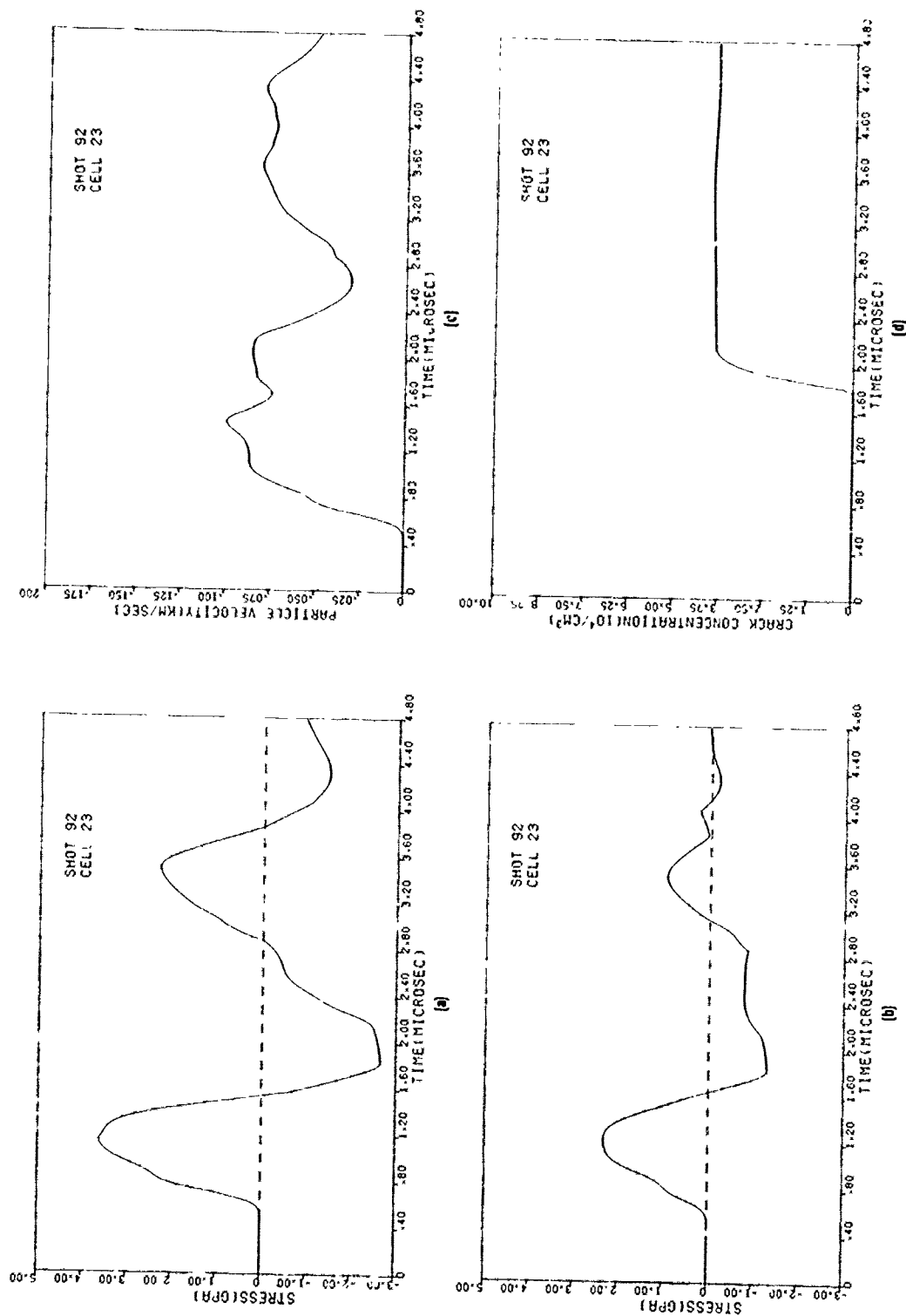


Figure H-3. Computed shock histories in cell 23 for Shot 92. (a) Parallel stress. (b) Perpendicular stress. (c) Partic levelocity. (d) Crack concentration.

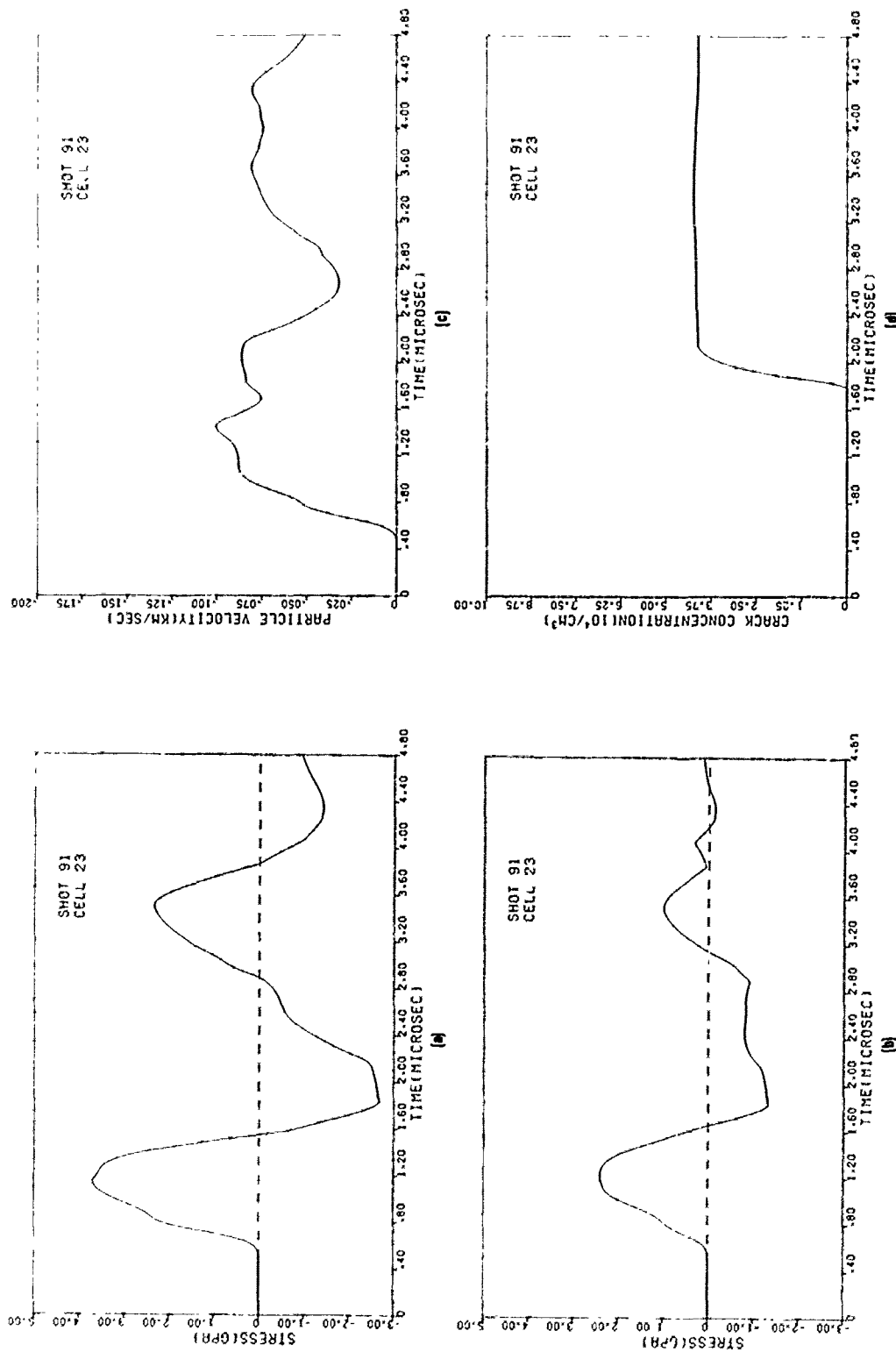


Figure H-4. Computed shock histories in cell 23 for Shot 91. (a) Parallel stress. (b) Perpendicular stress. (c) Particle velocity. (d) Crack concentration.

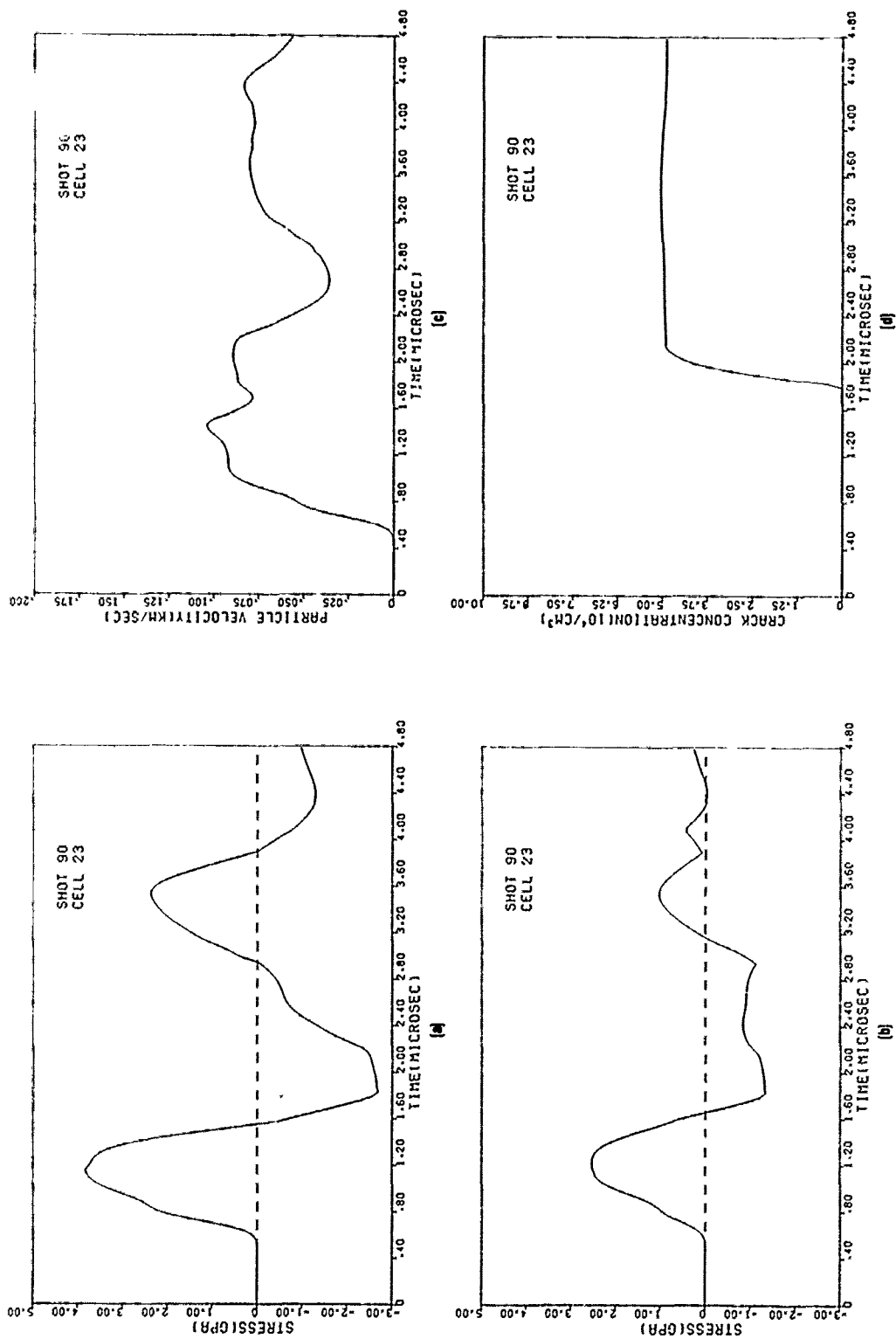


Figure H-5. Computed shock histories in cell 23 for Shot 90. (a) Parallel stress. (b) Perpendicular stress. (c) Particle velocity. (d) Crack concentration.

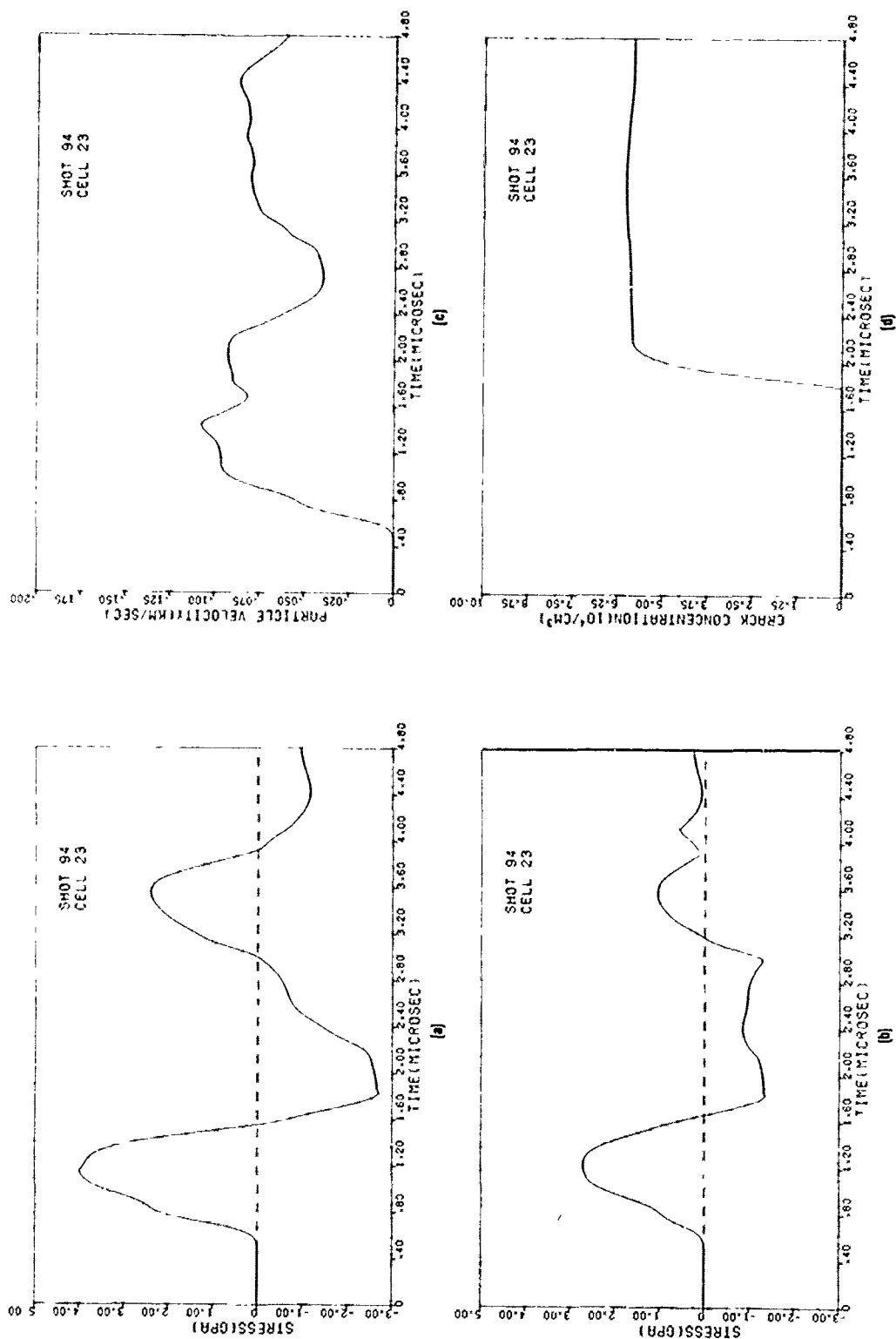


Figure H-6. Computed shock histories in cell 23 for Shot 94. (a) Parallel stress. (b) Perpendicular stress. (c) Particle velocity. (d) Crack concentration.

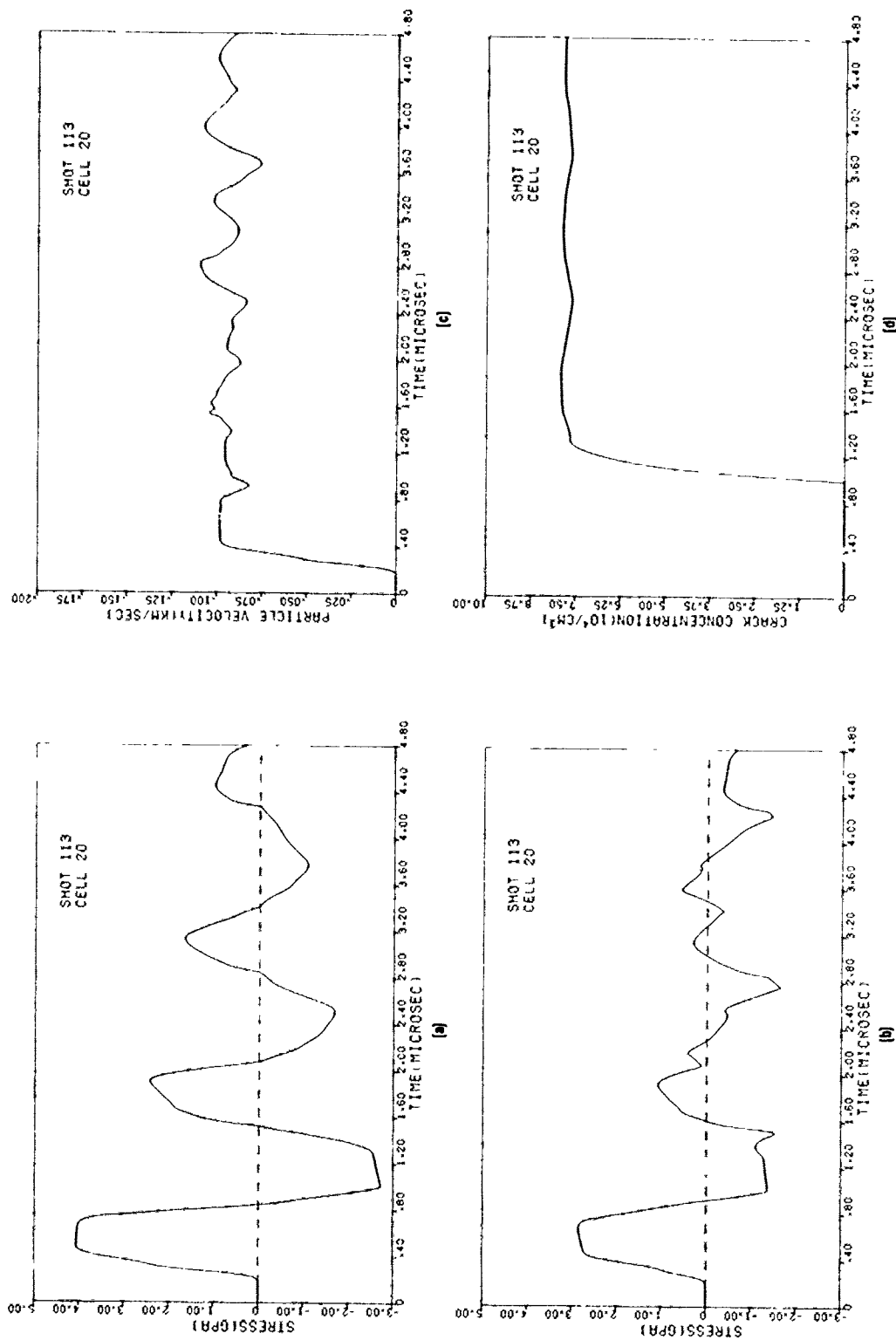


Figure H-7. Computed shock histories in cell 20 for Shot 113. (a) Parallel stress. (b) Perpendicular stress. (c) Particle velocity. (d) Crack concentration.

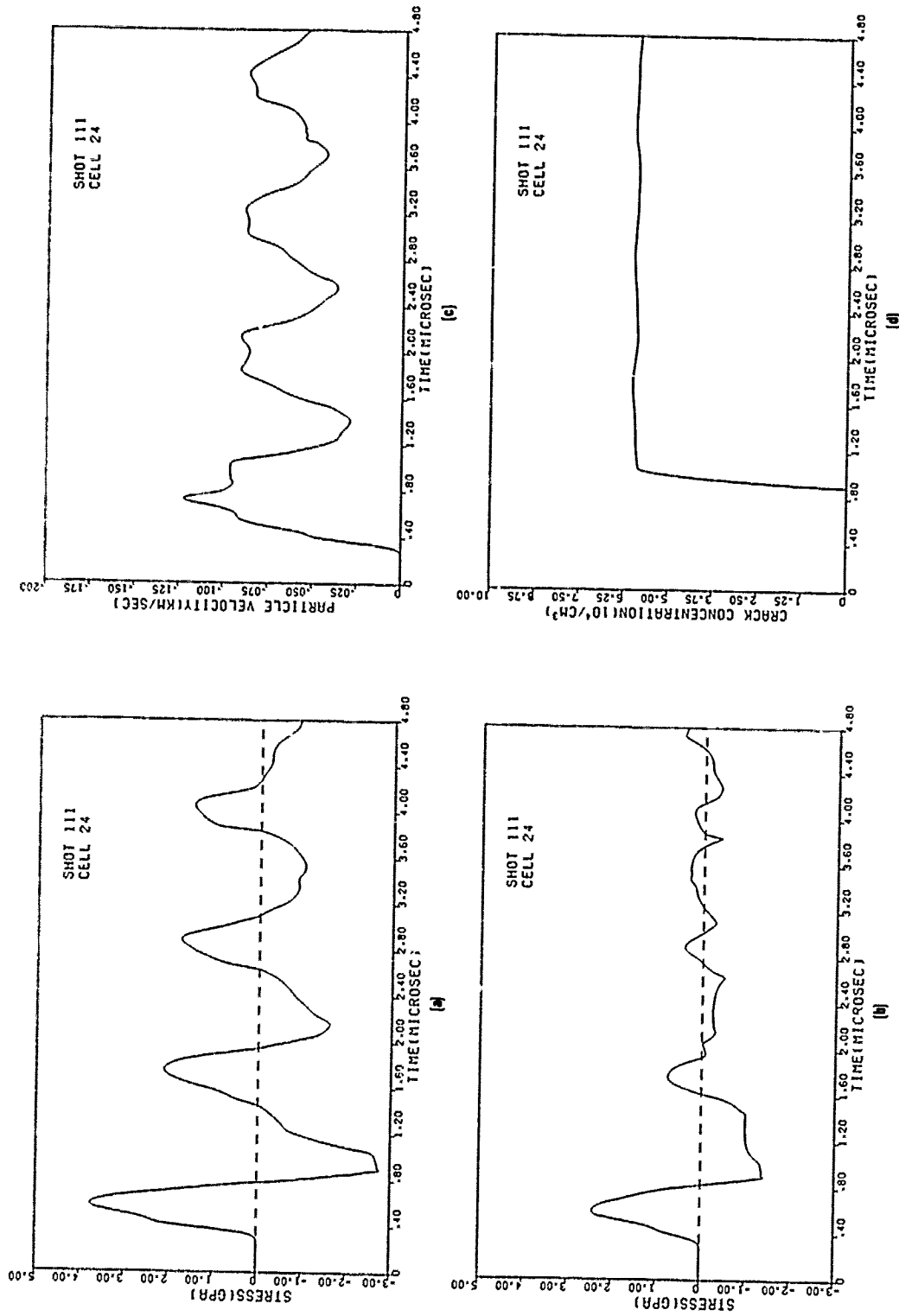


Figure H-8. Computed shock histories in cell 24 for Shot 111. (a) Parallel stress. (b) Perpendicular stress. (c) Particle velocity. (d) Crack concentration.

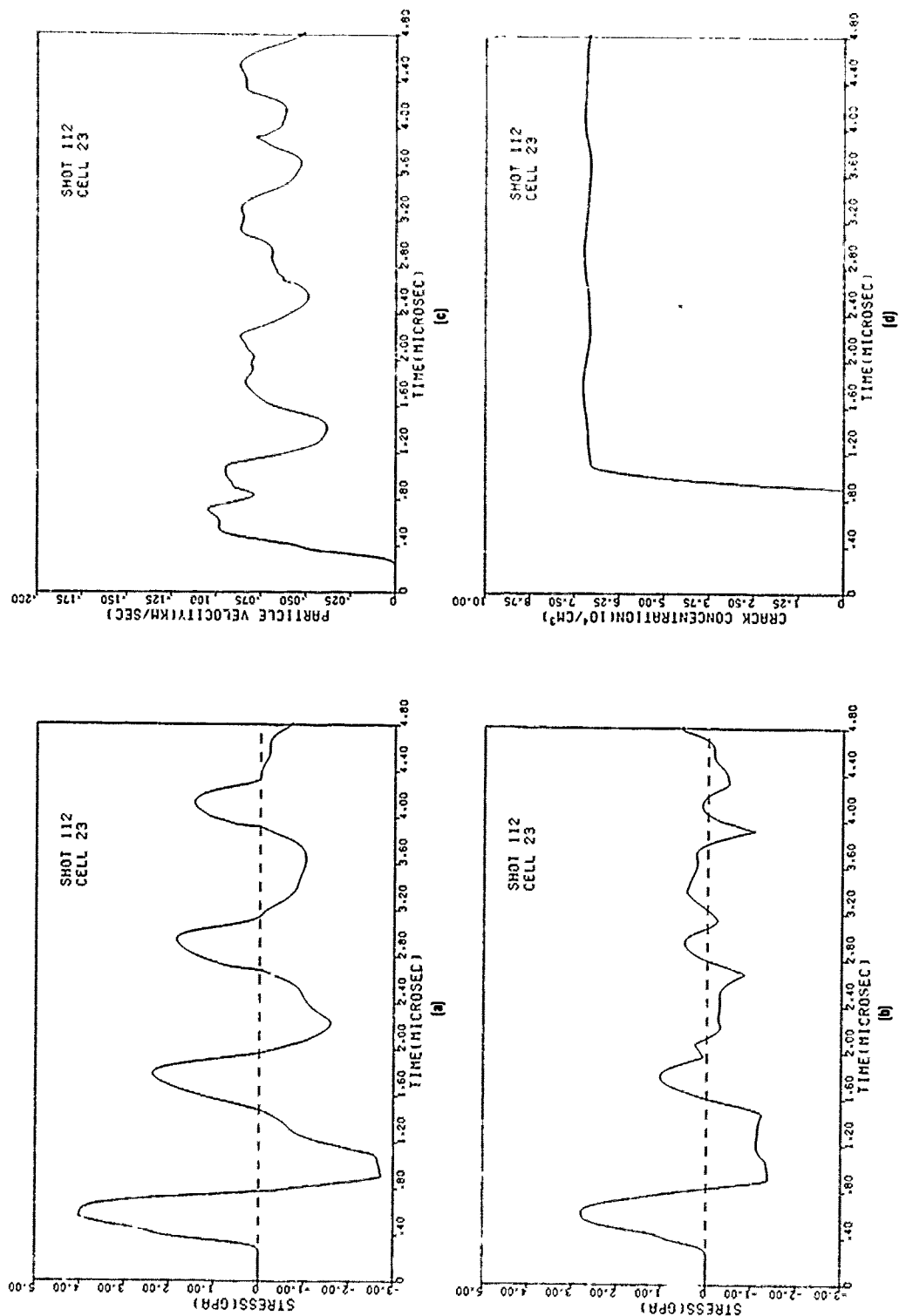


Figure H-9. Computed shock histories in cell 23 for Shot 112. (a) Parallel stress. (b) Perpendicular stress. (c) Particle velocity. (d) Crack concentration.

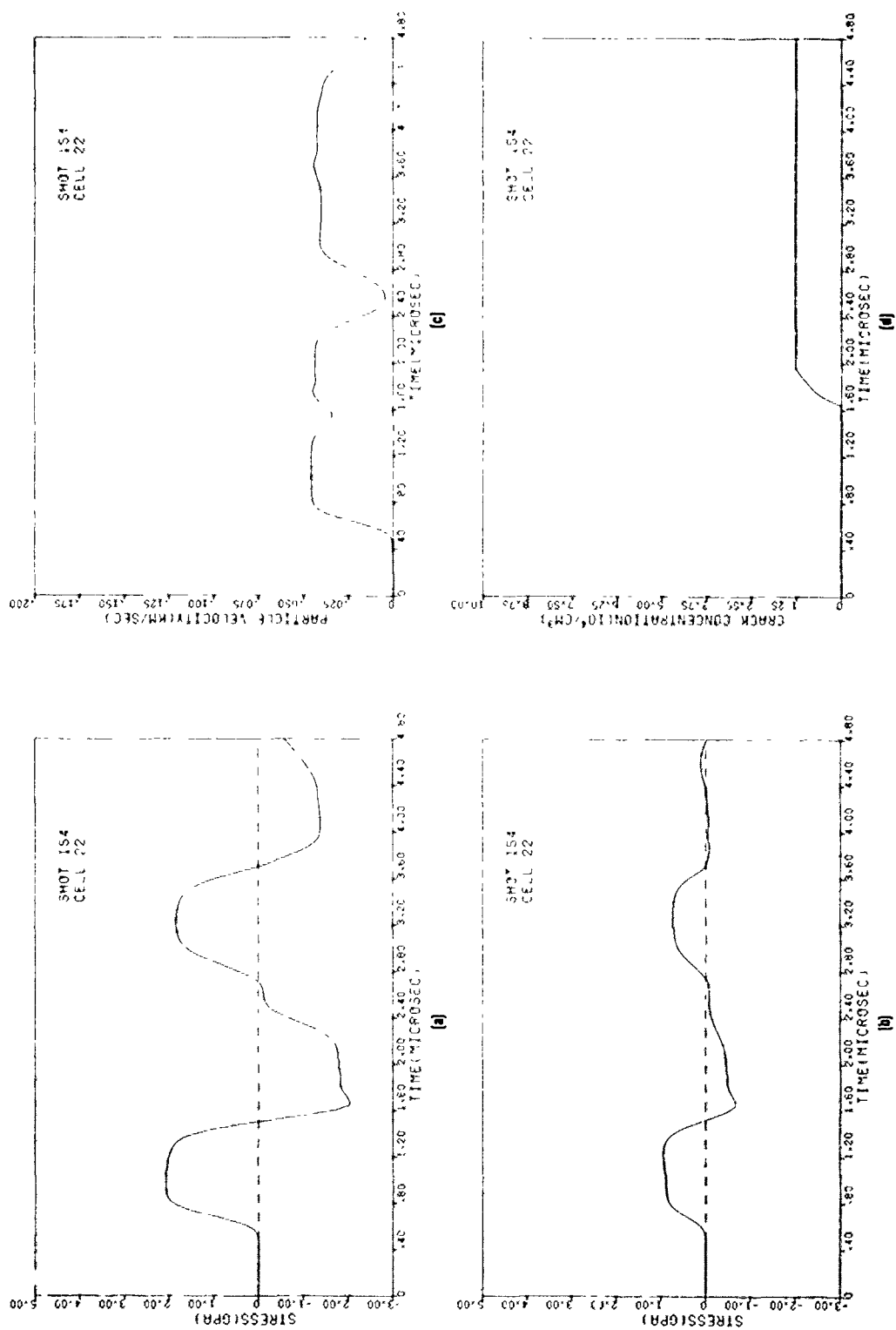


Figure H-10. Computed shock histories in cell 22 for Shot 154. (a) Parallel stress. (b) Perpendicular stress. (c) Particle velocity. (d) Crack concentration.

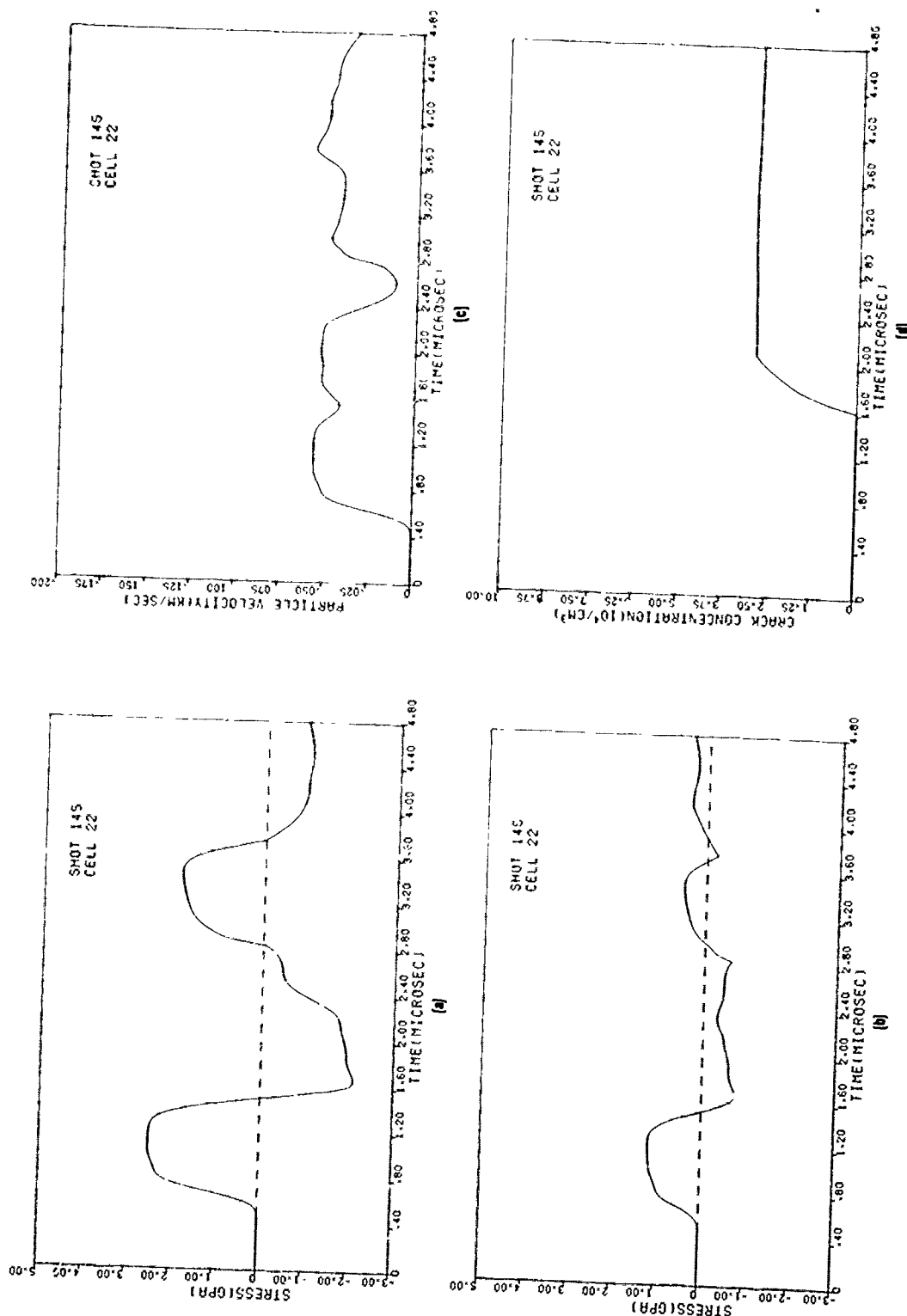


Figure H-11. Computed shock histories in cell 22 for Shot 145. (a) Parallel stress. (b) Perpendicular stress. (c) Particle velocity. (d) Crack concentration.

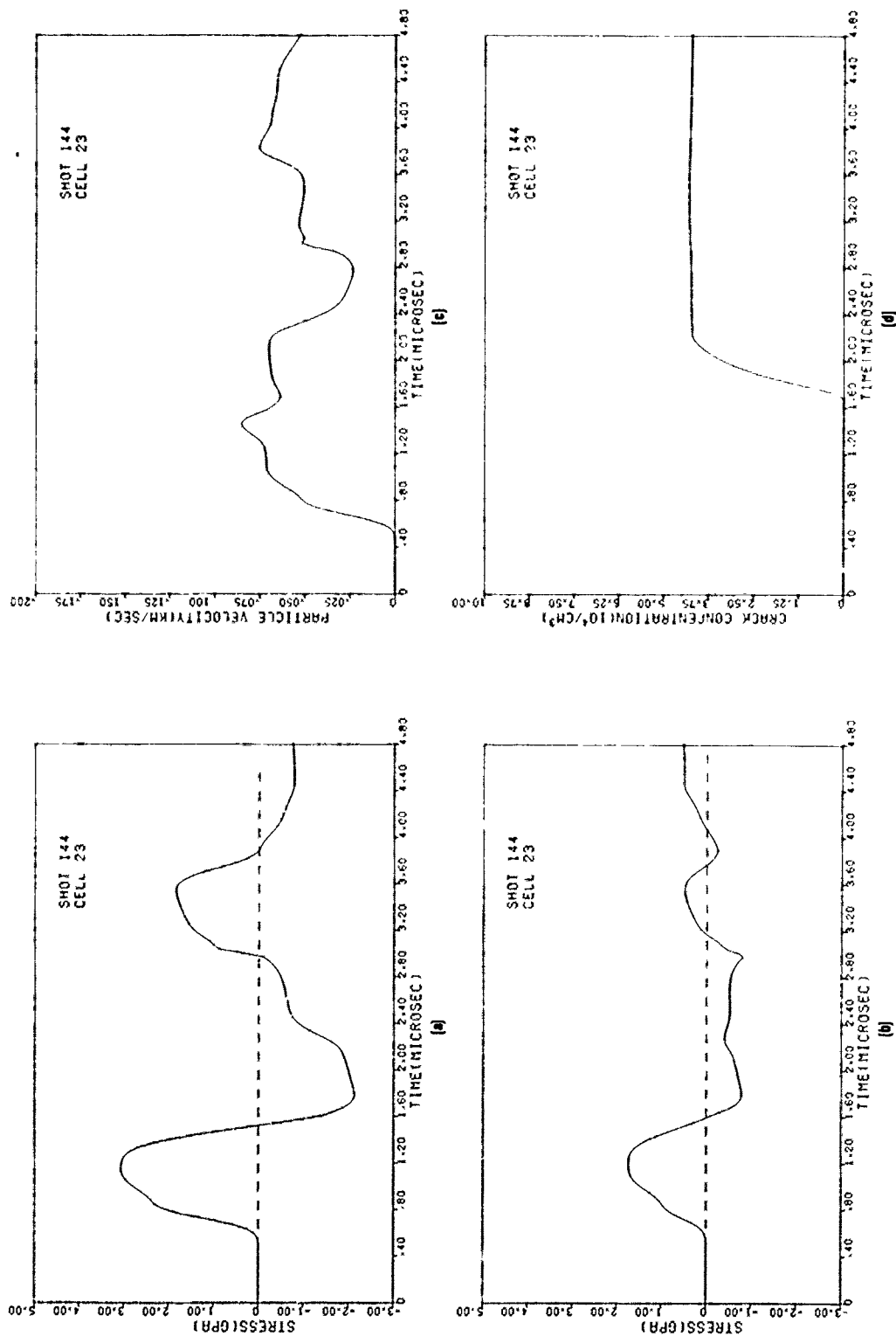


Figure H-12. Computed shock histories in cell 23 for Shot 144. (a) Parallel stress. (b) Perpendicular stress. (c) Particle velocity. (d) Crack concentration.

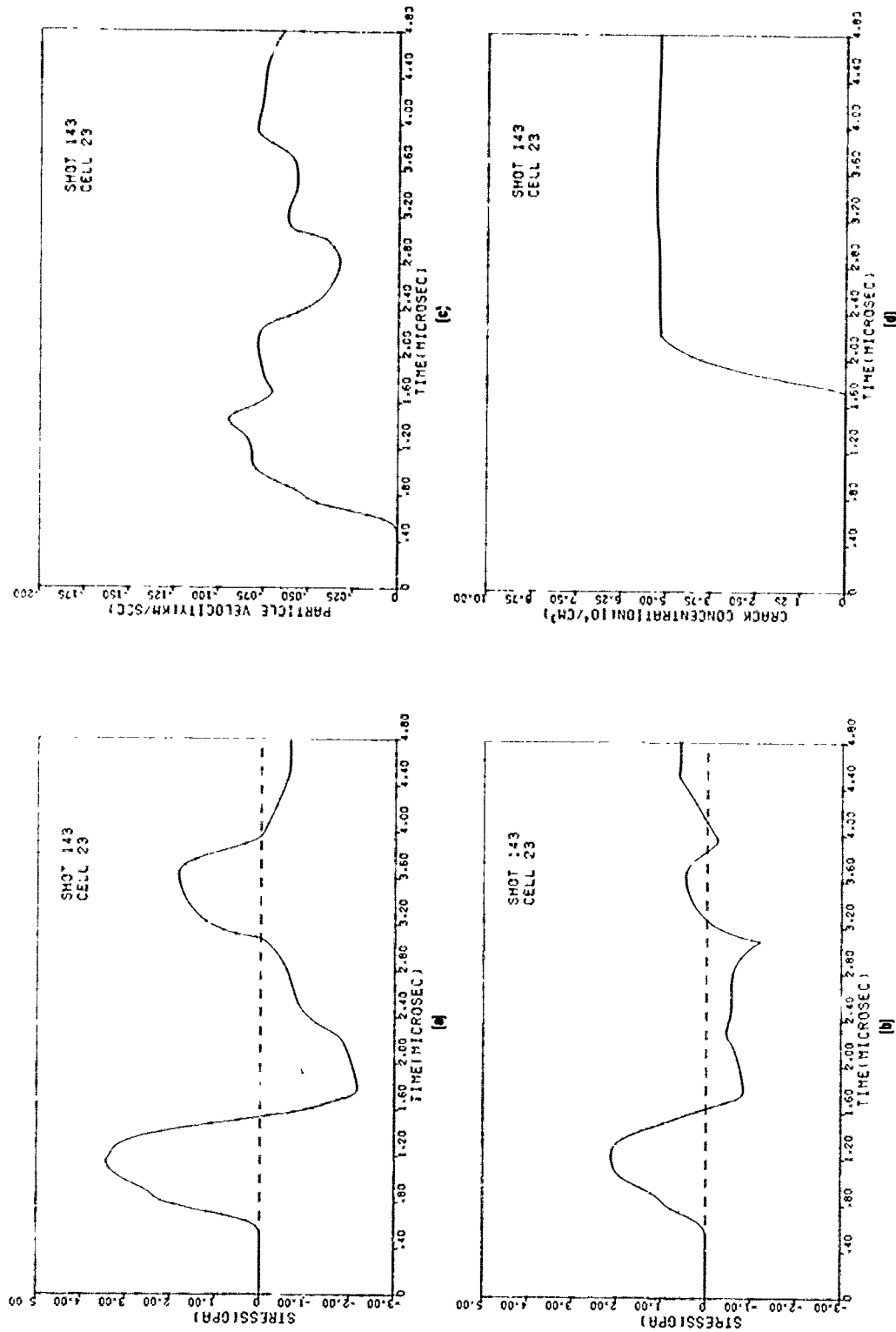


Figure H-13. Computed shock histories in cell 23 for Shot 143. (a) Parallel stress. (b) Perpendicular stress. (c) Particle velocity. (d) Crack concentration.

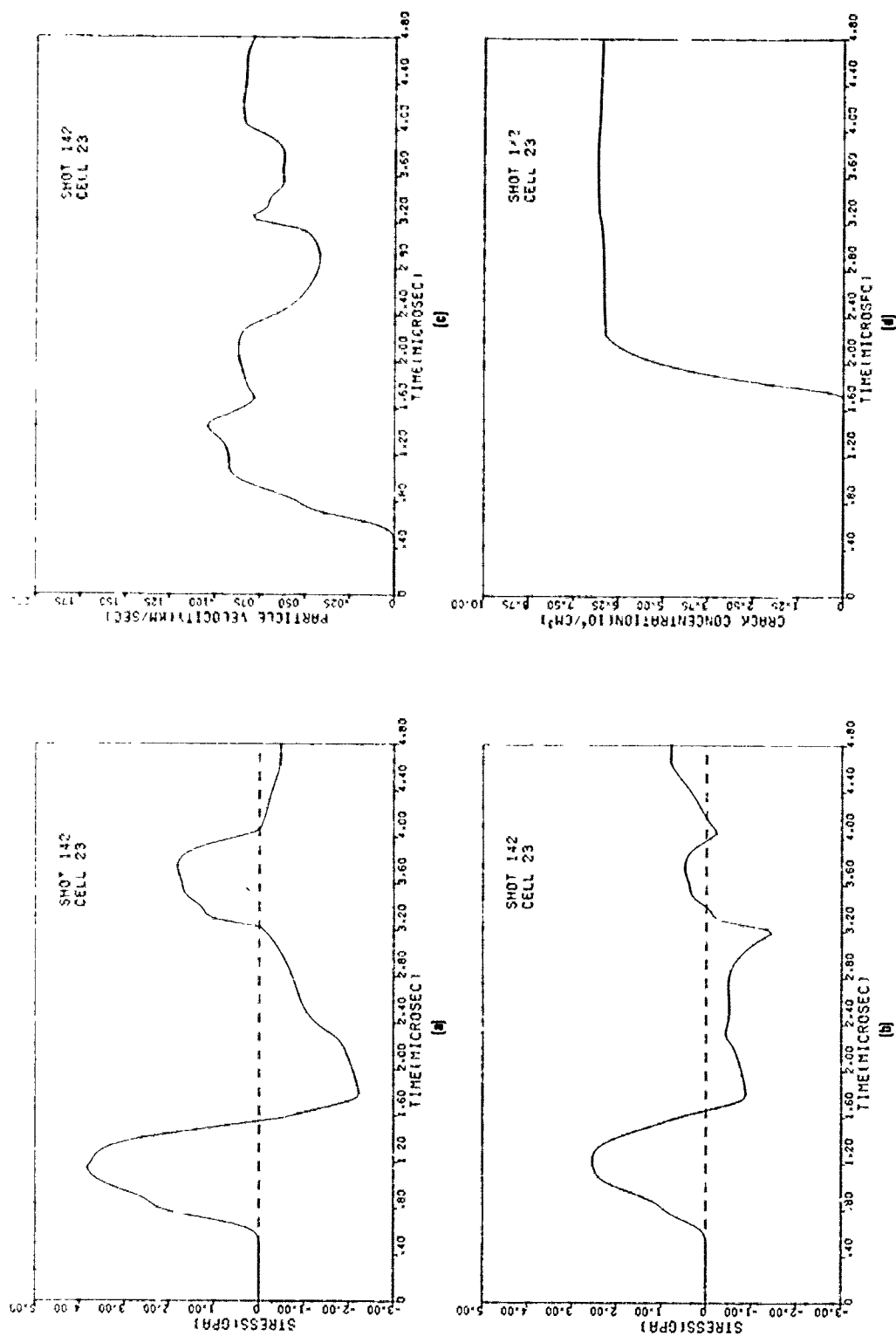


Figure H-14. Computed shock histories in cell 23 for Shot 142. (a) Parallel stress. (b) Perpendicular stress. (c) Particle velocity. (d) Crack concentration.

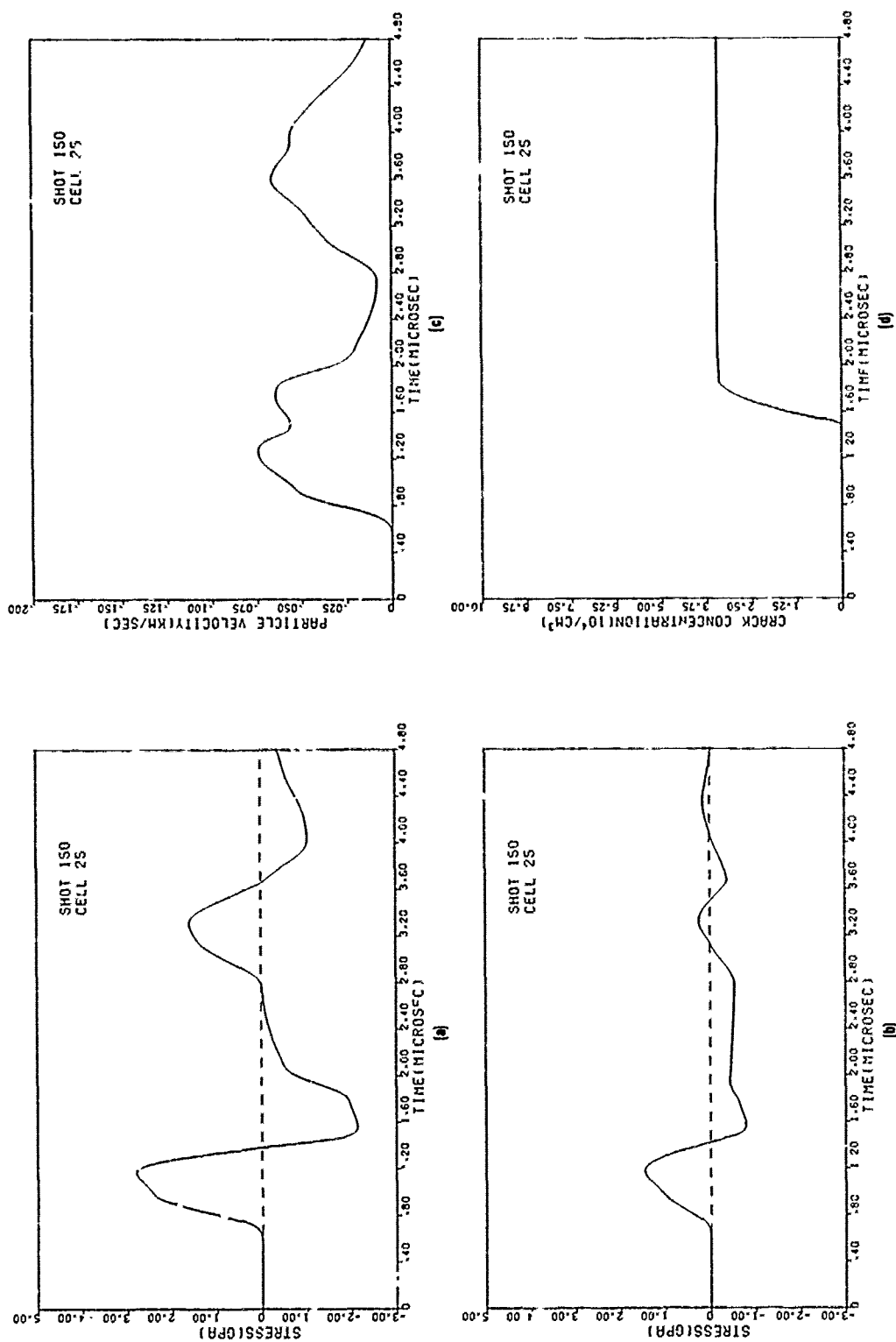


Figure H-15. Computed shock histories in cell 25 for Shot 150. (a) Parallel stress. (b) Perpendicular stress. (c) Particle velocity. (d) Crack concentration.

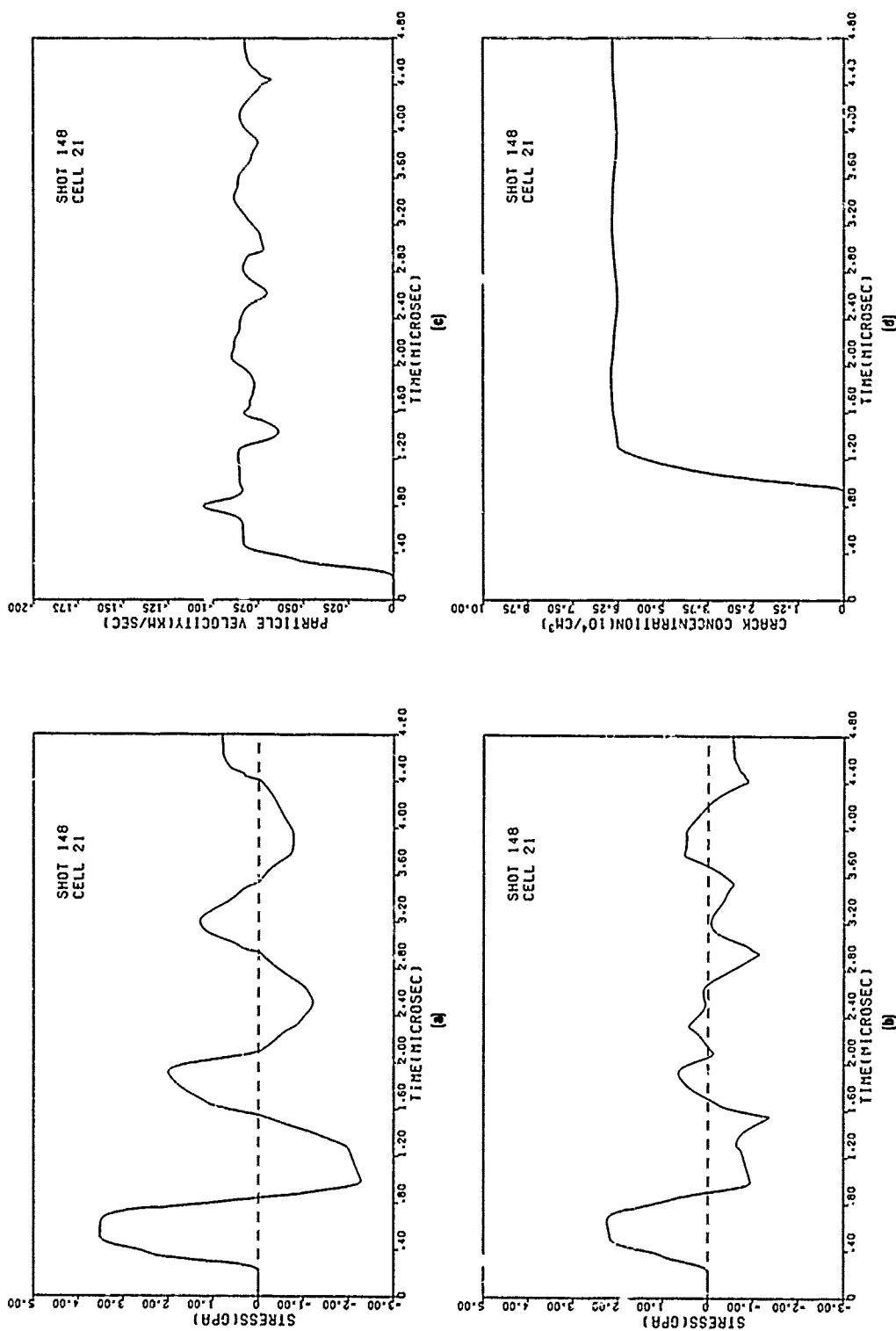


Figure H-16. Computed shock histories in cell 21 for Shot 148. (a) Parallel stress. (b) Perpendicular stress. (c) Particle velocity. (d) Crack concentration.

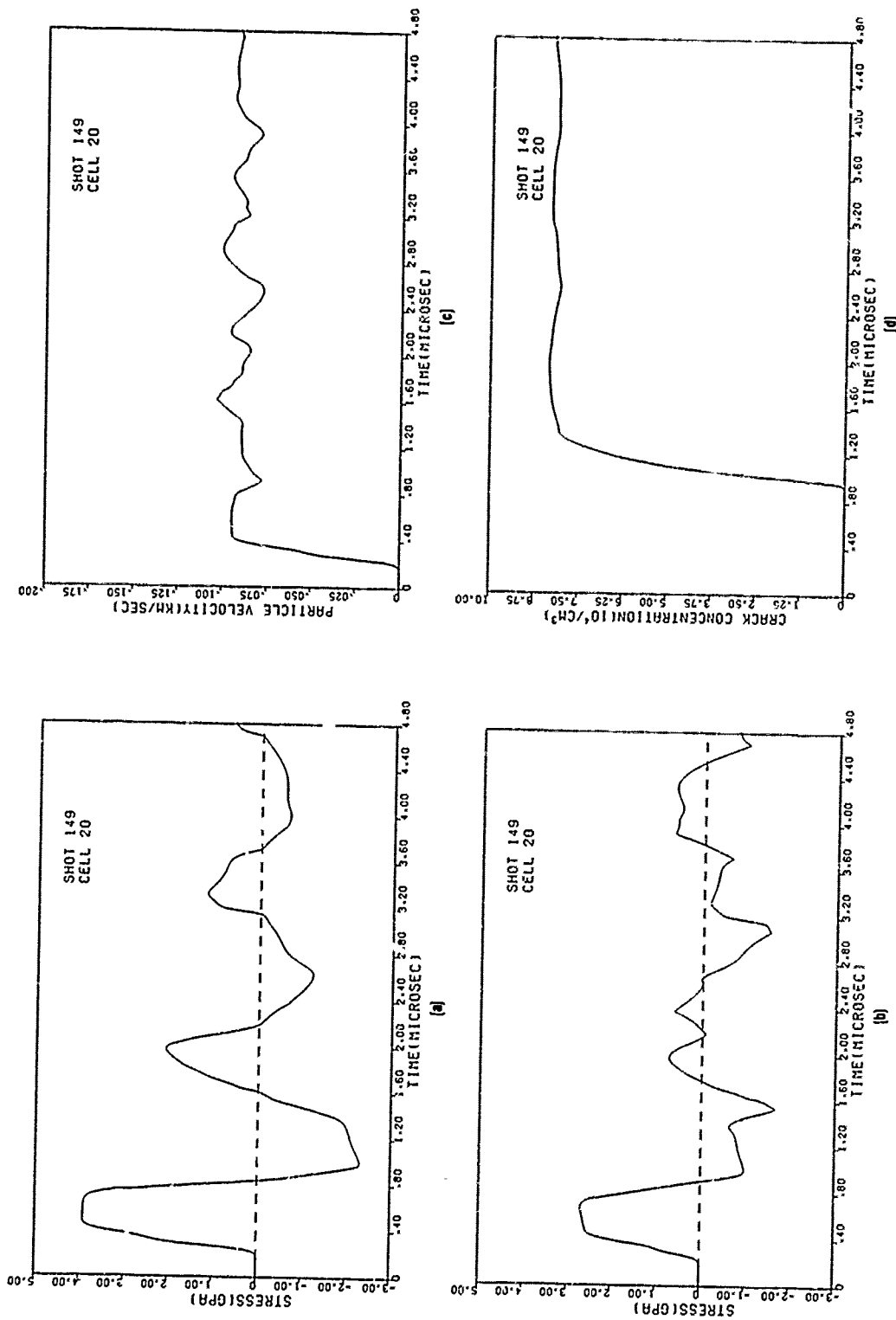


Figure H-17. Computed shock histories in cell 20 for Shot 149. (a) Parallel stress. (b) Perpendicular stress. (c) Particle velocity. (d) Crack concentration.

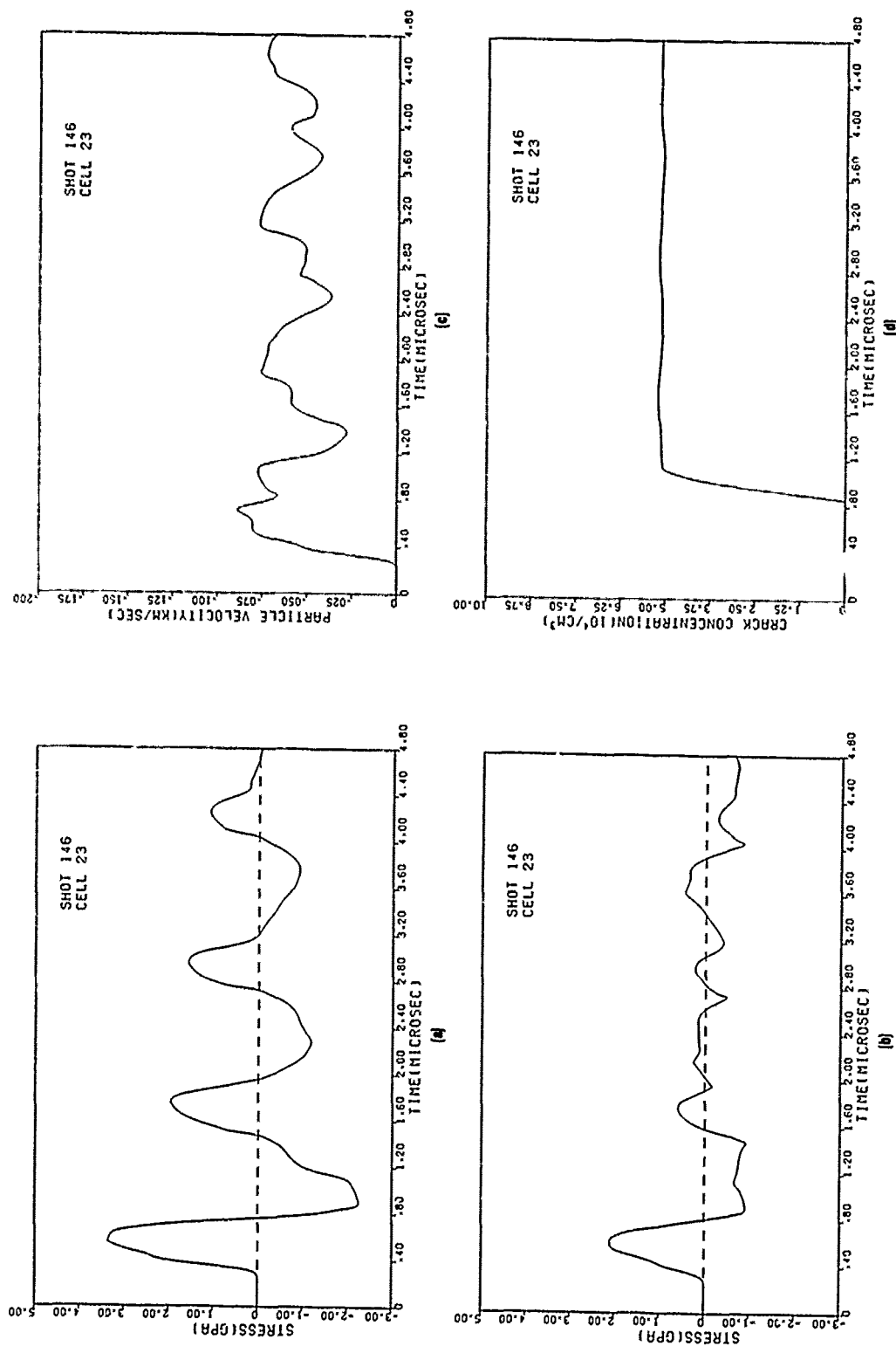


Figure H-18. Computed shock histories in cell 23 for Shot 146. (a) Parallel stress. (b) Perpendicular stress. (c) Particle velocity. (d) Crack concentration.

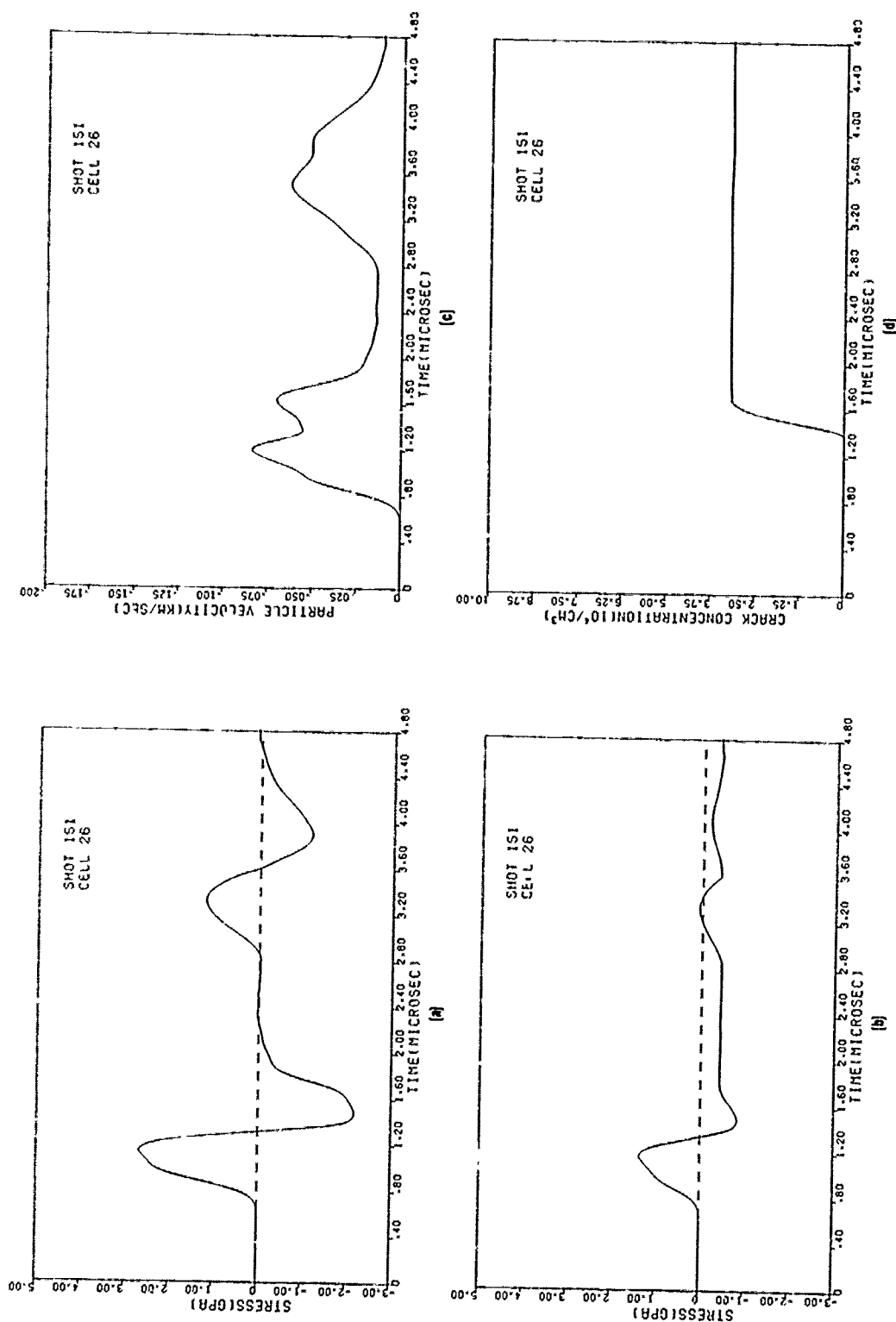
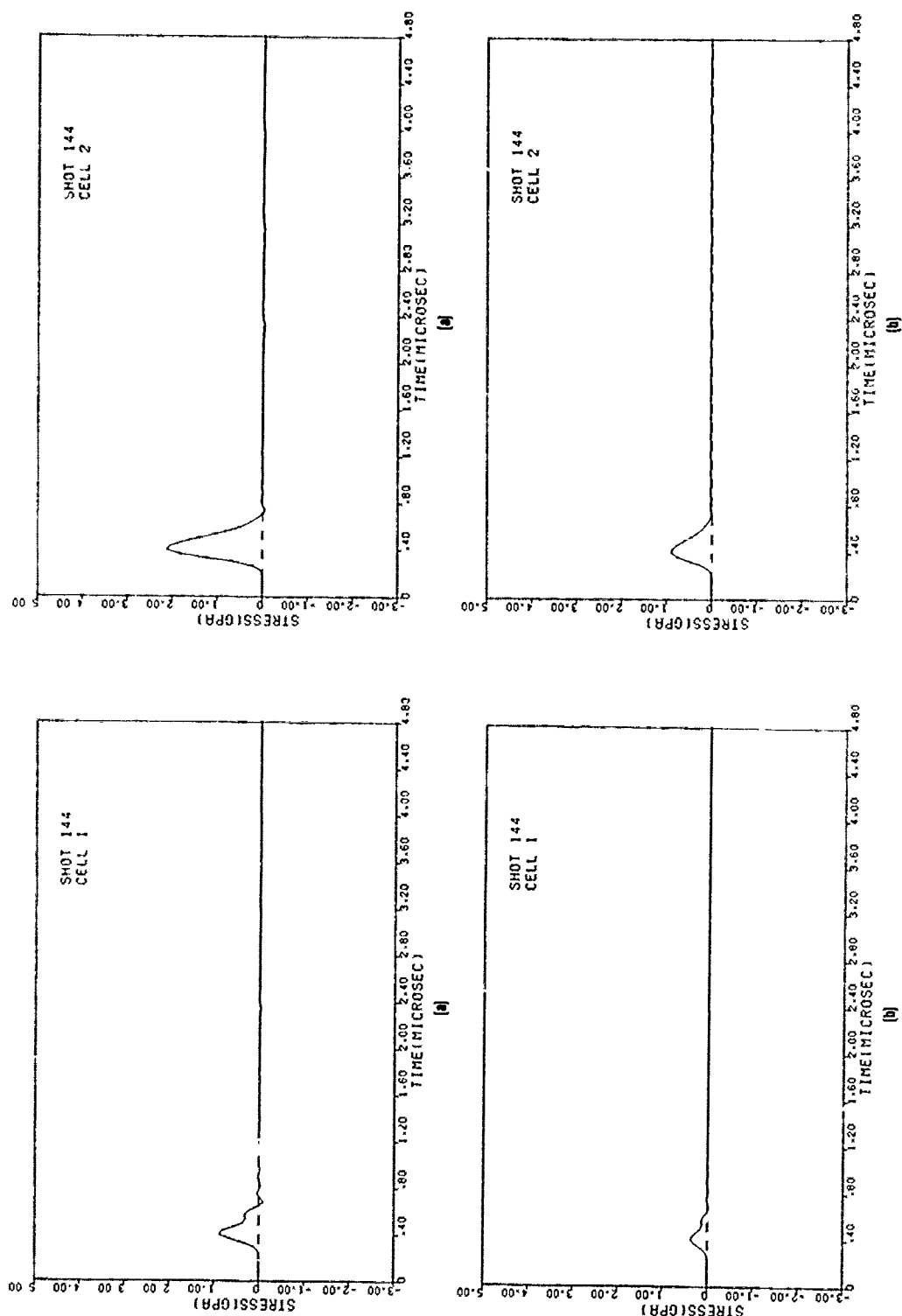


Figure H-19. Computed shock histories in cell 26 for Shot 151. (a) Parallel stress. (b) Perpendicular stress. (c) Particle velocity. (d) Crack concentration.

APPENDIX I

COMPUTED STRESS, PARTICLE VELOCITY, AND CRACK CONCENTRATION VERSUS TIME PLOTS FOR EACH COMPUTATIONAL CELL FOR THE HF-1 STEEL, HEAT TREATMENT B, SPALL FRACTURE SHOT 144

(For Shot 144, a 2.37-mm-thick disk impacted a 6.35-mm-thick specimen at 0.148 km/s. The input parameters in Figure G-6 (with the appropriate JEDIT parameters) were used in PUFF 8 computations to produce these plots. The impactor was divided into eight computational cells of equal width, numbered 1 through 8 beginning at the impactor free surface. The specimen was divided into 20 computational cells of equal width, numbered 10 through 29 beginning at the specimen impact surface. Plots (a) and (b) of Figures I-1 through I-28 give the principal stresses in the shock wave propagation direction and orthogonal to that direction, respectively. Compressive and tensile stress values are positive and negative, respectively. The stresses are computed at the cell midpoints. Figures I-29 through I-42 give the particle velocity in each cell in the shock wave propagation direction. The particle velocity values are computed at the cell edge nearest the impact surface. Figures I-43 through I-49 give crack concentrations in those computational cells in which tensile fracture occurred. Crack concentrations are computed at the cell midpoints and refer to cracks oriented in planes perpendicular to the shock wave propagation direction.)



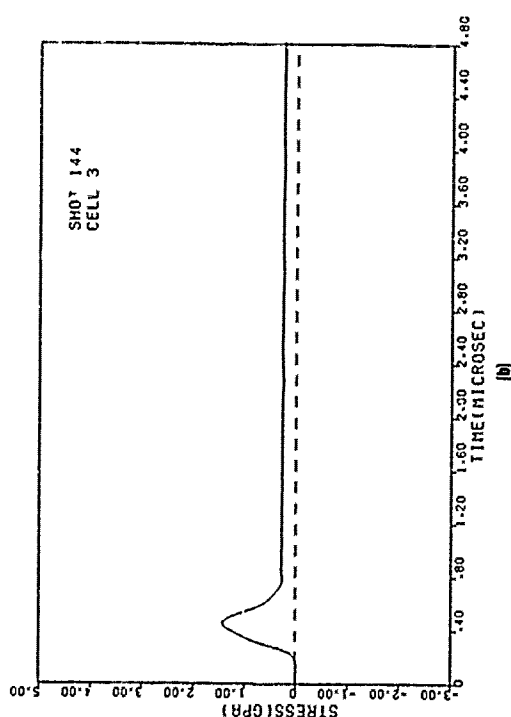
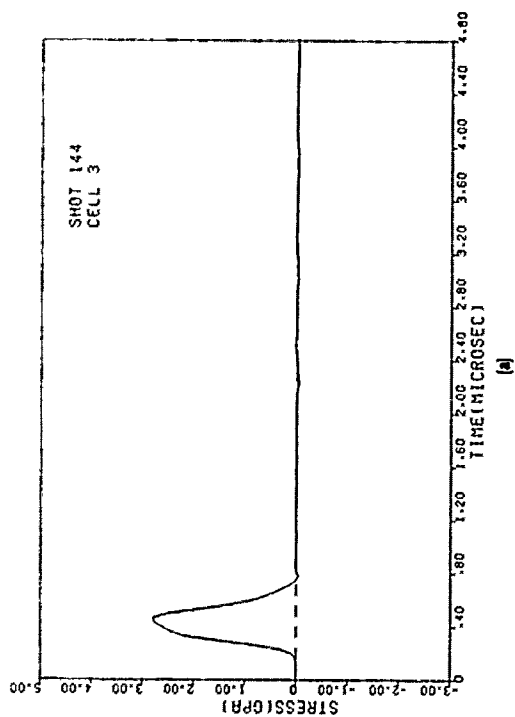


Figure I-3. Computed stress histories in cell 3 for Shot 144.
(a) Parallel and (b) perpendicular stresses.

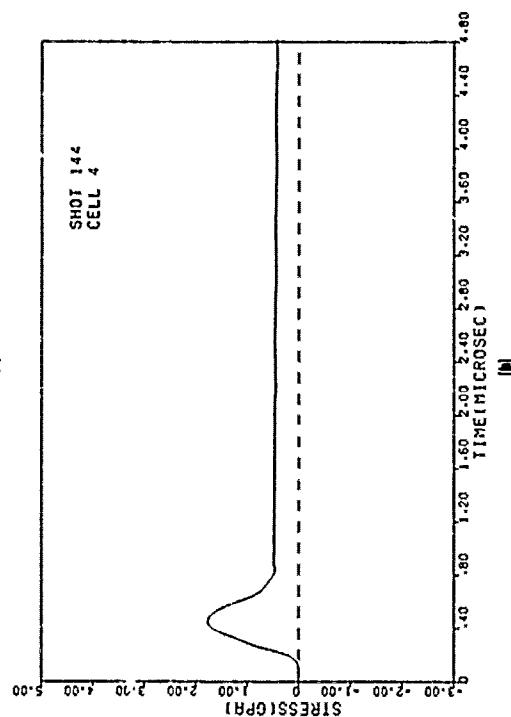
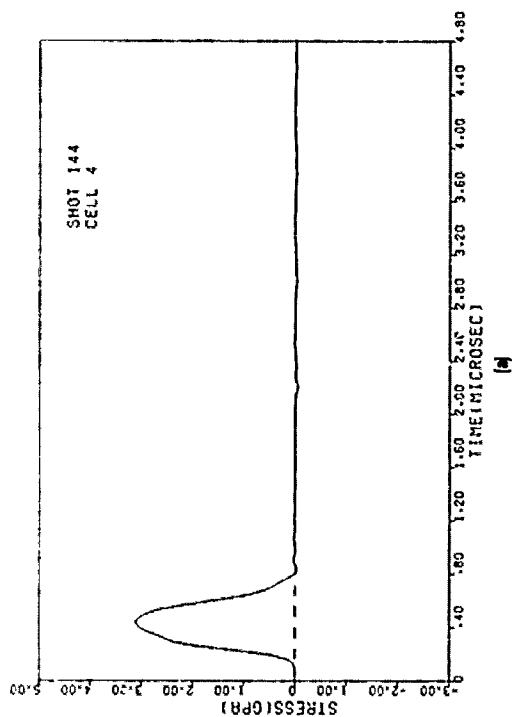


Figure I-4. Computed stress histories in cell 4 for Shot 144.
(a) Parallel and (b) perpendicular stresses.

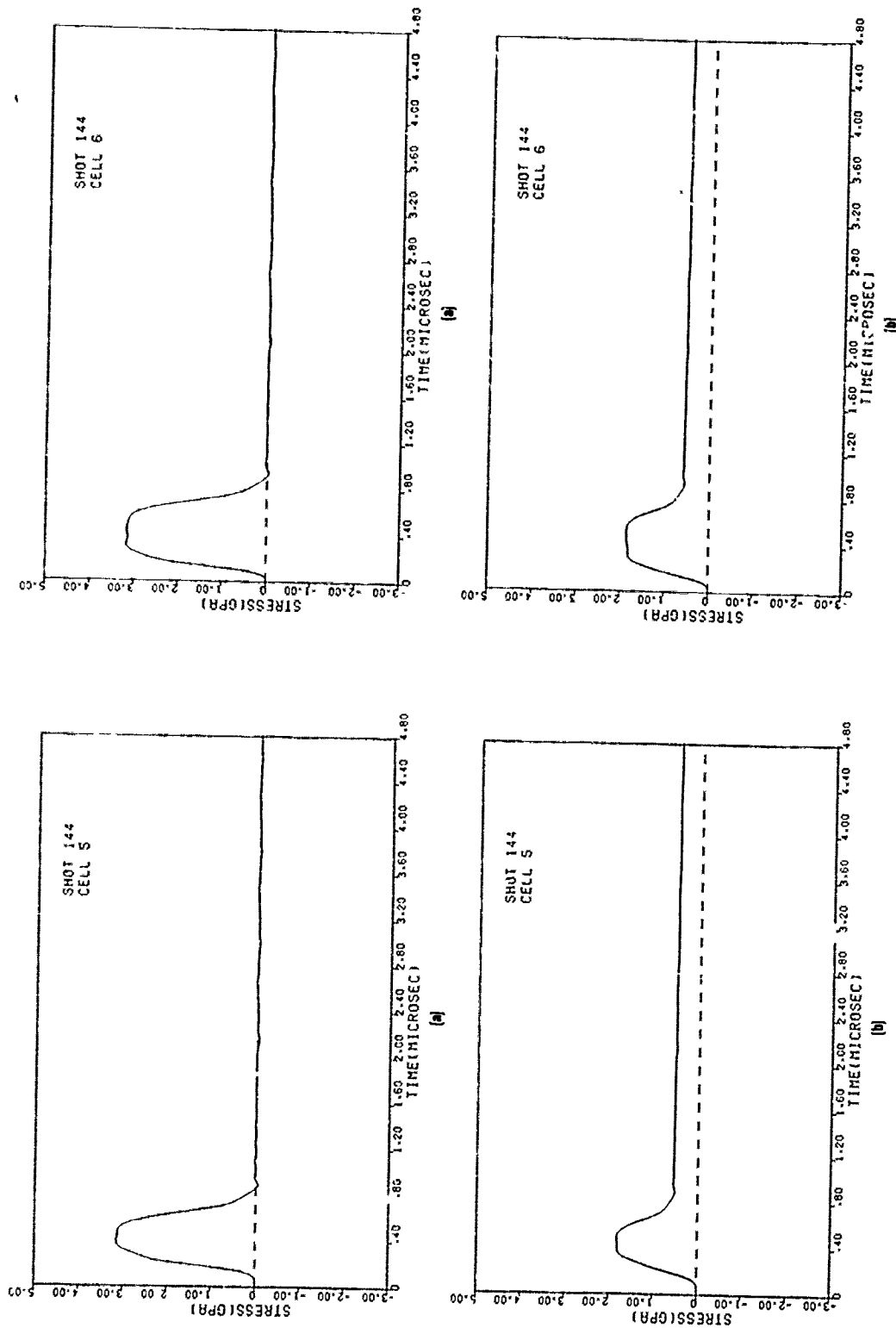


Figure I-5. Computed stress histories in cell 5 for Shot 144.
(a) Parallel and (b) perpendicular stresses.

Figure I-6. Computed stress histories in cell 6 for Shot 144.
(a) Parallel and (b) perpendicular stresses.

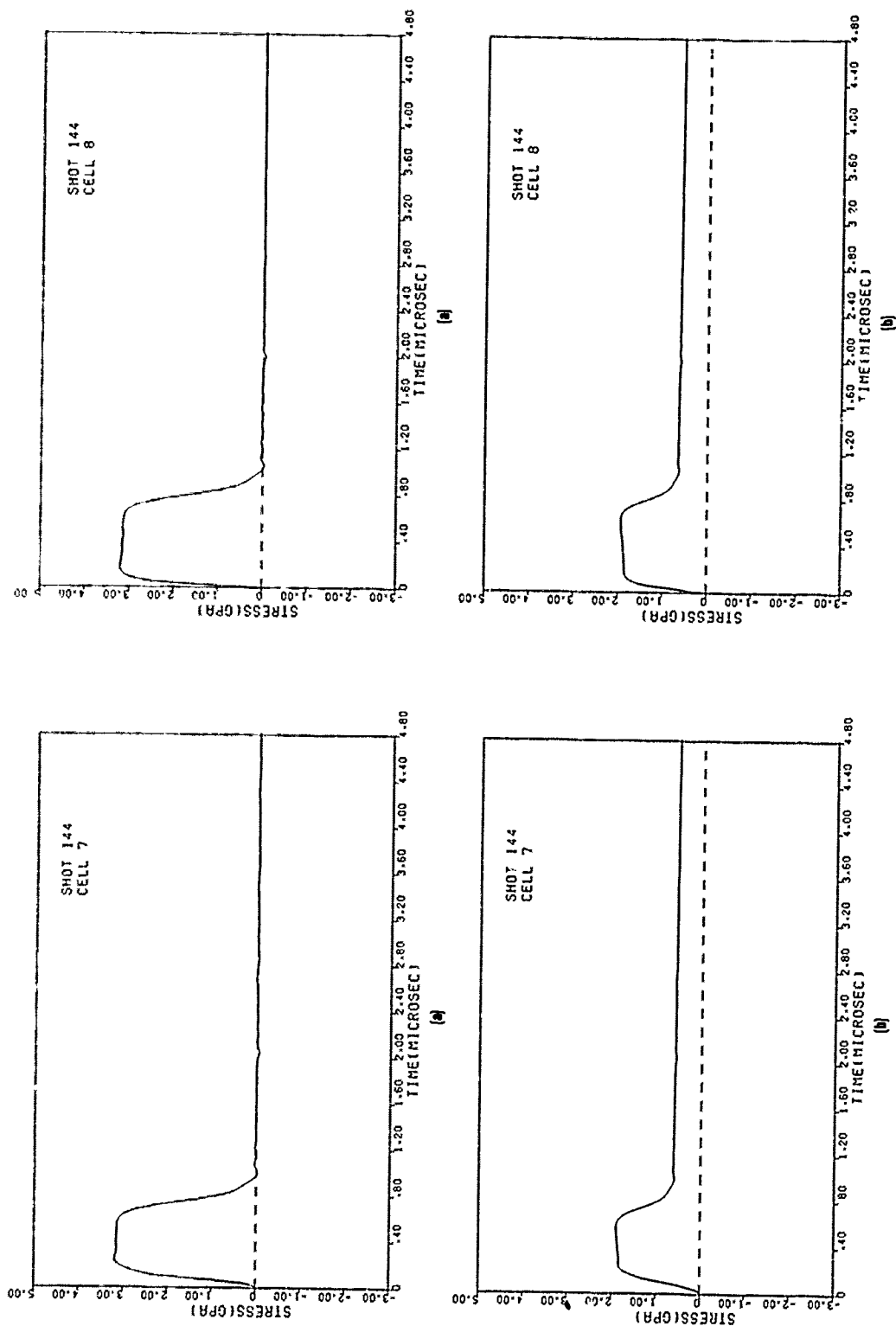


Figure I-7. Computed stress histories in cell 7 for Shot 144.
(a) Parallel and (b) perpendicular stresses.

Figure I-8. Computed stress histories in cell 8 for Shot 144.
(a) Parallel and (b) perpendicular stresses.

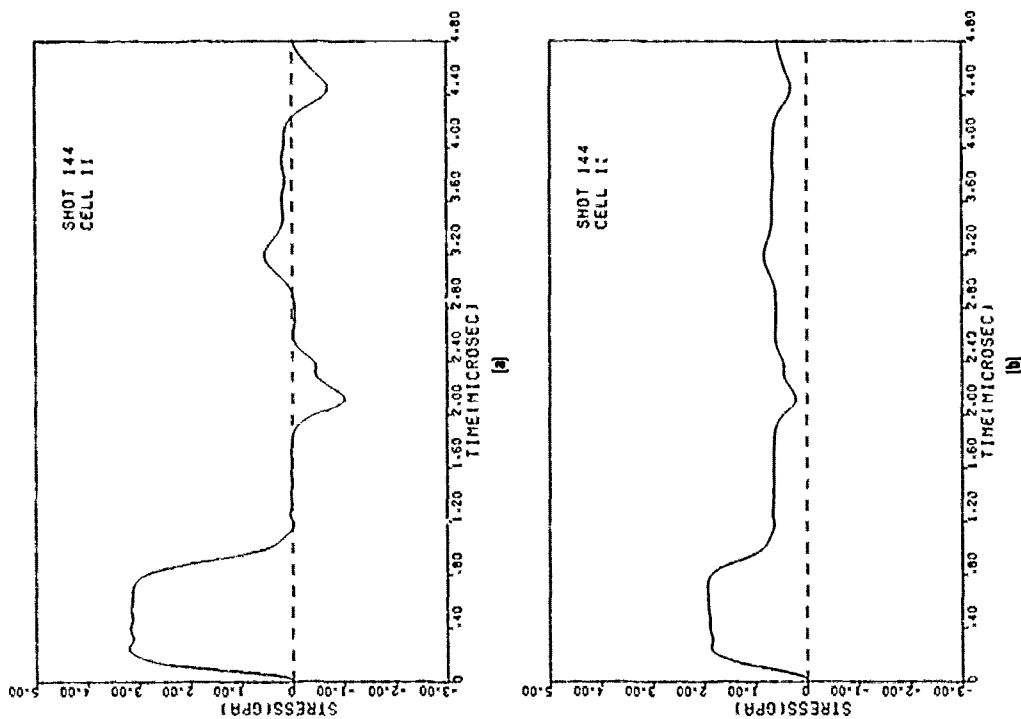


Figure I-9. Computed stress histories in cell 10 for Shot 144.
(a) Parallel and (b) perpendicular stresses.

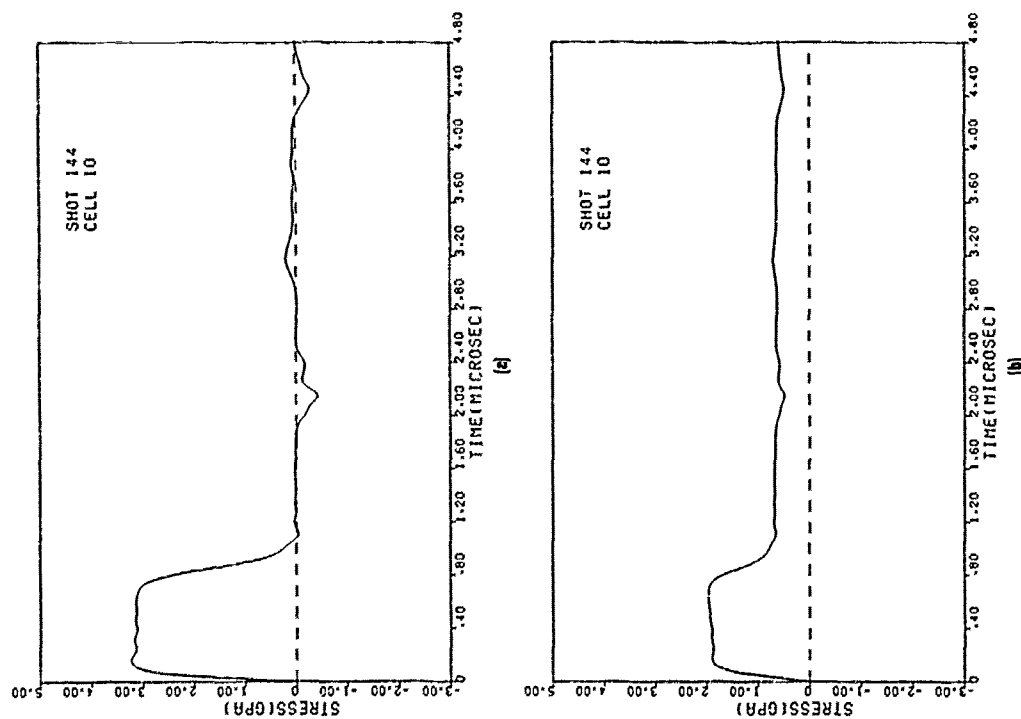


Figure I-10. Computed stress histories in cell 11 for Shot 144.
(a) Parallel and (b) perpendicular stresses.

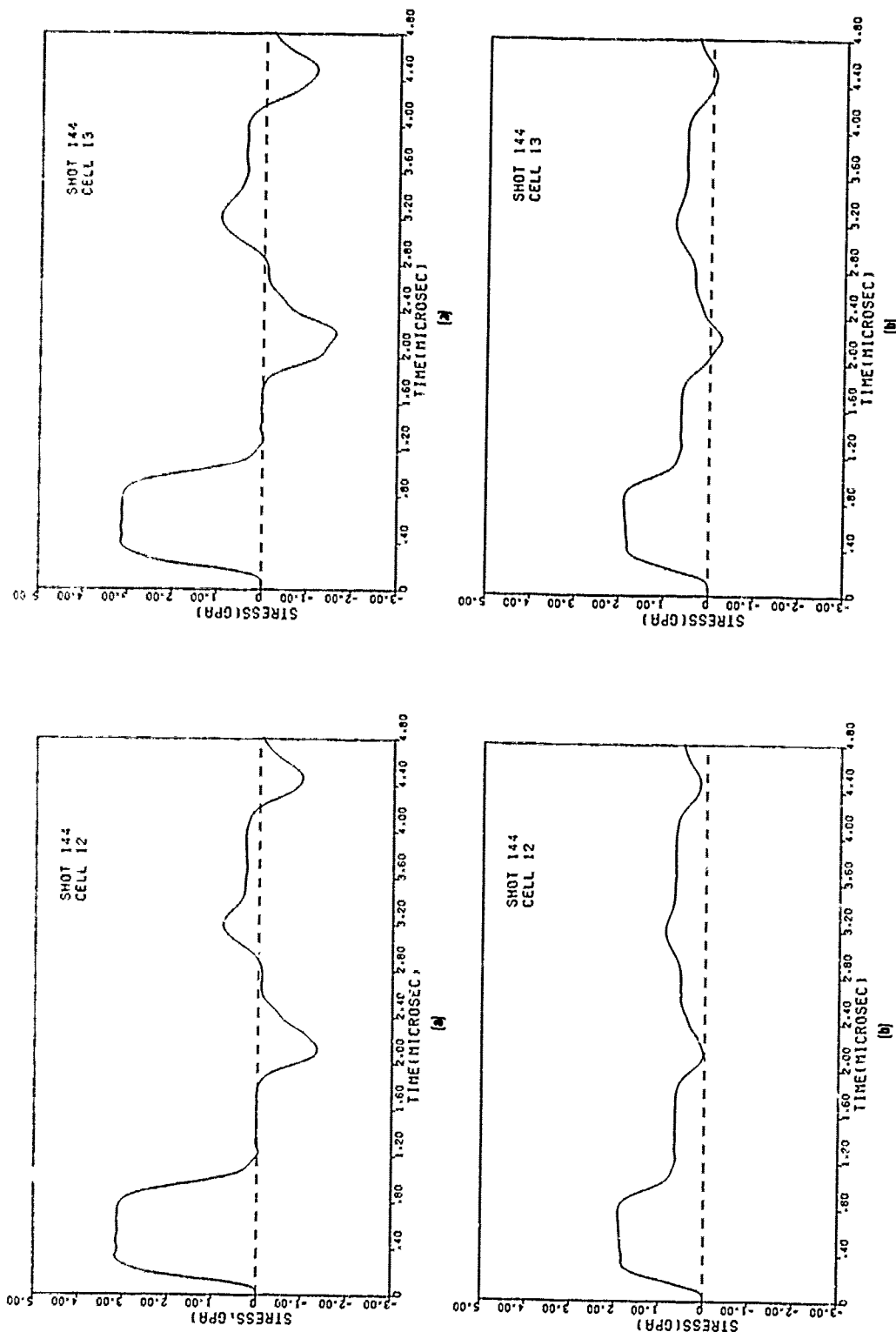


Figure 1-11. Computed stress histories in cell 12 for Shot 144.
(a) Parallel and (b) perpendicular stresses.

Figure 1-12. Computed stress histories in cell 13 for Shot 144.
(a) Parallel and (b) perpendicular stresses.

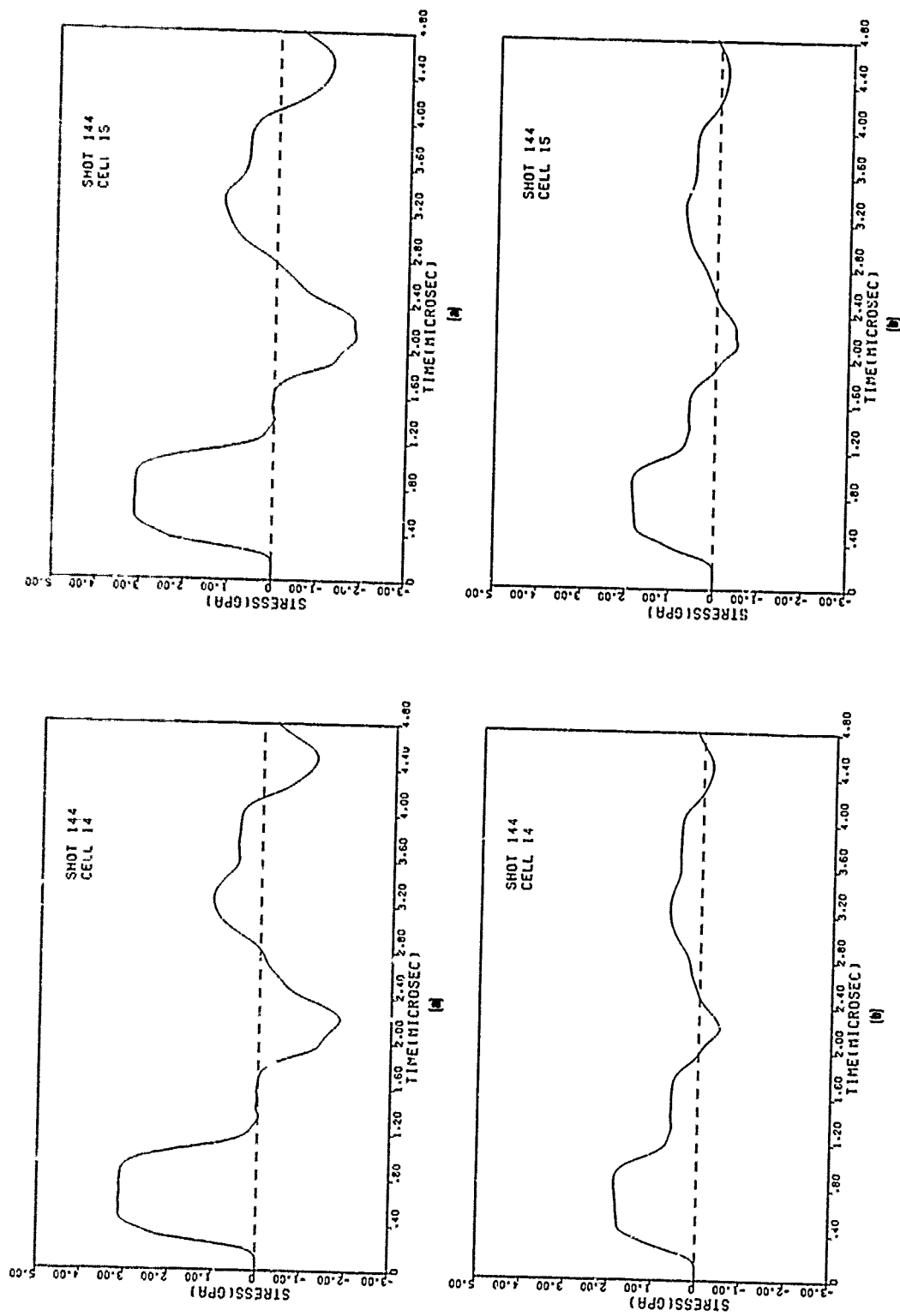


Figure I-13 Computed stress histories in cell 14 for Shot 144.
 (a) Parallel and (b) perpendicular stresses.

Figure I-14. Computed stress histories in cell 15 for Shot 144.
 (a) Parallel and (b) perpendicular stresses.

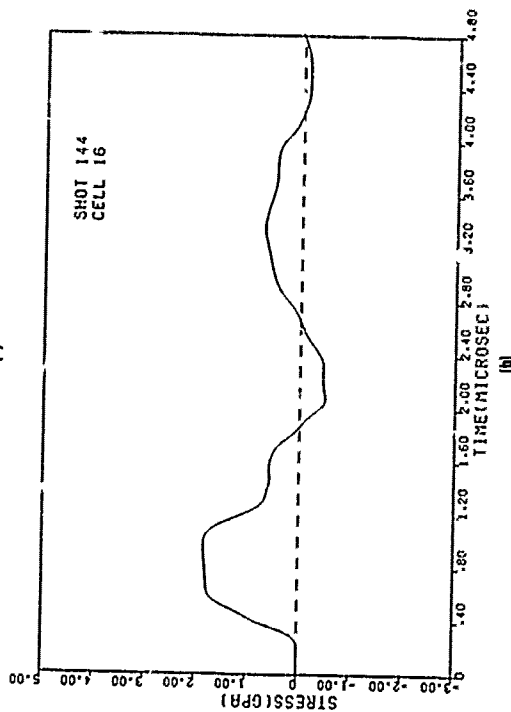
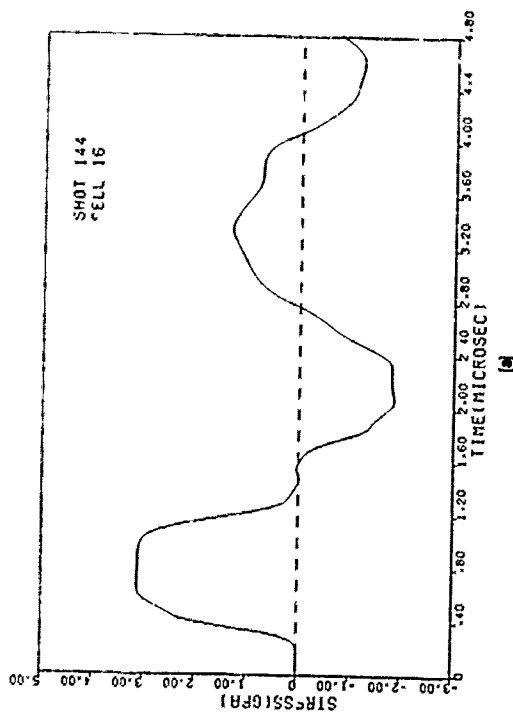


Figure I-15. Computed stress histories in cell 16 for Shot 144.
(a) Parallel and (b) perpendicular stresses.

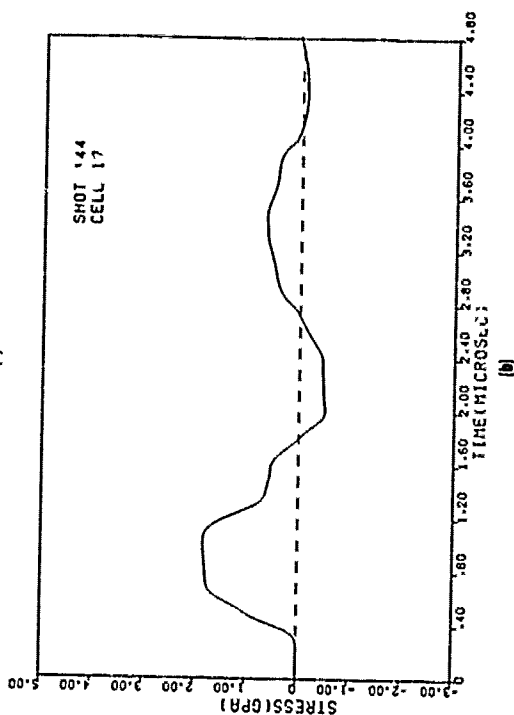
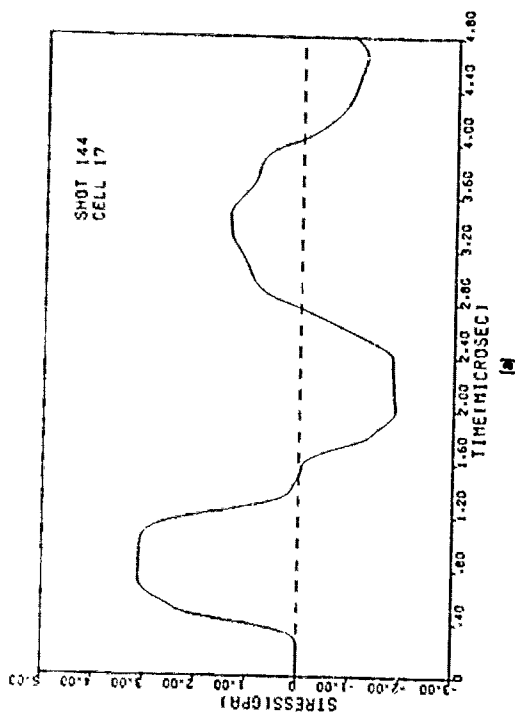


Figure I-16. Computed stress histories in cell 17 for Shot 144.
(a) Parallel and (b) perpendicular stresses.

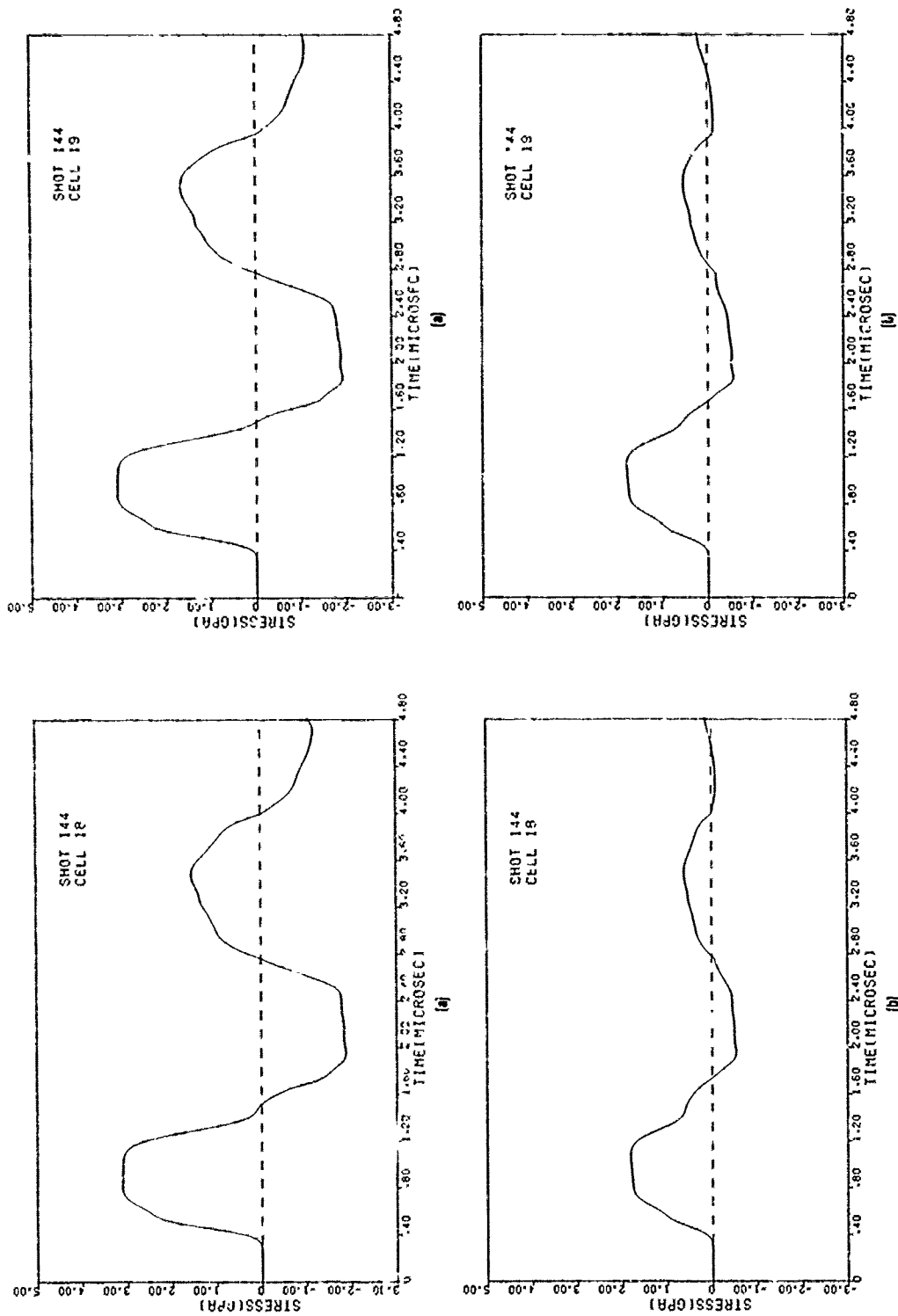


Figure I-17. Computed stress histories in cell 18 for Shot 144.
(a) Parallel and (b) perpendicular stresses.

Figure I-18. Computed stress histories in cell 19 for Shot 144.
(a) Parallel and (b) perpendicular stresses.

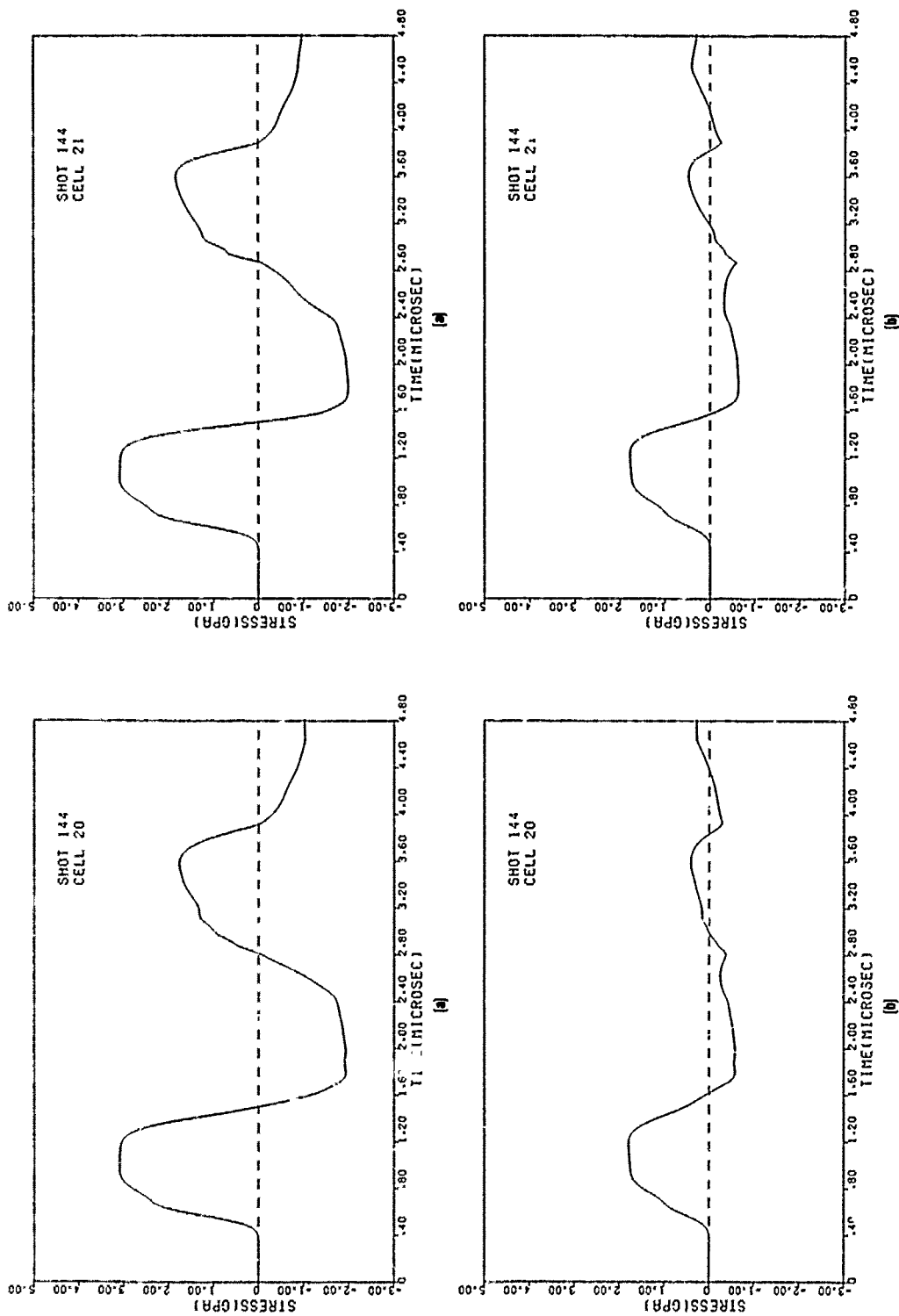


Figure I-19. Computed stress histories in cell 20 for Shot 144.
(a) Parallel and (b) perpendicular stresses.

Figure I-20. Computed stress histories in cell 21 for Shot 144.
(a) Parallel and (b) perpendicular stresses.

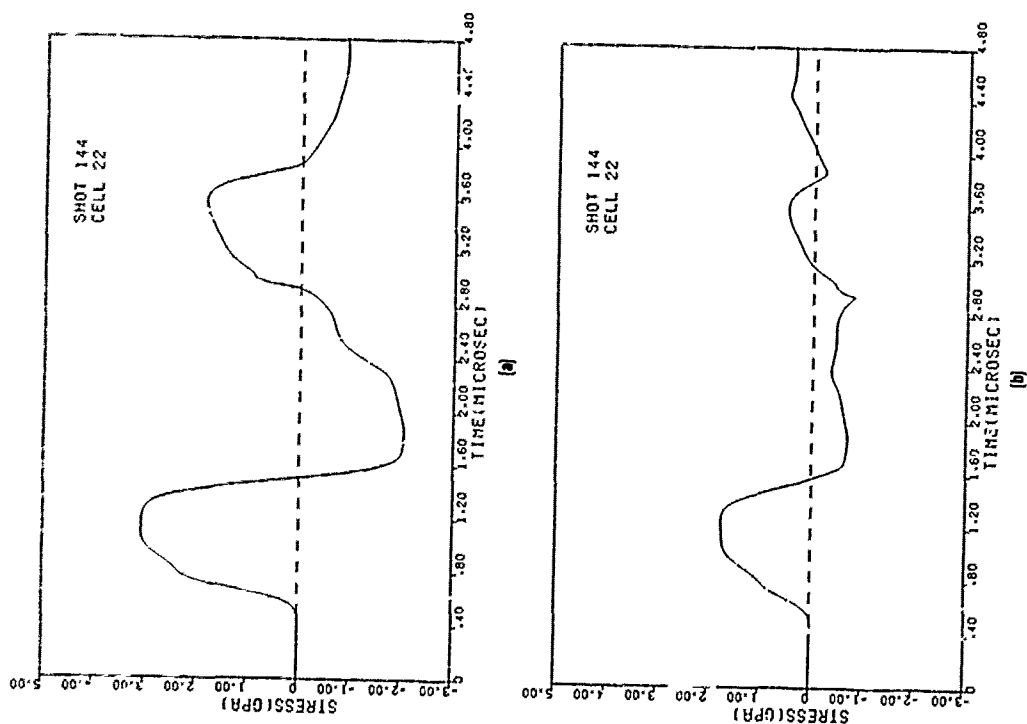


Figure I-21. Computed stress histories in cell 22 for Shot 144.
(a) Parallel and (b) perpendicular stresses.

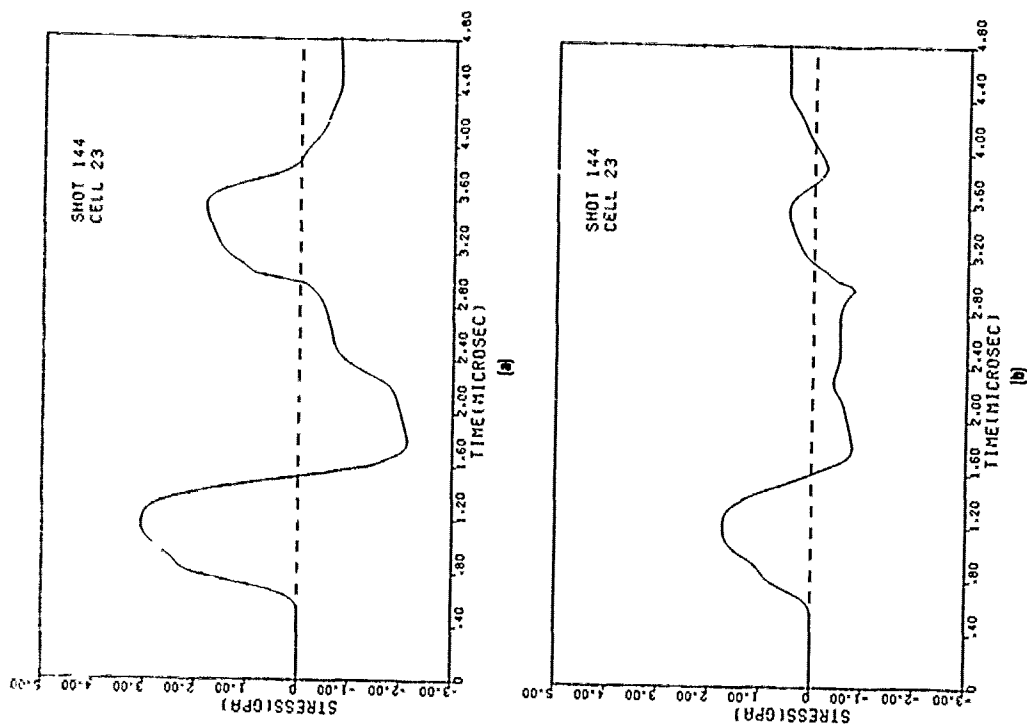


Figure I-22. Computed stress histories in cell 23 for Shot 144.
(a) Parallel and (b) perpendicular stresses.

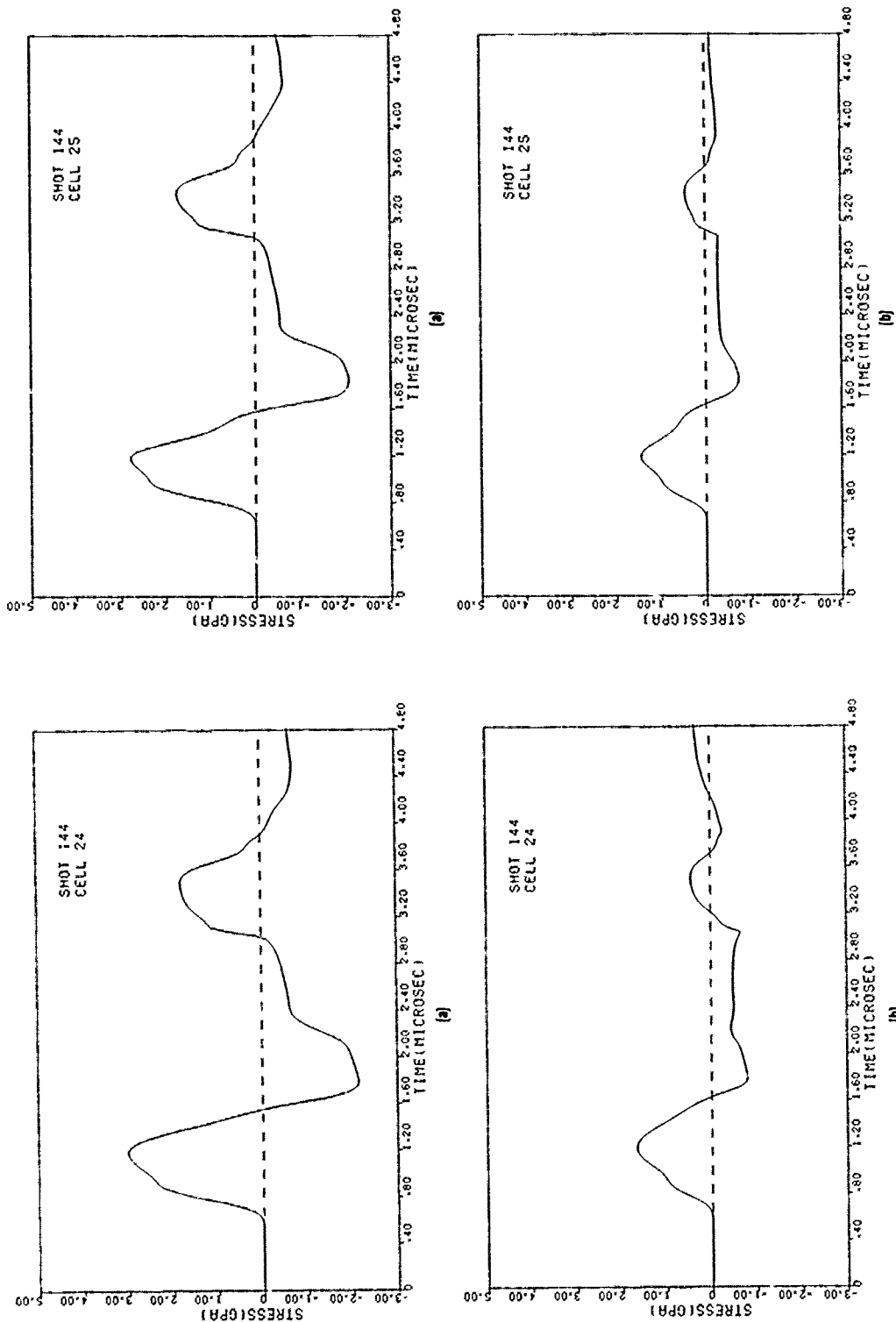


Figure I-24. Computed stress histories in cell 25 for Shot 144.
(a) Parallel and (b) perpendicular stresses.

Figure I-23. Computed stress histories in cell 24 for Shot 144.
(a) Parallel and (b) perpendicular stresses.

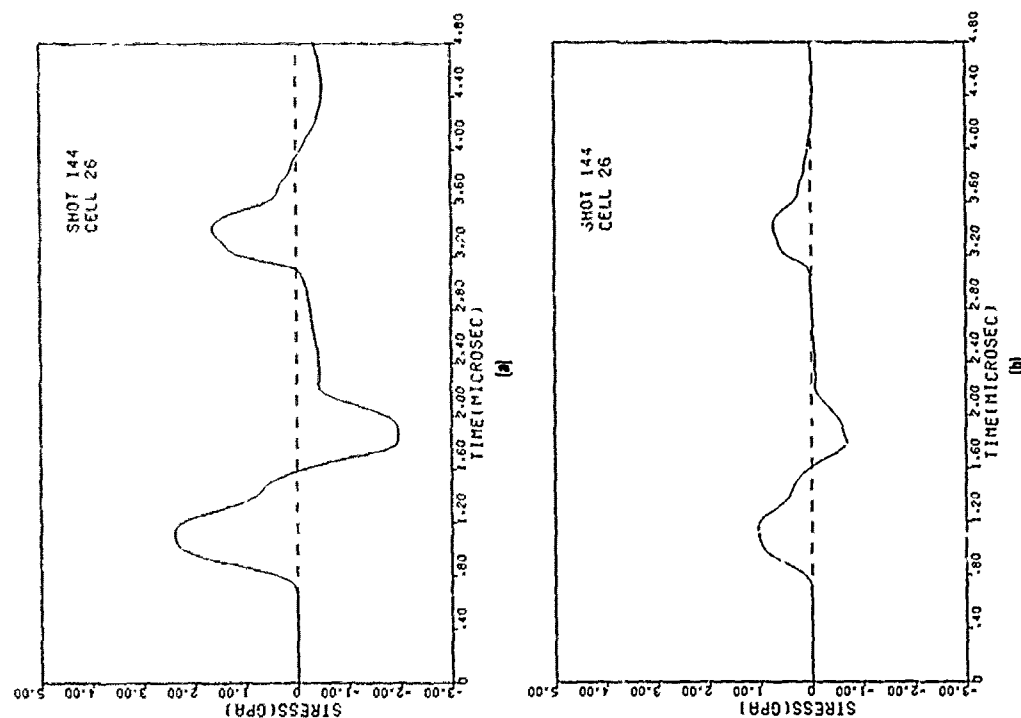


Figure I-25. Computed stress histories in cell 26 for Shot 144.
(a) Parallel and (b) perpendicular stresses.

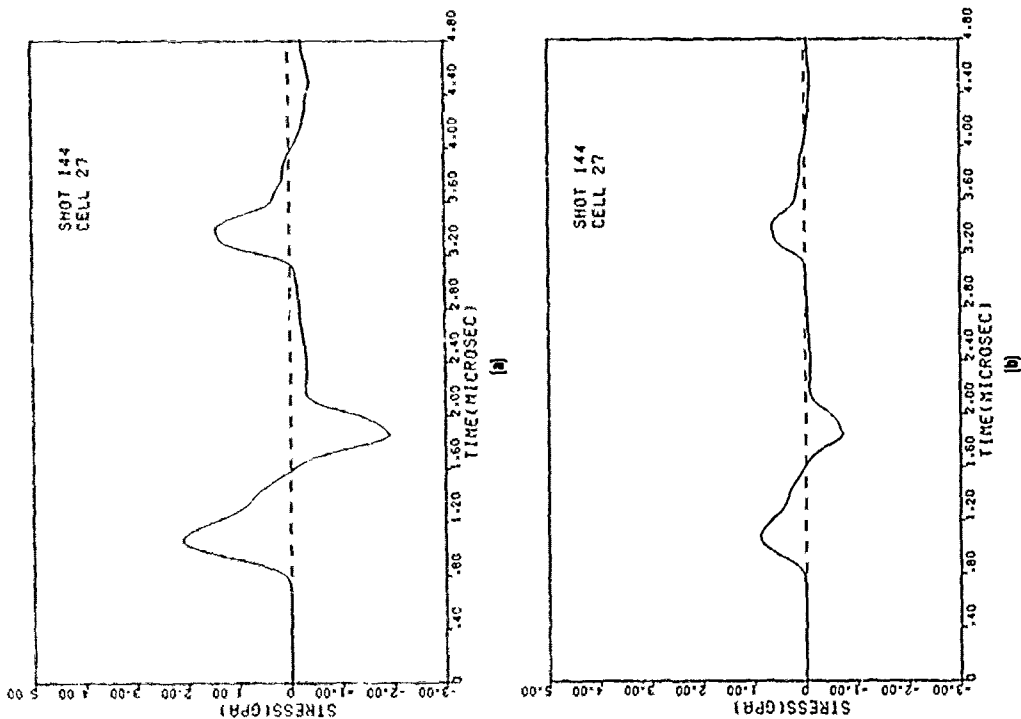


Figure I-26. Computed stress histories in cell 27 for Shot 144.
(a) Parallel and (b) perpendicular stresses.

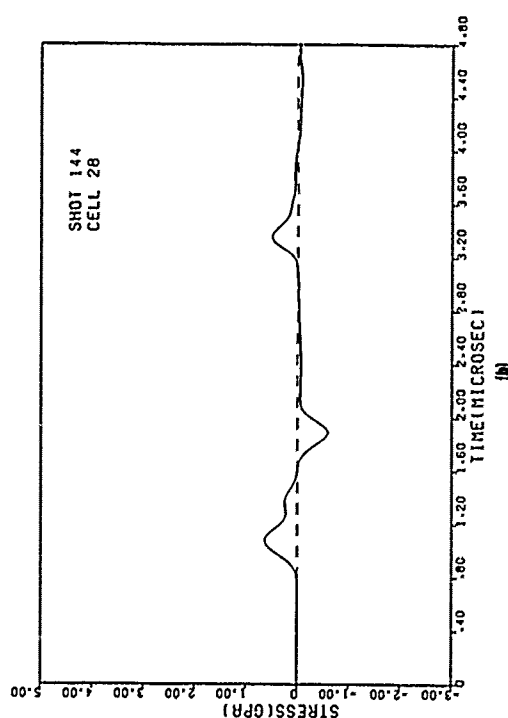
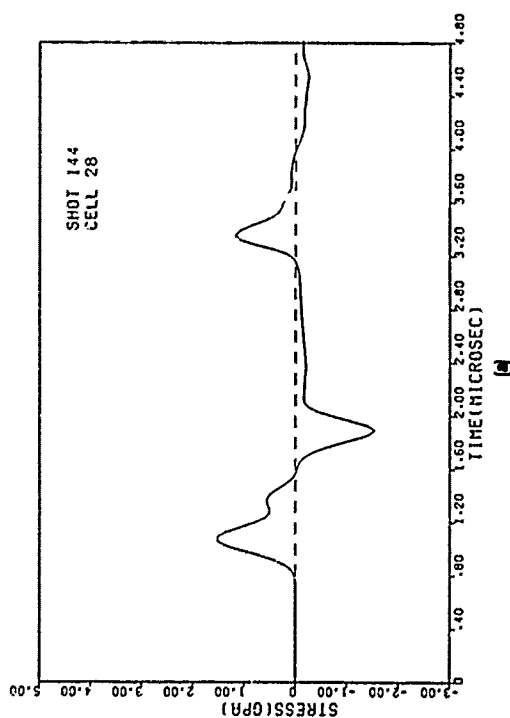


Figure I-27. Computed stress histories in cell 28 for Shot 144.
(a) Parallel and (b) perpendicular stresses.

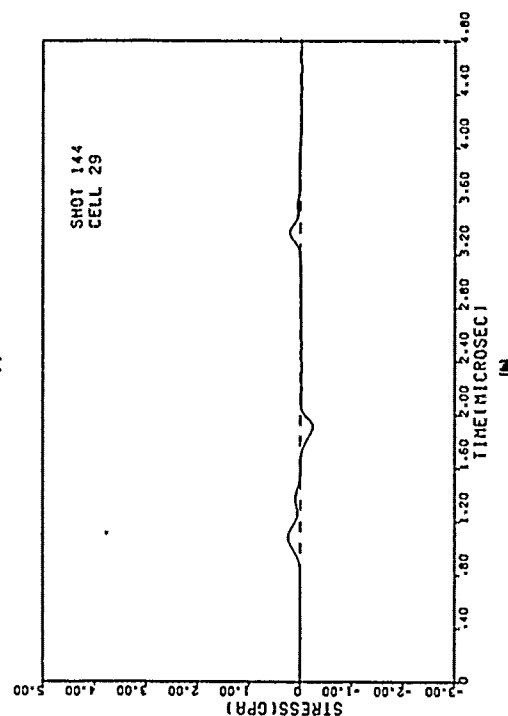
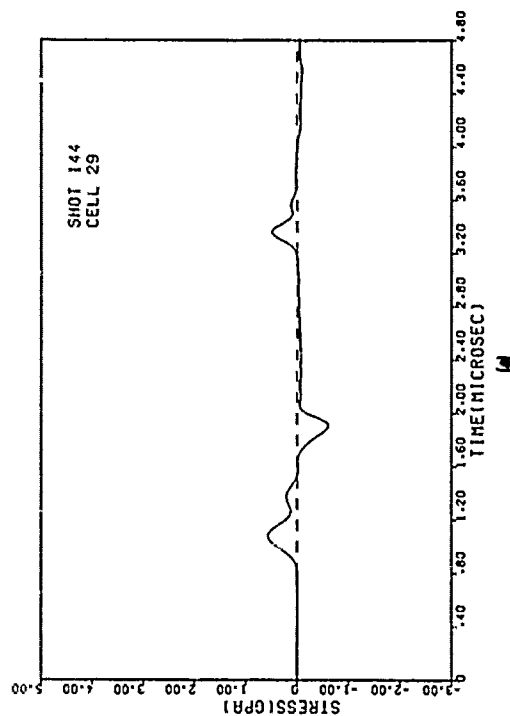


Figure I-28. Computed stress histories in cell 29 for Shot 144.
(a) Parallel and (b) perpendicular stresses.

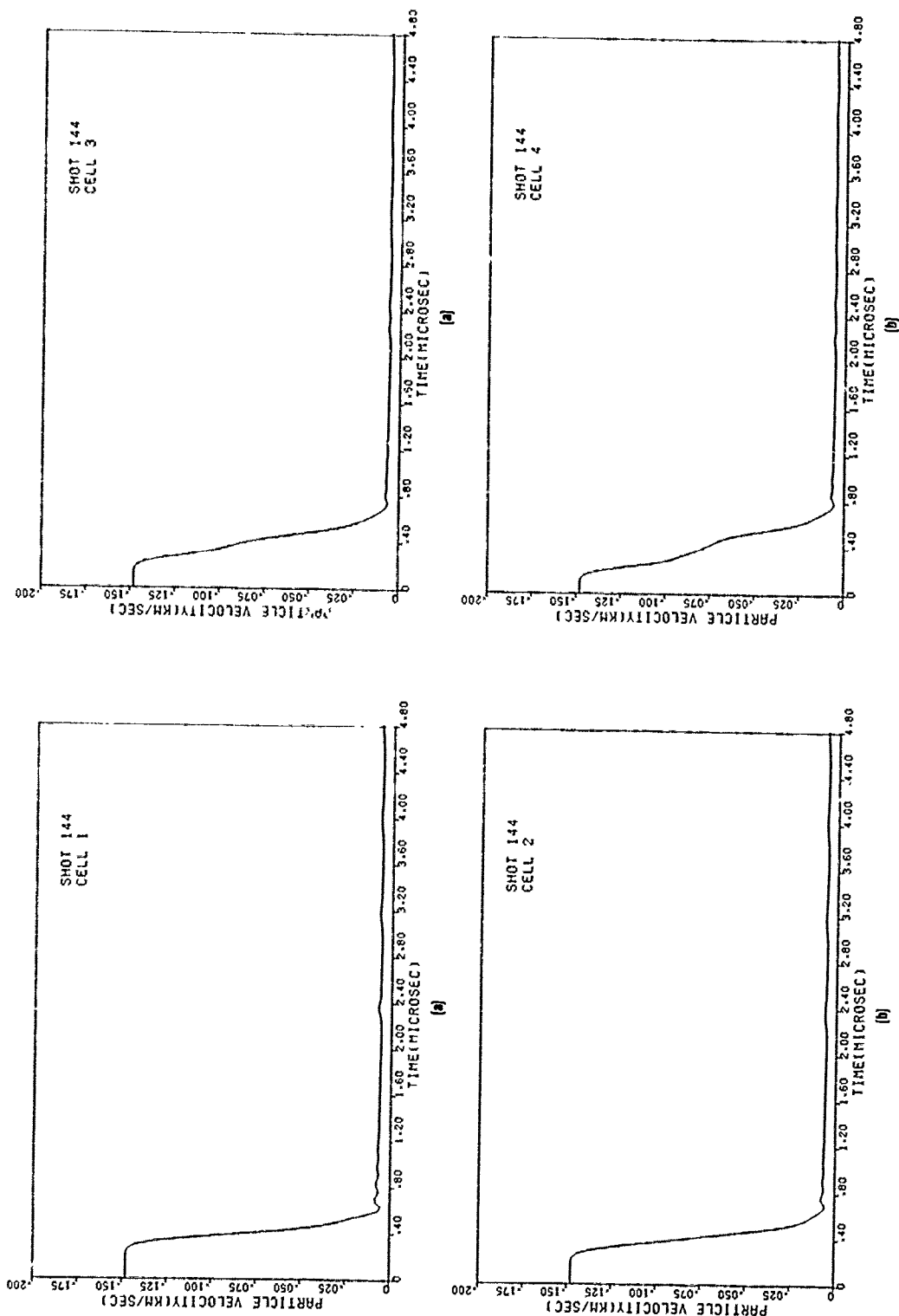


Figure I-29. Computed particle velocity histories in (a) cell 1 and (b) cell 2 for Shot 144.

Figure I-30. Computed particle velocity histories in (a) cell 3 and (b) cell 4 for Shot 144.

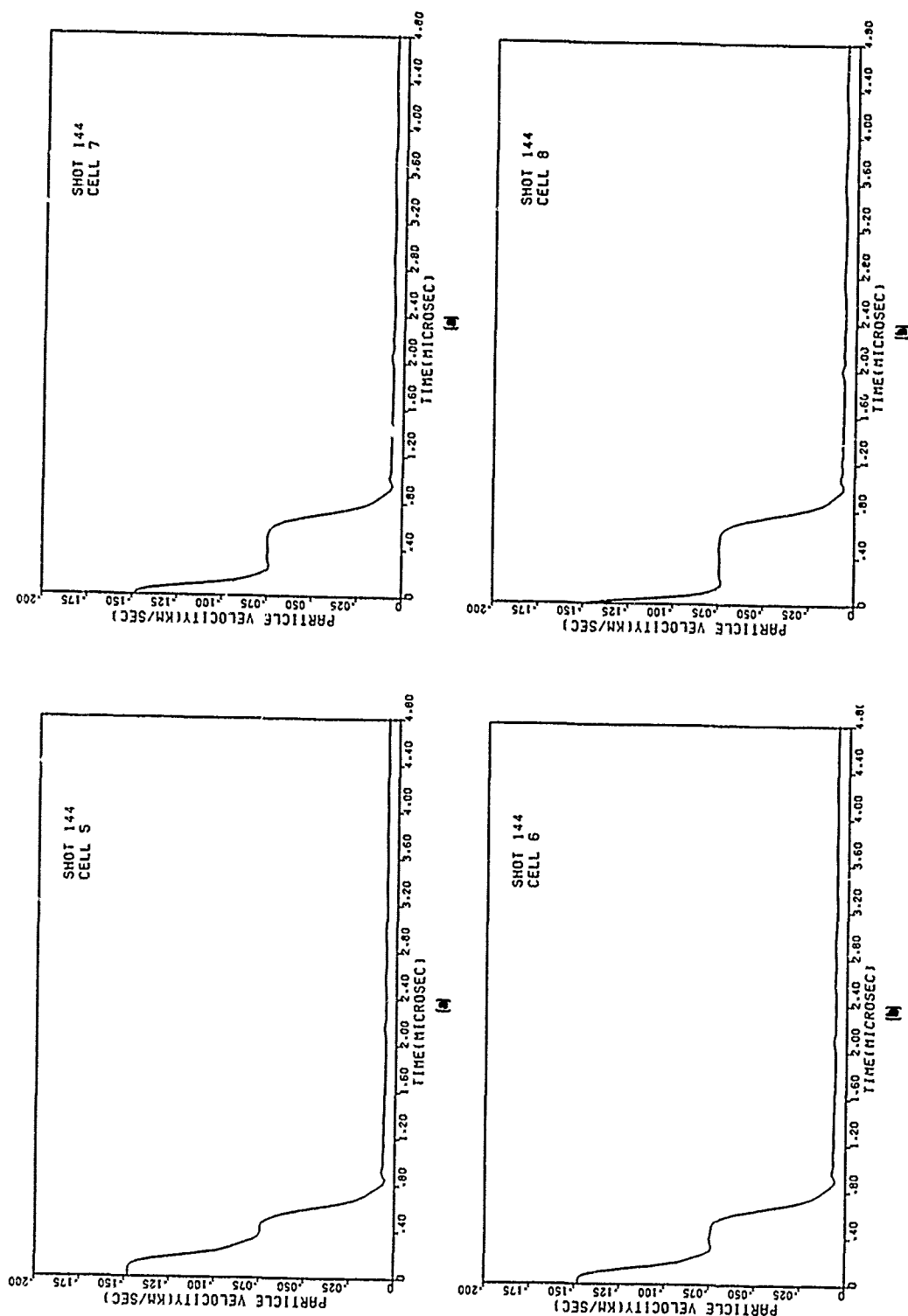


Figure I-31. Computed particle velocity histories in (a) cell 5 and (b) cell 6 for Shot 144.

Figure I-32. Computed particle velocity histories in (a) cell 7 and (b) cell 8 for Shot 144.

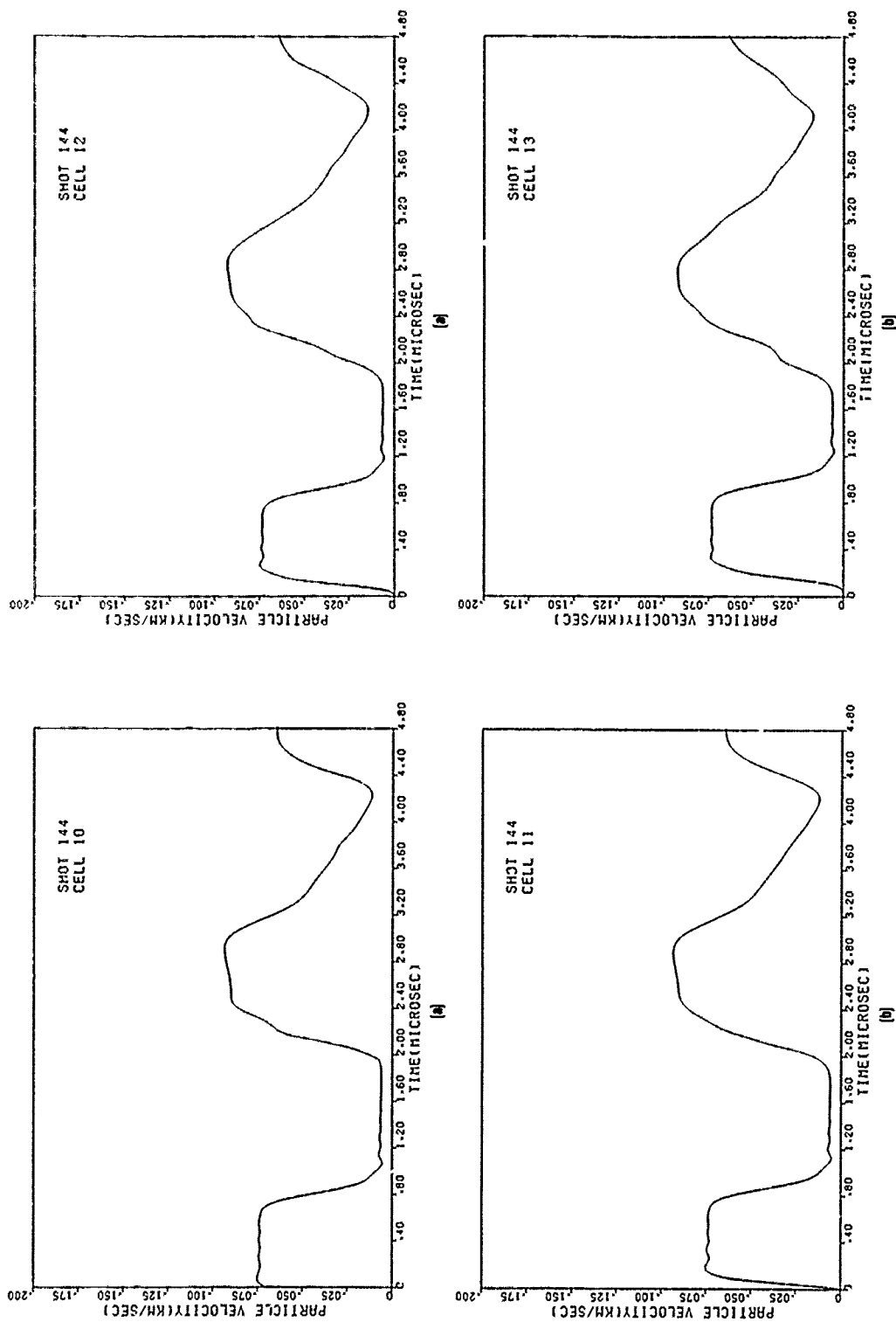


Figure I-33. Computed particle velocity histories in (a) cell 10 and (b) cell 11 for Shot 144.

Figure I-34. Computed particle velocity histories in (a) cell 12 and (b) cell 13 for Shot 144.

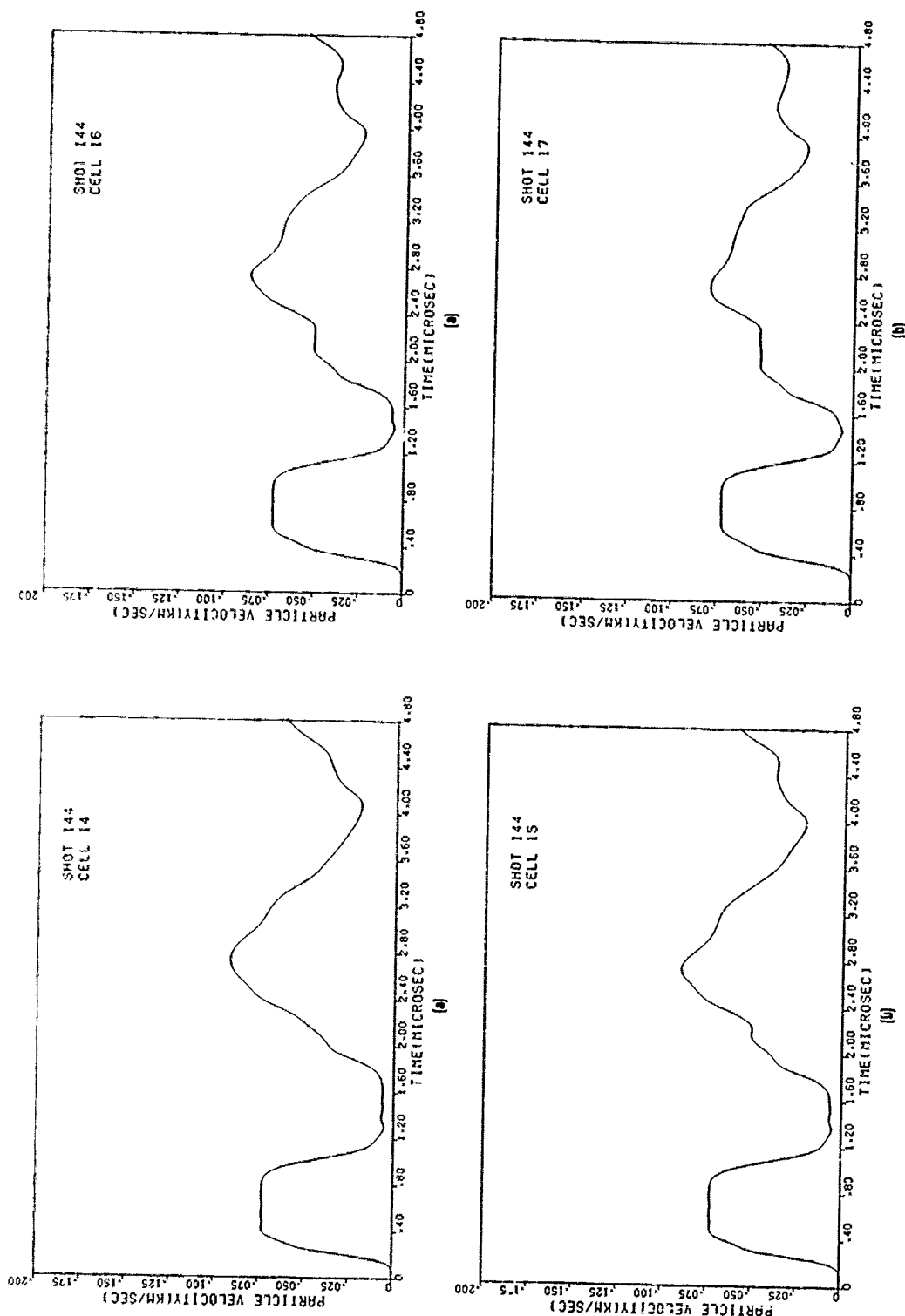


Figure I-35. Computed particle velocity histories in (a) cell 14 and (b) cell 15 for Shot 144.

Figure I-36. Computed particle velocity histories in (a) cell 16 and (b) cell 17 for Shot 144.

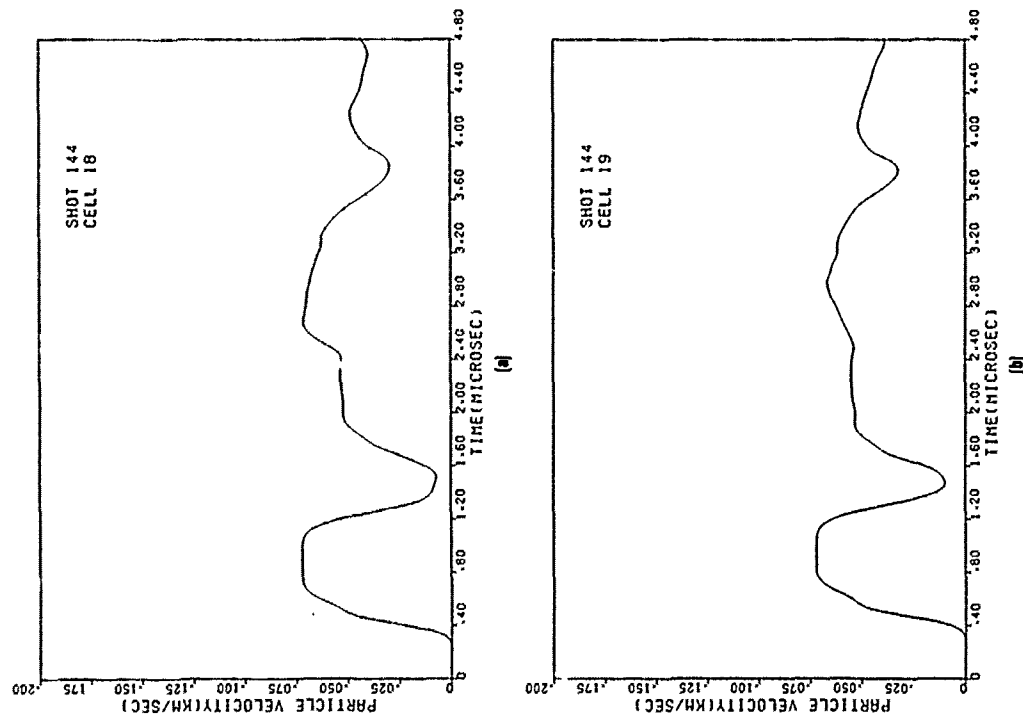


Figure 1-37. Computed particle velocity histories in (a) cell 18 and (b) cell 19 for Shot 144.

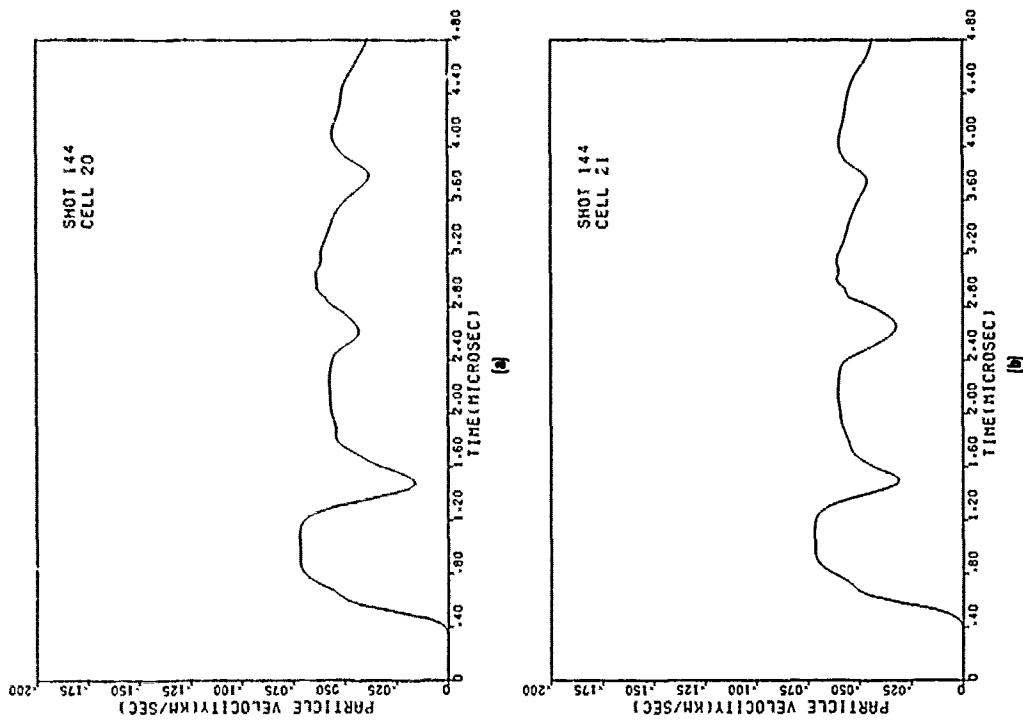


Figure 1-38. Computed particle velocity histories in (a) cell 20 and (b) cell 21 for Shot 144.

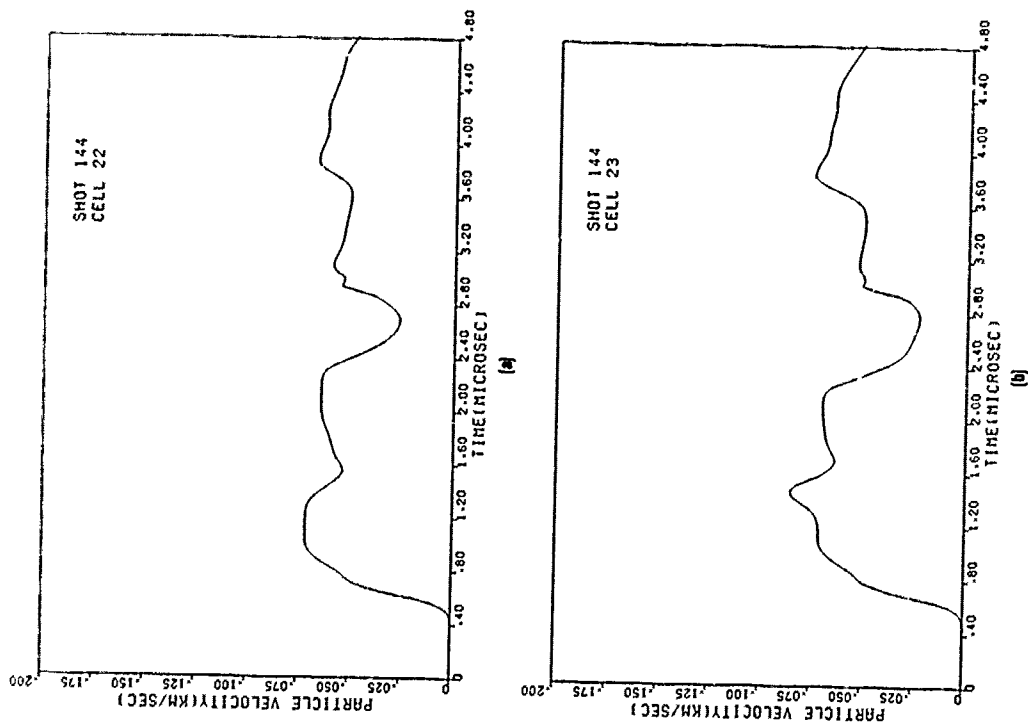


Figure I-39. Computed particle velocity histories in (a) cell 22 and (b) cell 23 for Shot 144.

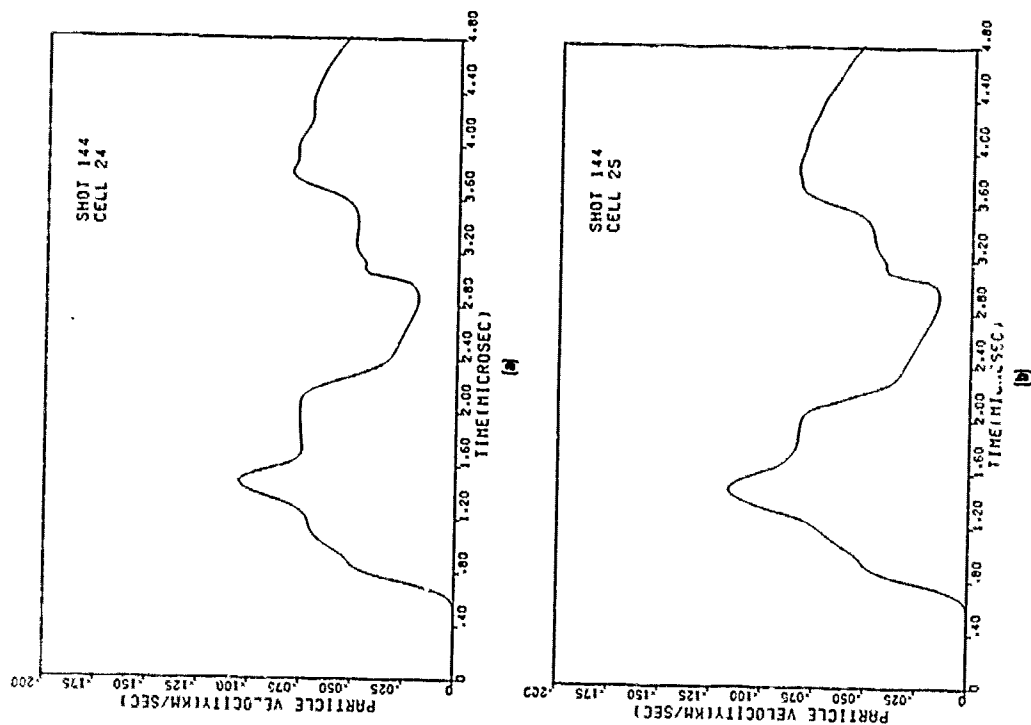


Figure I-40. Computed particle velocity histories in (a) cell 24 and (b) cell 25 for Shot 144.

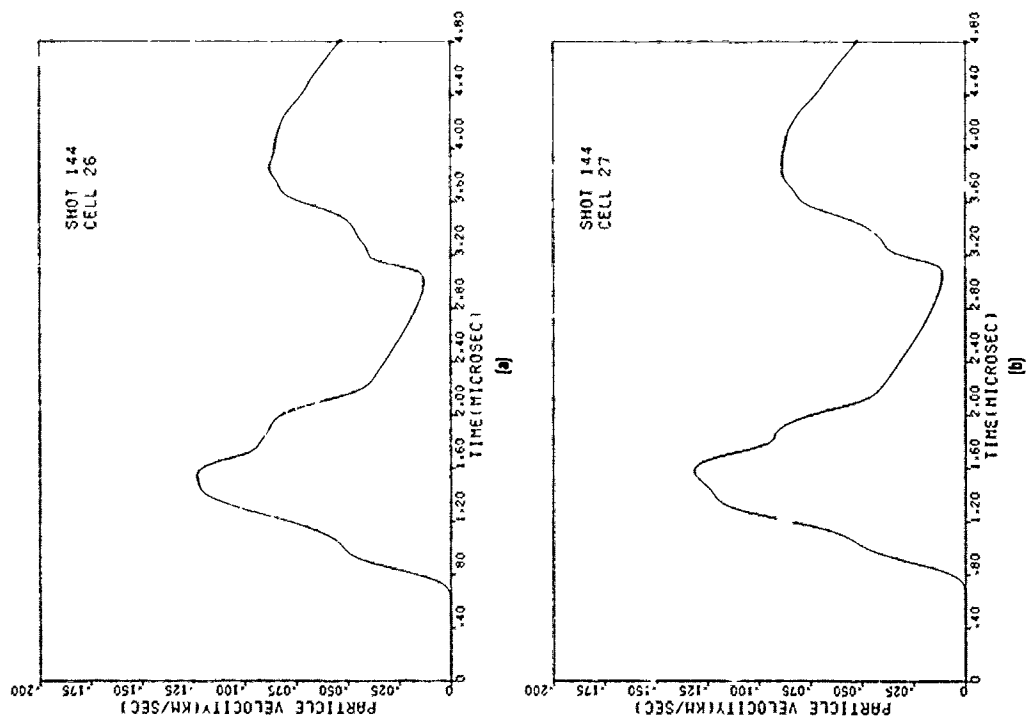


Figure I-41. Computed particle velocity histories in (a) cell 26 and (b) cell 27 for Shot 144.

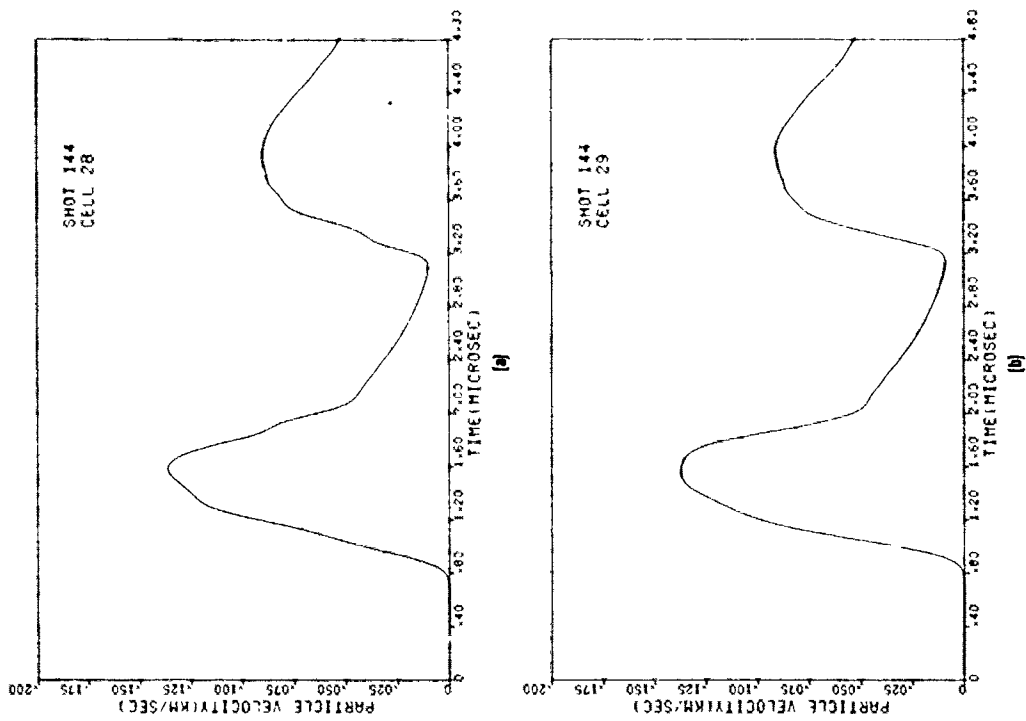


Figure I-42. Computed particle velocity histories in (a) cell 28 and (b) cell 29 for Shot 144.

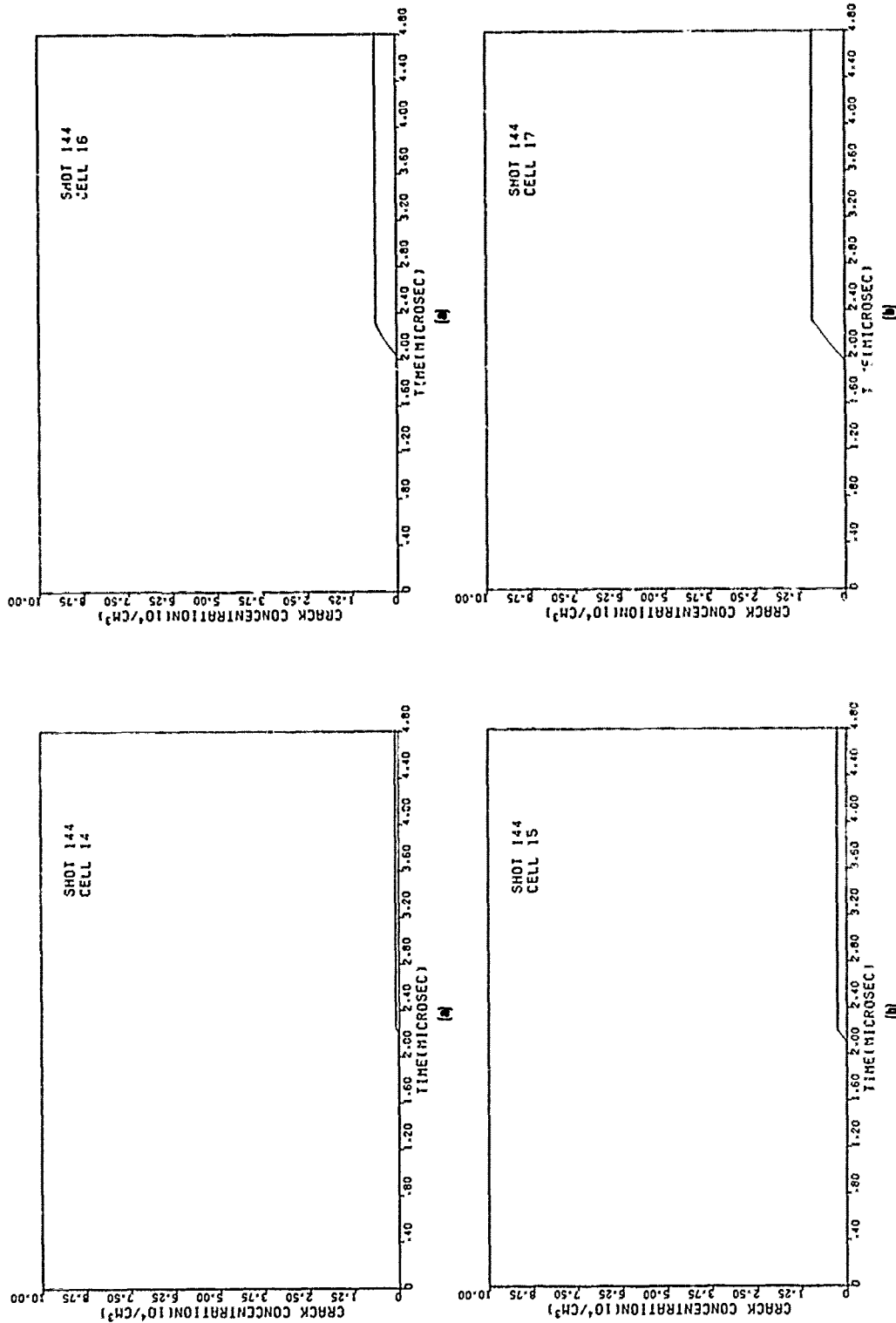


Figure I-43. Computed crack concentration histories in (a) cell 14 and (b) cell 15 for Shot 144.

Figure I-44. Computed crack concentration histories in (a) cell 16 and (b) cell 17 for Shot 144.

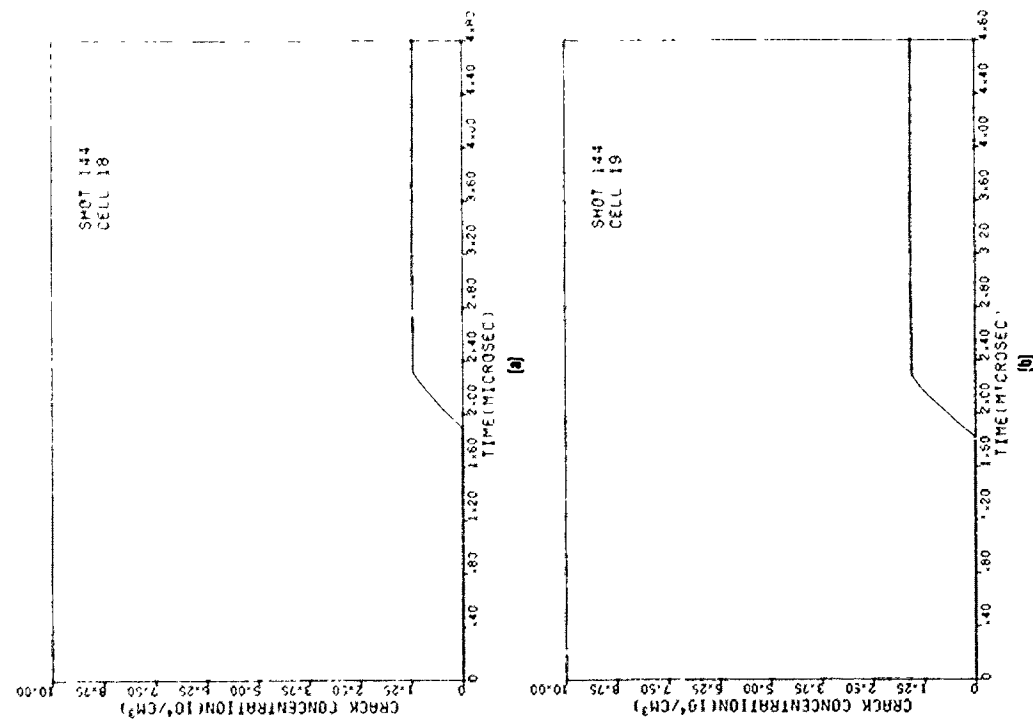


Figure I-45. Computed crack concentration histories in
(a) cell 18 and (b) cell 19 for Shot 144.

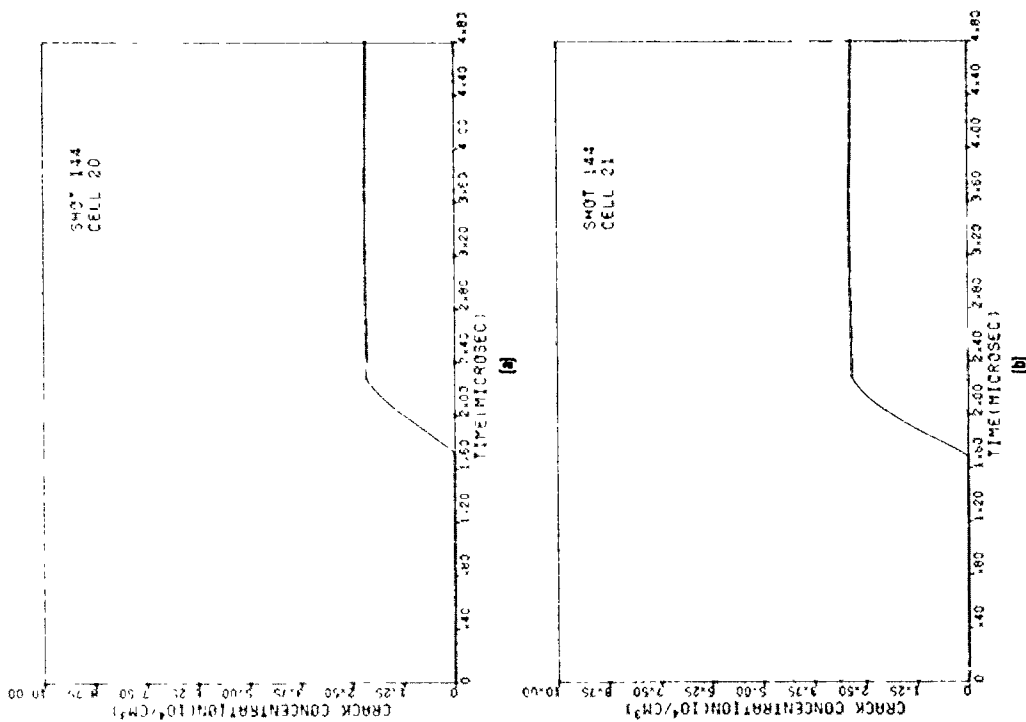


Figure I-46. Computed crack concentration histories in
(a) cell 20 and (b) cell 21 for Shot 144.

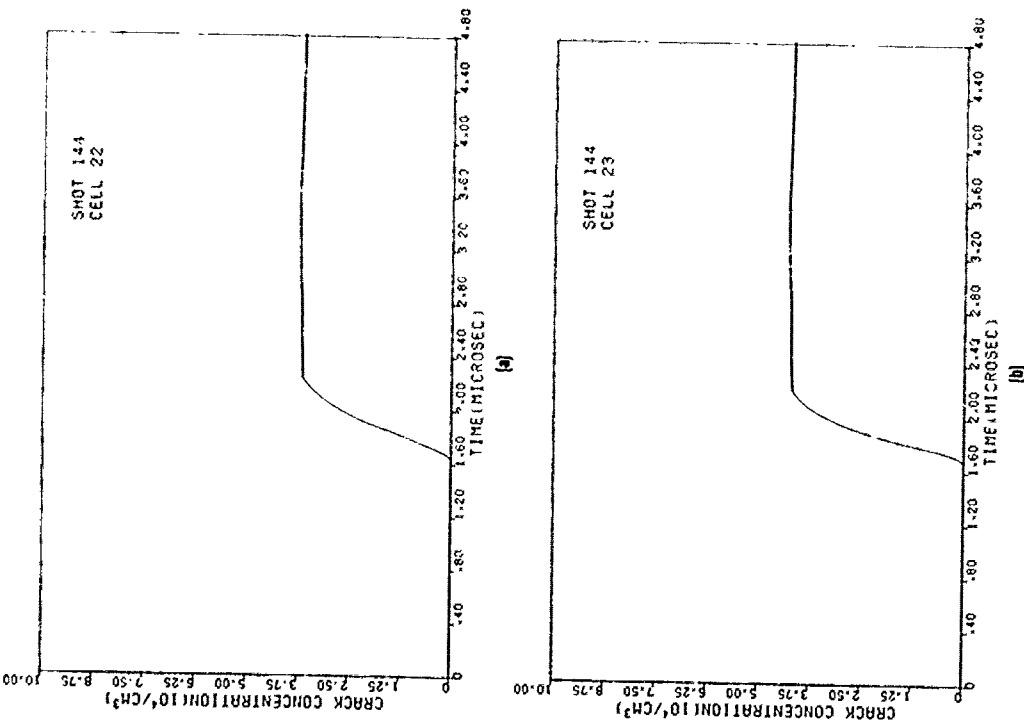


Figure I-47. Computed crack concentration histories in (a) cell 22 and (b) cell 23 for Shot 144.

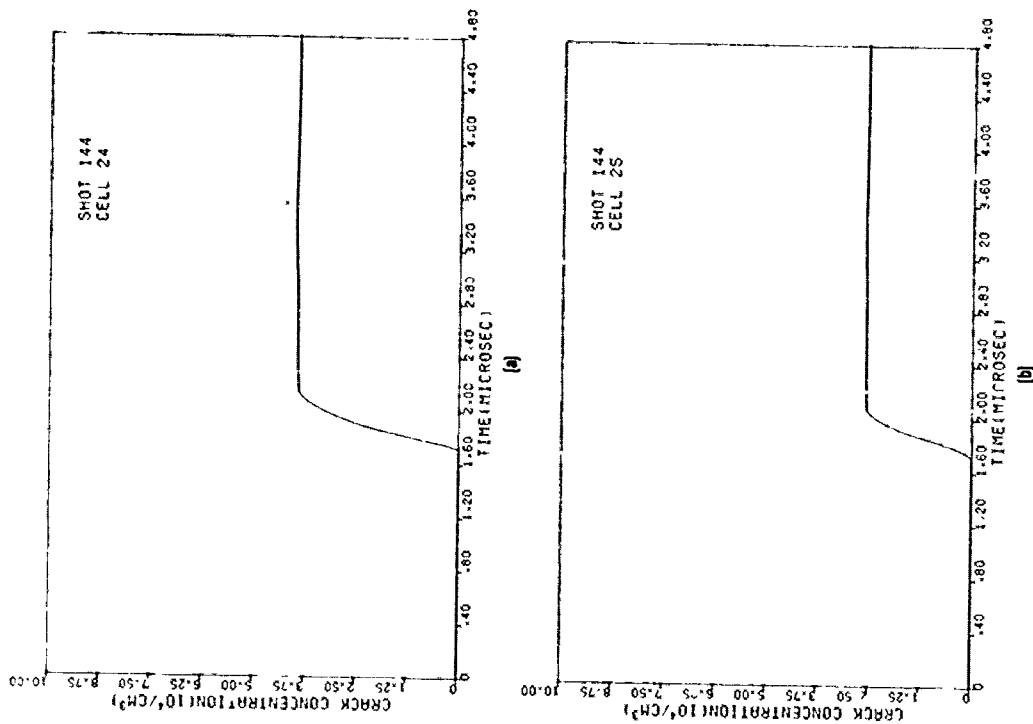


Figure I-48. Computed crack concentration histories in (a) cell 24 and (b) cell 25 for Shot 144.

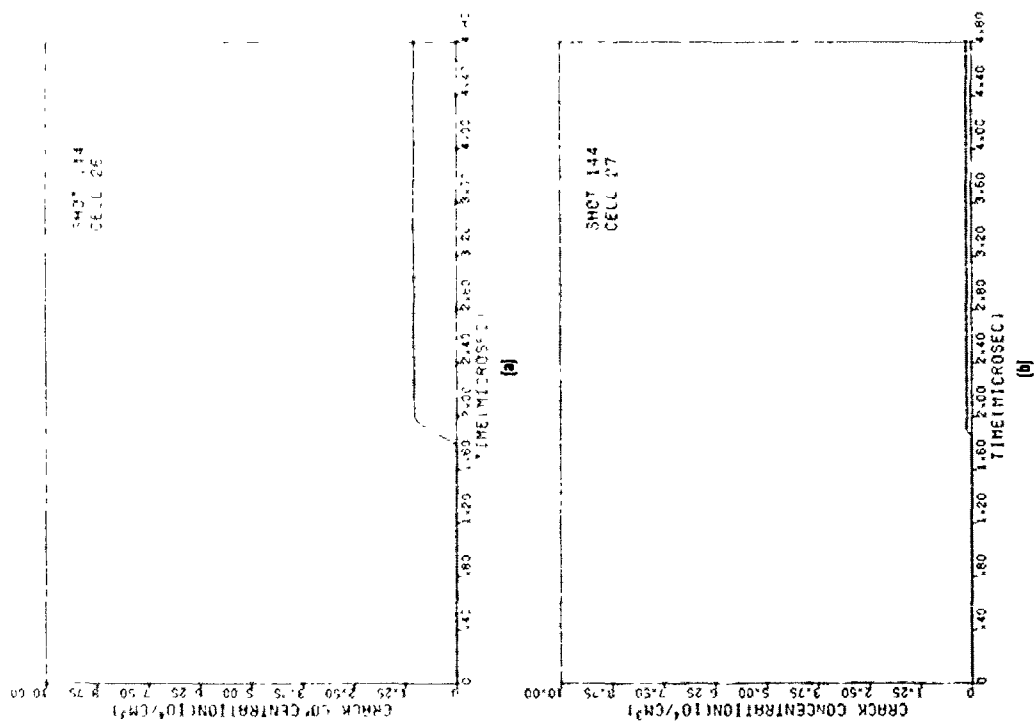


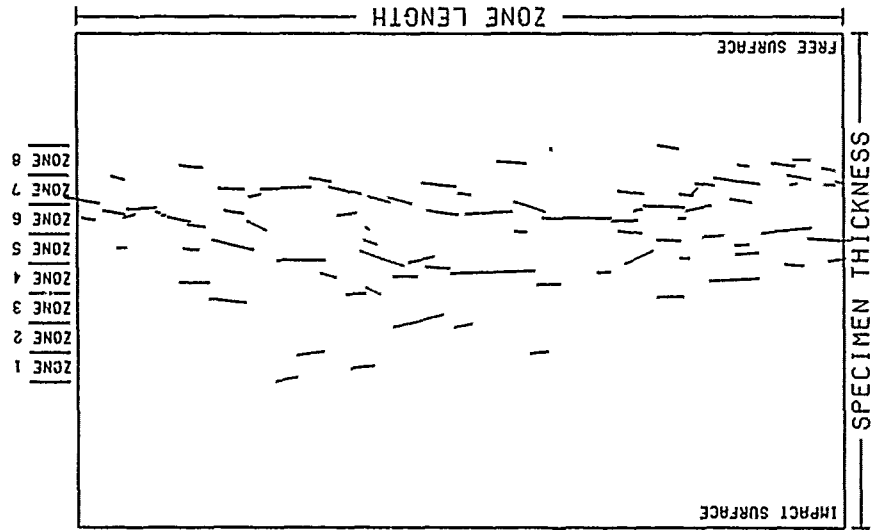
Figure 1-49. Computed crack concentration histories in
(a) cell 26 and (b) cell 27 for Shot 144.

APPENDIX J

COMPUTATION OF DYNAMIC FRACTURE PARAMETERS FOR HEAT TREATMENT A OF HF-1 STEEL WITH STRINGER CRACKS EXCLUDED

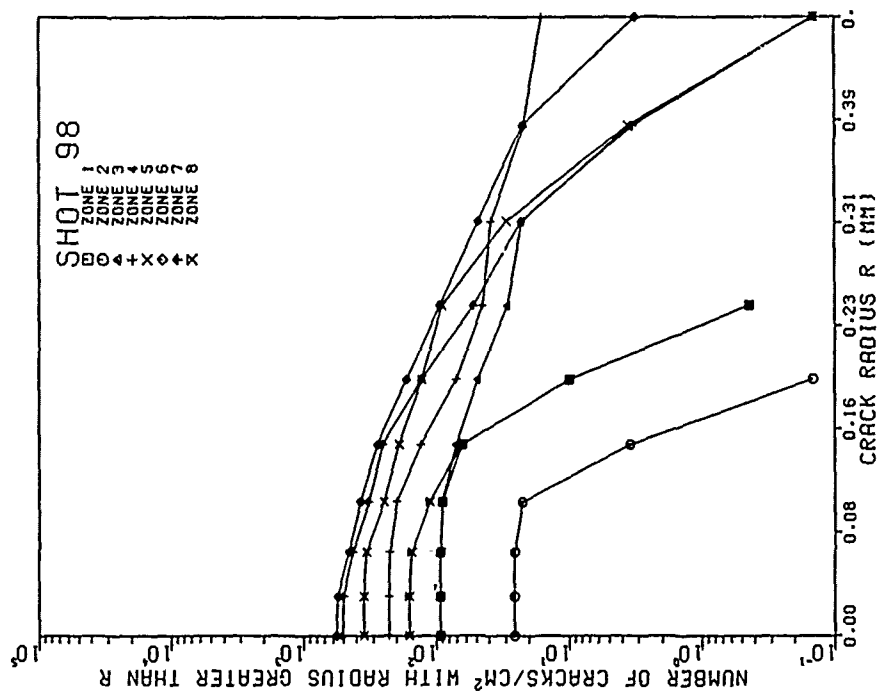
(To determine the importance of the stringer cracks, dynamic fracture parameters were calculated for heat treatment A material with these cracks excluded from the distributions. Stringer cracks are those cracks that occurred along the stringer impurities in the material. Stringer impurities are elongated impurity regions produced during the material fabrication process. For the HF-1 steel specimens the impurities were parallel to the shock wave propagation direction. The stringer cracks were therefore perpendicular to the majority of the cracks in a specimen. A total of 44 stringer cracks were measured: three for Shot 98, four for Shot 92, two for Shot 91, three for Shot 90, fourteen for Shot 94, nine for Shot 113, and nine for Shot 112. The digitized stringer crack coordinates are listed in Appendix F. Figures J-1 through J-7 give the crack distributions for these seven spall fracture specimens with stringer crack excluded. These distributions can be compared with those that include all the cracks given in Appendix E. Table J-1 summarizes the experimental volume crack-size distribution parameters for the heat treatment A specimens with stringer cracks excluded. Six iterations with the PUFF 8 computer program using the BFRACT2 subroutine were performed to obtain the dynamic fracture parameters. Table J-2 gives the experimental and computed nucleation and growth values obtained using the final set of parameters. These values are plotted in Figure J-8. The experimental and computed intercept and slope values for the nucleation rate curves in Figure J-8(a) are 7.48 and 8.30 cracks/cm³-ns and -14.1 and -13.4 GPa⁻¹, respectively. The experimental and computed intercept and slope values for the growth curves in Figure J-8(b) are 59.5 and 59.4 μ m and -0.161 and -0.164 GPa⁻¹ μ s⁻¹, respectively. For the experimental growth curve, the points for Shots 110, 91, and 113 were out of range of the majority of the points and were therefore not used in the least-squares fit. The dynamic fracture parameters are given in Table J-3. The exclusion of the stringer cracks appreciably affected only the nucleation threshold rate N_0 . This parameter decreased from 90 to 42 cracks/cm³-ns when excluding the stringer cracks. Figures J-9 through J-13 give the input listings for the PUFF 8 computations. Figures J-14 through J-22 give computed shock histories for the cell of maximum damage for each of the heat treatment A specimens with stringer cracks excluded. Plots (a) and (b) give the principal stresses in the direction of shock wave propagation and orthogonal to that direction, respectively. Plots (c) and (d) give particle velocity and crack concentration histories, respectively.)

SHOT 98
 IMPACTOR VELOCITY 0.160 KM/S
 IMPACTOR THICKNESS 2.37 MM
 SPECIMEN THICKNESS 6.35 MM
 NUMBER OF ZONES 86
 NUMBER OF ZONES 8
 ZONE LENGTH 10.16 MM
 ZONE WIDTH 0.38 MM
 IMPACT SURFACE TO ZONE1 1.87 MM

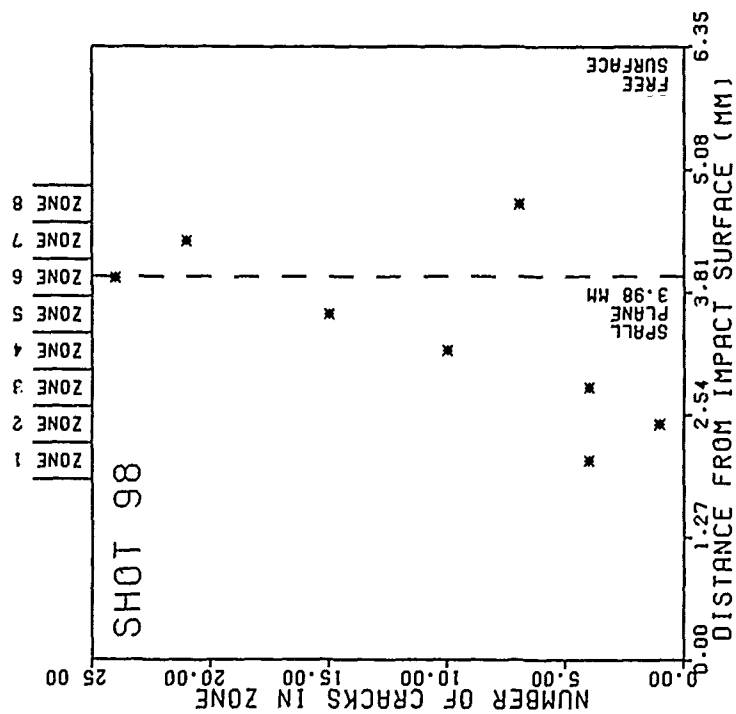


(a)

Figure J-1. Crack distributions for Shot 98 with stringer cracks excluded. (a) Digitized cracks on sectioned specimen surface. (b) Number of digitized cracks as a function of position. (c) Surface crack-size distributions. (d) Volume crack-size distributions. (e) Volume density of cracks as a function of position.

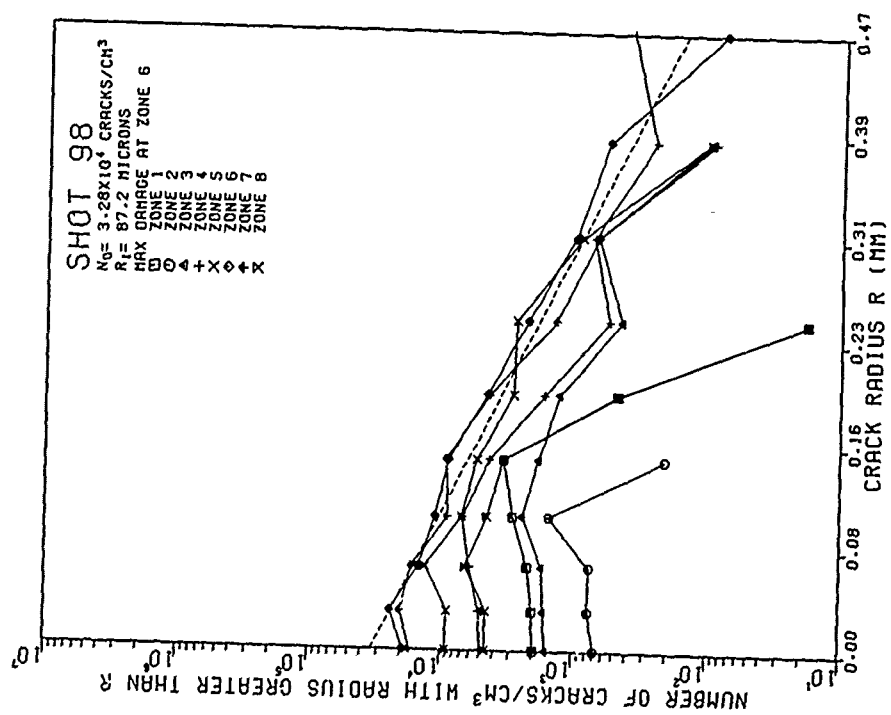


(c)

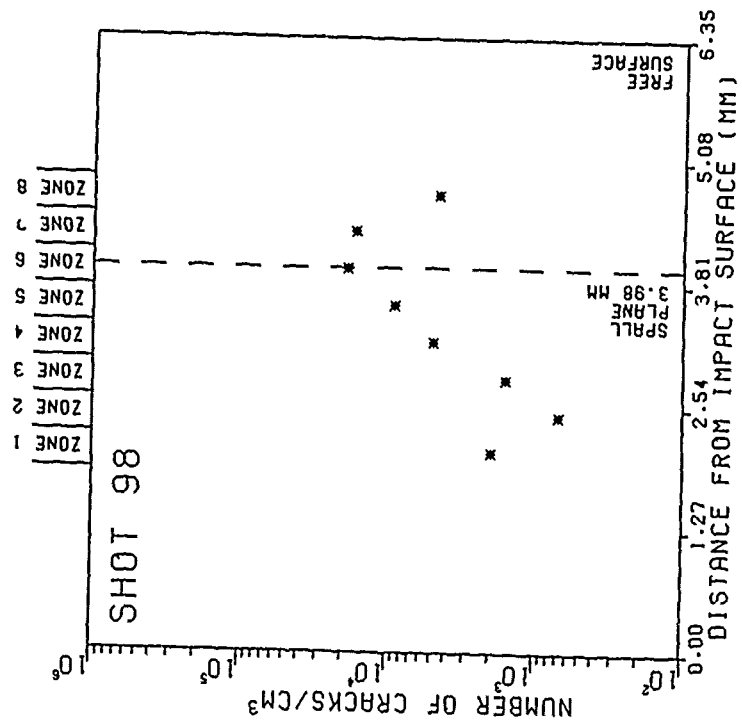


(b)

Figure J-1. (Continued)



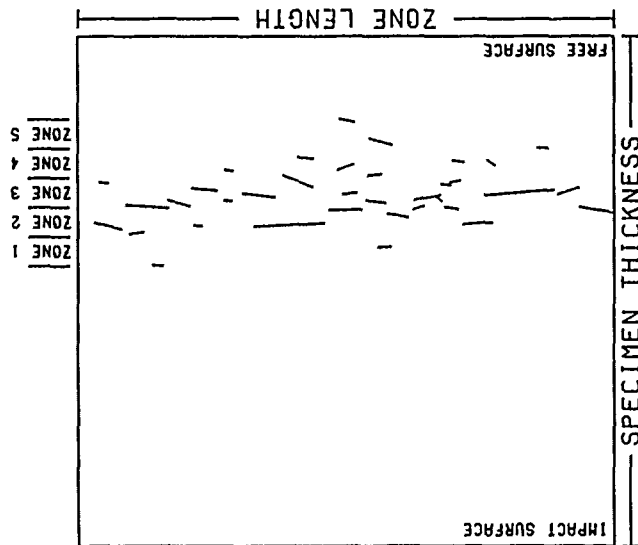
(d)



(e)

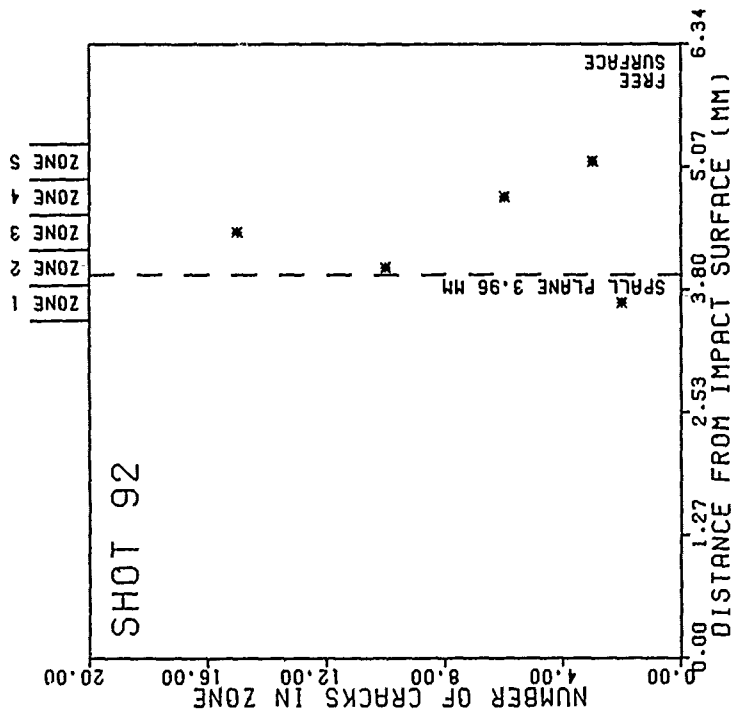
Figure J-1. (Continued)

SHOT 92
 IMPACTOR VELOCITY 0.180 KM/S
 IMPACTOR THICKNESS 2.38 MM
 SPECIMEN THICKNESS 6.34 MM
 NUMBER OF CRACKS 36
 NUMBER OF ZONES 5
 ZONE LENGTH 0.38 MM
 ZONE WIDTH 0.38 MM
 IMPACT SURFACE TO ZONE1 3.49 MM

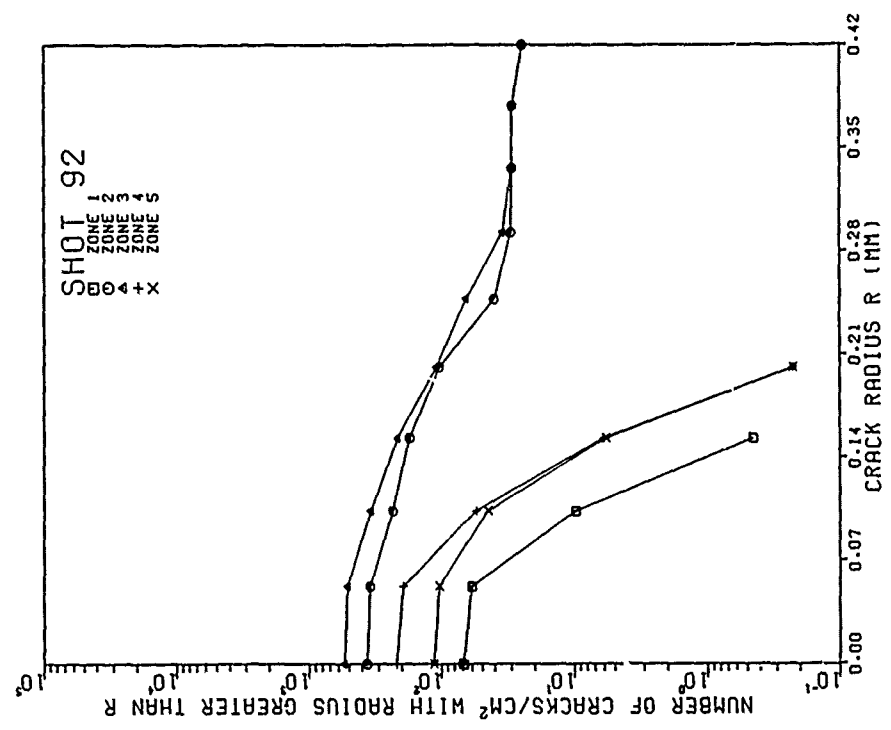


(a)

Figure J-2. Crack distributions for Shot 92 with stringer cracks excluded. (a) Digitized cracks on sectioned specimen surface. (b) Number of digitized cracks as a function of position. (c) Surface crack-size distributions. (d) Volume crack-size distributions. (e) Volume density of cracks as a function of position.

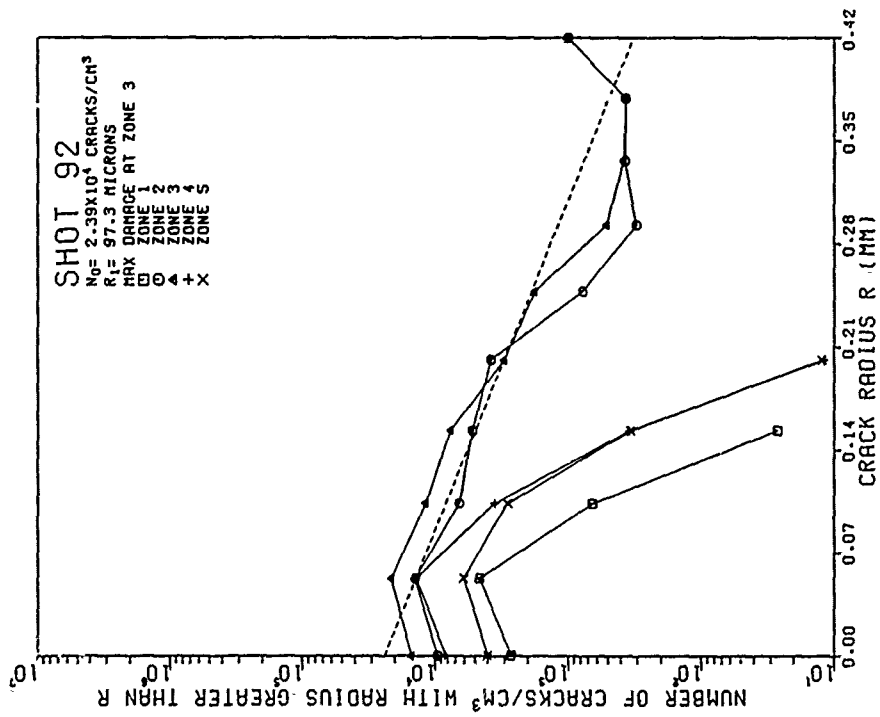


(b)

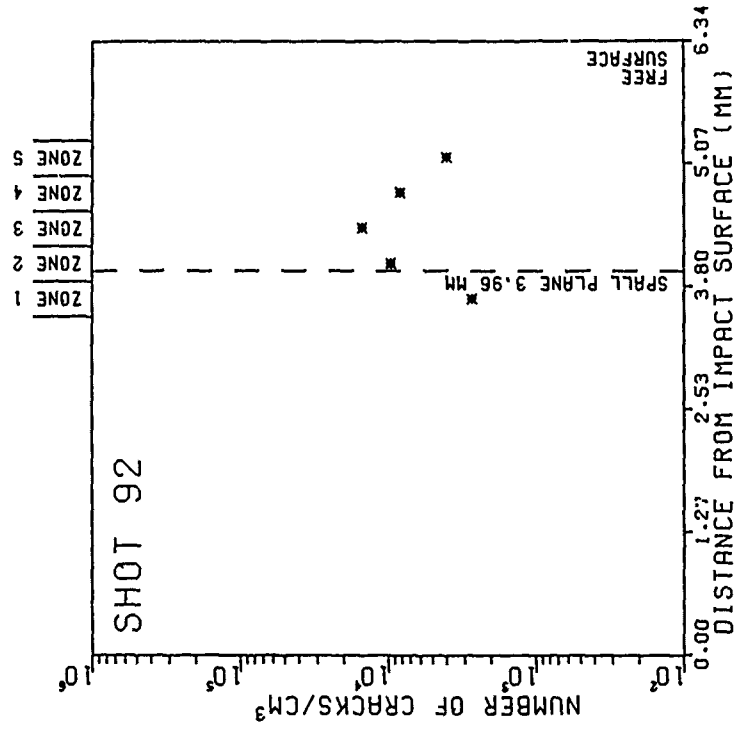


(c)

Figure J-2. (Continued)



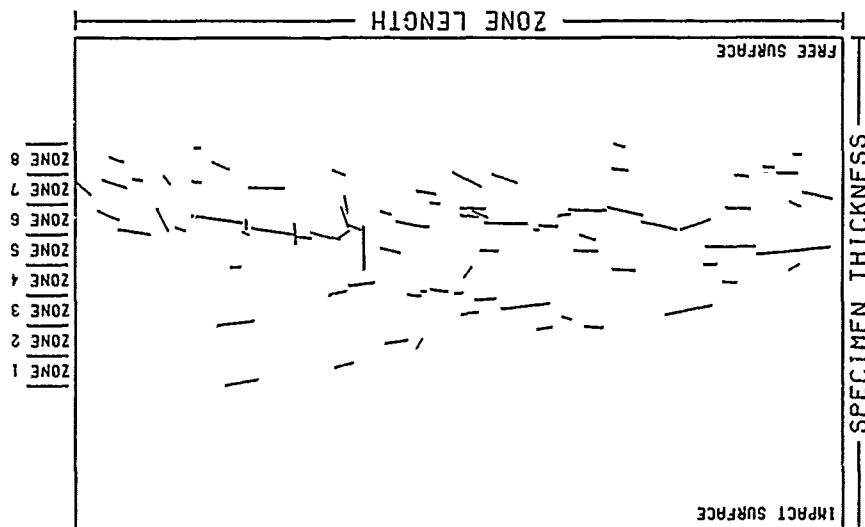
(d)



(e)

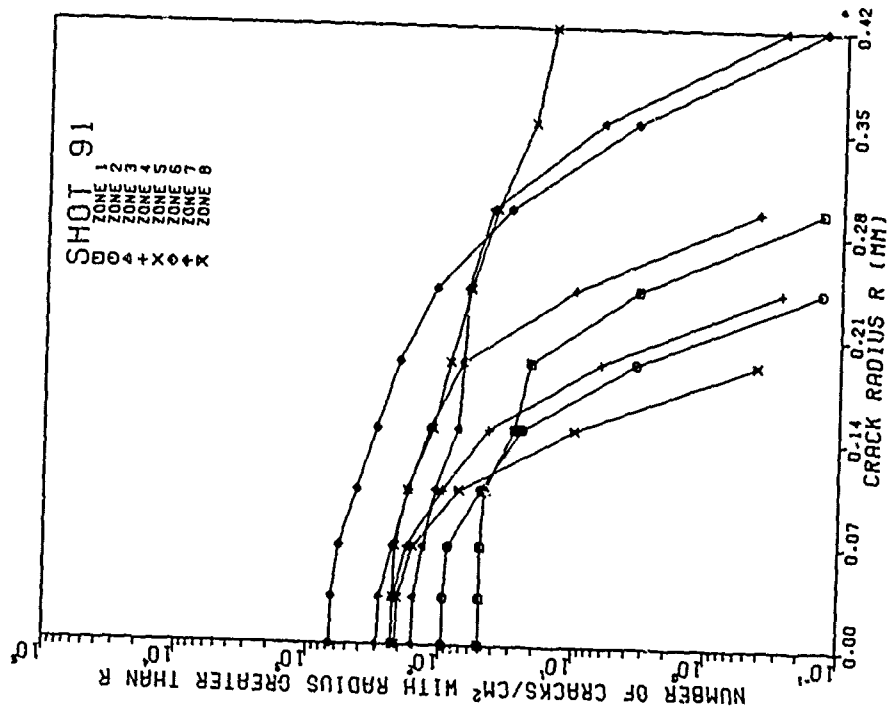
Figure J-2. (Continued)

SHOT 91
 IMPACTOR VELOCITY 0.193 KM/S
 SPECIMEN THICKNESS 2.37 MM
 SPECIMEN THICKNESS 6.34 MM
 NUMBER OF ZONES 82
 NUMBER OF ZONES 8
 ZONE LENGTH 10.16 MM
 ZONE WIDTH 0.39 MM
 IMPACT SURFACE TO ZONE1 1.85 MM

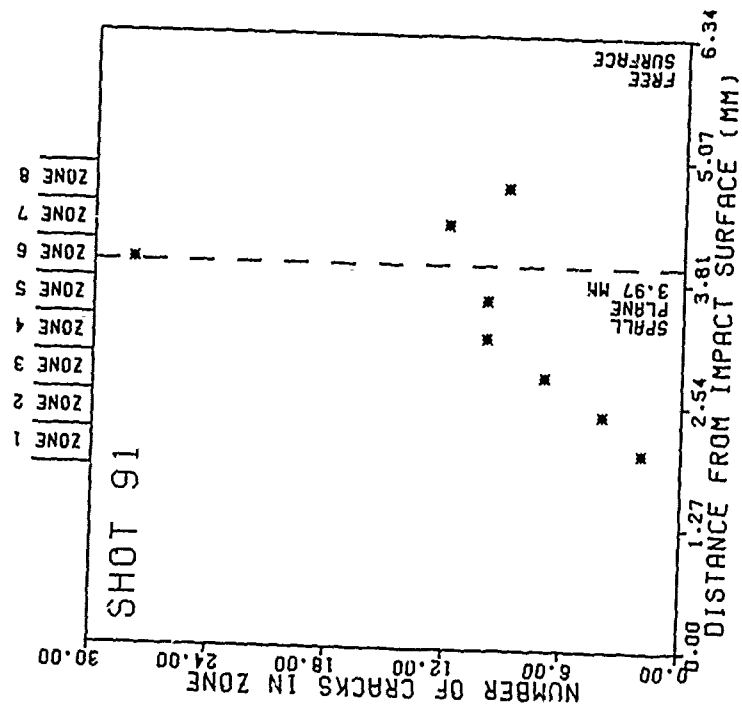


(a)

Figure J-3. Crack distributions for Shot 91 with stringer cracks excluded. (a) Digitized cracks on sectioned specimen surface. (b) Number of digitized cracks as a function of position. (c) Surface crack-size distributions. (d) Volume crack-size distributions. (e) Volume density of cracks as a function of position.

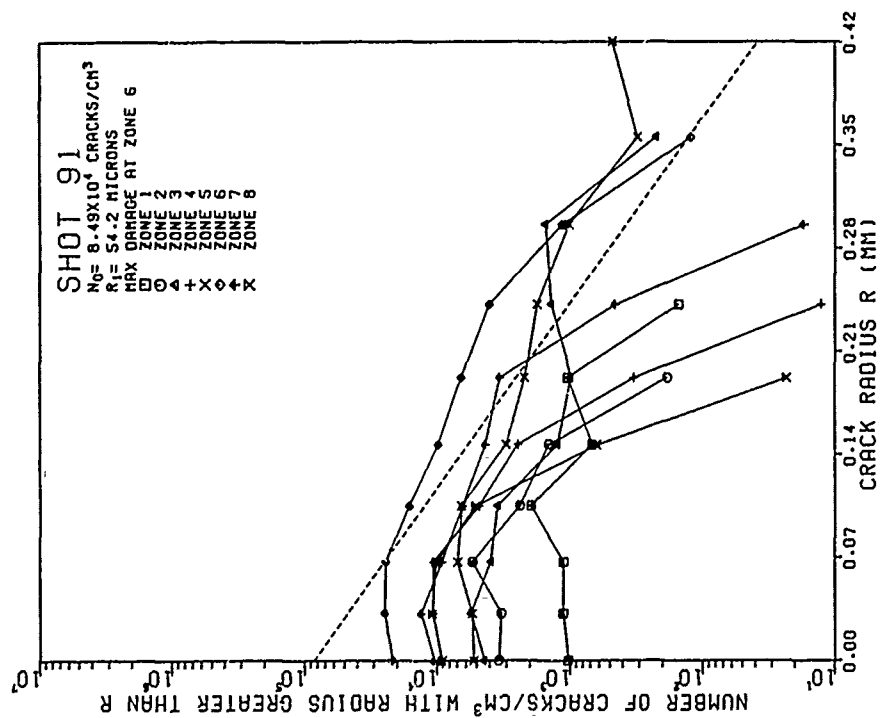


(c)

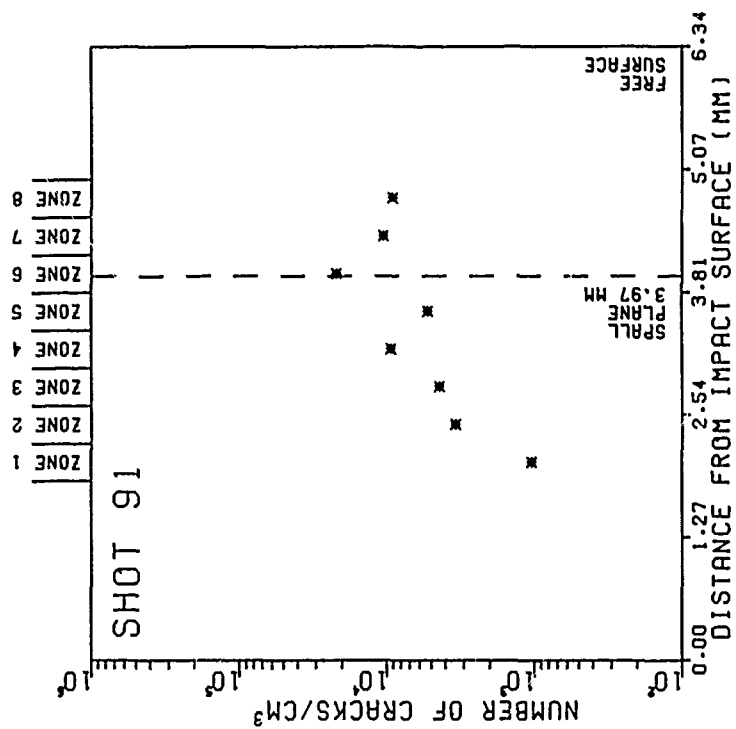


(b)

Figure J-3. (Continued)



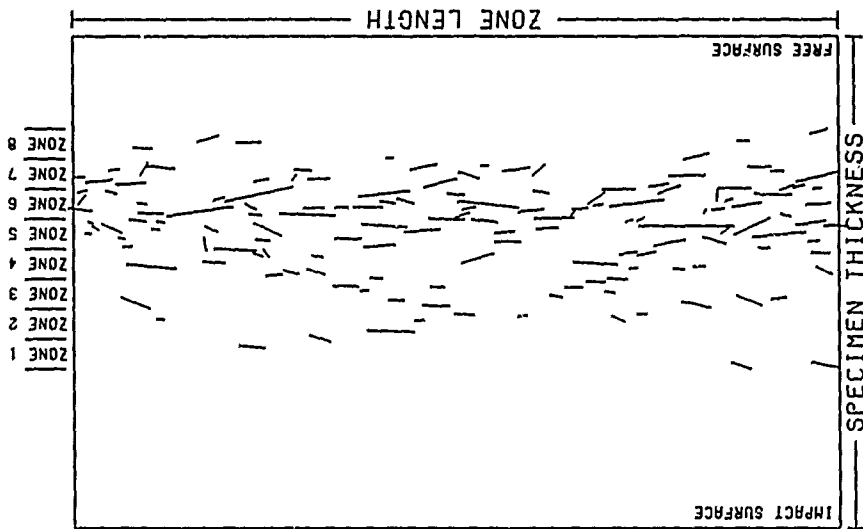
(d)



(e)

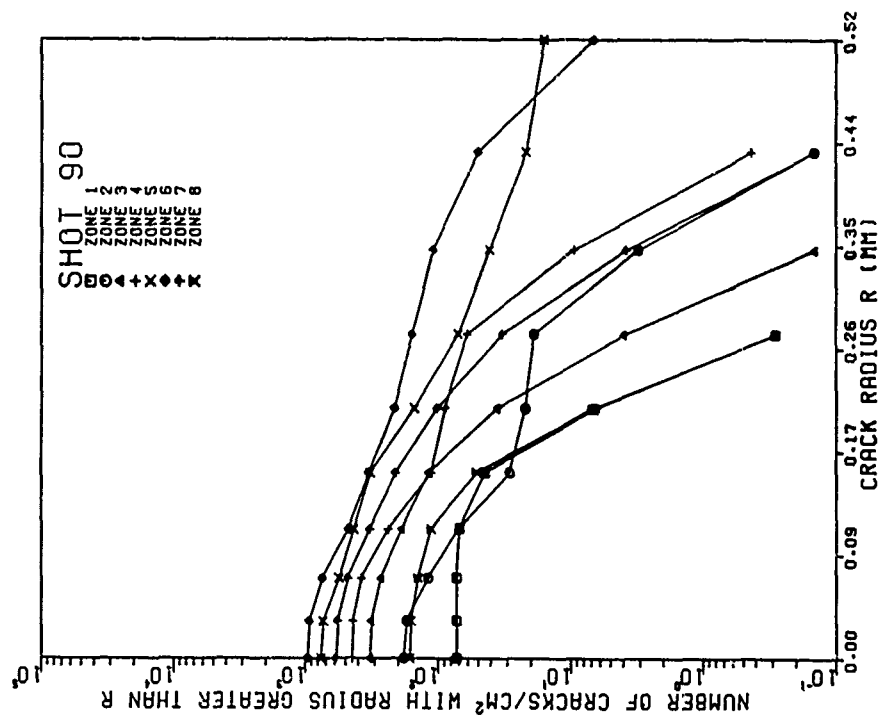
Figure J-3. (Continued)

SHOT 90
 IMPACTOR VELOCITY 0.191 KM/S
 IMPACTOR THICKNESS 2.37 MM
 SPECIMEN THICKNESS 8.35 MM
 NUMBER OF CRACKS 153
 NUMBER OF ZONES 8
 ZONE LENGTH 10.16 MM
 ZONE WIDTH 0.39 MM
 IMPACT SURFACE 0 ZONE1 2.05 MS

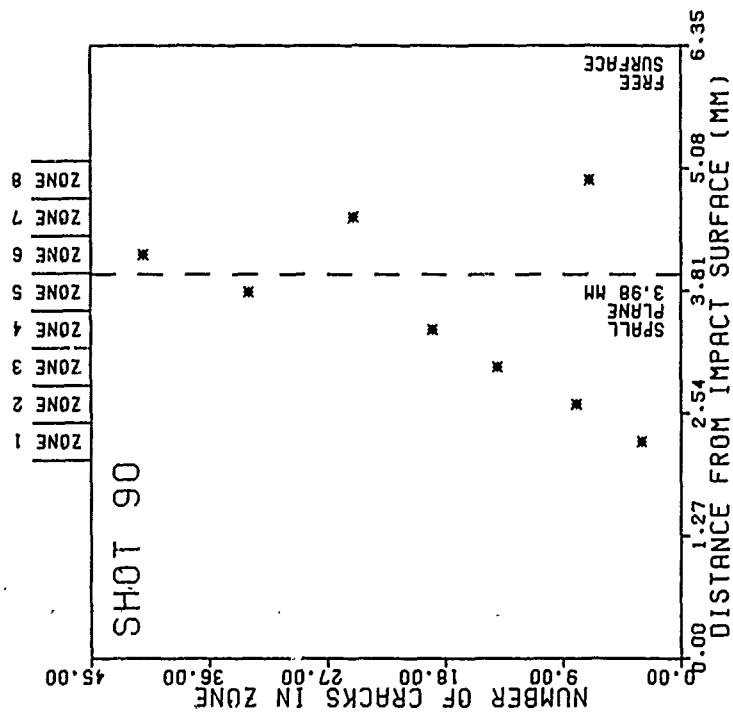


(a)

Figure J-4. Crack distributions for Shot 90 with stringer cracks excluded. (a) Digitized cracks on sectioned specimen surface. (b) Number of digitized cracks as a function of position. (c) Surface crack-size distributions. (d) Volume crack-size distributions. (e) Volume density of cracks as a function of position.

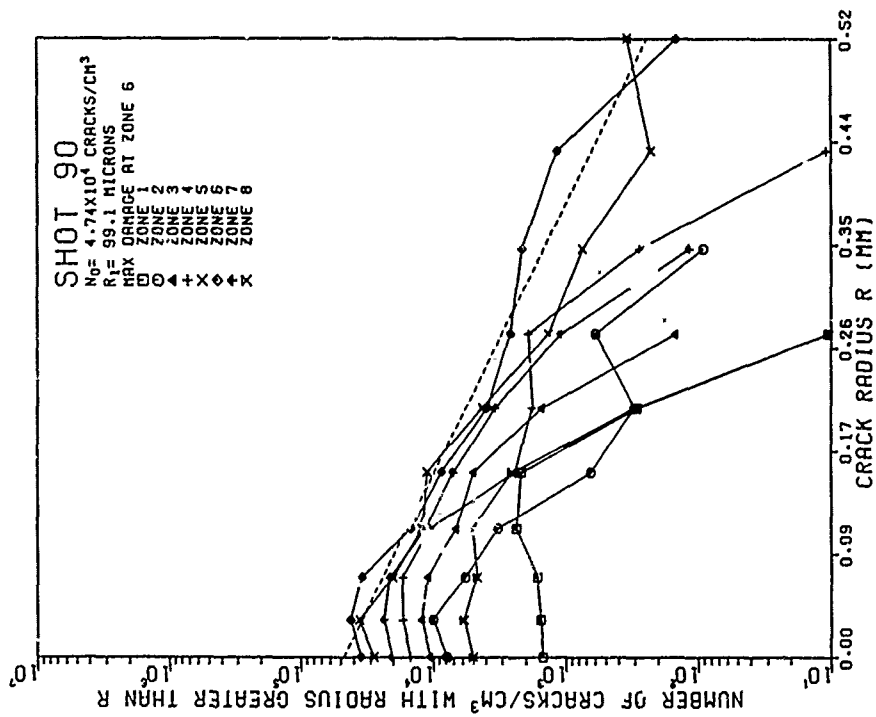


(c)

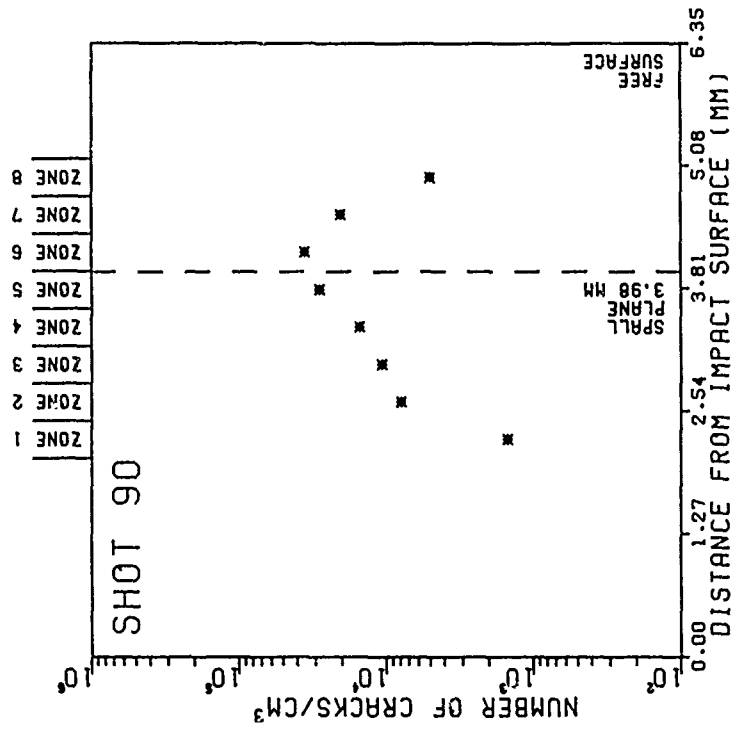


(b)

Figure J-4. (Continued)



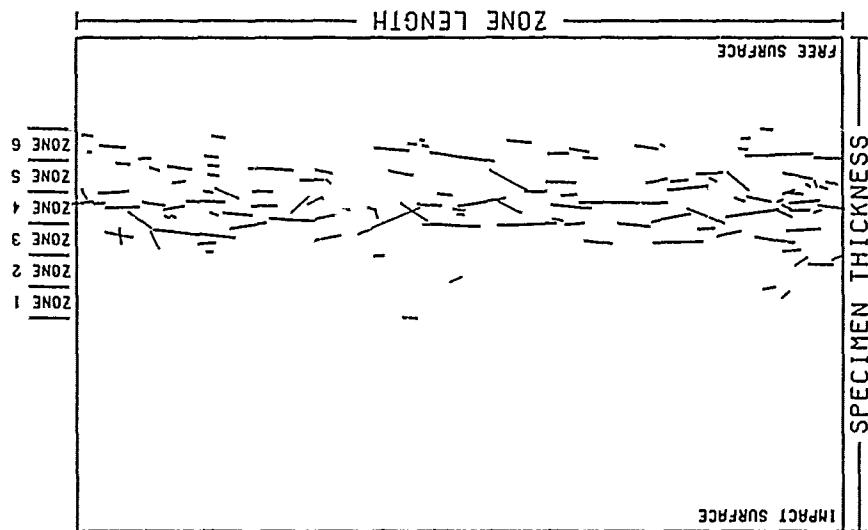
(d)



(e)

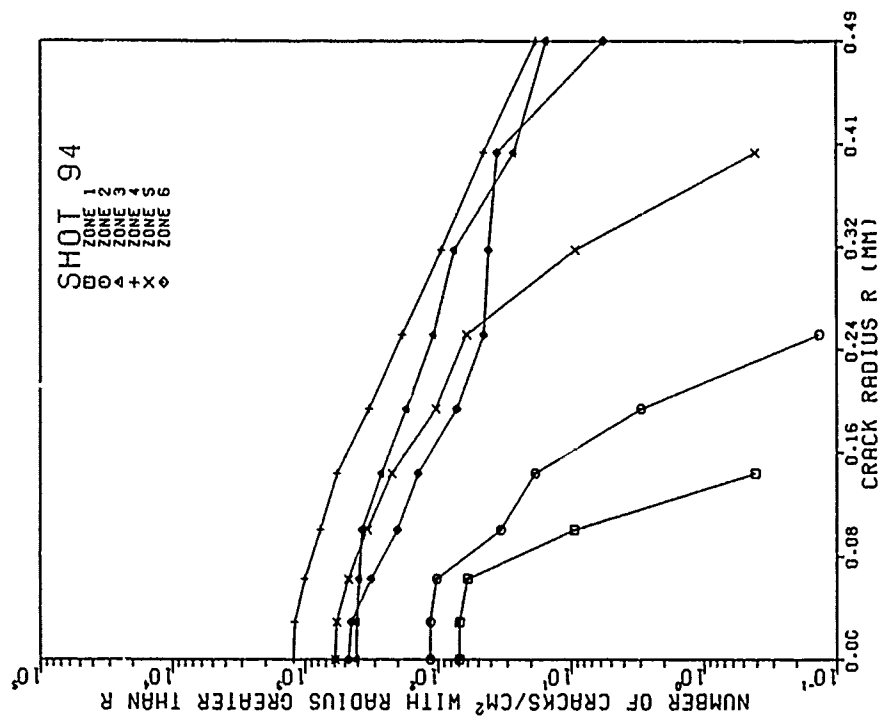
Figure J-4. (Continued)

SHOT 94
 IMPACTOR VELOCITY 0.200 KM/S
 IMPACTOR THICKNESS 2.37 MM
 SPECIMEN THICKNESS 6.36 MM
 NUMBER OF CRACKS 129
 ZONE LENGTH 0.6 MM
 ZONE HEIGHT 0.41 MM
 IMPACT SURFACE TO ZONE1 2.75 MM

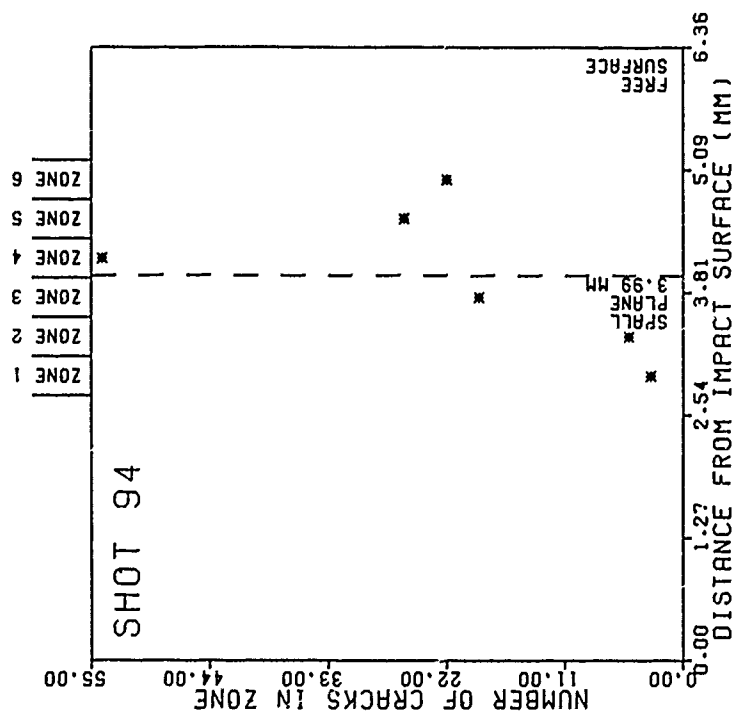


(a)

Figure J-5. Crack distributions for Shot 94 with stringer cracks excluded. (a) Digitized cracks on sectioned specimen surface. (b) Number of digitized cracks as a function of position. (c) Surface crack-size distributions. (d) Volume crack-size distributions. (e) Volume density of cracks as a function of position.

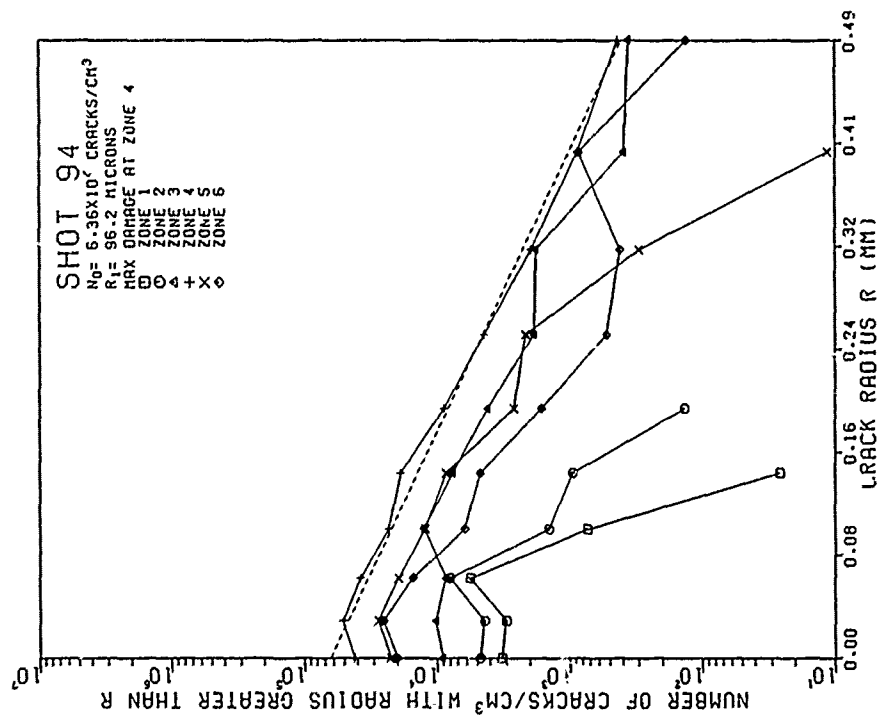


(c)

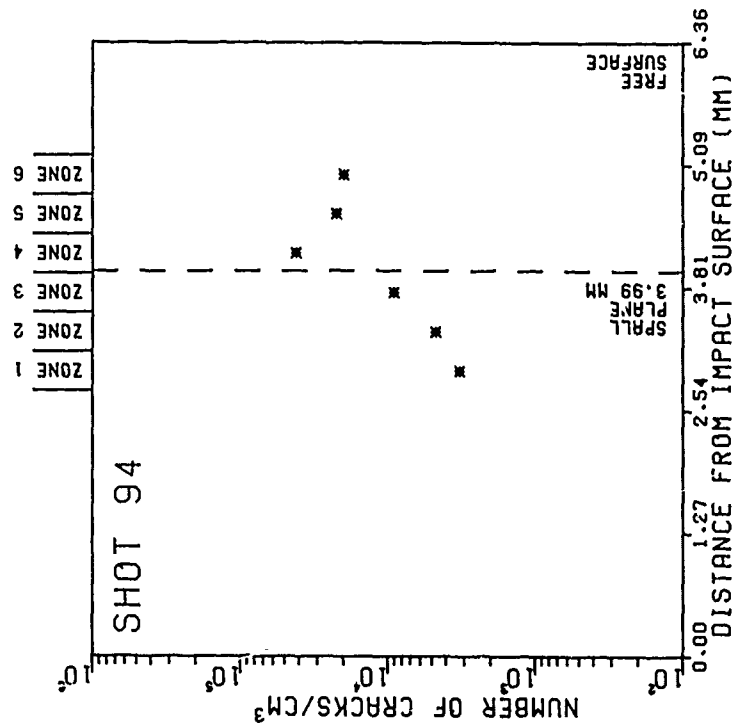


(b)

Figure J-5. (Continued)



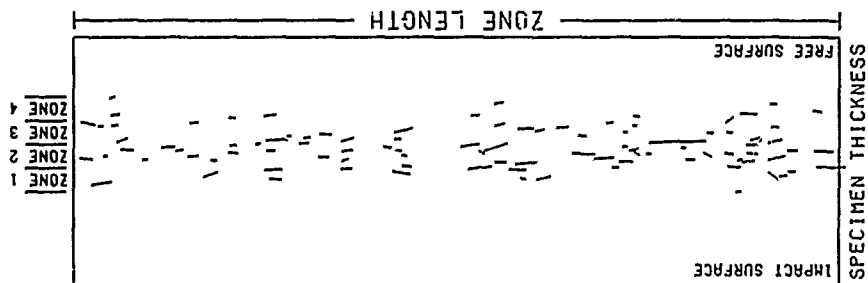
(d)



(e)

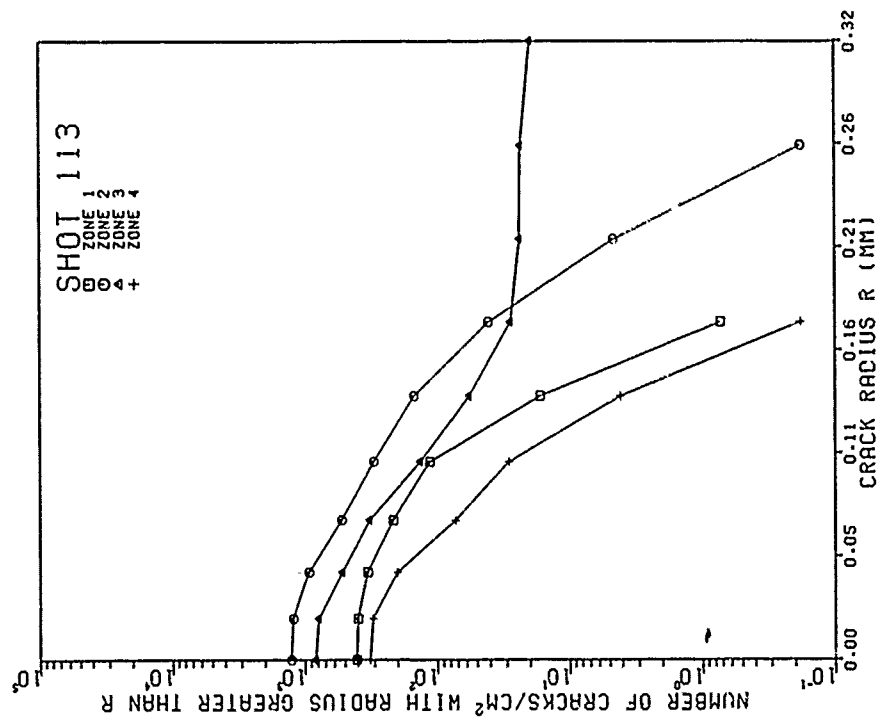
Figure J-5. (Continued)

SHOT 113
 IMPACTOR VELOCITY 0.202 KM/S
 IMPACTOR THICKNESS 1.60 MM
 SPECIMEN THICKNESS 3.19 MM
 NUMBER OF CRACKS 88
 NUMBER OF ZONES 4
 ZONE LENGTH 13.18 MM
 ZONE WIDTH 0.30 MM
 IMPACT SURFACE TO ZONE1 1.21 MM

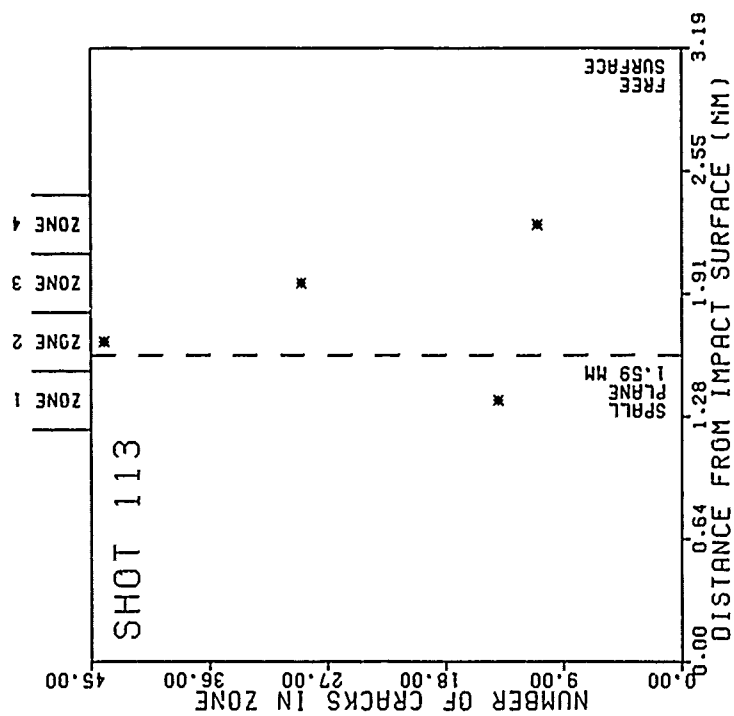


(a)

Figure J-6. Crack distributions for Shot 113 with stringer cracks excluded. (a) Digitized cracks on sectioned specimen surface. (b) Number of digitized cracks as a function of position. (c) Surface crack-size distributions. (d) Volume crack-size distributions. (e) Volume density of cracks as a function of position.

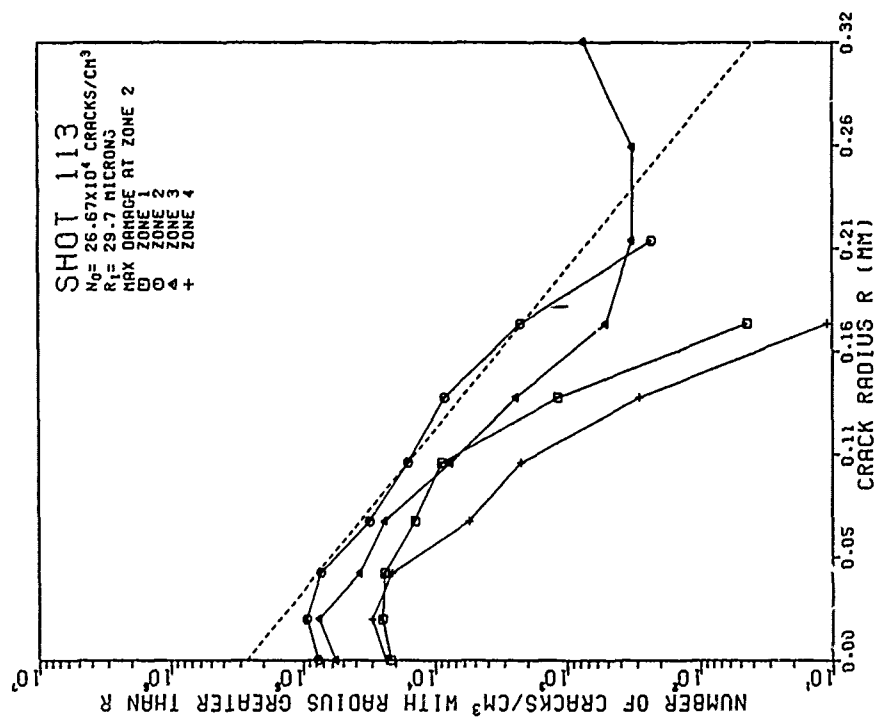


(c)

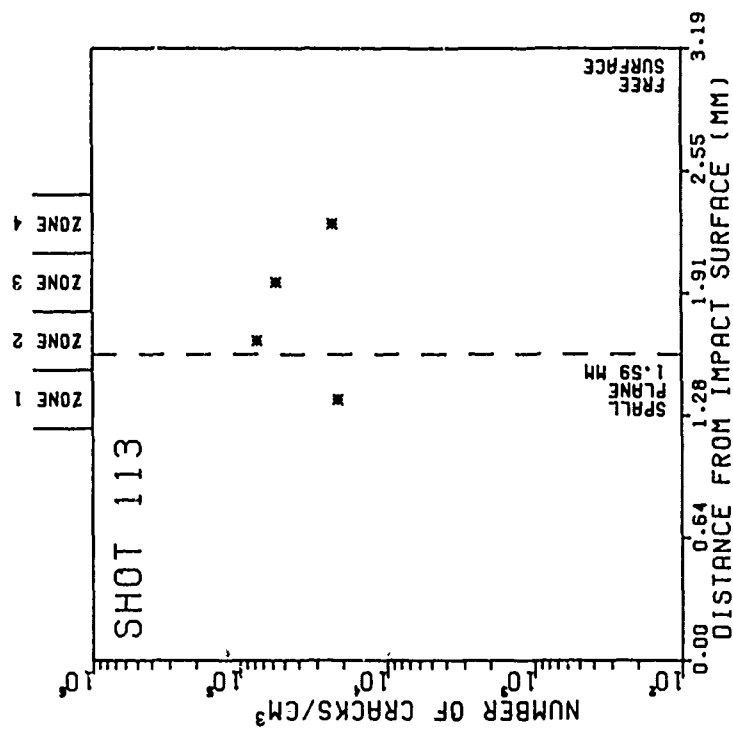


(b)

Figure J-6. (Continued)



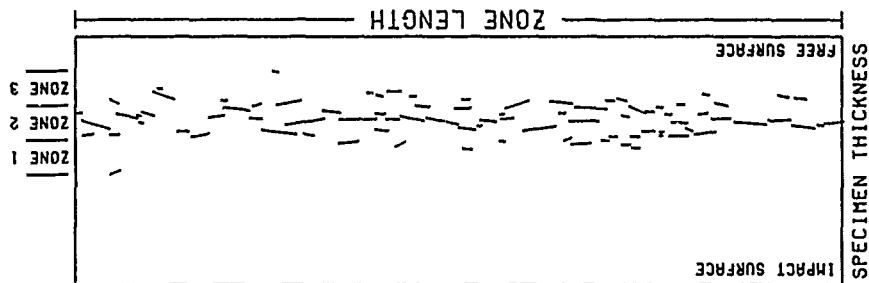
(d)



(e)

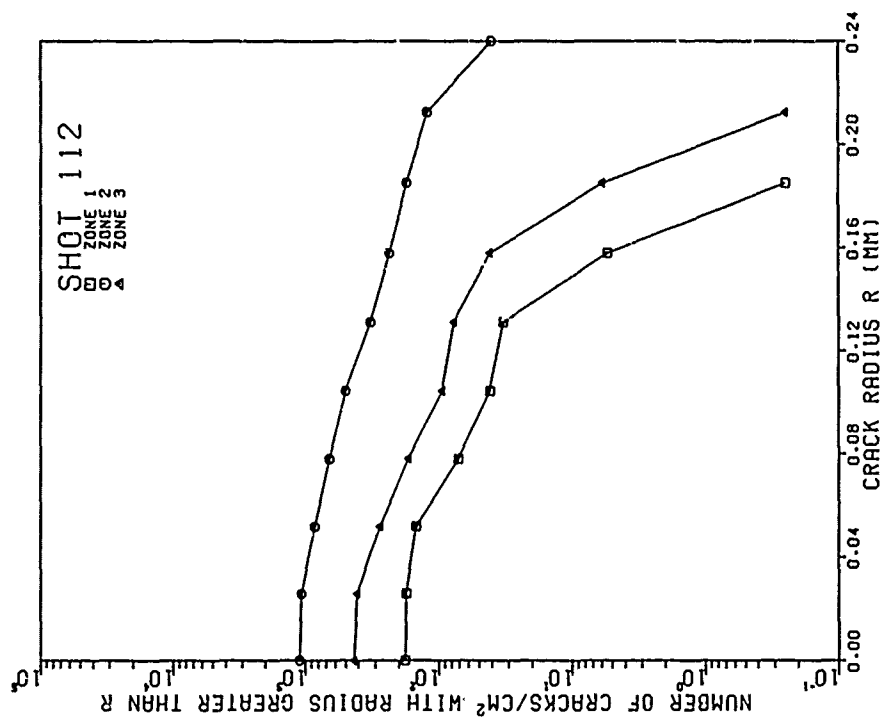
Figure J-6. (Continued)

SHOT 112
 IMPACTOR VELOCITY 0.204 KM/S
 IMPACTOR THICKNESS 1.18 MM
 SPECIMEN THICKNESS 3.19 MM
 NUMBER OF ZONES 36
 ZONE LENGTH 10.16 MM
 ZONE WIDTH 0.44 MM
 IMPACT SURFACE TO ZONE1 1.42 MM

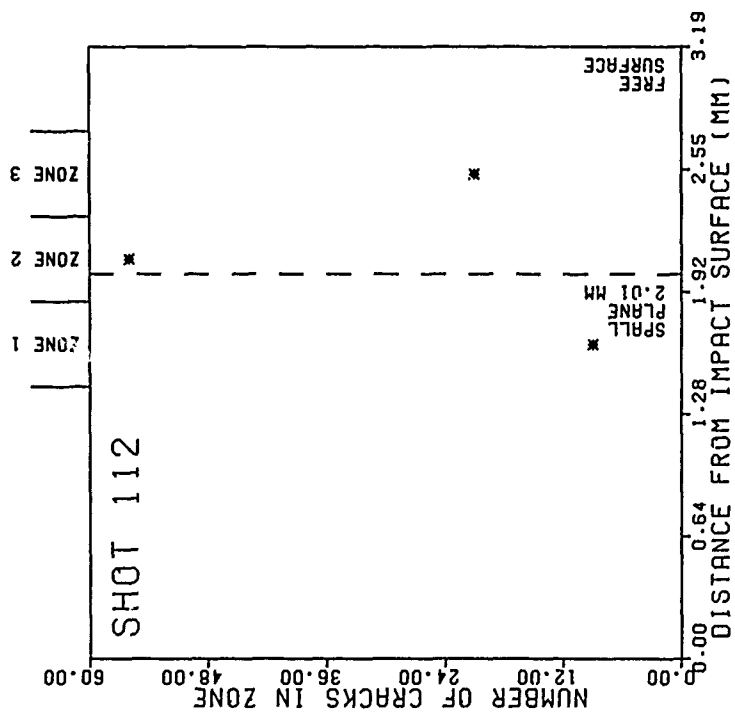


(a)

Figure J-7. Crack distributions for Shot 112 with stringer cracks excluded. (a) Digitized cracks on sectioned specimen surface. (b) Number of digitized cracks as a function of position. (c) Surface crack-size distributions. (d) Volume crack-size distributions. (e) Volume density of cracks as a function of position.

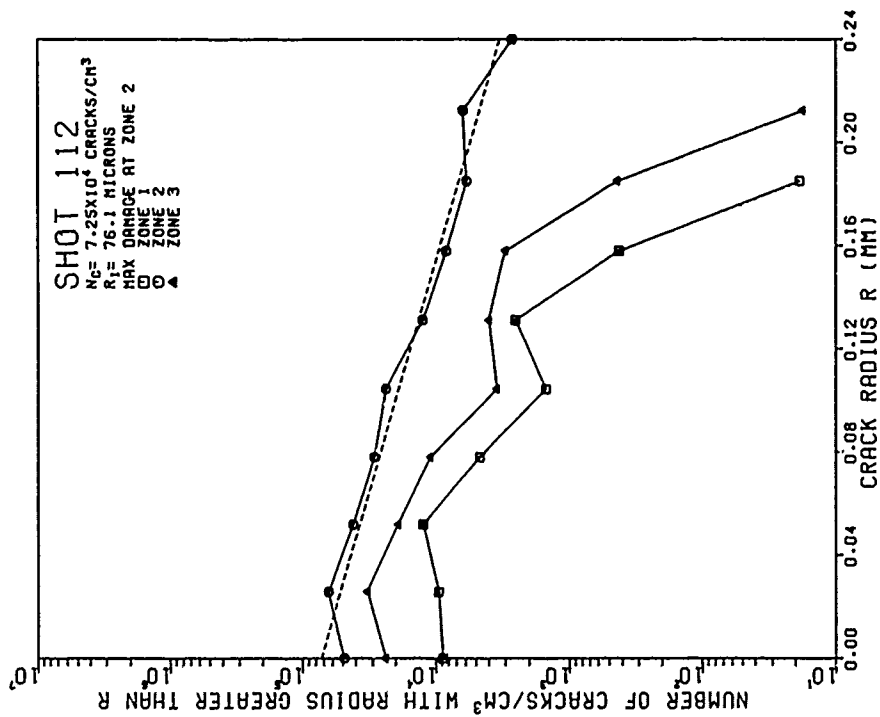


(c)

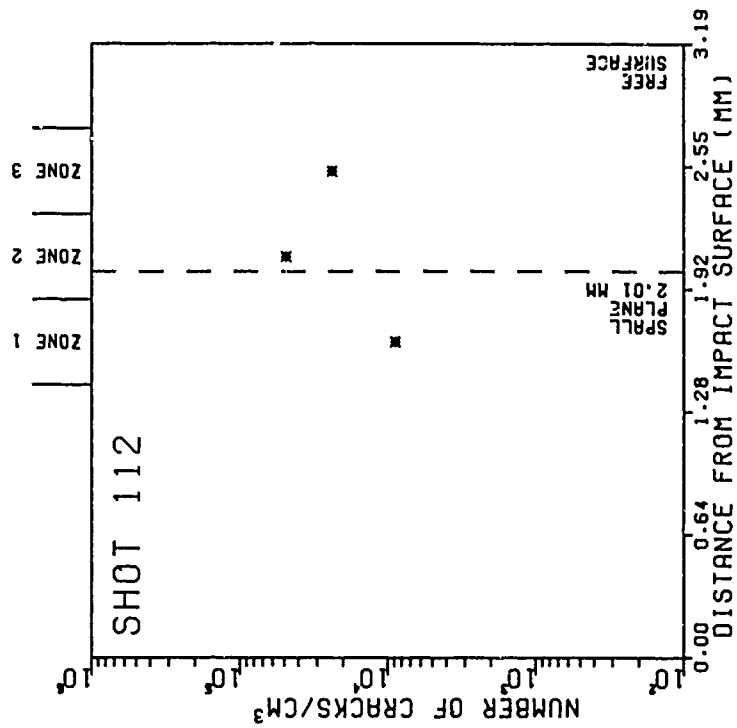


(b)

Figure J-7. (Continued)

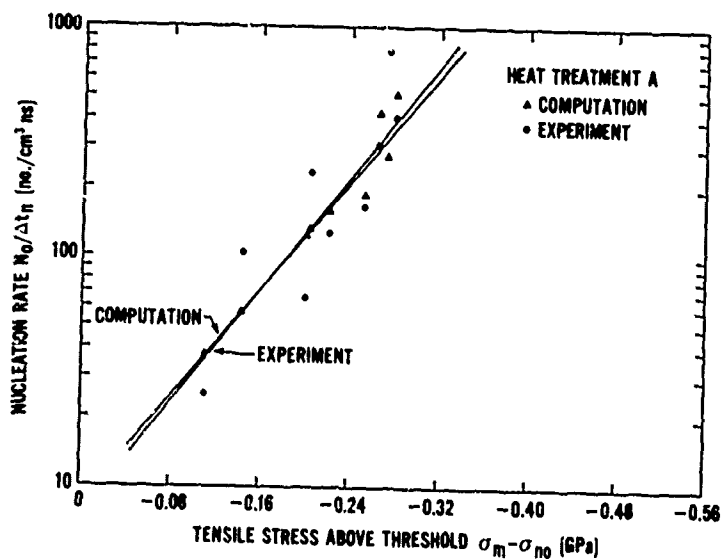


(d)

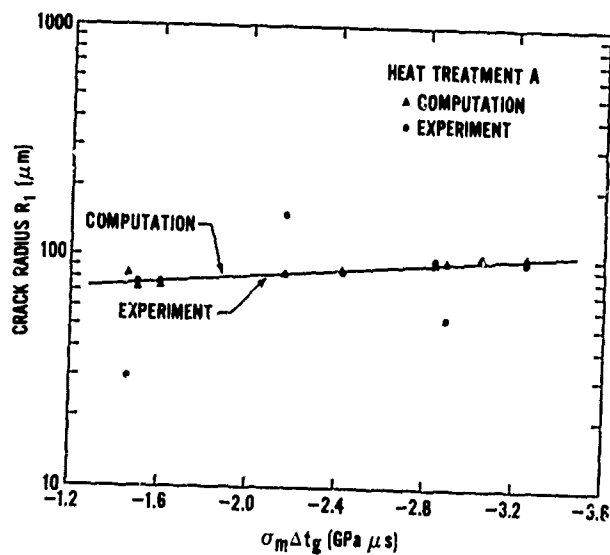


(e)

Figure J-7. (Continued)



(a)



(b)

Figure J-8 Experimental and computed nucleation rate and growth curves for HF-1 steel with heat treatment A with stringer cracks excluded. (a) Nucleation rate curves. (b) Growth curves. The points in these plots are from Table J-2 and were obtained by using the final set of dynamic fracture parameters for this heat treatment of HF-1 steel in a PUFF 8 computation.

DATE = 11/16/78
 IDENT HF-1 STEEL. SHOT 92. 590 FPS. DAMAGE.
 NTEOT= 0 NJEDIT= 3 NREZON= 0 NALPHA
 JEDITS= S1,10,11,12,13,14,15,16,17,18,19,20,21,22,23,24,25,26,27,28,29
 JEDITS= NEM,19,20,21,22,23,24,25,26,27,28
 JEDITS= NET,19,20,21,22,23,24,25,26,27,28
 NEDIT= 5 JCYCS= 150 CKS= 3.000E+00 TS= 1.037E-05 IN= 5 , , , CM, SEC
 NMTRLS= 1 MATFL= 1 UZERO= 1.000E+00 IN= 5 , , , CM/SEC
 HF1 STEEL RHOS= 7.774E+00 CFP = 050 OPV = 001 NVAR= 10
 EQST = 1.605E+12 3.561E+12 7.360E+10 1.660E+00 2.500E-01 3.687 +12 0.
 TSRI = -4.090E-05 -1.010E+09 5.870E-03 4.220E+10 -2.500E+10 -5.57 +08 0.
 TSRI = -2.500E+10 0. 2.500E-01 5.000E-01 4.000E-01 3.000E+00 0.
 Y8= 1.361E+10 7.912E+11 0. 0. 0. 0. 0.
 NLAYER= 2 JMAT= 1 1 0 0 0 0 0 0 0 0
 NZONES= 1 8 CELLS IN 2.372E-01 CM 0. 0. 0.
 NZONES= 1 2 CELLS IN 6.336E-01 CM 0. 0. 0.

(a)

DATE = 11/16/78
 IDENT HF-1 STEEL. SHOT 91. 501 FPS. DAMAGE.
 NTEOT= 0 NJEDIT= 3 NREZON= 0 NALPHA
 JEDITS= S1,10,11,12,13,14,15,16,17,18,19,20,21,22,23,24,25,26,27,28,29
 JEDITS= NEM,19,20,21,22,23,24,25,26,27,28
 JEDITS= NET,19,20,21,22,23,24,25,26,27,28
 NEDIT= 5 JCYCS= 150 CKS= 3.000E+00 TS= 1.000E-05 IN= 5 , , , CM, SEC
 NMTRLS= 1 MATFL= 1 UZERO= 1.030E+00 IN= 5 , , , CM/SEC
 HF1 STEEL RHOS= 7.774E+00 CFP = 050 OPV = 001 NVAR= 10
 EQST = 1.605E+12 3.561E+12 7.360E+10 1.660E+00 2.500E-01 3.687 +12 0.
 TSRI = -4.090E-05 -1.010E+09 5.870E-03 4.220E+10 -2.500E+10 -5.57 +08 0.
 TSRI = -2.500E+10 0. 2.500E-01 5.000E-01 4.000E-01 3.000E+00 0.
 Y8= 1.361E+10 7.912E+11 0. 0. 0. 0. 0.
 NLAYER= 2 JMAT= 1 1 0 0 0 0 0 0 0 0
 NZONES= 1 8 CELLS IN 2.372E-01 CM 0. 0. 0.
 NZONES= 1 2 CELLS IN 6.336E-01 CM 0. 0. 0.

(b)

Figure J-10. PUFF input parameters for (a) Shot 92 and (b) Shot 91 with stringer cracks excluded.


```

DATE = 11/16/78
IDENT HF-1 STEEL SHOT 113. 662 FPS DAMAGE.
NTEUT= 0 NJECT= 3 N. ONE
JEDITS= S1,13,11,12,13,14,15,16,17,18,19,20,21,22,23,24,25,26,27,28,29
JEDITS= NE1,16,17,18,19,20,21,22,23,24,25
JEDITS= NE1,16,17,18,19,20,21,22,23,24,25
NEDITS= 5 JCYCS= 150 CKS= 3.00E+00 TS= 1.000E-05 IN= 5 , , CM, SEC
NMTALS= 1 NATFL= 1 UZERO= 2.02E+04 000000000 IN= 5 , , CM/SEC

HF1 STEEL
EQST = 1.605E+12 3.561E+12 7.774E+08 CFP = 050 CFP = 001 NVAF= 10
TSR1 = -4.090E-05 -1.000E+03 1.660E+00 2.500E-01 3.583E+12 0.
TSR2 = -2.500E+10 0. 2.500E-03 5.670E-03 4.220E+10 -2.500E+10 -5.570E+05 0.
Y0= 1.361E+10 7.912E+11 0. 0. 0. 0. 0. 0.

NLAYER= 2 JNATE= 1 1 0 0 0 0 0 0
NZONES= 1 8 CELLS IN 1.596E-01 CM 0.
NZONES= 1 20 CELLS IN 3.149E-01 CM 0.

```

(a)

```

DATE = 11/16/78
IDENT HF-1 STEEL SHOT 111. 633 FPS DAMAGE.
NTEUT= 0 NJECT= 3 NREZON=
JEDITS= S1,10,11,12,13,14,15,16,17,18,19,20,21,22,23,24,25,26,27,28,29
JEDITS= NE1,19,20,21,22,23,24,25,26,27,28
JEDITS= NE1,19,20,21,22,23,24,25,26,27,28
NEDITS= 5 JCYCS= 150 CKS= 3.000E+00 TS= 1.000E-05 IN= 5 , , CM, SEC
NMTALS= 1 NATFL= 1 UZERO= 1.930E+04 000000000 IN= 5 , , CM/SEC

HF1 STEEL
EQST = 1.605E+12 3.561E+12 7.774E+08 CFP = 050 CFP = 001 NVAF= 10
TSR1 = -4.390E-05 -1.000E+03 1.660E+00 2.500E-01 3.583E+12 0.
TSR2 = -2.500E+10 0. 2.500E-03 5.670E-03 4.220E+10 -2.500E+10 -5.570E+05 0.
Y0= 1.361E+10 7.912E+11 0. 0. 0. 0. 0. 0.

NLAYER= 2 JNATE= 1 1 0 0 0 0 0 0
NZONES= 1 8 CELLS IN 1.156E-01 CM 0.
NZONES= 1 20 CELLS IN 3.145E-01 CM 0.

```

(b)

Figure J-12. PUFF input parameters for (a) Shot 113 and (b) Shot 111 with stringer cracks excluded.

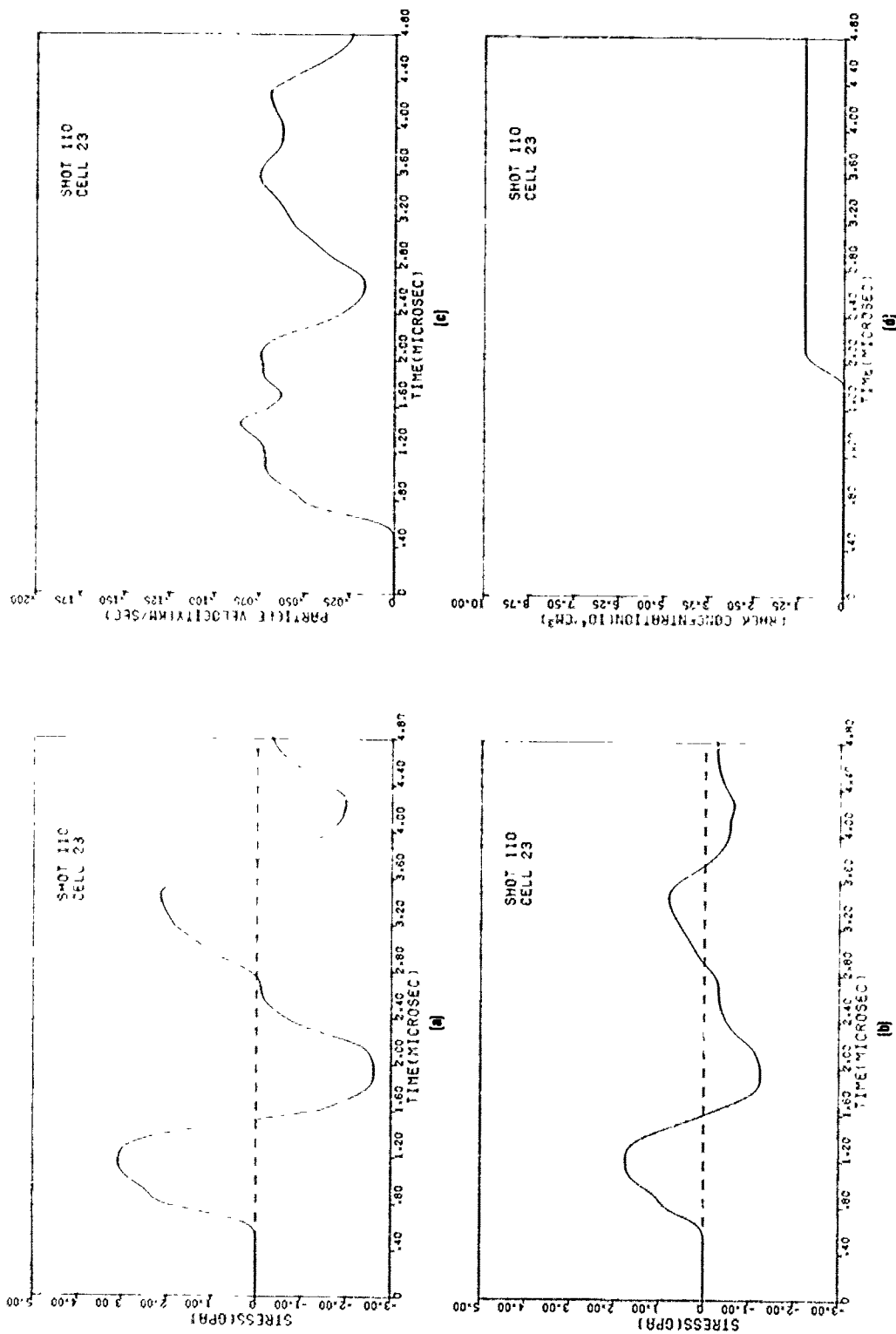


Figure J-14. Computed shock histories in cell 23 for Shot 110 with stringer cracks excluded. (a) Parallel stress. (b) Perpendicular stress. (c) Particle velocity. (d) Crack concentration.

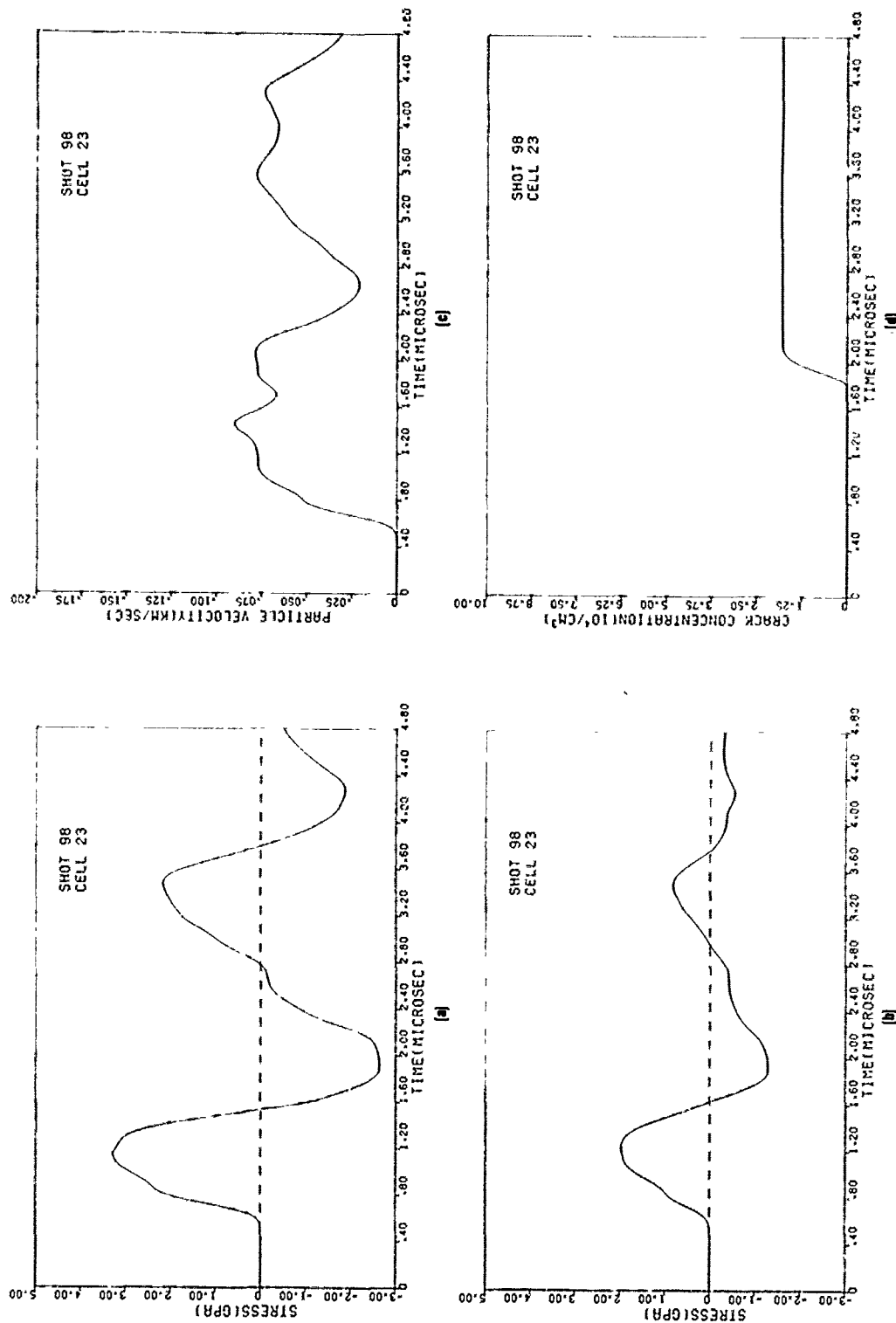


Figure J-15. Computed shock histories in cell 23 for Shot 98 with stringer cracks excluded. (a) Parallel stress. (b) Perpendicular stress. (c) Particle velocity. (d) Crack concentration.

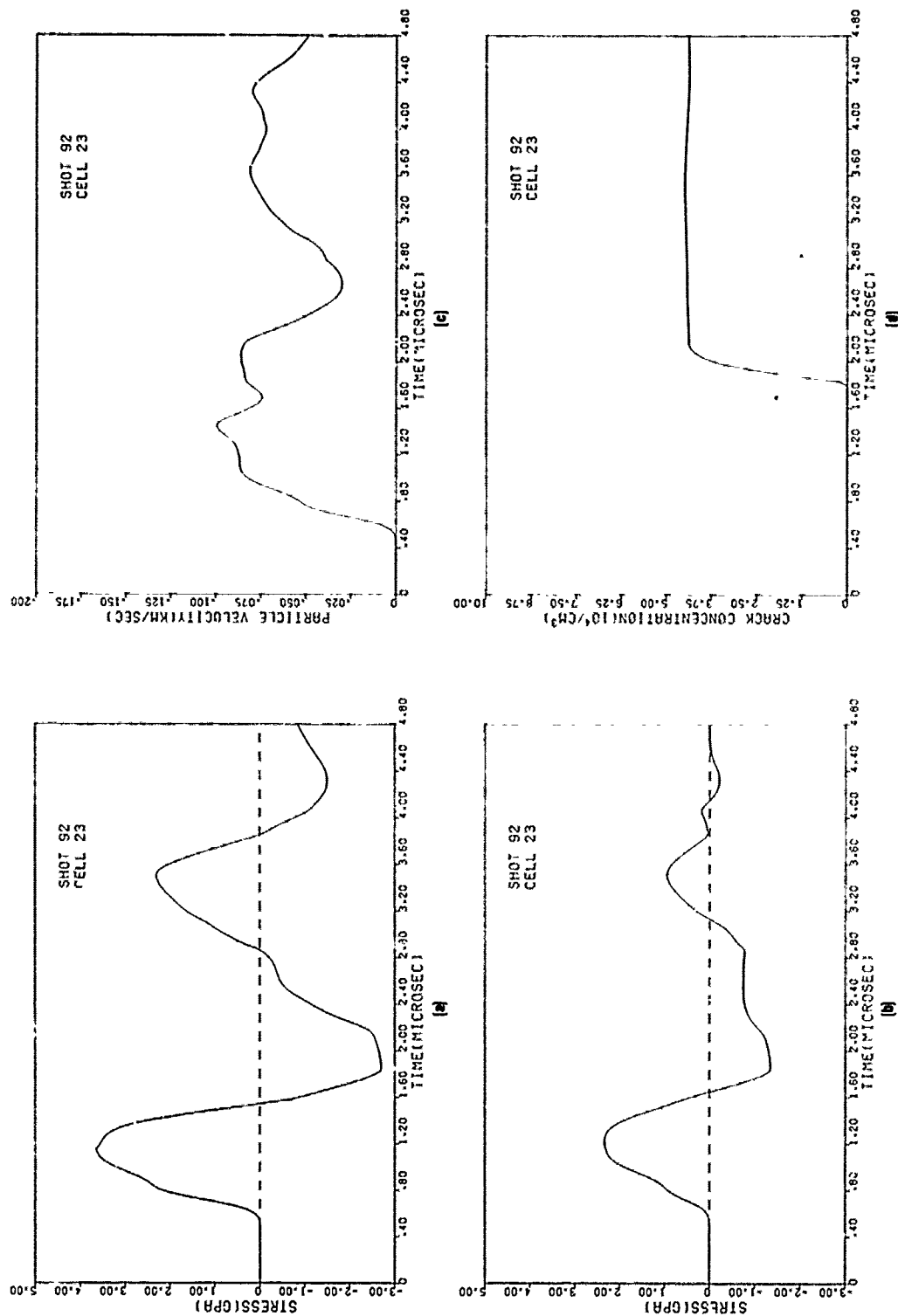


Figure J-16. Computed shock histories in cell 23 for Shot 92 with stringer cracks excluded. (a) Parallel stress. (b) Perpendicular stress. (c) Particle velocity. (d) Crack concentration.

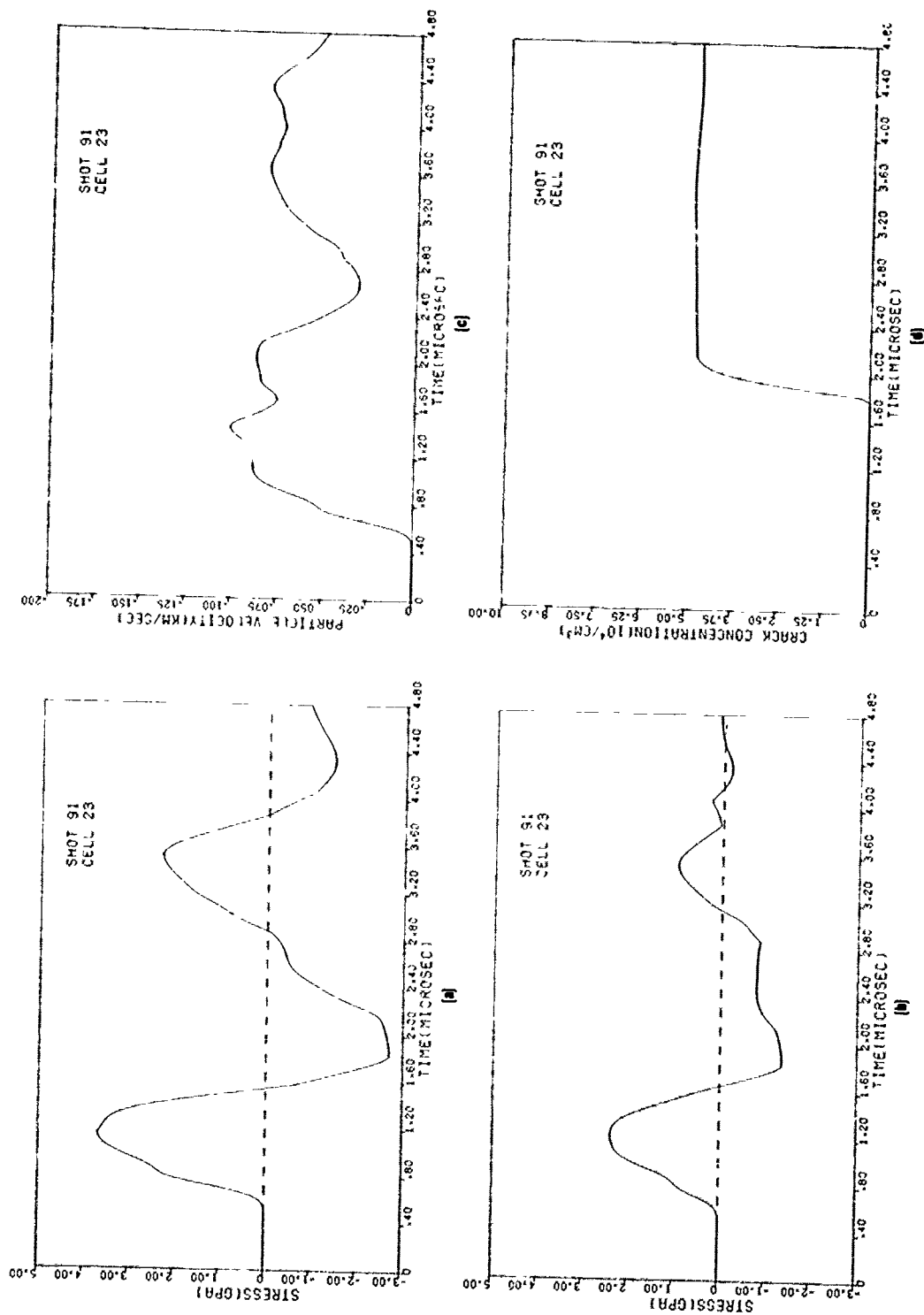


Figure J-17. Computed shock histories in cell 23 for Shot 91 with stringer cracks excluded. (a) Parallel stress. (b) Perpendicular stress. (c) Particle velocity. (d) Crack concentration.

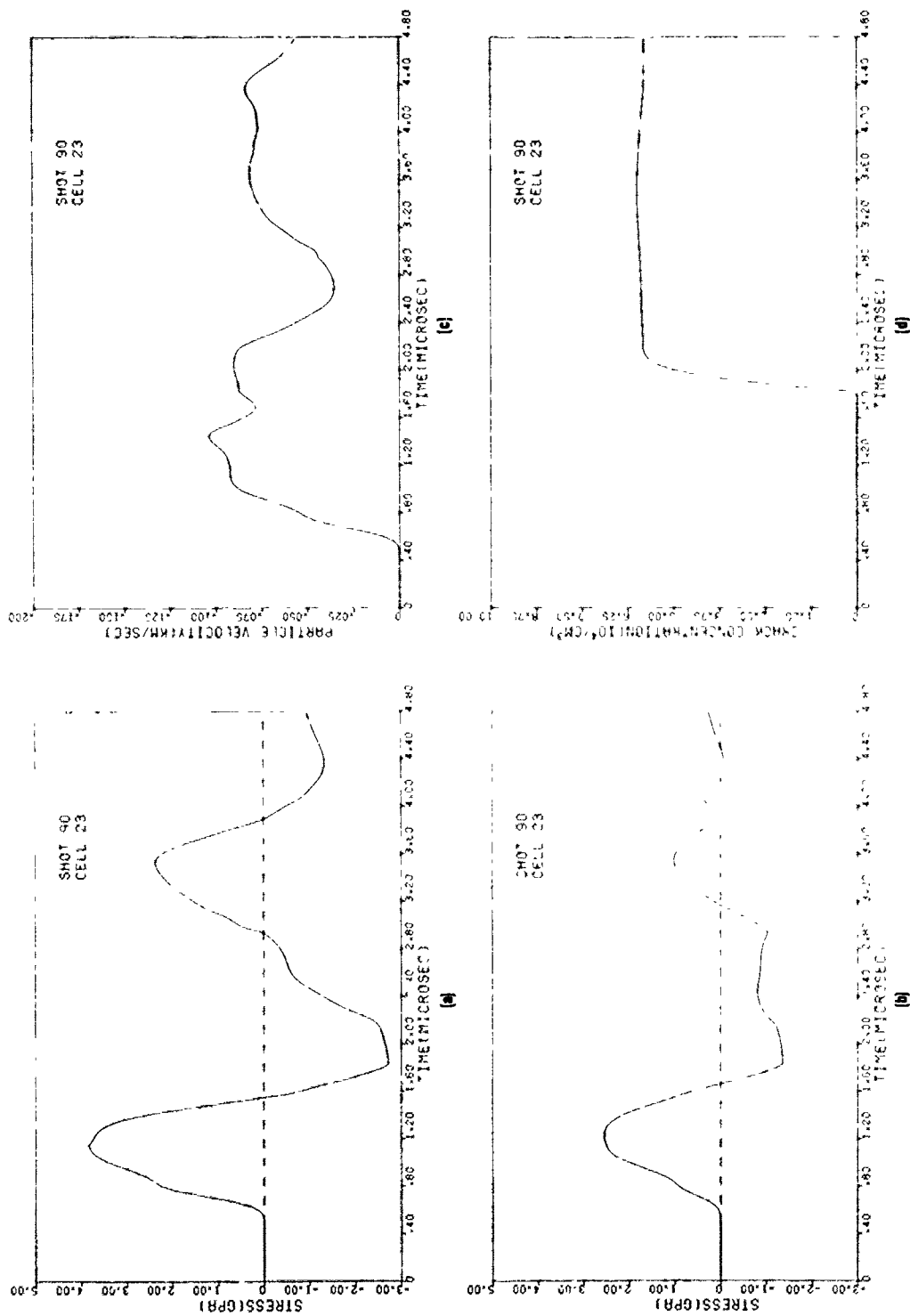


Figure J-18. Computed shock histories in cell 23 for Shot 90 with stringer cracks excluded. (a) Parallel stress. (b) Perpendicular stress. (c) Particle velocity. (d) Crack concentration.

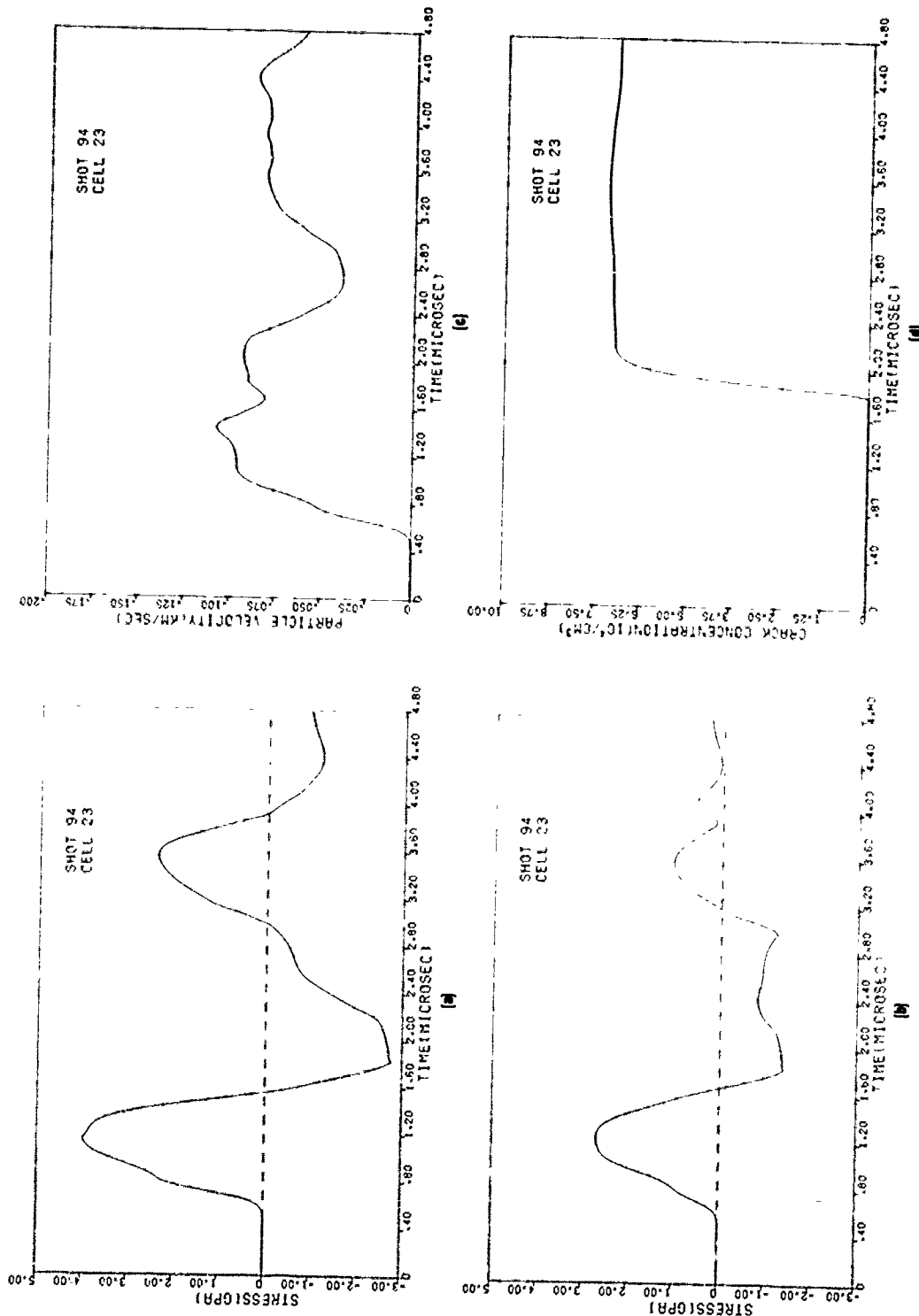


Figure J-19. Computed shock histories in cell 23 for Shot 94 with stringer cracks excluded. (a) Parallel stress. (b) Perpendicular stress. (c) Particle velocity. (d) Crack concentration.

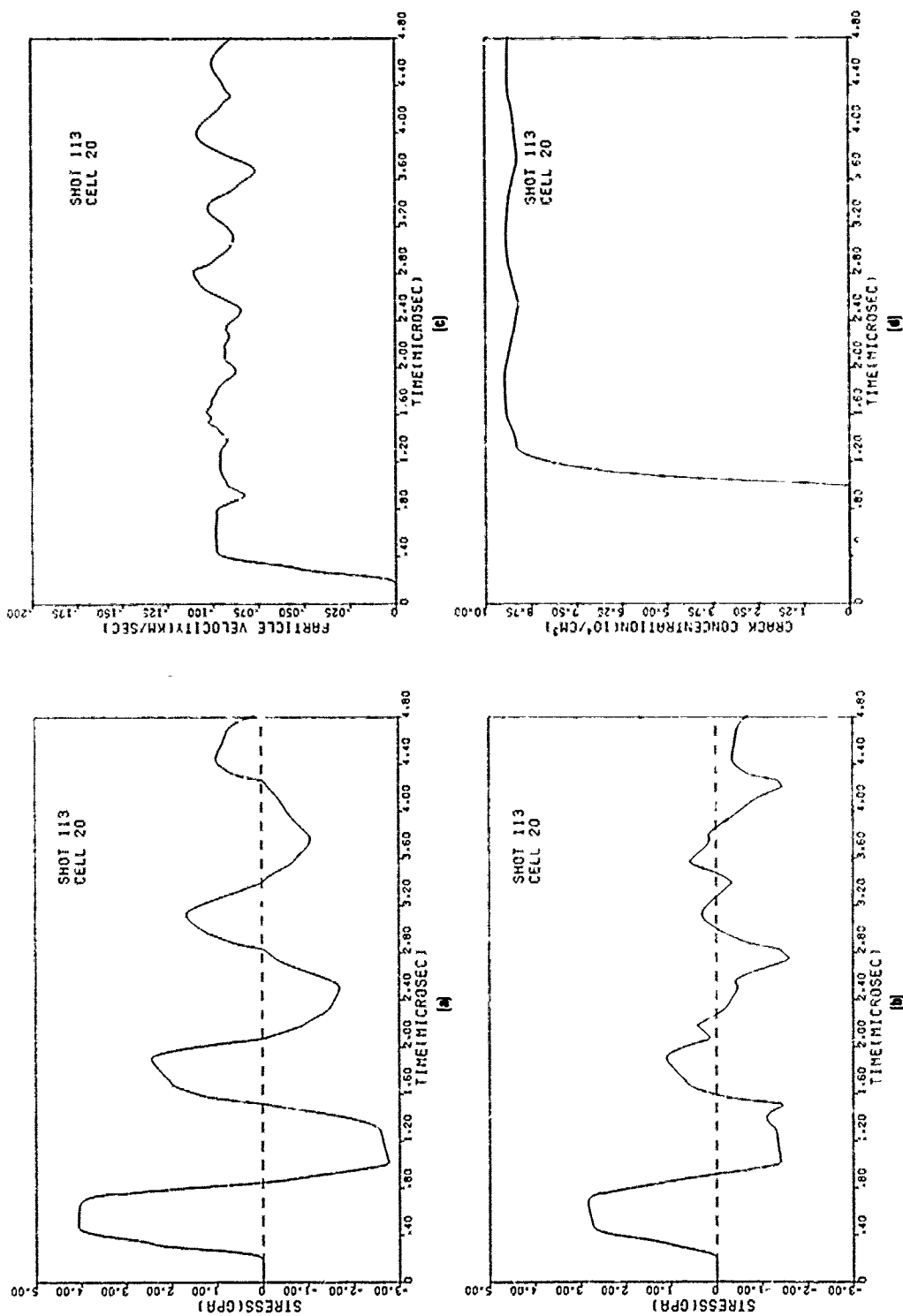


Figure J-20. Computed shock histories in cell 20 for Shot 113 with stringer cracks excluded. (a) Parallel stress. (b) Perpendicular stress. (c) Particle velocity. (d) Crack concentration.

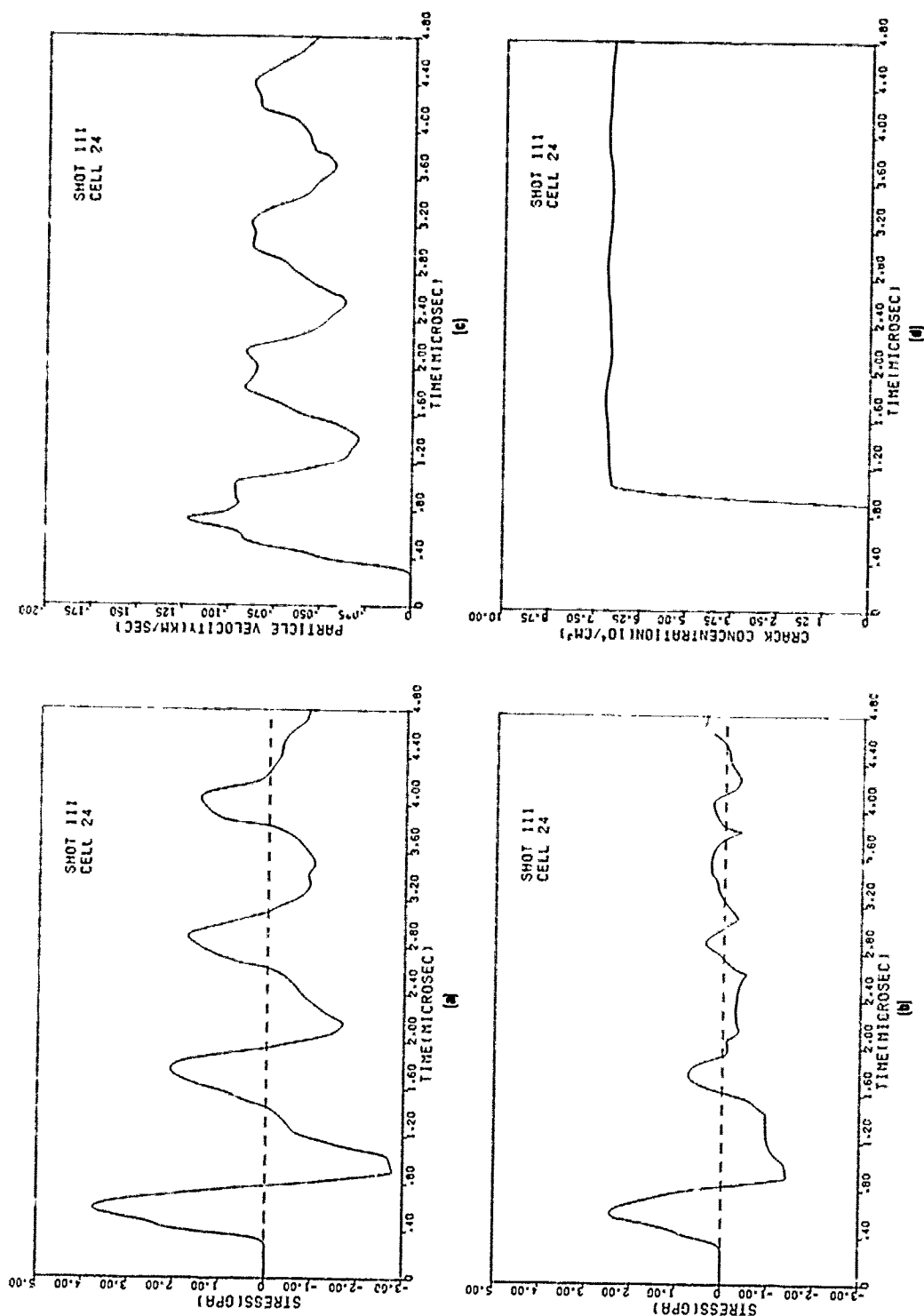


Figure J-21. Computed shock histories in cell 24 for Shot 111 with stringer cracks excluded. (a) Parallel stress. (b) Perpendicular stress. (c) Particle velocity. (d) Crack concentration.

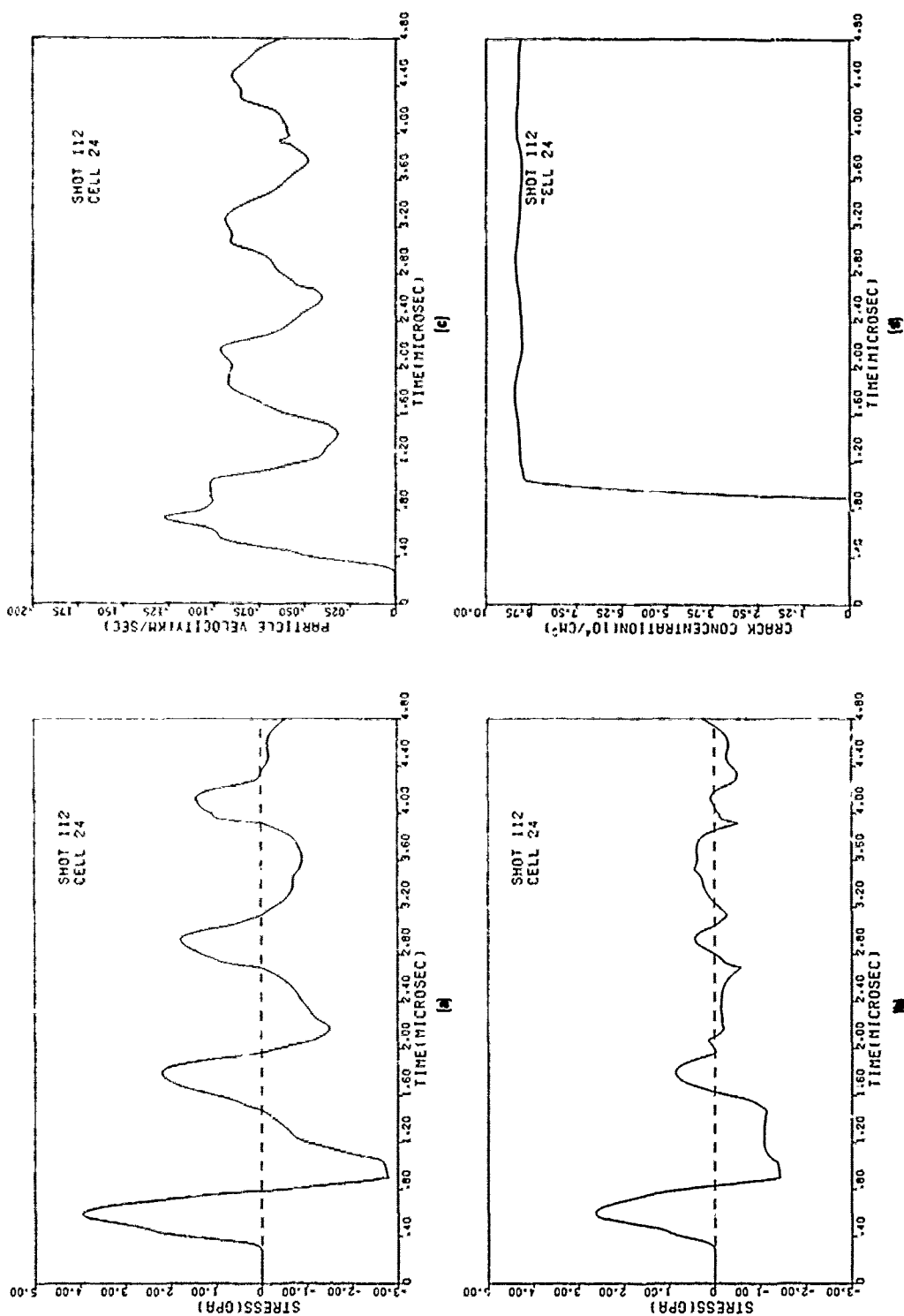


Figure J-22. Computed shock histories in cell 24 for Shot 112 with stringer cracks excluded. (a) Parallel stress. (b) Perpendicular stress. (c) Particle velocity. (d) Crack concentration.

Table J-1. Summary of experimental volume crack-size distribution parameters for spall fracture specimens of HF-1 steel with heat treatment A with stringer cracks excluded.^a

Shot No.	Number of Cracks per Unit Volume N_0 ($10^4/\text{cm}^3$)	Average Crack Radius R_1 (μm)	Distance from Specimen Impact Surface to Midpoint of Zone of Maximum Damage (mm)
95 ^b	0.03	-1822.2	2.73
110	0.74	150.3	4.04
98	3.28	87.2	3.96
92	2.39	97.3	4.40
91	8.49	54.2	4.00
90	4.74	99.1	4.19
94	6.36	96.2	4.17
89 ^c	—	—	—
113	26.67	29.7	1.66
88 ^d	3.92	107.6	1.51
111	5.36	75.5	2.19
112	7.25	76.1	2.09

^a The parameters N_0 and R_1 were obtained for each damage zone of each specimen by fitting the equation $N_g = N_0 \exp(-R/R_1)$ to the volume crack-size distribution. Here N_g is the number of cracks per unit volume with radius greater than R . Plots of the volume crack-size distributions for each damage zone of each specimen containing no stringer cracks are given in Appendix E (Shots 95, 110, 88, and 111) and this appendix (Shots 98, 92, 91, 90, 94, 113, and 112). The parameters N_0 and R_1 listed in this table are the values for the zone of maximum damage.

^b This shot was not used for determining dynamic fracture parameters due to the small number of measured cracks.

^c Cracks were not measured for the no-damage Shot 89.

^d This full-spall shot was not used for determining dynamic fracture parameters. Only cracks in one half of the specimen were digitized.

Table J-2. Summary of experimental and computed nucleation and growth values for spall fracture specimens of 1:F-1 steel with heat treatment A with stringer cracks excluded.^a

Shot No.	Distance from Specimen										Time at which Tensile Stress Exceeds Tensile Stress above Threshold									
	Experimental Crack Density ^c N_0 ($10^6/\text{cm}^3$)	Experimental Average Crack Radius ^c R_1 (μm)	Maximum Damaged	Coil of Crack	Distance to Midpoint of Crack	Computed Average Crack Radius R_1 (μm)	Time of Computed Crack Radius and Radius	Maximum Compressive Stress (GPa)	Time of Maximum Tensile Stress (μs)	Maximum Tensile Stress (GPa)	Time of Tensile Stress (μs)	Nucleation Time ^d Δt_n (μs)	Growth Time ^e Δt_g (μs)	Tensile Stress σ_{max} (GPa)	Product $\sigma_{\text{max}} \Delta t_n$ ($\text{GPa} \mu\text{s}$)	Experimental Nucleation Rate $N_0/\Delta t_n$ ($\text{no./cm}^3\text{-}\mu\text{s}$)	Computed Nucleation Rate $N_0/\Delta t_n$ ($\text{no./cm}^3\text{-}\mu\text{s}$)			
95 ^b	—	—	—	—	—	—	—	—	—	—	—	—	—	—	—	—	—			
110	0.74	150.3	23	4.28	—	83.0	2.83	3.09	1.16	-2.61	1.94	1.81	0.29	0.83	-2.16	25.1	37.2			
98	3.28	87.2	23	4.29	—	85.8	2.73	3.28	1.16	-2.64	1.50	1.81	0.31	0.92	-2.43	104	57.6			
92	2.39	97.3	23	4.28	—	94.2	2.91	3.64	1.16	-2.70	1.86	1.79	0.36	1.05	-0.20	-2.84	66.1			
91	8.49	54.2	23	4.28	—	95.5	2.91	3.69	1.16	-2.70	1.86	1.79	0.37	1.07	-0.20	-2.89	232			
90	4.74	99.1	23	4.29	—	98.9	2.91	3.84	1.16	-2.72	1.83	1.78	0.37	1.12	-0.22	-3.05	127			
94	6.36	56.2	23	4.29	—	102.8	2.91	4.00	1.15	-2.75	1.83	1.78	0.38	1.18	-0.25	-3.25	167			
89 ^b	—	—	—	—	—	—	—	—	—	—	—	—	—	—	—	—	—			
113	26.67	29.7	20	1.67	—	82.8	1.55	4.07	0.48	-2.77	1.02	0.98	0.34	0.53	-1.46	781	275			
88 ^b	—	—	—	—	—	—	—	—	—	—	—	—	—	—	—	—	—			
111	5.35	75.5	24	2.31	—	73.0	1.33	3.76	0.58	-2.77	0.92	0.88	0.17	0.54	-1.53	311	412			
112	7.25	76.1	24	2.31	—	74.6	1.50	3.95	0.58	-2.80	0.90	0.89	0.18	0.57	-1.60	405	508			

^a These computed nucleation and growth values for heat treatment A material with stringer cracks excluded were calculated using dynamic fracture parameters (Table J-3) obtained after six iterations with the PUFF 8 stress wave computer program for planar geometry.

^b These shots were not used for determining dynamic fracture parameters. Only a few spall fracture cracks were produced in Shot 95. No cracks were measured for the no-damage Shot 89. Shot 88 was a full-spall shot. Maximum tensile stresses of -2.5, -2.4, and -4.1 GPa were obtained for Shots 95, 89, and 88, respectively, from the initial no-damage PUFF - computations. The nucleation threshold stress for P-88 treatment A material was taken as -2.5 GPa, the maximum tensile stress value for Shot 95.

^c These experimental parameters were obtained from Table J-1 for the zone of maximum damage for each specimen (See Appendix E and this appendix).

^d The location of the coil of maximum damage does not necessarily correspond to the experimentally determined zone of maximum damage.

^e The nucleation time is the time interval that the initial tensile stress pulse exceeds the -2.5 GPa nucleation threshold stress.

^f The growth time is the time interval that the initial tensile stress pulse first exceeds the -2.5 GPa nucleation threshold stress until it decreases to the -0.1 GPa growth threshold stress.

Table J-3. Dynamic fracture parameters for heat treatment A of HF-1 steel with stringer cracks excluded.

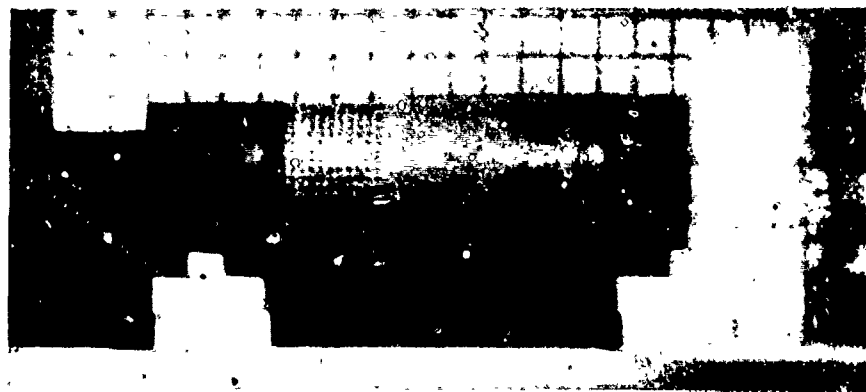
Parameter ^a	Description	Units	Value
T_1	Growth coefficient	$\text{GPa}^{-1} \mu\text{s}^{-1}$	-0.409
σ_{go}	Growth threshold stress	GPa	-0.1
R_0	Nucleation size parameter	μm	58.7
\dot{N}_0	Nucleation threshold rate	$\text{no.cm}^{-3} \text{ns}^{-1}$	42.2
σ_{no}	Nucleation threshold stress	GPa	-2.5
σ_1	Nucleation sensitivity parameter	GPa	-0.0577

^a In the BFRAC2 brittle fracture subroutine these parameters are listed as T1, T2, T3, T4, T5, and T6, respectively, with different units.

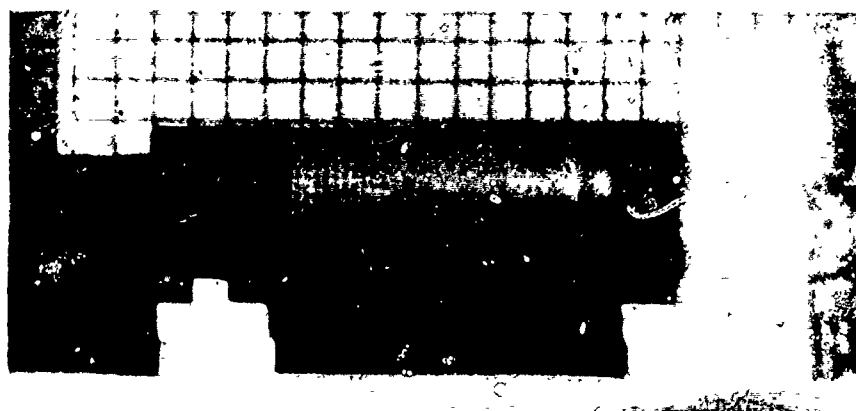
APPENDIX K

FRAMING CAMERA PHOTOGRAPHS FOR EXPLOSIVE-FILLED ARMCO IRON CYLINDER EXPERIMENT

(This appendix contains a series of 24 framing camera photographs for the explosive-filled Armco iron cylinder experiment. The frames are numbered 1 through 25; frame 13 is missing. The composition B explosive detonation front was located inside the cylinder in frames 1 through 10. The detonation front was assumed to be located at the left end of the cylinder in frame 11. The calculated axial position of the detonation front for these frames is given in Table 12. In these figures the time corresponding to each frame is taken as the time after the explosive detonation front has entered the cylinder. These times are probably uncertain by a few microseconds since the detonation front was probably not located exactly at the end of the cylinder in frame 11. The initial explosive detonation occurred about $8 \mu\text{s}$ prior to the entrance of the detonation front into the cylinder. The explosive extended about 64 mm beyond the metal cylinder on the initiation end.)

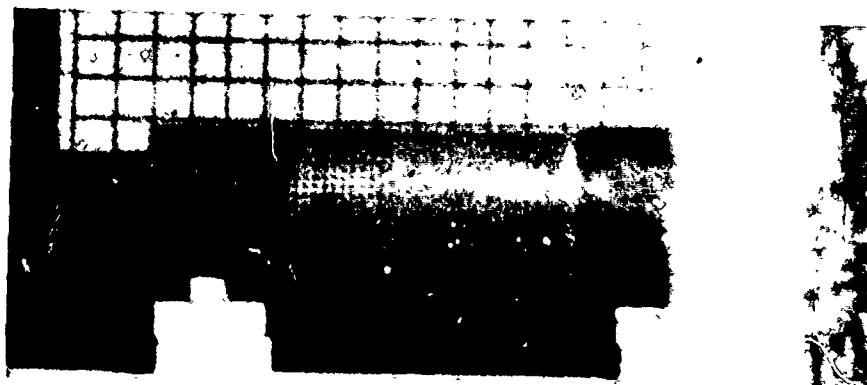


(a)

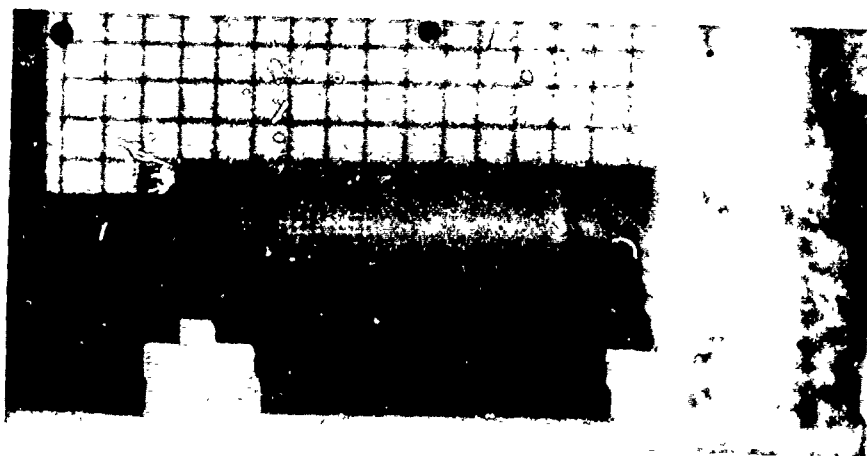


(b)

Figure K-1. Frames 1 and 2 for Armco iron framing camera experiment. (a) Frame 1 at $6 \mu\text{s}$ and (b) frame 2 at $10 \mu\text{s}$.

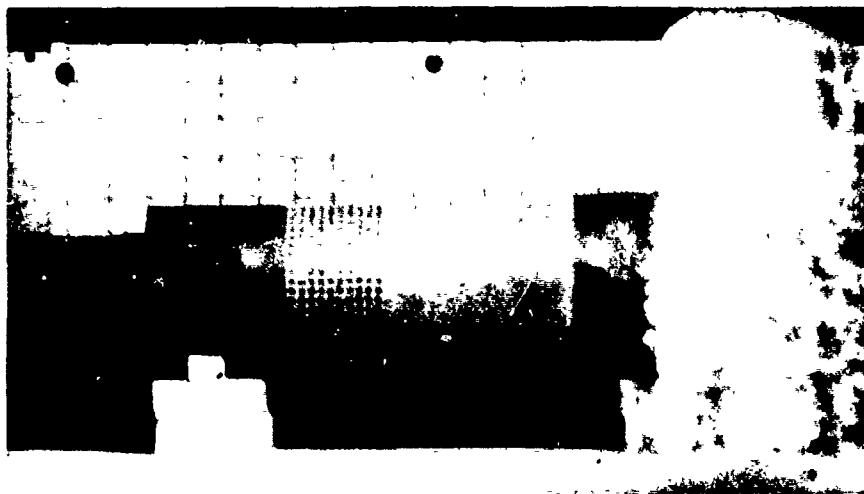


(a)

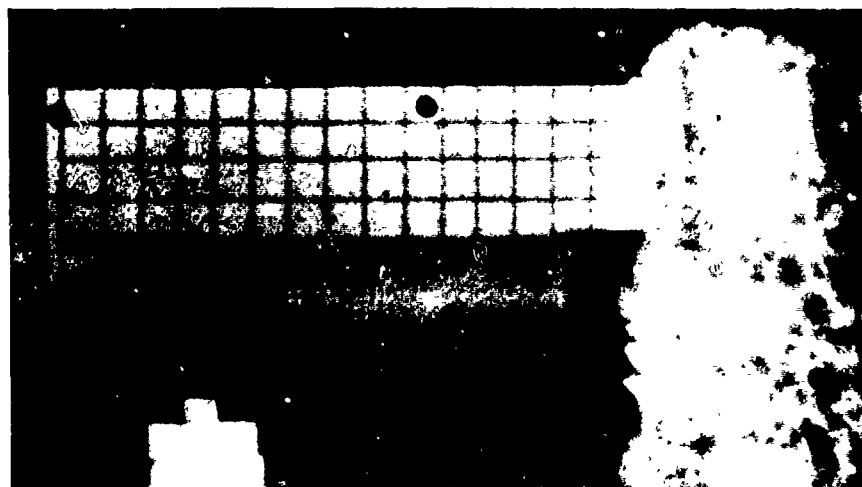


(b)

Figure K-2. Frames 3 and 4 for Armco iron framing camera experiment. (a) Frame 3 at $14 \mu\text{s}$ and (b) frame 4 at $18 \mu\text{s}$.

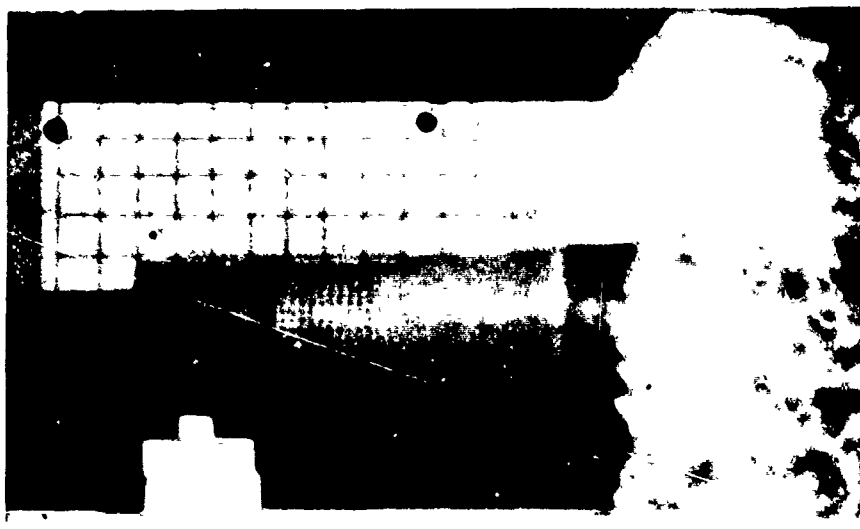


(a)

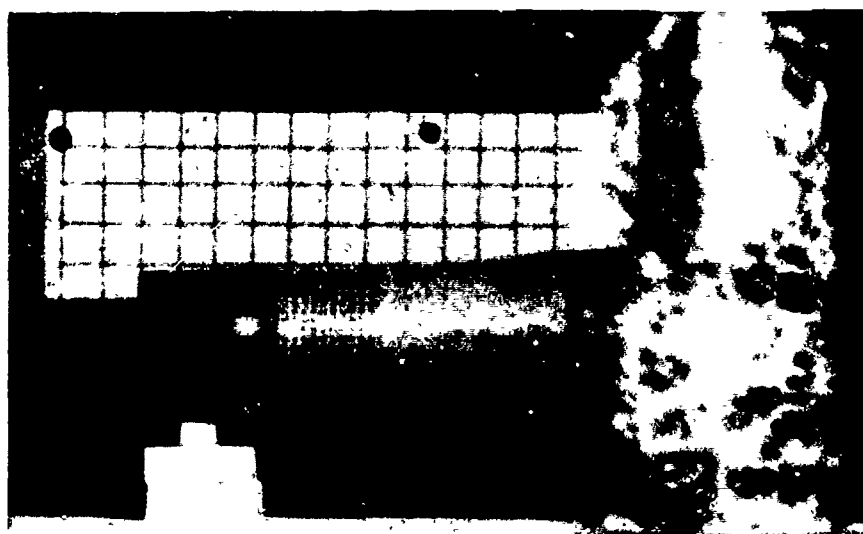


(b)

Figure K-3. Frames 5 and 6 for Armco iron framing camera experiment. (a) Frame 5 at $23 \mu\text{s}$ and (b) frame 6 at $27 \mu\text{s}$.

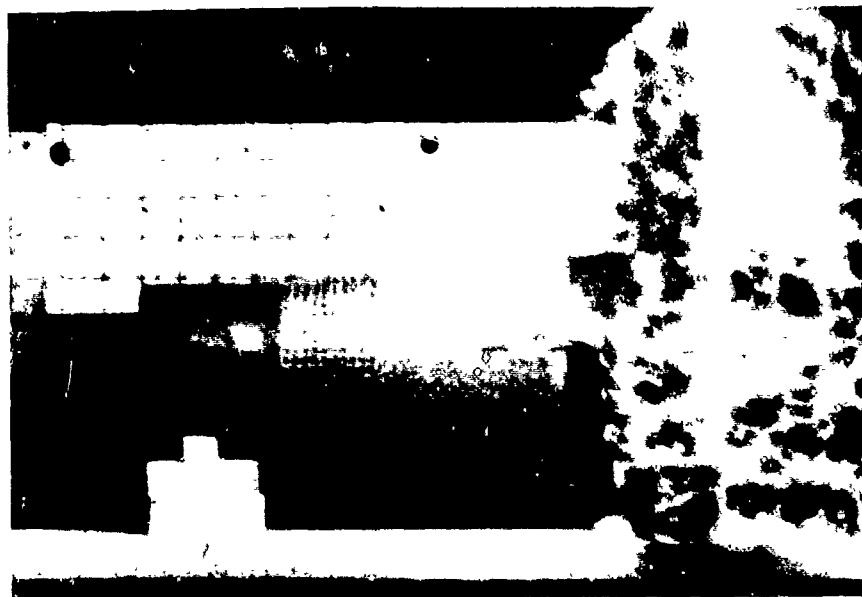


(a)

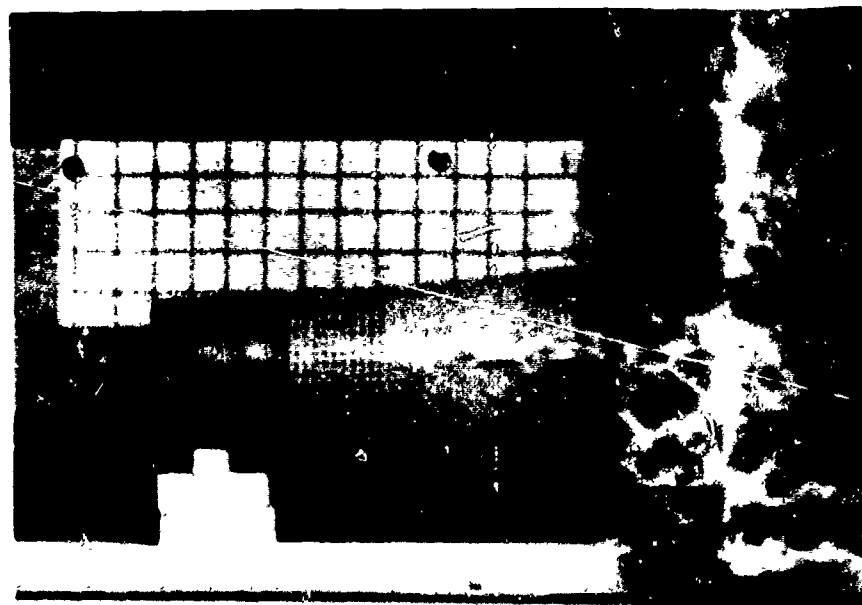


(b)

Figure K-4. Frames 7 and 8 for Armco iron framing camera experiment. (a) Frame 7 at $31 \mu\text{s}$ and (b) frame 8 at $35 \mu\text{s}$.



(a)

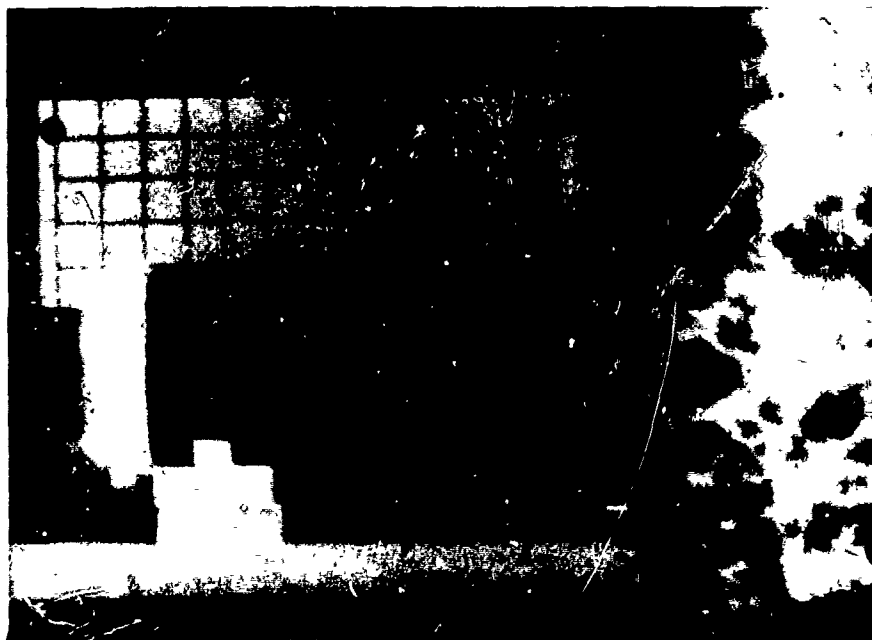


(b)

Figure K-5. Frames 9 and 10 for Armco iron framing camera experiment. (a) Frame 9 at $39 \mu\text{s}$ and (b) frame 10 at $43 \mu\text{s}$.



(a)



(b)

Figure K-6. Frames 11 and 12 for Armco iron framing camera experiment. (a) Frame 11 at $48 \mu s$ and (b) frame 12 at $52 \mu s$.

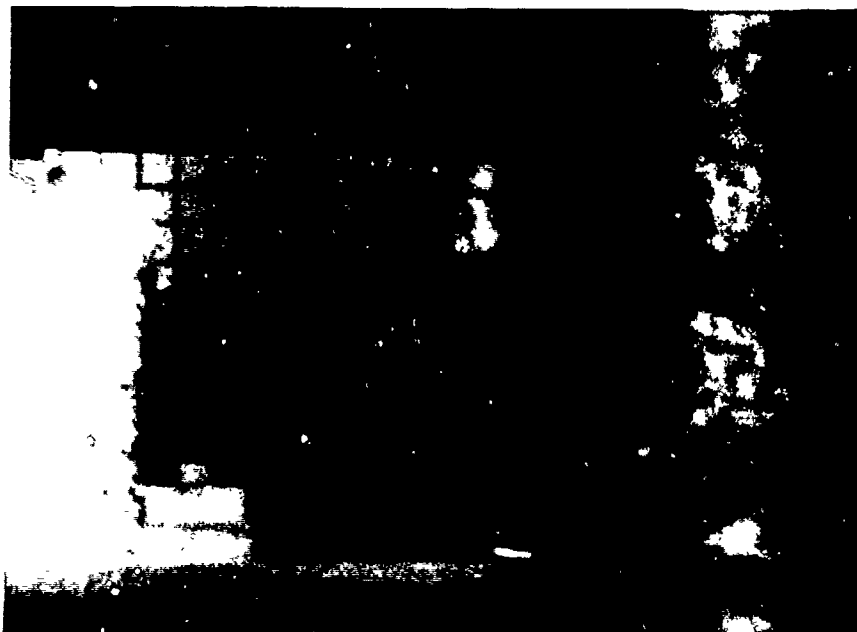


(a)



(b)

Figure K-7. Frames 14 and 15 for Armco iron framing camera experiment. (a) Frame 14 at $60 \mu\text{s}$ and (b) frame 15 at $64 \mu\text{s}$.



(a)



(b)

Figure K-8. Frames 16 and 17 for Armco iron framing camera experiment. (a) Frame 16 at $68 \mu\text{s}$ and (b) frame 17 at $73 \mu\text{s}$.

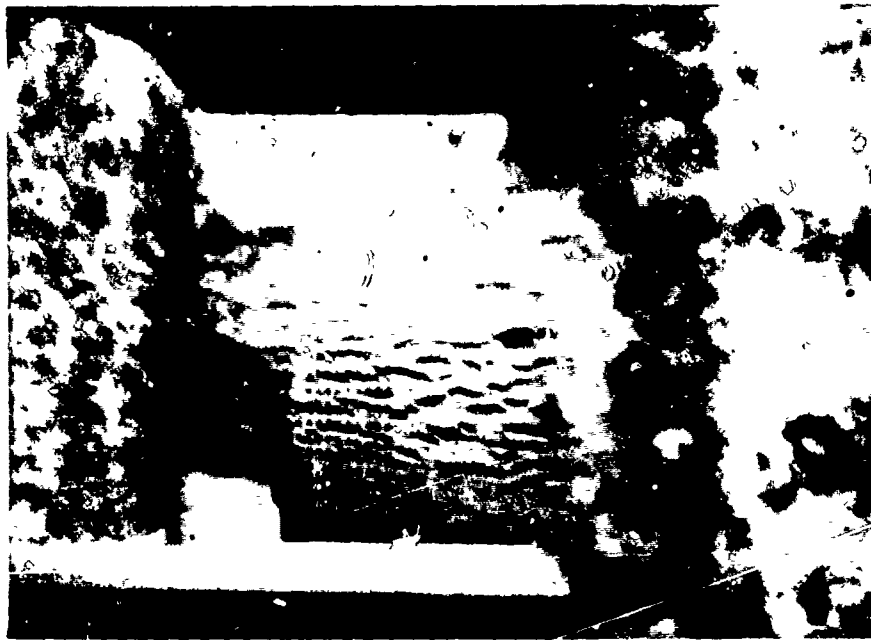


(a)

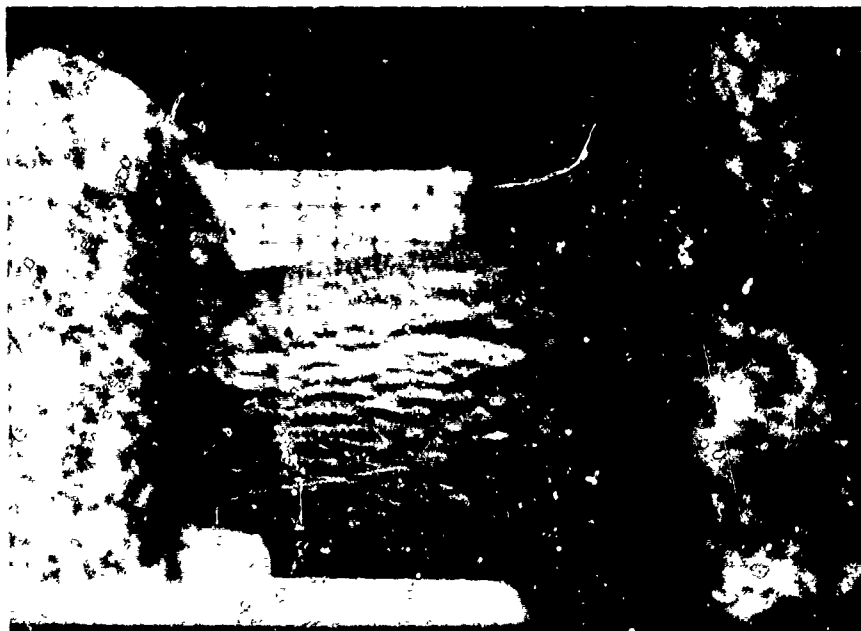


(b)

Figure K-9. Frames 18 and 19 for Armco iron framing camera experiment. (a) Frame 18 at $77 \mu\text{s}$ and (b) frame 19 at $81 \mu\text{s}$.

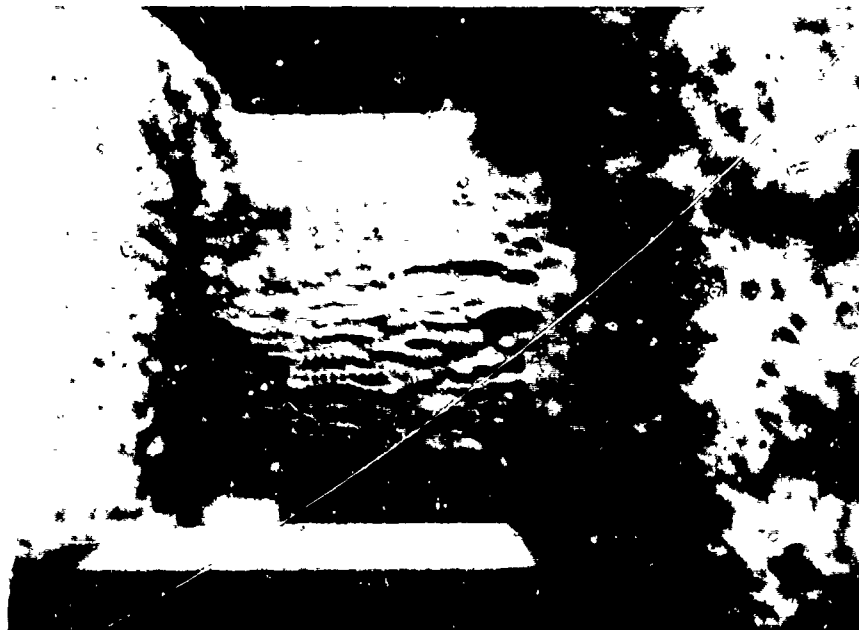


(a)



(b)

Figure K-10. Frames 20 and 21 for Armco iron framing camera experiment. (a) Frame 20 at $85 \mu\text{s}$ and (b) frame 21 at $89 \mu\text{s}$.

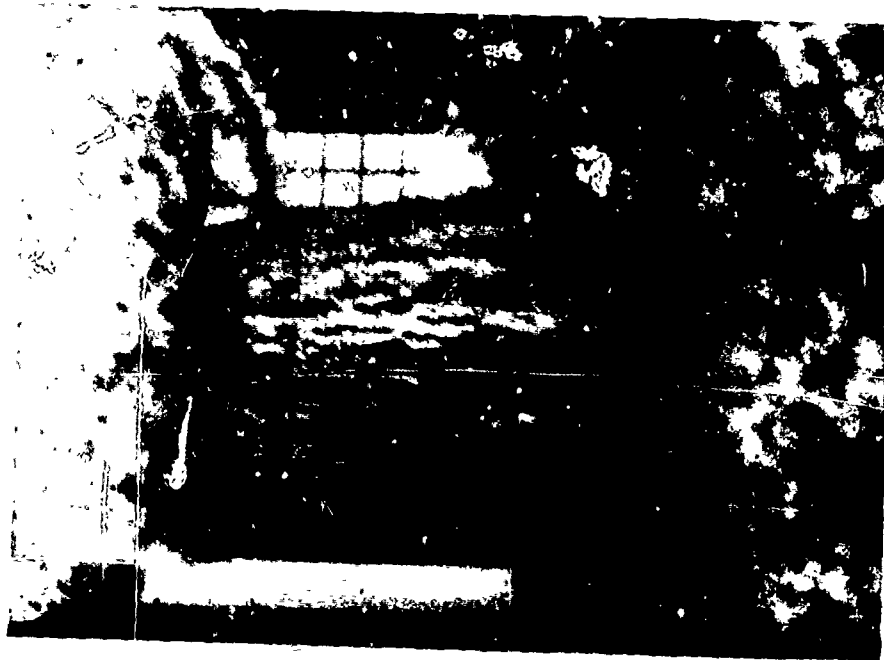


(a)



(b)

Figure K-11. Frames 22 and 23 for Armco iron framing camera experiment. (a) Frame 22 at $93 \mu\text{s}$ and (b) frame 23 at $98 \mu\text{s}$.



(a)



(b)

Figure K-12. Frames 24 and 25 for Armco iron framing camera experiment. (a) Frame 24 at $102 \mu\text{s}$ and (b) frame 25 at $106 \mu\text{s}$.

APPENDIX L

PHOTOGRAPHS OF FRAGMENT TYPES FROM ARMCO IRON AND HF-1 STEEL CYLINDER FRAGMENT RECOVERY EXPERIMENTS

(This appendix contains 24 figures. Figures L-1 through L-8 show Armco iron fragments from cylinder experiment 2. No type 4C fragments were observed for the Armco iron experiments. Figures L-9 through L-16 show HF-1 steel fragments with heat treatment A from cylinder experiment 4. Figures L-17 through L-24 show HF-1 steel fragments with heat treatment B from cylinder experiment 5. The fragment types are defined in Table 14. Schematic examples of the fragment types are shown in Figure 35).

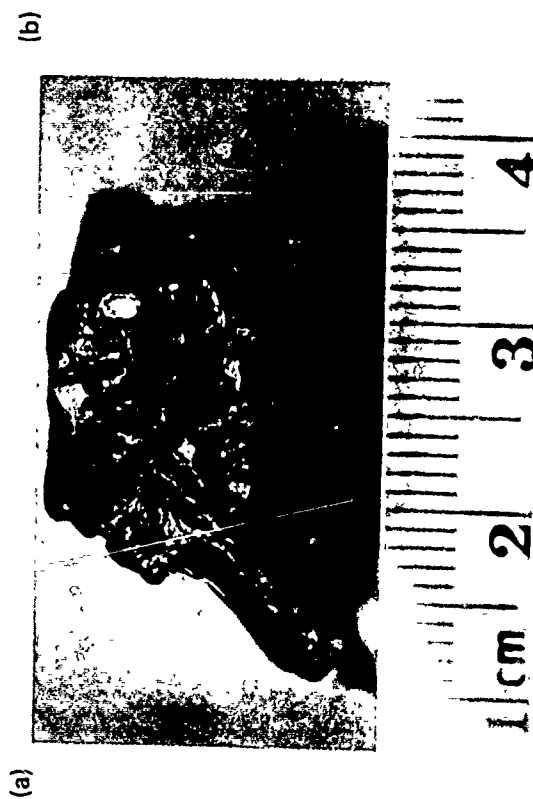
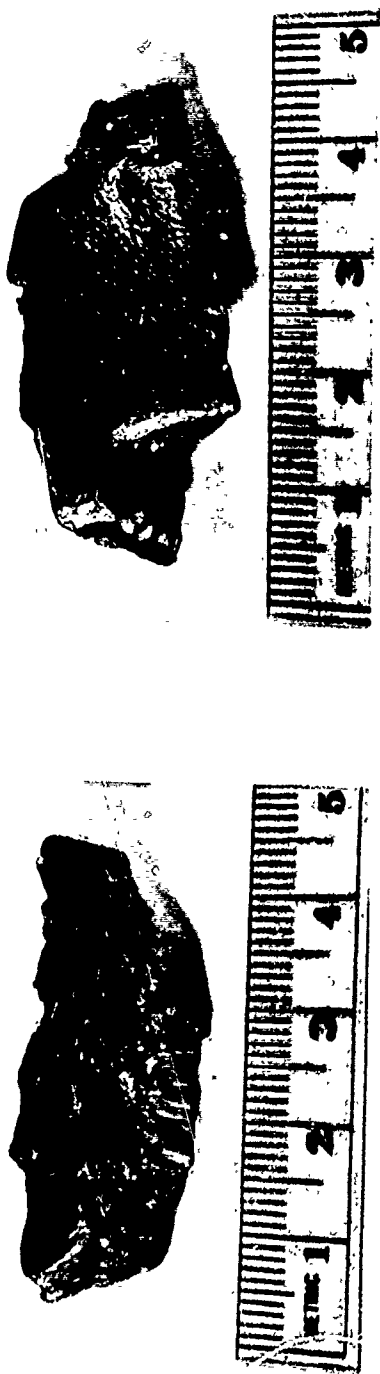


Figure L-1. Type 1 Armco iron cylinder fragment showing (a) cylinder outer surface, (b) cylinder inner surface, and (c) fragment end surface. Fragment mass: 1551.0 gr (100.50 g).



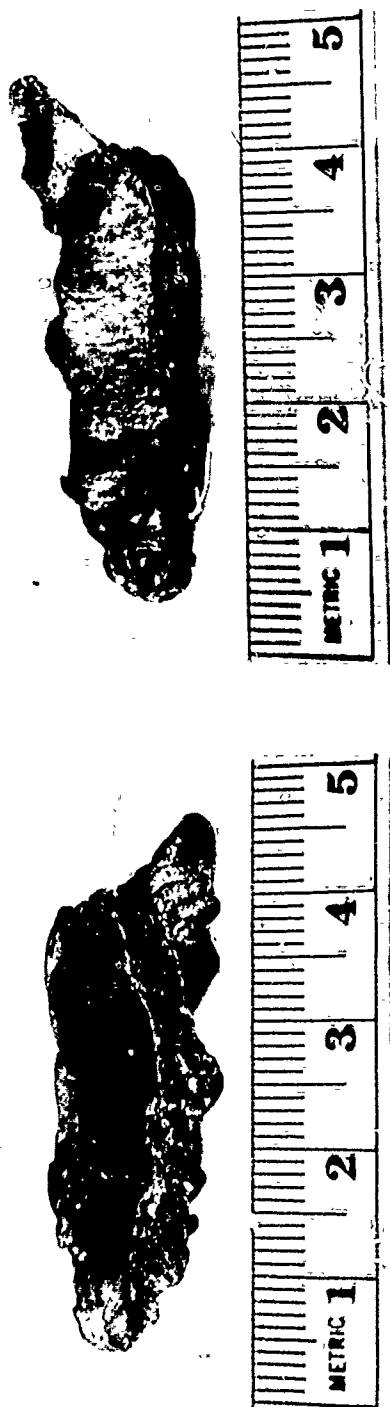
(a)

(b)



(c)

Figure L-2. Type 1 Armco iron cylinder fragment showing (a) cylinder outer surface, (b) cylinder inner surface, and (c) fragment end surface. Fragment mass: 437.4 gr (28.34 g).



(b)

(a)



(c)

Figure L-3. Type 2A Armco iron cylinder fragment showing (a) cylinder outer surface, (b) brittle and shear fracture surfaces, and (c) fragment end surface. Fragment mass: 276.9 gr (17.94 g).



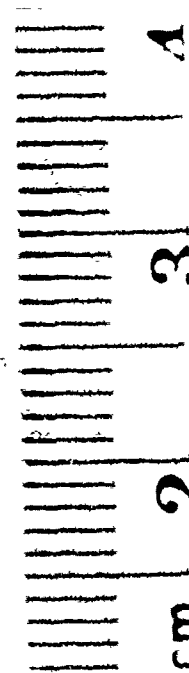
Figure L-4. Type 2B Armco iron cylinder fragment showing (a) cylinder outer surface, (b) brittle fracture surfaces, and (c) fragment end surface. Fragment mass: 104.8 gr (6.75 g).



(a)



(b)



(c)

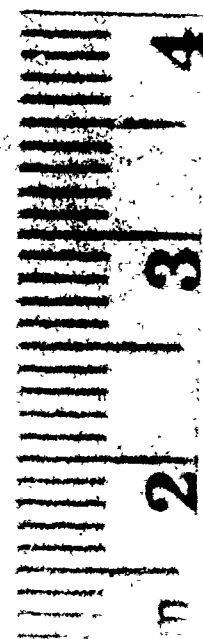
Figure L-5. Type 3A Armco iron cylinder fragment showing (a) brittle and shear fracture surfaces, (b) cylinder inner surface, and (c) fragment end surface. Fragment mass: 161.5 gr (10.47 g).



(a)

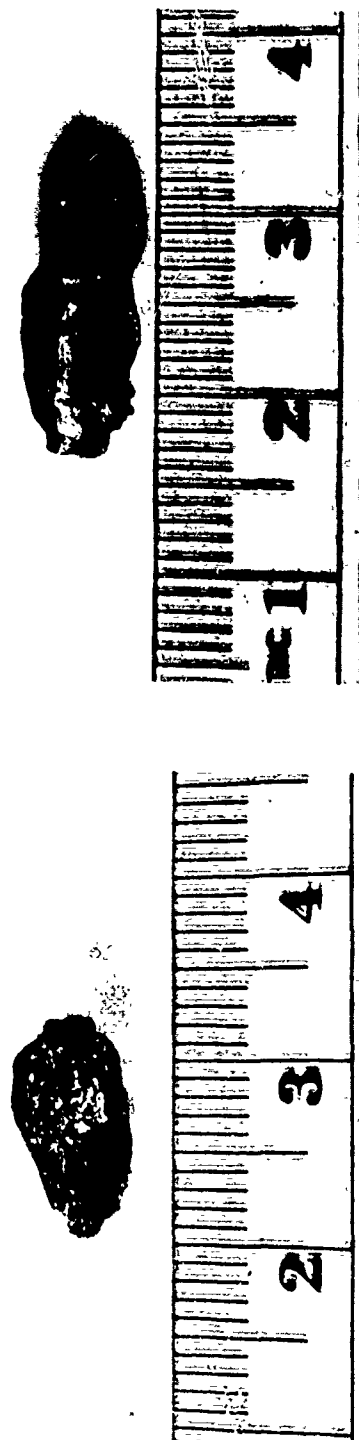


(b)



(c)

Figure L-6. Type 3B Armco iron cylinder fragment showing (a) shear fracture surfaces, (b) cylinder inner surface, and (c) fragment end surface. Fragment mass: 188.9 gr (12.24 g).



(a)

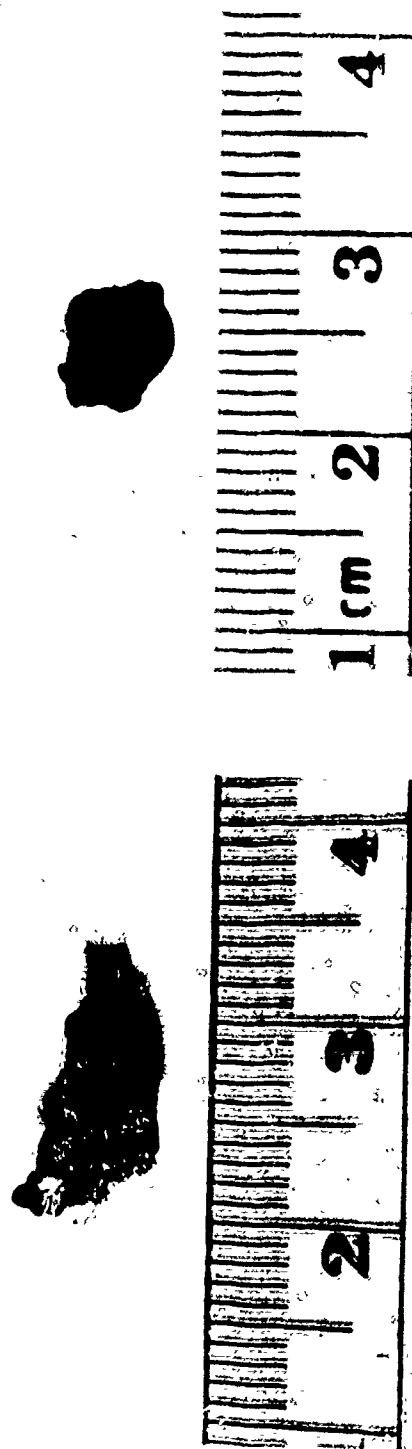
(b)

L-9



(c)

Figure L-7 Type 4A Armco iron cylinder fragment showing (a) brittle fracture surfaces, (b) shear fracture surfaces, and (c) fragment end surface. Fragment mass: 25.1 gr (1.63 g).



(a)

(b)

Figure L-8. Type 4B Armco iron cylinder fragment showing (a) brittle fracture surfaces and (b) fragment end surface.
Fragment mass: 14.9 gr (0.97 g).

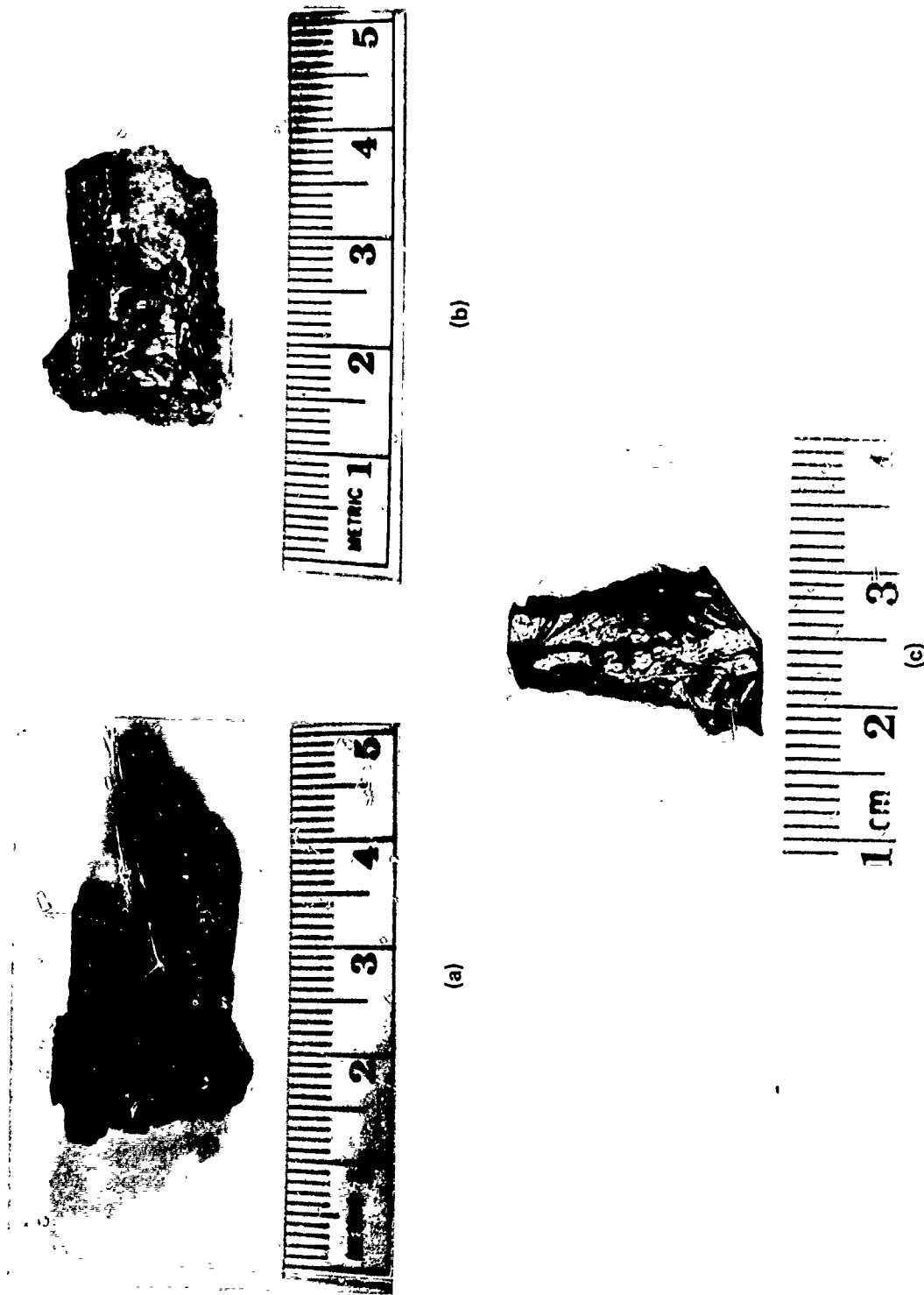


Figure L-9. Type 1 HF-1 steel cylinder fragment with heat treatment A showing (a) cylinder end surface, (b) cylinder outer surface, and (c) fragment end surface. Fragment mass: 347.3 gr (22.51 g).

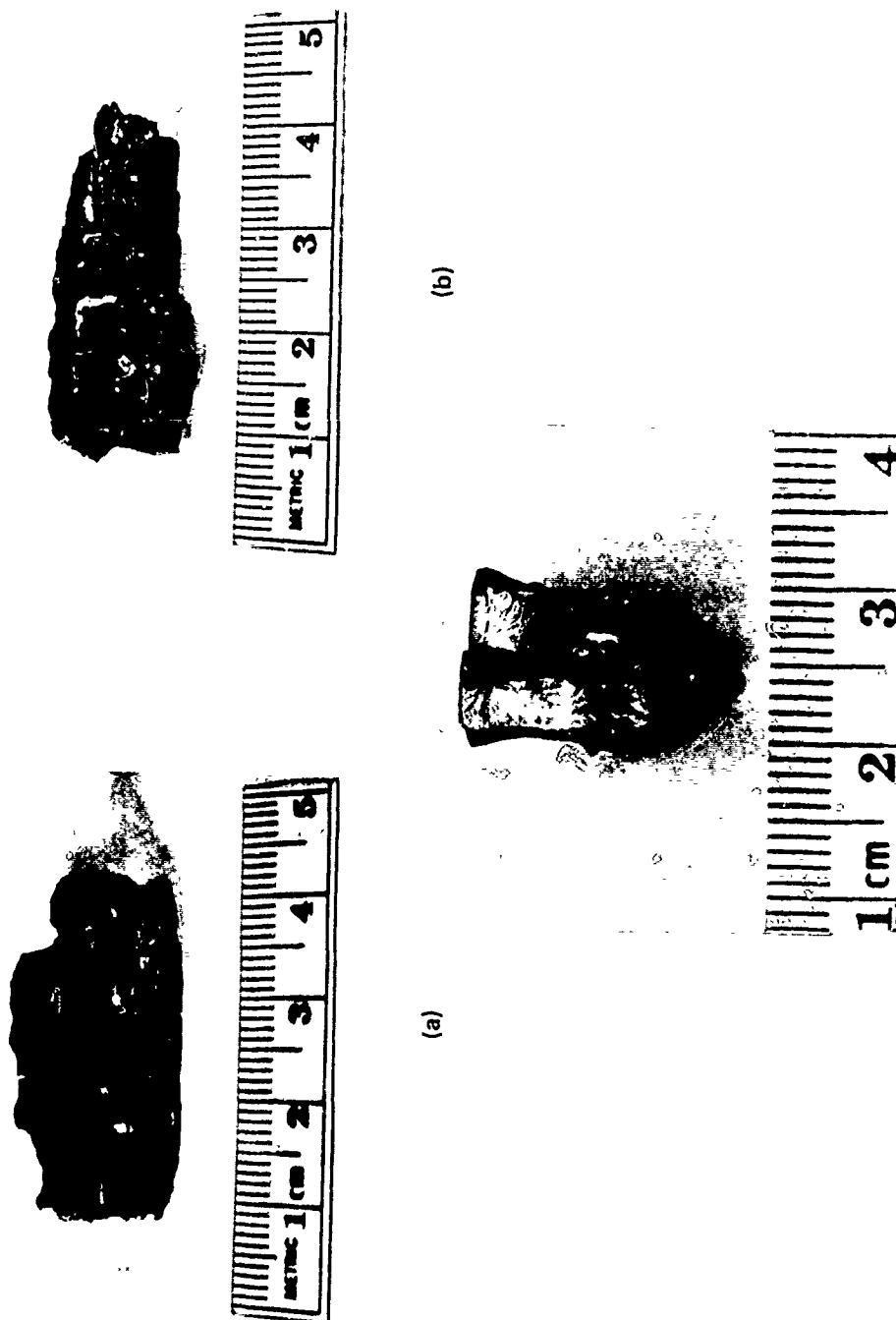
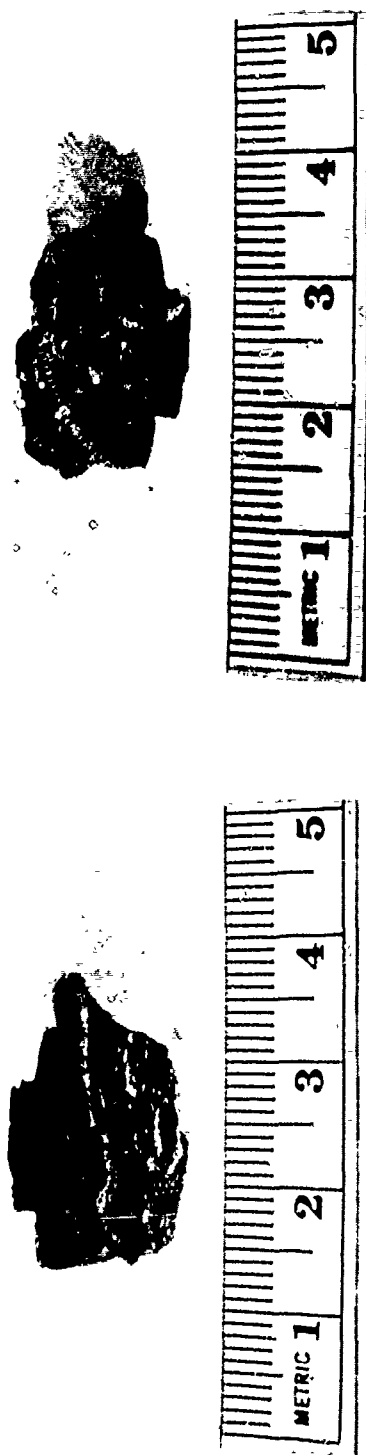
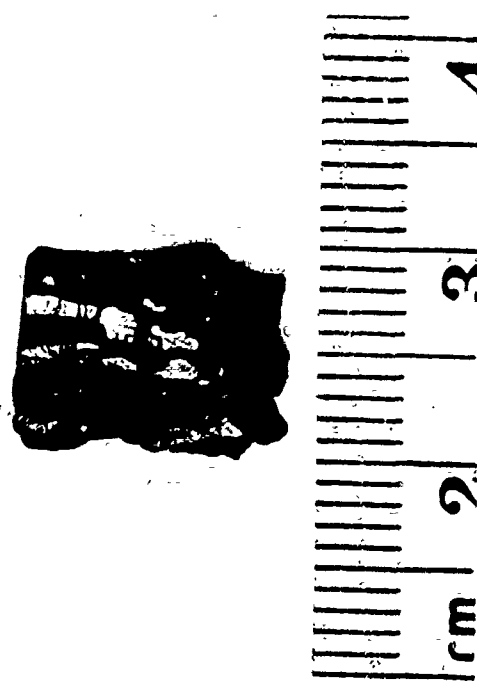


Figure L-10. Type 2A HF-1 steel cylinder fragment with heat treatment A showing (a) cylinder outer surface, (b) brittle and shear fracture surfaces, and (c) fragment end surface. Fragment mass: 373.2 gr (24.18 g).



(a)

(b)



(c)

Figure L-11. Type 2B HF-1 steel cylinder fragment with heat treatment A showing (a) cylinder outer surface, (b) brittle fracture surfaces, and (c) fragment end surface. Fragment mass: 165.9 gr (10.75 g).



(b)

(a)

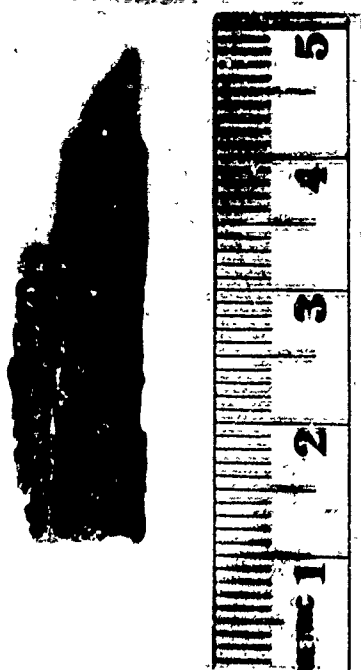


(c)

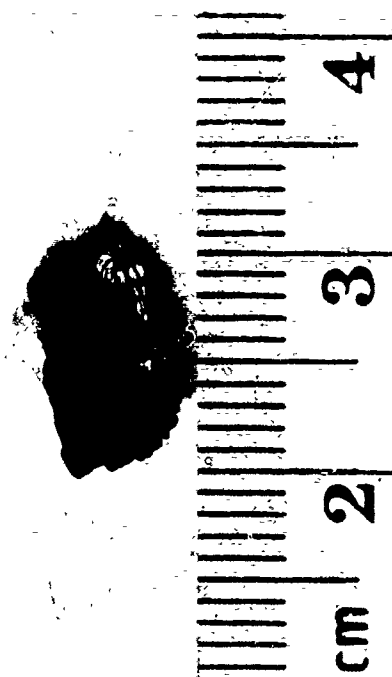
Figure L-12. Type 3A HF-1 steel cylinder fragment with heat treatment A showing (a) brittle and shear fracture surfaces, (b) cylinder inner surface, and (c) fragment end surface. Fragment mass: 275.7 gr (17.87 g).



(a)



(b)

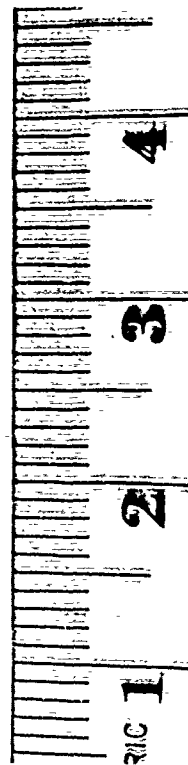


(c)

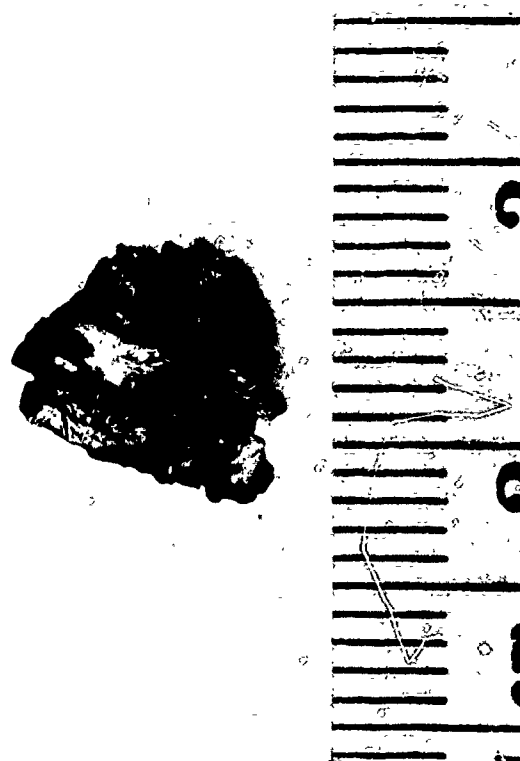
Figure L-13. Type 3B HF-1 steel cylinder fragment with heat treatment A showing (a) shear fracture surfaces, (b) cylinder inner surface, and (c) fragment end surface. Fragment mass: 77.1 gr (4.99 g).



Figure L-14. Type 4A HF-1 steel cylinder fragment with heat treatment A showing (a) brittle fracture surfaces, (b) shear fracture surfaces, and (c) fragment end surface. Fragment mass: 112.7 gr (7.30 g).

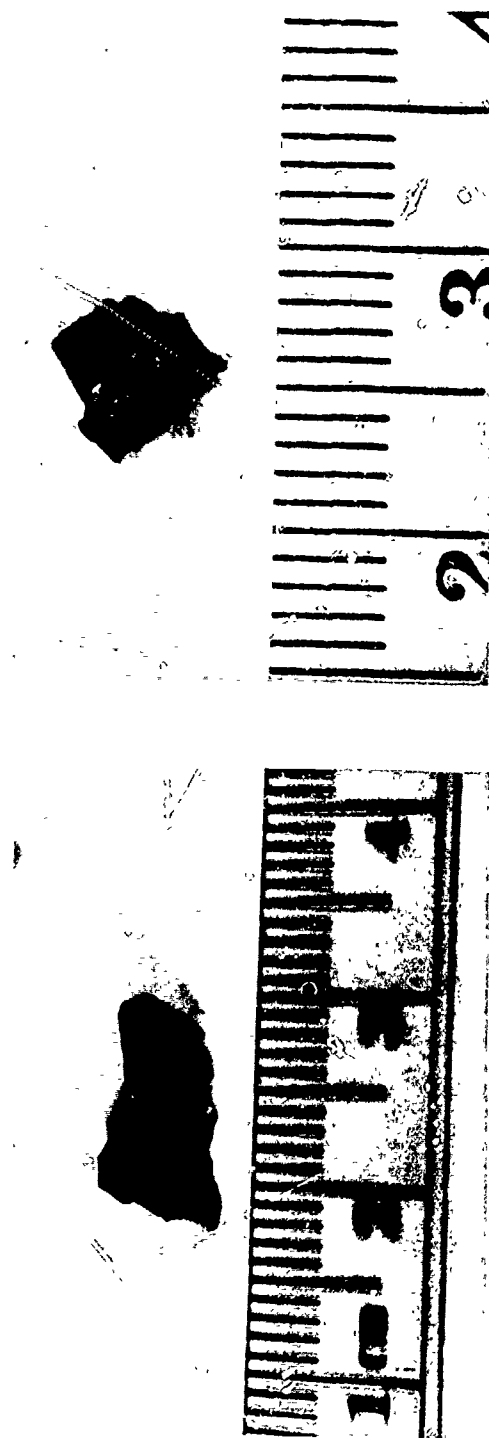


(a)



(b)

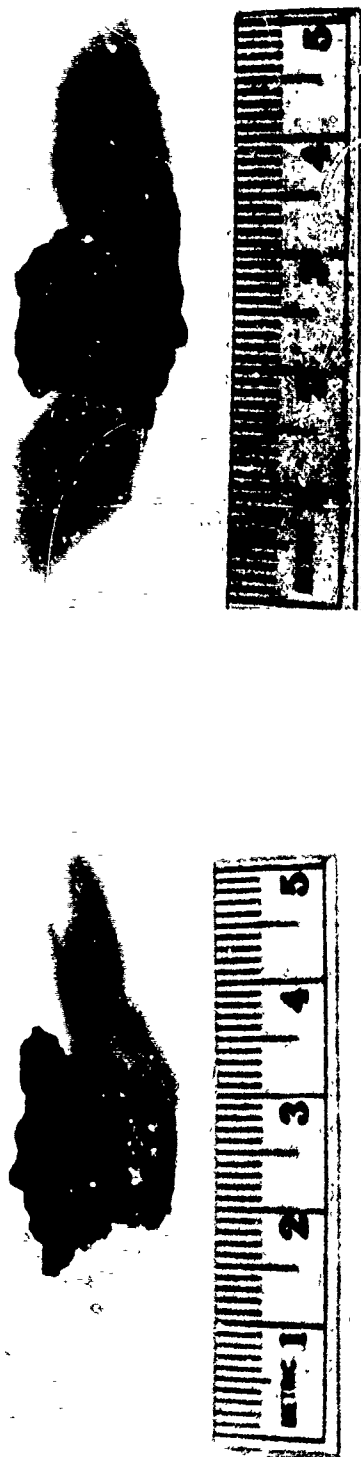
Figure L-15. Type 4B HF-1 steel cylinder fragment with heat treatment A showing (a) brittle fracture surfaces and (b) fragment end surface. Fragment mass: 42.8 gr (2.78 g).



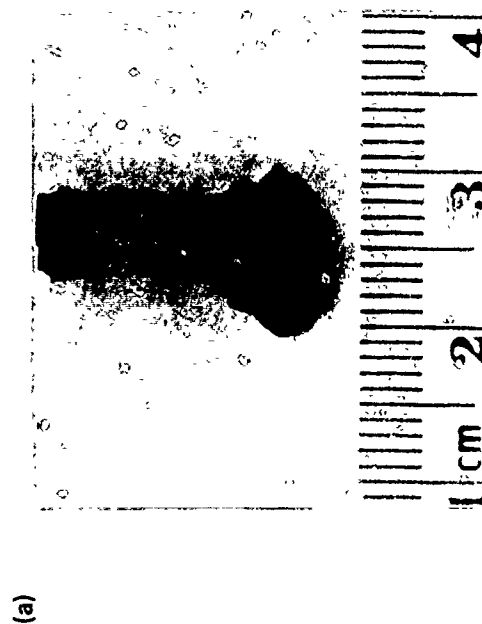
(a)

(b)

Figure L-16. Type 4C HF-1 steel cylinder fragment with heat treatment A showing (a) shear fracture surfaces and (b) fragment end surface. Fragment mass: 17.5 gr (1.13 g).

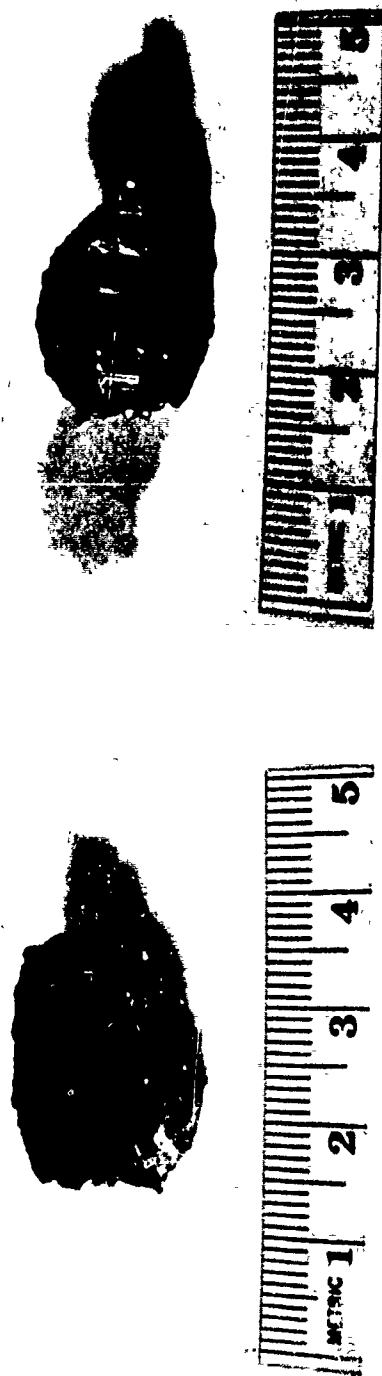


(b)



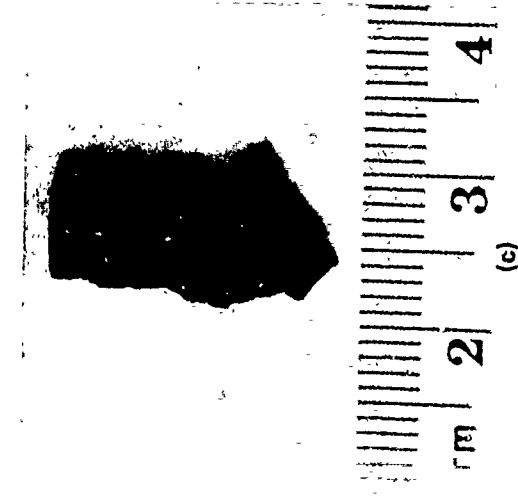
(c)

Figure L-17. Type 1 HF-1 steel cylinder fragment with heat treatment B showing (a) cylinder outer surface, (b) cylinder inner surface, and (c) fragment end surface. Fragment mass: 159.3 gr (10.32 g).



(a)

(b)



(c)

Figure L-18. Type 2A HF-1 steel cylinder fragment with heat treatment B showing (a) cylinder outer surface, (b) brittle and shear fracture surfaces, and (c) fragment end surface. Fragment mass: 231.9 gr (15.03 g).

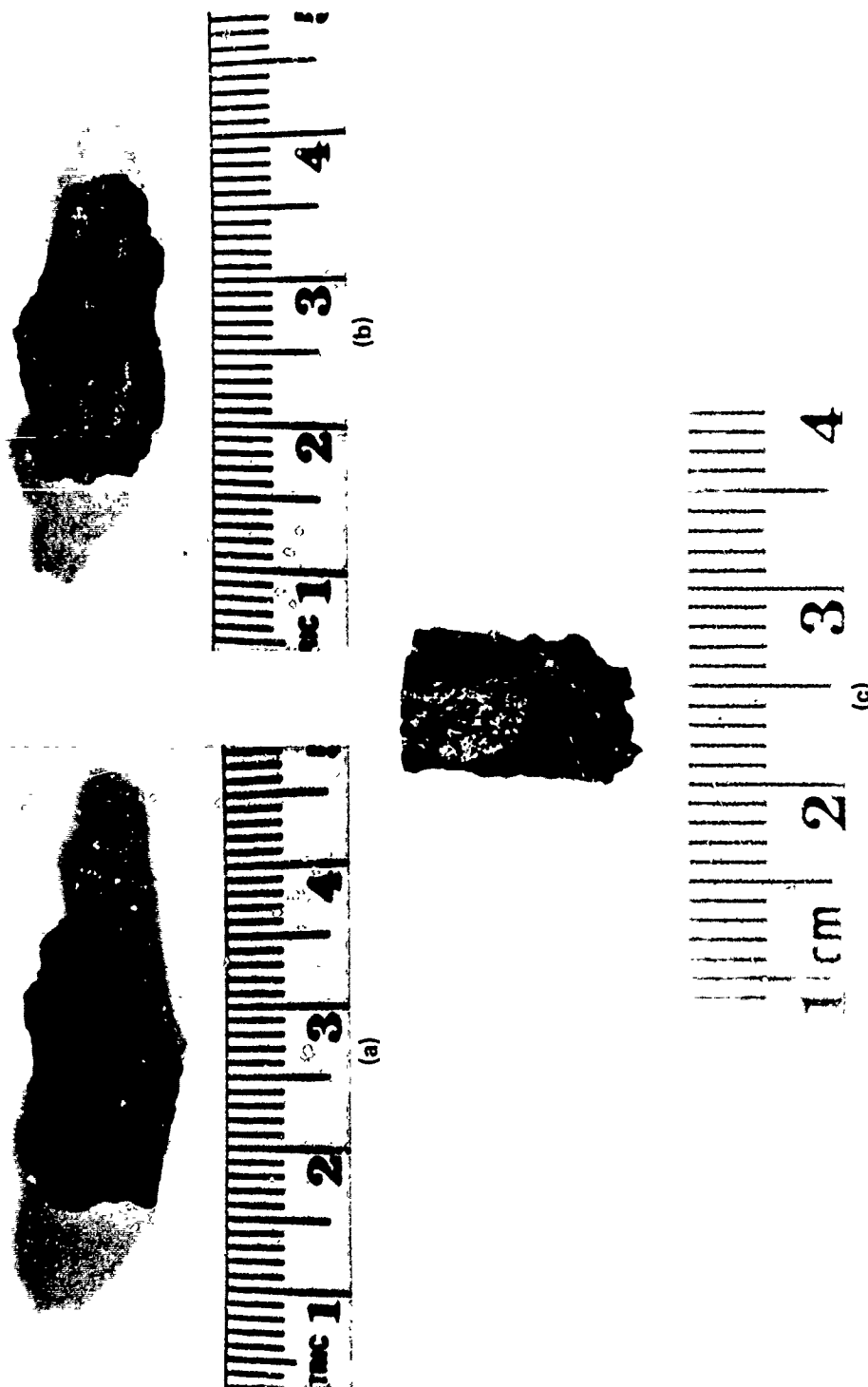
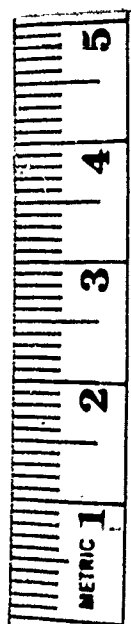


Figure L-19. Type 2B HF-1 steel cylinder fragment with heat treatment B showing (a) cylinder outer surface, (b) brittle fracture surface, and (c) fragment end surface. Fragment mass: 116.5 gr (7.55 g).



(a)



(b)



(c)

Figure L-20. Type 3A HF-1 steel cylinder fragment with heat treatment B showing (a) brittle and shear fracture surfaces, (b) cylinder inner surface, and (c) fragment end surface. Fragment mass: 172.3 gr (11.17 g).



Figure L-21. Type 3B HF-1 steel cylinder fragment with heat treatment B showing (a) shear fracture surfaces, (b) cylinder inner surface, and (c) fragment end surface. Fragment mass: 72.5 gr (4.70 g).



Figure L-22. Type 4A HF-1 steel cylinder fragment with heat treatment B showing (a) brittle fracture surfaces, (b) shear fracture surfaces, and (c) fragment end surface. Fragment mass: 51.7 gr (3.35 g).



3

2

3

2

4

(b)



(a)

Figure L-23. Type 4B HF-1 steel cylinder fragment with heat treatment B showing (a) brittle fracture surfaces and (b) fragment end surface. Fragment mass: 38.0 gr (2.46 g).

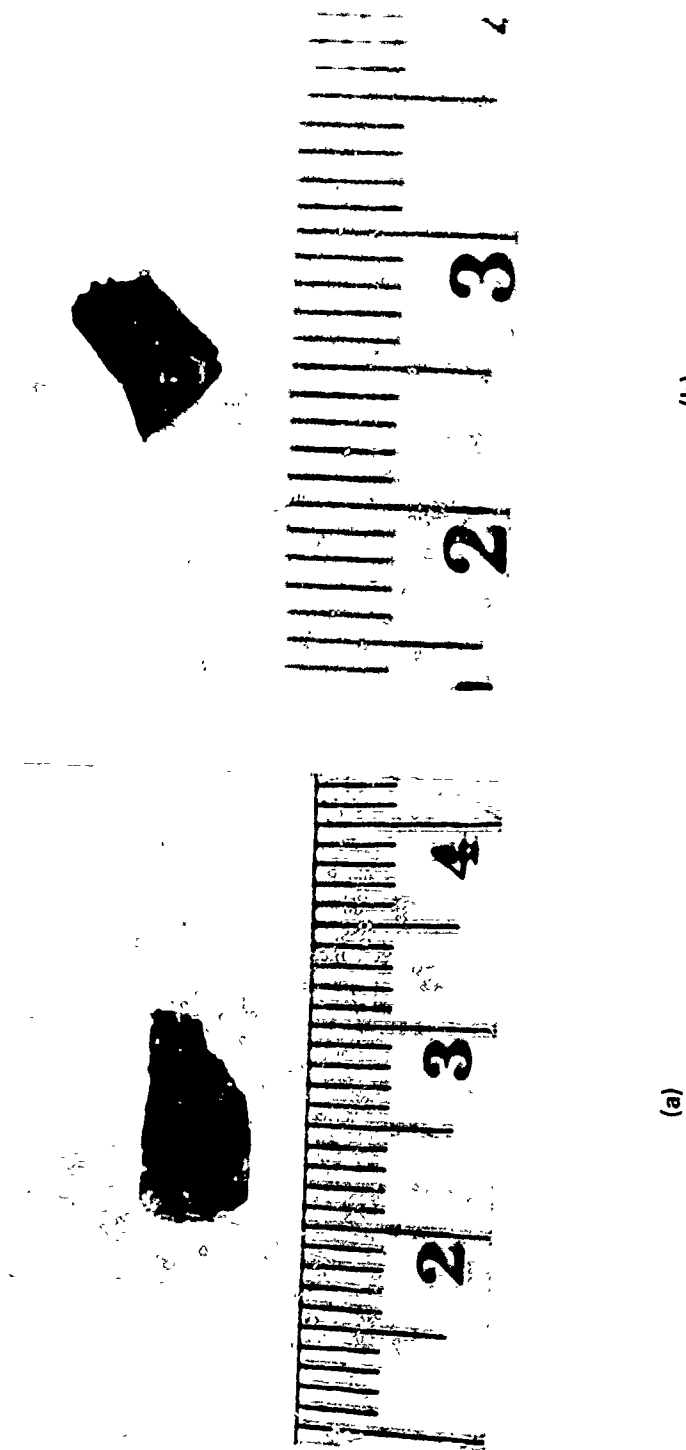


Figure L-24. Type 4C HF-1 steel cylinder fragment with heat treatment B showing (a) shear fracture surfaces and (b) fragment end surface. Fragment mass: 12.9 gr (0.84 g).

APPENDIX M

RESULTS OF THE ARMCO IRON CYLINDER, THE HF-1 STEEL CYLINDER, AND THE HF-1 STEEL PROJECTILE FRAGMENT RECOVERY EXPERIMENTS

(This appendix contains tables of the results of the Armco iron cylinder, the HF-1 steel cylinder, and the HF-1 steel projectile fragment recovery experiments. The configuration details for these experiments are given in Table 13. The results are summarized in Section VIII. Tables M-1 through M-7 give the mass distribution results for the typed fragments for the experiments. The fragments in the 0-1 gr mass group of each table were not counted due to their large numbers and small sizes. The recovered fragment mass was at least 98.9% of the initial metal mass in all the experiments. Tables M-8 through M-14 give dimension measurements and strain calculations for selected type 1 fragments from each experiment. All type 1 fragments from the HF-1 steel cylinder experiments were measured. Both English and SI units are used in these tables. (1 grain (gr) = 1/7000 pound = 0.06480 gram (g)).

Table M-1. Mass distribution and characterization of Armco iron cylinder fragments from experiment 1.^a

Mass Group (gr)	Type 1			Total		
	No.	Mass		No.	Mass	
		(gr)	(g)		(gr)	(g)
0-1 ^b				—	1326.7	85.97
1-5				637	1423.8	92.26
5-10				146	1055.4	68.39
10-15				84	1037.8	67.25
15-20				45	778.4	50.44
20-25				37	829.5	53.75
25-30	1	27.3	1.77	38	1047.8	67.90
30-40	2	70.8	4.58	41	1403.5	90.95
40-50	6	278.6	18.05	37	1673.0	108.41
50-75	18 ^c	1159.4	75.13	73	4514.0	292.51
75-100	13 ^d	1196.8	77.55	40	3594.8	232.94
100-125	12 ^e	1351.1	87.55	27	3012.2	195.19
125-150	16 ^f	2162.3	140.12	33	4484.3	290.58
150-200	10 ^g	1788.6	115.90	17	2966.0	192.20
200-300	24 ^h	5911.6	383.07	32	7927.1	513.68
300-600	47 ⁱ	21369.3	1384.73	48	21725.0	1407.78
600-1000	27 ^g	19884.0	1288.50	28	20539.8	1330.98
1000-1500	13 ^j	16982.1	1100.44	15	19658.0	1273.86
1500+	17 ^j	41128.9	2665.15	17	41128.9	2665.15

^a For this experiment only type 1 fragments were characterized. Six fragments (one fragment from the 125 - 150 gr group, two fragments from the 200 - 300 gr group, one fragment from the 600 - 1000 gr group, and two fragments from the 1000 - 1500 gr group) with a total mass of 0.216 kg were previously removed from the distribution for metallographic analysis and therefore were not characterized. Seventy-five of the 206 total type 1 fragments came from the end of the cylinder.

^b The fragments were not counted in this mass group.

^c One fragment came from the end of the cylinder.

^d Five fragments came from the end of the cylinder.

^e Four fragments came from the end of the cylinder.

^f Two fragments came from the end of the cylinder.

^g Eight fragments came from the end of the cylinder.

^h Nine fragments came from the end of the cylinder.

ⁱ Twenty-six fragments came from end of the cylinder.

^j Six fragments came from the end of the cylinder.

Table M-2. Mass distribution and characterization of Armco iron cylinder fragments from experiment 2.^a

Mass Group (gr)	Type 1 ^b	Type 2A	Type 2B	Type 3A	Type 3B	Type 4A	Type 4B	Type 4C	Total												
	No.	Mass (gr)	No.	Mass (gr)	No.	Mass (gr)	No.	Mass (gr)	No.	Mass (gr)											
0-1 ^c	15	111.6	69	482.2	31.25	26	185.1	11.99	38	281.4	18.23	17	111.8	7.24	5	55.4	2.29	646	1762.2	114.26	
1-5 ^d	7	85.9	5.57	26	435.5	28.22	8	100.1	6.49	22	269.4	17.46	9	105.3	6.82	2	28.7	6.82	170	1207.4	78.24
5-10	14	250.8	16.25	22	389.3	25.23	6	106.5	6.90	18	305.8	19.81	1	17.5	1.13			84	1025.0	66.42	
10-15	12	270.4	17.52	11	243.6	15.78	2	46.4	3.00	5	112.7	7.30						61	1069.9	69.33	
15-20	16	442.6	28.68	10	267.3	17.32	4	110.5	7.16	7	191.9	12.43	1	25.1	1.63			50	673.0	43.61	
20-25	8	255.0	16.52	5	163.0	10.56	4	126.0	8.17	1	34.0	2.20						38	1037.4	67.22	
25-30	9	311.6	21.44	7	261.8	16.97	11	416.4	26.98	4	147.7	9.57						20	642.9	41.66	
30-35	12	507.0	32.86	1	46.5	3.01	5	262.2	16.99	1	53.5	3.47						31	1157.4	75.00	
35-40	7	370.8	24.03	2	104.3	6.76	3	172.5	11.18	2	118.1	7.66						18	765.0	49.57	
40-45	2	114.5	7.4	4	226.7	14.69	3	187.1	12.12	2	125.0	8.10						13	621.9	40.30	
45-50	6	374.2	24.25	9	557.8	36.15	3	187.1	12.12	2	125.0	8.10						15	790.7	51.24	
50-55	6	374.2	24.25	9	557.8	36.15	3	187.1	12.12	2	125.0	8.10						11	631.8	40.94	
55-60	2	135.5	8.78	4	272.8	17.68	3	197.5	12.80	2	137.2	8.89						20	1244.2	80.63	
60-65	1	72.1	4.61	3	216.4	14.02	3	217.2	14.07	2	155.9	10.10						11	743.1	48.15	
65-70	1	76.1	4.93	1	78.3	5.07	3	230.6	14.94	2	160.4							7	505.7	32.77	
70-75	3	248.7	16.11	6	494.5	32.04	3	247.6	16.04									7	540.9	35.05	
75-80	1	56.4	3.50	8	698.3	45.25	1	35.2	5.52									12	990.8	64.20	
80-85	3	293.9	19.05	2	194.2	12.58	3	294.8	19.10	2	183.1	11.86						10	870.0	56.38	
85-90	1	102.6	6.65	1	102.5	6.64	3	292.1	18.93	1	97.8	6.34						5	477.9	30.97	
90-95	3	319.5	20.70	2	213.6	13.84	1	104.3	6.79	1	102.6	6.65						9	878.0	56.89	
95-100	2	224.7	14.56	1	114.3	7.41	5	537.2	34.94	1	102.6	6.65						5	516.7	33.48	
100-105	2 ^e	224.7	14.56	1	114.3	7.41	3	342.0	22.16									10	1072.3	69.48	
105-110	1 ^e	119.6	7.75	2	236.3	15.31												6	681.0	44.13	
110-115	2 ^e	247.8	16.05	4	487.0	31.56	2	246.4	15.96									3	355.9	23.06	
115-120	2	255.3	16.54	3	380.7	24.67	1	126.2	8.18									8	981.1	63.58	
120-125	3	396.8	25.71	1	130.3	6.44	4	529.4	34.30	1	134.5	8.71						6	762.2	49.39	
125-130	1	143.7	9.21				1	136.7	8.86	1	136.9	8.87						9	1190.9	77.17	
130-135	1	135.8	8.80				1	141.3	9.16									3	409.5	26.5	
135-140	4 ^e	589.1	38.17	2	296.7	19.22	1	131.0	9.78									2	285.0	18.4	
140-145	4 ^e	589.1	38.17	2	296.7	19.22	1	131.0	9.78									6	885.8	57.40	
145-150	4 ^e	606.3	39.29	2	304.7	19.74												7	1062.0	68.82	
150-155	4 ^e	606.3	39.29	2	304.7	19.74												7	1099.3	71.24	
155-160	5 ^f	784.0	50.81	1	158.6	10.28	2	323.4	20.96									3	486.3	31.51	
160-165	5 ^f	784.0	50.81	1	162.9	10.55	2	333.6	21.61									4	666.8	43.21	
165-170	2 ^e	333.2	21.59															3	519.8	33.68	
170-175	2 ^e	345.2	22.37	1	174.7	11.32												3	549.6	35.61	
175-175	2 ^e	345.2	22.37															3	549.6	35.61	
180-185	2	345.2	22.37															3	549.6	35.61	
185-190																		3	549.6	35.61	
190-195																		3	549.6	35.61	
195-200																		3	549.6	35.61	
200-205	1 ^e	202.8	13.14	1	200.2	12.97												1	188.9	12.24	
205-210	3 ^e	618.7	40.09	1	208.0	13.48												2	385.2	24.96	
210-215	2	421.4	27.31															1	197.3	12.78	
215-220	1	216.1	14.01															1	197.3	12.78	
220-225	1	224.0	14.52															1	197.3	12.78	
																		1	197.3	12.78	
																		1	197.3	12.78	
																		1	197.3	12.78	
																		1	197.3	12.78	
																		1	197.3	12.78	
																		1	197.3	12.78	
																		1	197.3	12.78	
																		1	197.3	12.78	
																		1	197.3	12.78	
																		1	197.3	12.78	
																		1	197.3	12.78	
																		1	197.3	12.78	
																		1	197.3	12.78	
																		1	197.3	12.78	
																		1	197.3	12.78	
																		1	197.3	12.78	
																		1	197.3	12.78	
																		1	197.3	12.78	
																		1	197.3	12.78	
																		1	197.3	12.78	
																		1	197.3	12.78	
																		1	197.3	12.78	
																		1	197.3	12.78	
																		1	197.3	12.78	
																		1	197.3	12.78	
																		1	197.3	12.78	
																		1	197.3	12.78	
																		1	197.3	12.78	
																		1	197.3	12.78	
																		1	197.3	12.78	
																		1	197.3	12.78	
											</										

Table M-2. Mass distribution and characterization of Armco iron cylinder fragments from experiment 2.^a (Continued)

Mass Group (g)	Type 1 ^b	Type 2A	Type 2B	Type 3A	Type 3B	Type 4A	Type 4B	Type 4C	Total
	No. (g)	No. (g)	No. (g)	No. (g)	No. (g)	No. (g)	No. (g)	No. (g)	No. (g)
225-230	1 228.6 14.81								1 228.6 14.81
230-235	1 ^c 231.0 14.97	1 210.6 14.94							2 461.6 29.91
235-240	1 235.9 15.28	1 238.4 15.45							2 474.3 30.73
245-250	2 495.1 32.09	1 248.7 16.12							3 743.9 48.20
255-270	2 ^c 533.6 34.58								2 533.7 34.58
270-275	3 ^c 820.8 53.19								3 820.8 53.19
275-280		1 276.9 17.94							1 276.9 17.94
280-285	2 ^c 565.4 36.63								2 565.4 36.63
285-290	2 572.2 37.08								2 572.2 37.08
290-295		1 292.9 18.98							1 292.9 18.98
295-300	3 ^c 895.0 58.02	1 296.8 19.23							4 1191.8 77.23
300-305	1 303.1 19.64								1 303.1 19.64
305-310	3 ^c 925.0 59.94								3 925.0 59.94
310-315	2 ^c 625.1 40.51								2 625.1 40.51
315-320	2 ^c 633.2 41.03								2 633.2 41.03
325-330		1 329.2 21.33							1 329.2 21.33
330-335	2 ^c 666.1 43.16								2 666.1 43.16
335-340	1 ^c 338.1 21.91	1 336.0 21.77							2 674.1 43.68
345-350	1 349.2 22.63								1 349.2 22.63
355-360	3 ^c 1068.0 69.21								3 1068.0 69.21
360-365	1 361.6 23.43								1 361.6 23.43
365-370	1 ^c 365.5 23.68	1 365.3 23.67							2 730.7 47.35
370-375	1 373.6 24.21								1 373.6 24.21
375-380	2 ^c 753.9 48.85								2 753.9 48.85
380-385	2 762.0 49.37								2 762.0 49.37
385-390	1 ^c 388.5 25.18	1 386.1 25.02							2 774.6 50.20
390-395	1 391.6 25.38								1 391.6 25.32
400-405	2 725.9 47.04								2 725.9 47.04
410-415	2 823.5 53.55								2 823.5 53.55
415-420	3 ^c 1287.5 82.13								3 1287.5 82.13
420-425	1 421.6 27.32								1 421.6 27.32
425-430	3 ^c 1287.1 83.15								3 1285.1 83.15
435-440	1 437.4 28.34								1 437.4 28.34
440-445	1 441.5 28.61								1 441.5 28.61
445-450	2 ^c 897.7 58.17								2 897.7 58.17
450-455	1 ^c 453.9 29.42								1 453.9 29.42
455-460	1 457.2 29.63								1 457.2 29.63
460-465	1 ^c 464.4 30.09								1 464.4 30.09
470-475	1 ^c 472.1 30.59								1 472.1 30.59
475-480	2 ^c 952.1 61.69								2 952.1 61.69
480-485	1 481.5 31.20								1 481.5 31.20
495-500	1 ^c 499.9 32.39								1 499.9 32.39
520-525	1 520.2 33.71								1 520.2 33.71
525-530	2 ^c 1052.8 68.22								2 1052.8 68.22

Table M-2. Mass Distribution and Characterization of Armco iron cylinder fragments from experiment 2.^a (Continued)

Mass Group (gr)	Type 1 ^b		Type 2A		Type 2B		Type 3A		Type 3B		Type 4A		Type 4B		Type 4C		Total	
	No.	Mass (gr)	No.	Mass (gr)	No.	Mass (gr)	No.	Mass (gr)	No.	Mass (gr)	No.	Mass (gr)	No.	Mass (gr)	No.	Mass (gr)	No.	Mass (gr)
540-545	1	541.7	3510														1	541.7
555-560	1 ^c	557.9	3615														1	557.9
630-635	1 ^c	630.4	40.85														1	630.4
645-650	1	646.1	41.87														1	646.1
675-680	1	677.2	43.88														1	677.2
690-695	3	2081.3	134.87														3	2081.3
705-710	1 ^c	710.0	46.01														1	710.0
715-720	1	718.5	50.45														1	718.5
725-730	2 ^c	1574.6	102.03														2	1574.6
810-815	1	812.5	52.65														1	812.5
830-835	1	833.7	54.02														1	833.7
835-840	1	837.3	54.25														1	837.3
855-860	1	860.0	55.73														1	860.0
860-865	1	863.7	55.97														1	863.7
865-870	1 ^c	866.7	56.16														1	866.7
885-890	1	888.7	57.59														1	888.7
895-900	1	898.0	58.19														1	898.0
900-905	1	904.5	58.61														1	904.5
925-930	1	928.7	60.18														1	928.7
945-950	1	946.2	61.31														1	946.2
955-960	1	958.0	62.08														1	958.0
960-965	1	963.6	62.44														1	963.6
965-970	1	968.6	62.76														1	968.6
985-990	3 ^c	2964.7	192.11														3	2964.7
990-995	1 ^c	992.5	64.32														1	992.5
1020-1025	1	1020.0	66.10														1	1020.0
1035-1040	2	2074.0	134.39														2	2074.0
1080-1085	1	1084.5	70.28														1	1084.5
1085-1090	1 ^c	1086.8	70.42														1	1086.8
1090-1095	1	1093.7	70.87														1	1093.7
1150-1155	1	1153.7	74.76														1	1153.7
1200-1225	1 ^c	1222.8	85.22														1	1222.8
1325-1330	1	1326.1	85.93														1	1326.1
1340-1345	1	1340.9	86.89														1	1340.9
1345-1350	1	1349.0	87.41														1	1349.0
1360-1365	1	1364.2	88.40														1	1364.2
1375-1380	1 ^c	1375.0	89.10														1	1375.0
1400-1405	1	1402.3	90.87														1	1402.3
1465-1470	1	1467.4	95.09														1	1467.4
1550-1555	1 ^c	1551.0	100.50														1	1551.0
1565-1570	1	1569.5	101.21														1	1569.5
1675-1680	1	1678.3	108.75														1	1678.3
1685-1690	1	1686.2	109.26														1	1686.2
1770-1775	1	1774.5	114.99														1	1774.5
1775-1780	1	1776.1	115.09														1	1776.1
1855-1860	1 ^c	1858.0	120.40														1	1858.0
1865-1870	1	1865.1	120.86														1	1865.1

Table M-2. Mass distribution and characterization of Armco iron cylinder fragments from experiment 2.^a (Continued)

Mass Group (g)	Type 1 ^b	Type 2A	Type 3B	Type 3A	Type 3B	Type 4A	Type 4B	Type 4C	Total
	No.	Mass (g)	No.	Mass (g)	No.	Mass (g)	No.	Mass (g)	No.
1910-1915	1 ^c	1912.8	123.95						1
2165-2170	1	2167.3	140.44						1
2175-2180	1 ^c	2175.9	141.26						1
2400-2405	1 ^c	2402.8	155.70						1
2595-2600	1	2599.7	168.46						1
2610-2615	1	2614.3	169.40						1
2620-2625	1 ^c	2622.1	169.91						1
2770-2775	1	2774.6	179.79						1
3330-3335	1 ^c	3333.0	215.98						1

^a If a mass group is not listed then no fragments were observed in that group. If there is no entry for a given type fragment in a mass group then no fragments of that type were observed.

^b Fifty-six of the 195 total type 1 fragments came from the end of the cylinder.

^c The fragments were not counted in this mass group. Only type 1 fragments were characterized.

^d Only type 1 fragments were characterized in this mass group.

^e One fragment came from the end of the cylinder.

^f Three fragments came from the end of the cylinder.

^g Two fragments came from the end of the cylinder.

Table M-3. Mass distribution and characterization of HF-1 steel cylinder fragments with heat treatment A from experiment 3.^a

Mass Group (gr)	Type 1			Total		
	No.	Mass		No.	Mass	
		(gr)	(g)		(gr)	(g)
0-1 ^b				—	8568.6	555.24
1-5				5521	12758.9	826.78
5-10				1482	10564.0	684.55
10-15				755	9264.6	600.35
15-20				464	8045.2	521.33
20-25				307	6888.8	446.39
25-30				232	6322.8	409.72
30-40				351	12089.4	783.39
40-50	1 ^c	41.5	2.69	234	10502.6	680.57
50-75	3	193.5	12.54	370	22785.1	1476.47
75-100	3	257.6	16.69	183	15836.0	1026.17
100-125	3	476.2	30.86	121	13562.1	878.82
125-150				47	6451.4	418.05
150-200	7 ^d	1261.8	81.77	58	9973.0	646.25
200-300	13 ^e	3158.4	204.66	47	11255.3	729.34
300-600	3 ^e	1096.6	71.06	9	3141.6	203.58

^a For this experiment only type 1 fragments were characterized. Six fragments (one fragment from the 150-200 gr group, two fragments from the 200-300 gr group, and three fragments from the 300-600 gr group) with a total mass of 0.117 kg were previously removed from the distribution for metallographic analysis and therefore were not characterized. Twelve of the 33 total type 1 fragments came from the end of the cylinder.

^b The fragments were not counted in this mass group. Only type 1 fragments were characterized.

^c One fragment came from the end of the cylinder.

^d Two fragments came from the end of the cylinder.

^e Eight fragments came from the end of the cylinder.

Table M-4. Mass distribution and characterization of HF-1 steel cylinder fragments with heat treatment A from experiment 4.3

Mass Group	Type 1 ^b	Type 2A	Type 2B	Type 3A	Type 3B	Type 4A	Type 4B	Type 4C	Total															
	No.	(gr)	No.	(gr)	No.	(gr)	No.	(gr)	No.	(gr)	No.	(gr)	No.	(gr)	No.	(gr)	No.	(gr)						
0-1 ^c	-	-	-	-	-	-	-	-	-	-	-	-	-	-	-	-	-	-						
1-5 ^d	-	-	-	-	-	-	-	-	-	-	-	-	-	-	-	-	-	-						
5-10	3	36.4	557	4056.0	262.83	132	972.5	63.02	32	232.0	15.04	376	2667.5	172.85	510	3493.7	226.39	1	9.0	0.59	5958	13581.7	880.09	
10-15	3	36.4	306	3720.8	241.11	84	1036.4	67.16	28	345.4	22.38	194	2370.7	153.62	125	1459.6	97.18	1	13.9	0.90	741	9023.3	584.71	
15-20	20	452.9	29.35	239	4119.6	266.95	71	1233.4	79.92	11	89.4	12.28	104	1789.4	115.95	46	777.9	50.41	1	17.5	1.13	472	8127.2	526.64
20-25	21	572.5	37.10	118	2644.9	171.39	55	1237.0	80.16	12	274.2	17.77	65	1473.4	95.48	17	379.9	24.62	287	6462.4	418.76			
25-30	23	572.5	37.10	99	2679.6	173.64	54	1451.6	94.06	8	216.7	14.04	38	1596.9	103.48	5	135.0	8.75	245	6652.3	431.07			
30-35	23	572.5	37.10	70	2261.2	146.53	46	1484.7	96.31	11	359.6	23.30	45	1469.5	95.22	6	190.3	12.33	201	6525.1	423.83			
35-40	28	1048.9	67.97	58	2175.5	140.97	31	1157.4	75.00	4	145.4	9.42	25	920.0	59.62	3	114.6	7.42	149	5561.8	360.41			
40-45	32	1368.7	88.69	52	2211.4	143.30	42	1783.9	115.59	3	129.1	8.36	20	849.5	55.05	2	82.8	5.37	151	6425.4	416.36			
45-50	25	1187.4	76.94	27	1273.6	82.53	23	1089.5	70.60	2	96.6	6.26	13	613.3	39.74	2	90.8	5.89	92	4351.2	281.96			
50-55	30	1578.5	102.28	25	1304.6	84.34	24	1259.3	81.60	6	315.9	20.47	13	677.4	43.89	98	5135.7	332.79	93	5391.0	349.34			
55-60	21	1212.3	78.56	28	1613.7	104.57	33	1925.6	124.78	3	176.6	11.45	4	462.8	29.99	7	247.9	16.07	73	4538.1	295.36			
60-65	30	1818.6	121.93	19	1179.4	76.43	20	1249.1	80.94	1	70.1	4.54	7	462.0	29.93	64	4308.5	279.19	64	4308.5	279.19			
65-70	7	507.1	32.86	11	798.9	51.77	17	1232.3	79.85	1	77.1	4.99	2	154.8	10.03	36	2608.4	169.03	36	2608.4	169.03			
70-75	19	1476.9	95.70	11	842.5	54.92	15	1162.0	75.29	1	84.9	5.50	1	90.0	5.83	48	3718.2	240.94	48	3718.2	240.94			
80-85	25	2060.4	133.51	9	718.9	47.88	17	1416.7	91.80	1	84.9	5.50	1	90.0	5.83	52	4300.8	274.70	52	4300.8	274.70			
85-90	15	1309.9	84.88	5	433.4	28.08	14	1221.8	79.17	1	84.9	5.50	1	90.0	5.83	38	3314.6	214.79	38	3314.6	214.79			
90-95	13	1210.5	78.44	2	185.7	12.03	14	1295.8	83.97	1	93.5	6.06	1	105.0	6.80	30	2185.4	140.50	30	2185.4	140.50			
95-100	8	728.0	50.42	4	395.0	25.60	8	779.3	50.50	1	103.4	6.70	1	105.0	6.80	26	2629.5	170.39	26	2629.5	170.39			
100-105	11	1131.0	71.29	4	373.1	24.18	9	917.0	59.42	1	103.4	6.70	1	105.0	6.80	25	2683.0	173.86	25	2683.0	173.86			
105-110	12	1286.2	83.34	2	214.0	13.87	11	1182.8	76.64	1	112.7	7.30	1	112.7	7.30	23	2577.0	166.99	23	2577.0	166.99			
110-115	1	110.6	7.17	6	669.3	43.37	3	342.1	22.17	12	1342.3	86.98	23	2462.6	159.58	21	2462.6	159.58	21	2462.6	159.58			
115-120	1 ^e	117.2	7.60	7	825.6	53.50	3	349.1	22.62	10	1170.6	75.86	21	2462.6	159.58	15	1837.4	119.06	15	1837.4	119.06			
120-125	2	245.2	15.89	4	489.2	31.70	1	121.6	7.88	8	981.4	63.60	24	3056.3	198.05	24	3056.3	198.05	24	3056.3	198.05			
125-130	2	256.3	16.61	11	1402.1	90.85	2	255.2	16.54	8	1013.2	65.66	14	1863.7	120.77	14	1863.7	120.77	14	1863.7	120.77			
130-135	5	660.2	42.78	1	133.6	8.66	2	273.2	17.20	2	273.2	17.20	11	1513.1	98.05	11	1513.1	98.05	11	1513.1	98.05			
135-140	1	139.4	9.04	3	1100.5	71.31	2	273.2	17.20	2	273.2	17.20	5	712.2	46.15	5	712.2	46.15	5	712.2	46.15			
140-145	1 ^e	143.8	9.32	3	426.1	27.61	2	294.8	19.10	4	586.8	38.03	10	1473.9	95.51	10	1473.9	95.51	10	1473.9	95.51			
145-150	4	592.3	38.38	2	294.8	19.10	4	586.8	38.03	6	908.3	58.86	10	1543.1	100.00	10	1543.1	100.00	10	1543.1	100.00			
150-155	1 ^e	154.4	10.00	2	327.3	21.21	1	153.1	9.92	6	908.3	58.86	15	2351.8	152.40	15	2351.8	152.40	15	2351.8	152.40			
155-160	1 ^e	158.5	10.03	10	1363.3	101.4	1	157.4	10.20	3	470.6	30.50	8	1297.3	84.06	8	1297.3	84.06	8	1297.3	84.06			
160-165	1 ^e	162.9	10.56	5	809.2	52.44	3	495.0	32.07	1	167.1	10.83	5	830.12	53.79	5	830.12	53.79	5	830.12	53.79			
165-170	1 ^e	158.1	10.89	3	531.2	34.42	1	174.6	11.31	4	692.2	44.85	8	1398.0	90.59	8	1398.0	90.59	8	1398.0	90.59			
170-175	1 ^e	158.1	10.89	3	531.2	34.42	1	174.6	11.31	4	692.2	44.85	5	886.2	57.43	5	886.2	57.43	5	886.2	57.43			
175-180	1 ^e	158.1	10.89	3	531.2	34.42	1	174.6	11.31	4	692.2	44.85	2	366.9	23.77	2	366.9	23.77	2	366.9	23.77			
180-185	1 ^e	158.1	10.89	3	531.2	34.42	1	174.6	11.31	4	692.2	44.85	6	1116.3	72.33	6	1116.3	72.33	6	1116.3	72.33			
185-190	3 ^e	557.3	36.15	1	187.0	12.12	2	371.4	24.07	2	371.4	24.07	2	371.4	24.07	2	371.4	24.07	2	371.4	24.07			

Table M-4. Mass distribution and characterization of HF-1 steel cylinder fragments with heat treatment 4.^a (Continued)

Mass Group (gr)	Type 1 ^b	Type 2A	Type 2B	Type 3A	Type 3B	Type 4A	Type 4B	Type 4C	Total
	No.	No.	No.	No.	No.	No.	No.	No.	No.
	Mass (gr)	Mass (gr)	Mass (gr)	Mass (gr)	Mass (gr)	Mass (gr)	Mass (gr)	Mass (gr)	Mass (gr)
190-195	2	384.0	24.88	5	963.9	62.46			7
195-200	2	394.3	25.55						2
200-205	3	610.5	39.56	1	205.0	13.22			4
205-210				2	414.0	26.82			2
210-215	1 ^c	211.7	13.72	2	424.4	27.50			2
215-220	1	215.0	13.93	3	434.2	28.13			6
220-225				1	221.0	14.32			1
225-230				1	226.4	14.67			1
230-235									1
235-240				1	238.0	15.42			3
240-245	1	241.6	15.66	1	244.5	15.84			2
245-250									1
250-255	1	253.2	16.41						2
255-260				1	267.4	17.33			1
265-270				1	274.8	17.81			1
270-275									1
275-280				1	281.7	18.25			1
280-285									1
285-290									1
290-295				1	291.7	18.90			1
295-300				1	296.1	19.19			1
300-305				1	305.4	19.79			1
305-310									1
310-315									1
315-320	1	318.7	20.65						2
320-325									1
325-330									2
330-335									2
335-340									2
340-345									2
345-350									2
350-355									2
355-360									2
360-365									2
365-370									2
370-375									2

^a If a mass group is not listed then no fragments were observed in that group. If there is no entry for a given type fragment in a mass group then no fragments of that type were observed.

^b Seven of the 25 total type 1 fragments came from the end of the cylinder.

^c The fragments were not counted in this mass group. Only type 1 fragments were characterized.

^d Only type 1 fragments were characterized in this mass group.

^e One fragment came from the end of the cylinder.

A-4

Table M-5. Mass distribution and characterization of HF-1 steel cylinder fragments with heat treatment B from experiments 5.²

Mass Group (gr)	Type 1 ^b No.	Type 1 ^b Mass (gr)	Type 2A No.	Type 2A Mass (gr)	Type 2B No.	Type 2B Mass (gr)	Type 3A No.	Type 3A Mass (gr)	Type 3B No.	Type 3B Mass (gr)	Type 4A No.	Type 4A Mass (gr)	Type 4B No.	Type 4B Mass (gr)	Type 4C No.	Type 4C Mass (gr)	Total Mass (gr)
0-1 ^c																	11601.5
1-2.5 ^d																	7040.0
2.5-5 ^d																	4395
5-7.5																	2309
7.5-10																	1147
10-12.5																	779
12.5-15																	6791.8
15-17.5																	6000.8
17.5-20																	5329.5
20-22.5																	5483.8
22.5-25																	4971.6
25-27.5																	4244.8
27.5-30																	3955.2
30-32.5																	4337.9
32.5-35																	3936.8
35-37.5																	3810.3
37.5-40																	3490.8
40-42.5																	3121.4
42.5-45																	2444.9
45-47.5																	2049.6
47.5-50																	2039.4
50-52.5																	204.6
52.5-55																	158.43
55-57.5																	158.43
57.5-60																	158.43
60-62.5																	158.43
62.5-65																	158.43
65-67.5																	158.43
67.5-70																	158.43
70-72.5																	158.43
72.5-75																	158.43
75-77.5																	158.43
77.5-80																	158.43
80-82.5																	158.43
82.5-85																	158.43
85-87.5																	158.43
87.5-90																	158.43
90-92.5																	158.43
92.5-95																	158.43
95-97.5																	158.43
97.5-100																	158.43
100-105																	158.43
105-110																	158.43
110-115																	158.43
115-120																	158.43
120-125																	158.43
125-130																	158.43

Table M-5. Mass distribution and characterization of HF-1 steel cylinder fragments with heat treatment B from experiments 5.^a (Continued)

Mass Group (gr)	Type 1 ^b No.	Type 1 ^b Mass (gr)	Type 2A No.	Type 2A Mass (gr)	Type 2B No.	Type 2B Mass (gr)	Type 3A No.	Type 3A Mass (gr)	Type 3B No.	Type 3B Mass (gr)	Type 4A No.	Type 4A Mass (gr)	Type 4B No.	Type 4B Mass (gr)	Type 4C No.	Type 4C Mass (gr)	Total No.	Total Mass (gr)
130-135	1	131.6	8.53	10	1326.1	85.93	1	130.5	8.46	3	399.4	25.88					15	1987.6
135-140	3 ^c	409.3	26.52	2	276.8	17.94				2	274.9	17.81					7	961.0
140-145	5 ^c	713.9	46.20	1	140.2	9.08	1	143.2	9.28	4	572.2	37.08					11	1569.5
145-150	2 ^c	294.7	19.10	1	148.0	9.59	1	148.3	9.61	2	296.6	19.22					6	887.6
150-155	1 ^c	151.4	9.81	1	151.5	9.82	3	457.0	29.61	3	457.0	29.61					5	759.9
155-160	4 ^c	627.1	40.64	1	155.7	10.09	1	156.7	10.15	2	313.3	20.30					8	1252.8
160-165				3	487.5	31.59	2	324.2	21.01								5	811.7
165-170	4	670.6	43.46														4	670.6
170-175	2	343.8	22.28	1	171.4	11.11	1	172.3	11.17								4	687.5
175-180	2	356.4	23.10	1	179.7	11.65											3	536.1
185-190	1 ^c	188.8	12.23														1	188.8
190-195	1 ^c	192.6	12.42														1	192.6
195-200	1 ^c	179.8	12.95	1	197.1	12.77											2	396.9
205-210	1 ^c	206.1	13.36	1	205.0	13.28											2	411.1
210-215	2	424.3	27.50	1	213.6	13.84											4	849.2
215-220	1	219.1	14.20				1	211.3	13.69								2	422.4
220-225	1 ^c	232.8	15.09	1	231.9	15.03											1	219.1
235-240	1 ^c	237.0	15.36														2	464.7
240-245	1 ^c	240.7	15.58														1	237.0
275-280	1	277.4	17.98														1	240.4
280-285				1	280.7	18.19											1	277.4
																	1	280.7

^a If a mass group is not listed then no fragments were observed in this group. If there is no entry for a given type fragment in a mass group then no fragments of that type were observed.

^b Twenty-one of the 55 total type 1 fragments came from the end of the cylinder.

^c The fragments were not counted in this mass group. Only type 1 fragments were characterized.

^d Only type 1 fragments were characterized in this mass group.

^e One fragment came from the end of the cylinder.

^f Two fragments came from the end of the cylinder.

Table M-6. Mass distribution and characterization of HF-1 steel cylinder fragments with heat treatment B from experiment 6.^a

Mass Group (gr)	Type 1			Total		
	No.	Mass		No.	Mass	
		(gr)	(g)		(gr)	(g)
0-1 ^b				—	11926.0	772.80
1-2.5				4680	7458.3	483.30
2.5-5				2616	9316.4	603.70
5-7.5				1268	7858.6	509.24
7.5-10				735	6375.4	413.13
10-12.5				546	6104.9	395.60
12.5-15				421	5757.0	373.05
15-17.5				327	5307.9	343.95
17.5-20				259	4833.7	313.22
20-22.5				241	5102.1	330.62
22.5-25				193	4593.6	297.67
25-27.5				190	5008.4	324.54
27.5-30				128	3667.4	237.65
30-32.5				131	4096.1	265.43
32.5-35				101	3422.5	221.78
35-37.5				94	3411.1	221.04
37.5-40				110	4252.5	275.56
40-42.5				75	2082.9	199.77
42.5-45				63	2756.5	178.62
45-47.5				56	2585.7	167.55
47.5-50				62	3025.6	196.06
50-52.5				46	2362.1	153.06
52.5-55				46	2484.1	160.97
55-57.5	1 ^c	55.1	3.57	46	2587.2	167.65
57.5-60				41	2415.8	156.54
60-62.5	1	61.1	3.96	36	2206.2	142.96
62.5-65				28	1776.6	115.12
65-67.5				36	2388.9	154.80
67.5-70				26	1787.2	115.81
70-72.5				21	1492.2	97.02
72.5-75				14	1032.9	66.93
75-77.5				18	1376.8	89.22
77.5-80	1 ^c	77.9	5.05	22	1731.6	112.21
80-82.5				22	1792.7	116.17
82.5-85				12	1005.7	65.17
85-87.5				6	519.0	33.63

Table M-6. Mass distribution and characterization of HF-1 steel cylinder fragments with heat treatment B from experiment 6.^a (Continued)

Mass Group (gr)	Type 1			Total		
	No.	Mass		No.	Mass	
		(gr)	(g)		(gr)	(g)
87.5-90				13	1152.0	74.65
90-92.5				12	1095.6	70.99
92.5-95				9	837.7	54.28
95-97.5				9	865.4	56.08
97.5-100				8	789.4	51.15
100-105	1	101.4	6.57	16	1634.7	105.03
105-110	1	107.3	6.95	17	1824.1	118.20
110-115	3	334.0	21.64	16	1800.3	116.66
115-120	1	115.2	7.47	13	1521.8	98.61
120-125	1	122.9	7.96	11	1351.9	87.60
125-130	4 ^c	508.5	32.95	12	1530.4	99.17
130-135	2	264.4	17.13	6	793.0	51.39
135-140	4 ^d	549.1	35.58	8	1097.1	71.09
140-145	2	283.4	18.36	8	1137.3	73.70
145-150	3 ^e	442.7	28.69	6	882.7	57.20
150-155	2 ^c	305.6	19.80	5	763.1	49.45
155-160	1 ^c	157.4	10.20	4	631.8	40.94
160-165	1	164.1	10.63	3	486.2	31.51
165-170	3 ^e	503.1	32.60	5	841.2	54.51
170-175	1	174.2	11.29	2	347.2	22.50
175-180	1 ^c	178.0	11.53	2	354.2	22.95
180-185	3 ^c	546.5	34.51	4	728.4	47.20
185-190	1	185.4	12.01	3	563.3	36.50
190-195	2 ^e	384.3	24.90	3	574.3	37.21
195-200				1	199.3	12.91
205-210	2 ^e	415.7	26.94	3	625.7	40.55
210-215				1	210.7	13.65
220-225	1 ^c	220.1	14.26	2	440.9	28.57
230-235	1 ^c	234.7	15.21	1	234.7	15.21
235-240				2	471.0	30.52
240-245				1	242.2	15.69
245-250	2 ^c	496.0	32.14	2	496.0	32.14
290-295	1 ^c	291.8	18.91	1	293.8	19.04
315-320	1	319.2	20.68	1	319.2	20.68
325-330	1	328.1	21.26	1	328.1	21.26

^a If a mass group is not listed then no fragments were observed in that group. For this experiment only type 1 fragments were characterized. Twenty-three of the 49 total type 1 fragments came from the end of the cylinder.

^b The fragments were not counted in this mass group.

^c One fragment came from the end of the cylinder.

^d Four fragments came from the end of the cylinder.

^e Two fragments came from the end of the cylinder.

Table M-7. Mass distribution and characterization of HF-1 steel projectile fragments with heat treatment A from experiment 7.2

Mass Group	Type 1 ^b	Type 2A ^c	Type 2B ^c	Type 3A	Type 3B	Type 4A	Type 4B	Type 4C	Total
(g)	No.	(g)	No.	(g)	No.	(g)	No.	(g)	(g)
0-1 ^d									
1-5 ^e									
5-10	5(5)	42.4	2.75	73(3)	599.3	36.24	692(135)	4584.8	323.01
10-15	15(15)	178.8	11.58	102(9)	1317.5	89.38	355(79)	4366.3	282.94
15-20	19(19)	314.8	21.69	88(9)	559.3	99.75	257(60)	4450.7	288.40
20-25	24(24)	544.6	35.29	101(17)	2273.8	147.34	131(48)	3813.1	247.09
25-30	14(14)	391.1	25.34	73(18)	1998.6	129.51	134(39)	3583.3	232.19
30-35	12(11)	380.3	24.64	74(21)	2377.0	154.03	98(34)	3173.8	205.66
35-40	13(12)	489.8	31.74	85(18)	3168.0	205.28	75(21)	2896.8	181.88
40-45	19(16)	810.0	52.49	66(21)	2819.0	182.67	54(11)	2289.7	148.37
45-50	11(10)	525.1	34.03	73(25)	3469.5	224.82	37(7)	1770.9	114.75
50-55	10(10)	578.0	34.22	68(25)	3571.0	231.49	37(8)	1756.1	111.85
55-60	8(8)	456.9	29.60	65(22)	3741.0	242.42	40(8)	2306.0	149.43
60-65	5(5)	308.6	19.99	57(24)	3749.8	230.03	20(6)	1244.7	80.66
65-70	6(4)	402.5	26.08	72(18)	4866.6	315.36	19(4)	1288.6	83.50
70-75	14(9)	1011.3	65.53	46(19)	3312.2	214.63	8	580.7	37.63
75-80	3(2)	235.0	15.23	42(16)	3257.6	211.10	15(1)	1154.0	74.78
80-85	9(7)	736.1	47.70	53(18)	4346.4	281.64	6	493.9	32.01
85-90	4(2)	346.6	22.46	35(14)	3063.9	198.54	13(1)	1142.2	74.01
90-95	6(3)	555.3	35.98	37(15)	3429.9	222.26	9(1)	833.3	54.00
95-100	7(4)	676.9	43.87	41(13)	3981.8	238.02	10(4)	969.2	62.81
100-105	3(1)	310.6	20.13	32(7)	3284.9	212.86	7	715.8	46.39
105-110	12(7)	1292.5	83.75	20(6)	2144.6	138.97	5	535.8	34.72
110-115	5(7)	561.5	36.39	20(10)	2241.1	145.22	4	448.4	29.05
115-120	15(7)	1761.8	114.17	17(3)	1998.2	129.48	3	349.4	22.64
120-125	4(2)	488.8	31.67	23(5)	2509.4	182.05	10(1)	120.2	7.79
125-130	8(2)	1026.4	66.51	22(7)	2787.1	180.60	2	254.5	16.49
130-135	6	803.3	52.06	14(2)	1830.1	119.89	3	402.0	26.05
135-140	11(2)	1516.5	98.27	15(5)	2060.4	133.51	3	413.3	26.78
140-145	7(2)	998.0	64.67	16(6)	2266.9	146.90	5	714.7	46.31
145-150	2	297.6	19.28	15(4)	2210.9	143.27	1	148.1	9.59
150-155	5(3)	1360.8	88.18	8(4)	1214.9	78.73	2	304.0	19.70
155-160	5	783.5	50.77	14(5)	2207.2	143.02	2	316.6	20.97
160-165	2(1)	324.4	21.02	12(1)	1950.0	126.36	2	323.5	20.97
165-170	5(1)	835.9	54.17	8(2)	1332.2	86.33			
170-175	4	690.0	44.71	7(1)	1210.9	78.46			
175-180	3	537.1	34.80	5	891.4	57.76			
180-185	3	545.9	35.38	4(1)	730.5	47.34			
185-190	4	746.7	48.39	3(2)	560.9	36.35			
190-195	6	1142.7	74.37	3	574.6	37.24			
195-200	2	391.9	25.40	4	795.4	51.54			
200-205	5(1)	1011.9	65.57	2	405.1	26.25			
205-210	6	1242.6	80.52	2	412.6	26.74			
210-215	5	1061.2	68.77	2(1)	422.4	27.37			
215-220	1	218.4	14.15	2	434.2	28.14			
220-225	2	445.8	28.89	2	447.2	28.98			
225-230	4	911.9	59.09						
230-235	2	464.2	30.08	3(1)	701.8	45.48			
235-240	2	474.3	30.74						
240-245	3	726.7	47.09	3	724.7	46.96			

Table M-7. Mass distribution and characterization of HF-1 steel projectile fragments with heat treatment A from experiment 7.^a (Continued)

Mass Group (gr)	No.	Type 1 ^b Mass (gr)	Type 2A ^c No.	Type 2A ^c Mass (gr)	Type 2B ^c No.	Type 2B ^c Mass (gr)	Type 3A No.	Type 3A Mass (gr)	Type 3B No.	Type 3B Mass (gr)	Type 4A No.	Type 4A Mass (gr)	Type 4B No.	Type 4B Mass (gr)	Type 4C No.	Type 4C Mass (gr)	Total Mass (gr)
245-250	1	248.7 16.12	3	741.6 48.06			2	495.2 32.09									6 1485.6 96.26
250-255	1	250.7 16.24	2	503.6 32.64			2	503.5 32.63									5 1257.9 81.51
255-260	2	510.3 33.07	1(1)	259.2 16.80			1	256.2 16.60									4 1025.7 66.47
260-265	5	1307.4 84.72					2	521.4 33.79									7 1828.8 118.51
265-270	2	535.9 34.72	1	269.1 17.44													3 805.0 52.16
270-275	2	547.2 35.46	1	272.0 17.63													4 1093.0 70.83
275-280	1	277.8 18.00	1	277.8 18.00													2 -55.6 36.00
280-285	3	848.2 54.96	1	280.0 18.15													4 1128.2 73.11
285-290	1	287.0 18.60	2	579.3 37.54													3 866.3 56.13
290-295					1	291.5 18.89											1 291.5 18.89
295-300	5	1487.3 96.38	2	591.7 38.34													7 2079.1 134.70
300-305	4	1214.0 78.67	2	606.9 39.33													6 1820.9 118.00
305-310	3	923.1 59.81	1	306.6 19.87													4 1229.7 79.68
310-315	3	936.0 60.65	1	312.7 20.26			1	311.2 20.17									5 1559.9 101.08
315-320	3	952.9 61.75	1	321.2 20.81													3 952.9 61.75
320-325	5	1637.0 106.08															1 321.2 20.81
325-330	3	998.3 64.69															5 1637.0 106.08
330-335	3	937.7 21.89															3 998.3 64.69
335-340	1	337.7 21.89															1 337.7 21.89
340-345	2	694.0 44.97															2 685.0 44.39
345-350	2	694.0 44.97															2 694.0 44.97
350-355	1	358.6 23.24															1 352.6 22.85
355-360	2	724.3 46.93															2 715.5 46.36
360-365	2	724.3 46.93															2 724.3 46.93
365-370	1	370.1 23.98	3	1099.0 71.22													3 1099.0 71.22
370-375	1	371.1 24.44	1	374.9 24.29													1 370.1 23.98
375-380	1	371.1 24.44	1	383.0 24.82			1	377.9 24.49									3 1130.0 73.22
380-385	2	763.2 49.46															3 1146.2 74.27
385-390	2	775.7 50.27															2 775.7 50.27
390-395	4	1583.4 102.61	1	392.1 25.41													5 1973.5 128.02
400-405	1	404.3 26.20															2 806.5 52.26
405-410	1	409.1 26.51															1 409.1 26.51
410-415	2	826.2 53.54															2 826.2 53.54
415-420	1	417.4 27.05	1	416.5 26.99													2 833.9 54.04
420-425	2	846.5 54.86	1	420.3 27.77													3 1267.3 82.12
425-430	2	855.8 55.46															2 855.8 55.46
430-435	3	1299.4 84.20	1	446.7 28.95			1	432.1 28.00									4 1731.8 112.21
445-450	1	452.4 29.32															1 446.7 28.95
450-455	1	457.5 29.65															1 457.5 29.65
455-460	1	465.0 30.07															1 465.0 30.07
465-470	1	467.0 30.26															1 465.0 30.07
490-495	1	492.0 31.88															1 492.0 31.88
500-505	1	503.7 32.64															1 492.0 31.88
505-510	1	509.8 33.04															1 503.7 32.64
515-520	1	516.8 33.49															1 509.8 33.04
525-530	1	525.5 34.05															1 516.8 33.49
530-535	1	534.0 34.61															1 525.5 34.05
535-540			1	536.2 34.75													1 534.0 34.61
																	1 536.2 34.75

Table M-7. Mass distribution and characterization of HF-1 steel projectile fragments with heat treatment A from experiment 7.^a (Continued)

Mass Group (g)	No.	Mass (g)	Type 1 ^b	Type 2A ^c	Type 3B ^c	Type 3A	Type 3B	Type 4A	Type 4B	Type 4C	Total
			No.	(g)	(g)	No.	(g)	No.	(g)	No.	(g)
540-545	1	542.3	35.14								542.3
550-555	2	1103.6	71.51								1103.6
570-575	1	579.9	36.99								579.9
625-630	2	1253.3	81.22								1253.3
635-640	2	1274.9	82.62								1274.9
640-645	1	641.3	41.56								641.3
650-655	1	652.9	42.31								652.9
665-670	1	668.4	43.31								668.4
680-685	1	684.6	44.36								684.6
685-690	1	689.0	44.71								689.0
740-745	1	742.7	48.13								742.7
765-770	1	766.4	49.66								766.4
770-775	1	771.4	49.99								771.4
790-795	2	1587.1	102.85								1587.1
795-800	1	798.4	47.85								798.4
800-805	1	800.2	51.85								800.2
810-815	1	810.4	52.51								810.4
860-865	1	864.7	56.03								864.7
865-870	1	866.0	56.12								866.0
895-900	1	898.2	58.20								898.2
925-930	2	1856.2	120.28								1856.2
930-935	2	1867.6	121.02								1867.6
935-940	1	936.9	60.71								936.9
940-945	1	944.7	61.22								944.7
1005-1010	2	2011.1	130.32								2011.1
1090-1095	1	1092.0	70.76								1092.0
1150-1155	1	1150.1	74.53								1150.1
1175-1180	1	1177.0	76.27								1177.0
1280-1285	1	1281.8	83.66								1281.8
1295-1300	1	1295.6	83.95								1295.6
1425-1430	1	1427.4	92.50								1427.4
1550-1555	1	1550.7	100.49								1550.7
1710-1715	1	1710.7	110.86								1710.7

^a If a mass group is not listed then no fragments were observed in that group. If there is no entry for a given type fragment in a mass group then no fragments of that type were observed. Includes only the fragments from the forward and aft projectile sections and not the fuse fragments.

^b A total of 210 type 1 fragments came from the joint region of the forward and aft projectile sections. For a given mass group the total number of type 1 fragments is listed first, followed by the number from the joint region in parentheses. Fifteen fragments came from the threaded fuse end of the forward section: three fragments from the 70-75 g group, one fragment from the 115-120 g group, one fragment from the 165-170 g group, one fragment from the 170-175 g group, one fragment from the 260-265 g group, two fragments from the 295-300 g group, one fragment from the 325-330 g group, one fragment from the 380-385 g group, one fragment from the 400-405 g group, and one fragment from the 460-465 g group.

^c A total of 867 type 2 (399 type 2A and 468 type 2B) fragments had knawling on their outer surface indicating that they came from the 107-mm-wide knawled region at the base of the aft projectile section. The knawled region consisted of eight 107-mm-wide knawled bands separated by 2.5-mm-wide unknawled bands. For a given mass group the total number of type 2A and type 2B fragments is listed first, followed by the number from the knawled region in parentheses. Also, four type 1 fragments came from the knawled region: one fragment from the 95-100 g group, one fragment from the 105-110 g group, one fragment from the 190-195 g group, and one fragment from the 335-340 g group.

^d The fragments were not counted in this mass group. Only type 1 fragments were characterized.

^e Only type 1 fragments were characterized in this mass group.

Table M-8. Measurements on twenty-five selected type 1 Armco iron cylinder fragments from experiment 1.^a

Fragment No.	Fragment Mass (gr) (g)		Wall Thickness ^b (mm)	Average Fraction of Wall Thickness with Brittle Fracture ^c	Maximum Fragment Width ^d (mm)	Maximum Fragment Length ^e (mm)	Engineering Radial Strain ^f	True Radial Strain ^g	Homogeneous Plastic Strain ^h
1	69.1	4.48	13.1	0.60	7	17	0.31	0.38	0.65
2	93.0	6.02	12.6	0.59	8	22	0.34	0.41	0.72
3	120.2	7.79	11.7	0.66	11	25	0.39	0.49	0.85
4	142.5	9.24	11.4	0.65	5	21	0.40	0.52	0.89
5 ⁱ	181.5	11.76	12.1	0.55	15	23	0.36	0.45	0.78
6	254.9	16.52	12.4	0.56	14	37	0.35	0.43	0.74
7 ⁱ	267.4	17.33	12.8	0.63	8	23	0.33	0.40	0.69
8	282.5	18.31	12.3	0.66	11	34	0.36	0.44	0.76
9	375.6	24.34	12.3	0.46	15	38	0.36	0.44	0.76
10	399.7	25.90	12.7	0.67	5	47	0.33	0.41	0.70
11	476.8	30.89	13.2	0.61	19	51	0.31	0.36	0.63
12 ⁱ	543.1	35.19	13.0	0.45	6	37	0.32	0.39	0.67
13	613.1	39.73	12.7	0.53	20	41	0.33	0.41	0.71
14 ⁱ	642.6	41.64	11.4	0.44	8	51	0.40	0.51	0.88
15	686.1	44.46	11.7	0.50	12	51	0.39	0.49	0.85
16 ⁱ	863.8	55.97	12.3	0.49	17	69	0.35	0.44	0.76
17	1127.1	73.04	13.6	0.51	18	89	0.29	0.34	0.59
18 ⁱ	1175.5	76.18	12.8	0.61	7	102	0.33	0.40	0.69
19	1271.3	82.38	13.0	0.59	8	111	0.32	0.39	0.67
20 ⁱ	1419.9	92.01	12.4	0.47	19	114	0.35	0.43	0.74
21 ⁱ	1700.4	110.18	13.0	0.47	17	130	0.32	0.39	0.67
22 ⁱ	2003.6	129.83	12.8	0.55	9	114	0.33	0.40	0.70
23	2241.7	145.26	13.9	0.47	22	127	0.27	0.31	0.54
24	3041.5	197.09	13.4	0.58	14	143	0.30	0.35	0.54
25	3118.5	202.08	12.7	0.55	18	121	0.33	0.41	0.71

^a The 25 fragments were chosen to represent the entire mass range for type 1 fragments.

^b The initial wall thickness was 19.1 mm.

^c These values are the average of measurements from the outer cylindrical surface to the beginning of the shear fracture surface on each side of the fragment. The estimated uncertainty in these values is 10-20%.

^d The two values listed for a fragment are, respectively, the maximum width of the brittle fracture region near the outer cylindrical surface and the maximum width of the shear fracture region near the inner cylindrical surface.

^e The fragment length is parallel to the cylindrical axis.

^f The engineering radial strain is $(a_0 - a_f)/a_0$ where a_0 and a_f are the initial and final wall thicknesses, respectively.

^g The true radial strain³ is $-\ln(a_f/a_0)$.

^h The homogeneous plastic strain³ is $-\sqrt{3} \ln(a_f/a_0)$.

ⁱ This fragment came from the end of the cylinder.

Table M-9. Measurements on twenty-five selected type 1 Armco iron cylinder fragments from experiment 2.^a

Fragment No.	Fragment Mass		Wall Thickness ^b	Average Fraction of Wall Thickness with Brittle Fracture ^c	Maximum Fragment Width ^c	Maximum Fragment Length ^c	Engineering Radial Strain ^c	True Radial Strain ^c	Homogeneous Plastic Strain ^c
	(gr)	(g)	(mm)		(mm)	(mm)			
1	32.1	2.08	9.7	0.82	6	10	0.49	0.68	1.18
2	43.9	2.85	8.2	0.69	6	11	0.57	0.84	1.45
3	63.8	4.13	9.9	0.62	7	14	0.48	0.66	1.14
4	82.1	5.32	10.1	0.63	13	13	0.47	0.64	1.11
5	107.1	6.94	12.5	0.46	11	18	0.35	0.43	0.74
6	150.4	9.75	13.3	0.54	7	22	0.30	0.36	0.63
7	206.3	13.37	12.1	0.56	14	27	0.36	0.45	0.78
8 ^d	282.3	18.29	12.2	0.51	9	31	0.36	0.44	0.77
9	334.2	21.66	12.2	0.56	13	43	0.36	0.45	0.77
10	412.5	26.73	13.4	0.57	10	38	0.30	0.35	0.61
11	481.5	31.20	12.6	0.56	18	57	0.34	0.41	0.71
12	677.2	43.88	12.5	0.50	16	57	0.34	0.42	0.73
13	778.5	50.45	13.3	0.57	3	51	0.30	0.36	0.62
14	904.5	58.61	13.3	0.63	15	83	0.30	0.36	0.62
15	2074.0	134.39	12.8	0.55	6	83	0.33	0.40	0.69
16 ^d	1322.8	85.72	11.5	0.53	11	79	0.40	0.51	0.88
17	1402.3	90.87	13.1	0.49	21	102	0.31	0.38	0.65
18	1569.5	101.71	13.3	0.59	17	108	0.30	0.36	0.63
19	1776.1	115.09	13.1	0.65	13	89	0.31	0.38	0.65
20 ^d	1912.9	123.95	13.1	0.60	22	95	0.31	0.37	0.65
21	2167.3	140.44	12.7	0.60	16	102	0.33	0.41	0.70
22 ^d	2402.8	155.70	13.3	0.61	19	159	0.30	0.36	0.63
23 ^d	2622.1	169.91	12.7	0.46	25	203	0.33	0.41	0.70
24	2774.6	179.79	14.9	0.53	14	127	0.22	0.24	0.42
25 ^d	3333.0	215.98	11.0	0.53	12	184	0.42	0.54	0.94
					25				
					24				

^a The 25 fragments were chosen to represent the entire mass range for type 1 fragments.

^b The initial wall thickness was 19.1 mm.

^c Defined in footnotes in Table M-8.

^d This fragment came from the end of the cylinder.

Table M-10. Measurements on the type 1 HF-1 steel cylinder fragments with heat treatment A from experiment 3.

Fragment No.	Fragment Mass (g)	Wall Thickness ^a (mm)	Average Fraction of Wall Thickness with Brittle Fracture ^b	Maximum Fragment Width ^b (mm)	Maximum Fragment Length ^b (mm)	Engineering Radial Strain ^b	True Radial Strain ^b	Homogeneous Plastic Strain ^b
1 ^c	41.5	2.69	0.84	3.0	15.2	0.16	0.18	0.31
2	62.8	4.07	0.77	7.1	11.6	0.12	0.13	0.23
3	64.9	4.20	0.75	5.7	10.6	0.13	0.14	0.25
4	65.8	4.26	0.88	2.9	12.6	0.11	0.11	0.19
5	78.0	5.05	0.73	4.5	18.9	0.13	0.14	0.24
6	83.3	5.40	0.83	6.1	16.5	0.12	0.12	0.21
7	96.4	6.25	0.61	4.0	16.1	0.10	0.10	0.18
8	101.2	6.56	0.87	7.5	20.1	0.12	0.13	0.23
9	104.8	6.79	0.80	6.7	20.2	0.09	0.10	0.17
10	115.9	7.51	0.73	3.9	28.9	0.10	0.10	0.18
11	151.1	9.79	0.83	7.6	28.1	0.10	0.10	0.18
12 ^c	171.4	11.1	0.87	10.2	18.5	0.13	0.14	0.25
13	179.8	11.6	0.76	5.5	24.8	0.08	0.09	0.15
14	183.0	11.9	0.78	10.7	19.6	0.11	0.12	0.21
15 ^c	185.4	12.0	0.63	11.9	23.0	0.15	0.16	0.27
16	191.4	12.4	0.91	7.5	25.0	0.11	0.12	0.21
17	199.9	13.0	0.81	8.0	21.0	0.11	0.11	0.19
18 ^c	200.4	13.0	0.68	9.8	17.6	0.14	0.15	0.26
19 ^c	208.0	13.4	0.78	8.4	19.3	0.13	0.14	0.25
20	219.2	14.2	0.77	9.0	27.6	0.10	0.10	0.18
21	220.7	14.7	0.71	8.2	17.8	0.11	0.12	0.21
22 ^c	223.9	14.5	0.78	9.9	17.7	0.14	0.15	0.26
23	226.0	14.6	0.65	13.6	21.5	0.12	0.13	0.22
24 ^c	227.8	14.8	0.71	10.6	22.7	0.11	0.12	0.21
25 ^c	248.4	16.1	0.84	9.9	20.1	0.12	0.13	0.22
26 ^c	259.2	16.8	0.81	9.8	23.5	0.14	0.15	0.25
27	263.7	17.1	0.80	11.7	26.1	0.11	0.11	0.19
28 ^c	277.5	18.0	0.85	13.6	26.2	0.12	0.13	0.22
29 ^c	286.0	18.5	0.84	14.3	26.7	0.12	0.12	0.21
30	291.6	18.9	0.78	9.5	26.9	0.12	0.12	0.21
31 ^c	311.8	20.2	0.75	10.6	27.6	0.12	0.12	0.21
32	224.6	21.0	0.60	12.3	31.3	0.11	0.12	0.20
33	460.2	29.8	0.52	7.6	37.3	0.09	0.09	0.16

^a The initial wall thickness was 22.3 mm

^b Defined in footnotes in Table M 8.

^c This fragment came from the end of the cylinder

Table M-11. Measurements on the type 1 HF-1 steel cylinder fragments with heat treatment A from experiment 4.

Fragment No.	Fragment Mass (g)	Fragment Mass (g)	Wall Thickness ^a (mm)	Average Fraction of Wall Thickness with Brittle Fracture ^b	Maximum Fragment Width ^b (mm)	Maximum Fragment Length ^b (mm)	Engineering Radial Strain ^b	True Radial Strain ^b	Homogeneous Plastic Strain ^b
1	68.3	4.42	19.8	0.79	6.8	14.8	0.11	0.12	0.20
2 ^c	85.1	5.51	19.4	0.90	8.0	18.2	0.13	0.14	0.24
3	89.5	5.80	19.9	0.90	9.2	16.7	0.10	0.11	0.19
4	110.6	7.17	19.7	0.83	3.7	18.1	0.12	0.12	0.21
5 ^c	117.2	7.60	19.7	0.72	7.7	18.5	0.11	0.12	0.21
6	121.2	7.85	20.2	0.79	6.0	17.9	0.09	0.10	0.17
7	124.1	8.04	20.0	0.66	7.1	19.4	0.10	0.11	0.19
8	127.7	8.28	20.2	0.72	7.0	21.8	0.09	0.10	0.17
9	128.5	8.33	19.7	0.82	6.2	13.0	0.11	0.12	0.21
10	139.4	9.04	20.0	0.66	7.0	21.1	0.10	0.10	0.18
11 ^c	143.8	9.32	19.7	0.78	5.3	21.8	0.11	0.12	0.21
12	154.4	10.00	19.8	0.81	7.8	24.0	0.11	0.12	0.20
13 ^c	158.5	10.03	19.3	0.74	9.1	21.9	0.13	0.14	0.25
14	162.9	10.56	20.4	0.76	8.7	16.7	0.08	0.09	0.15
15 ^c	168.1	10.89	19.9	0.79	11.2	21.8	0.11	0.11	0.19
16	185.1	12.00	20.1	0.64	6.5	26.0	0.10	0.10	0.18
17 ^c	186.2	12.07	19.9	0.76	9.3	23.7	0.11	0.11	0.19
18	186.5	12.09	19.8	0.71	9.1	27.5	0.11	0.12	0.21
19 ^c	211.7	13.72	19.9	0.65	8.7	19.4	0.10	0.11	0.19
20	215.0	13.93	20.0	0.69	6.1	27.8	0.10	0.11	0.19
21	241.6	15.66	20.0	0.61	8.2	19.1	0.10	0.11	0.19
22	253.2	16.41	20.1	0.83	11.3	22.0	0.10	0.10	0.17
23	318.7	20.65	20.1	0.57	7.1	22.9	0.10	0.10	0.18
24	347.3	22.51	19.9	0.81	12.6	24.1	0.10	0.11	0.19
25	351.7	22.79	19.9	0.74	8.9	28.4	0.11	0.11	0.20
					6.6				
					7.0				
					11.4				
					9.6				
					8.1				
					7.7				
					9.0				
					9.0				
					9.4				

^a The initial wall thickness was 22.3 mm.

^b Defined in footnotes in Table M-8.

^c This fragment came from the end of the cylinder.

Table M-12. Measurements on the type 1 HF-1 steel cylinder fragments with heat treatment B from experiment 5.

Fragment No.	Fragment Mass (g)	Wall Thickness ^a (mm)	Average Fraction of Wall Thickness with Brittle Fracture ^b	Maximum Fragment Width ^b (mm)	Maximum Fragment Length ^b (mm)	Engineering Radial Strain ^b	True Radial Strain ^b	Homogeneous Plastic Strain ^b	
1	55.5	3.60	19.2	0.86	3.1 6.5	16.3	0.13	0.14	0.24
2	58.3	3.78	19.8	0.81	7.4 7.8	10.4	0.16	0.11	0.19
3	60.2	3.90	18.7	0.90	5.8 5.8	9.2	0.15	0.17	0.29
4	62.7	4.06	19.2	0.89	8.1 6.7	8.8	0.13	0.14	0.24
5	62.7	4.07	19.1	0.84	3.6 5.7	12.0	0.13	0.14	0.25
6	80.3	5.20	19.9	0.97	6.7 5.2	11.1	0.10	0.10	0.18
7	85.9	5.57	19.1	0.74	5.6 7.9	15.5	0.14	0.15	0.25
8 ^c	94.9	6.15	18.5	0.85	4.3 10.7	16.7	0.16	0.18	0.30
9	95.2	6.17	20.5	0.71	5.1 12.9	11.8	0.07	0.07	0.13
10	99.3	6.43	19.5	0.68	5.2 10.6	15.4	0.12	0.12	0.21
11	100.4	6.51	19.3	0.59	5.0 8.6	21.3	0.12	0.13	0.23
12 ^c	103.8	6.73	18.7	0.87	6.9 6.8	18.8	0.15	0.17	0.29
13	106.1	6.88	19.5	0.83	9.5 9.5	12.4	0.12	0.12	0.21
14 ^c	108.1	7.01	18.3	0.83	5.2 8.7	20.1	0.17	0.18	0.32
15 ^c	115.7	7.50	18.2	0.95	5.4 5.7	18.0	0.18	0.20	0.34
16	121.7	7.89	19.3	0.76	4.6 9.0	22.0	0.12	0.13	0.23
17	124.7	8.08	19.5	0.80	7.4 13.1	11.2	0.12	0.13	0.21
18	125.6	8.14	19.4	0.70	6.0 7.6	19.3	0.12	0.13	0.22
19 ^c	125.8	8.15	18.4	0.92	11.1 5.9	11.6	0.16	0.18	0.31
20 ^c	128.8	8.35	18.4	0.82	7.1 7.7	21.8	0.17	0.18	0.32
21	131.6	8.53	19.5	0.68	5.6 9.7	18.6	0.12	0.12	0.21
22 ^c	135.4	8.77	18.3	0.95	9.4 5.4	14.8	0.17	0.19	0.33
23	136.1	8.82	18.2	0.82	8.1 8.1	20.3	0.17	0.19	0.33
24 ^c	137.8	8.93	18.6	0.85	6.2 9.2	20.7	0.16	0.17	0.30
25	140.6	9.11	19.2	0.84	7.2 8.6	21.2	0.13	0.14	0.24
26 ^c	142.5	9.23	18.7	0.84	10.7 8.8	20.2	0.15	0.17	0.29
27	143.4	9.29	19.1	0.74	4.3 10.0	26.5	0.14	0.15	0.25
28	143.7	9.31	18.9	0.73	5.5 8.5	22.9	0.14	0.15	0.27
29 ^c	143.9	9.32	18.7	0.85	10.0 8.2	19.1	0.15	0.16	0.28
30	147.0	9.53	19.2	0.73	3.3 13.3	24.5	0.13	0.14	0.24
31 ^c	147.8	9.58	18.6	0.85	8.8 6.1	20.0	0.16	0.17	0.30
32 ^c	151.4	9.81	18.3	0.79	11.7 10.7	16.6	0.17	0.19	0.32
33 ^c	155.1	10.05	18.8	0.88	11.3 10.8	19.6	0.15	0.16	0.28
34	155.6	10.08	19.3	0.79	6.8 10.3	24.4	0.13	0.13	0.23

Table M-12. Measurements on the type 1 HF-1 steel cylinder fragments with heat treatment B from experiment 5.(Continued)

Fragment No.	Fragment Mass (gr)	(g)	Wall Thickness ^a (mm)	Average Fraction of Wall Thickness with Brittle Fracture ^b	Maximum Fragment Width ^b (mm)	Maximum Fragment Length ^b (mm)	Engineering Radial Strain ^b	True Radial Strain ^b	Homogeneous Plastic Strain ^b
35 ^c	157.2	10.19	18.4	0.87	7.9 8.9	23.8	0.17	0.18	0.31
36	159.3	10.32	19.2	0.64	6.1 11.1	20.8	0.13	0.14	0.25
37	165.1	10.70	19.3	0.78	5.0 10.2	22.0	0.13	0.13	0.23
38	166.6	10.80	18.4	0.77	6.3 8.8	26.7	0.16	0.18	0.31
39	169.4	10.98	19.1	0.72	8.8 8.5	21.9	0.14	0.15	0.25
40	169.5	10.98	19.6	0.78	10.1 11.4	19.3	0.11	0.12	0.21
41	171.5	11.11	19.3	0.65	4.5 8.3	24.2	0.13	0.14	0.24
42	172.3	11.17	19.6	0.78	6.7 9.0	24.9	0.11	0.12	0.21
43	177.9	11.57	19.1	0.65	7.8 10.6	19.1	0.14	0.15	0.25
44	178.5	11.57	19.1	0.79	5.2 9.5	22.0	0.13	0.14	0.25
45 ^c	188.8	12.23	18.4	0.81	10.4 9.6	21.0	0.16	0.18	0.31
46 ^c	192.6	12.48	18.4	0.83	9.9 14.4	19.0	0.17	0.18	0.32
47 ^c	199.8	12.95	18.5	0.74	11.2 9.1	17.6	0.16	0.17	0.30
48 ^c	206.1	13.36	18.7	0.86	8.3 12.0	21.6	0.15	0.17	0.29
49	211.4	13.70	19.3	0.65	5.6 11.8	29.6	0.13	0.13	0.22
50	212.9	13.80	19.7	0.76	6.4 12.6	25.3	0.11	0.12	0.20
51	219.1	14.20	19.5	0.85	5.4 11.0	22.8	0.12	0.13	0.22
52 ^c	232.8	15.09	19.3	0.83	12.9 9.3	21.2	0.12	0.13	0.23
53 ^c	237.0	15.36	18.7	0.86	11.6 9.1	19.9	0.15	0.17	0.29
54 ^c	240.4	15.58	18.4	0.85	10.1 11.4	19.8	0.16	0.18	0.31
55	277.4	17.98	19.2	0.72	7.7 13.5	29.4	0.13	0.14	0.24

^a The initial wall thickness was 22.1 mm.

^b Defined in footnotes in Table M-8

^c This fragment came from the end of the cylinder.

Table M-13. Measurements on the type 1 HF-1 steel cylinder fragments with heat treatment B from experiment 6.

Fragment No.	Fragment Mass (g)		Wall Thickness ^a (mm)	Average Fraction of Wall Thickness with Brittle Fracture ^b	Maximum Fragment Width ^b (mm)	Maximum Fragment Length ^b (mm)	Engineering Radial Strain ^b	True Radial Strain ^b	Homogeneous Plastic Strain ^b
1 ^c	55.1	3.57	19.5	0.76	5.4 9.1	17.0	0.12	0.13	0.23
2	61.1	3.96	19.4	0.80	3.0 5.3	18.2	0.13	0.14	0.23
3 ^c	77.9	5.05	19.5	0.77	5.0 7.6	18.5	0.12	0.13	0.23
4	101.4	6.57	19.5	0.76	5.4 9.1	17.0	0.12	0.13	0.23
5	107.3	6.95	19.7	0.67	5.1 11.4	22.5	0.11	0.12	0.21
6	110.6	7.17	19.3	0.87	5.5 8.0	21.4	0.13	0.14	0.25
7	111.3	7.21	19.6	0.82	5.3 7.7	23.5	0.12	0.13	0.22
8	112.1	7.26	19.4	0.76	5.0 10.3	18.5	0.13	0.14	0.24
9	115.2	7.47	19.8	0.81	6.6 11.0	12.3	0.11	0.12	0.20
10	122.9	7.96	19.6	0.82	3.2 8.8	22.7	0.12	0.13	0.22
11	125.6	8.14	19.7	0.84	8.3 11.7	17.6	0.11	0.12	0.21
12	126.6	8.20	19.8	0.61	5.5 10.2	22.4	0.11	0.11	0.20
13	128.1	8.30	19.6	0.69	5.1 10.6	17.4	0.12	0.12	0.21
14 ^c	128.2	8.31	19.2	0.90	10.0 9.0	19.7	0.13	0.14	0.25
15	130.7	8.47	19.2	0.82	6.6 11.2	19.1	0.13	0.14	0.25
16	133.6	8.66	19.3	0.83	6.5 10.4	15.3	0.13	0.14	0.24
17 ^c	136.4	8.84	18.9	0.87	7.2 9.8	20.9	0.15	0.16	0.28
18 ^c	136.7	8.86	19.2	0.80	6.9 10.9	20.5	0.14	0.15	0.25
19 ^c	137.6	8.92	20.1	0.85	10.5 10.4	23.1	0.09	0.10	0.17
20 ^c	138.2	8.96	18.8	0.86	10.0 7.0	21.9	0.15	0.17	0.29
21	141.2	9.15	19.7	0.59	4.6 12.8	18.5	0.11	0.12	0.21
22	142.2	9.21	19.6	0.85	6.2 10.1	20.6	0.12	0.13	0.22
23 ^c	145.1	9.40	19.4	0.84	10.1 8.1	21.0	0.13	0.14	0.23
24	148.5	5.62	20.0	0.80	11.9 9.0	15.1	0.10	0.11	0.18
25 ^c	149.3	9.67	19.0	0.85	8.3 10.2	20.8	0.15	0.16	0.27
26	151.3	9.80	19.5	0.80	6.2 11.3	21.5	0.12	0.13	0.22
27 ^c	154.3	10.00	19.6	0.82	10.9 9.1	16.6	0.12	0.13	0.22
28 ^c	157.4	10.20	19.5	0.82	8.3 8.0	24.5	0.09	0.10	0.17
29	164.1	10.63	19.7	0.77	5.9 11.7	20.6	0.11	0.12	0.21
30	166.2	10.77	19.2	0.77	7.1 8.2	23.9	0.14	0.15	0.26
31 ^c	167.4	10.85	19.7	0.80	7.6 11.5	19.9	0.11	0.12	0.21

Table M-13. Measurements on the type 1 HF-1 steel cylinder fragments with heat treatment B from experiment 6.(Continued)

Fragment No.	Fragment Mass		Wall Thickness ^a (mm)	Average Fraction of Wall Thickness with Brittle Fracture ^b	Maximum Fragment Width ^b (mm)	Maximum Fragment Length ^b (mm)	Engineering Radial Strain ^b	True Radial Strain ^b	Homogeneous Plastic Strain ^b
(gr)	(g)								
32 ^c	169.4	10.98	19.4	0.89	8.3	23.1	0.13	0.14	0.23
33	174.2	11.29	19.7	0.78	9.0	19.6	0.11	0.12	0.21
34 ^c	178.0	11.53	19.6	0.82	6.9	21.2	0.12	0.13	0.22
35 ^c	180.8	11.72	19.4	0.89	8.1	18.7	0.13	0.14	0.23
36	181.4	11.75	19.3	0.81	8.8	22.7	0.13	0.14	0.25
37	184.3	11.94	19.8	0.78	8.8	22.5	0.11	0.12	0.20
38	185.4	12.01	19.4	0.72	11.1	24.2	0.13	0.14	0.24
39 ^c	190.1	12.32	19.3	0.80	6.5	25.9	0.13	0.14	0.24
40 ^c	194.2	12.58	19.9	0.81	9.9	24.3	0.11	0.11	0.19
41 ^c	207.6	13.45	20.1	0.78	11.2	23.4	0.09	0.10	0.17
42 ^c	208.2	13.49	19.9	0.86	6.2	22.6	0.11	0.11	0.19
43 ^c	220.1	14.26	19.4	0.87	7.4	22.6	0.13	0.14	0.24
44 ^c	234.7	15.21	19.5	0.89	7.2	28.1	0.12	0.13	0.23
45	247.5	16.04	19.7	0.72	8.6	21.8	0.11	0.12	0.21
46 ^c	248.5	16.10	19.4	0.90	11.2	23.0	0.13	0.14	0.23
47 ^c	291.8	18.91	19.8	0.82	10.4	26.7	0.11	0.12	0.20
48	319.2	20.68	19.7	0.85	10.1	32.1	0.11	0.12	0.21
49	328.1	21.26	19.8	0.67	14.6	32.4	0.11	0.12	0.20
					9.4				
					12.3				
					13.2				
					12.7				
					14.1				
					9.5				
					9.3				
					13.2				
					11.9				
					9.3				
					11.6				
					10.7				
					6.7				
					10.5				
					7.7				
					13.3				

^a The initial wall thickness was 22.3 mm.

^b Defined in footnotes in Table M-8.

^c This fragment came from the end of the cylinder.

Table M-14. Measurements on twenty selected type 1 HF-1 steel projectile fragments with heat treatment A from experiment 7.

Fragment No.	Fragment Mass (gr) (g)		Wall Thickness ^a (mm)	Average Fraction of Wall Thickness with Brittle Fracture ^a	Maximum Fragment Width ^a (mm)	Maximum Fragment Length ^a (mm)	Engineering Radial Strain ^a	True Radial Strain ^a	Homogeneous Plastic Strain ^a
1 ^b	794.3	51.47	16.0	0.56	16.5 16.3	58.8	0.11	0.12	0.20
2	639.6	41.44	15.9	0.43	8.2 5.8	67.2	0.12	0.12	0.22
3	516.8	33.49	15.7	0.47	7.7 6.4	58.2	0.13	0.14	0.24
4	466.9	30.26	15.5	0.75	10.7 10.0	53.5	0.14	0.15	0.25
5	428.4	27.76	16.3	0.59	13.2 12.2	28.3	0.09	0.10	0.17
6	348.3	22.57	16.3	0.86	14.4 6.4	37.5	0.10	0.10	0.17
7	298.6	19.35	15.4	0.72	12.4 10.5	33.3	0.15	0.16	0.27
8	204.9	13.28	16.3	0.90	9.2 7.4	27.1	0.09	0.10	0.17
9	153.2	9.93	16.3	0.65	11.3 4.3	23.1	0.09	0.10	0.17
10	104.2	6.75	16.3	0.93	6.0 4.5	22.2	0.09	0.10	0.17
11 ^c	152.3	9.87	8.9	1.00	7.6 7.6	22.0	0.08	0.08	0.14
12	102.9	6.67	8.7	1.00	7.8 7.8	22.6	0.10	0.11	0.18
13	82.7	5.36	8.6	0.94	7.5 6.9	17.1	0.11	0.11	0.19
14	74.6	4.83	8.9	0.57	5.7 5.3	20.5	0.07	0.08	0.13
15	41.6	2.70	8.5	1.00	4.5 5.0	14.1	0.12	0.12	0.21
16 ^d	202.9	13.15	7.2	1.00	9.1 9.5	34.7	0.17	0.19	0.33
17	74.71	4.84	7.3	0.94	6.4 5.2	19.3	0.17	0.18	0.32
18	42.4	2.75	7.3	0.96	6.2 6.2	17.8	0.16	0.18	0.30
19	24.3	1.57	7.5	0.00	3.8 4.3	13.1	0.13	0.15	0.25
20	12.4	0.80	7.2	1.00	2.3 2.9	10.5	0.17	0.19	0.32

^a Defined in footnotes in Table M-8.

^b Fragments 1 through 10 came from the 102-mm long uniform region of the aft projectile section. The initial wall thickness was 18.0 mm.

^c Fragments 11 through 15 came from the joint region of the forward projectile section. The initial wall thickness was 9.7 mm.

^d Fragments 16 through 20 came from the joint region of the aft projectile section. The initial wall thickness was 8.7 mm.

APPENDIX N

COMPUTER LISTINGS FOR THE ARMCO IRON AND HF-1 STEEL CYLINDRICAL PUFF AND TROTT COMPUTATIONS

(Computer listings of the PUFF computational results for the Armco iron and HF-1 steel cylinders and the TROTT computational results for the HF-1 steel projectile are given in this appendix. The BFRACT2 subroutine was used for the computations given in Figures N-1, N-2, N-3, and N-6. The BFRACT2 and SHEAR2 subroutines were used for the computations given in Figures N-4 and N-5. References 1 and 2 provide detailed explanations of the parameters used in the PUFF and TROTT computer codes, respectively. The crack distribution results for these computations are summarized in Appendix O. The fragment mass distribution results that are listed in the computer output for each brittle fracture computational cell were derived assuming spherical fragments and were not used in the present work. The details are given in Reference 3.)

```

DATE = 06/07/79
IDENT ARMCO IRON CYLINDER
NEDIT= 0 NEDIT= 3 NREZONE= 0 NALPHA
JEDIT= S1,1,2,3,4,5,6,7,8,9,10,12,13,14,15,16,17,18,19,20,21
JEDIT= S2,1,2,3,4,5,6,7,8,9,10,12,13,14,15,16,17,18,19,20,21
JEDIT= S3,1,2,3,4,5,6,7,8,9,10,12,13,14,15,16,17,18,19,20,21
NEDIT= 10 JCYCS= 600 CKS= 3.000E+01 TS=
NMTLS= 2 MATFL= 1 UZERG= 8.
COMPS RHOS= 1.720E+00 CFP = 000 DPY = 012 0 0
EQST = 1.000E+00 0. 1.000E+00 1.041E+00 0. 0.
QEAPL = 4.469E+10 0. 0.
EXPLODE-CONST. VOL. EXPLOSION WITH ENERGY= 4.469E+10 ERG/G
OUTPUT OF EXPLODE, DET= 7.950E+05, V(J)= 4.300E-01, ECJ= 6.611E+10, PCJ= 2.430E+11
TENS = -1.000E+03 0. -1.000E+00 0. 0. 0.
MELT = -1.000E+00 0. 0. 0. 0. 0.
ARMCO IRON RHOS= 7.850E+00 CFP = 050 DPY = 011 NVAR= 11
EQST = 1.589E+12 5.170E+12 7.360E+10 1.690E+00 2.500E-01 5.170E+13 0.
TSR1 = -5.500E-04 -1.000E+08 5.000E-05 4.800E+12 -1.800E+09 -5.270E+09 0.
TSR2 = -1.800E+03 0. 2.500E-01 5.000E-01 4.000E-01 3.800E+00 0.
Y0= 1.800E+09 8.190E+11 2.100E+09 0. 0. 0.
NLAYER= 2 JHAT= 1 2 0 0 0 0 0 0 0 0 0 0
NZONES= 1 10 CELLS IN 3.010E+00 CM 0.
NZONES= 1 10 CELLS IN 1.905E+00 CM 0.

```

(a)

Figure N-1. Computer listing of (a) input parameters and (b) output results at 600 time cycles for the Armco iron cylindrical PUFF computation using the BFRAC22 subroutine.

CELL 1 12	CL = 0. CN = 0.	0. 0.	9.338E-05 2.583E+05	7.357E-03 3.630E+06	CL-AVG = CN-TOT =	7.199E-03 3.889E+06	PI*PR**2=	617.	ROT=	0. NO.=	FU=.3116 6.692E+05
CELL 1 13	CL = 0. CN = 0.	0. 0.	1.246E-04 3.172E+05	7.740E-03 3.927E+06	CL-AVG = CN-TOT =	7.542E-03 4.244E+06	PI*PR**2=	739.	ROT=	0. NO.=	FU=8.8900 1.081E+06
CELL 1 14	CL = 0. CN = 0.	0. 0.	6.186E-05 1.256E+05	6.818E-03 3.241E+06	CL-AVG = CN-TOT =	6.732E-03 3.367E+06	PI*PR**2=	473.	ROT=	0. NO.=	FU=.7836 2.494E+05
CELL 1 15	CL = 0. CN = 0.	6.735E-05 9.071E+04	1.092E-04 3.683E+05	9.442E-03 1.378E+06	CL-AVG = CN-TOT =	8.443E-03 1.928E+06	PI*PR**2=	386.	ROT=	8. NO.=	FU=.5792 2.828E+05
CELL 1 16	CL = 1.763E-04 CN = 9.333E+05	3.174E-04 1.251E+06	9.371E-04 1.637E+06	6.602E-03 3.400E+06	CL-AVG = CN-TOT =	4.872E-03 8.472E+06	PI*PR**2=	471.	ROT=	0. NO.=	FU=.7479 5.348E+05
CELL 1 17	CL = 3.941E-04 CN = 1.369E+06	8.530E-04 1.747E+06	2.211E-03 2.323E+06	6.011E-03 4.348E+06	CL-AVG = CN-TOT =	4.384E-03 1.153E+07	PI*PR**2=	538.	ROT=	8. NO.=	FU=.7557 7.844E+05
CELL 1 18	CL = 3.534E-04 CN = 1.356E+06	8.322E-04 1.734E+06	2.531E-03 2.309E+06	5.936E-03 4.442E+06	CL-AVG = CN-TOT =	4.374E-03 1.157E+07	PI*PR**2=	546.	ROT=	8. NO.=	FU=.7586 6.988E+05
CELL 1 19	CL = 2.146E-04 CN = 9.538E+05	7.017E-04 1.642E+06	2.622E-03 2.172E+06	7.393E-03 4.309E+06	CL-AVG = CN-TOT =	5.498E-03 1.072E+07	PI*PR**2=	792.	ROT=	0. NO.=	FU=8.8888 2.680E+06
CELL 1 20	CL = 2.145E-04 CN = 2.661E+05	5.072E-04 1.586E+06	2.191E-03 2.194E+06	7.440E-03 4.351E+06	CL-AVG = CN-TOT =	5.641E-03 9.883E+06	PI*PR**2=	775.	ROT=	8. NO.=	FU=.8843 2.460E+06
CELL 1 21	CL = 1.232E-04 CN = 1.701E+05	4.754E-04 2.185E+05	1.852E-03 1.883E+06	7.388E-03 4.332E+06	CL-AVG = CN-TOT =	6.554E-03 6.922E+06	PI*PR**2=	822.	ROT=	8. NO.=	FU=8.8888 1.731E+06

N= 600, JSTAR= 22, TIME= 7.363E-05, CALC TIME= 613.970 SECS, JTS= 12 DTNH= 7.570E-06 SHAX= 3.821E+08 JSMAX= 6

(b)

Figure N-1 (Continued)


```

***** SRI PUFF 8 *****
DATE = 06/06/79
IDENT HF-1 STEEL CYLINDER HEAT TREATMENT A
NTEOT= 0 NJEOT= 3 NREZON= 0 NALPHA
JEDITS= S1,1,2,3,4,5,6,7,8,9,10,12,13,14,15,16,17,18,19,20,21
JEDITS= S2,1,2,3,4,5,6,7,8,9,10,12,13,14,15,16,17,18,19,20,21
JEDITS= S3,1,2,3,4,5,6,7,8,9,10,12,13,14,15,16,17,18,19,20,21
JEDITS= S4,1,2,3,4,5,6,7,8,9,10,12,13,14,15,16,17,18,19,20,21
NMTZLS= 10 JCYCS= 500 CKS= 3.000E+01 TS=
2 MATFL= 1 UZERO= 0.
COMP8 RHOS= 1.720E+00 CFP = 000 DPY = 012
EQST = 1.000E+00 0. 1.300E+00 1.641E+00 0.
QEXPL = 4.469E+10 0.
EXPLODE-CONST. VOL. EXPLOSION WITH ENERGY= 4.469E+10 ERG/G
OUTPUT OF EXPLODE, DET= 7.950E+05, VCJ= 4.300E-01, ECJ= 6.611E+10, PCJ= 2.630E+11
TENS = -1.000E+09 0. -1.000E+00 0. 0. 0.
MELT = -1.000E+00 0. 0. 0. 0. 0.
HF1 STEEL RHOS= 7.774E+00 CFP = 050 DPY = 001 NVAF= 11
EQST = 1.605E+12 3.561E+12 7.360E+10 1.660E+00 2.500E-01 3.683E+12 0.
TSR1 = -3.770E-05-1.000E+09 6.560E-03 9.000E+10-1.000E+10-5.680E+08 0.
TSR2 = -1.040E+10 0. 2.500E-01 5.000E-01 4.000E-01 1.000E+00 0.
Y0= 1.040E+10 7.912E+11 9.400E+09 0. 0. 0.
NAYER= 2 JMAT= 1 2 0 0 0 0 0 0 0 0 0 0
NZONES= 1 10 CELLS IN 3.610E+00 CM 0.
NZONES= 1 10 CELLS IN 2.225E+00 CM 0.

```

(a)

Figure N-2. Computer listing of (a) input parameters and (b) output results at 500 time cycles for the HF-1 steel, heat treatment A, cylindrical PUFF computation using the BFRAC2 subroutine.

CELL 1 12	CL = 0. CN = 0.	0. 0.	7.241E-03 0. 1.306E+04 0.	1.431E-02 3.254E+05	CL-AVG = 1.415E-02 CN-TOT = 3.385E+05	PI*N*R**2= 212. FRAGMENT RAD.= 7.075E-03	ROT= 0. NO.= 1.968E+04	FU= .7675
CELL 1 13	CL = 0. CN = 0.	0. 0.	8.353E-03 0. 6.486E+03 0.	1.858E-02 2.191E+05	CL-AVG = 1.834E-02 CN-TOT = 2.255E+05	PI*N*R**2= 237. FRAGMENT RAD.= 9.171E-03	ROT= 0. NO.= 3.599E+04	FU= .3618
CELL 1 14	CL = 0. CN = 0.	0. 0.	9.305E-03 0. 2.202E+04 0.	1.540E-02 3.997E+05	CL-AVG = 1.518E-02 CN-TOT = 4.217E+05	PI*N*R**2= 304. FRAGMENT RAD.= 7.592E-03	ROT= 0. NO.= 7.563E+04	FU= .2826
CELL 1 15	CL = 0. CN = 0.	0. 0.	8.467E-03 0. 5.262E+03 0.	2.278E-02 1.160E+05	CL-AVG = 2.247E-02 CN-TOT = 1.213E+05	PI*N*R**2= 190. FRAGMENT RAD.= 1.123E-02	ROT= 0. NO.= 1.889E+04	FU= .3772
CELL 1 16	CL = 0. CN = 0.	0. 0.	8.118E-03 0. 1.095E+04 0.	1.828E-02 2.361E+05	CL-AVG = 1.803E-02 CN-TOT = 2.471E+05	PI*N*R**2= 250. FRAGMENT RAD.= 9.815E-03	ROT= 0. NO.= 4.266E+04	FU= .3893
CELL 1 17	CL = 0. CN = 0.	0. 0.	7.405E-03 0. 1.443E+04 0.	2.532E-02 6.349E+04	CL-AVG = 2.370E-02 CN-TOT = 7.793E+04	PI*N*R**2= 130. FRAGMENT RAD.= 1.185E-02	ROT= 0. NO.= 5.947E+03	FU= .6947
CELL 1 18	CL = 0. CN = 0.	0. 0.	8.480E-03 0. 1.670E+04 0.	2.209E-02 1.370E+05	CL-AVG = 2.131E-02 CN-TOT = 1.537E+05	PI*N*R**2= 214. FRAGMENT RAD.= 1.066E-02	ROT= 0. NO.= 2.795E+04	FU= .2725
CELL 1 19	CL = 0. CN = 0.	0. 0.	8.788E-03 0. 1.513E+04 0.	2.250E-02 1.307E+05	CL-AVG = 2.174E-02 CN-TOT = 1.459E+05	PI*N*R**2= 212. FRAGMENT RAD.= 1.087E-02	ROT= 0. NO.= 2.694E+04	FU= .2612
CELL 1 20	CL = 0. CN = 0.	0. 0.	8.556E-03 0. 1.687E+04 0.	1.877E-02 1.486E+05	CL-AVG = 1.817E-02 CN-TOT = 1.654E+05	PI*N*R**2= 168. FRAGMENT RAD.= 9.886E-03	ROT= 0. NO.= 1.492E+04	FU= .7368
CELL 1 21	CL = 0. CN = 0.	0. 0.	1.257E-02 0. 2.473E+04 0.	2.443E-02 1.187E+05	CL-AVG = 2.315E-02 CN-TOT = 1.634E+05	PI*N*R**2= 235. FRAGMENT RAD.= 1.159E-02	ROT= 0. NO.= 3.585E+04	FU= 0.0800

N= 500, JSTAR= 22, TIME= 7.470E-05, CALC TIME= 630.440 SECS, JTS= 12 DTNH= 9.663E-08 SHAX= 7.764E+08 JSNAX= 15

(b)

Figure N-2 (Continued)

Figure N-2 (Continued)

CELL 1 12	CL = 0. CN = 0.	0. 0.	9.212E-03 0. 1.002E+04 0.	2.121E-02 1.010E+05	CL-AVG = 2.060E-02 CN-TOT = 1.111E+05	PI*N*R**2 = 145. FRAGMENT RAD. = 1.030E-02	0. 0.	FU = .7566 NO. = 6.760E+03
CELL 1 13	CL = 0. CN = 0.	0. 0.	1.066E-02 0. 6.850E+03 0.	2.476E-02 7.936E+04	CL-AVG = 2.414E-02 CN-TOT = 8.621E+04	PI*N*R**2 = 155. FRAGMENT RAD. = 1.207E-02	0. 0.	FU = .5292 NO. = 1.015E+04
CELL 1 14	CL = 0. CN = 0.	0. 0.	1.143E-02 0. 1.605E+04 0.	2.072E-02 1.479E+05	CL-AVG = 2.015E-02 CN-TOT = 1.639E+05	PI*N*R**2 = 206. FRAGMENT RAD. = 1.006E-02	0. 0.	FU = .4092 NO. = 2.421E+04
CELL 1 15	CL = 0. CN = 0.	0. 0.	1.055E-02 0. 6.170E+03 0.	3.149E-02 4.364E+04	CL-AVG = 3.019E-02 CN-TOT = 4.981E+04	PI*N*R**2 = 136. FRAGMENT RAD. = 1.509E-02	0. 0.	FU = .3621 NO. = 7.655E+03
CELL 1 16	CL = 0. CN = 0.	0. 0.	1.047E-02 0. 6.046E+03 0.	2.517E-02 8.714E+04	CL-AVG = 2.465E-02 CN-TOT = 9.319E+04	PI*N*R**2 = 176. FRAGMENT RAD. = 1.233E-02	0. 0.	FU = .3575 NO. = 1.497E+04
CELL 1 17	CL = 0. CN = 0.	0. 0.	9.790E-03 0. 9.586E+03 0.	3.341E-02 2.963E+04	CL-AVG = 3.051E-02 CN-TOT = 3.922E+04	PI*N*R**2 = 107. FRAGMENT RAD. = 1.526E-02	0. 0.	FU = .6218 NO. = 3.706E+03
CELL 1 18	CL = 0. CN = 0.	0. 0.	1.090E-02 0. 8.643E+03 0.	2.993E-02 5.165E+04	CL-AVG = 2.850E-02 CN-TOT = 6.049E+04	PI*N*R**2 = 149. FRAGMENT RAD. = 1.425E-02	0. 0.	FU = .3533 NO. = 9.780E+03
CELL 1 19	CL = 0. CN = 0.	0. 0.	1.166E-02 0. 8.643E+03 0.	3.079E-02 5.392E+04	CL-AVG = 2.938E-02 CN-TOT = 6.257E+04	PI*N*R**2 = 164. FRAGMENT RAD. = 1.469E-02	0. 0.	FU = .1782 NO. = 1.255E+04
CELL 1 20	CL = 0. CN = 0.	0. 0.	1.151E-02 0. 9.083E+03 0.	2.719E-02 5.842E+04	CL-AVG = 2.601E-02 CN-TOT = 6.750E+04	PI*N*R**2 = 139. FRAGMENT RAD. = 1.300E-02	0. 0.	FU = .5532 NO. = 7.539E+03
CELL 1 21	CL = 0. CN = 0.	0. 0.	1.645E-02 0. 1.083E+04 0.	3.154E-02 5.512E+04	CL-AVG = 2.999E-02 CN-TOT = 6.593E+04	PI*N*R**2 = 181. FRAGMENT RAD. = 1.499E-02	0. 0.	FU = .0017 NO. = 1.645E+04

N= 500, JSTAR= 22, TIME= 7.492E-05, CALC TIME= 624.500 SECS, JTS= 12 DTNH= 9.534E-06 SMAX= 4.450E+06 JSMAX= 6

(b)

Figure N-3 (Continued)

**** CRITERION FOR STOP ****
 N = 500, JCYCS = 500, TIME = 7.492E-05, IS = 8.000E-05, X(JSHAX) = 5.592E+00, CKS = 3.000E+01, LSUB(7) = 0, DTNH = 9.534E-08

DATE = 06/06/79 IDENT HF-1 STEEL CYLINDER HEAT TREATMENT B

TIME EDIT NO. 50 AT N = 500, TIME = 7.49177E-05 SECS, JSTAP = 22, CALC TIME IS 62.465 SECS, DTNH = 9.534E-08 SECS

J	CELL	X	CH	U	CH/SEC	3HL	DYN/CH2	PHL	DYN/CH2	SHL	CHL/CH2	CHL/SEC	CONO	COMB	MOM	FURN	NET
1	1.000000	0.	2.704E+08	2.704E+08	2.704E+08	2.704E+08	2.704E+08	2.704E+08	2.704E+08	2.704E+08	2.704E+08	2.704E+08	S S M	COMP8	0.	1.000E+00	0.
2	1.139995	14584.	2.725E+08	2.725E+08	2.725E+08	2.725E+08	2.725E+08	2.725E+08	2.725E+08	2.725E+08	2.725E+08	2.725E+08	S S M	COMP8	1.806E+03	1.000E+00	0.
3	2.272109	24959.	2.555E+08	2.555E+08	2.555E+08	2.555E+08	2.555E+08	2.555E+08	2.555E+08	2.555E+08	2.555E+08	2.555E+08	S S M	COMP8	1.650E+04	1.000E+00	0.
4	3.429481	36146.	2.709E+08	2.709E+08	2.709E+08	2.709E+08	2.709E+08	2.709E+08	2.709E+08	2.709E+08	2.709E+08	2.709E+08	S S M	COMP8	5.434E+04	1.000E+00	0.
5	4.552860	45231.	3.601E+08	3.601E+08	3.601E+08	3.601E+08	3.601E+08	3.601E+08	3.601E+08	3.601E+08	3.601E+08	3.601E+08	S S M	COMP8	1.249E+05	1.000E+00	0.
6	5.591696	52721.	4.450E+08	4.450E+08	4.450E+08	4.450E+08	4.450E+08	4.450E+08	4.450E+08	4.450E+08	4.450E+08	4.450E+08	S S M	COMP8	2.342E+05	1.000E+00	0.
7	6.574469	64013.	3.970E+08	3.970E+08	3.970E+08	3.970E+08	3.970E+08	3.970E+08	3.970E+08	3.970E+08	3.970E+08	3.970E+08	S S M	COMP8	3.932E+05	1.000E+00	0.
8	7.611894	77551.	3.117E+08	3.117E+08	3.117E+08	3.117E+08	3.117E+08	3.117E+08	3.117E+08	3.117E+08	3.117E+08	3.117E+08	S S M	COMP8	6.212E+05	1.000E+00	0.
9	8.742635	87337.	3.028E+08	3.028E+08	3.028E+08	3.028E+08	3.028E+08	3.028E+08	3.028E+08	3.028E+08	3.028E+08	3.028E+08	S S M	COMP8	9.275E+05	1.000E+00	0.
10	9.882180	96683.	2.955E+08	2.955E+08	2.955E+08	2.955E+08	2.955E+08	2.955E+08	2.955E+08	2.955E+08	2.955E+08	2.955E+08	S S M	COMP8	1.315E+06	1.000E+00	9.
11	11.041502	109893.	0.	0.	0.	0.	0.	0.	0.	0.	0.	0.	S L 8	COMP8	1.801E+06	1.000E+00	0.
J													CONO			Y/NEM/RVV	SD/NET/ENV
12	11.041502	109893.	3.390E+08	3.390E+08	3.390E+08	3.390E+08	3.390E+08	3.390E+08	3.390E+08	3.390E+08	3.390E+08	3.390E+08	S P A	HF1 STEEL	1.801E+06	2.437E-01	1.111E+05
13	11.120266	109075.	4.026E+08	4.026E+08	4.026E+08	4.026E+08	4.026E+08	4.026E+08	4.026E+08	4.026E+08	4.026E+08	4.026E+08	S N I A	HF1 STEEL	3.274E+06	4.708E-01	8.621E+04
14	11.202710	108259.	4.369E+08	4.369E+08	4.369E+08	4.369E+08	4.369E+08	4.369E+08	4.369E+08	4.369E+08	4.369E+08	4.369E+08	S N I A	HF1 STEEL	4.813E+06	5.508E-01	1.539E+05
15	11.288859	107411.	4.331E+08	4.331E+08	4.331E+08	4.331E+08	4.331E+08	4.331E+08	4.331E+08	4.331E+08	4.331E+08	4.331E+08	S N I A	HF1 STEEL	6.433E+06	6.179E-01	4.981E+04
16	11.378545	106541.	3.354E+08	3.354E+08	3.354E+08	3.354E+08	3.354E+08	3.354E+08	3.354E+08	3.354E+08	3.354E+08	3.354E+08	S N I A	HF1 STEEL	8.117E+06	6.425E-01	9.319E+04
17	11.471766	105656.	3.494E+08	3.494E+08	3.494E+08	3.494E+08	3.494E+08	3.494E+08	3.494E+08	3.494E+08	3.494E+08	3.494E+08	S N I A	HF1 STEEL	9.665E+06	3.782E-01	3.922E+04
18	11.563340	104767.	2.712E+08	2.712E+08	2.712E+08	2.712E+08	2.712E+08	2.712E+08	2.712E+08	2.712E+08	2.712E+08	2.712E+08	S N I A	HF1 STEEL	1.169E+07	6.467E-01	6.049E+04
19	11.668267	103857.	1.120E+08	1.120E+08	1.120E+08	1.120E+08	1.120E+08	1.120E+08	1.120E+08	1.120E+08	1.120E+08	1.120E+08	S N I A	HF1 STEEL	1.356E+07	8.218E-01	6.257E+04
20	11.771571	102763.	6.780E+07	6.780E+07	6.780E+07	6.780E+07	6.780E+07	6.780E+07	6.780E+07	6.780E+07	6.780E+07	6.780E+07	S N I A	HF1 STEEL	1.551E+07	4.468E-01	6.750E+04
21	11.878046	101930.	1.772E+07	1.772E+07	1.772E+07	1.772E+07	1.772E+07	1.772E+07	1.772E+07	1.772E+07	1.772E+07	1.772E+07	S N I A	HF1 STEEL	1.751E+07	-9.904E-01	6.593E+04
22	12.004494	100725.	0.	0.	0.	0.	0.	0.	0.	0.	0.	0.	S L 8	HF1 STEEL	1.956E+07	1.040E+10	0.

(b)

Figure N-3 (Continued)

```

***** SRI PUFF 8 *****
DATE = 08/25/79
IDENT HF-1 STEEL CYLINDER HEAT TREATMENT A
NTEOT= 8 NJEQIT= 0 NREZONE= 0 NALPHA
NEDIT= 5 JCYCS= 500 CKS= 3.000E+01 TS= 0
NNTRLS= 2 MATFL= 1 UZERO= 0.
COMPB RHOS= 1.720E+00 CFP= 0.00 DPF= .012 0 0
EOST= 1.000E+00 0. 1.000E+00 1.041E+00 0. 0.
QEXPL= 4.469E+10 0. 0.
EXPLODE-CONST.VOL.EXPLOSION WITH ENERGY= 4.469E+10 ERG/G
OUTPUT OF EXPLODE, DET= 7.950E+05, VCJ= 4.300E-01, ECJ= 6.011E+10, PCJ= 2.830E+11
TENS= -1.000E+09 0. -1.000E+00 0. 0. 0. 0. 0.
MELT= -1.000E+00 0. 0. 0. 0. 0. 0. 0.
HF1 STEEL RHOS= 7.774E+00 CFP= 0.40 DPF= .002 NVAR= 58
EQST= 1.605E+12 3.561E+12 7.360E+10 1.660E+00 2.500E-01 3.663E+12 0.
SH2 .300E+02 .200E+00 .100E-01 .100E-02 .170E+00 .710E-01 .700E-01
.140E+01 .300E-07 .300E+09 .600E+01 .210E+00 .170E+10 .700E+10
NSIZE 0 0 0 0 0 0 0 0
TSR1= -3.770E-05-1.000E+09 6.560E-03 9.000E+10-1.040E+10-5.000E+00 0.
TSR2= -1.040E+13 0. 2.500E-01 5.000E-01 4.000E-01 3.000E+00 0.
MELT= 1.005E+10 6.460E+09 5.000E-02 7.000E-01-1.700E-01 0. 0.
Y0= 1.040E+10 7.912E+11 9.400E+09 0. 0. 0. 0.
NLAYER= 2 MAT= 1 2 0 0 0 0 0 0
NZONES= 1 10 CELLS IN 3.010E+00 CM 0.
NZONES= 1 10 CELLS IN 2.225E+00 CM 0.

```

(a)

Figure N-4. Computer listing of (a) input parameters and (b) output results at 500 time cycles for the HF-1 steel, heat treatment A, cylindrical PUFF computation using the BFRAC2 and SHEAR2 subroutines.

K=	12	J=	12	IN3=	25	ROT=	0.	EN=	.392E+03	TAU=	.11E+01	EP=	.785E+00
NG=	4												
CN=	.272E+03			.176E+03		.995E+02		.479E+02		.107E+02		.546E+01	.108E+01
CL=	.226E-01			.541E-01		.983E-01		.160E+00		.247E+00		.368E+00	.536E+00
NG=	5												
CN=	.475E+02			.318E+02		.144E+02		.889E+01		.336E+01		.921E+00	.145E+00
CL=	.792E-02			.190E-01		.345E-01		.562E-01		.867E-01		.129E+00	.189E+00
NG=	6												
CN=	.718E+02			.409E+02		.212E+02		.981E+01		.384E+01		.115E+01	.235E+00
CL=	.241E-01			.578E-01		.155E+00		.171E+00		.264E+00		.393E+00	.569E+00
TAU=	0.00000			0.00000		0.00000		.881748		.806033		.281762	.209
K=	12	J=	12	EP=	.785E+00	TOT PL STRAIN =	0.000	EN=	.412E+03	TAU=	.11E+01	EP=	.792E+00
K=	13	J=	13	IN3=	25	ROT=	0.						
NG=	4												
CN=	.219E+03			.139E+03		.774E+02		.370E+02		.146E+02		.441E+01	.948E+00
CL=	.243E-01			.584E-01		.106E+00		.173E+00		.266E+00		.397E+00	.580E+00
NG=	5												
CN=	.854E+02			.547E+02		.258E+02		.131E+02		.443E+01		.107E+01	.135E+00
CL=	.114E-01			.250E-01		.455E-01		.741E-01		.114E+00		.170E+00	.249E+00
NG=	6												
CN=	.117E+03			.553E+02		.243E+02		.913E+01		.294E+01		.772E+00	.145E+00
CL=	.248E-01			.596E-01		.108E+00		.177E+00		.272E+00		.406E+00	.543E+00
TAU=	0.00000			0.00000		0.00000		.883912		.818203		.183180	.212
K=	13	J=	13	EP=	.7918E+00	TOT PL STRAIN =	0.000	EN=	.226E+03	TAU=	.10E+01	EP=	.793E+00
K=	14	J=	14	IN3=	25	ROT=	0.						
NG=	4												
CN=	.174E+03			.109E+03		.686E+02		.288E+02		.111E+02		.327E+01	.654E+00
CL=	.268E-01			.644E-01		.117E+00		.191E+00		.294E+00		.438E+00	.640E+00
NG=	5												
CN=	.210E+02			.147E+02		.921E+01		.494E+01		.214E+01		.690E+00	.148E+00
CL=	.118E-01			.258E-01		.469E-01		.765E-01		.118E+00		.178E+00	.257E+00
NG=	6												
CN=	.315E+02			.214E+02		.130E+02		.673E+01		.281E+01		.865E+00	.176E+00
CL=	.256E-01			.614E-01		.112E+00		.182E+00		.280E+00		.418E+00	.640E+00
TAU=	0.00000			0.00000		0.00000		.814450		.010234		.176345	.216
K=	14	J=	14	EP=	.7920E+00	TOT PL STRAIN =	0.000	EN=	.169E+03	TAU=	.931E+00	EP=	.788E+00
K=	15	J=	15	IN3=	21	ROT=	0.						
NG=	4												
CN=	.133E+03			.824E+02		.452E+02		.213E+02		.814E+01		.239E+01	.457E+00
CL=	.297E-01			.713E-01		.130E+00		.211E+00		.325E+00		.489E+00	.709E+00
NG=	5												
CN=	.169E+02			.115E+02		.695E+01		.356E+01		.147E+01		.451E+00	.942E+01
CL=	.121E-01			.298E-01		.527E-01		.858E-01		.132E+00		.197E+00	.248E+00
NG=	6												
CN=	.191E+02			.125E+02		.736E+01		.373E+01		.153E+01		.478E+00	.988E+01
CL=	.276E-01			.663E-01		.110E+00		.196E+00		.303E+00		.451E+00	.659E+00
TAU=	0.00000			0.00000		0.00000		.798974		.009772		.122214	.218
K=	15	J=	15	EP=	.7879E+00	TOT PL STRAIN =	0.000	EN=	.0.000	0.000	0.000	0.000	.237

(b)

Figure N-4 (Continued)

K= 16 J= 16 IH3= 19 ROT= 0. EN= .136E+83 TAU= .818E+80 EP= .771E+00
 NG= 4
 CN= .15E+03 .536E+02 .345E+02 .164E+02 .644E+01 .194E+01 .359E+00 .476E-01
 CL= .35E-01 .755E-01 .137E+00 .224E+00 .344E+00 .514E+00 .758E+00 .103E+01
 NG= 5
 CN= .153E+02 .101E+02 .566E+01 .286E+01 .111E+01 .319E+00 .604E-01 .653E-02
 CL= .11E-01 .266E-01 .483E-01 .786E-01 .121E+00 .181E+00 .214E+00 .381E+00
 NG= 6
 CN= .154E+02 .983E+01 .568E+01 .270E+01 .144E+01 .293E+00 .547E-01 .585E-02
 CL= .237E-01 .520E-01 .945E-01 .154E+00 .237E+00 .354E+00 .517E+00 .746E+00
 TAUZ= 0.000000 0.000000 0.000000 .765522 .005569 .038857
 K= 16 J= 16 EP= .7705E+00 TOT PL STRAIN = 0.000 0.000 0.000 .222 .226 .241
 SX,SY,SZ= .559E+08 .559E+08 .112E+09 P= .559E+08 ST= -.277E+04 -.277E+04 .178E+09 0.
 EX,EY= -.939E-03 .940E-03 DH= 7.73146 PS= 1.178E+07
 ST= 1.442E+09-1.538E+09 1.257E+08 0.
 SX,SY,SZ= .413E+08 .413E+08 -.826E+08 P= .499E+08 ST= 0. .124E+09 0.
 EX,EY= -.939E-03 .940E-03 DH= 7.73146 EN= .116E+03 TAU= .733E+00 EP= .737E+00
 K= 17 J= 17 IH3= 17 ROT= 0. EN= .116E+03 TAU= .733E+00 EP= .737E+00
 NG= 4
 CN= .866E+02 .490E+02 .257E+02 .115E+02 .428E+01 .122E+01 .239E+00 .275E-01
 CL= .355E-01 .851E-01 .155E+00 .252E+00 .388E+00 .579E+00 .845E+00 .115E+01
 NG= 5
 CN= .146E+02 .869E+01 .587E+01 .294E+01 .118E+01 .349E+00 .610E-01 .781E-02
 CL= .814E-02 .195E-01 .355E-01 .578E-01 .891E-01 .133E+00 .194E+00 .280E+00
 NG= 6
 CN= .147E+02 .977E+01 .575E+01 .288E+01 .115E+01 .343E+00 .676E-01 .768E-02
 CL= .149E-01 .266E-01 .520E-01 .848E-01 .131E+00 .195E+00 .245E+00 .410E+00
 TAUZ= 0.000000 0.000000 0.000000 .723536 .002368 .007310 .225 .217 .227
 K= 17 J= 17 EP= .7371E+00 TOT PL STRAIN = 0.000 0.000 0.000
 CELL CL = 0. 0. 0. 8.508E-02 0. 3.382E-02 CL-AVG = 3.333E-02 PI*NR**2= 100. ROT= 0. FU= .6634
 I 18 CN = 0. 0. 0. 1.254E+03 0. 2.765E+04 CN-TOT = 2.891E+04 FRAGMENT RAD.= 1.666E-02 MO.= 2.433E+03
 CELL CL = 0. 0. 0. 8.386E-03 0. 2.697E-02 CL-AVG = 2.618E-02 PI*NR**2= 144. ROT= 0. FU= .5125
 I 19 CN = 0. 0. 0. 6.818E+03 0. 6.257E+04 CN-TOT = 6.858E+04 FRAGMENT RAD.= 1.389E-02 NO.= 8.359E+03
 CELL CL = 0. 0. 0. 9.255E-03 0. 2.362E-02 CL-AVG = 2.312E-02 PI*NR**2= 168. ROT= 0. FU= .4927
 I 20 CN = 0. 0. 0. 6.777E+03 0. 9.457E+04 CN-TOT = 1.013E+05 FRAGMENT RAD.= 1.356E-02 NO.= 1.285E+04
 CELL CL = 0. 0. 0. 1.153E-02 0. 2.232E-02 CL-AVG = 2.119E-02 PI*NR**2= 193. ROT= 0. FU= .4138
 I 21 CN = 0. 0. 0. 2.586E+04 0. 1.168E+05 CN-TOT = 1.425E+05 FRAGMENT RAD.= 1.854E-02 NO.= 2.088E+04
 N= 500, JSTAR= 22, TIME= 7.530E-05, CALC TIME= 1419.630 SECS, JTS= 12 DTNH= 9.811E-08 SHAX= 4.812E+08 JSNAX= 5

(b)

Figure N-4 (Continued)

N-15

```

**** SRI PUFF 8 ****
DATE = 30/25/79
IDENT HF-1 STEEL CYLINDER HEAT TREATMENT 8
NTEDIT= 0 NJEDIT= 0 NREZON= 0 NALPHA
NEDIT= 5 JCYCS= 500 CKS= 3.000E+01 TS= 8.000E-05 IN= 5
NMTLS= 2 MATFL= 1 UZERO= 0. 0000000000 IN= 5 , , CM, SEC
, IN= 5 , , CM/SEC

COMP8 RHOS= 1.720E+00 CFP = 000 DPY = 012 0 IN= 5 G/CM3
EOST = 1.000E+00 0. 1.000E+00 1.841E+00 0. 0. IN= 5
QEXPL = 4.459E+10 0. 0. 0. IN= 5 DYN/CM2,=, ERG/G, , DYN/CM2, ERG/G
EXPLODE-CONST.VOL-EXPLOSION WITH ENERGY= 4.459E+10 ERG/G
OUTPUT CF EXPLODE, DET= 7.950E+05, VCJ= 4.300E-01, ECJ= 6.611E+10, PCJ= 2.839E+11
TENS = -1.000E+09 0. -1.000E+00 0. 0. 0. IN= 5 CYN/CM2,=
MELT = -1.000E+00 0. 0. 0. 0. 0. IN= 5 ERG/G,
, IN= 5 ERG/G,

HF1 STEEL RHOS= 7.774E+00 CFP = 040 DPY = 002 NVAR= 58 0 IN= 5 G/CM3
EOST = 1.605E+12 3.561E+12 7.360E+10 1.660E+00 2.500E-01 3.683E+12 0. IN= 5 DYN/CM2,=, ERG/G, , DYN/CM2, ERG/G
SH2 = 3.00E+02 200E+00 110E-01 1.00E-02 170E+00 700E-01 700E-01 IN= 5
140E+01 300E-07 300E+09 500E+01 200E+00 170E+00 700E+10 IN= 5
NSIZE 0 0 0 0 0 0 0 IN= 5
TSR1 = -3.870E-05-1.000E+09 8.180E-03 1.240E+11-1.040E+10-1.740E+09 0. IN= 5
TSR2 = -1.040E+10 0. 2.500E-01 5.000E-01 4.000E-01 3.000E+00 0. IN= 5
MELT = 1.045E+10 6.400E+09 5.000E-02 7.000E-01-1.700E-01 0. 0. IN= 5 ERG/G,
YB= 1.840E+10 7.912E+11 9.400E+09 0. 0. 0. 0. IN= 5 CYN/CM2, DYN/CM2,
, IN= 5 ERG/G,

NLAYER= 2 JMAT= 1 2 0 0 0 0 0 0 0 0 IN= 5
NZONES= 1 10 CELLS IN 3.795E+00 CM IN= 5 CM, CM,
10 CELLS IN 2.215E+00 CM 0. 0. IN= 5 CM, CM,

```

(a)

Figure N-5. Computer listing of (a) input parameters and (b) output results at 500 time cycles for the HF-1 steel, heat treatment B, cylindrical PUFF computation using the BFRAC2 and SHEAR2 subroutines.

A = A

K= 12 J= 12 IH3= 25 ROT= 0.	EN= .393E+03 TAU= .101E+01 EP= .784E+00	
NG= 4		
CN= .273E+03	.176E+03	.995E+02
CL= .224E-01	.537E-01	.971E-01
NG= 5		
CN= .461E+02	.311E+02	.182E+02
CL= .782E-02	.100E-01	.341E-01
NG= 6		
CN= .735E+02	.422E+02	.220E+02
CL= .234E-01	.570E-01	.104E+00
TAU7= 0.00000	0.00000	0.00000
K= 12 J= 12 EP= .784E+03 TOT PL STRAIN = 0.000	.802787	.005892
K= 13 J= 13 IH3= 25 ROT= 0.	EN= .375E+03 TAU= .181E+01 EP= .796E+00	
NG= 4		
CN= .235E+03	.133E+03	.723E+02
CL= .227E-01	.610E-01	.112E+00
NG= 5		
CN= .712E+02	.451E+02	.240E+02
CL= .115E-01	.252E-01	.450E-01
NG= 6		
CN= .894E+02	.471E+02	.215E+02
CL= .253E-01	.606E-01	.110E+00
TAU7= 0.00000	0.00000	0.00000
K= 13 J= 13 EP= .795E+03 TOT PL STRAIN = 0.000	.802275	.016219
K= 14 J= 14 IH3= 25 ROT= 0.	EN= .230E+03 TAU= .130E+01 EP= .793E+00	
NG= 4		
CN= .179E+03	.112E+03	.617E+02
CL= .268E-01	.643E-01	.117E+00
NG= 5		
CN= .216E+02	.146E+02	.920E+01
CL= .105E-01	.253E-01	.459E-01
NG= 6		
CN= .309E+02	.210E+02	.120E+02
CL= .256E-01	.615E-01	.112E+00
TAU7= 0.00000	0.00000	0.00000
K= 14 J= 14 EP= .792E+03 TOT PL STRAIN = 0.000	.816276	.009666
K= 15 J= 15 IH3= 21 ROT= 0.	EN= .174E+03 TAU= .921E+00 EP= .787E+00	
NG= 4		
CN= .159E+03	.873E+02	.487E+02
CL= .205E-01	.685E-01	.124E+00
NG= 5		
CN= .166E+02	.114E+02	.689E+01
CL= .110E-01	.279E-01	.500E-01
NG= 6		
CN= .189E+02	.124E+02	.734E+01
CL= .270E-01	.647E-01	.118E+00
TAU7= 0.00000	0.00000	0.00000
K= 15 J= 15 EP= .786E+03 TOT PL STRAIN = 0.000	.791121	.008741

(b)

Figure N-5 (Continued)

K= 16 J= 16 IH3= 19 POT= C. EN= .137E+03 TAU= .807E+00 EP= .766E+00
 NG= 4
 CN= .17E+03 .651E+02 .357E+02 .171E+02 .676E+01 .205E+01 .473E+00 .535E-01
 CL= .319E-01 .743E-01 .135E+00 .220E+00 .339E+00 .505E+00 .738E+00 .102E+01
 NG= 5
 CN= .150E+02 .101E+02 .594E+01 .295E+01 .117E+01 .346E+00 .680E-01 .773E-02
 CL= .105E-01 .252E-01 .459E-01 .747E-01 .115E+00 .172E+00 .251E+00 .362E+00
 NG= 6
 CN= .152E+02 .983E+01 .564E+01 .275E+01 .107E+01 .311E+00 .681E-01 .672E-02
 CL= .211E-01 .507E-01 .922E-01 .150E+00 .231E+00 .345E+00 .504E+00 .727E+00
 TAUZ= 0.000000 0.000000 0.000000 .764330 .005091 .037709
 K= 16 J= 16 EP= .7663E+00 TOT PL STRAIN = 0.000 C.003 6.000 .221 .240
 EX,SV,SZ= .281E+09 .281E+09 -5.62E+09 P= .261E+09 ST= -.938E+05 -.938E+05 .856E+09 C.
 ST= 1.297E+09 -1.776E+09 6.444E+08 0. PS= 5.636E+07
 EX,SV,SZ= .213E+09 .213E+09 -.425E+09 P= .254E+09 ST= 0. 0. .638E+09 C.
 EX,EV= -.951E-03 .991E-03 0H= 7.73172
 K= 17 J= 17 IH3= 17 ROT= 0. EN= .115E+07 TAU= .739E+00 EP= .739E+00
 NG= 4
 CN= .465E+02 .499E+02 .258E+02 .116E+02 .432E+01 .123E+01 .241E+00 .278E-01
 CL= .355E-01 .851E-01 .155E+00 .252E+00 .388E+00 .579E+00 .845E+00 .114E+01
 NG= 5
 CN= .146E+02 .992E+01 .590E+01 .295E+01 .118E+01 .347E+00 .682E-01 .764E-02
 CL= .854E-02 .205E-01 .372E-01 .607E-01 .935E-01 .139E+00 .204E+00 .294E+00
 NG= 6
 CN= .139E+02 .938E+01 .559E+01 .282E+01 .114E+01 .340E+00 .672E-01 .758E-02
 CL= .123E-01 .296E-01 .537E-01 .875E-01 .135E+00 .201E+00 .294E+00 .424E+00
 TAUZ= 0.000000 0.000000 0.000000 .728743 .002728 .001931
 K= 17 J= 17 EP= .7393E+00 TOT PL STRAIN = 0.000 8.000 0.000 .225 .217 .229
 CELL CL = 0. 0. 1.090E-02 0. 4.763E-02 CL-AVG = 4.512E-02 FI*P*2= 73. ROT= 0. FU= .6287
 1 18 CN = 0. 0. 1.482E+03 0. 1.010E+04 CN-TOT = 1.156E+04 FRAGMENT RAD.= 2.286E-02 NO.= 1.075E+03
 CELL CL = 0. 0. 0. 0. 1.123E-02 0. 3.518E-02 CL-AVG = 3.402E-02 FI*P*2= 111. ROT= 0. FU= .5097
 1 19 CN = 0. 0. 3.094E+03 0. 2.826E+04 CN-TOT = 3.135E+04 FRAGMENT RAD.= 1.701E-02 NO.= 3.843E+03
 CELL CL = 0. 0. 0. 0. 1.249E-02 0. 3.210E-02 CL-AVG = 3.861E-02 FI*P*2= 131. ROT= 0. FU= .4262
 1 20 CN = 0. 0. 6.493E+03 0. 3.966E+04 CN-TOT = 4.613E+04 FRAGMENT RAD.= 1.531E-02 NO.= 6.618E+03
 CELL CL = 0. 0. 0. 0. 1.504E-02 0. 2.985E-02 CL-AVG = 2.814E-02 FI*P*2= 161. ROT= 0. FU= .4474
 1 21 CN = 0. 0. 1.154E+04 C. 4.744E+04 CN-TOT = 5.859E+04 FRAGMENT RAD.= 1.402E-02 NO.= 8.149E+03
 N= 500, JSTAR= 22, TIME= 7.485E-05, CALC TIME= 1380.730 SECS, JTS= 12 DTAN= 1.004E-07 SPAX= 4.054E+00 JSMAX= 5

(b)

Figure N-5 (Continued)

**** CRITERION FOR STOP ****

N = 500, JCYCS = 500, TIME = 7.485E-05, TS = 0.000E-05, X(JSMAX) = 4.503E+00, CKS = 3.000E+01, LSUB(7) = 0, DTNH = 1.004E-07

DATE = 08/25/79 IDENT HF-1 STEEL CYLINDER HEAT TREATMENT 8

TIME EDIT NO.100 AT N = 500, TIME = 7.48531E-05 SECS, JSTAR = 22, CALC TIME IS 138.091 SECS, DTNH = 1.004E-07 SECS

J	CELL	X	CM	CH/SEC	U	RHL	DYN/CH2	PHL	DYN/CH2	SHL	ERGS	DHL	CM/SEC	CHL	COND	MON	TAPS	FURN	NET
1	0.000000			0.	2.299E+08	2.299E+06	2.299E+06	2.299E+06	2.299E+06	6.324E+08	1804	6.017E+04	S	S	M	CCMPB	0.	1.000E+00	0.
2	1.372553			13553.	2.508E+08	2.508E+06	2.508E+06	2.508E+06	2.508E+06	7.242E+08	1871	6.171E+04	S	S	M	CCMPB	1.679E+03	1.000E+00	0.
3	2.313395			24548.	2.619E+08	2.619E+06	2.619E+06	2.619E+06	2.619E+06	7.507E+08	1895	6.266E+04	S	S	M	CCMPB	1.584E+04	1.000E+00	0.
4	3.448764			33668.	3.375E+08	3.375E+06	3.375E+06	3.375E+06	3.375E+06	8.860E+08	2069	6.807E+04	S	S	M	CCMPB	5.170E+04	1.000E+00	0.
5	4.503451			39627.	4.054E+08	4.054E+06	4.054E+06	4.054E+06	4.054E+06	9.975E+08	2207	7.223E+04	S	S	M	CCMPB	1.150E+05	1.000E+00	0.
6	5.512489			51523.	3.919E+08	3.919E+06	3.919E+06	3.919E+06	3.919E+06	9.757E+08	2182	7.143E+04	S	S	M	CCMPB	2.166E+05	1.000E+00	0.
7	6.549808			67102.	3.920E+08	3.920E+06	3.920E+06	3.920E+06	3.920E+06	9.765E+08	2181	7.146E+04	S	S	M	CCMPB	3.782E+05	1.000E+00	0.
8	7.595115			78985.	3.560E+08	3.560E+06	3.560E+06	3.560E+06	3.560E+06	9.171E+08	2107	6.928E+04	S	S	M	CCMPB	6.134E+05	1.000E+00	0.
9	8.679837			87954.	3.136E+08	3.136E+06	3.136E+06	3.136E+06	3.136E+06	8.473E+08	2010	6.657E+04	S	S	M	CCMPB	9.236E+05	1.000E+00	0.
10	9.813657			97235.	3.016E+08	3.016E+06	3.016E+06	3.016E+06	3.016E+06	8.370E+08	1957	6.616E+04	S	S	M	CCMPB	1.314E+06	1.000E+00	0.
11	10.971777			109033.	0.	0.	0.	0.	0.	4.469E+10	1.7200	7.950E+05	S	L	B	CCMPB	1.799E+06	1.000E+00	0.
J		X	CM	CH/SEC	U	RHL	DYN/CH2	PHL	DYN/CH2	SHL	ERGS	DHL	CM/SEC	CHL	COND	MON	TAPS	FURN	NET
12	10.971777			109033.	3.064E+08	3.064E+06	3.064E+06	3.064E+06	3.064E+06	9.829E+08	7.7139	5.649E+05	S	R	Y	HF1 STEEL	1.799E+06	1.010E+00	3.826E+02
13	11.053956			108251.	2.808E+08	2.808E+06	2.808E+06	2.808E+06	2.808E+06	9.026E+08	7.7188	5.849E+05	S	N	Y	HF1 STEEL	3.260E+06	1.007E+00	3.747E+02
14	11.133961			107455.	2.522E+08	2.522E+06	2.522E+06	2.522E+06	2.522E+06	8.316E+08	7.7231	5.849E+05	S	N	Y	HF1 STEEL	4.793E+06	1.008E+00	2.301E+02
15	11.220758			106541.	2.165E+08	2.165E+06	2.165E+06	2.165E+06	2.165E+06	7.793E+08	7.7263	5.849E+05	S	N	Y	HF1 STEEL	6.356E+06	9.210E+00	1.743E+02
16	11.311120			105808.	1.463E+08	1.463E+06	1.463E+06	1.463E+06	1.463E+06	7.282E+08	7.7293	5.849E+05	S	N	Y	HF1 STEEL	8.060E+06	6.071E+01	1.360E+02
17	11.405169			104981.	4.160E+07	2.544E+08	4.160E+08	4.160E+08	4.160E+08	6.794E+08	7.7317	5.849E+05	S	N	Y	HF1 STEEL	9.808E+06	7.394E+01	1.151E+02
18	11.502589			104116.	7.940E+05	7.940E+05	7.940E+05	7.940E+05	7.940E+05	2.419E+08	7.7369	5.849E+05	S	N	Y	HF1 STEEL	1.161E+07	3.713E+01	1.151E+02
19	11.603150			103227.	-2.160E+06	-2.160E+06	-2.160E+06	-2.160E+06	-2.160E+06	1.684E+08	7.7629	5.849E+05	S	N	Y	HF1 STEEL	1.348E+07	4.904E+01	1.151E+02
20	11.706993			102325.	-3.994E+06	-3.994E+06	-3.994E+06	-3.994E+06	-3.994E+06	1.369E+08	7.7626	5.849E+05	S	N	Y	HF1 STEEL	1.541E+07	5.740E+01	3.133E+04
21	11.814809			101455.	-3.314E+06	-3.314E+06	-3.314E+06	-3.314E+06	-3.314E+06	8.087E+07	7.7679	5.849E+05	S	N	Y	HF1 STEEL	1.741E+07	5.526E+01	4.613E+04
22	11.924268			100558.	0.	0.	0.	0.	0.	0.	7.7740	5.849E+05	S	L	B	HF1 STEEL	1.946E+07	1.040E+00	5.099E+04

(b)

Figure N-5 (Continued)

```

DATE = 10/23/79
HF-1 FRAG ROUND WITH RUNNING, DETONATION HEAT TREATMENT A
NSTAR 0 NFLOT 50 NCUMP 999 IMAX= 600 IPRIN 50 0 0
IJBUND 2 NBLOCK 10 NMTLS 3 NJED= 45 0 0
TS = .15CE-03 IVTYPE= 0 NVALK = 0
COSQ= .400E+01 CLIN = .100E+00 TRIO= .500E-01
JEOT,K,J= 315 5 415 5 1315 5 1415 5 1515 5 315 6 415 6
          1315 6 1415 6 1515 6 315 7 415 7 1315 7 1415 7
          1515 7 321 5 421 5 1321 5 1421 5 1521 5 321 6 421 6
          1321 6 1421 6 1521 6 321 7 421 7 1321 7 1421 7
          1521 7 327 5 427 5 1327 5 1427 5 1527 5 327 6 427 6
          1327 6 1427 6 1527 6 327 7 427 7 1327 7 1427 7
          1527 7
HF1 STEEL
EGST = RHOS= .777E+01 CFP = 020 OPY = 001 NTRI= 0 NVAR= 20
TSR1 = .161E+13 .356E+13 .736E+11 .166E+01 .250E+00 .368E+13 0.
TSR2 = -.377E-04 -.100E+10 .656E-02 .900E+11 -.114E+11 -.588E+89 0.
Y0= -.104E+11 0. .256E+00 .500E+00 .410E+00 .310E+01 8.
      .104E+11 .791E+12 .940E+10
PBXN-106
EQST = RHOS= .163E+01 CFP = 000 OPY = 010 NTRI= 0 NVAR= 2
MTYPE = .100E+01 0. C. .200E+01 .200E+01 0.
      2 0EXFL = 3.900E+10 5.507E+01 0. 2.010E+00
FRCH EXPLODE, DET, VCJ, ECJ, PCJ= 7.899E+05 4.590E-01 5.850E+10 2.549E+11
      INO= , IN= 5 -EXPLODE-
CH6
EQST = RHOS= .177E+01 CFP = 001 OPY = 010 NTRI= 0 NVAR= 2
MTYPE = .100E+01 0. 0. .170E+01 .170E+01 0.
      2 0EXFL = 5.811E+10 5.410E+11 0. 2.010E+00
FRCH EXPLODE, DET, VCJ, ECJ, PCJ= 8.550E+05 4.113E-01 6.481E+10 3.505E+11
      SP= 5.049E+05 7.899E+05 8.550E+05 0.
      INO= , IN= 5 -EXPLODE-

```

(a)

Figure N-6. Computer listing of (a) input parameters, (b) grid layout, and (c) output results at 500 time cycles for the HF-1 steel, heat treatment A, TROTT computation using the BFRAC22 subroutine.

J	K	H	L	V	A	X	Y	A	D	Z	YIELD	XC	YD
1	1	0	0	0	0.00000	0.00000	0.00000	0.00000	0.00000	0.00000	0.	0.	0
2	1	0	0	0	0.00000	0.00000	0.00000	0.00000	0.00000	0.00000	0.	0.	0
3	1	0	0	5	0.00000	0.00000	0.00000	0.00000	0.00000	0.00000	0.	0.	0
4	1	0	0	9	0.00000	0.00000	0.00000	0.00000	0.00000	0.00000	0.	0.	0
5	1	0	0	13	0.00000	0.00000	0.00000	0.00000	0.00000	0.00000	0.	0.	0
6	1	0	0	17	0.00000	0.00000	0.00000	0.00000	0.00000	0.00000	0.	0.	0
7	1	0	0	21	0.00000	0.00000	0.00000	0.00000	0.00000	0.00000	0.	0.	0
8	1	0	0	25	0.00000	0.00000	0.00000	0.00000	0.00000	0.00000	0.	0.	0
9	1	0	0	29	0.00000	0.00000	0.00000	0.00000	0.00000	0.00000	0.	0.	0
10	2	0	0	33	0.00000	0.00000	0.00000	0.00000	0.00000	0.00000	0.	0.	0
11	2	0	0	37	0.00000	0.00000	0.00000	0.00000	0.00000	0.00000	0.	0.	0
12	2	1	0	41	0.00000	0.00000	0.00000	0.00000	0.00000	0.00000	0.	0.	0
13	2	1	0	45	0.00000	0.00000	0.00000	0.00000	0.00000	0.00000	0.	0.	0
14	2	1	1	49	0.00000	0.00000	0.00000	0.00000	0.00000	0.00000	0.	0.	0
15	2	1	1	53	0.00000	0.00000	0.00000	0.00000	0.00000	0.00000	0.	0.	0
16	2	1	1	57	0.00000	0.00000	0.00000	0.00000	0.00000	0.00000	0.	0.	0
17	2	1	1	61	0.00000	0.00000	0.00000	0.00000	0.00000	0.00000	0.	0.	0
18	2	1	1	65	0.00000	0.00000	0.00000	0.00000	0.00000	0.00000	0.	0.	0
19	2	1	1	69	0.00000	0.00000	0.00000	0.00000	0.00000	0.00000	0.	0.	0
20	2	1	1	73	0.00000	0.00000	0.00000	0.00000	0.00000	0.00000	0.	0.	0
21	2	1	1	77	0.00000	0.00000	0.00000	0.00000	0.00000	0.00000	0.	0.	0
22	2	1	1	81	0.00000	0.00000	0.00000	0.00000	0.00000	0.00000	0.	0.	0
23	2	1	1	85	0.00000	0.00000	0.00000	0.00000	0.00000	0.00000	0.	0.	0
24	2	1	1	89	0.00000	0.00000	0.00000	0.00000	0.00000	0.00000	0.	0.	0
25	2	1	1	93	0.00000	0.00000	0.00000	0.00000	0.00000	0.00000	0.	0.	0
26	2	1	1	97	0.00000	0.00000	0.00000	0.00000	0.00000	0.00000	0.	0.	0
27	2	1	1	101	0.00000	0.00000	0.00000	0.00000	0.00000	0.00000	0.	0.	0
28	2	1	1	105	0.00000	0.00000	0.00000	0.00000	0.00000	0.00000	0.	0.	0
29	2	1	1	109	0.00000	0.00000	0.00000	0.00000	0.00000	0.00000	0.	0.	0
30	2	1	1	113	0.00000	0.00000	0.00000	0.00000	0.00000	0.00000	0.	0.	0
31	2	1	1	117	0.00000	0.00000	0.00000	0.00000	0.00000	0.00000	0.	0.	0
32	2	1	1	121	0.00000	0.00000	0.00000	0.00000	0.00000	0.00000	0.	0	

Figure N-6 (Continued)

1	2	3	4	5	6	7	8	9	10	11	12	13	14	15	16	17	18	19	20	21	22	23	24	25	26	27	28	29	30	31	32	33	34	35	36	37	38	39	40	41	42	43	44	45	46	47	48	49	50	51	52	53	54	55	56	57	58	59	60	61	62	63	64	65	66	67	68	69	70	71	72	73	74	75	76	77	78	79	80	81	82	83	84	85	86	87	88	89	90	91	92	93	94	95	96	97	98	99	100																																																																																																																																																																																																																																																																																																																																																																																																																																																																																																																																																																																																																																																																																																																																																															
7.620000	7.704667	7.789333	7.874000	7.958667	8.043333	8.128000	8.212667	8.297333	8.382000	8.466667	8.551333	8.636000	8.720667	8.805333	8.890000	8.974667	9.059333	9.144000	9.228667	9.313333	9.398000	9.482667	9.567333	9.652000	9.736667	9.821333	9.906000	9.990667	10.075333	10.160000	10.244667	10.329333	10.414000	10.498667	10.583333	10.668000	10.752667	10.837333	10.922000	11.006667	11.091333	11.176000	11.260667	11.345333	11.430000	11.514667	11.599333	11.684000	11.768667	11.853333	11.938000	12.022667	12.107333	12.192000	12.276667	12.361333	12.446000	12.530667	12.615333	12.700000	12.784667	12.869333	12.954000	13.038667	13.123333	13.208000	13.292667	13.377333	13.462000	13.546667	13.631333	13.716000	13.800667	13.885333	13.970000	14.054667	14.139333	14.224000	14.308667	14.393333	14.478000	14.562667	14.647333	14.732000	14.816667	14.901333	14.986000	15.070667	15.155333	15.240000	15.324667	15.409333	15.494000	15.578667	15.663333	15.748000	15.832667	15.917333	16.002000	16.086667	16.171333	16.256000	16.340667	16.425333	16.510000	16.594667	16.679333	16.764000	16.848667	16.933333	17.018000	17.102667	17.187333	17.272000	17.356667	17.441333	17.526000	17.610667	17.695333	17.780000	17.864667	17.949333	18.034000	18.118667	18.203333	18.288000	18.372667	18.457333	18.542000	18.626667	18.711333	18.796000	18.880667	18.965333	19.050000	19.134667	19.219333	19.304000	19.388667	19.473333	19.558000	19.642667	19.727333	19.812000	19.896667	19.981333	20.066000	20.150667	20.235333	20.320000	20.404667	20.489333	20.574000	20.658667	20.743333	20.828000	20.912667	21.000000	21.084667	21.169333	21.254000	21.338667	21.423333	21.508000	21.592667	21.677333	21.762000	21.846667	21.931333	22.016000	22.100667	22.185333	22.270000	22.354667	22.439333	22.524000	22.608667	22.693333	22.778000	22.862667	22.947333	23.032000	23.116667	23.201333	23.286000	23.370667	23.455333	23.540000	23.624667	23.709333	23.794000	23.878667	23.963333	24.048000	24.132667	24.217333	24.302000	24.386667	24.471333	24.556000	24.640667	24.725333	24.810000	24.894667	24.979333	25.064000	25.148667	25.233333	25.318000	25.402667	25.487333	25.572000	25.656667	25.741333	25.826000	25.910667	26.000000	26.084667	26.169333	26.254000	26.338667	26.423333	26.508000	26.592667	26.677333	26.762000	26.846667	26.931333	27.016000	27.100667	27.185333	27.270000	27.354667	27.439333	27.524000	27.608667	27.693333	27.778000	27.862667	27.947333	28.032000	28.116667	28.201333	28.286000	28.370667	28.455333	28.540000	28.624667	28.709333	28.794000	28.878667	28.963333	29.048000	29.132667	29.217333	29.302000	29.386667	29.471333	29.556000	29.640667	29.725333	29.810000	29.894667	29.979333	30.064000	30.148667	30.233333	30.318000	30.402667	30.487333	30.572000	30.656667	30.741333	30.826000	30.910667	31.000000	31.084667	31.169333	31.254000	31.338667	31.423333	31.508000	31.592667	31.677333	31.762000	31.846667	31.931333	32.016000	32.100667	32.185333	32.270000	32.354667	32.439333	32.524000	32.608667	32.693333	32.778000	32.862667	32.947333	33.032000	33.116667	33.201333	33.286000	33.370667	33.455333	33.540000	33.624667	33.709333	33.794000	33.878667	33.963333	34.048000	34.132667	34.217333	34.302000	34.386667	34.471333	34.556000	34.640667	34.725333	34.810000	34.894667	34.979333	35.064000	35.148667	35.233333	35.318000	35.402667	35.487333	35.572000	35.656667	35.741333	35.826000	35.910667	36.000000	36.084667	36.169333	36.254000	36.338667	36.423333	36.508000	36.592667	36.677333	36.762000	36.846667	36.931333	37.016000	37.100667	37.185333	37.270000	37.354667	37.439333	37.524000	37.608667	37.693333	37.778000	37.862667	37.947333	38.032000	38.116667	38.201333	38.286000	38.370667	38.455333	38.540000	38.624667	38.709333	38.794000	38.878667	38.963333	39.048000	39.132667	39.217333	39.302000	39.386667	39.471333	39.556000	39.640667	39.725333	39.810000	39.894667	39.979333	40.064000	40.148667	40.233333	40.318000	40.402667	40.487333	40.572000	40.656667	40.741333	40.826000	40.910667	41.000000	41.084667	41.169333	41.254000	41.338667	41.423333	41.508000	41.592667	41.677333	41.762000	41.846667	41.931333	42.016000	42.100667	42.185333	42.270000	42.354667	42.439333	42.524000	42.608667	42.693333	42.778000	42.862667	42.947333	43.032000	43.116667	43.201333	43.286000	43.370667	43.455333	43.540000	43.624667	43.709333	43.794000	43.878667	43.963333	44.048000	44.132667	44.217333	44.302000	44.386667	44.471333	44.556000	44.640667	44.725333	44.810000	44.894667	44.979333	45.064000	45.148667	45.233333	45.318000	45.402667	45.487333	45.572000	45.656667	45.741333	45.826000	45.910667	46.000000	46.084667	46.169333	46.254000	46.338667	46.423333	46.508000	46.592667	46.677333	46.762000	46.846667	46.931333	47.016000	47.100667	47.185333	47.270000	47.354667	47.439333	47.524000	47.608667	47.693333	47.778000	47.862667	47.947333	48.032000	48.116667	48.201333	48.286000	48.370667	48.455333	48.540000	48.624667	48.709333	48.794000	48.878667	48.963333	49.048000	49.132667	49.217333	49.302000	49.386667	49.471333	49.556000	49.640667	49.725333	49.810000	49.894667	49.979333	50.064000	50.148667	50.233333	50.318000	50.402667	50.487333	50.572000	50.656667	50.741333	50.826000	50.910667	51.000000	51.084667	51.169333	51.254000	51.338667	51.423333	51.508000	51.592667	51.677333	51.762000	51.846667	51.931333	52.016000	52.100667	52.185333	52.270000	52.354667	52.439333	52.524000	52.608667	52.693333	52.778000	52.862667	52.947333	53.032000	53.116667	53.201333	53.286000	53.370667	53.455333	53.540000	53.624667	53.709333	53.794000	53.878667	53.963333	54.048000	54.132667	54.217333	54.302000	54.386667	54.471333	54.556000	54.640667	54.725333	54.810000	54.894667	54.979333	55.064000	55.148667	55.233333	55.318000	55.402667	55.487333	55.572000	55.656667	55.741333	55.826000	55.910667	56.000000	56.084667	56.169333	56.254000	56.338667	56.423333	56.508000	56.592667	56.677333	56.762000	56.846667	56.931333	57.016000	57.100667	57.185333	57.270000	57.354667	57.439333	57.524000	57.608667	57.693333	57.778000	57.862667	57.947333	58.032000	58.116667	58.201333	58.286000	58.370667	58.455333	58.540000	58.624667	58.709333	58.794000	58.878667	58.963333	59.048000	59.132667	59.217333	59.302000	59.386667	59.471333	59.556000	59.640667	59.725333	59.810000	59.894667	59.979333	60.064000	60.148667	60.233333	60.318000	60.402667	60.487333	60.572000	60.656667	60.741333	60.826000	60.910667	61.000000	61.084667	61.169333	61.254000	61.338667	61.423333	61.508000	61.592667	61.677333	61.762000	61.846667	61.931333	62.016000	62.100667	62.185333	62.270000	62.354667	62.439333	62.524000	62.608667	62.693333	62.778000	62.862667	62.947333	63.032000	63.116667	63.201333	63.286000	63.370667	63.455333	63.540000	63.624667	63.709333	63.794000	63.878667	63.963333	64.048000	64.132667	64.217333	64.302000	64.386667	64.471333	64.556000	64.640667	64.725333	64.810000	64.894667	64.979333	65.064000	65.148667	65.233333	65.318000	65.402667	65.487333	65.572000	65.656667	65.741333	65.826000	65.910667	66.000000	66.084667	66.169333	66.254000	66.338667	66.423333	66.508000	66.592667	66.677333	66.762000	66.846667	66.931333	67.016000	67.100667	67.185333	67.270000	67.354667	67.439333	67.524000	67.608667	67.693333	67.778000	67.862667	67.947333	68.032000	68.116667	68.201333	68.286000	68.370667	68.455333	68.540000	68.624667	68.709333	68.794000	68.878667	68.963333	69.048000	69.132667	69.217333	69.302000	69.386667	69.471333	69.556000	69.640667	69.725333	69.810000	69.894667	69.979333	70.064000	70.148667	70.233333	70.318000	70.402667	70.487333	70.572000	70.656667	70.741333	70.826000	70.910667	71.000000	71.084667	71.169333	71.254000	71.338667	71.423333	71.508000	71.592667	71.677333	71.762000	71.846667	71.931333	72.016000	72.100667	72.185333	72.270000	72.354667	72.439333	72.524000	72.608667	72.693333	72.778000	72.862667	72.947333	73.032000	73.116667	73.201333	73.286000	73.370667	73.455333	73.540000	73.624667	73.709333	73.794000	73.878667	73.963333	74.048000	74.132667	74.217333	74.302000	74.386667	74.471333	74.556000	74.640667	74.725333	74.810000	74.894667	74.979333	75.064000	75.148667	75.233333	75.318000	75.402667	75.487333	75.572000	75.656667	75.741333	75.826000	75.910667	76.000000	76.084667	76.169333	76.254000	76.338667	76.423333	76.508000	76.592667	76.677333	76.762000	76.846667	76.931333	77.016000	77.100667	77.185333	77.270000	77.354667	77.439333	77.524000	77.608667	77.693333	77.778000	77.862667	77.947333	78.032000	78.116667	78.201333	78.286

(b)

Figure N-6 (Continued)

CELL	CL = 0.	2.079E-02	0.	0.	2.188E-02	CL-AVG =	2.188E-02	PI*N*R**2=	263.	ROT=	-0.	FU= .0077	
3	6	1.7415	5.1199	0.0000	0.0000	CN-TOT =	1.065E+05	FRAGMENT	RAD.=	1.059E-02	NO.=	4.626E+04	
6	1.7415	5.1199	0.0000	0.0000	0.0000	CN-TOT =	2.600	6.423764	0.1000	16.354	-322.124	466.301	
CELL	CL = 0.	0.	0.	0.	0.	CL-AVG =	2.453E-02	PI*N*R**2=	227.	ROT=	-0.	FU= .0039	
3	7	1.7677	5.5801	0.0000	0.0000	CN-TOT =	1.203E+05	FRAGMENT	RAD.=	1.227E-02	NO.=	2.996E+04	
7	1.7677	5.5801	0.0000	0.0000	0.0000	CN-TOT =	14.0	6.137372	0.0000	17.130	-363.121	486.444	
COLUMN	K= 4, N= 500,	TIME= .8995E-04, X=	4.773, Y=	0.0000	0.0000	CN-TOT =	14.0	6.137372	0.0000	17.130	-363.121	486.444	
J	X	Y	TYXW	TYZW	TYXW	TYZW	P	E	D	C	SPSQ	XCNH	
CELL	CL = 0.	0.	0.	0.	0.	CL-AVG =	2.814E-02	PI*N*R**2=	159.	ROT=	0.	FU= .0051	
4	2	.8347	1.4549	0.0000	0.0000	CN-TOT =	7.613E+04	FRAGMENT	RAD.=	1.395E-02	NO.=	2.018E+04	
2	.8347	1.4549	0.0000	0.0000	0.0000	CN-TOT =	76.1	5.387206	0.0000	15.771	-587.657	237.761	
CELL	CL = 0.	0.	0.	0.	0.	CL-AVG =	3.139E-02	PI*N*R**2=	178.	ROT=	0.	FU= .0003	
4	3	1.3685	2.7147	0.0000	0.0000	CN-TOT =	5.754E+04	FRAGMENT	RAD.=	1.570E-02	NO.=	1.438E+04	
3	1.3685	2.7147	0.0000	0.0000	0.0000	CN-TOT =	88.4	6.343315	0.0000	16.567	-467.819	373.216	
CELL	CL = 0.	0.	0.	0.	0.	CL-AVG =	5.056E-02	PI*N*R**2=	112.	ROT=	0.	FU= 0.0000	
4	4	2.2427	4.0082	0.0000	0.0000	CN-TOT =	1.396E+04	FRAGMENT	RAD.=	2.528E-02	NO.=	3.490E+03	
4	2.2427	4.0082	0.0000	0.0000	0.0000	CN-TOT =	0.0000	0.0000	0.0000	16.611	-328.064	545.447	
CELL	CL = 0.	0.	0.	0.	0.	CL-AVG =	3.220E-02	PI*N*R**2=	176.	ROT=	-0.	FU= 0.0000	
4	5	2.6930	4.8315	0.0000	0.0000	CN-TOT =	5.397E+04	FRAGMENT	RAD.=	1.610E-02	NO.=	1.349E+04	
5	2.6930	4.8315	0.0000	0.0000	0.0000	CN-TOT =	0.0000	58.2	6.566317	0.0000	16.005	-285.609	598.877
CELL	CL = 0.	0.	0.	0.	0.	CL-AVG =	2.227E-02	PI*N*R**2=	251.	ROT=	-0.	FU= 0.0000	
4	6	2.9585	5.8531	0.0000	0.0000	CN-TOT =	1.611E+05	FRAGMENT	RAD.=	1.114E-02	NO.=	4.028E+04	
6	2.9585	5.8531	0.0000	0.0000	0.0000	CN-TOT =	0.0000	26.7	6.331006	0.0000	16.606	-288.052	635.562
CELL	CL = 0.	0.	0.	0.	0.	CL-AVG =	2.485E-02	PI*N*R**2=	224.	ROT=	-0.	FU= .0043	
4	7	3.0547	6.5064	0.0000	0.0000	CN-TOT =	1.156E+05	FRAGMENT	RAD.=	1.243E-02	NO.=	2.879E+04	
7	3.0547	6.5064	0.0000	0.0000	0.0000	CN-TOT =	0.0000	14.7	5.451206	0.0000	17.435	-325.505	632.876
COLUMN	K= 5, N= 500,	TIME= .8995E-04, X=	2.1296, Y=	0.0000	0.0000	CN-TOT =	0.0000	14.7	5.451206	0.0000	17.435	-325.505	632.876
J	X	Y	TYXW	TYZW	TYXW	TYZW	P	E	D	C	SPSQ	XCNH	
2	2.4500	1.4533	-184.8042	-184.8042	0.0000	184.8042	233.5	.395109	0.0000	52.480	-312.005	204.574	
3	3.0166	2.8913	-238.8119	-238.8119	0.0000	238.8119	278.5	.428819	0.0000	62.480	-232.689	466.533	
4	3.4688	4.4414	-345.2739	-345.2739	0.0000	345.2739	359.4	.480313	0.0000	62.480	-240.003	736.081	
CELL	CL = 0.	0.	0.	0.	0.	CL-AVG =	3.273E-02	PI*N*R**2=	172.	ROT=	-0.	FU= 0.0000	
5	5	3.7610	5.2021	0.0000	0.0000	CN-TOT =	5.113E+04	FRAGMENT	RAD.=	1.636E-02	NO.=	2.278E+04	
5	3.7610	5.2021	0.0000	0.0000	0.0000	CN-TOT =	0.0000	77.2	6.626636	0.0000	15.861	-248.366	740.547
CELL	CL = 0.	0.	0.	0.	0.	CL-AVG =	2.609E-02	PI*N*R**2=	214.	ROT=	-0.	FU= 0.0000	
5	6	4.0474	6.0374	0.0000	0.0000	CN-TOT =	1.003E+05	FRAGMENT	RAD.=	1.385E-02	NO.=	2.507E+04	
6	4.0474	6.0374	0.0000	0.0000	0.0000	CN-TOT =	0.0000	34.5	6.814135	0.0000	15.429	-263.840	730.342
CELL	CL = 0.	0.	0.	0.	0.	CL-AVG =	2.496E-02	PI*N*R**2=	223.	ROT=	-0.	FU= .0045	
5	7	4.1633	6.8905	0.0000	0.0000	CN-TOT =	1.141E+05	FRAGMENT	RAD.=	1.248E-02	NO.=	2.841E+04	
7	4.1633	6.8905	0.0000	0.0000	0.0000	CN-TOT =	15.6	6.175065	0.0000	17.023	-259.369	729.277	

(c)

Figure N-6 (Continued)

COLUMN K= 9, N= 500, TIME= .6995E-04, X= 8.1142, Y= 0.0000															
J	X	Y	TXM	TYM	TZM	TXM	TYM	TZM	P	E	O	C	YCNH	YCNH	P
2	8.2707	2.3070	-175.3135	-175.3135	-175.3135	0.0000	0.0000	0.0000	175.3135	227.7	.385041	0.0000	0.0000	0.0000	0.0000
3	8.4568	4.4682	-247.1038	-247.1038	-247.1038	0.0000	0.0000	0.0000	247.1038	286.8	.430865	0.0000	0.0000	0.0000	0.0000
4	8.1763	6.5218	-303.8528	-303.8528	-303.8528	0.0000	0.0000	0.0000	303.8528	328.2	.462359	0.0000	0.0000	0.0000	0.0000
CELL CL = 0.0, CN = 0.0, TXM = 0.0000, TYM = 0.0000, TZM = 0.0000															
5	8.3454	7.0924	0.0000	0.0000	0.0000	0.0000	0.0000	0.0000	0.0000	86.3	7.054307	0.0000	0.0000	0.0000	0.0000
CELL CL = 0.0, CN = 0.0, TXM = 0.0000, TYM = 0.0000, TZM = 0.0000															
6	8.4524	7.6973	0.0000	0.0000	0.0000	0.0000	0.0000	0.0000	0.0000	45.4	6.599461	0.0000	0.0000	0.0000	0.0000
CELL CL = 0.0, CN = 0.0, TXM = 0.0000, TYM = 0.0000, TZM = 0.0000															
7	8.4584	8.3762	0.0000	0.0000	0.0000	0.0000	0.0000	0.0000	0.0000	15.7	6.276786	0.0000	0.0000	0.0000	0.0000
CELL CL = 0.0, CN = 0.0, TXM = 0.0000, TYM = 0.0000, TZM = 0.0000															
8	9.5923	2.5146	-161.2804	-161.2804	-161.2804	0.0000	0.0000	0.0000	161.2804	233.4	.385327	0.0000	0.0000	0.0000	0.0000
9	9.7107	4.8343	-252.4666	-252.4666	-252.4666	0.0000	0.0000	0.0000	252.4666	298.5	.434610	0.0000	0.0000	0.0000	0.0000
10	9.3693	7.0392	-292.0116	-292.0116	-292.0116	0.0000	0.0000	0.0000	292.0116	320.1	.456072	0.0000	0.0000	0.0000	0.0000
CELL CL = 0.0, CN = 0.0, TXM = 0.0000, TYM = 0.0000, TZM = 0.0000															
11	9.5135	7.5674	0.0000	0.0000	0.0000	0.0000	0.0000	0.0000	0.0000	86.7	6.991469	0.0000	0.0000	0.0000	0.0000
CELL CL = 0.0, CN = 0.0, TXM = 0.0000, TYM = 0.0000, TZM = 0.0000															
12	9.5221	8.1234	0.0000	0.0000	0.0000	0.0000	0.0000	0.0000	0.0000	46.2	6.859151	0.0000	0.0000	0.0000	0.0000
CELL CL = 0.0, CN = 0.0, TXM = 0.0000, TYM = 0.0000, TZM = 0.0000															
13	9.5737	8.7567	0.0000	0.0000	0.0000	0.0000	0.0000	0.0000	0.0000	15.4	6.082315	0.0000	0.0000	0.0000	0.0000
CELL CL = 0.0, CN = 0.0, TXM = 0.0000, TYM = 0.0000, TZM = 0.0000															
14	10.9273	2.7322	-167.0029	-167.0029	-167.0029	0.0000	0.0000	0.0000	167.0029	220.3	.379327	0.0000	0.0000	0.0000	0.0000
15	11.0182	5.8299	-237.7755	-237.7755	-237.7755	0.0000	0.0000	0.0000	237.7755	279.7	.425880	0.0000	0.0000	0.0000	0.0000
16	10.6129	7.5639	-270.9739	-270.9739	-270.9739	0.0000	0.0000	0.0000	270.9739	305.7	.443257	0.0000	0.0000	0.0000	0.0000
CELL CL = 0.0, CN = 0.0, TXM = 0.0000, TYM = 0.0000, TZM = 0.0000															
17	10.7301	8.0386	0.0000	0.0000	0.0000	0.0000	0.0000	0.0000	0.0000	87.4	6.886565	0.0000	0.0000	0.0000	0.0000
CELL CL = 0.0, CN = 0.0, TXM = 0.0000, TYM = 0.0000, TZM = 0.0000															
18	10.7684	8.5103	0.0000	0.0000	0.0000	0.0000	0.0000	0.0000	0.0000	46.7	6.71089	0.0000	0.0000	0.0000	0.0000
CELL CL = 0.0, CN = 0.0, TXM = 0.0000, TYM = 0.0000, TZM = 0.0000															
19	10.7243	9.1267	0.0000	0.0000	0.0000	0.0000	0.0000	0.0000	0.0000	15.1	5.681726	0.0000	0.0000	0.0000	0.0000

(c)

Figure N-6 (Continued)

COLUMN K= 15, N= 500, TIME= .8995E-04, X= 16.1883, Y= 0.0000										
J	X	Y	TXM	TYM	TXM	TYM	P	E	D	XCNT, YONH=
2	16.2380	3.0792	-106.7667	-106.7667	-106.7667	-106.7667	106.7667	16.4.0	.325668	0.0000
3	16.3339	5.8436	-162.4018	-162.4018	-162.4018	-162.4018	162.4018	218.4	.371875	0.0000
4	15.8439	8.8571	-204.1143	-204.1143	-204.1143	-204.1143	204.1143	257.2	.355684	0.0000
CELL	CL = 0.	0.	0.	0.	0.	0.	5.004E-02	CL-AVG = 5.404E-02	PI*N*R**2= 112.	ROT=
15	5	CN = 0.	0.	0.	0.	0.	1.420E+04	CN-TOT = 1.420E+04	FRAGMENT RAD.= 2.562E-02	NO.= 3.551E+03
5	15.8382	9.0565	0.0000	0.0000	0.0000	0.0000	0.0000	0.4.9	6.750197	0.0000
CELL	CL = 0.	0.	0.	0.	0.	0.	3.109E-02	CL-AVG = 3.109E-02	PI*N*R**2= 179.	ROT=
15	6	CN = 0.	0.	0.	0.	0.	5.910E+04	CN-TOT = 5.910E+04	FRAGMENT RAD.= 1.555E-02	NO.= 1.475E+04
6	15.7742	9.4946	0.0000	0.0000	0.0000	0.0000	0.0000	4.5.6	6.622305	0.0000
CELL	CL = 0.	0.	0.	0.	0.	0.	2.557E-02	CL-AVG = 2.557E-02	PI*N*R**2= 220.	ROT=
15	7	CN = 0.	0.	0.	0.	0.	1.069E+05	CN-TOT = 1.069E+05	FRAGMENT RAD.= 1.278E-02	NO.= 2.673E+04
7	15.6740	10.8271	0.0000	0.0000	0.0000	0.0000	0.0000	1.5.1	5.843275	0.0000
COLUMN K= 16, N= 500, TIME= .8995E-04, X= 17.5001, Y= 0.0000										
J	X	Y	TXM	TYM	TXM	TYM	P	E	D	XCNT, YONH=
2	17.5573	3.1280	-100.0288	-100.0288	-100.0288	-100.0288	100.0288	156.7	.319244	0.0000
3	17.6126	5.9428	-150.0804	-150.0804	-150.0804	-150.0804	150.0804	208.5	.363369	0.0000
4	17.0512	8.8806	-187.7148	-187.7148	-187.7148	-187.7148	187.7148	243.4	.385554	0.0000
CELL	CL = 0.	0.	0.	0.	0.	0.	5.735E-02	CL-AVG = 5.735E-02	PI*N*R**2= 58.	ROT=
16	5	CN = 0.	0.	0.	0.	0.	9.491E+03	CN-TOT = 9.491E+03	FRAGMENT RAD.= 2.667E-02	NO.= 2.373E+03
5	17.0412	9.2174	0.0000	0.0000	0.0000	0.0000	0.0000	8.6.0	6.816328	0.0000
CELL	CL = 0.	0.	0.	0.	0.	0.	3.104E-02	CL-AVG = 3.104E-02	PI*N*R**2= 179.	ROT=
16	6	CN = 0.	0.	0.	0.	0.	5.924E+04	CN-TOT = 5.924E+04	FRAGMENT RAD.= 1.552E-02	NO.= 1.472E+04
6	16.9719	9.6518	0.0000	0.0000	0.0000	0.0000	0.0000	4.5.6	6.717181	0.0000
CELL	CL = 0.	0.	0.	0.	0.	0.	2.568E-02	CL-AVG = 2.568E-02	PI*N*R**2= 220.	ROT=
16	7	CN = 0.	0.	0.	0.	0.	1.061E+05	CN-TOT = 1.061E+05	FRAGMENT RAD.= 1.284E-02	NO.= 2.653E+04
7	16.8633	10.1805	0.0000	0.0000	0.0000	0.0000	0.0000	1.5.0	5.910957	0.0000
COLUMN K= 17, N= 500, TIME= .8995E-04, X= 18.6102, Y= 0.0000										
J	X	Y	TXM	TYM	TXM	TYM	P	E	D	XCNT, YONH=
2	18.8605	3.1880	-93.1659	-93.1659	-93.1659	-93.1659	93.1659	150.2	.310217	0.0000
3	18.8921	6.0895	-139.1435	-139.1435	-139.1435	-139.1435	139.1435	195.5	.355532	0.0000
4	18.2484	8.5846	-171.3495	-171.3495	-171.3495	-171.3495	171.3495	221.3	.373603	0.0000
CELL	CL = 0.	0.	0.	0.	0.	0.	5.928E-02	CL-AVG = 5.928E-02	PI*N*R**2= 94.	ROT=
17	5	CN = 0.	0.	0.	0.	0.	8.539E+03	CN-TOT = 8.539E+03	FRAGMENT RAD.= 2.564E-02	NO.= 2.135E+03
5	18.2341	9.3787	0.0000	0.0000	0.0000	0.0000	0.0000	8.6.5	6.787005	0.0000
CELL	CL = 0.	0.	0.	0.	0.	0.	3.100E-02	CL-AVG = 3.100E-02	PI*N*R**2= 181.	ROT=
17	6	CN = 0.	0.	0.	0.	0.	5.982E+04	CN-TOT = 5.982E+04	FRAGMENT RAD.= 1.555E-02	NO.= 1.496E+04
6	18.1815	9.8098	0.0000	0.0000	0.0000	0.0000	0.0000	4.5.4	6.656838	0.0000
CELL	CL = 0.	0.	0.	0.	0.	0.	2.539E-02	CL-AVG = 2.539E-02	PI*N*R**2= 222.	ROT=
17	7	CN = 0.	0.	0.	0.	0.	1.094E+05	CN-TOT = 1.094E+05	FRAGMENT RAD.= 1.271E-02	NO.= 2.735E+04
7	18.0573	10.3370	0.0000	0.0000	0.0000	0.0000	0.0000	1.4.6	5.817503	0.0000

(c)

Figure N-6 (Continued)

COLUMN K=18, N=500, TIME=.6995E-04, X=20.10E3, Y=0.0000

J	X	Y	TXM	TYM	TZM	TXM	TYM	TZM	P	E	D	XCNT	YDNT	SPSG	YDNT	YDNT
2	20.1556	3.2844	-84.6065	-84.6065	-84.6065	0.0000	0.0000	0.0000	84.6065	139.7	302767	0.0000	0.0000	62.400	62.400	62.400
3	20.1630	6.2063	-127.2913	-127.2913	-127.2913	0.0000	0.0000	0.0000	127.2913	184.4	335120	0.0000	0.0000	62.400	62.400	62.400
4	19.4418	9.1474	-154.8888	-154.8888	-154.8888	0.0000	0.0000	0.0000	154.8888	214.6	360676	0.0000	0.0000	62.400	62.400	62.400

CELL CL=0.0, CN=0.0, TXM=0.0000, TYM=0.0000, TZM=0.0000

18 5 CN=0.0, TXM=0.0000, TYM=0.0000, TZM=0.0000

5 19.4250 9.5386 0.0000 0.0000 0.0000

CELL CL=0.0, CN=0.0, TXM=0.0000, TYM=0.0000, TZM=0.0000

18 6 CN=0.0, TXM=0.0000, TYM=0.0000, TZM=0.0000

6 19.3510 9.5677 0.0000 0.0000 0.0000

CELL CL=0.0, CN=0.0, TXM=0.0000, TYM=0.0000, TZM=0.0000

18 7 CN=0.0, TXM=0.0000, TYM=0.0000, TZM=0.0000

7 19.2460 10.4942 0.0000 0.0000 0.0000

COLUMN K=19, N=500, TIME=.6995E-04, X=21.4013, Y=0.0000

J	X	Y	TXM	TYM	TZM	TXM	TYM	TZM	P	E	D	XCNT	YDNT	SPSG	YDNT	YDNT
2	21.4490	3.3149	-74.6223	-74.6223	-74.6223	0.0000	0.0000	0.0000	74.6223	120.3	250865	0.0000	0.0000	62.400	62.400	62.400
3	21.4335	6.3196	-113.8806	-113.8806	-113.8806	0.0000	0.0000	0.0000	113.8806	171.1	332886	0.0000	0.0000	62.400	62.400	62.400
4	20.6349	9.3167	-135.0220	-135.0220	-135.0220	0.0000	0.0000	0.0000	135.0220	199.7	348411	0.0000	0.0000	62.400	62.400	62.400

CELL CL=0.0, CN=0.0, TXM=0.0000, TYM=0.0000, TZM=0.0000

19 5 CN=0.0, TXM=0.0000, TYM=0.0000, TZM=0.0000

5 20.6165 9.6365 0.0000 0.0000 0.0000

CELL CL=0.0, CN=0.0, TXM=0.0000, TYM=0.0000, TZM=0.0000

19 6 CN=0.0, TXM=0.0000, TYM=0.0000, TZM=0.0000

6 20.5413 10.1243 0.0000 0.0000 0.0000

CELL CL=0.0, CN=0.0, TXM=0.0000, TYM=0.0000, TZM=0.0000

19 7 CN=0.0, TXM=0.0000, TYM=0.0000, TZM=0.0000

7 20.4352 10.6505 0.0000 0.0000 0.0000

COLUMN K=20, N=500, TIME=.6995E-04, X=22.7229, Y=0.0000

J	X	Y	TXM	TYM	TZM	TXM	TYM	TZM	P	E	D	XCNT	YDNT	SPSG	YDNT	YDNT
2	22.7546	3.3492	-64.4544	-64.4544	-64.4544	0.0000	0.0000	0.0000	64.4544	117.3	274810	0.0000	0.0000	62.400	62.400	62.400
3	22.7016	6.4339	-100.7716	-100.7716	-100.7716	0.0000	0.0000	0.0000	100.7716	157.1	320705	0.0000	0.0000	62.400	62.400	62.400
4	21.6300	9.4657	-124.1485	-124.1485	-124.1485	0.0000	0.0000	0.0000	124.1485	184.5	336442	0.0000	0.0000	62.400	62.400	62.400

CELL CL=0.0, CN=0.0, TXM=0.0000, TYM=0.0000, TZM=0.0000

20 5 CN=0.0, TXM=0.0000, TYM=0.0000, TZM=0.0000

5 21.8110 9.6528 0.0000 0.0000 0.0000

CELL CL=0.0, CN=0.0, TXM=0.0000, TYM=0.0000, TZM=0.0000

20 6 CN=0.0, TXM=0.0000, TYM=0.0000, TZM=0.0000

6 21.7347 10.2793 0.0000 0.0000 0.0000

CELL CL=0.0, CN=0.0, TXM=0.0000, TYM=0.0000, TZM=0.0000

20 7 CN=0.0, TXM=0.0000, TYM=0.0000, TZM=0.0000

7 21.6293 10.8064 0.0000 0.0000 0.0000

(c)

Figure N-6 (Continued)

COLUMN K= 21, N= 500, TIME= .6995E-04, X= 24.6445, Y= 0.0000										XCNH, YCNH=									
J	X	Y	TXM	TYM	TZM	P	E	D	C	SPSC	YCNH	YCNH	YCNH	YCNH	YCNH				
2	24.0731	3.4471	-55.2323	-55.2323	-55.2323	55.2323	105.2	2.262509	0.0000	62.400	62.400	62.400	62.400	62.400	62.400				
3	23.9920	6.5514	-88.8802	-88.8802	-88.8802	88.8802	145.6	3.15257	0.0000	62.400	62.400	62.400	62.400	62.400	62.400				
4	23.0325	9.6194	-111.1021	-111.1021	-111.1021	111.1021	172.5	3.32204	0.0000	62.400	62.400	62.400	62.400	62.400	62.400				
CELL	CL = 0.	0.	0.	0.	0.	0.	5.135E-02	PI*N**2=	109.	ROT=	-C.	FU=0.0000	675.494	0.000	0.000				
21	5	0.	0.	0.	0.	0.	1.318E+04	FRAGMENT	RAD.= 2.567E-02	NO.= 3.295E+03	-58.944	1109.643	1						
5	23.0029	10.0040	0.0000	0.0000	0.0000	0.0000	84.0	6.454016	0.0000	16.294	-C.	FU=0.0012							
CELL	CL = 0.	0.	0.	0.	0.	0.	2.955E-02	PI*N**2=	189.	ROT=	-C.	FU=0.0012							
21	6	0.	0.	0.	0.	0.	6.885E+04	FRAGMENT	RAD.= 1.478E-02	NO.= 1.719E+04	-C.	FU=0.0012							
6	22.9340	10.4300	0.0000	0.0000	0.0000	0.0000	44.9	6.333365	0.0000	16.603	-C.	FU=0.0012							
CELL	CL = 0.	0.	0.	0.	0.	0.	2.499E-02	PI*N**2=	224.	ROT=	-C.	FU=0.0000							
21	7	0.	0.	0.	0.	0.	1.141E+05	FRAGMENT	RAD.= 1.249E-02	NO.= 2.852E+04	-C.	FU=0.0000							
7	22.8300	10.5574	0.0000	0.0000	0.0000	0.0000	14.6	5.454787	0.0000	15.137	-C.	FU=0.0000							
COLUMN K= 22, N= 500, TIME= .6995E-04, X= 25.3864, Y= 0.0000																			
J	X	Y	TXM	TYM	TZM	P	E <td>D</td> <td>C</td> <td>SPSC</td> <td>YCNH</td> <td>YCNH</td> <td>YCNH</td> <td>YCNH</td> <td>YCNH</td>	D	C	SPSC	YCNH	YCNH	YCNH	YCNH	YCNH				
2	25.4074	3.5148	-47.3953	-47.3953	-47.3953	47.3953	94.0	2.49046	0.0000	62.400	62.400	62.400	62.400	62.400	62.400				
3	25.2808	6.6644	-78.3636	-78.3636	-78.3636	78.3636	133.6	2.93203	0.0000	62.400	62.400	62.400	62.400	62.400	62.400				
4	24.2369	9.7822	-99.8553	-99.8553	-99.8553	99.8553	159.4	3.13137	0.0000	62.400	62.400	62.400	62.400	62.400	62.400				
CELL	CL = 0.	0.	0.	0.	0.	0.	5.054E-02	PI*N**2=	111.	ROT=	-C.	FU=0.0000							
22	5	0.	0.	0.	0.	0.	1.380E+04	FRAGMENT	RAD.= 2.527E-02	NO.= 3.450E+03	-54.434	1109.251	1						
5	24.2146	10.1471	0.0000	0.0000	0.0000	0.0000	84.6	6.354487	0.0000	16.548	-C.	FU=0.0000							
CELL	CL = 0.	0.	0.	0.	0.	0.	2.963E-02	PI*N**2=	147.	ROT=	-C.	FU=0.0000							
22	6	0.	0.	0.	0.	0.	6.796E+04	FRAGMENT	RAD.= 1.481E-02	NO.= 1.682E+04	-C.	FU=0.0000							
6	24.1375	10.5726	0.0000	0.0000	0.0000	0.0000	45.0	6.232466	0.0000	16.873	-C.	FU=0.0000							
CELL	CL = 0.	0.	0.	0.	0.	0.	2.528E-02	PI*N**2=	222.	ROT=	-C.	FU=0.0000							
22	7	0.	0.	0.	0.	0.	1.108E+05	FRAGMENT	RAD.= 1.264E-02	NO.= 2.770E+04	-C.	FU=0.0000							
7	24.0349	11.1006	0.0000	0.0000	0.0000	0.0000	14.0	5.405290	0.0000	19.453	-C.	FU=0.0000							
COLUMN K= 23, N= 500, TIME= .6995E-04, X= 26.7421, Y= 0.0000																			
J	X	Y	TXM	TYM	TZM	P	E <td>D</td> <td>C</td> <td>SPSC</td> <td>YCNH</td> <td>YCNH</td> <td>YCNH</td> <td>YCNH</td> <td>YCNH</td>	D	C	SPSC	YCNH	YCNH	YCNH	YCNH	YCNH				
2	26.7517	3.5844	-40.9590	-40.9590	-40.9590	40.9590	86.0	2.30247	0.0000	62.400	62.400	62.400	62.400	62.400	62.400				
3	26.5233	6.7604	-65.3894	-65.3894	-65.3894	65.3894	122.9	2.82211	0.0000	62.400	62.400	62.400	62.400	62.400	62.400				
4	25.4461	9.9013	-90.1329	-90.1329	-90.1329	90.1329	148.0	3.02839	0.0000	62.400	62.400	62.400	62.400	62.400	62.400				
CELL	CL = 0.	0.	0.	0.	0.	0.	5.131E-02	PI*N**2=	112.	ROT=	-C.	FU=0.0000							
23	5	0.	0.	0.	0.	0.	1.404E+04	FRAGMENT	RAD.= 2.515E-02	NO.= 3.510E+03	-48.913	1095.545	1						
5	25.4241	10.2836	0.0000	0.0000	0.0000	0.0000	85.1	6.261369	0.0000	16.755	-C.	FU=0.0000							
CELL	CL = 0.	0.	0.	0.	0.	0.	3.100E-02	PI*N**2=	182.	ROT=	-C.	FU=0.0000							
23	6	0.	0.	0.	0.	0.	6.035E+04	FRAGMENT	RAD.= 1.550E-02	NO.= 1.510E+04	-C.	FU=0.0000							
6	25.3467	10.7887	0.0000	0.0000	0.0000	0.0000	45.0	6.133528	0.0000	17.145	-C.	FU=0.0000							
CELL	CL = 0.	0.	0.	0.	0.	0.	2.512E-02	PI*N**2=	223.	ROT=	-C.	FU=0.0000							
23	7	0.	0.	0.	0.	0.	1.124E+05	FRAGMENT	RAD.= 1.256E-02	NO.= 2.811E+04	-C.	FU=0.0000							
7	25.2455	11.2360	0.0000	0.0000	0.0000	0.0000	14.6	5.308365	0.0000	15.809	-C.	FU=0.0000							

(c)

Figure N-6 (Continued)

(c)

N-37

COLUMN K= 27, N= 500, TIME= .8995E-04, X= 32.3423, Y= 0.0000									
J	X	Y	TXM	TYM	TZM	P	E	D	XCNT, YCNH=
2	32.2805	3.8019	-24.3575	-24.3575	-24.3575	24.3575	60.5	.20111E	712.801
3	31.9335	7.0942	-46.1172	-46.1172	-46.1172	46.1172	93.2	.24743E	XCNH
4	30.4278	10.3396	-62.7972	-62.7972	-62.7972	62.7972	117.4	.267551	640.165
									421.522
									789.660
									.038
									1064.015
									2
									2
CELL	CL = 0.	0.	0.	0.	0.	CL-AVG = 5.212E-02	PI*NR**2= 110.	ROT=	-6.
27	5	CN = 0.	0.	0.	0.	CN-TOT = 1.284E+04	FRAGMENT RAD.= 2.606E-02	NO.= 3.289E+03	
5	30.4118	10.7156	0.0000	0.0000	0.0000	0.0000	85.8	5.77492	NO.= 2.789
									1060.520
									1
CELL	CL = 0.	0.	0.	0.	0.	CL-AVG = 2.763E-02	PI*NR**2= 205.	ROT=	-0.
27	6	CN = 0.	0.	0.	0.	CN-TOT = 8.555E+04	FRAGMENT RAD.= 1.382E-02	NO.= 2.139E+04	
6	30.3422	11.1421	0.0000	0.0000	0.0000	0.0000	44.2	5.57738	NO.= 4.366
									1058.564
									1
CELL	CL = 0.	0.	0.	0.	0.	CL-AVG = 2.476E-02	PI*NR**2= 226.	ROT=	-0.
27	7	CN = 0.	0.	0.	0.	CN-TOT = 1.171E+05	FRAGMENT RAD.= 1.232E-02	NO.= 2.925E+04	
7	30.2639	11.6872	0.0000	0.0000	0.0000	0.0000	14.0	4.71456	NO.= 2.161
									1061.132
									1
COLUMN K= 28, N= 500, TIME= .8995E-04, X= 33.7923, Y= 0.0000									
J	X	Y	TXM	TYM	TZM	P	E	D	XCNT, YCNH=
2	33.7637	3.8362	-21.7943	-21.7943	-21.7943	21.7943	56.3	.193402	723.851
3	33.2818	7.1630	-42.7070	-42.7070	-42.7070	42.7070	89.2	.239427	XCNH
4	31.7549	10.3979	-58.3051	-58.3051	-58.3051	58.3051	112.4	.259371	426.010
									474.352
									775.365
									2
									2
CELL	CL = 0.	0.	0.	0.	0.	CL-AVG = 5.583E-02	PI*NR**2= 101.	ROT=	-6.
28	5	CN = 0.	0.	0.	0.	CN-TOT = 1.029E+04	FRAGMENT RAD.= 2.791E-02	NO.= 2.573E+03	
5	31.7373	10.7673	0.0000	0.0000	0.0000	0.0000	84.6	5.606158	NO.= 15.245
									1042.813
									1
CELL	CL = 0.	0.	0.	0.	0.	CL-AVG = 2.691E-02	PI*NR**2= 211.	ROT=	-0.
28	6	CN = 0.	0.	0.	0.	CN-TOT = 9.290E+04	FRAGMENT RAD.= 1.346E-02	NO.= 2.322E+04	
6	31.6633	11.4924	0.0000	0.0000	0.0000	0.0000	43.4	5.403757	NO.= 18.179
									1042.722
									1
CELL	CL = 0.	0.	0.	0.	0.	CL-AVG = 2.520E-02	PI*NR**2= 231.	ROT=	-0.
28	7	CN = 0.	0.	0.	0.	CN-TOT = 1.157E+05	FRAGMENT RAD.= 1.260E-02	NO.= 2.892E+04	
7	31.5850	11.7409	0.0000	0.0000	0.0000	0.0000	13.5	4.548938	NO.= 21.091
									1046.130
									1
COLUMN K= 29, N= 500, TIME= .8995E-04, X= 35.2774, Y= 0.0000									
J	X	Y	TXM	TYM	TZM	P	E	D	XCNT, YCNH=
2	35.1683	3.8742	-19.3942	-19.3942	-19.3942	19.3942	52.4	.185171	735.978
3	34.6497	7.1924	-40.2657	-40.2657	-40.2657	40.2657	86.1	.233843	XCNH
4	33.1632	10.4306	-53.7893	-53.7893	-53.7893	53.7893	106.3	.253108	654.575
									466.775
									756.075
									2
									2
CELL	CL = 0.	0.	0.	0.	0.	CL-AVG = 4.969E-02	PI*NR**2= 113.	ROT=	-6.
29	5	CN = 0.	0.	0.	0.	CN-TOT = 1.462E+04	FRAGMENT RAD.= 2.485E-02	NO.= 3.651E+03	
5	33.1164	10.7942	0.0000	0.0000	0.0000	0.0000	84.5	5.403620	NO.= 47.381
									1023.751
									1
CELL	CL = 0.	0.	0.	0.	0.	CL-AVG = 2.742E-02	PI*NR**2= 227.	ROT=	-6.
29	6	CN = 0.	0.	0.	0.	CN-TOT = 8.770E+04	FRAGMENT RAD.= 1.371E-02	NO.= 2.193E+04	
6	33.0186	11.2244	0.0000	0.0000	0.0000	0.0000	42.6	5.159561	NO.= 45.758
									1024.672
									1
CELL	CL = 0.	0.	0.	0.	0.	CL-AVG = 2.556E-02	PI*NR**2= 225.	ROT=	-6.
29	7	CN = 0.	0.	0.	0.	CN-TOT = 1.097E+05	FRAGMENT RAD.= 1.627E-02	NO.= 2.743E+04	
7	32.9249	11.7846	0.0000	0.0000	0.0000	0.0000	13.7	4.591161	NO.= 47.632
									1029.620
									1

(c)

Figure N-6 (Continued)

COLUMN K= 30, N= 500, TIME= .6995E-04, X= 36.9113, Y= 0.0000									
J	X	Y	TXM	TYM	P	E	D	C	SPSC
2	36.761E	3.7768	-17.2127	0.0000	17.2127	48.5	.117564	0.0000	62.400
3	36.2547	6.5148	-35.2979	0.0000	35.2979	78.5	.223598	0.0000	62.400
4	34.7377	10.2770	-51.4650	0.0000	51.4650	105.9	.243050	0.0000	62.400
CELL CL = 0.0, CN = 0.0, FU=0.0000									
30	5	34.6489	10.6619	0.0000	0.0000	81.2	5.169596	0.0000	20.336
CELL CL = 0.0, CN = 0.0, FU=0.0000									
30	6	34.5289	11.1110	0.0000	0.0000	40.7	4.919747	0.0000	21.071
CELL CL = 0.0, CN = 0.0, FU=0.0000									
30	7	34.4271	11.6519	0.0000	0.0000	13.4	4.160110	0.0000	25.372
COLUMN K= 31, N= 500, TIME= .6995E-04, X= 36.5421, Y= 0.0000									
J	X	Y	TXM	TYM	P	E	D	C	SPSC
2	36.3801	3.6632	-15.1869	0.0000	15.1869	44.8	.169663	0.0000	62.400
3	37.8414	6.7894	-32.2318	0.0000	32.2318	74.6	.215927	0.0000	62.400
4	36.1554	10.0920	-47.7772	0.0000	47.7772	104.2	.235992	0.0000	62.400
CELL CL = 0.0, CN = 0.0, FU=0.0000									
31	5	36.1029	10.4685	0.0000	0.0000	71.7	5.279644	0.0000	15.515
CELL CL = 0.0, CN = 0.0, FU=0.0000									
31	6	35.9828	10.5477	0.0000	0.0000	39.6	5.070757	0.0000	20.735
CELL CL = 0.0, CN = 0.0, FU=0.0000									
31	7	35.8558	11.5365	0.0000	0.0000	13.6	4.151231	0.0000	25.085
COLUMN K= 32, N= 500, TIME= .6995E-04, X= 40.1683, Y= 0.0000									
J	X	Y	TXM	TYM	P	E	D	C	SPSC
2	39.9772	3.5636	-13.5973	0.0000	13.5973	44.2	.164843	0.0000	62.400
3	39.3653	6.6334	-29.7499	0.0000	29.7499	70.4	.211226	0.0000	62.400
4	37.5634	9.8766	-45.5545	0.0000	45.5545	97.6	.233383	0.0000	62.400
CELL CL = 0.0, CN = 0.0, FU=0.0000									
32	5	37.4500	10.2801	0.0000	0.0000	70.3	5.388410	0.0000	15.514
CELL CL = 0.0, CN = 0.0, FU=0.0000									
32	6	37.3740	10.7444	0.0000	0.0000	38.4	5.232739	0.0000	20.094
CELL CL = 0.0, CN = 0.0, FU=0.0000									
32	7	37.3001	11.3367	0.0000	0.0000	13.8	4.346465	0.0000	24.191

(c)

Figure N-6 (Continued)

(c)

Figure N-6 (Continued)

COLUMN K= 39, N= 500, TIME= .8995E-04, X= 50.5470, Y= 0.0000									
J	2	50.0594	3.0976	TXM	TXM	TXM	TXM	TXM	TXM
		-4.7389	-4.7389	0.0000	0.0000	0.0000	0.0000	0.0000	0.0000
3	40.9466	5.4463	-15.6131	0.0000	0.0000	0.0000	0.0000	0.0000	0.0000
4	46.7201	7.5391	-28.4929	0.0000	0.0000	0.0000	0.0000	0.0000	0.0000
CELL	CL = 0.	0.	0.	0.	0.	0.	0.	0.	0.
39	5	CL = 0.	0.	0.	0.	0.	0.	0.	0.
5	46.6161	8.3784	0.0000	0.0000	0.0000	0.0000	0.0000	0.0000	0.0000
CELL	CL = 0.	0.	0.	0.	0.	0.	0.	0.	0.
39	6	CL = 0.	0.	0.	0.	0.	0.	0.	0.
6	46.5170	8.6840	0.0000	0.0000	0.0000	0.0000	0.0000	0.0000	0.0000
CELL	CL = 0.	0.	0.	0.	0.	0.	0.	0.	0.
39	7	CL = 0.	0.	0.	0.	0.	0.	0.	0.
7	46.4485	9.5465	0.0000	0.0000	0.0000	0.0000	0.0000	0.0000	0.0000
COLUMN K= 40, N= 500, TIME= .8995E-04, X= 51.7231, Y= 0.0000									
J	2	51.3021	3.0721	TXM	TXM	TXM	TXM	TXM	TXM
		-4.1078	-4.1078	0.0000	0.0000	0.0000	0.0000	0.0000	0.0000
3	50.2245	5.3187	-14.0983	0.0000	0.0000	0.0000	0.0000	0.0000	0.0000
4	48.0112	7.6322	-25.1322	0.0000	0.0000	0.0000	0.0000	0.0000	0.0000
CELL	CL = 0.	0.	0.	0.	0.	0.	0.	0.	0.
40	5	CL = 0.	0.	0.	0.	0.	0.	0.	0.
5	47.8589	8.0779	0.0000	0.0000	0.0000	0.0000	0.0000	0.0000	0.0000
CELL	CL = 0.	0.	0.	0.	0.	0.	0.	0.	0.
40	6	CL = 0.	0.	0.	0.	0.	0.	0.	0.
6	47.7545	8.5954	0.0000	0.0000	0.0000	0.0000	0.0000	0.0000	0.0000
CELL	CL = 0.	0.	0.	0.	0.	0.	0.	0.	0.
40	7	CL = 0.	0.	0.	0.	0.	0.	0.	0.
7	47.7621	9.2659	0.0000	0.0000	0.0000	0.0000	0.0000	0.0000	0.0000
COLUMN K= 41, N= 500, TIME= .8995E-04, X= 52.7315, Y= 0.0000									
J	2	52.3169	3.0842	TXM	TXM	TXM	TXM	TXM	TXM
		-4.1278	-4.1278	0.0000	0.0000	0.0000	0.0000	0.0000	0.0000
3	51.3427	5.2654	-13.4492	0.0000	0.0000	0.0000	0.0000	0.0000	0.0000
4	49.2881	7.3753	-21.3473	0.0000	0.0000	0.0000	0.0000	0.0000	0.0000
CELL	CL = 0.	0.	0.	0.	0.	0.	0.	0.	0.
41	5	CL = 0.	0.	0.	0.	0.	0.	0.	0.
5	49.1610	7.8209	0.0000	0.0000	0.0000	0.0000	0.0000	0.0000	0.0000
CELL	CL = 0.	0.	0.	0.	0.	0.	0.	0.	0.
41	6	CL = 0.	0.	0.	0.	0.	0.	0.	0.
6	49.0407	8.3422	0.0000	0.0000	0.0000	0.0000	0.0000	0.0000	0.0000
CELL	CL = 0.	0.	0.	0.	0.	0.	0.	0.	0.
41	7	CL = 0.	0.	0.	0.	0.	0.	0.	0.
7	48.9580	9.0107	0.0000	0.0000	0.0000	0.0000	0.0000	0.0000	0.0000

(c)

Figure N-6 (Continued)

COLUMN K= 42, N= 500, TIME= .6995E-04, X= 53.5196, Y= 0.0000										
J	X	Y	TXM	TYM	TXM	TYM	P	E	D	YCNH, YDNH=
2	53.0268	3.0800	-5.0249	-5.0249	0.0000	0.0000	5.0249	21.2	.118720	386.643
3	52.2633	5.2172	-14.3544	-14.3544	0.0000	0.0000	14.3544	43.0	.166770	305.400
4	50.5182	7.2206	-17.2259	-17.2259	0.0000	0.0000	17.2259	50.6	.169553	225.609
CELL CL = P, CN = 0, 0.0000										
42	5	0.0000	0.0000	0.0000	0.0000	0.0000	CL-AVG = 4.088E-02	PI*NR**2= 139.	ROT=	-0. FU=0.0000
5	50.3886	7.6615	0.0000	0.0000	0.0000	0.0000	CN-TOT = 2.639E+04	FRAGMENT RAD.= 2.044E-02	NO.= 6.598E+03	
CELL CL = 0, CN = 0, 0.0000										
42	6	0.0000	0.0000	0.0000	0.0000	0.0000	CL-AVG = 2.240E-02	PI*NR**2= 250.	ROT=	-0. FU=0.0000
6	50.2712	8.1799	0.0000	0.0000	0.0000	0.0000	CN-TOT = 1.589E+05	FRAGMENT RAD.= 1.120E-02	NO.= 3.973E+04	
CELL CL = 0, CN = 0, 0.0000										
42	7	0.0000	0.0000	0.0000	0.0000	0.0000	CL-AVG = 2.767E-02	PI*NR**2= 201.	ROT=	-0. FU=0.0000
7	50.1752	8.8453	0.0000	0.0000	0.0000	0.0000	CN-TOT = 6.359E+04	FRAGMENT RAD.= 1.383E-02	NO.= 2.071E+04	
COLUMN K= 43, N= 500, TIME= .8995E-04, X= 54.1207, Y= 0.0000										
J	X	Y	TXM	TYM	TXM	TYM	P	E	D	YCNH, YDNH=
2	53.6740	3.0407	-6.2085	-6.2085	0.0000	0.0000	6.2085	24.0	.159412	342.629
3	52.9230	5.3203	-17.3129	-17.3129	0.0000	0.0000	17.3129	47.4	.162730	263.379
4	51.6287	7.2347	-13.7748	-13.7748	0.0000	0.0000	13.7748	42.3	.162819	182.565
CELL CL = 0, CN = 0, 0.0000										
43	5	0.0000	0.0000	0.0000	0.0000	0.0000	CL-AVG = 2.586E-02	PI*NR**2= 224.	ROT=	-0. FU=0.0000
5	51.5790	7.6566	0.0000	0.0000	0.0000	0.0000	CN-TOT = 1.066E+05	FRAGMENT RAD.= 1.293E-02	NO.= 2.664E+04	
CELL CL = 0, CN = 0, 0.0000										
43	6	0.0000	0.0000	0.0000	0.0000	0.0000	CL-AVG = 2.238E-02	PI*NR**2= 254.	ROT=	-0. FU=0.0000
6	51.4892	8.1715	0.0000	0.0000	0.0000	0.0000	CN-TOT = 1.617E+05	FRAGMENT RAD.= 1.119E-02	NO.= 4.041E+04	
CELL CL = 0, CN = 0, 0.0000										
43	7	0.0000	0.0000	0.0000	0.0000	0.0000	CL-AVG = 2.730E-02	PI*NR**2= 209.	ROT=	-0. FU=0.0000
7	51.3609	8.8456	0.0000	0.0000	0.0000	0.0000	CN-TOT = 6.946E+04	FRAGMENT RAD.= 1.365E-02	NO.= 2.237E+04	
COLUMN K= 44, N= 500, TIME= .6995E-04, X= 54.1115, Y= 0.0000										
J	X	Y	TXM	TYM	TXM	TYM	P	E	D	YCNH, YDNH=
2	54.2428	2.9220	-8.9945	-8.9945	0.0000	0.0000	8.9945	46.7	.158566	305.698
3	53.4697	5.4128	-21.6346	-21.6346	0.0000	0.0000	21.6346	87.6	.152225	233.283
4	52.5003	7.4164	-17.1236	-17.1236	0.0000	0.0000	17.1236	74.1	.135907	160.254
CELL CL = 0, CN = 0, 0.0000										
44	5	0.0000	0.0000	0.0000	0.0000	0.0000	CL-AVG = 2.520E-02	PI*NR**2= 223.	ROT=	-0. FU=0.0000
5	52.5664	7.7711	0.0000	0.0000	0.0000	0.0000	CN-TOT = 1.119E+05	FRAGMENT RAD.= 1.261E-02	NO.= 2.795E+04	
CELL CL = 0, CN = 0, 0.0000										
44	6	0.0000	0.0000	0.0000	0.0000	0.0000	CL-AVG = 2.223E-02	PI*NR**2= 256.	ROT=	-0. FU=0.0000
6	52.5593	8.2374	0.0000	0.0000	0.0000	0.0000	CN-TOT = 1.653E+05	FRAGMENT RAD.= 1.111E-02	NO.= 4.131E+04	
CELL CL = 0, CN = 0, 0.0000										
44	7	0.0000	0.0000	0.0000	0.0000	0.0000	CL-AVG = 2.519E-02	PI*NR**2= 228.	ROT=	-0. FU=0.0000
7	52.4655	8.5023	0.0000	0.0000	0.0000	0.0000	CN-TOT = 1.144E+05	FRAGMENT RAD.= 1.259E-02	NO.= 2.861E+04	

(c)

Figure N-6 (Continued)

COLUMN K= 45, N= 500, TIME= .89952E-04, X= 55.6645, Y= 0.0000									
J	XXH	YYH	ZZH	TXH	TYH	P	E	D	0.0000
2	55.1064	2.6852	-6.4727	-6.4727	-6.4727	8.4727	57.7	-0.86300	0.0000
3	54.2982	5.0554	-21.8270	-21.8270	-21.8270	21.8270	105.1	-1.22202	0.0000
4	53.7591	7.2573	-17.8718	-17.8718	-17.8718	17.8718	92.7	-1.13372	0.0000
CELL CL = 0.0, CN = 0.0, 0.0000, 0.0000, 0.0000, 0.0000, 0.0000, 0.0000, 0.0000, 0.0000									
45	5	53.8430	7.5300	0.0000	0.0000	0.0000	95.2	3.62476	0.0000
CELL CL = 0.0, CN = 0.0, 0.0000, 0.0000, 0.0000, 0.0000, 0.0000, 0.0000, 0.0000, 0.0000									
45	5	53.8437	8.0100	0.0000	0.0000	0.0000	30.0	3.12042	0.0000
CELL CL = 0.0, CN = 0.0, 0.0000, 0.0000, 0.0000, 0.0000, 0.0000, 0.0000, 0.0000, 0.0000									
45	7	53.9578	6.7170	0.0000	0.0000	0.0000	16.6	2.360573	0.0000
COLUMN K= 46, N= 500, TIME= .89952E-04, X= 57.5099, Y= 0.0000									
J	XXH	YYH	ZZH	TXH	TYH	P	E	D	0.0000
2	56.5360	1.9973	-6.3168	-6.3168	-6.3168	6.3168	42.6	-0.87321	0.0000
3	55.9534	3.6695	-15.9231	-15.9231	-15.9231	15.9231	76.6	-1.22248	0.0000
4	55.4687	5.3737	-18.5857	-18.5857	-18.5857	18.5857	83.6	-1.30778	0.0000
CELL CL = 0.0, CN = 0.0, 0.0000, 0.0000, 0.0000, 0.0000, 0.0000, 0.0000, 0.0000, 0.0000									
46	5	55.3103	6.1680	0.0000	0.0000	0.0000	74.4	2.009897	0.0000
CELL CL = 0.0, CN = 0.0, 0.0000, 0.0000, 0.0000, 0.0000, 0.0000, 0.0000, 0.0000, 0.0000									
46	6	55.3200	6.2741	0.0000	0.0000	0.0000	25.0	2.000121	0.0000
CELL CL = 0.0, CN = 0.0, 0.0000, 0.0000, 0.0000, 0.0000, 0.0000, 0.0000, 0.0000, 0.0000									
46	7	55.6630	7.5791	0.0000	0.0000	0.0000	16.6	1.618706	0.0000
COLUMN K= 47, N= 500, TIME= .69952E-04, X= 57.8092, Y= 0.0000									
J	XXH	YYH	ZZH	TXH	TYH	P	E	D	0.0000
2	57.5592	0.0000	-1000.9810	-1000.9810	-1000.9810	1000.9810	139.6	7.735833	0.0000
CELL CL = 0.0, CN = 0.0, 0.0000, 0.0000, 0.0000, 0.0000, 0.0000, 0.0000, 0.0000, 0.0000									
47	3	56.8074	2.0188	0.0000	0.0000	0.0000	103.4	3.129549	0.0000
CELL CL = 0.0, CN = 0.0, 0.0000, 0.0000, 0.0000, 0.0000, 0.0000, 0.0000, 0.0000, 0.0000									
47	4	56.4739	3.3578	0.0000	0.0000	0.0000	93.3	3.013529	0.0000
CELL CL = 0.0, CN = 0.0, 0.0000, 0.0000, 0.0000, 0.0000, 0.0000, 0.0000, 0.0000, 0.0000									
47	5	56.3592	4.4452	0.0000	0.0000	0.0000	53.1	2.833714	0.0000

(c)

Figure N-6 (Continued)

(c)

Figure N-6 (Continued)

COLUMN K= 50, N= 500, TIME= .6995E-04, X= 56.6984, Y= 0.0000

J	X	Y	TXM	TYM	TZM	TXM	TYM	TZM	P	E	O	XCNH	YCNIH	SPSO	XCNIH	YCNIH
CELL	CL = 0.	0.	2.906E-02	0.	0.	3.005E-02	CL-AVG = 2.599E-02	PI*FR**2= 151.	ROT=			0.	FU=0.0000		0.	FU=0.0000
50 3	CN = 0.	0.	1.150E+04	0.	0.0000	5.664E+04	CN-TOT = 6.813E+04	FRAGMENT RAD.= 1.494E-02				MO.= 1.703E+04		57.082	31.651	1
3 58.8533	.7526	0.0000	0.0000	0.0000	0.0000	0.0000	0.0000	9.9	4.064510	0.0000	0.0000	25.076				
CELL	CL = 0.	0.	2.062E-02	0.	0.	3.517E-02	CL-AVG = 3.273E-02	PI*FR**2= 171.	ROT=			0.	FU=0.0000		0.	FU=0.0000
50 4	CN = 0.	0.	1.283E+04	0.	0.0000	3.950E+04	CN-TOT = 5.231E+04	FRAGMENT RAD.= 1.635E-02				MO.= 1.306E+04		59.566	35.540	1
4 58.9109	1.4218	0.0000	0.0000	0.0000	0.0000	0.0000	0.0000	8.1	5.413189	0.0000	0.0000	15.434				
CELL	CL = 0.	0.	0.	0.	0.	3.521E-02	CL-AVG = 3.521E-02	PI*FR**2= 161.	ROT=			0.	FU=0.0000		0.	FU=0.0000
50 5	CN = 0.	0.	0.	0.	0.0000	4.126E+04	CN-TOT = 4.126E+04	FRAGMENT RAD.= 1.761E-02				MO.= 1.032E+04		65.590	32.452	1
5 58.9581	2.0490	0.0000	0.0000	0.0000	0.0000	0.0000	0.0000	6.8	6.117096	0.0000	0.0000	17.195				
CELL	CL = 0.	0.	0.	0.	0.	4.119E-02	CL-AVG = 4.019E-02	PI*FR**2= 140.	ROT=			0.	FU=0.0000		0.	FU=0.0000
50 6	CN = 0.	0.	0.	0.	0.0000	2.754E+04	CN-TOT = 2.754E+04	FRAGMENT RAD.= 2.009E-02				MO.= 6.885E+03		77.520	22.884	1
6 59.0349	2.6469	0.0000	0.0000	0.0000	0.0000	0.0000	0.0000	4.8	6.916200	0.0000	0.0000	15.217				
CELL	CL = 0.	0.	0.	0.	0.	6.394E-02	CL-AVG = 6.394E-02	PI*FR**2= 19.	ROT=			0.	FU=0.0000		0.	FU=0.0000
50 7	CN = 0.	0.	0.	0.	0.	1.482E+03	CN-TOT = 1.482E+03	FRAGMENT RAD.= 0.				MO.= 0.		124.355	23.636	1
7 59.1558	3.2566	-619.9597	-235.6460	448.0395	-4.3452	135.8508	16.1	7.570265	0.0000	0.0000	0.0000	13.167				
COLUMN K= 51, N= 500, TIME= .6995E-04, X= 59.3775, Y= 0.0000																
CELL	CL = 0.	0.	0.	0.	0.	3.486E-02	CL-AVG = 3.486E-02	PI*FR**2= 162.	ROT=			0.	FU=0.0000		0.	FU=0.0000
51 3	CN = 0.	0.	1.404E+04	0.	0.0000	2.835E+04	CN-TOT = 4.239E+04	FRAGMENT RAD.= 1.743E-02				MO.= 1.066E+04		80.886	0.680	1
3 60.1344	0.0000	0.0000	0.0000	0.0000	0.0000	0.0000	5.0	4.830195	0.0000	0.0000	21.770					
CELL	CL = 0.	0.	0.	0.	0.	3.873E-02	CL-AVG = 3.873E-02	PI*FR**2= 146.	ROT=			0.	FU=0.0000		0.	FU=0.0000
51 4	CN = 0.	0.	0.	0.	0.0000	3.105E+04	CN-TOT = 3.105E+04	FRAGMENT RAD.= 1.936E-02				MO.= 7.761E+03		79.644	-1.574	1
4 60.1372	.7609	0.0000	0.0000	0.0000	0.0000	0.0000	3.9	6.013472	0.0000	0.0000	17.453					
CELL	CL = 0.	0.	0.	0.	0.	4.170E-02	CL-AVG = 4.170E-02	PI*FR**2= 133.	ROT=			0.	FU=0.0000		0.	FU=0.0000
51 5	CN = 0.	0.	0.	0.	0.0000	2.442E+04	CN-TOT = 2.442E+04	FRAGMENT RAD.= 2.009E-02				MO.= 6.056E+03		78.845	-2.336	1
5 60.1451	1.5233	0.0000	0.0000	0.0000	0.0000	0.0000	2.4	6.578422	0.0000	0.0000	15.993					
CELL	CL = 0.	0.	0.	0.	0.	5.951E-02	CL-AVG = 5.951E-02	PI*FR**2= 54.	ROT=			0.	FU=0.0000		0.	FU=0.0000
51 6	CN = 0.	0.	0.	0.	0.	8.452E+03	CN-TOT = 8.452E+03	FRAGMENT RAD.= 2.575E-02				MO.= 2.113E+03		79.766	-1.524	1
6 60.1578	2.2784	0.0000	0.0000	0.0000	0.0000	0.0000	1.9	7.190507	0.0000	0.0000	14.633					
7 60.1643	3.0425	-457.7137	11.7833	697.6612	150.9804	-96.3527	4.4	7.765565	12.3758	34.216	34.216	83.286				
COLUMN K= 52, N= 500, TIME= .6995E-04, X= 61.4102, Y= 0.0000																
CELL	CL = 0.	0.	0.	0.	0.	3.763E-02	CL-AVG = 3.763E-02	PI*FR**2= 67.	ROT=			0.	FU=0.9197		0.	FU=0.9197
52 4	CN = 0.	0.	1.496E+04	0.	0.0000	14.4506	CN-TOT = 1.496E+04	FRAGMENT RAD.= 1.881E-02				MO.= 3.003E+02		75.971	.867	1
4 61.4102	.6775	305.0689	54.4295	21.7251	0.0000	-146.6442	.6	7.687139	19.5650	34.216	34.216	83.286				
CELL	CL = 0.	0.	0.	0.	0.	7.832E-02	CL-AVG = 7.832E-02	PI*FR**2= 23.	ROT=			0.	FU=1.0000		0.	FU=1.0000
52 5	CN = 0.	0.	0.	0.	0.	1.179E+03	CN-TOT = 1.179E+03	FRAGMENT RAD.= 0.				MO.= 0.		76.564	1.155	1
5 61.4118	1.3528	-21.0282	17.1344	75.7482	-6.5397	-37.7901	.5	7.714550	13.8362	34.216	34.216	83.286				
6 61.4163	2.0322	-7.3335	-35.3299	199.1150	62.9366	-55.0950	.6	7.770529	4.2738	31.216	31.216	78.516				
7 61.4213	2.7121	-403.3151	-106.6226	-306.4421	204.3837	258.0750	1.9	7.785315	14.1182	34.216	34.216	77.377				

(c)

Figure N-6 (Continued)

APPENDIX O

SUMMARY OF THE COMPUTATIONAL CRACK DISTRIBUTION RESULTS AND THE CALCULATED FRAGMENT MASS DISTRIBUTION RESULTS FOR THE ARMCO IRON AND HF-1 STEEL CYLINDER EXPERIMENTS AND THE HF-1 STEEL PROJECTILE EXPERIMENT

(Tables O-1, O-3, O-5, O-7, O-9, and O-11 summarize the crack distribution results for the PUFF and TROTT computations given in Appendix N. Tables O-2, O-4, O-6, O-8, O-10, and O-11 give the calculated fragment mass distribution results using the crack distribution results.)

Table O-1. Summary of brittle fracture crack distribution results for the Armco iron cylindrical PUFF computation.^a

Computational Cell No.	Initial Outer Radius of Cell (mm)	Initial Axial Area of Cell (mm ²)	Initial Volume of Cell ^b (cm ³)	Fraction of Cylinder Volume per Cell	Cracks Normal to Direction of 45° Between Radial and Circumferential Axes ^c				Cracks Normal to Direction of 45° Between Radial and Circumferential Axes ^c				Axial Cracks ^d	
					N ₀ (10 ⁶ /cm ³)	R ₁ (μm)	N ₀ (10 ⁶ /cm ³)	R ₁ (μm)	N ₀ (10 ⁶ /cm ³)	R ₁ (μm)	N ₀ (10 ⁶ /cm ³)	R ₁ (μm)	N ₀ (10 ⁶ /cm ³)	R ₁ (μm)
12	40.01	467.4	94.9	0.082	-	-	-	-	0.26	0.93	-	-	3.63	73.57
13	41.91	490.2	99.5	0.086	-	-	-	-	0.32	1.25	-	-	3.93	77.40
14	43.82	513.0	104.1	0.090	-	-	-	-	0.13	0.62	-	-	3.24	68.18
15	45.72	535.8	108.8	0.094	-	-	0.09	0.67	0.37	1.09	0.09	0.67	1.38	94.42
16	47.63	558.6	113.4	0.098	0.93	1.76	1.25	3.67	1.64	9.37	1.25	3.17	3.40	66.02
17	49.53	581.4	118.0	0.102	1.37	3.94	1.75	8.53	2.32	22.11	1.75	8.53	4.35	60.11
18	51.44	604.2	122.7	0.106	1.36	3.53	1.73	8.32	2.31	25.31	1.73	8.32	4.44	59.36
19	53.34	627.1	127.3	0.110	0.95	2.15	1.64	7.02	2.17	26.22	1.64	7.02	4.31	73.93
20	55.25	649.9	131.9	0.114	0.27	2.15	1.59	5.07	2.19	21.91	1.59	5.07	4.25	74.40
21	57.15	672.7	136.5	0.118	0.17	1.23	0.22	4.75	1.88	18.52	0.22	4.75	4.43	75.88

^a Figure N-1 gives the input parameters and output results for this computation. Cells 1 through 10 contain composition B explosive. Cells 12 through 21 contain Armco iron. The cell dimensions given in this table were calculated using the input parameters in Figure N-1(a) and the 203.0-mm cylinder length. The computed crack distribution values are for 600 time cycles. This corresponds to 73.4 μs after constant-volume explosive detonation. The five columns in Figure N-1(b) correspond (from left to right) to crack orientation bins 1 through 5. ^b If crack values are not listed then no cracks were nucleated for that orientation in that cell.

^b The total Armco iron cylinder volume is 1157.2 cm³.

^c N₀ and R₁ are the crack density and average crack radius, respectively. Average crack density (N₀) and average crack radius (R₁) values were calculated for each orientation with Equations (9) and (10), respectively, and the values in this table. The values were averaged over all ten cells. The average values are as follows: N₀ = 0.53 x 10⁶/cm³ and R₁ = 1.94 μm for the radial cracks, N₀ = 0.88 x 10⁶/cm³ and R₁ = 6.53 μm for each orientation of 45° cracks, N₀ = 1.45 x 10⁶/cm³ and R₁ = 19.96 μm for the circumferential cracks, and N₀ = 3.79 x 10⁶/cm³ and R₁ = 73.49 μm for the axial cracks. The total average crack area density (or R₁²N₀) for each orientation is 6.24 mm²/cm³ for the radial cracks, 118.1 mm²/cm³ for each orientation of 45° cracks, 1811.8 mm²/cm³ for the circumferential cracks, and 64232 mm²/cm³ for the axial cracks. Since the crack area for the radial cracks and each orientation of 45° cracks is only 0.37 and 6.52%, respectively, of the circumferential crack area, the radial cracks and 45° cracks were therefore not used in calculating the Armco iron fragment mass distribution. The total number of axial and circumferential cylinder cracks is 4.38 x 10⁹ and 1.68 x 10⁹, respectively. There are 2.6 axial cracks for each circumferential crack.

Table O-2. Calculated fragment mass distribution results for the Armco iron cylinder using the brittle fracture crack distribution results from Table O-1.^a

Number of Fragments ^b	Total Number of Axial Cracks ^b	Total Number of Circumferential Cracks ^b	Minimum Axial Crack Radius ^c (mm)	Number of Axial Cracks per Fracture Surface ^d	Area per Axial Fracture Surface ^e (mm ²)	Minimum Circumferential Crack Radius ^f (mm)	Number of Circumferential Cracks per Fracture Surface ^d	Area per Circumferential Fracture Surface ^g (mm ²)	Fragment Length ^h (mm)	Fragment Volume ⁱ (cm ³)	Fragment Mass ^j (g)
2	1.50×10^3	5.72×10^2	1.10	750	2851.0	0.28	286	70.4	3.70	10.54	82.76
20	1.50×10^4	5.72×10^3	0.93	750	2016.0	0.24	286	51.8	2.72	5.48	42.99
2×10^2	1.50×10^5	5.72×10^4	0.76	750	1361.0	0.20	286	35.9	1.89	2.57	20.16
2×10^3	1.50×10^6	5.72×10^5	0.58	750	792.6	0.15	286	20.2	1.06	0.84	6.60
2×10^4	1.50×10^7	5.72×10^6	0.43	750	425.6	0.11	286	10.9	0.57	0.24	1.90
2×10^5	1.50×10^8	5.72×10^7	0.25	750	147.3	0.06	286	3.23	0.17	0.03	0.20
											3.0

^a All fragments are assumed to be type 1. Each fragment contains the inner and outer cylindrical surfaces, two fracture surfaces with axial cracks perpendicular to the cylinder axis, and two fracture surfaces with circumferential cracks perpendicular to the cylinder circumference. All fragments are assumed to have the same number of cracks. Each fragment is assumed to have 2.6 axial cracks for each circumferential crack in agreement with the crack distribution results in Table O-1.

^b Two fragments can be formed from 1500 axial cracks and 572 circumferential cracks since the amount of fragment area is twice the amount of crack area.

^c Obtained for the total number of axial cracks using the axial crack distribution for the Armco iron cylinder in Figure 4.5.

^d Each fragment has 750 cracks per axial fracture surface and 286 cracks per circumferential fracture surface.

^e Equals 750 times the minimum axial crack area.

^f Obtained for the total number of circumferential cracks using the circumferential crack distribution for the Armco iron cylinder in Figure 4.5.

^g Equals 286 times the minimum circumferential crack area.

^h Parallel to the cylinder axis. Equals the area of the circumferential fracture surface divided by the 19.05-mm wall thickness value.

ⁱ Equals the fragment length times the axial fracture surface area.

^j Equals the fragment volume times the 7.85-Mg/in³ Armco iron density value.

Table O-3. Summary of brittle fracture crack distribution results for the HF-1 steel, heat treatment A, cylindrical PUFF computation.^a

Computational Cell No.	Initial Outer Radius of Cell (mm)	Initial Axial Area of Cell (mm ²)	Initial Volume of Cell ^b (cm ³)	Fraction of Cylinder Volume per Cell	Circumferential Cracks ^c		Axial Cracks ^c	
					N_0 (10 ⁴ /cm ³)	R_1 (μm)	N_0 (10 ⁴ /cm ³)	R_1 (μm)
12	40.33	548.2	111.3	0.080	1.31	72.41	32.54	143.1
13	42.55	579.3	117.6	0.084	0.64	83.53	21.91	185.0
14	44.78	610.4	123.9	0.089	2.20	93.05	39.97	154.0
15	47.00	641.5	130.2	0.093	0.53	84.67	11.60	227.8
16	49.23	672.6	136.5	0.098	1.10	81.18	23.61	182.8
17	51.45	703.7	142.9	0.102	1.44	74.05	6.35	253.2
18	53.68	734.8	149.2	0.107	1.67	84.80	13.70	220.9
19	55.90	765.9	155.5	0.111	1.51	87.80	13.07	225.0
20	58.13	797.0	161.8	0.116	1.69	85.56	14.86	187.7
21	60.35	828.1	168.1	0.120	2.47	125.7	11.87	244.3

^a Figure N-2 gives the input parameters and output results for this computation. Cells 1 through 10 contain composition B explosive. Cells 12 through 21 contain HF-1 steel with heat treatment A. The initial cell dimensions given in this table were calculated using the input parameters in Figure N-2(a) and the 203.0-mm cylinder length. The computed crack distribution values are for 500 time cycles. This corresponds to 74.7 μs after constant-volume explosive detonation. The five columns in Figure N-2(b) correspond (from left to right) to crack orientation bins 1 through 5. ^b Only circumferential and axial cracks were nucleated in this computation.

^b The total HF-1 steel cylinder volume is 1397.0 cm³. ^c N_0 and R_1 are the crack density and average crack radius, respectively. Average crack density (\bar{N}_0) and average crack radius (\bar{R}_1) values were calculated for each orientation with Equations (9) and (10), respectively, and the values in this table. The values were averaged over all ten cells. The average values are as follows: $\bar{N}_0 = 1.50 \times 10^4/\text{cm}^3$ and $\bar{R}_1 = 92.21 \mu\text{m}$ for the circumferential cracks, and $\bar{N}_0 = 18.09 \times 10^4/\text{cm}^3$ and $\bar{R}_1 = 188.7 \mu\text{m}$ for the axial cracks. The total average crack area density ($\pi \bar{R}_1^2 \bar{N}_0$) is 399.9 mm²/cm³ for the circumferential cracks and 20234 mm²/cm³ for the axial cracks. The total number of circumferential and axial cracks for the cylinder is 2.09×10^5 and 25.27×10^7 , respectively. There are 12.1 axial cracks for each circumferential crack.

Table O-4. Calculated fragment mass distribution results for the HF-1 steel cylinder with heat treatment A using the brittle fracture crack distribution results from Table O-3.^a

Number of Fragments ^b	Total Number of Axial Cracks ^b	Total Number of Circumferential Cracks ^b	Minimum Axial Crack Radius ^c (mm)	Number of Axial Cracks per Fracture Surface ^d	Area per Axial Fracture Surface ^e (mm ²)	Minimum Circumferential Crack Radius ^c (mm)	Number of Circumferential Cracks per Fracture Surface ^d	Area per Circumferential Fracture Surface ^e (mm ²)	Fragment Length ^h (mm)	Fragment Volume ⁱ (cm ³)	Fragment Mass ^j (g)	Fragment Mass ^j (gr)
2	1.92×10^2	16	2.66	96	2134.0	1.29	8	41.8	1.88	4.01	31.18	481.2
6	5.76×10^2	48	2.45	96	1810.0	1.18	8	35.0	1.57	2.85	22.13	341.6
10	9.60×10^2	80	2.35	96	1666.0	1.15	8	33.2	1.50	2.50	19.43	299.8
20	1.92×10^3	1.60×10^2	2.22	96	1486.0	1.08	8	29.3	1.32	1.96	15.22	234.9
1×10^2	9.60×10^3	8.0×10^2	1.91	96	1100.0	0.93	8	21.7	0.98	1.08	8.39	129.5
2×10^2	1.92×10^4	1.60×10^3	1.78	96	955.6	0.88	8	19.2	0.86	0.83	6.42	99.1
2×10^3	1.92×10^5	1.60×10^4	1.35	96	549.7	0.61	8	9.4	0.42	0.23	1.80	27.7
1×10^4	9.60×10^5	8.0×10^4	1.05	96	332.5	0.51	8	6.5	0.30	0.10	0.76	11.8
2×10^4	1.92×10^6	1.60×10^5	0.93	96	258.1	0.45	8	5.1	0.23	0.06	0.46	7.1
2×10^5	1.92×10^7	1.60×10^6	0.48	96	69.5	0.23	8	1.3	0.060	0.004	0.03	0.5

^a All fragments are assumed to be type 1. Each fragment contains the inner and outer cylindrical surfaces, two fracture surfaces with axial cracks perpendicular to the cylinder axis, and two fracture surfaces with circumferential cracks perpendicular to the cylinder circumference. All fragments are assumed to have the same number of cracks. Each fragment is assumed to have 12 axial cracks for each circumferential crack. In agreement with the crack distribution results in Table O-3.

^b Two fragments can be formed from 192 axial cracks and 16 circumferential cracks since the amount of fragment area is twice the amount of crack area.

^c Obtained for the total number of axial cracks using the axial crack distribution for the HF-1 steel cylinder with heat treatment A in Figure 45.

^d Each fragment has 96 cracks per axial fracture surface and 8 cracks per circumferential fracture surface.

^e Equals 96 times the minimum axial crack area.

^f Obtained for the total number of circumferential cracks using the circumferential crack distribution for the HF-1 steel cylinder with heat treatment A in Figure 45.

^g Equals 8 times the minimum circumferential crack area.

^h Parallel to the cylinder axis. Equals the area of the circumferential fracture surface divided by the 22.25-mm wall thickness value.

ⁱ Equals the fragment length times the axial fracture surface area.

^j Equals the fragment volume times the 7.77-Mg/m³ HF-1 steel density value.

Table O-5. Summary of brittle fracture crack distribution results for the HF-1 steel, heat treatment B, cylindrical PUFF computation.^a

Computational ^a Cell No.	Initial Outer Radius of Cell (mm)	Initial Axial Area of Cell ^b (mm ²)	Initial Volume of Cell ^b (cm ³)	Fraction of Cylinder Volume per Cell	Circumferential Cracks ^c		Axial Cracks ^c	
					\bar{N}_0 (10 ⁴ /cm ³)	\bar{R}_1 (μ m)	\bar{N}_0 (10 ⁴ /cm ³)	\bar{R}_1 (μ m)
12	40.17	543.6	110.0	0.080	1.01	92.13	10.10	212.1
13	42.38	574.4	116.2	0.084	0.69	106.6	7.94	247.5
14	44.60	605.2	121.5	0.089	1.61	118.3	14.79	207.2
15	46.81	636.1	128.7	0.093	0.62	105.5	4.36	314.9
16	49.03	666.9	134.9	0.098	0.60	104.7	8.71	251.7
17	51.24	697.7	141.2	0.102	0.96	97.90	2.96	334.1
18	53.46	728.5	147.4	0.107	0.86	109.0	5.19	299.3
19	55.67	759.4	153.7	0.111	0.86	116.6	5.39	307.9
20	57.89	790.2	159.9	0.116	0.91	115.1	5.84	217.9
21	60.10	821.0	166.1	0.120	1.08	164.5	5.51	315.4

^a Figure N-3 gives the input parameters and output results for this computation. Cells 1 through 10 contain composition B explosive. Cells 12 through 21 contain HF-1 steel with heat treatment B. The initial cell dimensions given in this table were calculated using the input parameters in Figure N-3(a) and the 202.4-mm cylinder length. The computed crack distribution values are for 500 time cycles. This corresponds to 74.9 μ s after constant-volume explosive detonation. The five columns in Figure N-3(b) correspond (from left to right) to crack orientation bins 1 through 5, O-1. Only circumferential and axial cracks were nucleated in this computation.

^b The total HF-1 steel cylinder volume is 1380.6 cm³.
^c \bar{N}_0 and \bar{R}_1 are the crack density and average crack radius, respectively. \bar{N}_0 values were calculated for each orientation with Equations (9) and (10), respectively, and the values in this table. The average values are as follows: $\bar{N}_0 = 0.92 \times 10^4/\text{cm}^3$ and $\bar{R}_1 = 116.5 \mu\text{m}$ for the circumferential cracks, and $\bar{N}_0 = 6.84 \times 10^4/\text{cm}^3$ and $\bar{R}_1 = 257.1 \mu\text{m}$ for the axial cracks. The total average crack area density ($\pi \bar{R}_1 \bar{N}_0$) is 391.7 nm²/cm³ for the circumferential cracks and 14207 nm²/cm³ for the axial cracks. The total number of circumferential and axial cracks is 1.27×10^7 , and 9.44×10^7 , respectively. There are 7.4 axial cracks for each circumferential crack.

Table O-6. Calculated fragment mass distribution results for the HF-1 steel cylinder with heat treatment B using the brittle fracture crack distribution results from Table O-5.^a

Number of Fragments ^b	Total Number of Axial Cracks ^b	Total Number of Circumferential Cracks ^b	Minimum Axial Crack Radius ^c (mm)	Number of Axial Cracks per Fracture Surface ^d	Area per Axial Fracture Surface ^e (mm ²)	Minimum Circumferential Crack Radius ^f (mm)	Number of Circumferential Cracks per Fracture Surface ^d	Area per Circumferential Fracture Surface ^g (mm ²)	Fragment Length ^h (mm)	Fragment Volume ⁱ (cm ³)	Fragment Mass ^j (g)	Fragment Mass ^j (gr)
2	76	10	3.61	38	1556.0	1.63	5	41.7	1.88	2.93	22.79	351.7
4	1.52×10^2	20	3.43	38	1404.0	1.55	5	37.7	1.70	2.39	18.60	287.1
10	3.8×10^2	50	3.19	38	1215.0	1.45	5	33.0	1.49	1.81	14.08	217.3
20	7.6×10^2	1×10^2	3.02	38	1089.0	1.36	5	29.1	1.31	1.43	11.10	171.3
2×10^2	7.6×10^3	1×10^3	2.42	38	699.1	1.10	5	19.0	0.86	0.60	4.66	72.0
2×10^3	7.6×10^4	1×10^4	1.83	38	397.6	0.83	5	10.7	0.48	0.19	1.49	23.0
6×10^3	2.28×10^5	3×10^4	1.55	38	286.8	0.70	5	7.7	0.35	0.10	0.77	12.0
2×10^4	7.6×10^5	1×10^5	1.23	38	180.6	0.56	5	4.9	0.22	0.04	0.31	4.8
4×10^4	1.52×10^6	2×10^5	0.98	38	114.7	0.48	5	3.6	0.16	0.02	0.15	2.2
2×10^5	7.6×10^6	1×10^6	0.64	38	48.9	0.30	5	1.4	0.06	0.003	0.02	0.4

^a All fragments are as assumed to be type 1. Each fragment contains the inner and outer cylindrical surfaces, two fracture surfaces with axial cracks perpendicular to the cylinder axis, and two fracture surfaces with circumferential cracks perpendicular to the cylinder circumference. All fragments are assumed to have the same number of cracks. Each fragment is assumed to have 7.4 axial cracks for each circumferential crack in agreement with the crack distribution results in Table O-5.

^b Two fragments can be formed from 76 axial cracks and 10 circumferential cracks since the amount of fragment area is twice the amount of crack area.

^c Obtained for the total number of axial cracks using the axial crack distribution for the HF-1 steel cylinder with heat treatment B in Figure 45.

^d Each fragment has 38 cracks per axial fracture surface and 5 cracks per circumferential fracture surface.

^e Equals 38 times the minimum axial crack area.

^f Obtained for the total number of circumferential cracks using the circumferential crack distribution for the HF-1 steel cylinder with heat treatment A in Figure 45.

^g Equals 5 times the minimum circumferential crack area.

^h Parallel to the cylinder axis. Equals the area of the circumferential fracture surface divided by the 22.15-mm wall thickness value.

ⁱ Equals the fragment length times the axial fracture surface area.

^j Equals the fragment volume times the 7.77-Mg/m³ HF-1 steel density value.

Table O-7. Summary of brittle and shear fracture crack distribution results for the HF-1 steel, heat treatment A, cylindrical PUFF computation.^a

Computational Cell No.	Initial Outer Radius of Cell (mm)	Initial Axial Area of Cell (mm ²)	Initial Volume of Cell ^b (cm ³)	Fraction of Cylinder Volume per Cell	Shear Cracks on 45° Planes Between Radial and Circumferential Axes ^c				Brittle Circumferential Cracks ^c		Brittle Axial Cracks ^c	
					N ₀ (10 ² /cm ³)	R ₁ (μm)	N ₀ (10 ⁴ /cm ³)	R ₁ (μm)	N ₀ (10 ⁴ /cm ³)	R ₁ (μm)	N ₀ (10 ⁴ /cm ³)	R ₁ (μm)
12	40.33	548.2	111.3	0.080	2.72	973	-	-	-	-	-	-
13	42.55	579.3	117.6	0.084	2.19	1060	-	-	-	-	-	-
14	44.78	610.4	123.9	0.089	1.74	1150	-	-	-	-	-	-
15	47.00	641.5	130.2	0.093	1.33	1230	-	-	-	-	-	-
16	49.23	672.6	136.5	0.098	1.05	1320	-	-	-	-	-	-
17	51.45	703.7	142.9	0.102	0.87	1390	-	-	-	-	-	-
18	53.68	734.8	149.2	0.107	-	-	0.13	85.68	2.77	338.2	-	-
19	55.90	765.9	155.5	0.111	-	-	0.60	83.86	6.26	269.7	-	-
20	58.13	797.0	161.8	0.116	-	-	0.68	92.55	9.46	236.2	-	-
21	60.35	828.1	168.1	0.120	-	-	2.59	115.3	11.66	223.2	-	-

^a Figure N-4 gives the input parameters and output results for this computation. The input parameters for the SHEAR2 subroutine were obtained from Reference 1. Cells 1 through 10 contain composition B explosive. Cells 12 through 21 contain HF-1 steel with heat treatment A. The cell dimensions in this table were calculated using the input parameters in Figure N-4 (a) and the 203.0-mm cylinder length. The computed crack distribution values are for 500 time cycles. This corresponds to 75.3 μs after constant-volume explosive detonation. Shear fracture cracks were activated in cells 12 through 17. Figure N-4(b) indicates that shear bands with three orientations were activated in each shear cell. The orientations are 45° between the radial and circumferential directions (NG = 4), 45° between the radial and axial directions (NG = 5), and 45° between the circumferential and axial directions (NG = 6). Only the NG=4 area for the NG = 5 and 6 orientations is no more than 2 and 25%, respectively, of the area for the NG = 4 orientation (as indicated by the TAUIZ values in Figure N-4(b)). Only the NG=4 orientation shear bands were used to form fragments. Eight shear band size groups are listed for each orientation in Figure N-4(b). Each size group gives a shear band radius and the number of shear bands per cubic centimeter with a radius larger than that value. The N₀ (crack density) and R₁ (average crack radius) values given in this table for cells 12 through 17 were determined from straight-line fits to semi-logarithmic plots of the size group values for the NG = 4 orientation. Brittle fracture cracks were activated in cells 18 through 21. The five columns in Figure N-4(b) correspond (from left to right) to crack orientation bins 1 through 5. Only circumferential and axial cracks were activated. The computed N₀ and R₁ values from Figure N-4(b) are given in this table.

^b The total HF-1 steel cylinder volume is 1397.0 cm³. The volume of cells 12 through 17 is 762.4 cm³; the volume of cells 18 through 21 is 634.6 cm³. Average crack density (N₀) and average crack radius (R₁) values were calculated for each orientation with Equations (9) and (10), respectively, and the values in this table. The values for the shear cracks were averaged over cells 12 through 17; the values for the brittle cracks were averaged over cells 18 through 21. The values are as follows: N₀ = 1.60 x 10²/cm³ and R₁ = 1140 μm for the shear cracks, N₀ = 1.04 x 10⁴/cm³ and R₁ = 106.2 μm for the brittle circumferential cracks, and N₀ = 7.68 x 10⁴/cm³ and R₁ = 246.3 μm for the brittle axial cracks. The total average crack area density (πR₁²N₀) is 653.8 mm²/cm³ for the shear cracks, 365.7 mm²/cm³ for the brittle circumferential cracks, and 14642 mm²/cm³ for the brittle axial cracks. The total number of shear cracks for the cylinder (cells 12 through 17) is 1.22 x 10⁵. The total number of brittle circumferential cracks for the cylinder (cells 18 through 21) is 6.57 x 10⁶. The total number of brittle axial cracks for the cylinder (in order to form fragments it is assumed that axial cracks with the axial crack density are activated in cells 12 through 17 in addition to cells 18 through 21) is 1.07 x 10⁸. There are 16.3 axial cracks for each circumferential crack and 877 axial cracks for each shear crack.

Table O-9. Summary of brittle and shear fracture crack distribution results for the HF-1 steel, heat treatment B, cylindrical PUFF computation.^a

Computational Cell No.	Initial Outer Radius of Cell (mm)	Initial Axial Area of Cell (mm ²)	Initial Volume of Cell ^b (cm ³)	Fraction of Cylinder Volume per Cell	Shear Cracks on 45° Planes Between Radial and Circumferential Axes ^c				Brittle Circumferential Cracks ^c		Brittle Axial Cracks ^c	
					N ₀ (10 ² /cm ³)	R ₁ (μm)	N ₀ (10 ⁴ /cm ³)	R ₁ (μm)	N ₀ (10 ⁴ /cm ³)	R ₁ (μm)	N ₀ (10 ⁴ /cm ³)	R ₁ (μm)
12	40.17	543.6	110.0	0.080	2.73	973	-	-	-	-	-	-
13	42.38	574.4	116.2	0.084	2.15	1060	-	-	-	-	-	-
14	44.60	605.2	121.5	0.089	1.79	1150	-	-	-	-	-	-
15	46.81	636.1	128.7	0.093	1.39	1230	-	-	-	-	-	-
16	49.03	666.9	134.9	0.098	1.07	1320	-	-	-	-	-	-
17	51.24	697.7	141.2	0.102	0.87	1390	-	-	-	-	-	-
18	53.46	728.5	147.4	0.107	-	-	0.15	109.0	1.01	478.3	-	-
19	55.67	759.4	153.7	0.111	-	-	0.31	112.3	2.83	351.8	-	-
20	57.89	790.2	159.9	0.116	-	-	0.65	124.9	3.96	321.0	-	-
21	60.10	821.0	166.1	0.120	-	-	1.15	150.4	4.74	298.5	-	-

^a Figure N-5 gives the input parameters and output results for this computation. The input parameters for the SHEAR2 subroutine were obtained from References 1. Cells 1 through 10 contain composition B explosive. Cells 12 through 21 contain HF-1 steel with heat treatment B. The cell dimensions in this table were calculated using the input parameter in Figure N-5 (a) and the 202.4-mm cylinder length. The computed crack distribution values are for 500 time cycles. This corresponds to 74.9 μs after constant-volume explosive detonation. Shear fracture cracks were activated in cells 12 through 17. Figure N-5(b) indicates that shear bands with three orientations were activated in each shear cell. The orientations are 45° between the radial and circumferential directions (NG = 4), 45° between the radial and axial directions (NG = 5), and 45° between the circumferential and axial directions (NG = 6). Since the shear band area for the NG = 5 and 6 orientations is no more than 2 and 25%, respectively, of the area for the NG = 4 orientation (as indicated by the TAUZ values in Figure N-5(b)), only the NG=4 orientation shear bands were used to form fragments. Eight shear band size groups are listed for each orientation in Figure N-5(b). Each size group gives a shear band radius and the number of shear bands per cubic centimeter with a radius larger than that value. The N₀ (crack density) and R₁ (average crack radius) values given in this table for cells 12 through 17 were determined from straight - line fits to semi-logarithmic plots of the size group values for the NG = 4 orientation. Brittle fracture cracks were activated in cells 18 through 21. The five columns in Figure N-5(b) correspond (from left to right) to crack orientation bins 1 through 5. Only circumferential and axial cracks were activated. The computed N₀ and R₁ values from Figure N-5(b) are given in this table.

^b The total HF-1 steel cylinder volume is 1380.6 cm³. The volume of cells 12 through 17 is 753.5 cm³; the volume of cells 18 through 21 is 627.1 cm³.
^c Average crack density (\bar{N}_0) and average crack radius (\bar{R}_1) values were calculated for each orientation with Equations (9) and (10), respectively, and the values in this table. The values for the shear cracks were averaged over cells 12 through 17; the values for the brittle cracks were averaged over cells 18 through 21. The values are as follows: $\bar{N}_0 = 1.61 \times 10^2/\text{cm}^3$ and $\bar{R}_1 = 1160 \mu\text{m}$ for the shear cracks, $\bar{N}_0 = 0.58 \times 10^4/\text{cm}^3$ and $\bar{R}_1 = 135.7 \mu\text{m}$ for the brittle circumferential cracks, and $\bar{N}_0 = 3.20 \times 10^4/\text{cm}^3$ and $\bar{R}_1 = 330.5 \mu\text{m}$ for the brittle axial cracks. The total average crack area density ($\pi \bar{R}_1^2 \bar{N}_0$) is 671.1 mm²/cm³ for the shear cracks, 336.7 mm²/cm³ for the brittle circumferential cracks, and 10972 mm²/cm³ for the brittle axial cracks. The total number of shear cracks for the cylinder (cells 12 through 17) is 1.21×10^5 . The total number of brittle circumferential cracks for the cylinder (cells 18 through 21) is 3.65×10^6 . The total number of brittle axial cracks for the cylinder (in order to form fragments it is assumed that axial cracks with the axial crack density are activated in cells 12 through 17 in addition to cells 18 through 21) is 4.41×10^7 . There are 12.1 axial cracks for each circumferential crack and 364 axial cracks for each shear crack.

Table O-10. Calculated fragment mass distribution results for the HF-1 steel cylinder with heat treatment B using the brittle and shear fracture crack distribution results from Table O-9.^a

Number of Axial Fragments ^b	Number of Brittle Axial Cracks ^b	Total Number of Brittle Axial Cracks ^b	Total Number of Brittle Axial Cracks ^b	Minimum Axial Crack Radius ^c	Number of Axial Fracture Surfaces ^d	Area per Axial Fracture Surface ^e	Minimum Circumferential Crack Radius ^f	Number of Circumferential Fracture Surfaces ^d	Area per Circumferential Fracture Surface ^g	Fragment Length in Circumferential Fracture Region (Cells 18 through 21) ^h	Minimum Shear Crack Radius ⁱ	Number of Shear Fracture Surfaces ^d	Area per Shear Fracture Surface ^j	Fragment Length in Shear Fracture Region (Cells 12 through 17) ^k	Fragment Volume ^l	Fragment Mass ^m
2	42	3.47	0.116	4.58	21	1384.0	1.85	1.74	18.7	2.11	16.05	0.038	46.8	2.49	3.18	24.72
20	4.2 x 10 ²	34.7	1.16	3.82	21	962.7	1.56	1.74	13.2	1.50	13.40	0.038	32.6	1.73	1.56	12.10
2 x 10 ²	4.2 x 10 ³	3.47 x 10 ²	11.6	3.07	21	621.8	1.25	1.74	8.9	0.96	10.68	0.038	20.7	1.10	0.64	4.99
2 x 10 ³	4.2 x 10 ⁴	3.47 x 10 ³	1.16 x 10 ²	2.28	21	343.0	0.94	1.74	4.8	0.54	8.05	0.038	11.8	0.63	0.20	1.56
2 x 10 ⁴	4.2 x 10 ⁵	3.47 x 10 ⁴	1.16 x 10 ³	1.52	21	152.4	0.63	1.74	2.1	0.24	5.50	0.038	5.5	0.29	0.04	0.32
2 x 10 ⁵	4.2 x 10 ⁶	3.47 x 10 ⁵	1.16 x 10 ⁴	0.77	21	39.1	0.32	1.74	0.6	0.06	2.68	0.038	1.3	0.07	0.003	0.02

^a All fragments are assumed to be type 1. Each fragment contains the inner and outer cylindrical surfaces, two fracture surfaces with brittle axial cracks perpendicular to the cylinder axis, two fracture surfaces with brittle circumferential cracks perpendicular to the cylinder circumference, and two fracture surfaces with shear cracks on planes 45° between the radial and circumferential axes. All fragments are assumed to have the same number of cracks. There are 12.1 axial cracks for each circumferential crack and 364 axial cracks for each shear crack in agreement with the crack distribution results in Table O-9.

^b Two fragments can be formed from 42 brittle axial cracks, 3.47 brittle circumferential cracks, and 0.116 shear cracks since the amount of fragment area is twice the amount of crack area.

^c Obtained for the total number of axial cracks using the axial crack distribution for the HF-1 steel cylinder with heat treatment B in Figure 46.

^d Each fragment has 21 cracks per axial fracture surface, 1.82 cracks per circumferential fracture surface, and 0.038 cracks per shear fracture surface.

^e Equals 21 times the minimum axial crack area.

^f Obtained for the total number of circumferential cracks using the circumferential crack distribution for the HF-1 steel cylinder with heat treatment B in Figure 46.

^g Equals 1.82 times the minimum circumferential crack area.

^h Parallel to the cylinder axis. Equals the area of the circumferential fracture surface divided by the 8.86-mm wall thickness for cells 18 through 21.

ⁱ Obtained for the total number of shear cracks using the shear crack distribution for the HF-1 steel cylinder with heat treatment B in Figure 46.

^j Equals 0.038 times the minimum shear crack area.

^k Parallel to the cylinder axis. Equals the projection of the shear fracture area in the radial direction (cos 45° times the area of the shear fracture surface) divided by the 13.29-mm wall thickness for cells 12 through 17.

^l Equals the average of the fragment lengths for the circumferential and shear regions times the axial fracture surface area.

^m Equals the fragment volume times the 7.77-Mg/m³ HF-1 steel density value.

Table O-11. Calculated fragment mass distribution results for the HF-1 steel projectile with heat treatment A using the brittle fracture crack distribution results from the TROTT computation.^{a, b}

Number of Fragments ^c	Total Number of Axial Cracks ^c	Total Number of		Minimum Axial ^e	Number of		Area per		Minimum Circumferential Crack Radius ^d (mm)	Cracks per Axial Fracture Surface ^e		Area per Axial Fracture Surface ^f (mm ²)		Minimum Circumferential Crack Radius ^g (mm)		Cracks per Circumferential Fracture Surface ^e		Area per Circumferential Fracture Surface ^h (mm ²)		Fragment Length ⁱ (mm)		Fragment Volume ^j (cm ³)		Fragment Mass ^k (g)	
		Total	Number of Circumferential Cracks ^c		Minimum Axial	Cracks per Axial	Fracture Surface ^e	Area per Axial Fracture Surface ^f		Cracks per Circumferential	Fracture Surface ^e	Area per Circumferential Fracture Surface ^h	Cracks per Axial Fracture Surface ^e	Area per Axial Fracture Surface ^f	Cracks per Circumferential	Fracture Surface ^e	Area per Circumferential Fracture Surface ^h	Fragment Length ⁱ	Fragment Volume ^j	Fragment Mass ^k					
2	18	18	4.23	9	505.9	4.23	9	505.9	4.23	9	505.9	20.95	10.60	82.41	1278.0										
10	90	90	3.80	9	408.3	3.80	9	408.3	3.80	9	408.3	16.91	6.90	53.67	828.3										
20	1.8 × 10 ²	1.8 × 10 ²	3.62	9	370.5	3.62	9	370.5	3.62	9	370.5	15.35	5.69	44.20	682.1										
50	4.5 × 10 ²	4.5 × 10 ²	3.37	9	321.1	3.37	9	321.1	3.37	9	321.1	13.30	4.27	33.20	512.3										
2 × 10 ²	1.8 × 10 ³	1.8 × 10 ³	3.00	9	254.5	3.00	9	254.5	3.00	9	254.5	10.54	2.63	20.85	321.8										
8 × 10 ²	7.2 × 10 ³	7.2 × 10 ³	2.62	9	194.1	2.62	9	194.1	2.62	9	194.1	8.04	1.56	12.13	187.2										
2 × 10 ³	1.8 × 10 ⁴	1.8 × 10 ⁴	2.37	9	158.8	2.37	9	158.8	2.37	9	158.8	6.58	1.04	8.12	125.3										
2 × 10 ⁴	1.8 × 10 ⁵	1.8 × 10 ⁵	1.74	9	85.6	1.74	9	85.6	1.74	9	85.6	3.55	0.30	2.36	36.4										
2 × 10 ⁵	1.8 × 10 ⁶	1.8 × 10 ⁶	1.14	9	36.7	1.14	9	36.7	1.14	9	36.7	1.52	0.006	0.43	6.7										

^a Figure N-6 gives the input parameters and output results for this computation. For TROTT computations with cylindrical symmetry the x, y, and z axes are in the axial, radial, and circumferential directions, respectively. (For cylindrical PUFF computations the x, y, and z axes are in the radial, circumferential, and axial directions, respectively.) The initial cell and coordinate layout for this computation is given by the K, J, x, and y values. This computation has 323 cells: 197 cells contain HF-1 steel, 117 cells contain PBXN-106 explosive, and 9 cells contain CH6 explosive. Figure N-6(b) is an output listing of some variables and array quantities for each cell and each coordinate for this computation. The Z column, which equals (1.5/π) times the cell mass, is used for calculating average crack density (\bar{N}_0) and average crack radius (\bar{R}_1) values for this computation. Figure N-6(c) is an output listing at 500 times cycles. This corresponds to 90.0 μs after explosive detonation. The computed CL and CN crack distribution values for each cell are given as five columns in Figure N-6(c) that correspond to orientation bins 1 through 5. ⁰⁻¹ For this computation circumferential cracks (bin 5) were activated in 159 of the 197 cells with HF-1 steel. Cracks with other orientations were activated in a few cells at the ends of the projectile. Only circumferential cracks were used for computing the fragment mass distribution. An average crack density value $\bar{N}_0 = 3.75 \times 10^4/\text{cm}^3$ and an average crack radius value $\bar{R}_1 = 268.6 \mu\text{m}$ were calculated using the circumferential crack distribution values for the HF-1 steel cells from K = 2 through 52 (174 cells) in Figure N-6(c) and the Z values in Figure N-6(b). The total average crack density (\bar{N}_0) is $8500 \text{ mm}^{-2}/\text{cm}^3$. The 23 cells from K = 53 through 58 were not used for calculating average crack distribution values. This computational region, which corresponds to the fuse section of the projectile, is 76.2 mm long and has an HF-1 steel mass of 0.634 kg. No cracks were activated in these cells. The total number of circumferential cracks is 1.22×10^8 . This value was calculated using the measured HF-1 steel mass of 25.2 kg. The computational HF-1 steel mass between K = 2 and 52 is 28.0 kg.

^b Since for the computation only circumferential cracks were activated, an axial crack distribution equivalent to the circumferential crack distribution is assumed in order to form fragments. All fragments are assumed to be type 1. Each fragment contains the projectile inner and outer surfaces, two fracture surfaces with axial cracks perpendicular to the projectile axis, and two fracture surfaces w_1 , circumferential cracks perpendicular to the projectile circumference. All fragments are assumed to have the same number of cracks. Each fragment is assumed to have the same number of axial and circumferential cracks.

^c Two fragments can be formed from 18 axial cracks and 18 circumferential cracks since the amount of fragment area is twice the amount of crack area.

^d Obtained for the total number of axial cracks using the circumferential crack distribution for the HF-1 steel projectile with heat treatment A in Figure 45.

^e Each fragment has 9 cracks per axial fracture surface and 9 cracks per circumferential fracture surface.

^f Equals 9 times the minimum axial crack area.

^g Obtained for the total number of circumferential cracks using the circumferential crack distribution for the HF-1 steel projectile with heat treatment A in Figure 45.

^h Equals 9 times the minimum circumferential crack area.

ⁱ Parallel to the projectile axis. Equals the area of the circumferential fracture surface divided by the 24.14-mm average wall thickness value. The average wall thickness value was obtained by dividing the 14718 mm² xy area of the HF-1 steel cells between K = 2 and 52 (174 cells) by the 609.6-mm axial length of these cells.

^j Equals the fragment length times the axial fracture surface area.

^k Equals the fragment volume times the 7.77-Mg/m³ HF-1 steel density value.

REFERENCE

- O-1. L. Seaman and D. A. Shockey, *Models for Ductile and Brittle Fracture for Two-Dimensional Propagation Calculations*, Contract DAAG46-72-C-0182, Army Materials and Mechanics Research Center, Watertown, MA (February 1975).
- O-2. D. C. Erlich, L. Seaman, D. A. Shockey, and D. R. Curran, *Development and Application of a Computational Shear Band Model*, Contract DAAD05-76-C-0762, Army Ballistic Research Laboratory, Aberdeen Proving Ground, MD (May 1977).

APPENDIX P

COMPUTED STRESS, PARTICLE VELOCITY, AND CRACK CONCENTRATION VERSUS TIME PLOTS FOR EACH COMPUTATIONAL CELL FOR THE HF-1 STEEL, HEAT TREATMENT B, CYLINDER EXPERIMENTS

(These plots were produced using cylindrical PUFF computations with the BFRACT 2 subroutine and the input parameters from Figure N-3(a) (with the appropriate JEDIT parameters). The JEDIT parameters S1, S2, S3, U, COM9, and COM11 used for these plots correspond to the radial stress, circumferential stress, axial stress, radial particle velocity, circumferential crack concentration, and axial crack concentration, respectively. Cells 1 through 10 contain composition B explosive. Cells 12 through 21 contain HF-1 steel with heat treatment B. Plots (a), (b), and (c) of Figures P-1 through P-20 are the principal stresses in the radial, circumferential, and axial directions, respectively. Compressive and tensile stress values are positive and negative, respectively. The stresses are computed at the cell midpoints. Figures P-21 through P-30 give the radial particle velocity in the cells. A particle velocity refers to the cell edge. Plots (a) and (b) of Figures 31 through 40 give the circumferential and axial crack concentrations, respectively, for the fractured HF-1 steel cells. Crack concentrations are computed at the cell midpoints).

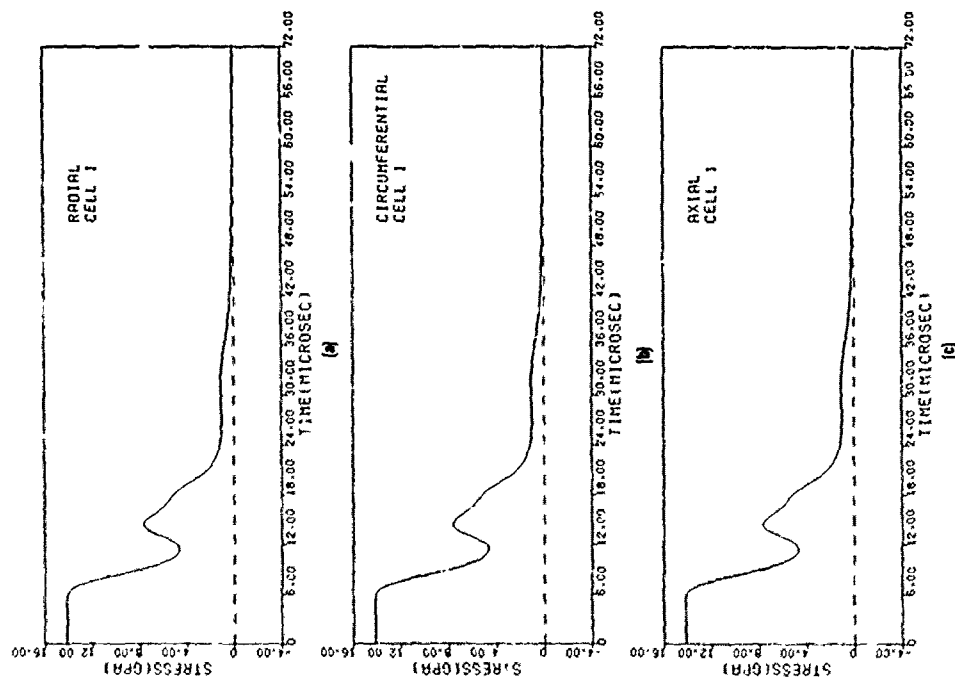


Figure P-1. Computed stress histories in cell 1 for the HF-1 steel, heat treatment B, cylinder experiments. (a) Radial, (b) circumferential, and (c) axial stresses.

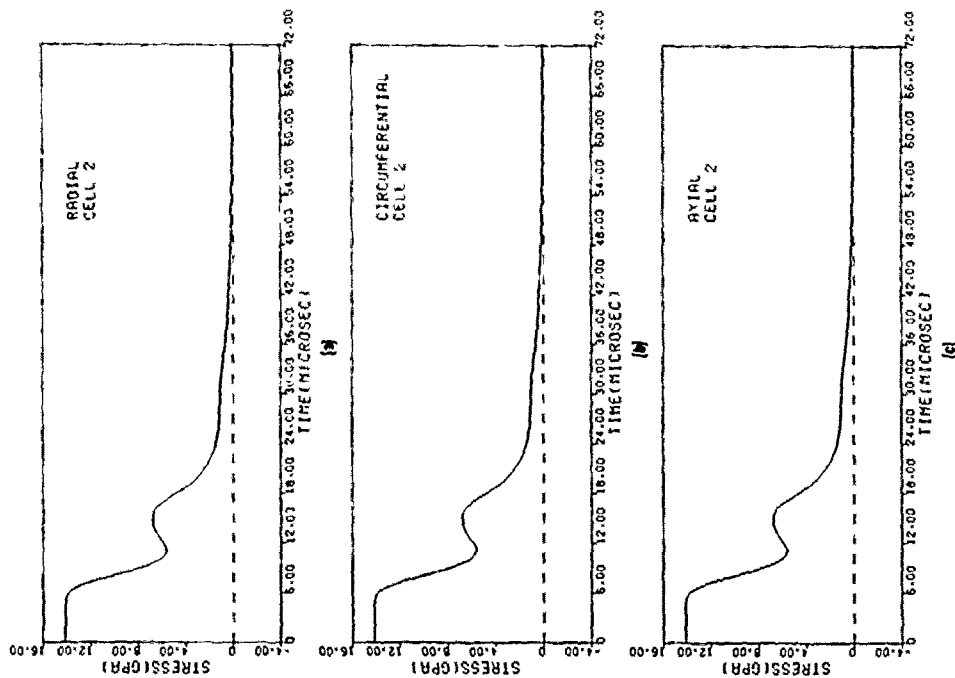


Figure P-2. Computed stress histories in cell 2 for the HF-1 steel, heat treatment B, cylinder experiments. (a) Radial, (b) circumferential, and (c) axial stresses.

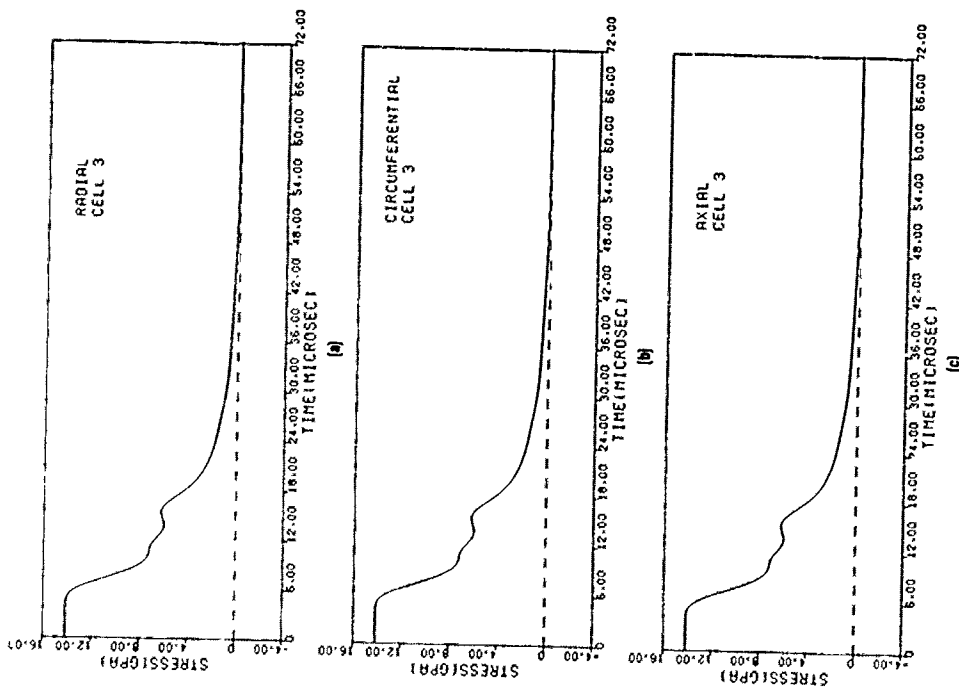


Figure P-3. Computed stress histories in cell 3 for the HF-1 steel, heat treatment B, cylinder experiments. (a) Radial, (b) circumferential, and (c) axial stresses.

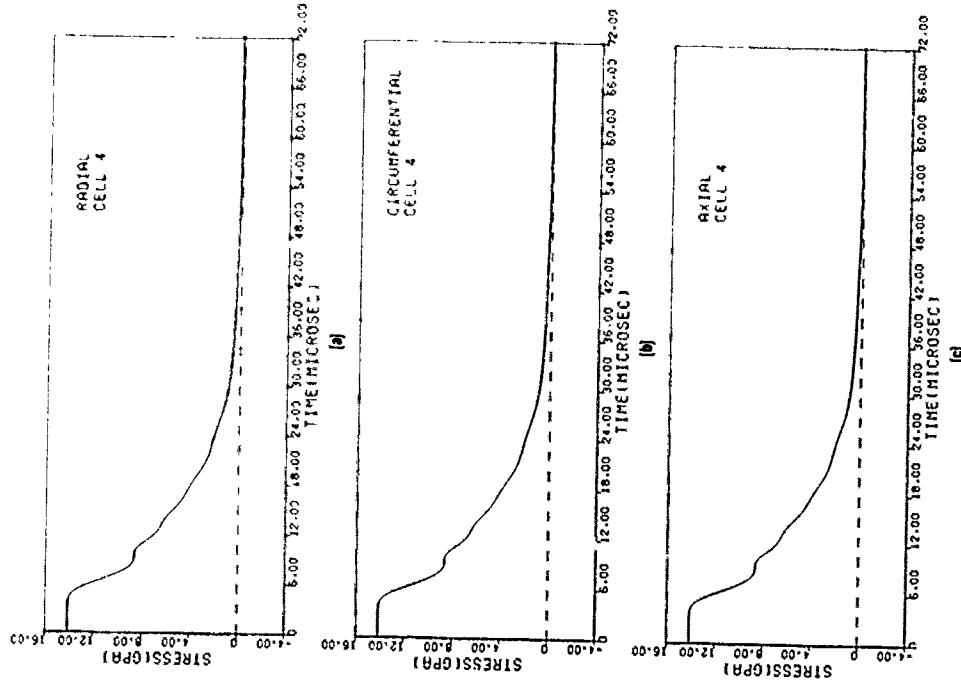


Figure P-4. Computed stress histories in cell 4 for the HF-1 steel, heat treatment B, cylinder experiments. (a) Radial, (b) circumferential, and (c) axial stresses.

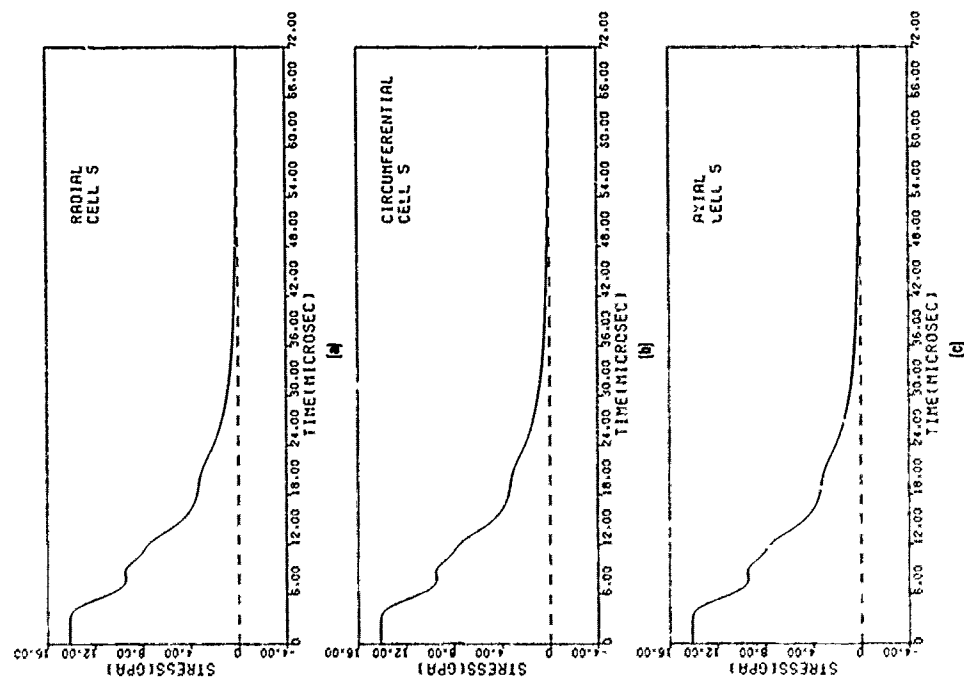


Figure P-5. Computed stress histories in cell 5 for the HF-1 steel, heat treatment B, cylinder experiments.
(a) Radial, (b) circumferential, and (c) axial stresses.

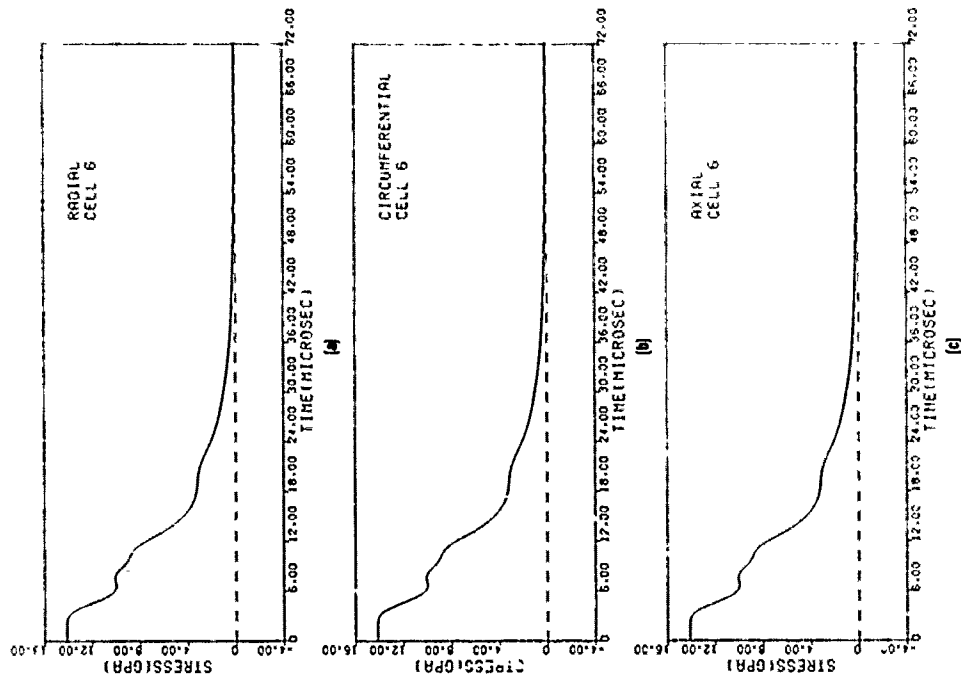


Figure P-6. Computed stress histories in cell 6 for the HF-1 steel, heat treatment B, cylinder experiments.
(a) Radial, (b) circumferential, and (c) axial stresses.

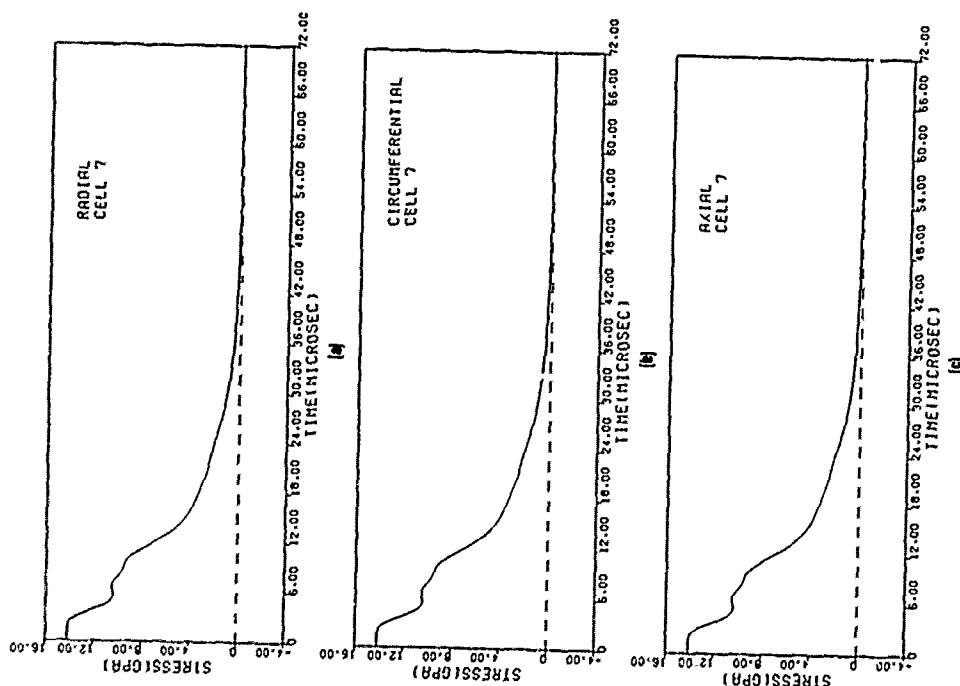


Figure P-7. Computed stress histories in cell 7 for the HF-1 steel, heat treatment B, cylinder experiments.
(a) Radial, (b) circumferential, and (c) axial stresses.

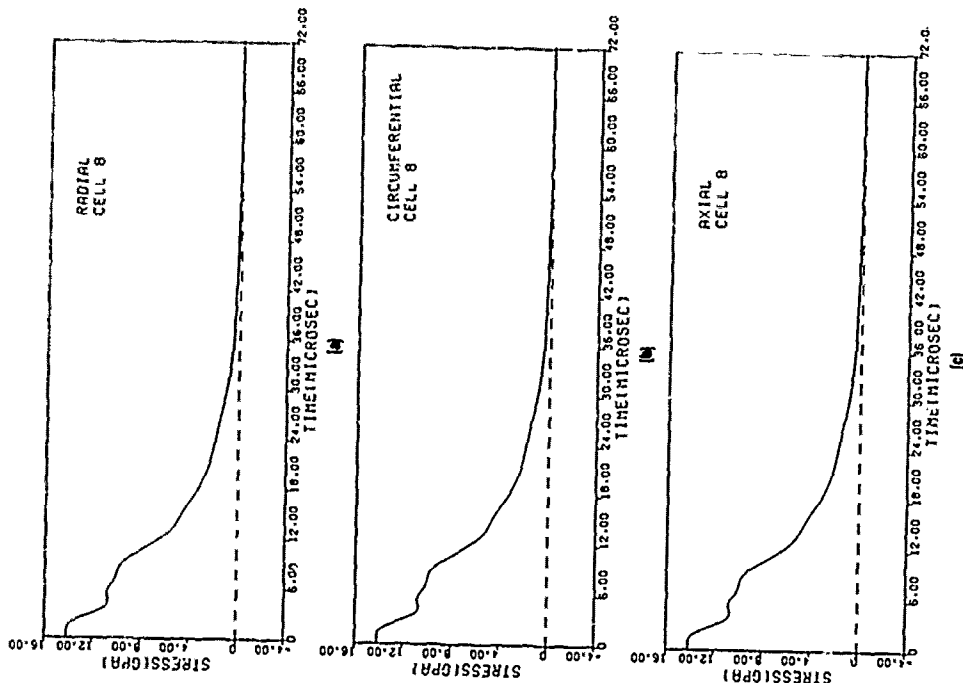


Figure P-8. Computed stress histories in cell 8 for the HF-1 steel, heat treatment B, cylinder experiments.
(a) Radial, (b) circumferential, and (c) axial stresses.

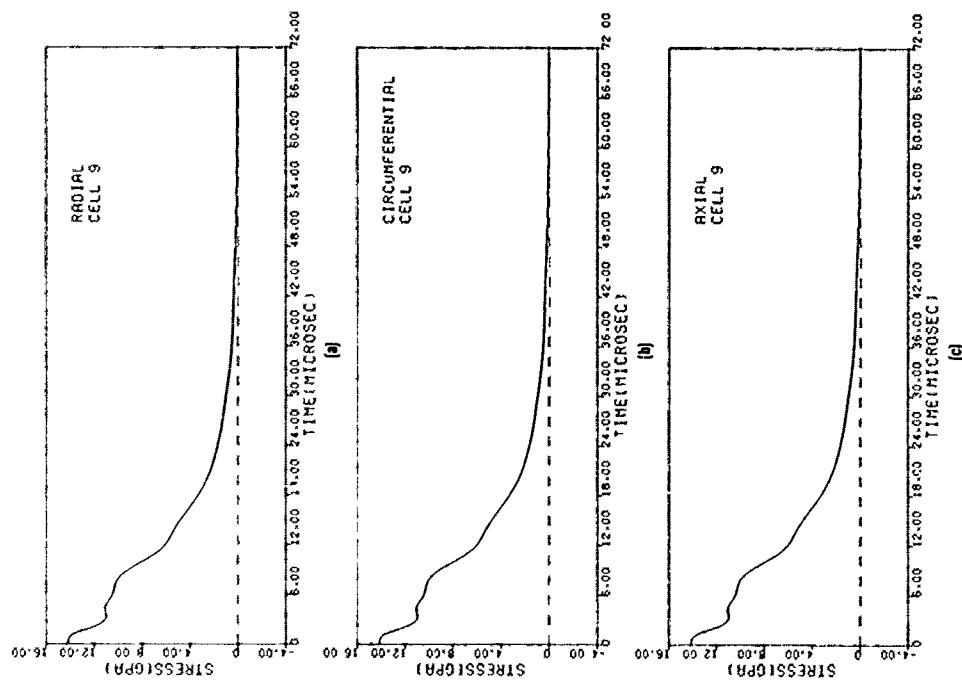


Figure P-9. Computed stress histories in cell 9 for the HF-1 steel, heat treatment B, cylinder experiments. (a) Radial, (b) circumferential, and (c) axial stresses.

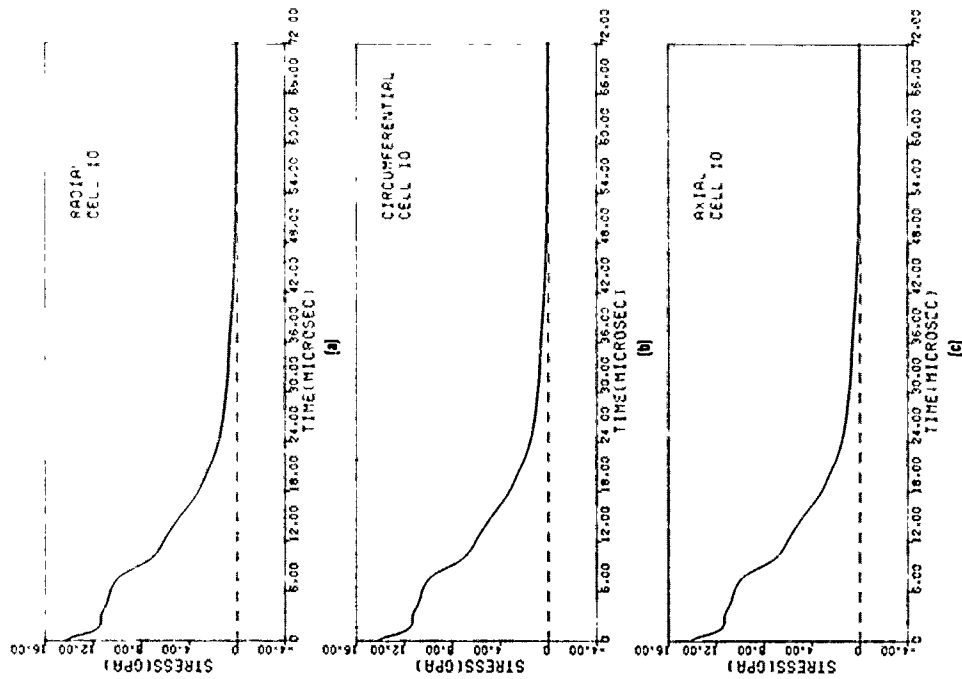


Figure P-10. Computed stress histories in cell 10 for the HF-1 steel, heat treatment B, cylinder experiments. (a) Radial, (b) circumferential, and (c) axial stresses.

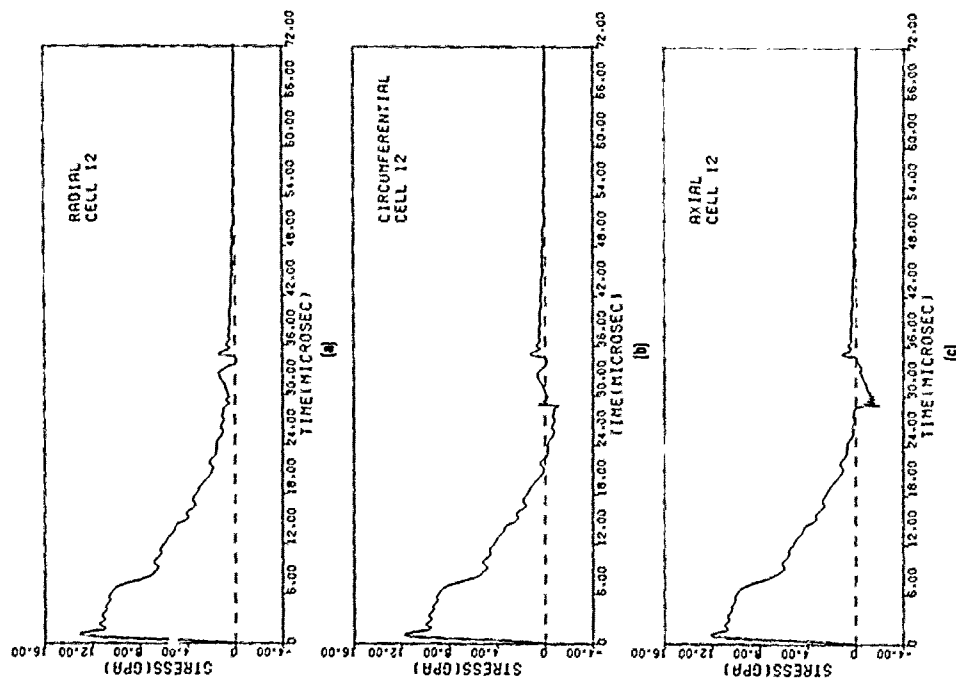


Figure P-11. Computed stress histories in cell 12 for the HF-1 steel, heat treatment B, cylinder experiments.
(a) Radial, (b) circumferential, and (c) axial stresses.

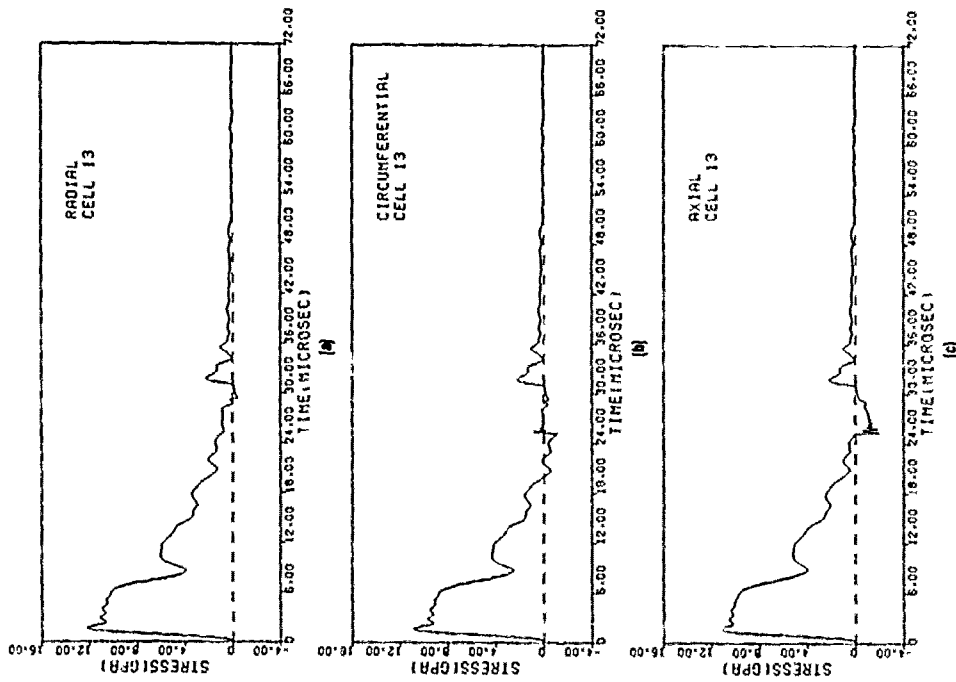


Figure P-12. Computed stress histories in cell 13 for the HF-1 steel, heat treatment B, cylinder experiments.
(a) Radial, (b) circumferential, and (c) axial stresses.

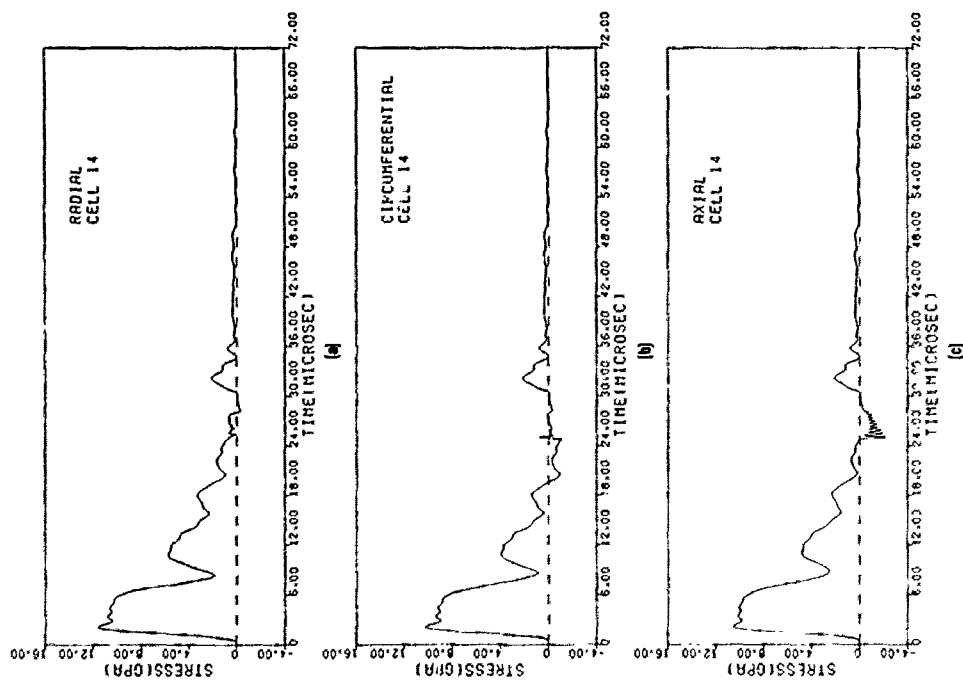


Figure P-13. Computed stress histories in cell 14 for the HF-1 steel, heat treatment B, cylinder experiments.
(a) Radial, (b) circumferential, and (c) axial stresses.

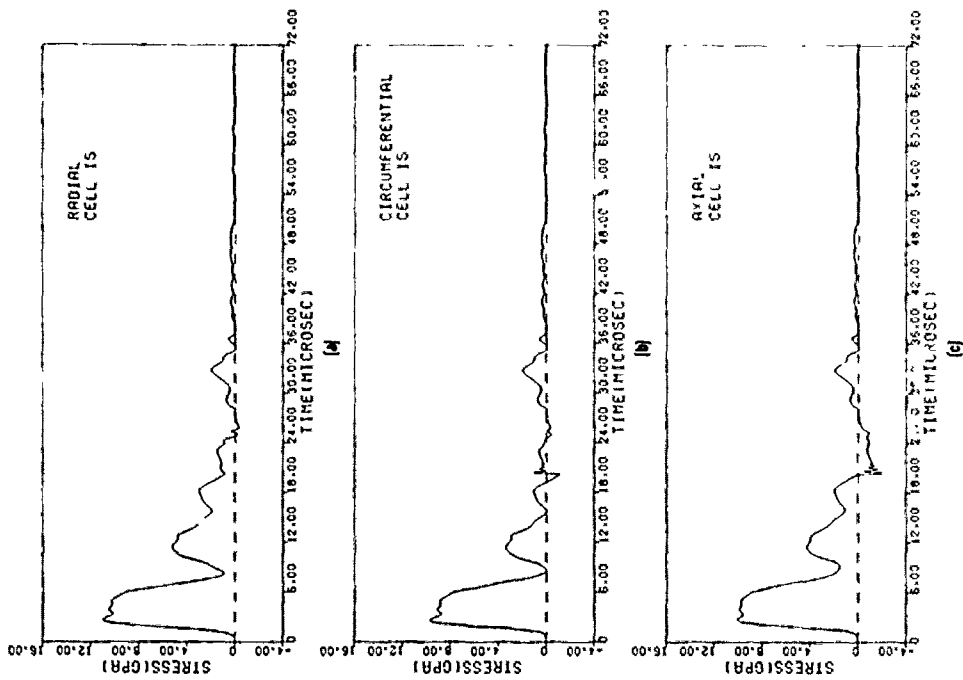


Figure P-14. Computed stress histories in cell 15 for the HF-1 steel, heat treatment B, cylinder experiments.
(a) Radial, (b) circumferential, and (c) axial stresses.

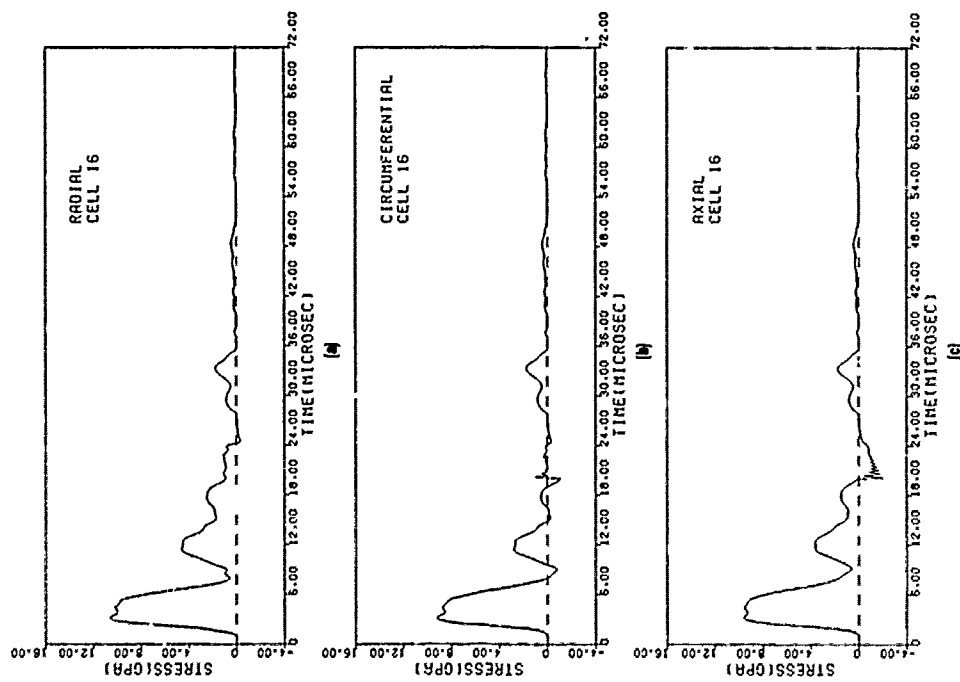


Figure P-15. Computed stress histories in cell 16 for the HF-1 steel, heat treatment B, cylinder experiments.
(a) Radial, (b) circumferential, and (c) axial stresses.

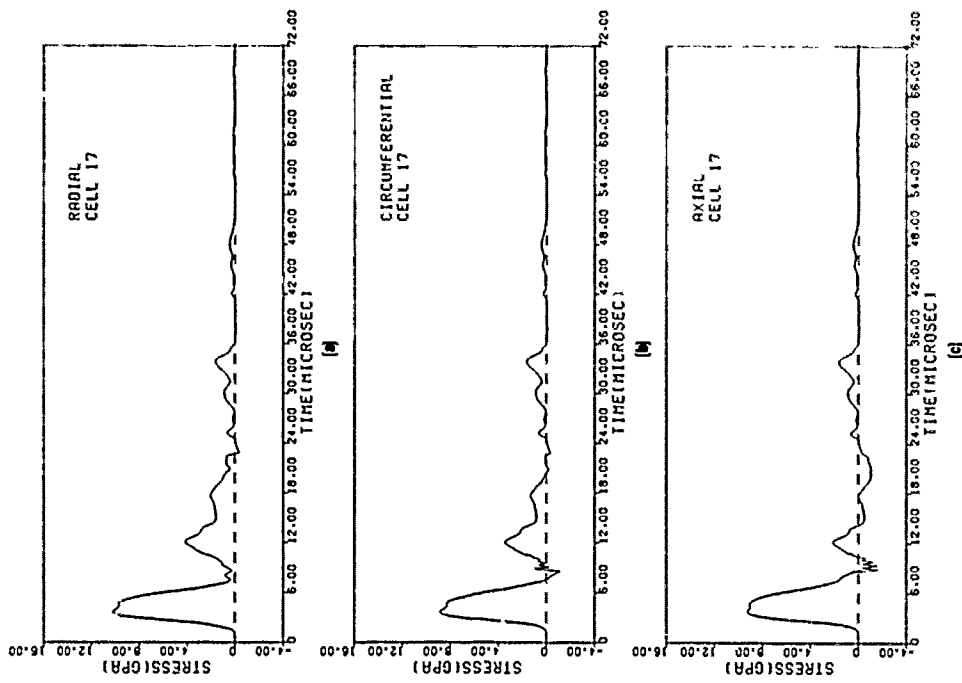


Figure P-16. Computed stress histories in cell 17 for the HF-1 steel, heat treatment B, cylinder experiments.
(a) Radial, (b) circumferential, and (c) axial stresses.

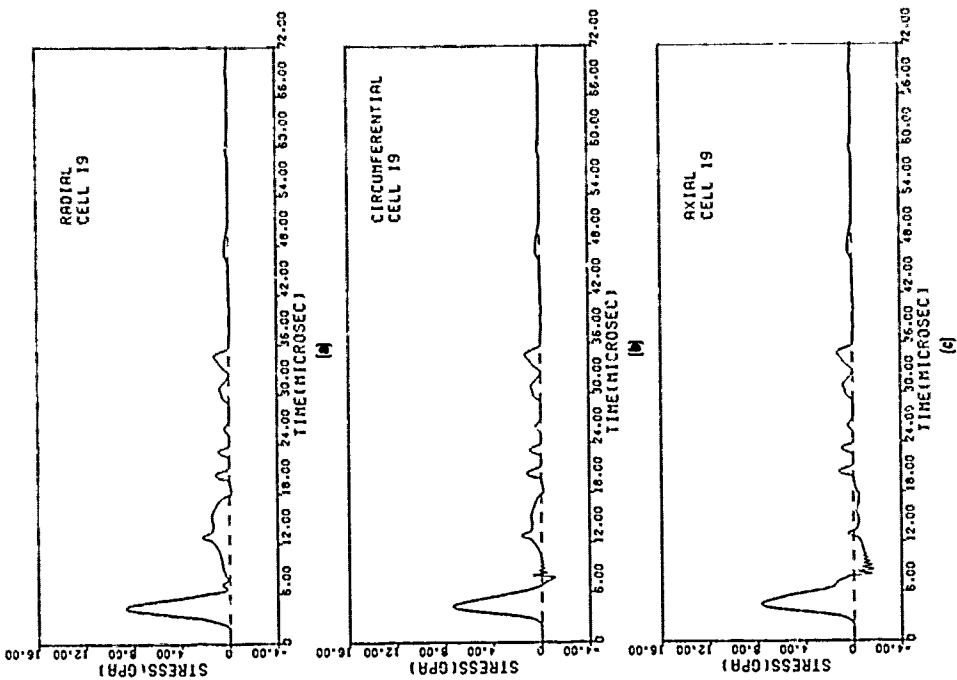


Figure P-17. Computed stress histories in cell 18 for the HF-1 steel, heat treatment B, cylinder experiments.
(a) Radial, (b) circumferential, and (c) axial stresses.

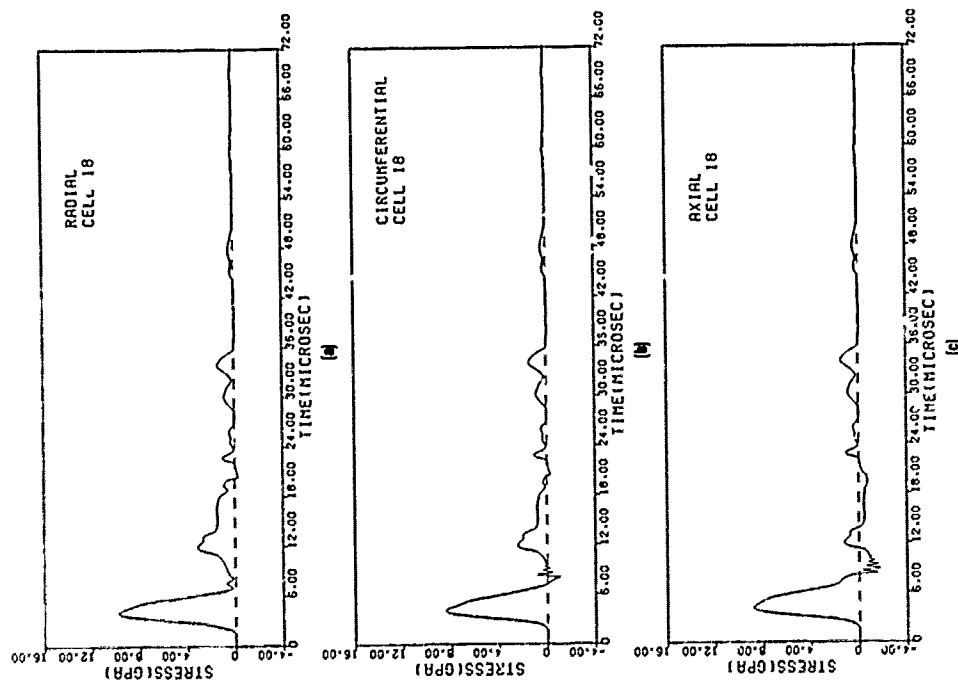


Figure P-18. Computed stress histories in cell 19 for the HF-1 steel, heat treatment B, cylinder experiments.
(a) Radial, (b) circumferential, and (c) axial stresses.

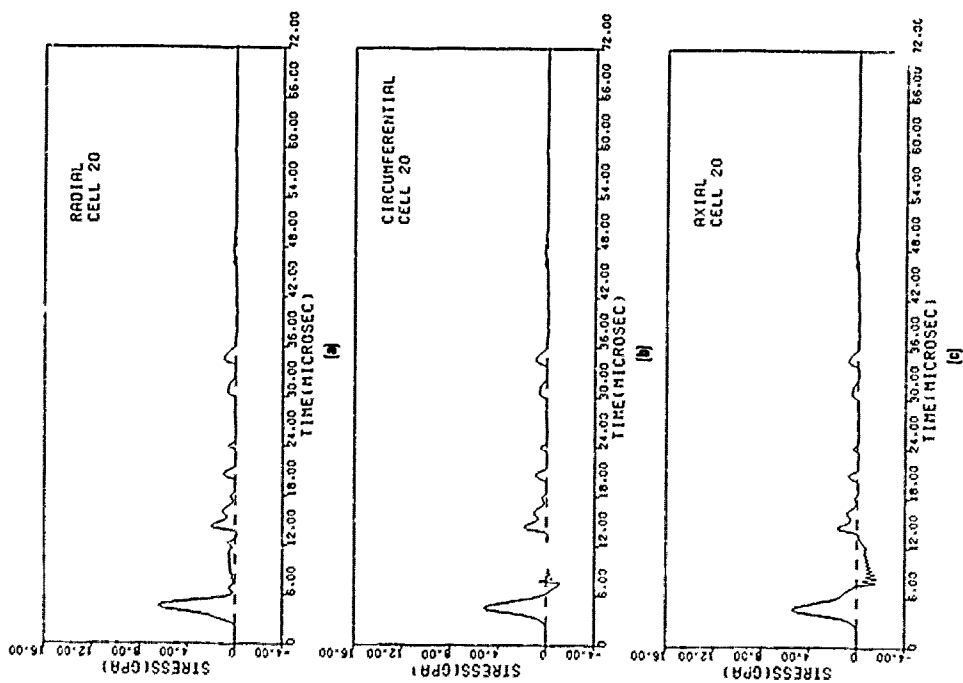


Figure P-19. Computed stress histories in cell 20 for the HF-1 steel, heat treatment B, cylinder experiments.
(a) Radial, (b) circumferential, and (c) axial stresses.

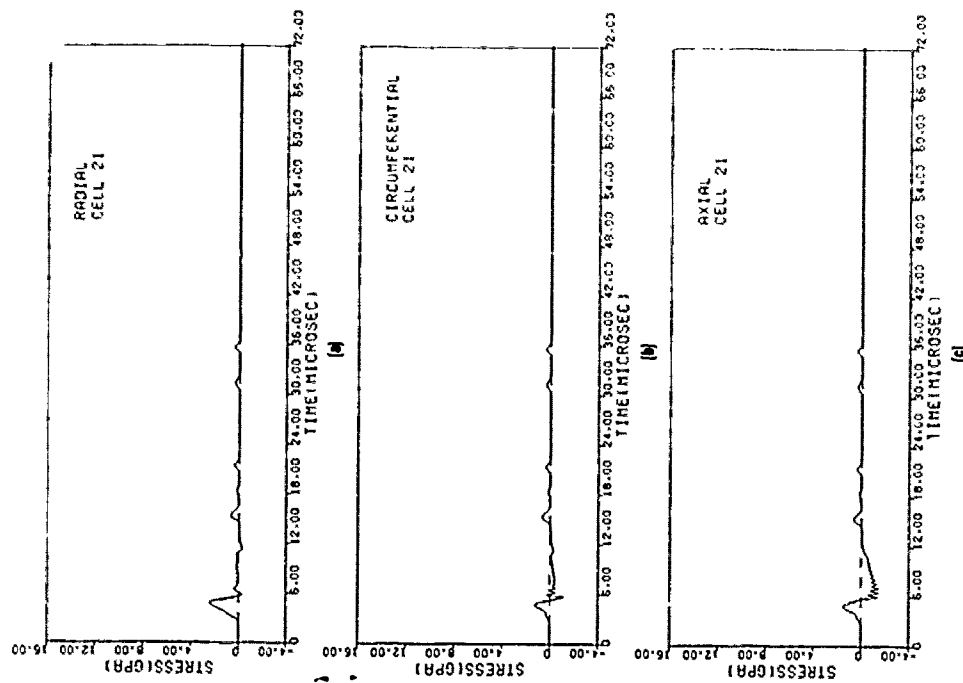


Figure P-20. Computed stress histories in cell 21 for the HF-1 steel, heat treatment B, cylinder experiments.
(a) Radial, (b) circumferential, and (c) axial stresses.

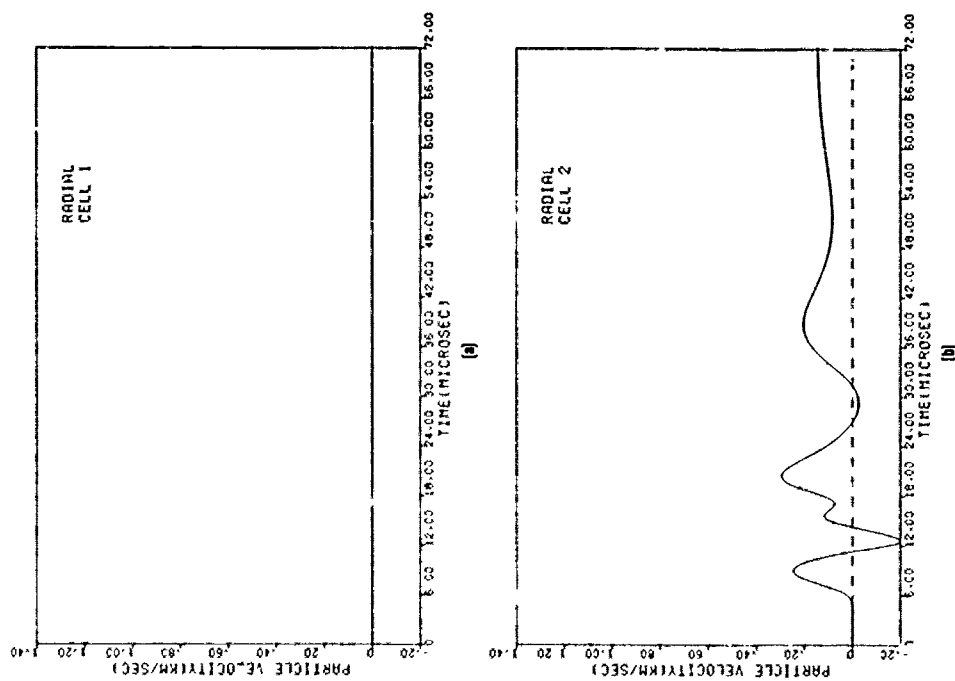


Figure P-21. Computed particle velocity histories in (a) cell 1 and (b) cell 2 for the HF-1 steel, heat treatment B, cylinder experiments.

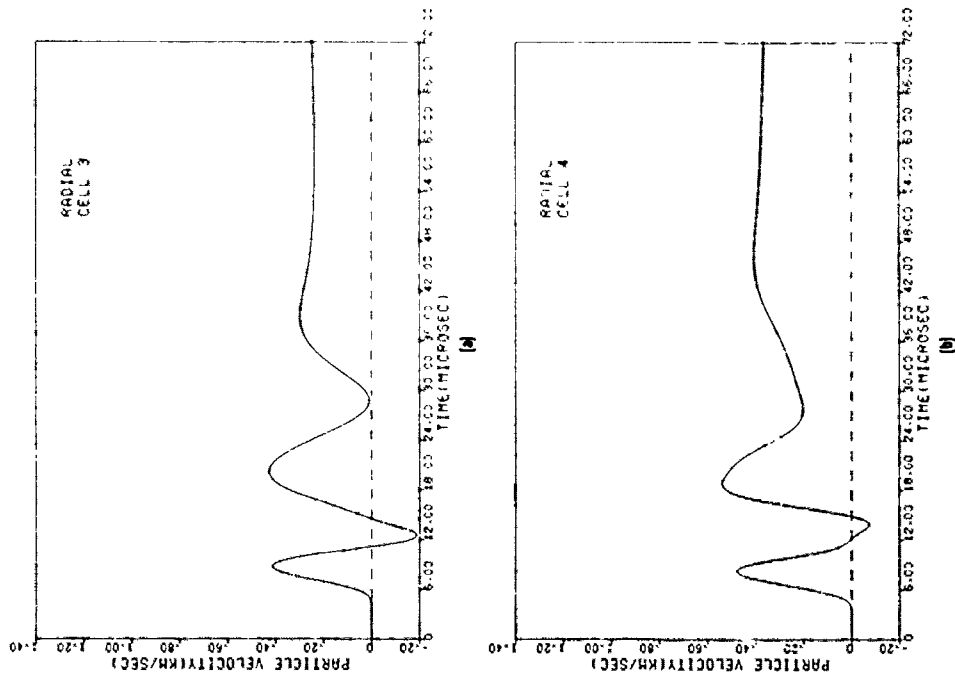


Figure P-22. Computed particle velocity histories in (a) cell 3 and (b) cell 4 for the HF-1 steel, heat treatment B, cylinder experiments.

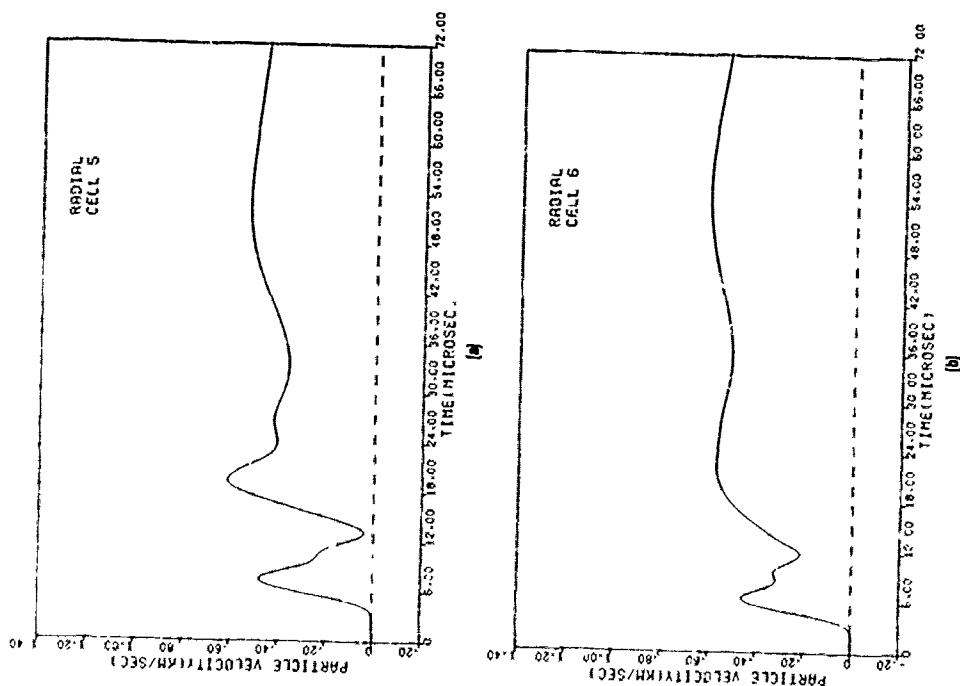


Figure P-23. Computed particle velocity histories in (a) cell 5 and (b) cell 6 for the HF-1 steel, heat treatment B, cylinder experiments.

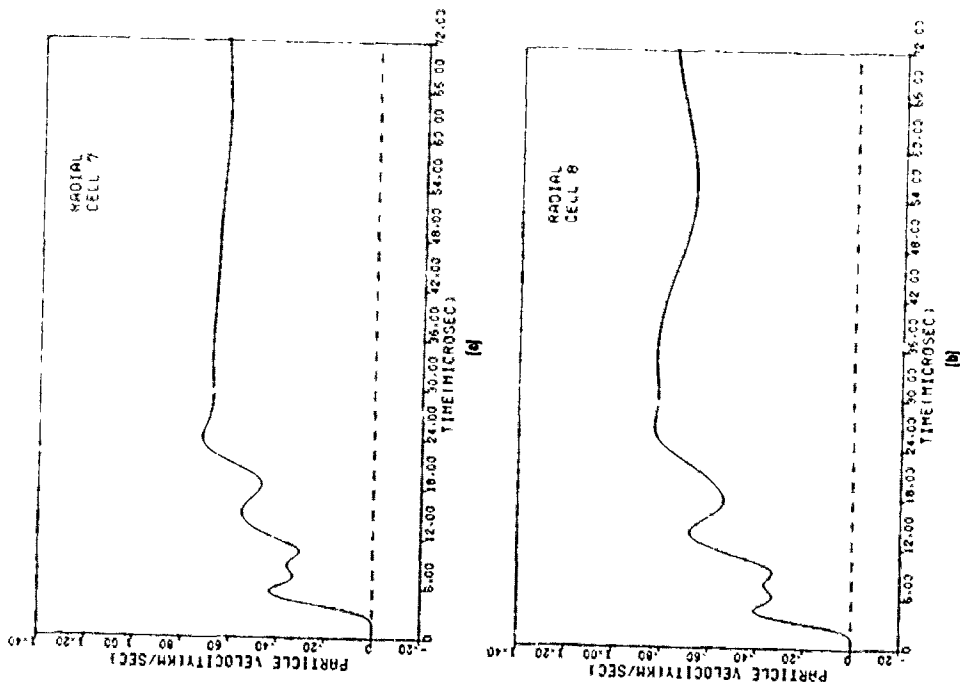


Figure P-24. Computed particle velocity histories in (a) cell 7 and (b) cell 8 for the HF-1 steel, heat treatment B, cylinder experiments.

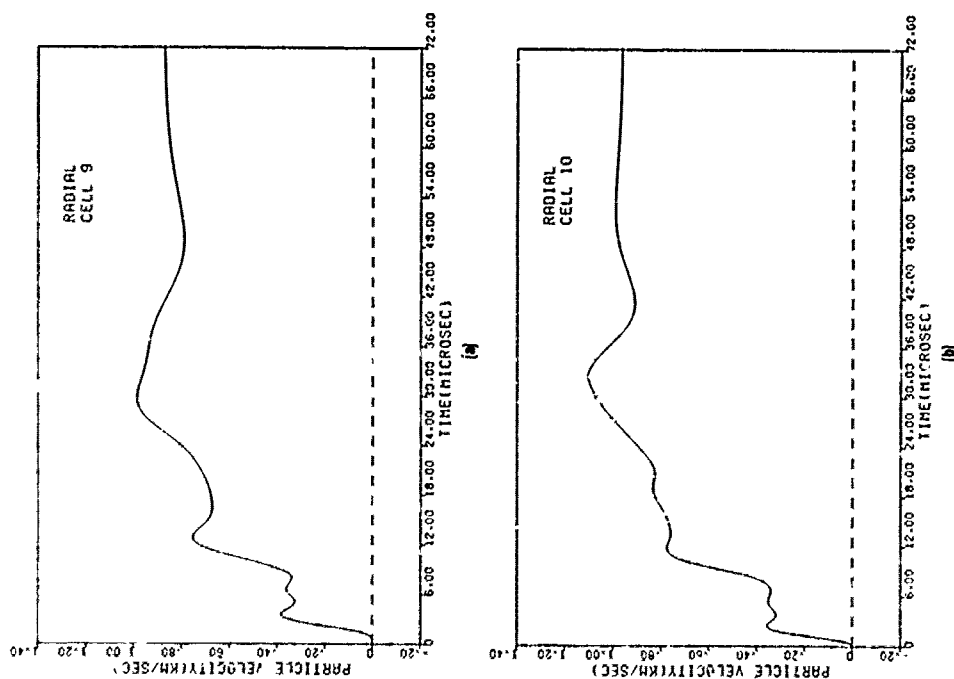


Figure P-25. Computed particle velocity histories in (a) cell 9 and (b) cell 10 for the HF-1 steel, heat treatment B, cylinder experiments.

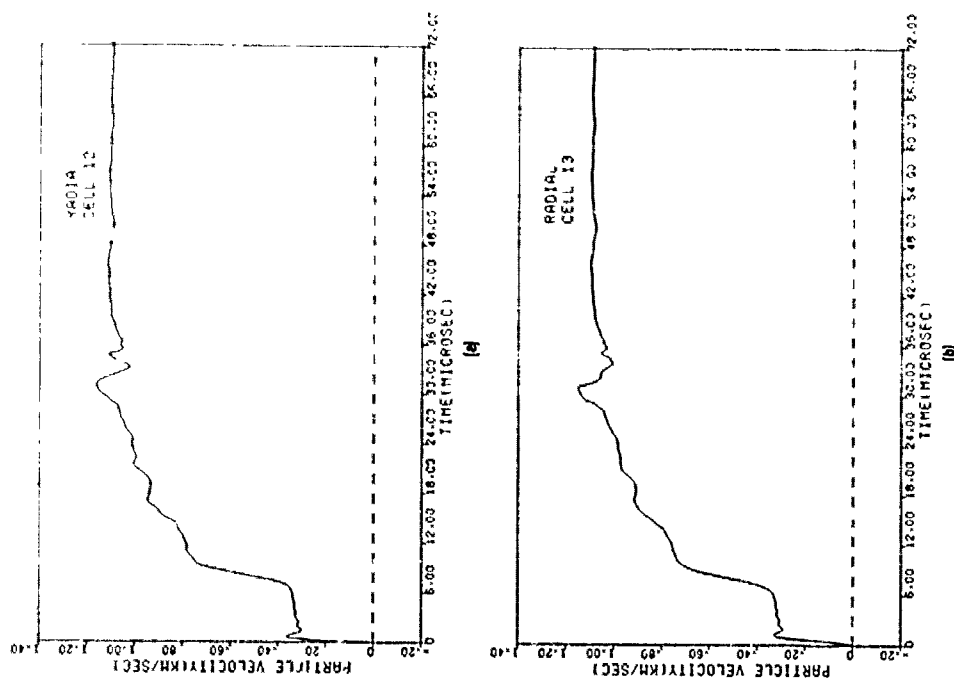


Figure P-26. Computed particle velocity histories in (a) cell 12 and (b) cell 13 for the HF-1 steel, heat treatment B, cylinder experiments.

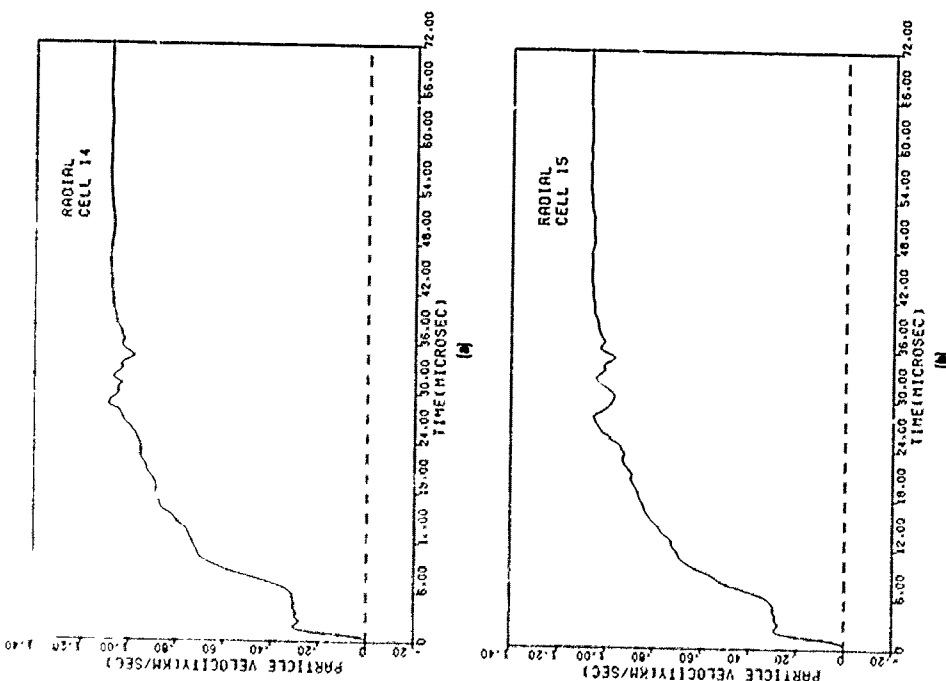


Figure P-27. Computed particle velocity histories in (a) cell 14 and (b) cell 15 for the HF-1 steel, heat treatment B, cylinder experiments.

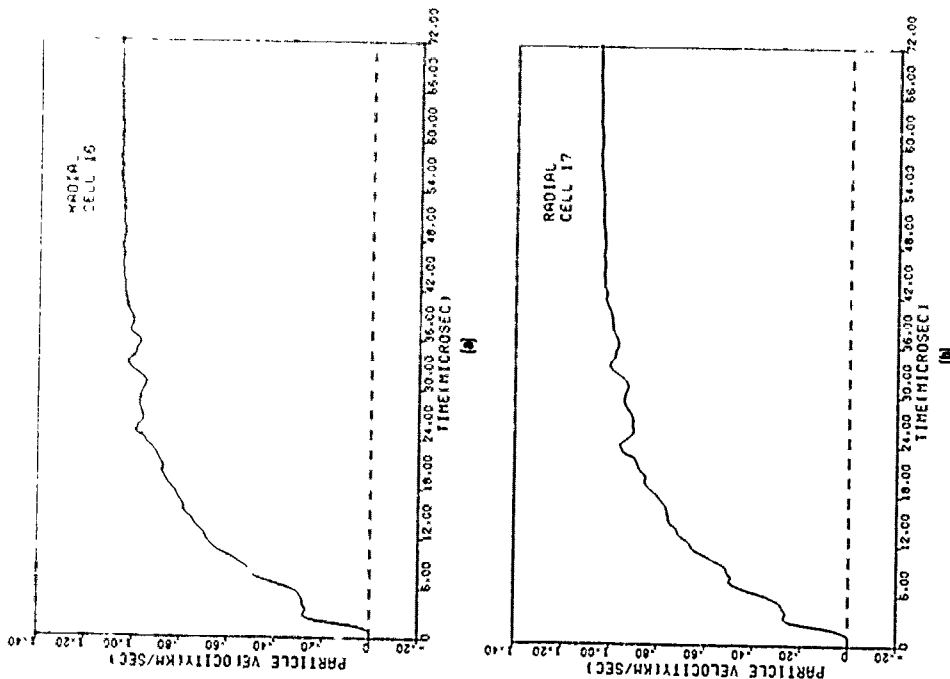


Figure P-28. Computed particle velocity histories in (a) cell 16 and (b) cell 17 for the HF-1 steel, heat treatment B, cylinder experiments.

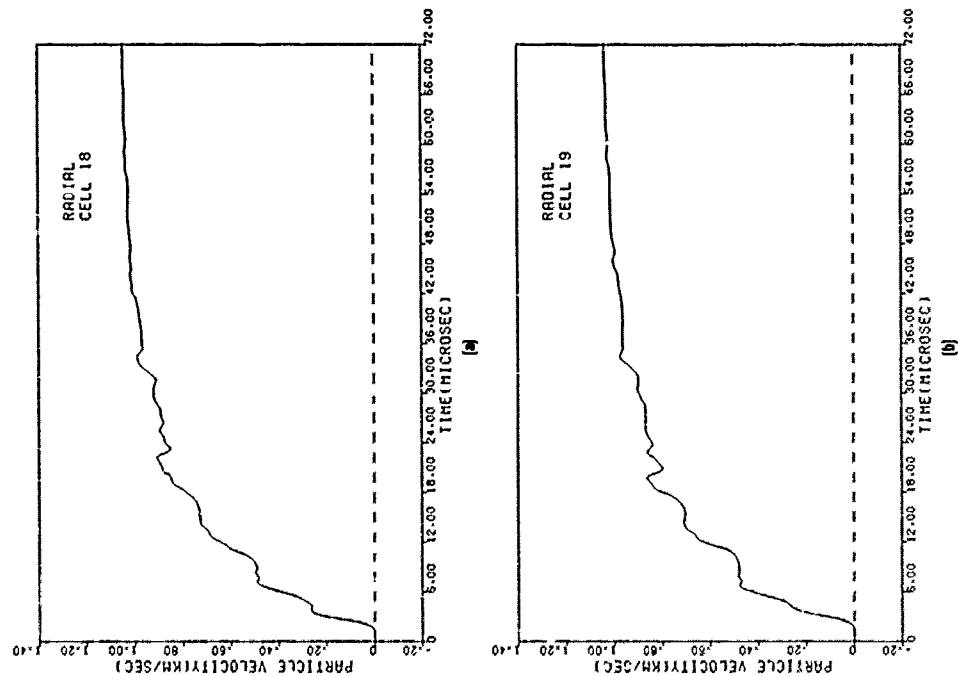


Figure P-29. Computed particle velocity histories in (a) cell 18 and (b) cell 19 for the HF-1 steel, heat treatment B, cylinder experiments.

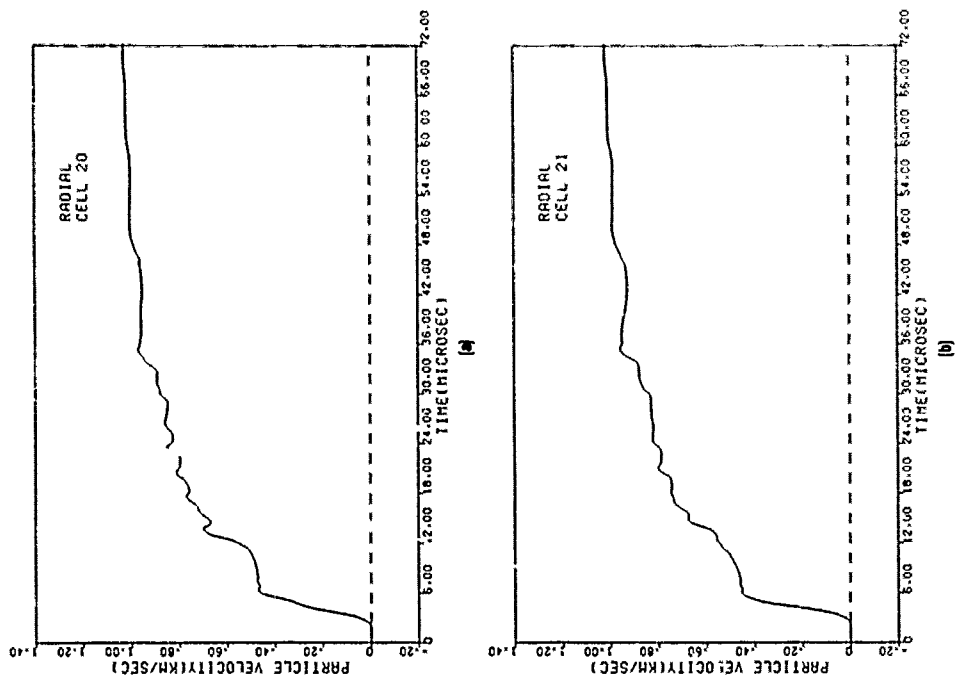


Figure P-30. Computed particle velocity histories in (a) cell 20 and (b) cell 21 for the HF-1 steel, heat treatment B, cylinder experiments.

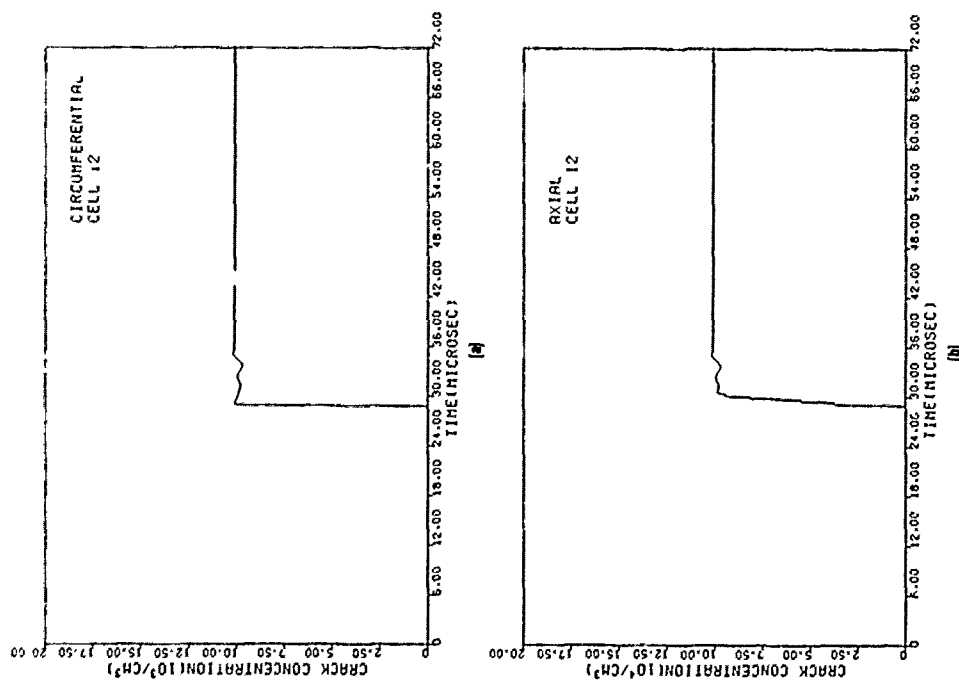


Figure P-31. Computed crack concentration histories in cell 12 for the HF-1 steel, heat treatment B, cylinder experiments. (a) Circumferential and (b) axial crack concentrations.

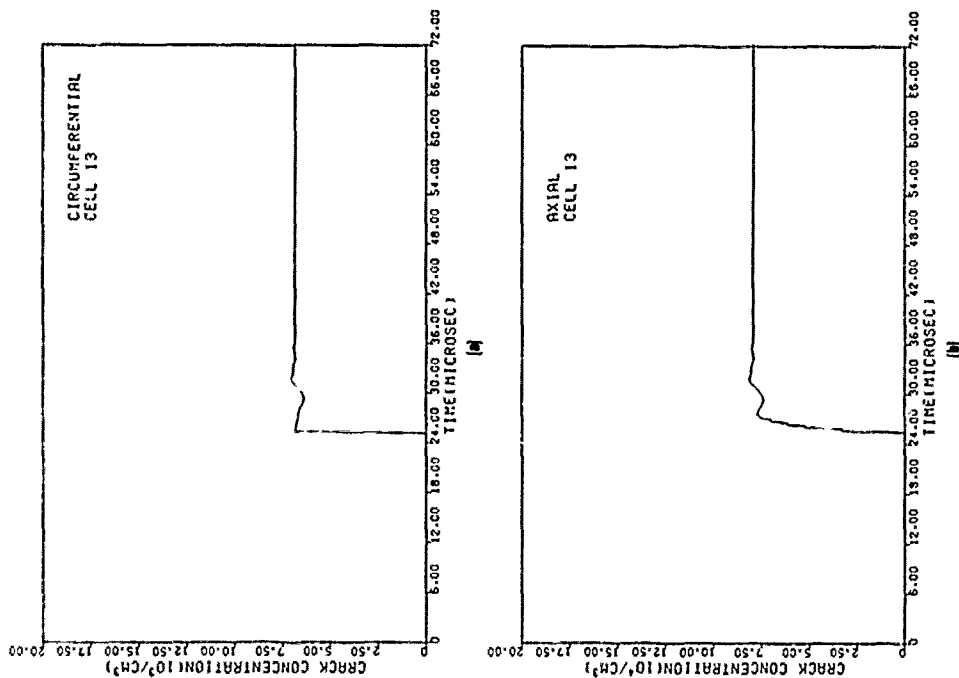


Figure P-32. Computed crack concentration histories in cell 13 for the HF-1 steel, heat treatment B, cylinder experiments. (a) Circumferential and (b) axial crack concentrations.

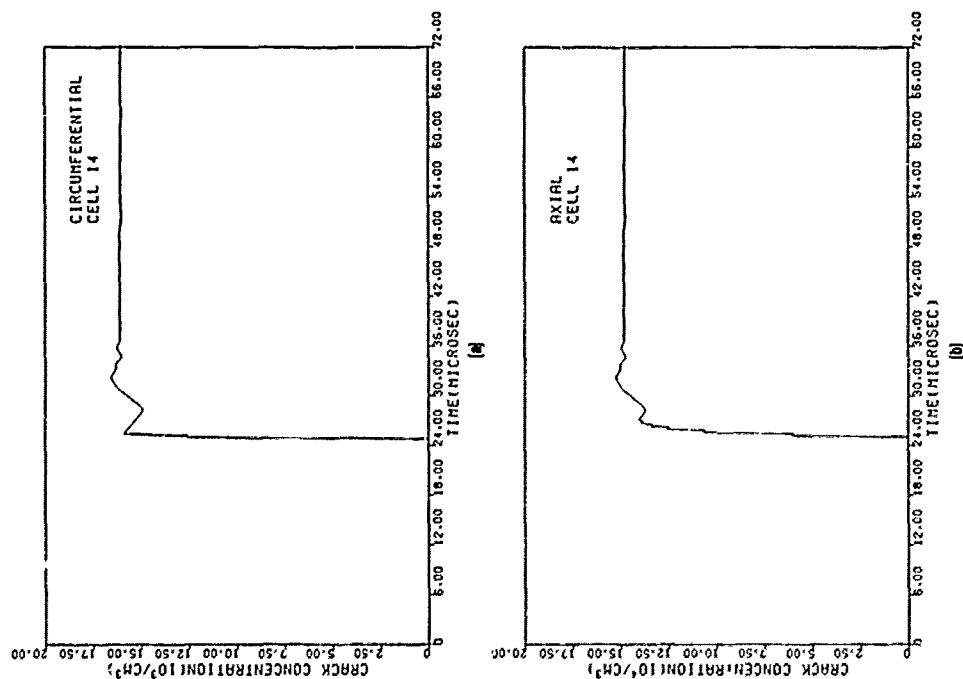


Figure P-33. Computed crack concentration histories in cell 14 for the HF-1 steel, heat treatment B, cylinder experiments. (a) Circumferential and (b) axial crack concentrations.

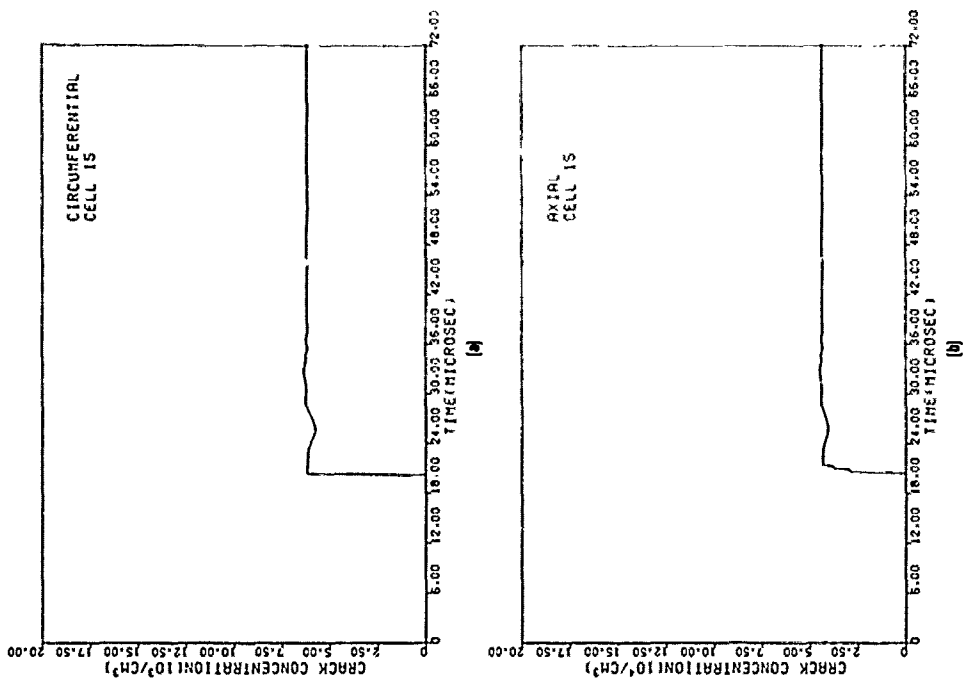


Figure P-34. Computed crack concentration histories in cell 15 for the HF-1 steel, heat treatment B, cylinder experiments. (a) Circumferential and (b) axial crack concentrations.

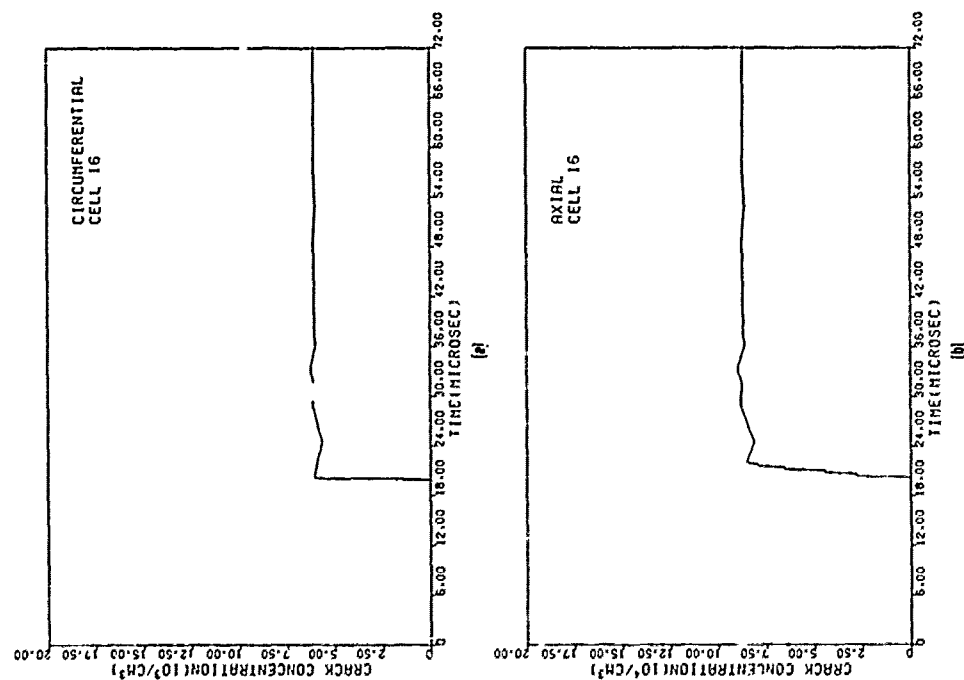


Figure P-35. Computed crack concentration histories in cell 16 for the HF-1 steel, heat treatment B, cylinder experiments. (a) Circumferential and (b) axial crack concentrations.

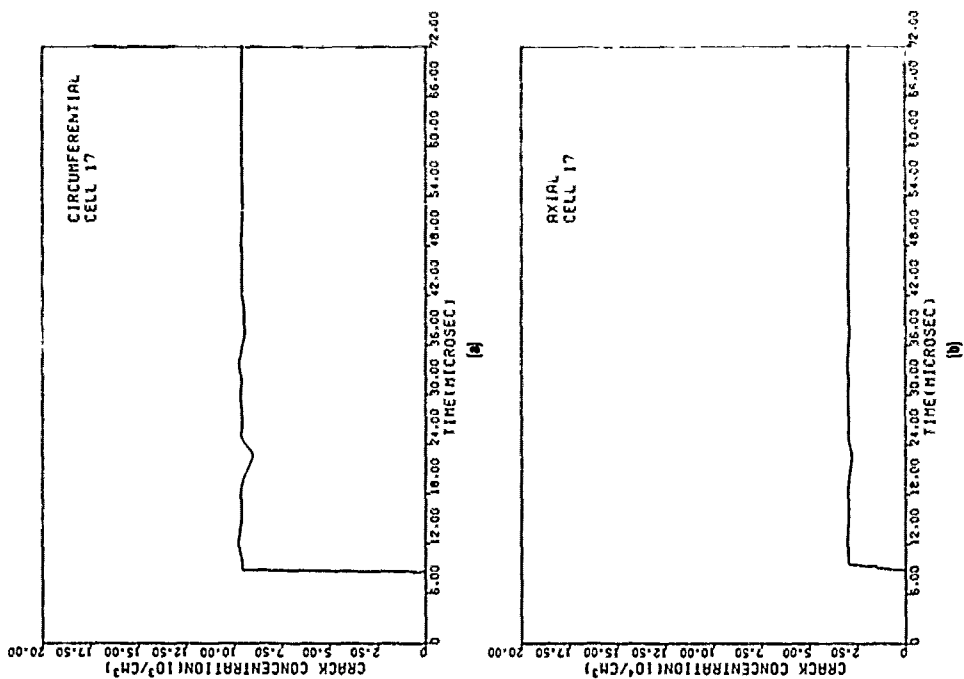


Figure P-36. Computed crack concentration histories in cell 17 for the HF-1 steel, heat treatment B, cylinder experiments. (a) Circumferential and (b) axial crack concentrations.

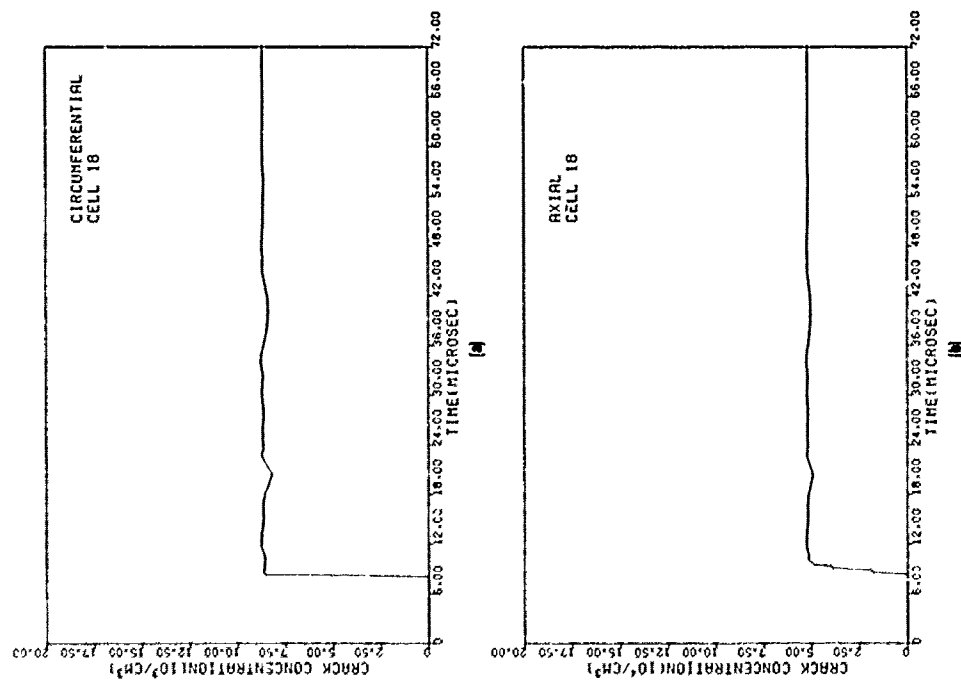


Figure P-37. Computed crack concentration histories in cell 18 for the HF-1 steel, heat treatment B, cylinder experiments. (a) Circumferential and (b) axial crack concentrations.

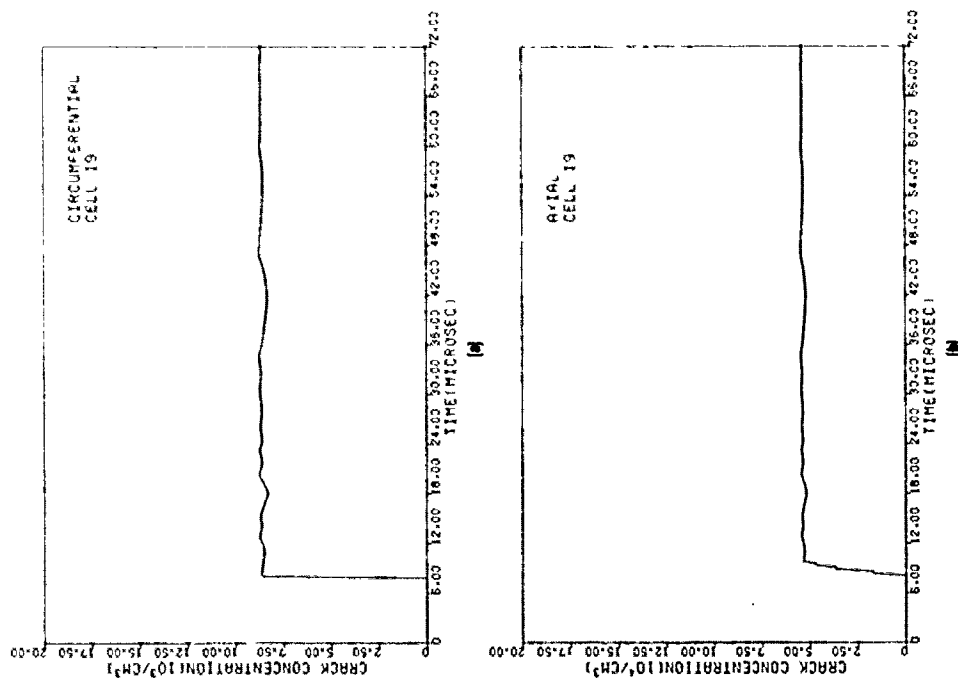


Figure P-38. Computed crack concentration histories in cell 19 for the HF-1 steel, heat treatment B, cylinder experiments. (a) Circumferential and (b) axial crack concentrations.

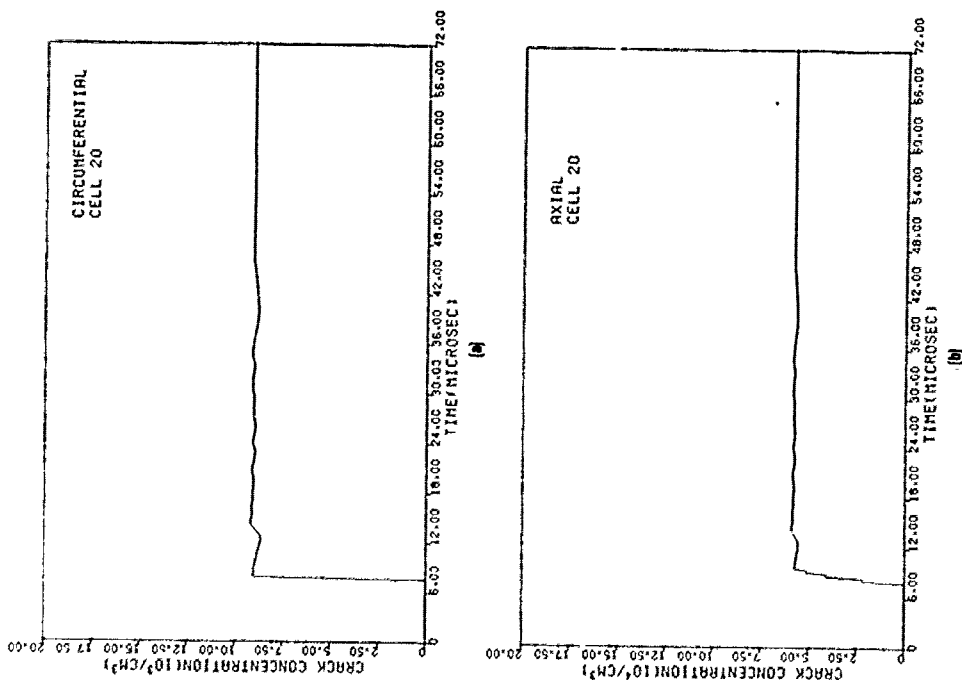


Figure P-39. Computed crack concentration histories in cell 20 for the HF-1 steel, heat treatment B, cylinder experiments. (a) Circumferential and (b) axial crack concentrations.

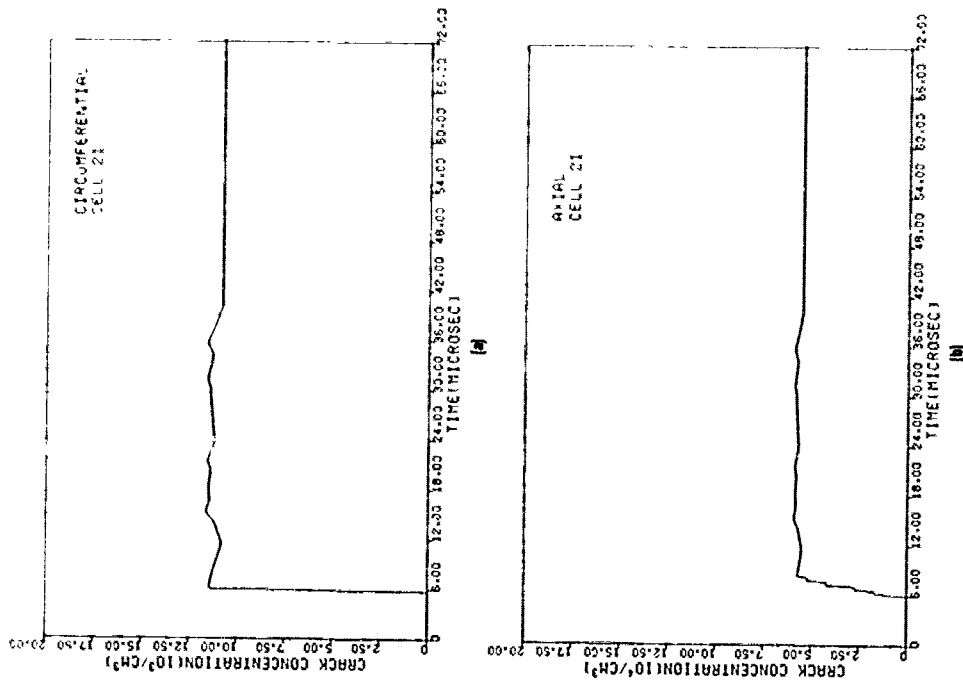


Figure P-40. Computed crack concentration histories in cell 21 for the HF-1 steel, heat treatment B, cylinder experiments. (a) Circumferential and (b) axial crack concentrations.

DISTRIBUTION

Commander
Naval Sea Systems Command
Washington, DC 20360
ATTN: SEA-003 (S. R. Marcus)
SEA-05R (G. N. Sorkin)
SEA-05R22 (S. J. Matesky)
SEA-62R (W. W. Blaine)
SEA-62R31 (R. A. Bailey)
SEA-62R32 (G. Edwards)
SEA-62R4 (M. A. Kinna)
SEA-62R41 (L. Pasiuk)
SEA-62R54 (B. Lubin)
SEA-62Y13C (L. H. Hawver)
SEA-62Z3 (J. Whelan)
SEA-62Z31E (M. E. Schoner)
PMS-400M (R. D. Cuddy)
PMS-400M3 (J. Lindberg)

Commander
Naval Air Systems Command
Washington, DC 20360
ATTN: AIR-310B (J. W. Willis)
AIR-320 (T. F. Kearns)
AIR-350 (H. B. Berfield)
AIR-5163 (C. Berscia)
AIR-5324 (S. Englander)

Office of Naval Technology
Department of the Navy
Boston Towers Bldg. No. 1
800 N. Quincy St.
Arlington, VA 22217

Office of Naval Research
Department of the Navy
Washington, DC 20360
ATTN: ONR-420 (T. G. Berlincourt)
ONR-465 (E. I. Salkovitz)

Office of Naval Research
536 S. Clark St.
Chicago, IL 60605
ATTN: George Sandoz

DISTRIBUTION (Continued)

Office of Naval Research
Bldg. 114 Section D
666 Summer St.
Boston, MA 02210
ATTN: L. H. Peebles, Jr.

Commander
Naval Research Laboratory
Washington, DC 20375
ATTN: 7908 (A. Williams)

Commander
Naval Weapons Center
China Lake, CA 93555
ATTN: M. D. Alexander

M. E. Backman
R. L. Ballenger
J. Pearson
H. D. Pieper
E. B. Royce
R. G. Sewell
L. H. Smith
T. R. Zulkoski

Director
Army Ballistic Research Laboratory
Aberdeen Proving Ground, MD 21005
ATTN: W. S. deRosset

W. Gillich
G. E. Hauver
G. Moss
R. Vitali

Commander
Army Materials and Mechanics Research Center
Watertown, MA 02172
ATTN: D. T. Dandekar
J. F. Mescall
M. Staker

DISTRIBUTION (Continued)

Commander
Army Research and Development Command
Dover, NJ 07801
ATTN: J. Beetle
F. J. Owens

Commander
Army Waterways Experiment Station
Vicksburg, MS 39180
ATTN: D. R. Coltharp

Los Alamos Scientific Laboratory
Los Alamos, NM 87544
ATTN: J. M. Holt, Jr.
J.N. Johnson
R. Morales
J. A. Morgan
Technical Library

(2)

Sandia Laboratories
Albuquerque, NM 87115
ATTN: Lee Davison
D. E. Grady
R. A. Graham
J. E. Kennedy
Technical Library

(2)

Lawrence Livermore Laboratory
University of California
Livermore, CA 94550
ATTN: S. Cochran
W. H. Gust
E. Nidick, Jr.
M. L. Wilkins

New Mexico Institute of Mining and Technology
Campus Station
Socorro, NM 87801
ATTN: P. D. Buckley
H. L. Giclas
M. L. Kempton

DISTRIBUTION (Continued)

SRI International
333 Ravenswood Avenue
Menlo Park, CA 94025
ATTN: D. Curran
 L. Seaman
 D. Shockey

Bendix Advanced Technology Center
9140 Old Annapolis Rd.
Columbia, MD 21045
ATTN: O. H. Griffin

Denver Research Institute
University of Denver
Denver, CO 80208
ATTN: R. F. Recht

Shock Dynamics Laboratory
Washington State University
Pullman, WA 99163
ATTN: G. E. Duvall
 G. R. Fowles

Defense Research Establishment Valcartier
Armaments Division
P. O. Box 880
Courcellette, Quebec GOA 1K0, Canada
ATTN: C. Briercliffe
 C. Lahaye

Royal Armament Research and Development Establishment
Fort Halstead, Sevenoaks
Kent TN 14 7TB, England
ATTN: R. H. Lynch

DISTRIBUTION (Continued)

Australian Defence Scientific Service
Materials Research Laboratories
Maribyrnong Victoria, Australia
ATTN: I. R. Lanborn
F. G. J. May
R. L. Woodward

Defense Technical Information Center
Cameron Station
Alexandria, VA 22314

(12)

Library of Congress
Washington, DC 20540
ATTN: Gift and Exchange Division

(4)

GIDEP Operations Office
Corona, CA 91720

Local

C
D
E1A
E41
F
F10
F12 (Berger)
G
G10
G102
G103
G13
G13 (Wasmund)
G13 (Hock)
G13 (Dickinson)
G20
G25
G25 (Bolt)
G25 (Elliott)

DISTRIBUTION (Continued)

G25 (Hales)
G25 (D. Smith)
G25 (T. Smith)
G30
G301
G302
G31
G32
G33
G34
G35
G35 (Adams)
G35 (Mock)
G35 (Holt)
G35 (Peterson)
G35 (Wishard)
G35 (Waggener)
G40
G50
G60
K21
K21 (Blackmon)
R
R04
R10
R12
R12 (Erkman)
R12 (Lutzky)
R13
R13 (Coleburn)
R13 (Forbes)
R13 (Roslund)
R13 (Short)
R30
R32
R32 (Crowe)
X210